

AD-A243 563



DTIC
ELECTE
DEC 27 1991
S C D

KALMAN FILTER TRACKING OF A REFLECTIVE
TARGET USING FOWARD LOOKING INFRARED
AND DOPPLER RETURN MEASUREMENTS

THESIS

Theodore D. Herrera
Captain, USAF

AFIT/GE/ENG/91D-25

Best Available Copy

91-19050



91 12 24 083

REPORT DOCUMENTATION PAGE

Form Approved
OMB No. 0704-0188

This report documents the collection of information estimated to take a total of four hours response, including the time for reviewing published information, searching for information, preparing the report, and completing and reviewing the collection of information. Send comments on this collection of information, including suggestions for reducing the burden, to Washington Headquarters Services, Directorate for Information Operations and Reports, 1215 Jefferson Davis Highway, Suite 1204, Arlington, VA 22202-4302, and to the Office of Management and Budget, Paperwork Project (0704-0188), Washington, DC 20503.

1. AGENCY USE ONLY (leave blank)	2. REPORT DATE December 1991	3. REPORT TYPE AND DATES COVERED Master's Thesis
4. TITLE AND SUBTITLE Kalman Filter Tracking of a Reflective Target Using Forward-Looking Infrared and Doppler Return Measurements		5. FUNDING NUMBERS
6. AUTHOR(S) Theodore D. Herrera Captain, USAF		
7. PERFORMING ORGANIZATION NAME(S) AND ADDRESS(ES) Air Force Institute of Technology WPAFB OH 45433-6583		8. PERFORMING ORGANIZATION REPORT NUMBER AFIT/GE/ENG/91D-25
9. SPONSORING/MONITORING AGENCY NAME(S) AND ADDRESS(ES) Capt Joseph Bergin Phillips Laboratory/LITT Kirtland AFB, NM 87117		10. SPONSORING/MONITORING AGENCY REPORT NUMBER
11. SUPPLEMENTARY NOTES		
12a. DISTRIBUTION STATEMENT Approved for Public Release; Distribution Unlimited.		12b. DISTRIBUTION CODE

13. ABSTRACT (Maximum 200 words)

Plume phenomenology experiments conducted in 1990 uncovered the existence of plume speckle reflectance emanating from the exhaust of a solid-propellant rocket motor due to the presence of metallic particulates in the plume. This impeded attempts, that are dependent upon the speckle return of an actively illuminated target hardbody, to discern the plume/hardbody interface. This thesis investigates the feasibility of employing the Doppler return phenomenon in discerning the plume/hardbody interface and locating the hardbody center-of-mass. The potential of the Doppler phenomenon's utilization lies in the fact that the Doppler return frequency spectra of the plume and the hardbody respectively possess distinct properties and are differentiable from each other. Hence, these differences can be exploited in the attempt to discern the plume/hardbody interface. For this study, two center-of-mass Kalman filters are developed to receive the Doppler return measurements: a one-state filter and two-state Modified Maximum a Posteriori Multiple Model Adaptive filter. A sensitivity analysis is conducted wherein the performances of the one-state filter and two-state filter are evaluated with variations in transmitted wavelength, signal-to-noise (SNR), and probability-of-miss. Results show the center-of-mass filters are sensitive to increases in probability-of-miss, whereas decreases in SNR produced insignificant degradation in performance. The two-state Modified MAP MMAF achieved the best performance, and clearly has the potential to accomplish the task of locating and tracking the hardbody center-of-mass.

Best Available Copy

Kalman Filter, Tracking, Plume, Infrared, Doppler

451

GENERAL INSTRUCTIONS FOR COMPLETING SF 298

The Report Documentation Page (RDP) is used in announcing and cataloging reports. It is important that this information be consistent with the rest of the report, particularly the cover and title page. Instructions for filling in each block of the form follow. It is important to stay within the lines to meet optical scanning requirements.

Block 1. Agency Use Only (Leave blank).

Block 2. Report Date. Full publication date including day, month, and year, if available (e.g. 1 Jan 88). Must cite at least the year.

Block 3. Type of Report and Dates Covered. State whether report is interim, final, etc. If applicable, enter inclusive report dates (e.g. 1 Jun 87 - 30 Jun 88).

Block 4. Title and Subtitle. A title is taken from the part of the report that provides the most meaningful and complete information. When a report is prepared in more than one volume, repeat the primary title, add volume number, and include subtitle for the specific volume. On classified documents enter the title classification in parentheses.

Block 5. Funding Numbers. To include contract and grant numbers; may include program element number(s), project number(s), task number(s), and work unit number(s). Use the following labels:

C - Contract	PR - Project
G - Grant	TA - Task
PE - Program Element	WU - Work Unit Accession No.

Block 6. Author(s). Name(s) of person(s) responsible for writing the report, performing the research, or credited with the content of the report. If editor or compiler, this should follow the name(s)

Block 7. Performing Organization Name(s) and Address(es) Self-explanatory

Block 8. Performing Organization Report Number. Enter the unique alphanumeric report number(s) assigned by the organization performing the work

Block 9. Sponsoring/Monitoring Agency Name(s) and Address(es) Self-explanatory

Block 10. Sponsoring/Monitoring Agency Report Number (If known)

Block 11. Supplementary Notes. Enter information that is not included elsewhere on the form. This information may include information that is not available in the report, information that is not available in the report, information that is not available in the report, information that is not available in the report.

Block 12a. Distribution/Availability Statement. Denotes public availability or limitations. Cite any availability to the public. Enter additional limitations or special markings in all capitals (e.g. NOFORN, REL, ITAR).

DOD - See DoDD 5230.24, "Distribution Statements on Technical Documents."

DOE - See authorities.

NASA - See Handbook NHB 2200.2.

NTIS - Leave blank.

Block 12b. Distribution Code.

DOD - Leave blank.

DOE - Enter DOE distribution categories from the Standard Distribution for Unclassified Scientific and Technical Reports.

NASA - Leave blank.

NTIS - Leave blank.

Block 13. Abstract. Include a brief (Maximum 200 words) factual summary of the most significant information contained in the report.

Block 14. Subject Terms. Keywords or phrases identifying major subjects in the report.

Block 15. Number of Pages. Enter the total number of pages.

Block 16. Price Code. Enter appropriate price code (NTIS only).

Blocks 17. - 19. Security Classifications. Self-explanatory. Enter U.S. Security Classification in accordance with U.S. Security Regulations (i.e., UNCLASSIFIED). If form contains classified information, stamp classification on the top and bottom of the page

Block 20. Limitation of Abstract. This block must be completed to assign a limitation to the abstract. Enter either UL (unlimited) or SAR (same as report). An entry in this block is necessary if the abstract is to be limited. If blank, the abstract is assumed to be unlimited.

Best Available Copy

KALMAN FILTER TRACKING OF A
REFLECTIVE TARGET USING FORWARD
LOOKING INFRARED MEASUREMENTS
AND DOPPLER RETURNS

THESIS

Presented to the Faculty of the School of Engineering
of the Air Force Institute of Technology

Air University

In Partial Fulfillment of the
Requirements for the Degree of
Master of Science in Electrical Engineering

Theodore D. Herrera, B.S.E., M.B.M.

Captain, USAF

Accession For	
DTIC GRAFI	<input checked="" type="checkbox"/>
DTIC TAB	<input type="checkbox"/>
Unannounced	<input type="checkbox"/>
Justification	
By	
Distribution/	
Availability Codes	
Dist	Avail and/or Special
A-1	



Approved for public release; distribution unlimited

Acknowledgement

This thesis, sponsored by the Phillips Laboratory, at Kirtland AFB, New Mexico, investigates the feasibility of using the Doppler return phenomenon to locate and track the center-of-mass of a missile hardbody. This endeavor epitomizes the challenges, labor, and rewards of my 18 months at AFIT. Throughout the course of this study, I had the fortune to be advised by Dr. Peter Maybeck, who not only provided the much-needed guidance and motivation, but also shared with me his balanced perspective on engineering and the priorities of the family.

This accomplishment is shared with my family, who have been, and still are, a constant source of happiness. I thank my talented and gifted children, Luerne and Kristian, for their understanding why there were times I couldn't be there for them. With this work behind me, I hope to make up for the lost times. My deepest gratitude goes to my friend-in-life, Cynthia, who has always been with me during the good and not-so-good times, and who put up with the male prima donna in the family.

Finally, this work is dedicated to my father, Donato, who remains in the islands and had to endure the earthquake and Mt. Pinatubo.

Ted Herrera

Table of Contents

Acknowledgement	ii
List of Figures	ix
List of Tables	xxiv
Abstract	xxv
I. Introduction	1-1
1.1 Background	1-2
1.2 Summary of Previous AFIT Research	1-4
1.3 Thesis Objectives	1-21
1.3.1 Doppler Phenomenon Modeling	1-22
1.3.2 Alternative Scan Techniques	1-23
1.3.3 Performance Evaluation	1-24
1.4 Thesis Overview	1-25
II. The Kalman Filter Algorithm	2-1
2.1 Introduction	2-1
2.2 Linear Kalman Filter	2-3
2.3 Multiple Model Adaptive algorithm	2-7
2.4 Summary	2-11
III. Simulation Space	3-1
3.1 Introduction	3-1
3.2 Coordinate Frames	3-1
3.2.1 Inertial Reference Frame	3-1

3.2.2	Target Plume Reference Frame	3-2
3.2.3	$\alpha - \beta - r$ Reference Frame	3-3
3.2.3.1	$\alpha - \beta$ (FLIR Image) Plane	3-3
3.2.3.2	Absolute α - β - r Reference Frame	3-4
3.2.3.3	Trans-FLIR Plane	3-4
3.2.3.4	ALT/ACT Plane	3-4
3.3	FLIR Image Plane	3-5
3.3.1	FLIR Field-Of-View	3-6
3.3.2	Target Models on the FLIR Plane	3-6
3.3.2.1	Target Plume Model on the FLIR Plane	3-7
3.3.2.2	Target Plume Projection onto the FLIR Plane	3-9
3.3.2.3	Target Plume Velocity Projection onto the FLIR Plane	3-12
3.4	FLIR Sensor Pointing Controller	3-15
3.5	Summary	3-15
IV.	Truth Model	4-1
4.1	Introduction	4-1
4.2	Dynamics Model	4-3
4.2.1	Target Model State Description	4-7
4.2.2	Atmospheric Jitter Model	4-11
4.2.3	Bending/Vibration Model	4-14
4.2.4	Plume Pogo Model	4-17
4.3	Measurement Models	4-20
4.3.1	FLIR Model	4-22
4.3.2	Low-Energy Laser Speckle Reflection Model	4-26

4.3.2.1	The Hardbody Reflectivity Model	4-27
4.3.2.2	Plume Reflectance Model	4-34
4.3.3	The Doppler Measurement Model	4-37
4.3.3.1	The Doppler Effect	4-38
4.3.3.2	Hardbody Doppler Return	4-42
4.3.3.3	Plume Doppler Return	4-43
4.3.3.4	Doppler Measurement Noises	4-46
4.4	Truth Model Parameters	4-50
4.4.1	Target Trajectory Initial Conditions	4-50
4.4.2	Target Model, Dimensions, and Orientation	4-50
4.4.3	Intensity Functions	4-51
4.4.4	Atmospheric Jitter	4-51
4.4.5	Bending/Vibration	4-51
4.4.6	Plume Pogo Characteristics	4-51
4.4.7	Spatially Correlated Background Noise	4-51
4.4.8	Low-Energy Laser Speckle Return Measurement Dimensions	4-52
4.4.9	Plume Reflectance Model	4-52
4.4.10	Low-Energy Doppler Return Measurement Dimensions	4-52
4.4.11	Hardbody Reflectivity Measurement Model	4-52
4.5	Summary	4-53
V.	Filter Models	5-1
5.1	Introduction	5-1
5.2	Six-State FLIR Filter	5-2
5.2.1	Dynamics Model	5-2

5.3.3.5	Two-State Modified MAP MMAF: Initial Conditions	5-34
5.3.3.6	Two-State Modified MAP MMAF: Tuning Values	5-35
5.4	Summary	5-36
VI.	Procedures and Results	6-1
6.1	Introduction	6-1
6.2	One-State Filter with Speckle Return Measurements	6-3
6.3	One-State Filter with Doppler Return Measurements	6-4
6.4	Two-State Modified MAP MMAF	6-12
6.4.1	Case 1: The Loss of Both Returns	6-13
6.4.2	Case 2: Continuously Available Speckle Returns	6-17
6.5	Comparison of the One-state Filter and the Two-State Modified MAP MMAF	6-20
6.6	Summary	6-23
VII.	Conclusions and Recommendations	7-1
7.1	Introduction	7-1
7.2	Conclusions	7-1
7.2.1	One-State Filter with Doppler Return Measurements	7-3
7.2.2	Two-State Modified MAP MMAF	7-4
7.2.2.1	Case 1: The Loss of Both Returns	7-4
7.2.2.2	Case 2: Continuous Speckle Returns	7-5
7.2.3	Filter Comparison	7-6
7.3	Recommendations	7-7
7.3.1	Increased Number of Monte Carlo Runs	7-7
7.3.2	Plume/Hardbody Interface Doppler Return	7-7
7.3.3	Consolidation of Cases 1 and 2 of the Two-State Modified MAP MMAF	7-8

7.3.4	Alternative Low-Energy Scan Techniques	7-8
7.3.5	Oscillation of the Plume's Speckle Reflectance	7-8
7.3.6	Plume/Hardbody Interface Speckle Return	7-9
7.3.7	Bayesian Approach to the Plume Speckle Reflectance and MMAF	7-9
Appendix A	Data Processing Statistics Method	A-1
Appendix B	Examples of Performance Plots	B-1
Appendix C	One-State Center-of-Mass Filter with Doppler Return Measurements	C-1
Appendix D	Two-State Modified MAP MMAF Tuning Runs	D-1
Appendix E	Two-State Modified MAP MMAF: Case 1	E-1
Appendix F	Two-State Modified MAP MMAF: Case 2	F-1
Appendix G	RMS Error Plots: One-State Doppler Filter and Two-State Modified MAP MMAF	G-1
Appendix H	Tables	H-1
Bibliography		Bib-1
Vita		Vita-1

List of Figures

Figure 1.1 Multiple Model Adaptive Filter	1-8
Figure 1.2 Data Processing Scheme using FFT and IFFT	1-9
Figure 1.3 Linear Kalman Filter/Enhanced Correlator Algorithm	1-11
Figure 1.4 Discrete Implementation of Cross-Sectional Reflectivity Function	1-20
Figure 3.1 Three Primary Coordinate Frames in Simulation Space	3-2
Figure 3.2 FLIR Plane, Trans-FLIR Plane, and ALT-ACT Plane	3-5
Figure 3.3 Target Plume Image in 8 x 8 FLIR Field-of-View (FOV)	3-7
Figure 3.4 Spatial Relationship of Target Plume Gaussian Intensity Functions	3-9
Figure 3.5 Target Plume Intensity Centroid Projection Geometry	3-10
Figure 3.6 Intensity Centroid Dispersion Axes in FLIR Plane	3-11
Figure 3.7 Inertial Velocity FLIR Plane Projection Geometry	3-14
Figure 4.1 Plume Intensity Function Position on FLIR Image Plane	4-2
Figure 4.2 Target Centroid Image on α - β Plane with "Pseudo" Angles	4-8
Figure 4.3 Plume Pogo Oscillation	4-20
Figure 4.4 Composite Plume Intensity Function on FLIR Plane	4-23
Figure 4.5 Empirical Radar Reflection Data of Cylinder	4-28
Figure 4.6 3-d Hardbody Reflectivity Model Relative to FLIR Image Plane	4-29
Figure 4.7 Discrete Implementation of Cross-Sectional Reflectivity Function	4-30
Figure 4.8 Projection Geometry onto FLIR Image Plane	4-31
Figure 4.9 Ideal Low-Energy Laser Scan	4-33
Figure 4.10 Sweep Technique of Laser Scan	4-34
Figure 4.11 Biased Offset Measurement Caused by Plume Reflectance	4-36

Figure 4.12 Spectra of Received Signals	4-39
Figure 4.13 Pulsed Signal Frequency Spectrum	4-41
Figure 4.14 Spectra of Coherent and Non-Coherent Pulsed Signals	4-42
Figure 4.15 Spectra of Plume and Hardbody-Induced Doppler Returns	4-44
Figure 4.16 Detection Characteristics	4-49
Figure 5.1 Linear Kalman Filter/Enhanced Correlator Algorithm	5-9
Figure 5.2 Filter Estimate of Offset Distance (Ideal Conditions)	5-19
Figure 5.3 Two-State Modified MAP MMAF Structure	5-25
Figure 5.4 Modified MAP MMAF Algorithm	5-30
Figure 6.1 One-State Speckle Return Filter Biased Offset Error	6-5
Figure 6.2 One-State Speckle Return Filter Biased Offset Error at t_i^-	6-5
Figure 6.3. One-State Speckle Return Filter Biased Offset Error at t_i^+	6-6
Figure B.1 Example of Time History Plot of Filter vs. Actual errors	B-3
Figure B.2 Example Time History Plot of Filter Error Statistics (Mean $\pm 1\sigma$)	B-3
Figure C.1.1 0.53 μm Doppler Return One-State Filter Offset Error, SNR = 10, $P_m = 0.0$	C-4
Figure C.1.2 0.53 μm Doppler Return One-State Filter Offset Error at t_i^- , SNR=10, $P_m = 0.0$	C-4
Figure C.1.3 0.53 μm Doppler Return One-State Filter Offset Error at t_i^+ , SNR=10, $P_m = 0.0$	C-5
Figure C.1.4 0.53 μm Doppler Return One-State Filter Offset RMS Error, SNR=10, $P_m=0.05$	C-6
Figure C.1.5 0.53 μm Doppler Return One-State Filter Offset Error, SNR=10, $P_m=0.05$, at t_i^-	C-6
Figure C.1.6 0.53 μm Doppler Return One-State Filter Offset Error, SNR=10, $P_m=0.05$, at t_i^+	C-7
Figure C.1.7 0.53 μm Doppler Return One-State Filter Offset Error, SNR=10, $P_m = 0.30$	C-8
Figure C.1.8 0.53 μm Doppler Return One-State Filter Offset Error, SNR=10, $P_m = 0.30$, at t_i^-	C-8
Figure C.1.9 0.53 μm Doppler Return One-State Filter Offset Error, SNR=10, $P_m=0.30$, at t_i^+	C-9
Figure C.2.1 0.53 μm Doppler Return One-State Filter Offset Error, with SNR = 4, $P_m = 0.0$	C-11

Figure C.2.2	0.53 μm Doppler Return One-State Filter Offset Error, SNR = 4, $P_m = 0.0$ at t_i^-	C-11
Figure C.2.3	0.53 μm Doppler Return One-State Filter Offset Error, SNR = 4, $P_m = 0.0$ at t_i^+	C-12
Figure C.2.4	0.53 μm Doppler Return One-State Filter Offset Error, SNR = 4, $P_m = 0.05$	C-13
Figure C.2.5	0.53 μm Doppler Return One-State Filter Offset Error, SNR=4, $P_m = 0.05$, at t_i^-	C-13
Figure C.2.6	0.53 μm Doppler Return One-State Filter Offset Error, SNR=4, $P_m = 0.05$, at t_i^+	C-14
Figure C.2.7	0.53 μm Doppler Return One-State Filter Offset Error, SNR = 4, $P_m = 0.30$	C-15
Figure C.2.8	0.53 μm Doppler Return One-State Filter Offset Error, SNR=4, $P_m = 0.30$, at t_i^-	C-15
Figure C.2.9	0.53 μm Doppler Return One-State Filter Offset Error, SNR=4, $P_m = 0.30$, at t_i^+	C-16
Figure C.3.1	2.01 μm Doppler Return One-State Filter Offset Error with SNR = 10, $P_m = 0.0$	C-18
Figure C.3.2	2.01 μm Doppler Return One-State Filter Offset Error, SNR = 10, $P_m = 0.0$ at t_i^-	C-18
Figure C.3.3	2.01 μm Doppler Return One-State Offset Filter, with SNR = 10, $P_m = 0.0$ at t_i^+	C-19
Figure C.3.4	2.01 μm Doppler Return One-State Filter Offset Error, SNR = 10, $P_m = 0.05$	C-20
Figure C.3.5	2.01 μm Doppler Return One-State Filter Offset Error, SNR=10, $P_m = 0.05$, at t_i^-	C-20
Figure C.3.6	2.01 μm Doppler Return One-State Filter Offset Error, SNR=10, $P_m=0.05$, at t_i^+	C-21
Figure C.3.7	2.01 μm Doppler Return One-State Filter Offset Error, SNR = 10, $P_m = 0.30$	C-22
Figure C.3.8	2.01 μm Doppler Return One-State Filter Offset Error, SNR=10, $P_m = 0.30$, at t_i^-	C-22
Figure C.3.9	2.01 μm Doppler Return One-State Filter Offset Error, SNR=10, $P_m=0.30$, at t_i^+	C-23
Figure C.4.1	2.01 μm Doppler Return One-State Filter Offset Error with SNR = 4, $P_m = 0.0$	C-25
Figure C.4.2	2.01 μm Doppler Return One-State Filter Offset Error, SNR = 4, $P_m = 0.0$ at t_i^-	C-25
Figure C.4.3	2.01 μm Doppler Return One-State Filter Offset Error, SNR = 4, $P_m = 0.0$ at t_i^+	C-26
Figure C.4.4	2.01 μm Doppler Return One-State Filter Offset Error with SNR = 4, $P_m = 0.05$	C-27
Figure C.4.5	2.01 μm Doppler Return One-State Filter Offset Error, SNR=4, $P_m = 0.05$, at t_i^-	C-27
Figure C.4.6	2.01 μm Doppler Return One-State Filter Offset Error, SNR=4, $P_m = 0.05$, at t_i^+	C-28
Figure C.4.7	2.01 μm Doppler Return One-State Filter Offset Error with SNR = 4, $P_m = 0.30$	C-29

Figure C.4.8	2.01 μm Doppler Return One-State Filter Offset Error, SNR=4, $P_m = 0.30$, at t_i^-	C-29
Figure C.4.9	2.01 μm Doppler Return One-State Filter Offset Error, SNR=4, $P_m = 0.30$, at t_i^+	C-30
Figure C.5.1	10.5 μm Doppler Return One-State Filter Offset Error with SNR = 10, $P_m = 0.0$	C-32
Figure C.5.2	10.5 μm Doppler Return One-State Filter Offset Error, SNR = 10, $P_m = 0.0$ at t_i^-	C-32
Figure C.5.3	10.5 μm Doppler Return One-State Filter Offset Error, SNR = 10, $P_m = 0.0$ at t_i^+	C-33
Figure C.5.4	10.5 μm Doppler Return One-State Filter Offset Error, SNR = 10, $P_m = 0.05$	C-34
Figure C.5.5	10.5 μm Doppler Return One-State Filter Offset Error, SNR=10, $P_m = 0.05$, at t_i^-	C-34
Figure C.5.6	10.5 μm Doppler Return One-State Filter Offset Error, SNR=10, $P_m=0.05$, at t_i^+	C-35
Figure C.5.7	10.5 μm Doppler Return One-State Filter Offset Error, SNR = 10, $P_m = 0.30$	C-36
Figure C.5.8	10.5 μm Doppler Return One-State Filter Offset Error, SNR=10, $P_m = 0.30$, at t_i^-	C-36
Figure C.5.9	10.5 μm Doppler Return One-State Filter Offset Error, SNR=10, $P_m=0.30$, at t_i^+	C-37
Figure C.6.1	10.5 μm Doppler Return One-State Filter Offset Error with SNR = 4, $P_m = 0.0$. . .	C-39
Figure C.6.2	10.5 μm Doppler Return One-State Filter Offset Error, SNR = 4, $P_m = 0.0$ at t_i^-	C-39
Figure C.6.3	10.5 μm Doppler Return One-State Filter Offset Error, SNR = 4, $P_m = 0.0$ at t_i^+	C-40
Figure C.6.4	10.5 μm Doppler Return One-State Filter Offset Error, SNR = 4, $P_m = 0.05$	C-41
Figure C.6.5	10.5 μm Doppler Return One-State Filter Offset Error, SNR=4, $P_m = 0.05$, at t_i^-	C-41
Figure C.6.6	10.5 μm Doppler Return One-State Filter Offset with SNR = 4, $P_m = 0.05$, at t_i^+	C-42
Figure C.6.7	10.5 μm Doppler Return One-State Filter Offset Error with SNR = 4, $P_m = 0.30$	C-43
Figure C.6.8	10.5 μm Doppler Return One-State Filter Offset Error, SNR=4, $P_m = 0.30$, at t_i^-	C-43
Figure C.6.9	10.5 μm Doppler Return One-State Filter Offset Error, SNR=4, $P_m = 0.30$, at t_i^+	C-44
Figure D.1	Two-State Modified MAP MMAF Offset Error, $q_{df11} = 0.7$, $q_{df22} = 0.7$	D-5
Figure D.2	Two-State Modified MAP MMAF Offset Error at t_i^- , $q_{df11} = 0.7$, $q_{df22} = 0.7$	D-6
Figure D.3	Two-State Modified MAP MMAF Offset Error at t_i^+ , $q_{df11} = 0.7$, $q_{df22} = 0.7$	D-7
Figure D.4	Two-State Modified MAP MMAF Bias Error, $q_{df11} = 0.7$, $q_{df22} = 0.7$	D-8

Figure D.5	Two-State Modified MAP MMAF Bias Error at t_i^- , $q_{df 11} = 0.7$, $q_{df 22} = 0.7$	D-4
Figure D.6	Two-State Modified MAP MMAF Bias Error at t_i^+ , $q_{df 11} = 0.7$, $q_{df 22} = 0.7$	D-9
Figure D.7	Two-State Modified MAP MMAF Offset Error, $q_{df 11} = 0.7$, $q_{df 22} = 0.07$	D-6
Figure D.8	Two-State Modified MAP MMAF Offset Error at t_i^- , $q_{df 11} = 0.7$, $q_{df 22} = 0.07$	D-8
Figure D.9	Two-State Modified MAP MMAF Offset Error at t_i^+ , $q_{df 11} = 0.7$, $q_{df 22} = 0.07$	D-10
Figure D.10	Two-State Modified MAP MMAF Bias Error, $q_{df 11} = 0.7$, $q_{df 22} = 0.07$	D-7
Figure D.11	Two-State Modified MAP MMAF Bias Error at t_i^- , $q_{df 11} = 0.7$, $q_{df 22} = 0.07$	D-11
Figure D.12	Two-State Modified MAP MMAF Bias Error at t_i^+ , $q_{df 11} = 0.7$, $q_{df 22} = 0.07$	D-12
Figure D.13	Two-State Modified MAP MMAF Offset Error, $q_{df 11} = 0.07$, $q_{df 22} = 0.0007$	D-9
Figure D.14	Two-State Modified MAP MMAF Offset Error at t_i^- , $q_{df 11} = 0.07$, $q_{df 22} = 0.007$	D-13
Figure D.15	Two-State Modified MAP MMAF Offset Error at t_i^+ , $q_{df 11} = 0.07$, $q_{df 22} = 0.007$	D-14
Figure D.16	Two-State Modified MAP MMAF Bias Error, $q_{df 11} = 0.07$, $q_{df 22} = 0.007$	D-10
Figure D.17	Two-State Modified MAP MMAF Bias Error at t_i^- , $q_{df 11} = 0.07$, $q_{df 22} = 0.007$	D-15
Figure D.18	Two-State Modified MAP MMAF Bias Error at t_i^+ , $q_{df 11} = 0.07$, $q_{df 22} = 0.007$	D-16
Figure D.19	Two-State Modified MAP MMAF Offset Error, $q_{df 11} = 0.007$, $q_{df 22} = 0.0007$	D-11
Figure D.20	Two-State Modified MAP MMAF Offset Error at t_i^- , $q_{df 11} = 0.007$, $q_{df 22} = 0.0007$	D-12
Figure D.21	Two-State Modified MAP MMAF Offset Error at t_i^+ , $q_{df 11} = 0.007$, $q_{df 22} = 0.0007$	D-12
Figure D.22	Two-State Modified MAP MMAF Bias Error, $q_{df 11} = 0.007$, $q_{df 22} = 0.0007$	D-13
Figure D.23	Two-State Modified MAP MMAF Bias Error at t_i^- , $q_{df 11} = 0.007$, $q_{df 22} = 0.0007$	D-14
Figure D.24	Two-State Modified MAP MMAF Bias Error at t_i^+ , $q_{df 11} = 0.007$, $q_{df 22} = 0.0007$	D-14
Figure D.25	Two-State Modified MAP MMAF Offset Error, $q_{df 11} = 0.03$, $q_{df 22} = 0.001$	D-15
Figure D.26	Two-State Modified MAP MMAF Offset Error at t_i^- , $q_{df 11} = 0.03$, $q_{df 22} = 0.001$	D-16
Figure D.27	Two-State Modified MAP MMAF Offset Error at t_i^+ , $q_{df 11} = 0.03$, $q_{df 22} = 0.001$	D-16
Figure D.28	Two-State Modified MAP MMAF Bias Error, $q_{df 11} = 0.03$, $q_{df 22} = 0.001$	D-17

Figure D.29	Two-State Modified MAP MMAF Bias Error at t_i^- , $q_{df11} = 0.03$, $q_{df22} = 0.001$. . .	D-17
Figure D.30	Two-State Modified MAP MMAF Bias Error at t_i^+ , $q_{df11} = 0.03$, $q_{df22} = 0.001$. . .	D-18
Figure E.1.1	0.53 μm Two-State Modified MAP MMAF Offset Error, SNR=10, $P_m=0.0$	E-4
Figure E.1.2	0.53 μm Two-State Modified MAP MMAF Offset Error, SNR=10, $P_m=0.0$, at t_i^- . . .	E-4
Figure E.1.3	0.53 μm Two-State Modified MAP MMAF Offset Error, SNR=10, $P_m=0.0$, at t_i^+	E-5
Figure E.1.4	0.53 μm Two-State Modified MAP MMAF Bias Error, SNR=10, $P_m=0.0$	E-5
Figure E.1.5	0.53 μm Two-State Modified MAP MMAF Bias Error, SNR=10, $P_m=0.0$, at t_i^-	E-6
Figure E.1.6	0.53 μm Two-State Modified MAP MMAF Bias Error, SNR=10, $P_m=0.0$, at t_i^+	E-6
Figure E.1.7	0.53 μm Two-State Modified MAP MMAF Offset Error, SNR = 10, $P_m = 0.05$. . .	E-7
Figure E.1.8	0.53 μm Two-State Modified MAP MMAF Offset Error, SNR=10, $P_m=0.05$, at t_i^- . . .	E-7
Figure E.1.9	0.53 μm Two-State Modified MAP MMAF Offset Error, SNR=10, $P_m=0.05$, at t_i^+ . . .	E-8
Figure E.1.10	0.53 μm Two-State Modified MAP MMAF Bias Error, SNR = 10, $P_m = 0.05$. . .	E-8
Figure E.1.11	0.53 μm Two-State Modified MAP MMAF Bias Error, SNR=10, $P_m=0.05$, at t_i^- . . .	E-9
Figure E.1.12	0.53 μm Two-State Modified MAP MMAF Bias Error, SNR=10, $P_m=0.05$, at t_i^+ . . .	E-9
Figure E.1.13	0.53 μm Two-State Modified MAP MMAF Offset Error, SNR = 10, $P_m = 0.30$. .	E-10
Figure E.1.14	0.53 μm Two-State Modified MAP MMAF Offset Error, SNR=10, $P_m=0.30$, at t_i^- .	E-10
Figure E.1.15	0.53 μm Two-State Modified MAP MMAF Offset Error, SNR=10, $P_m=0.30$, at t_i^+ .	E-11
Figure E.1.16	0.53 μm Two-State Modified MAP MMAF Bias Error, SNR = 10, $P_m = 0.30$. . .	E-11
Figure E.1.17	0.53 μm Two-State Modified MAP MMAF Bias Error, SNR=10, $P_m=0.30$, at t_i^- . .	E-12
Figure E.1.18	0.53 μm Two-State Modified MAP MMAF Bias Error, SNR=10, $P_m=0.30$, at t_i^+ . .	E-12
Figure E.2.1	0.53 μm Two-State Modified MAP MMAF Offset Error, SNR=4, $P_m=0.0$	E-14
Figure E.2.2	0.53 μm Two-State Modified MAP MMAF Offset Error, SNR=4, $P_m=0.0$, at t_i^- . . .	E-14
Figure E.2.3	0.53 μm Two-State Modified MAP MMAF Offset Error, SNR=4, $P_m=0.0$, at t_i^+	E-15
Figure E.2.4	0.53 μm Two-State Modified MAP MMAF Bias Error, SNR=4, $P_m=0.0$	E-15

Figure E.2.5	0.53 μm Two-State Modified MAP MMAF Bias Error, SNR=4, $P_m=0.0$, at t_i^-	E-16
Figure E.2.6	0.53 μm Two-State Modified MAP MMAF Bias Error, SNR=4, $P_m=0.0$, at t_i^+	E-16
Figure E.2.7	0.53 μm Two-State Modified MAP MMAF Offset Error, SNR = 4, $P_m = 0.05$. . .	E-17
Figure E.2.8	0.53 μm Two-State Modified MAP MMAF Offset Error, SNR=4, $P_m=0.05$, at t_i^- . .	E-17
Figure E.2.9	0.53 μm Two-State Modified MAP MMAF Offset Error, SNR=4, $P_m=0.05$, at t_i^+ . . .	E-18
Figure E.2.10	0.53 μm Two-State Modified MAP MMAF Bias Error, SNR = 4, $P_m = 0.05$. . .	E-18
Figure E.2.11	0.53 μm Two-State Modified MAP MMAF Bias Error, SNR=4, $P_m=0.05$, at t_i^- . . .	E-19
Figure E.2.12	0.53 μm Two-State Modified MAP MMAF Bias Error, SNR=4, $P_m=0.05$, at t_i^+ . . .	E-19
Figure E.2.13	0.53 μm Two-State Modified MAP MMAF Offset Error, SNR = 4, $P_m = 0.30$. . .	E-20
Figure E.2.14	0.53 μm Two-State Modified MAP MMAF Offset Error, SNR=4, $P_m=0.30$, at t_i^- . .	E-20
Figure E.2.15	0.53 μm Two-State Modified MAP MMAF Offset Error, SNR=4, $P_m=0.30$, at t_i^+ . .	E-21
Figure E.2.16	0.53 μm Two-State Modified MAP MMAF Bias Error, SNR = 4, $P_m = 0.30$	E-21
Figure E.2.17	0.53 μm Two-State Modified MAP MMAF Bias Error, SNR=4, $P_m=0.30$, at t_i^- . . .	E-22
Figure E.2.18	0.53 μm Two-State Modified MAP MMAF Bias Error, SNR=4, $P_m=0.30$, at t_i^+ . . .	E-22
Figure E.3.1	2.01 μm Two-State Modified MAP MMAF Offset Error, SNR=10, $P_m=0.0$	E-24
Figure E.3.2	2.01 μm Two-State Modified MAP MMAF Offset Error, SNR=10, $P_m=0.0$, at t_i^- . .	E-24
Figure E.3.3	2.01 μm Two-State Modified MAP MMAF Offset Error, SNR=10, $P_m=0.0$, at t_i^+ . . .	E-25
Figure E.3.4	2.01 μm Two-State Modified MAP MMAF Bias Error, SNR=10, $P_m=0.0$	E-25
Figure E.3.5	2.01 μm Two-State Modified MAP MMAF Bias Error, SNR=10, $P_m=0.0$, at t_i^- . . .	E-26
Figure E.3.6	2.01 μm Two-State Modified MAP MMAF Bias Error, SNR=10, $P_m=0.0$, at t_i^+	E-26
Figure E.3.7	2.01 μm Two-State Modified MAP MMAF Offset Error, SNR = 10, $P_m = 0.05$. .	E-27
Figure E.3.8	2.01 μm Two-State Modified MAP MMAF Offset Error, SNR=10, $P_m=0.05$, at t_i^- . .	E-27
Figure E.3.9	2.01 μm Two-State Modified MAP MMAF Offset Error, SNR=10, $P_m=0.05$, at t_i^+ . .	E-28
Figure E.3.10	2.01 μm Two-State Modified MAP MMAF Bias Error, SNR = 10, $P_m = 0.05$. .	E-28

Figure E.3.11	2.01 μm Two-State Modified MAP MMAF Bias Error, SNR=10, $P_m=0.05$, at t_i^-	..	E-29
Figure E.3.12	2.01 μm Two-State Modified MAP MMAF Bias Error, SNR=10, $P_m=0.05$, at t_i^+	..	E-29
Figure E.3.13	2.01 μm Two-State Modified MAP MMAF Offset Error, SNR = 10, $P_m = 0.30$..	E-30
Figure E.3.14	2.01 μm Two-State Modified MAP MMAF Offset Error, SNR=10, $P_m=0.30$, at t_i^-	..	E-30
Figure E.3.15	2.01 μm Two-State Modified MAP MMAF Offset Error, SNR=10, $P_m=0.30$, at t_i^+	..	E-31
Figure E.3.16	2.01 μm Two-State Modified MAP MMAF Bias Error, SNR = 10, $P_m = 0.30$...	E-31
Figure E.3.17	2.01 μm Two-State Modified MAP MMAF Bias Error, SNR=10, $P_m=0.30$, at t_i^-	..	E-32
Figure E.3.18	2.01 μm Two-State Modified MAP MMAF Bias Error, SNR=10, $P_m=0.30$, at t_i^+	..	E-32
Figure E.4.1	2.01 μm Two-State Modified MAP MMAF Offset Error, SNR=4, $P_m=0.0$	E-34
Figure E.4.2	2.01 μm Two-State Modified MAP MMAF Offset Error, SNR=4, $P_m=0.0$, at t_i^-	...	E-34
Figure E.4.3	2.01 μm Two-State Modified MAP MMAF Offset Error, SNR=4, $P_m=0.0$, at t_i^+	...	E-35
Figure E.4.4	2.01 μm Two-State Modified MAP MMAF Bias Error, SNR=4, $P_m=0.0$	E-35
Figure E.4.5	2.01 μm Two-State Modified MAP MMAF Bias Error, SNR=4, $P_m=0.0$, at t_i^-	...	E-36
Figure E.4.6	2.01 μm Two-State Modified MAP MMAF Bias Error, SNR=4, $P_m=0.0$, at t_i^+	...	E-36
Figure E.4.7	2.01 μm Two-State Modified MAP MMAF Offset Error, SNR = 4, $P_m = 0.05$...	E-37
Figure E.4.8	2.01 μm Two-State Modified MAP MMAF Offset Error, SNR=4, $P_m=0.05$, at t_i^-	..	E-37
Figure E.4.9	2.01 μm Two-State Modified MAP MMAF Offset Error, SNR=4, $P_m=0.05$, at t_i^+	..	E-38
Figure E.4.10	2.01 μm Two-State Modified MAP MMAF Bias Error, SNR = 4, $P_m = 0.05$...	E-38
Figure E.4.11	2.01 μm Two-State Modified MAP MMAF Bias Error, SNR=4, $P_m=0.05$, at t_i^-	..	E-39
Figure E.4.12	2.01 μm Two-State Modified MAP MMAF Bias Error, SNR=4, $P_m=0.05$, at t_i^+	..	E-39
Figure E.4.13	2.01 μm Two-State Modified MAP MMAF Offset Error, SNR = 4, $P_m = 0.30$...	E-40
Figure E.4.14	2.01 μm Two-State Modified MAP MMAF Offset Error, SNR=4, $P_m=0.30$, at t_i^-	..	E-40
Figure E.4.15	2.01 μm Two-State Modified MAP MMAF Offset Error, SNR=4, $P_m=0.30$, at t_i^+	..	E-41
Figure E.4.16	2.01 μm Two-State Modified MAP MMAF Bias Error, SNR = 4, $P_m = 0.30$...	E-41

Figure E.4.17	2.01 μ m Two-State Modified MAP MMAF Bias Error,SNR=4, $P_m=0.30$, at t_i^-	...	E-42
Figure E.4.18	2.01 μ m Two-State Modified MAP MMAF Bias Error,SNR=4, $P_m=0.30$,at t_i^+	...	E-42
Figure E.5.1	10.5 μ m Two-State Modified MAP MMAF Offset Error,SNR=10, $P_m=0.0$	E-44
Figure E.5.2	10.5 μ m Two-State Modified MAP MMAF Offset Error,SNR=10, $P_m=0.0$, at t_i^-	..	E-44
Figure E.5.3	10.5 μ m Two-State Modified MAP MMAF Offset Error,SNR=10, $P_m=0.0$,at t_i^+	...	E-45
Figure E.5.4	10.5 μ m Two-State Modified MAP MMAF Bias Error,SNR=10, $P_m=0.0$	E-45
Figure E.5.5	10.5 μ m Two-State Modified MAP MMAF Bias Error,SNR=10, $P_m=0.0$, at t_i^-	...	E-46
Figure E.5.6	10.5 μ m Two-State Modified MAP MMAF Bias Error,SNR=10, $P_m=0.0$,at t_i^+	E-46
Figure E.5.7	10.5 μ m Two-State Modified MAP MMAF Offset Error, SNR = 10, $P_m = 0.05$..	E-47
Figure E.5.8	10.5 μ m Two-State Modified MAP MMAF Offset Error,SNR=10, $P_m=0.05$,at t_i^-	..	E-47
Figure E.5.9	10.5 μ m Two-State Modified MAP MMAF Offset Error,SNR=10, $P_m=0.05$,at t_i^+	..	E-48
Figure E.5.10	10.5 μ m Two-State Modified MAP MMAF Bias Error, SNR = 10, $P_m = 0.05$..	E-48
Figure E.5.11	10.5 μ m Two-State Modified MAP MMAF Bias Error,SNR=10, $P_m=0.05$,at t_i^-	..	E-49
Figure E.5.12	10.5 μ m Two-State Modified MAP MMAF Bias Error,SNR=10, $P_m=0.05$,at t_i^+	..	E-49
Figure E.5.13	10.5 μ m Two-State Modified MAP MMAF Offset Error, SNR = 10, $P_m = 0.30$..	E-50
Figure E.5.14	10.5 μ m Two-State Modified MAP MMAF Offset Error,SNR=10, $P_m=0.30$, at t_i^-	..	E-50
Figure E.5.15	10.5 μ m Two-State Modified MAP MMAF Offset Error,SNR=10, $P_m=0.30$.at t_i^+	..	E-51
Figure E.5.16	10.5 μ m Two-State Modified MAP MMAF Bias Error, SNR = 10, $P_m = 0.30$..	E-51
Figure E.5.17	10.5 μ m Two-State Modified MAP MMAF Bias Error,SNR=10, $P_m=0.30$, at t_i^-	..	E-52
Figure E.5.18	10.5 μ m Two-State Modified MAP MMAF Bias Error,SNR=10, $P_m=0.30$,at t_i^+	..	E-52
Figure E.6.1	10.5 μ m Two-State Modified MAP MMAF Offset Error,SNR=4, $P_m=0.0$	E-54
Figure E.6.2	10.5 μ m Two-State Modified MAP MMAF Offset Error,SNR=4, $P_m=0.0$, at t_i^-	...	E-54
Figure E.6.3	10.5 μ m Two-State Modified MAP MMAF Offset Error,SNR=4, $P_m=0.0$,at t_i^+	E-55
Figure E.6.4	10.5 μ m Two-State Modified MAP MMAF Bias Error,SNR=4, $P_m=0.0$	E-55

Figure E.6.5	10.5 μm Two-State Modified MAP MMAF Bias Error, SNR=4, $P_m=0.0$, at t_i^-	...	E-56
Figure E.6.6	10.5 μm Two-State Modified MAP MMAF Bias Error, SNR=4, $P_m=0.0$, at t_i^+	...	E-56
Figure E.6.7	10.5 μm Two-State Modified MAP MMAF Offset Error, SNR = 4, $P_m = 0.05$...	E-57
Figure E.6.8	10.5 μm Two-State Modified MAP MMAF Offset Error, SNR=4, $P_m=0.05$, at t_i^-	...	E-57
Figure E.6.9	10.5 μm Two-State Modified MAP MMAF Offset Error, SNR=4, $P_m=0.05$, at t_i^+	...	E-58
Figure E.6.10	10.5 μm Two-State Modified MAP MMAF Bias Error, SNR = 4, $P_m = 0.05$...	E-58
Figure E.6.11	10.5 μm Two-State Modified MAP MMAF Bias Error, SNR=4, $P_m=0.05$, at t_i^-	...	E-59
Figure E.6.12	10.5 μm Two-State Modified MAP MMAF Bias Error, SNR=4, $P_m=0.05$, at t_i^+	...	E-59
Figure E.6.13	10.5 μm Two-State Modified MAP MMAF Offset Error, SNR = 4, $P_m = 0.30$...	E-60
Figure E.6.14	10.5 μm Two-State Modified MAP MMAF Offset Error, SNR=4, $P_m=0.30$, at t_i^-	...	E-60
Figure E.6.15	10.5 μm Two-State Modified MAP MMAF Offset Error, SNR=4, $P_m=0.30$, at t_i^+	...	E-61
Figure E.6.16	10.5 μm Two-State Modified MAP MMAF Bias Error, SNR = 4, $P_m = 0.30$...	E-61
Figure E.6.17	10.5 μm Two-State Modified MAP MMAF Bias Error, SNR=4, $P_m=0.30$, at t_i^-	...	E-62
Figure E.6.18	10.5 μm Two-State Modified MAP MMAF Bias Error, SNR=4, $P_m=0.30$, at t_i^+	...	E-62
Figure F.1.1	0.53 μm Two-State Modified MAP MMAF Offset Error, SNR=10, $P_m=0.0$...	F-4
Figure F.1.2	0.53 μm Two-State Modified MAP MMAF Offset Error, SNR=10, $P_m=0.0$, at t_i^-	...	F-4
Figure F.1.3	0.53 μm Two-State Modified MAP MMAF Offset Error, SNR=10, $P_m=0.0$, at t_i^+	...	F-5
Figure F.1.4	0.53 μm Two-State Modified MAP MMAF Bias Error, SNR=10, $P_m=0.0$...	F-5
Figure F.1.5	0.53 μm Two-State Modified MAP MMAF Bias Error, SNR=10, $P_m=0.0$, at t_i^-	...	F-6
Figure F.1.6	0.53 μm Two-State Modified MAP MMAF Bias Error, SNR=10, $P_m=0.0$, at t_i^+	...	F-6
Figure F.1.7	0.53 μm Two-State Modified MAP MMAF Offset Error, SNR = 10, $P_m = 0.05$...	F-7
Figure F.1.8	0.53 μm Two-State Modified MAP MMAF Offset Error, SNR=10, $P_m=0.05$, at t_i^-	...	F-7
Figure F.1.9	0.53 μm Two-State Modified MAP MMAF Offset Error, SNR=10, $P_m=0.05$, at t_i^+	...	F-8
Figure F.1.10	0.53 μm Two-State Modified MAP MMAF Bias Error, SNR = 10, $P_m = 0.05$...	F-8

Figure F.1.11	0.53 μm Two-State Modified MAP MMAF Bias Error,SNR=10, $P_m=0.05$,at t_i^-	...	F-9
Figure F.1.12	0.53 μm Two-State Modified MAP MMAF Bias Error,SNR=10, $P_m=0.05$,at t_i^+	...	F-9
Figure F.1.13	0.53 μm Two-State Modified MAP MMAF Offset Error, SNR = 10, $P_m = 0.30$..	F-10
Figure F.1.14	0.53 μm Two-State Modified MAP MMAF Offset Error,SNR=10, $P_m=0.30$, at t_i^-	.	F-10
Figure F.1.15	0.53 μm Two-State Modified MAP MMAF Offset Error,SNR=10, $P_m=0.30$,at t_i^+	.	F-11
Figure F.1.16	0.53 μm Two-State Modified MAP MMAF Bias Error, SNR = 10, $P_m = 0.30$...	F-11
Figure F.1.17	0.53 μm Two-State Modified MAP MMAF Bias Error,SNR=10, $P_m=0.30$, at t_i^-	..	F-12
Figure F.1.18	0.53 μm Two-State Modified MAP MMAF Bias Error,SNR=10, $P_m=0.30$,at t_i^+	..	F-12
Figure F.2.1	0.53 μm Two-State Modified MAP MMAF Offset Error,SNR=4, $P_m=0.0$	F-14
Figure F.2.2	0.53 μm Two-State Modified MAP MMAF Offset Error,SNR=4, $P_m=0.0$, at t_i^-	...	F-14
Figure F.2.3	0.53 μm Two-State Modified MAP MMAF Offset Error,SNR=4, $P_m=0.0$,at t_i^+	F-15
Figure F.2.4	0.53 μm Two-State Modified MAP MMAF Bias Error,SNR=4, $P_m=0.0$	F-15
Figure F.2.5	0.53 μm Two-State Modified MAP MMAF Bias Error,SNR=4, $P_m=0.0$, at t_i^-	F-16
Figure F.2.6	0.53 μm Two-State Modified MAP MMAF Bias Error,SNR=4, $P_m=0.0$,at t_i^+	F-16
Figure F.2.7	0.53 μm Two-State Modified MAP MMAF Offset Error, SNR = 4, $P_m = 0.05$...	F-17
Figure F.2.8	0.53 μm Two-State Modified MAP MMAF Offset Error,SNR=4, $P_m=0.05$,at t_i^-	...	F-17
Figure F.2.9	0.53 μm Two-State Modified MAP MMAF Offset Error,SNR=4, $P_m=0.05$,at t_i^+	...	F-18
Figure F.2.10	0.53 μm Two-State Modified MAP MMAF Bias Error, SNR = 4, $P_m = 0.05$...	F-18
Figure F.2.11	0.53 μm Two-State Modified MAP MMAF Bias Error,SNR=4, $P_m=0.05$,at t_i^-	...	F-19
Figure F.2.12	0.53 μm Two-State Modified MAP MMAF Bias Error,SNR=4, $P_m=0.05$,at t_i^+	...	F-19
Figure F.2.13	0.53 μm Two-State Modified MAP MMAF Offset Error, SNR = 4, $P_m = 0.30$...	F-20
Figure F.2.14	0.53 μm Two-State Modified MAP MMAF Offset Error,SNR=4, $P_m=0.30$, at t_i^-	..	F-20
Figure F.2.15	0.53 μm Two-State Modified MAP MMAF Offset Error,SNR=4, $P_m=0.30$,at t_i^+	..	F-21
Figure F.2.16	0.53 μm Two-State Modified MAP MMAF Bias Error, SNR = 4, $P_m = 0.30$	F-21

Figure F.2.17	0.53 μ m Two-State Modified MAP MMAF Bias Error,SNR=4, P_m =0.30, at t_i^- . . .	F-22
Figure F.2.18	0.53 μ m Two-State Modified MAP MMAF Bias Error,SNR=4, P_m =0.30,at t_i^+ . . .	F-22
Figure F.3.1	2.01 μ m Two-State Modified MAP MMAF Offset Error,SNR=10, P_m =0.0	F-24
Figure F.3.2	2.01 μ m Two-State Modified MAP MMAF Offset Error,SNR=10, P_m =0.0, at t_i^- . .	F-24
Figure F.3.3	2.01 μ m Two-State Modified MAP MMAF Offset Error,SNR=10, P_m =0.0,at t_i^+ . . .	F-25
Figure F.3.4	2.01 μ m Two-State Modified MAP MMAF Bias Error,SNR=10, P_m =0.0	F-25
Figure F.3.5	2.01 μ m Two-State Modified MAP MMAF Bias Error,SNR=10, P_m =0.0, at t_i^- . . .	F-26
Figure F.3.6	2.01 μ m Two-State Modified MAP MMAF Bias Error,SNR=10, P_m =0.0,at t_i^+	F-26
Figure F.3.7	2.01 μ m Two-State Modified MAP MMAF Offset Error, SNR = 10, P_m = 0.05 . .	F-27
Figure F.3.8	2.01 μ m Two-State Modified MAP MMAF Offset Error,SNR=10, P_m =0.05,at t_i^- . .	F-27
Figure F.3.9	2.01 μ m Two-State Modified MAP MMAF Offset Error,SNR=10, P_m =0.05,at t_i^+ . .	F-28
Figure F.3.10	2.01 μ m Two-State Modified MAP MMAF Bias Error, SNR = 10, P_m = 0.05 . . .	F-28
Figure F.3.11	2.01 μ m Two-State Modified MAP MMAF Bias Error,SNR=10, P_m =0.05,at t_i^- . .	F-29
Figure F.3.12	2.01 μ m Two-State Modified MAP MMAF Bias Error,SNR=10, P_m =0.05,at t_i^+ . .	F-29
Figure F.3.13	2.01 μ m Two-State Modified MAP MMAF Offset Error, SNR = 10, P_m = 0.30 .	F-30
Figure F.3.14	2.01 μ m Two-State Modified MAP MMAF Offset Error,SNR=10, P_m =0.30, at t_i^- .	F-30
Figure F.3.15	2.01 μ m Two-State Modified MAP MMAF Offset Error,SNR=10, P_m =0.30,at t_i^+ .	F-31
Figure F.3.16	2.01 μ m Two-State Modified MAP MMAF Bias Error, SNR = 10, P_m = 0.30 . . .	F-31
Figure F.3.17	2.01 μ m Two-State Modified MAP MMAF Bias Error,SNR=10, P_m =0.30, at t_i^- . .	F-32
Figure F.3.18	2.01 μ m Two-State Modified MAP MMAF Bias Error,SNR=10, P_m =0.30,at t_i^+ . .	F-32
Figure F.4.1	2.01 μ m Two-State Modified MAP MMAF Offset Error,SNR=4, P_m =0.0	F-34
Figure F.4.2	2.01 μ m Two-State Modified MAP MMAF Offset Error,SNR=4, P_m =0.0, at t_i^- . . .	F-34
Figure F.4.3	2.01 μ m Two-State Modified MAP MMAF Offset Error,SNR=4, P_m =0.0,at t_i^+	F-35
Figure F.4.4	2.01 μ m Two-State Modified MAP MMAF Bias Error,SNR=4, P_m =0.0	F-35

Figure F.4.5	2.01 μm Two-State Modified MAP MMAF Bias Error, SNR=4, $P_m=0.0$, at t_i^-	F-36
Figure F.4.6	2.01 μm Two-State Modified MAP MMAF Bias Error, SNR=4, $P_m=0.0$, at t_i^+	F-36
Figure F.4.7	2.01 μm Two-State Modified MAP MMAF Offset Error, SNR = 4, $P_m = 0.05$. . .	F-37
Figure F.4.8	2.01 μm Two-State Modified MAP MMAF Offset Error, SNR=4, $P_m=0.05$, at t_i^- . . .	F-37
Figure F.4.9	2.01 μm Two-State Modified MAP MMAF Offset Error, SNR=4, $P_m=0.05$, at t_i^+ . . .	F-38
Figure F.4.10	2.01 μm Two-State Modified MAP MMAF Bias Error, SNR = 4, $P_m = 0.05$. . .	F-38
Figure F.4.11	2.01 μm Two-State Modified MAP MMAF Bias Error, SNR=4, $P_m=0.05$, at t_i^- . . .	F-39
Figure F.4.12	2.01 μm Two-State Modified MAP MMAF Bias Error, SNR=4, $P_m=0.05$, at t_i^+ . . .	F-39
Figure F.4.13	2.01 μm Two-State Modified MAP MMAF Offset Error, SNR = 4, $P_m = 0.30$. . .	F-40
Figure F.4.14	2.01 μm Two-State Modified MAP MMAF Offset Error, SNR=4, $P_m=0.30$, at t_i^- . .	F-40
Figure F.4.15	2.01 μm Two-State Modified MAP MMAF Offset Error, SNR=4, $P_m=0.30$, at t_i^+ . .	F-41
Figure F.4.16	2.01 μm Two-State Modified MAP MMAF Bias Error, SNR = 4, $P_m = 0.30$	F-41
Figure F.4.17	2.01 μm Two-State Modified MAP MMAF Bias Error, SNR=4, $P_m=0.30$, at t_i^- . . .	F-42
Figure F.4.18	2.01 μm Two-State Modified MAP MMAF Bias Error, SNR=4, $P_m=0.30$, at t_i^+ . . .	F-42
Figure F.5.1	10.5 μm Two-State Modified MAP MMAF Offset Error, SNR=10, $P_m=0.0$	F-44
Figure F.5.2	10.5 μm Two-State Modified MAP MMAF Offset Error, SNR=10, $P_m=0.0$, at t_i^- . .	F-44
Figure F.5.3	10.5 μm Two-State Modified MAP MMAF Offset Error, SNR=10, $P_m=0.0$, at t_i^+ . . .	F-45
Figure F.5.4	10.5 μm Two-State Modified MAP MMAF Bias Error, SNR=10, $P_m=0.0$	F-45
Figure F.5.5	10.5 μm Two-State Modified MAP MMAF Bias Error, SNR=10, $P_m=0.0$, at t_i^- . . .	F-46
Figure F.5.6	10.5 μm Two-State Modified MAP MMAF Bias Error, SNR=10, $P_m=0.0$, at t_i^+	F-46
Figure F.5.7	10.5 μm Two-State Modified MAP MMAF Offset Error, SNR = 10, $P_m = 0.05$. .	F-47
Figure F.5.8	10.5 μm Two-State Modified MAP MMAF Offset Error, SNR=10, $P_m=0.05$, at t_i^- . .	F-47
Figure F.5.9	10.5 μm Two-State Modified MAP MMAF Offset Error, SNR=10, $P_m=0.05$, at t_i^+ . .	F-48
Figure F.5.10	10.5 μm Two-State Modified MAP MMAF Bias Error, SNR = 10, $P_m = 0.05$. . .	F-48

Figure F.5.11	10.5 μm Two-State Modified MAP MMAF Bias Error, SNR=10, $P_m=0.05$, at t_i^- . .	F-49
Figure F.5.12	10.5 μm Two-State Modified MAP MMAF Bias Error, SNR=10, $P_m=0.05$, at t_i^+ . .	F-49
Figure F.5.13	10.5 μm Two-State Modified MAP MMAF Offset Error, SNR = 10, $P_m = 0.30$. .	F-50
Figure F.5.14	10.5 μm Two-State Modified MAP MMAF Offset Error, SNR=10, $P_m=0.30$, at t_i^- .	F-50
Figure F.5.15	10.5 μm Two-State Modified MAP MMAF Offset Error, SNR=10, $P_m=0.30$, at t_i^+ .	F-51
Figure F.5.16	10.5 μm Two-State Modified MAP MMAF Bias Error, SNR = 10, $P_m = 0.30$. . .	F-51
Figure F.5.17	10.5 μm Two-State Modified MAP MMAF Bias Error, SNR=10, $P_m=0.30$, at t_i^- . .	F-52
Figure F.5.18	10.5 μm Two-State Modified MAP MMAF Bias Error, SNR=10, $P_m=0.30$, at t_i^+ . .	F-52
Figure F.6.1	10.5 μm Two-State Modified MAP MMAF Offset Error, SNR=4, $P_m=0.0$	F-54
Figure F.6.2	10.5 μm Two-State Modified MAP MMAF Offset Error, SNR=4, $P_m=0.0$, at t_i^- . . .	F-54
Figure F.6.3	10.5 μm Two-State Modified MAP MMAF Offset Error, SNR=4, $P_m=0.0$, at t_i^+	F-55
Figure F.6.4	10.5 μm Two-State Modified MAP MMAF Bias Error, SNR=4, $P_m=0.0$	F-55
Figure F.6.5	10.5 μm Two-State Modified MAP MMAF Bias Error, SNR=4, $P_m=0.0$, at t_i^-	F-56
Figure F.6.6	10.5 μm Two-State Modified MAP MMAF Bias Error, SNR=4, $P_m=0.0$, at t_i^+	F-56
Figure F.6.7	10.5 μm Two-State Modified MAP MMAF Offset Error, SNR = 4, $P_m = 0.05$. . .	F-57
Figure F.6.8	10.5 μm Two-State Modified MAP MMAF Offset Error, SNR=4, $P_m=0.05$, at t_i^- . . .	F-57
Figure F.6.9	10.5 μm Two-State Modified MAP MMAF Offset Error, SNR=4, $P_m=0.05$, at t_i^+ . . .	F-58
Figure F.6.10	10.5 μm Two-State Modified MAP MMAF Bias Error, SNR = 4, $P_m = 0.05$. . .	F-58
Figure F.6.11	10.5 μm Two-State Modified MAP MMAF Bias Error, SNR=4, $P_m=0.05$, at t_i^- . . .	F-59
Figure F.6.12	10.5 μm Two-State Modified MAP MMAF Bias Error, SNR=4, $P_m=0.05$, at t_i^+ . . .	F-59
Figure F.6.13	10.5 μm Two-State Modified MAP MMAF Offset Error, SNR = 4, $P_m = 0.30$. . .	F-60
Figure F.6.14	10.5 μm Two-State Modified MAP MMAF Offset Error, SNR=4, $P_m=0.30$, at t_i^- . .	F-60
Figure F.6.15	10.5 μm Two-State Modified MAP MMAF Offset Error, SNR=4, $P_m=0.30$, at t_i^+ . .	F-61
Figure F.6.16	10.5 μm Two-State Modified MAP MMAF Bias Error, SNR = 4, $P_m = 0.30$	F-61

Figure F.6.17	10.5 μ m Two-State Modified MAP MMAF Bias Error, SNR=4, $P_m=0.30$, at t_i^- . . .	F-62
Figure F.6.18	10.5 μ m Two-State Modified MAP MMAF Bias Error, SNR=4, $P_m=0.30$, at t_i^+ . . .	F-62
Figure G.1.1	RMS Errors for $P_m = 0.0$ at t_i^+	G-4
Figure G.1.2	RMS Errors for $P_m = 0.01$ at t_i^+	G-5
Figure G.1.3	RMS Errors for $P_m = 0.05$ at t_i^+	G-6
Figure G.1.4	RMS Errors for $P_m = 0.10$ at t_i^+	G-7
Figure G.1.5	RMS Errors for $P_m = 0.20$ at t_i^+	G-8
Figure G.1.6	RMS Errors for $P_m = 0.30$ at t_i^+	G-9
Figure G.1.7	RMS Errors for $P_m = 0.0$ at t_i^-	G-10
Figure G.1.8	RMS Errors for $P_m = 0.01$ at t_i^-	G-11
Figure G.1.9	RMS Errors for $P_m = 0.05$ at t_i^-	G-12
Figure G.1.10	RMS Errors for $P_m = 0.10$ at t_i^-	G-13
Figure G.1.11	RMS Errors for $P_m = 0.20$ at t_i^-	G-14
Figure G.1.12	RMS Errors for $P_m = 0.30$ at t_i^-	G-15
Figure G.2.1	RMS Errors for SNR = 10 at t_i^+	G-17
Figure G.2.2	RMS Errors for SNR = 8 at t_i^+	G-18
Figure G.2.3	RMS Errors for SNR = 6 at t_i^+	G-19
Figure G.2.4	RMS Errors for SNR = 4 at t_i^+	G-20
Figure G.2.5	RMS Errors for SNR = 10 at t_i^-	G-21
Figure G.2.6	RMS Errors for SNR = 8 at t_i^-	G-22
Figure G.2.7	RMS Errors for SNR = 6 at t_i^-	G-23
Figure G.2.8	RMS Errors for SNR = 4 at t_i^-	G-24

List of Tables

Table 1.1	Kalman Filter and Correlation Tracker Statistics Comparison	1-6
Table 5.1	Two-State Modified MAP MMAF Tuning Statistics	5-35
Table 6.1	Offset Distance Statistics of One-State Speckle Return Filter	6-4
Table 6.2	Values of Parameter Variations	6-7
Table 6.3	Measurement Noise Variances for Transmitted Wavelength and SNR	6-7
Table 6.4	One-State Doppler Filter Error Statistics (in Pixels)	6-10
Table 6.5	One-State Speckle Return Filter Statistics Without Plume Reflectance	6-12
Table 6.6	Two-State Modified MAP MMAF Offset Error Statistics for Case 1 (in Pixels)	6-15
Table 6.7	Two-State Modified MAP MMAF Offset Error Statistics for Case 2 (in Pixels)	6-18
Table D.1	Tuning Values for Dynamics Noise Variances (in Pixels ²)	D-4
Table H.1	One-State Doppler Filter Offset Error Statistics (in Pixels)	H-4
Table H.2	Two-State Modified MAP MMAF Offset Error Statistics (in Pixels) for Case 1	H-11
Table H.3	Two-State Modified MAP MMAF Offset Error Statistics (in Pixels) for Case 2	H-18

Abstract

For thirteen years, the Air Force Institute of Technology (AFIT) has been engaged in studying the applicability of the Kalman filter to locate and track airborne targets precisely. A majority of the research explored linear, extended (nonlinear) filters and multiple model adaptive filter structures in conjunction with an enhanced correlator tracker to estimate the position and velocity of the target exhaust plume. The tracking concept centers upon the use of a forward-looking infrared sensor (FLIR) to detect the intensity centroid of the target plume. Raw FLIR data is provided to an enhanced correlator algorithm that generates linear elevation and azimuth FLIR image plane offsets as "measurements" for the Kalman filter. In comparison to conventional correlation trackers, the AFIT Kalman filter tracker yields superior performance in both short and long range tracking scenarios with target trajectories that range from benign to highly dynamic maneuvers up to 20 g's. With the tracking problem of the exhaust plume resolved, recent AFIT theses have shifted attention to tracking the missile hardbody and locating its center-of-mass.

Beginning in 1989, research efforts to locate the hardbody center-of-mass used a low-energy laser to actively illuminate the hardbody. A low-energy scan would originate at the estimated position of the target plume's intensity centroid, and continue along the target's estimated velocity vector to intercept the hardbody. The hardbody's dimensions would be apparent from the low-energy laser speckle return of the hardbody, upon which the location of the center-of-mass can be derived. However, plume phenomenology experiments in 1990 uncovered the existence of plume speckle reflectance emanating from the exhaust of a solid-propellant rocket motor (due to the presence of metallic particulates) that made the plume/hardbody interface

difficult to discern. In view of this shortcoming of the low-energy speckle return, the Phillips Laboratory requested AFIT to explore the feasibility of using the Doppler phenomenon to locate the hardbody.

The potential of the Doppler phenomenon's utilization in the AFIT tracking scenario lies in the fact that the Doppler return frequency spectra of the plume and the hardbody respectively possess distinct properties and are differentiable from each other. The plume and missile hardbody have opposite velocity vectors which result in opposite Doppler shifts. In addition, the frequency spectrum bandwidth of the plume-induced Doppler return has been observed to be *significantly* broader than that of the hardbody-induced Doppler return spectrum, due to the diverse velocity orientations of the numerous particulates in the plume. Hence, these differences can be exploited in the attempt to discern the plume/hardbody interface.

This thesis investigates the feasibility of employing the Doppler return phenomenon in discerning the plume/hardbody interface and locating the hardbody center-of-mass. To accomplish this objective, a Doppler return model is developed that also incorporates a probability-of-miss parameter that represents instances when the target aspect angle approaches an orientation that results in no Doppler shift of either plume or hardbody, as well as representing bending of the low-energy laser by atmospheric effects so that the hardbody is not actually intercepted. Doppler return measurement noise variances are determined as a function of laser transmitted wavelength and signal-to-noise ratio. The speckle return model is also modified to include the effects of the plume speckle reflectance. For this study, two center-of-mass Kalman filters are developed to receive the Doppler return measurements: a one-state filter and two-state Modified Maximum a Posteriori Multiple Model Adaptive filter (MAP MMAF). The two-state Modified MAP MMAF receives both speckle and Doppler return measurements and uses the speckle return measurement

to compensate for occurrences of no Doppler shift measurement. A sensitivity analysis is conducted wherein the performances of the one-state filter and two-state filter are evaluated with variations in transmitted wavelength, signal-to-noise (SNR), and probability-of-miss. Results show the center-of-mass filters are sensitive to increases in probability-of-miss, whereas decreases in SNR produced insignificant degradation in performance. The two-state Modified MAP MMAF achieves the best performance, and clearly has the potential to accomplish the task of locating and tracking the hardbody center-of-mass.

KALMAN FILTERING OF A REFLECTIVE TARGET USING FORWARD-LOOKING INFRARED AND DOPPLER RETURN MEASUREMENTS

I. Introduction

The concept of a defensive posture capable of nullifying a ballistic missile attack has had worldwide ramifications. One can point to the recent dynamic changes in the Soviet-US Arms Control Treaty and progress in the Strategic Arms Reduction Talks as attributable to the US government's commitment to Strategic Defense Initiative (SDI) research [1]. During the Desert Storm operation, the world watched the success of the ground-based Patriot ballistic missile defense system under actual war conditions. Still, technology issues continue to challenge the scientific and engineering community regarding, in particular, the space-based contingent of SDI.

Of paramount concern is locating and tracking the ballistic target in the presence of its plume and atmospheric background, whether the mode of intercept is achieved by kinetic or direct energy means. Only the autonomous and precise tracking of the target over long ranges, can ensure that these space-based anti-ballistic weapon systems achieve the goals of SDI.

This research, in conjunction with prior studies, addresses the intricacies of locating and discerning the missile hardbody in the presence of its plume. It probes the feasibility of employing Doppler frequency spectrum returns as a means of discerning the missile hardbody/plume interface. Conventional tracking techniques, using a laser illuminator and measuring the speckle return, have shown that the plume reflectance of a solid-propellant rocket

motor is of the same magnitude as that of the hardbody [2]. This condition causes an ambiguity in the position of the hardbody with respect to the plume. At the plume/hardbody interface, a unique Doppler function is expected and may, therefore, be used to define that interface precisely.

1.1 Background

For the past thirteen years, the Air Force Institute of Technology (AFIT) has been engaged in the research and development of long and short range ballistic target trackers under the sponsorship of the Phillips Laboratory (formerly the Air Force Weapons Laboratory/AWFL) at Kirtland Air Force Base, New Mexico [5-7,10-12,14,21-25,27,29,32,33,35-37,40-43]. Central to these trackers is a 300 x 500 pixel array Forward-Looking Infrared (FLIR) sensor which passively detects the infrared radiation emitted by the missile plume. Each pixel in the array detects infrared energy through an angle of 15 microradians in two orthogonal directions (azimuth and elevations)[35]. The array utilizes an 8 x 8 pixel sub-array field-of-view (FOV) as a window for tracking purposes [33,35].

Information from the excited 8 x 8 FOV is provided to an enhanced image correlator algorithm that produces position offsets as pseudo-measurements to a linear Kalman filter. In the Fourier domain, the enhanced correlator algorithm correlates the current raw FLIR data frame with a template that represents an estimate of the target plume's intensity function. Two linear position offsets, x_c and y_c , are created that yield maximum correlation of the current data and the template. The Kalman filter treats these offsets as measurements and computes optimum estimates of the position offsets and furnishes these estimates to a pointing controller that centers the plume centroid in the FOV. Since the high-energy laser is optically boresighted with the FLIR FOV, the laser continuously points to the target's estimated position.

Previous research concentrated upon tracking the plume centroid while the target exhibits benign trajectories to harsh dynamic target maneuvers up to 20 g's. However, the intended target for the laser is the missile hardbody, which cannot be distinguished solely from information provided by the FLIR measurements. Thus, the two most recent theses [5,6] have focused upon locating and discerning the missile hardbody utilizing the speckle return of a low-energy laser. These returns are fed as additional inputs to the Kalman filter algorithm in order to estimate the hardbody center-of-mass as well as the infrared target image centroid.

Prior to AFIT research into the Kalman filter algorithm, AWFL utilized a standard correlation algorithm to perform the tracking function. This algorithm cross-correlates the FLIR image with a previously sampled image to generate position offsets, assuming that a translation in the image corresponds to a spatial translation of the target. The advantage of the correlation algorithm is that it does not require a priori knowledge of the type of target and is therefore a robust tracker. However, it does have several shortcomings.

First, the correlation algorithm inherently neglects any knowledge of the target type, shape, and motion characteristics. This *a priori* information may be exploited to estimate the target position adaptively and enhance tracker performance. Second, computation of the correlation function and subsequent pointing of the tracker produces a finite time lag. Lastly, the correlation tracker is unable to distinguish between true target motion and "apparent" target motion caused by identifiable disturbances such as atmospheric jitter [27], distorted wavefronts of the inbound IR energy, vibration/bending of the platform and optical system [12], and missile plume "pogo" effects [35].

These deficiencies of the correlation tracker have been resolved by incorporating Kalman filtering methodology [5,6,8,10,11,12,14,27,29,32,33,35,36,37,40,41]. By developing accurate models of the disturbances mentioned above, the Kalman filter assigns the appropriate weight to the FLIR data to yield the optimum estimate of the target's position. Furthermore, *a priori* knowledge of the target type, shape, and dynamic characteristics are modelled and incorporated in the Kalman filter algorithm. This target model is propagated forward in time to establish an estimate of the target's future position for use in laser pointing and target tracking.

1.2 Summary of Previous AFIT Research

Beginning in 1978, AFIT has been engaged in research investigating the use of Kalman filtering techniques for ballistic missile and other airborne target tracking. As a result, there exist numerous papers and theses devoted to this area of study. By far, the majority of this research lies in sixteen previous theses accomplished by AFIT graduate students. As a stand-alone document, each thesis contains an overview of previous theses. The overview presented by Roger Evans [6] is noted for its completeness and is reproduced for this section.

Research in this area was initiated by Mercier [27] in 1978, who compared the extended Kalman filter (EKF) performance to that of the AWFL correlation tracker under identical conditions. An eight-state truth model was developed for simulation purposes, consisting of two target position states and six atmospheric jitter states. The position states defined the target location in each of two FLIR plane coordinate directions (azimuth and elevation), by accurately portraying target trajectories in three-dimensional space and projecting onto the FLIR plane. The atmospheric jitter was modeled by a third order shaping filter driven by white noise for each FLIR plane axis, as provided by The Analytic Sciences Corporation (TASC) [17]; three states defined

the atmospheric distortion in each of the two FLIR plane coordinate directions. The Kalman filter dynamics model consisted of four states: two states representing target position, and two representing the atmospheric jitter (based on reduced order models, versus the six states of the truth model). In both the truth model and filter dynamics model, the position states and atmospheric jitter states were defined in each of the two FLIR plane coordinate directions. In the filter, the position and jitter states were each modeled as a first-order, zero-mean, Gauss-Markov process. The FLIR provided sampled data measurements to the filter at a 30 Hertz (Hz) rate. The FLIR measurement noise due to background clutter effects and internal FLIR noises were modeled in the filter as both temporally and spatially uncorrelated. The target was considered as a point source of light (i.e., a long range target) having benign dynamics. The corresponding Airy disc on the FLIR image plane was modeled as a bivariate Gaussian distribution with circular equal intensity contours. The conventional correlation tracker and the extended Kalman filter were compared across three different signal-to-noise ratios (SNR), using a ten-run Monte Carlo analysis to obtain the tracker error statistics. The results of the comparison are shown in Table 1.1 for a Gaussian intensity function dispersion, σ_p , equal to one pixel. (For a Gaussian intensity function dispersion equal to one pixel, most of the useful information is contained in an area of about five pixels square.)

While the correlation tracker showed dramatic performance degradation as the SNR was decreased, the Kalman filter showed only a minor change in its performance at the lowest SNR tested. The extended Kalman filter was shown to be superior to the correlation tracker by an order of magnitude in the root mean square (rms) tracking error, provided the models incorporated into the filter were a valid depiction of the tracking scenario. This success motivated a follow-on thesis to improve filter modeling and thereby to enhance the performance.

Table 1.1 Kalman Filter and Correlation Tracker Statistics Comparison

Signal-to Noise Ratio	Correlation Tracker		Extended Kalman Filter	
	Mean Error	1 σ	Mean Error	1 σ
20	7.0	8.0	0.0	0.2
10	8.0	10.0	0.0	0.2
1	15.0	30.0	0.0	0.8

The research accomplished by Harnly and Jenson [10,21] investigated modeling improvements in the filter and tested more dynamic target simulations. A comparison was made between a new six-state filter and a new eight-state filter. The six-state filter dynamics target model included the four previous states as well as two velocity states in the FLIR plane coordinates (azimuth and elevation); the dynamics model of the eight-state filter included two acceleration states in the FLIR coordinates as well. The acceleration was modeled as Brownian motion (BM) ($\dot{a} = w$, where w is a zero-mean white Gaussian noise). The filter was also designed to perform residual monitoring, which allowed the filter to react adaptively, and maintain track, by quickly increasing the covariance values in the filter-computed P matrix, which in turn increased the filter gain K . A recommendation was also made to examine increasing the FOV during target jinking maneuvers to avoid losing lock. The constant-intensity contours of the target were modeled as elliptical patterns as opposed to the earlier circular equal-intensity contours in order to simulate closer range targets. The major axis of the target FLIR image was aligned with the estimated velocity vector. A number of different target trajectories were tested against the six-

state and eight-state filters, and while the six-state filter performed well during moderate jinking maneuvers, the eight-state filter performed better while tracking high-g target maneuvers.

Other approaches to modeling the dynamics of the target in the filter were considered by Flynn [8]. He used a Brownian motion (BM) acceleration target dynamics model [10] and a constant turn-rate (CTR) dynamics model. The CTR model portrayed the target behavior by modeling the acceleration as that associated with CTR dynamics. Concatenating such constant turn-rate segments together provides an accurate portrayal of manned target evasive maneuver trajectories. Additionally, a Bayesian multiple model adaptive filter (MMAF) was developed using the BM dynamics model. A MMAF (Figure 1.1) consists of a bank of K independent Kalman filters, each of which is tuned to a specified target dynamics characteristic or parameter (a_1, a_2, \dots, a_K in Figure 1.1). The time histories of the residuals ($r_k(t)$ in Figure 1.1) of these K Kalman filters are processed to compute the conditional probability ($p_k(t)$ in Figure 1.1) that each discrete parameter value is "correct." The residuals of the Kalman filter, based upon the "correct" model, are expected to be consistently smaller (relative to the filter's internally computed residual rms values) than the residuals of the other mismatched filters (i.e., based upon "incorrect" models) [8]. If that is true, then the MMAF algorithm appropriately weights that particular Kalman filter more heavily than the other Kalman filters. These values are used as weighting coefficients to produce a probability-weighted average of the elemental filter outputs [8]. Therefore, the state estimate ($\hat{x}_{mmaf}(t_i)$ in Figure 1.1) is actually the probabilistically weighted average of the state estimates generated by each of the K separate Kalman filters ($\hat{x}_k(t_i)$ in Figure 1.1). Testing of the three filter models was conducted for three different flight trajectories which included 2-g, 10-g, and 20-g pull-up maneuvers. Unfortunately, the residuals of the K Kalman filter did not differ from each other enough to perform the weighting function properly, and MMAF did not track

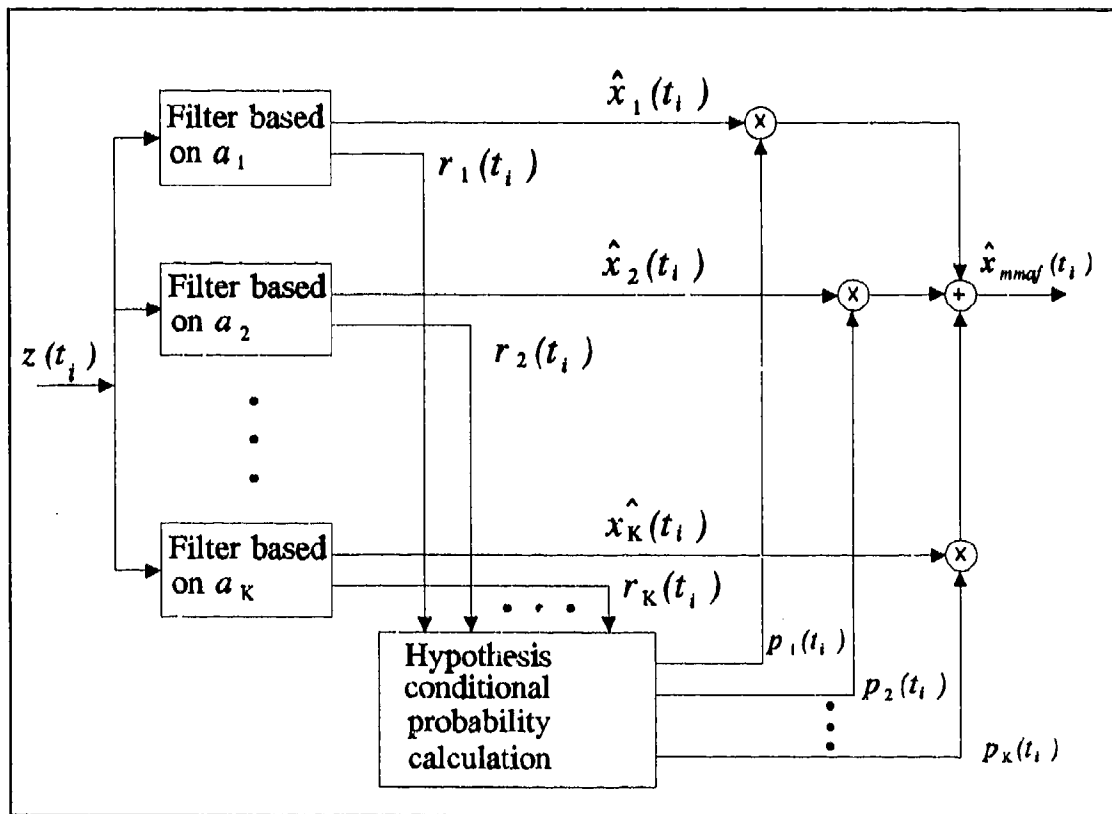


Figure 1.1 Multiple Model Adaptive Filter

well. The BM and CTR filters both performed equally well at 2-g's. The CTR filter was found to be substantially better than the BM filter for 10-g and 20-g pull-up maneuvers.

Mercier had assumed that the filter had *a priori* knowledge of the target shape and intensity profile. Singletery [37] improved the realism in the target model by developing a model in the FLIR plane which included multiple hot spots. However, he returned to the case of very benign targets. The filter did not assume *a priori* knowledge of the target size, shape, or location. A new data processing scheme (Figure 1.2) was developed which included the use of the Fast Fourier Transform (FFT) and the Inverse Fast Fourier Transform (IFFT), each of which can be produced with a lens if optical processing is used. The plan included two data paths for

processing the intensity measurements $z(t_i)$. On the first path, the 8×8 array of intensity measurements from the FLIR are arranged into a 64-dimensional measurement vector. This measurement vector is applied to the extended Kalman filter (as in prior work). The purpose of the second path is to provide centered target shape functions to be time-averaged with previous centered shape functions in order to generate the estimated target template (h in Figure 1.2) and partial derivatives of it with respect to the states (H in Figure 1.2), as needed by the extended Kalman filter. This invokes the shifting theorem of Fourier transforms. The shift theorem states that a translation of an image in the spatial domain results in a linear phase shift in the spatial frequency domain. To negate the translational effects of an uncentered target image in the spatial

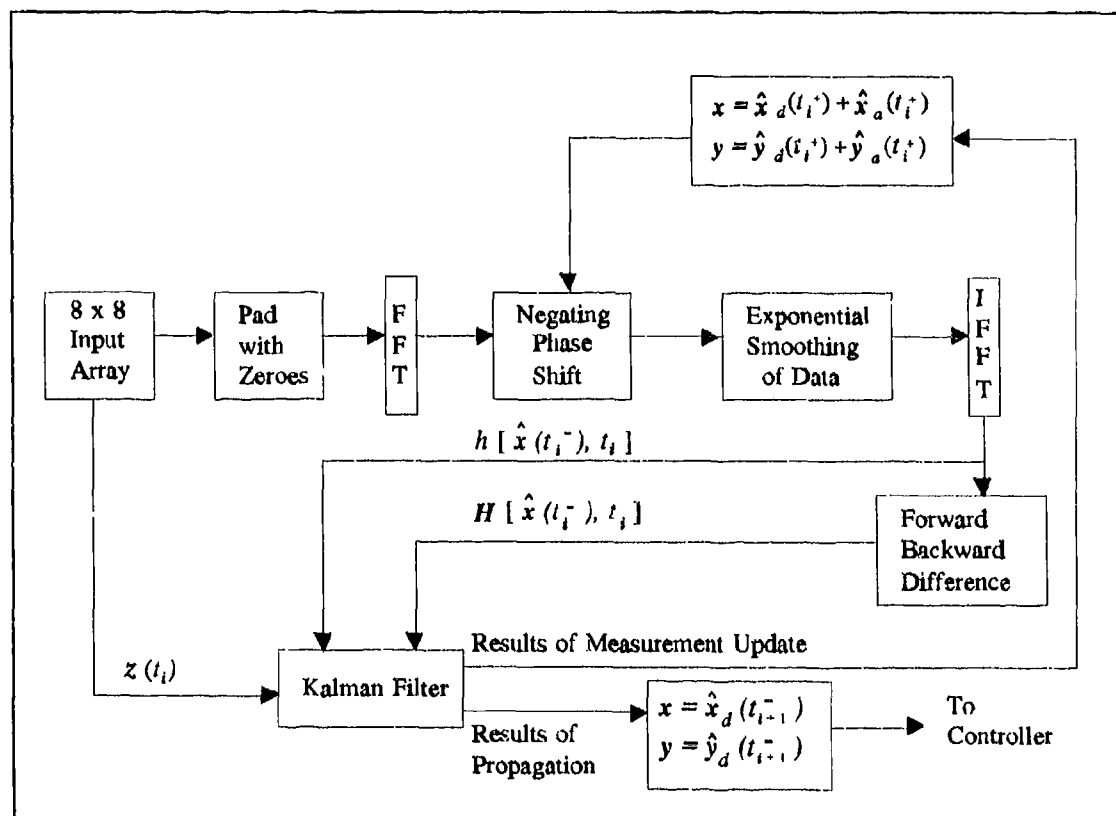


Figure 1.2 Data Processing Scheme using FFT and IFFT

domain, the Fourier transform of the translated image is multiplied by the complex conjugate of the desired linear phase shift [37]. The extended Kalman filter model, in path one, which was developed by Mercier [27], was used to provide the optimal estimate of the linear translation. The filter state estimates are used to develop the complex conjugate of the linear phase shift and provide the centered measurement functions. Before the IFFT is taken, the resulting pattern is exponentially smoothed to yield an approximation to averaging the result with previously centered frames of data, to minimize the effect of measurement noise. The result is a centered pattern with noise effects substantially reduced. Following the application of the IFFT to form the nonlinear function of intensity measurements (h of Figure 1.2), the spatial derivative is used to determine the linearized function of intensity measurements (H of Figure 1.2). These are both used by the Kalman filter in processing the next sampled measurement [37]. The results of this data processing scheme were inconclusive due to filter divergence problems. Despite the problems encountered with the filter, the concept was considered to have filter performance potential.

Rogers [36] continued the work of developing a Kalman filter tracker which could handle multiple-hotspots with no *a priori* information as to the size, shape, intensity, or location of the target. However, he continued the application to benign target motion, as Singletary [37] had done before, in order to concentrate on the feasibility of adaptively identifying the target shape. Using digital signal processing on the FLIR data (as described above) to identify the target shape, the filter uses the information to estimate target offset from the center of the FOV, which in turn drives a controller to center the image in the FLIR plane. Algorithm improvements included replacing the Forward-Backward Difference block of Figure 1.2 with a partial differentiation operation accomplished as a simple multiplication before the IFFT block.

Rogers also considered an alternative design that used the target image h (as generated in Figure 1.2) as a template for an enhanced correlator, as shown in Figure 1.3. The position offsets produced as outputs from the correlator were then used as "pseudo-measurement" inputs to a linear Kalman filter. The improved correlation algorithm of Figure 1.3 compares the FLIR image to an estimated template instead of the previous image, as is done in the standard correlator. This tracking concept is thus a hybrid of correlation tracking and Kalman filtering [36]. Its performance was compared to the results of earlier extended Kalman filters that used the raw FLIR data as measurements [10]. Although the extended Kalman filter performed well without *a priori* knowledge of the shape and location of the intensity centroid, the improved correlator

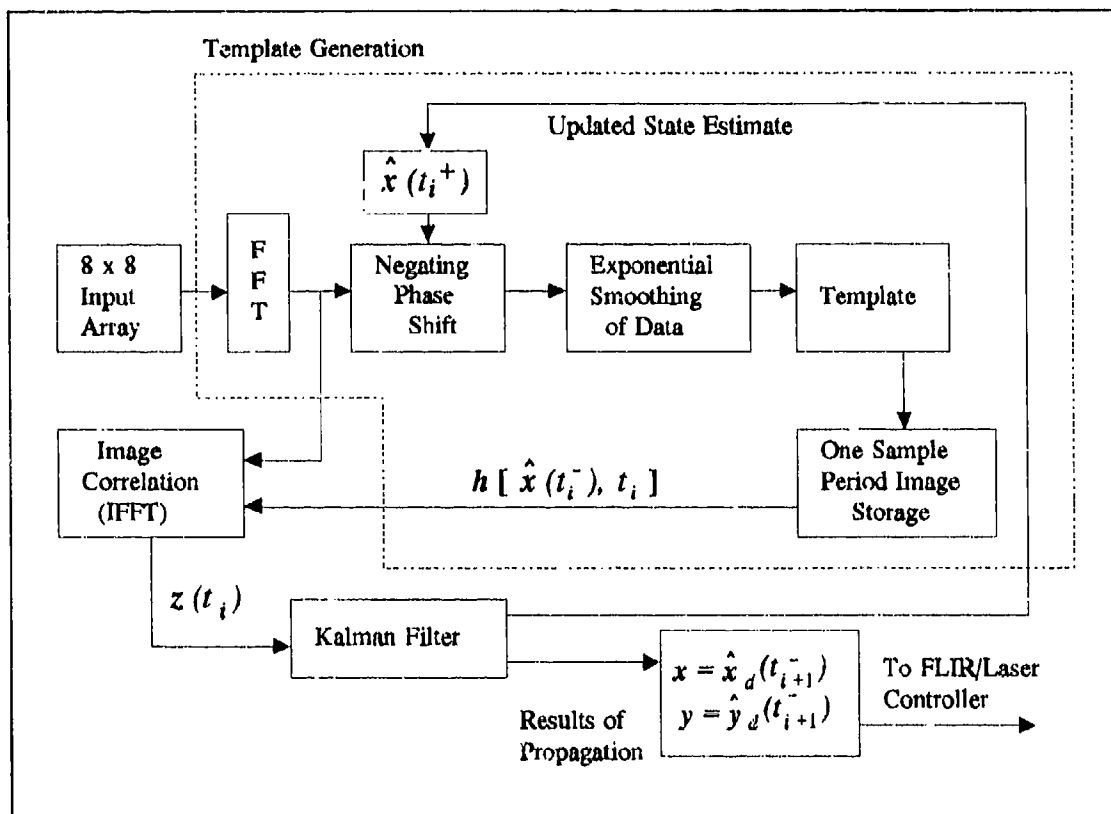


Figure 1.3 Linear Kalman Filter/Enhanced Correlator Algorithm

used with the linear Kalman filter outperformed the extended Kalman filter while providing reduced computational loading.

Millner [29] and Kozemchak [11] tested an extended Kalman filter and the linear Kalman filter/enhanced correlation algorithm against close range, highly maneuverable targets. The linear four-state filter used in the previous research was replaced by an eight-state filter consisting of position, velocity, acceleration, and atmospheric jitter states in the two coordinates of the FLIR plane (azimuth and elevation). Two target dynamics models were also developed. The target was first modeled as a first-order Gauss-Markov acceleration process, and secondly with a constant turn-rate model. Both filters performed well without *a priori* knowledge of the target size, shape, and location, using the FFT data processing method for identifying the target shape function [36,37]. However, at maneuvers approaching 5-g's, the filter performance degraded considerably. It was noted that the tracking was substantially better when the Kalman filter dynamics model closely matched the target trajectory.

The Bayesian MMAF technique [8] was reinvestigated by Suizu [40] based on the recommendations of the previous work. The MMAF (Figure 1.1) consisted of two elemental Kalman filters. One elemental filter was tuned for benign target maneuvers and obtained sampled measurement information from an 8 x 8 pixel FOV in the FLIR plane. A second filter was tuned for dynamic maneuvers and obtained sampled measurement information from a 24 x 24 pixel FOV in the FLIR plane. The technique allowed the MMAF to maintain track on benign target trajectories up to 20-g's at a distance of 20 kilometers. The MMAF was configured for both the linear Kalman filter/enhanced correlation algorithm [36] and the extended Kalman filter. Both filtering schemes exhibited comparable rms tracking performance results, with the correlator/linear

Kalman filter having smaller mean errors and larger standard deviations than the extended Kalman filter, as seen in earlier work of Rogers [36]. The state rms tracking error was on the order of 0.2 to 0.4 pixels (one pixel being equivalent to 20 μ rad on a side).

The potential of the MMAF technique with the FFT processing method was continued by Loving [14]. A third filter was added to the bank of filters, tuned for intermediate target maneuvers and obtaining sampled measurement information from the 8 x 8 FOV in the FLIR plane. This MMAF showed significant performance advantages over all the previous filters. Additionally, a Maximum A Posteriori (MAP) algorithm was developed and compared with the Bayesian MMAF. The MAP algorithm differs from the Bayesian MMAF in that the MAP algorithm uses the residuals of the separate filters to select the one filter with the highest probabilistic validity, while the Bayesian MMAF uses a probability-weighted average of all filters in the bank. The Bayesian and the MAP techniques produced similiar results and delivered performance that surpassed previous filters.

Netzer [32] expanded the study of the MMAF algorithm. He investigated a steady-state bias error that resulted when tracking a target exhibiting a high-g constant turn-rate maneuver. A major cause of this bias is the MMAF mistuning the x -direction (azimuth) while maintaining lock on the highly dynamic y -direction (elevation) transient. This motivates the concept of individual x - and y -channel target-motion filters in the MMAF, which would allow adaptive filtering for maneuvers in the x - and y -channels independently [32]. The size of the FOV was also investigated. When a target came to within five kilometers of the FLIR platform, the 8 x 8 FOV was saturated with the intensity centroid image, resulting in a loss of track. This analysis motivates a changing FOV to maintain lock for targets and also warrants the possibility of adding

another Kalman filter which is tuned for extremely harsh manuevers at close ranges. A study of the aspect ratio (AR) associated with target's intensity centroid was also accomplished to identify filter tracking characteristics for various target image functions [32]. This study used "greyscale plots" to support the analysis. A greyscale plot is a pictorial display of an image in which shading of the image is used to indicate similar parameters. In this case, the plot indicates regions of varying levels of the intensity of the filter-reconstructed target image in a 24 x 24 pixel FOV. Four different AR values of 0.2, 0.5, 5, and 10 were compared to the nominal AR of 1. The results showed that tracking was slightly impaired for images with AR as high as 5. The reduced performance is primarily along the semi-major axis of an elliptically modeled intensity centroid. Additionally, a target-decoy experiment was conducted in which a high density decoy was also located in the FOV with the target. Since the decoy was modeled with different dynamics not given to the filter, it was hoped that the filter would reject the decoy. This was not the case; the filter locked onto the hotter decoy image. This indicates that the inability of the current filter algorithm to reject this type of bright hotspot requires isolating the target image in a small FOV or some other concept to ensure tracking of the desired target.

The previous research efforts [14,32,40] used Gauss-Markov acceleration models in the development of the MMAF. Tobin [41] implemented the CTR dynamics model in another MMAF. His results showed that the Gauss-Markov MMAF exhibited smaller bias errors while the CTR MMAF gave smaller steady state standard deviation errors; both filters had comparable rms errors. Motivated by earlier research [32], he also developed an 8 x 24 pixel FOV for both the x- and y-directions of the FLIR image plane to be used with filters designed to anticipate harsh target accelerations in a specific direction (along which the longer side of the FOV would be oriented). The results showed that the filter maintained lock on a target during a highly dynamic

maneuver in the y -direction while maintaining substantially better steady state bias performance in the benign x -direction.

Leeney [12] expanded the previous used Gauss-Markov truth model by incorporating bending vibrational states. The elemental filters in the MMAF were not modeled with this information through explicit state variables, but performed well up to a 10-g maneuver. A performance investigation was also conducted as to the effects of increasing the measurement update rate from the previously used 30 Hz to 50 Hz. The sampling rate of 50 Hz showed a minor performance improvement, but also increased the computational loading because of the higher rate. A preliminary study was also done on replacing the 8 x 24 pixel FOV in the x - and y -directions [41] on the FLIR plane with a single 8 x 24 pixel FOV, which is also known as the rotating rectangular-field-of-view (RRFOV). The idea was to align the long side of the rectangular FOV with an estimate of the acceleration vector. The higher precision velocity estimate was actually used instead of the noisier acceleration estimate, and it was assumed that the acceleration direction would be essentially orthogonal to the velocity vector direction. Additionally, the five elemental Kalman filters in the MMAF bank would be reduced to four by using this FOV rotation scheme. The results were not conclusive, but the insight provided motivation to continue the study.

The RRFOV research was continued by Norton [33]. He discovered that the appropriate choice of the filter dynamics driving noise strength Q dictated the filter's response to a high-g jinking maneuver, and that the size of the FOV could be reduced to an 8 x 8 pixel rotating FOV, also known as the rotating square field of view (RSFOV). His investigation showed that a non-rotating square FOV could provide good performance, but that the dynamics noise strength Q

matrix value must be large in the elements corresponding to the direction of the acceleration vector. A mathematical matrix transformation was developed which rotated the Q matrix to keep the larger values aligned with the acceleration vector. A study of both the rotating FOV and rotating the Q matrix provided advantages and disadvantages for each method. Both methods are affected by the tuning parameters used to represent the rms level of acceleration of the target, which also contributes to error biases. The rotating FOV improves the x -direction (azimuth) estimation for dominant y -direction (elevation) dynamics from previous MMAF algorithms, but does not improve y -direction estimation for dominant y -direction dynamics. Rotating the Q matrix adaptively improves estimation of both x - and y -directions and improves the jink maneuver error transients, but is dependent on the orthogonality of the velocity and acceleration vectors and proper initial tuning parameters. The conclusion was that both methods employed together provide the ability to adjust filter characteristics to differentiate between harsh and benign dynamics in any orientation of target acceleration (rotating Q) while at the same time maintaining appropriate view resolution in the directions of both benign and harsh dynamics (rotating FOV). Therefore, the combination allows for tracking highly maneuvering targets without sacrificing the resolution provided by the smaller RSFOV [33].

The research up to this point was primarily directed towards tracking aircraft and missiles from a ground-based FLIR plane. Rizzo [35] initiated research on a space-based platform which could track targets using the same filtering techniques. Since the linear Kalman filter/enhanced correlator algorithm had proven to be computationally more efficient than the extended Kalman filter, it was chosen as the system filter. The plume "pogo" (oscillation) phenomenon of a missile in the boost phase of flight was modeled in the truth model and in one of two filters used for the analysis. The pogo was modeled as a second-order Gauss-Markov process, and applied in the

direction of the missile velocity vector. The plan was to go adaptive on the pogo states using the MMAF algorithm, treating the pogo amplitude and oscillation frequency as uncertain parameters. Although the elemental filters were developed, no MMAF performance was accomplished, due to elemental filter performance difficulties.

Three rotation schemes were also developed and tested. The first scheme, referred to as the rotating field-of-view (RFOV), involved using the 8 x 8 FOV filter and aligning a single axis of the FLIR plane with the estimated velocity vector of the target; therefore one of the coordinate axes of the FOV would stay aligned with the oscillation of the plume. The second scheme, referred to as the diagonal rotating field-of-view (DRFOV), used the 8 x 8 FOV with the diagonal aligned with the oscillation of the plume. The motivation behind this scheme is that the 8 x 8 FOV is oriented in such a fashion will be able to "see" more of the target's intensity image, thus enabling the sensor to obtain more measurement information [35]. The third tracking scheme was the rotating rectangular field-of-view (RRFOV) algorithm developed from previous research [12,41]. The RFOV, DRFOV, and the RRFOV algorithms [32] were tested along with the non-rotating field-of-view (NRFOV) filter. The NRFOV is the standard tracker used in previous studies [12,32,41]. The DRFOV scheme was shown to be superior to the other three tested for providing enhanced tracking of a missile hardbody whose plume is undergoing a pogo phenomenon.

The eight-state filter (without pogo states; two target position states, two target velocity states, two target acceleration states, and two atmospheric jitter states) and the ten-state filter (with pogo states) surfaced a problem that may have gone unnoticed in previous work. Following tuning of the filters with the twelve-state truth model, it was discovered that the eight-state filter

outperformed the ten-state filter. An investigation into the cause of the irregularity revealed that there was a serious observability problem in the both filters. The affected states were velocity and acceleration. A recommendation was made to remove the acceleration states in the ten-state filter, and to model the velocity states in this new eight-state filter as a first-order Gauss-Markov process.

Eden [5] resumed the research of the space-based FLIR platform. The scope of the tracking problem was expanded by requiring the filter to track the hardbody of the missile rather than just the intensity centroid of the FLIR. Since the FLIR could not supply the needed information about the hardbody location relative to the image center of intensity to the Kalman filter, another measurement source was developed. Under the advisement of the Phillips Laboratory, the new measurement source was identified as a low-energy laser. The laser actively acquires measurement data while the FLIR obtains its measurement information passively. This scheme calls for a six-state Kalman filter (consisting of two position states, two velocity states, and two atmospheric jitter states) to provide a velocity vector estimate for the target plume. The low-energy laser is scanned along this vector from the target plume image intensity center to intercept the hardbody. The hardbody is modeled as a rectangle with binary reflectivity. When the low-energy laser (modeled with a beam width of 2.75 meters at the target) illuminates the hardbody, the reflection is received by a low-energy laser sensor on the platform. This speckle information is provided to a single-state Kalman filter which estimates the distance between the center of mass and the center of intensity along the velocity vector direction. The center of mass is defined as the midpoint of the scan across the hardbody if the centerline of the laser beam crosses the aft end of the missile and the top (nose) of the hardbody, or if the laser beam crosses the aft end and one of the sides of the hardbody. The results of the laser scan show that the

interception of the laser with the hardbody occurs only 10-20% of the time. This low ratio of hitting the target is attributed to the six-state filter being tuned for estimating only the intensity centroid location on the FLIR plane and not for precise velocity estimation. Since the velocity vector must be accurately estimated for active illumination of the target to be a viable concept, it was recommended that the filter also be tuned for accurate velocity estimates.

Tracking the center-of-mass of a missile hardbody using FLIR measurements and low-energy laser illumination was further investigated by Evans [6]. He surmised that the tracking error, represented by a straight line between the estimated target center-of-mass and the true center-of-mass [5], could provide more insight if it were separated into the x - and y - (azimuth and elevation) components, or into along-track and across-track (2-d perpendicular axes of the hardbody) components. Evans proposed the latter method would provide better information relative to the principle axes directions of the error phenomenon. An eight-state filter was developed by augmenting Eden's six-state filter [5] with two additional bias states used to estimate the hardbody center-of-mass [6]. A comparison between the eight-state filter and Eden's one-state filter used in conjunction with the six-state FLIR filter, resulted in negligible difference in performance. Evans' analysis of the eight-state filter's error statistics showed that the tracking error is much greater in the along-track direction than in the across-track direction, and thus the separate one-state filter and six-state FLIR filter performed as well as the eight-state filter.

Aside from investigating the tracking error statistics, Evans enhanced Eden's 2-d hardbody model (which treated reflectivity as a binary on/off function) with a 3-d hardbody reflectivity model to provide increased realism in the simulation. Two reflectivity functions, cross-sectional and longitudinal, were defined based upon empirical data obtained from a radar return off a 20

x 249 inch cylinder with hemispherical endcaps, rotated longitudinally in the plane of the radar source [7]. As shown in Figure 1.4, the cross-sectional and longitudinal reflectivity functions were incorporated into Eden's rectangular hardbody model as 29 discrete weighted line segments along the longitudinal axis of the hardbody.

Evans also found that the sensitivity level of the low-energy sensor is a factor in determining the reflectivity received at the sensor [6]. The sensitivity level represents a threshold below which the reflected return is indistinguishable from sensor noise. A sensitivity factor, μ , is incorporated in the simulation to define the appropriate sensitivity level required to detect a hardbody's return as well as represent the physical limitations of the sensor.

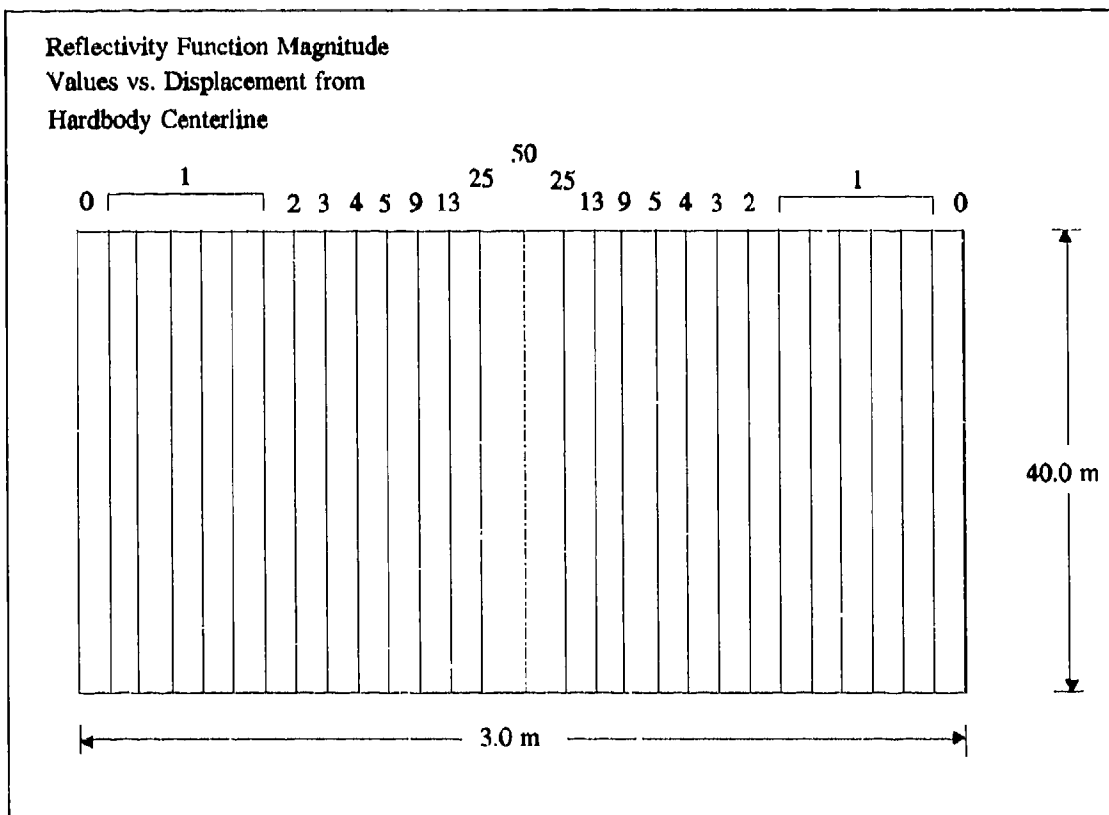


Figure 1.4 Discrete Implementation of Cross-Sectional Reflectivity Function

Performance data collection from the eight-state filter and one-state/six-state filter combination hinged upon the successful illumination of the hardbody by the low-energy laser. Evans was faced with a low target intercept rate (10% - 20%), which inhibited any useful error analysis of the center-of-mass filters. Realizing this, Evans generated an ad hoc technique of offsetting the low-energy laser scan relative to the FLIR estimated velocity vector and "sweeping" the scan across the hardbody, thus providing constant hardbody illumination information. However, the "sweep" is not an optimal tool and should only be used to test the center-of-mass filters in the simulation [6]. Both the 3-d reflectivity hardbody model and laser sweep were employed to evaluate the performance of the eight-state filter and one-state/six-state filter combination center-of-mass estimators.

1.3 Thesis Objectives

The vast amount of previous research is evidence of the complexity of the tracking problem which grows more sophisticated with each thesis. As the progression of research shows, the development of a tracking algorithm, employing Kalman filtering techniques, has evolved from passively tracking the missile plume using infrared measurements to actively locating and tracking the missile hardbody with the aid of information available from laser speckle returns. The prior works of Eden and Evans [5,6] have confirmed the usefulness of laser speckle returns in discerning the hardbody from the missile plume. Unfortunately, the plume physical characteristics affect the degree to which the missile hardbody/plume speckle returns may be precisely defined [2]. Experiments have shown that the laser speckle return of a solid-propellant rocket motor is of the same magnitude as that of the hardbody, as a result of the metallic particles present in this type of propellant [2]. Moreover, this causes a non-negligible bias (25 - 30 meters, occurring at

least 90% of the time) in the estimate of the location of the missile hardbody center-of-mass that was not reflected in the previous analysis [6], and this should be properly incorporated into the current performance analysis. However, it has been observed that the Doppler return of the plume, utilizing a pulsed coherent laser, exhibited both unique frequency shift and broadening attributes which may be strongly distinguishable from that of a hardbody [2]. Thus, the primary focus of this thesis is to investigate the feasibility of employing the Doppler phenomenon to discern the missile hardbody from its plume. The specific objectives of this endeavor are outlined below.

1.3.1 Doppler Phenomenon Modeling. Eden and Evans have established the methodology of incorporating hardbody center-of-mass estimates into the linear Kalman filter/correlator algorithm. The six-state filter (with two position states, two velocity states, and two atmospheric states) augmented with the one-state filter that estimates the distance between the plume centroid and the hardbody center-of-mass, performed well as long as hardbody measurements (i.e., Doppler return for the current research) to the one-state filter are consistently provided. This filter structure shall be used for this thesis.

For this preliminary investigation into the Doppler phenomenon, a modeling of the physical processes of transmitting the pulsed coherent laser, or sensing the Doppler return shall not be attempted. Instead, this effort concentrates upon specifying the form of measurement data presented to the Kalman filter from these processes.

The Doppler return can be described by two characteristics: the magnitude of the frequency shift, and the spread of the return spectrum. The direction of the hardbody's velocity is presumed to be in the opposite direction of the plume's velocity [26]. Hence, the plume and

hardbody-induced Doppler return are expected to exhibit contrasting frequency shifts. The respective spectrum spread of the hardbody's and plume's Doppler returns shall be seen to be distinguishable from each other due to differences in mass density and particle velocities. In essence, the plume will exhibit a broader spectrum spread as compared to the hardbody. On the basis of these two factors, the Doppler return of the hardbody can be easily discriminated from the Doppler return of the plume.

The angular resolution, expressed in tracking angle rms errors (a function of wavelength and signal-to-noise ratio - to be developed in Chapter IV), is used to define the noise inherent in the measurements [16,26]. Furthermore, a probability-of-miss is incorporated to account for the probability of no detected plume/hardbody interface due to: bending of the laser path (so that actual scan doesn't intersect the hardbody even though the intended scan does); and cases where the Doppler receiver cannot discern the presence of two separate returns from the hardbody and the plume (i.e., both plume and hardbody velocities are normal to the sensor plane, resulting in no Doppler shift).

Eden's binary rectangular hardbody model is utilized from the onset. Eventually, the hardbody reactivity model developed by Evans will also be modified to exhibit the appropriate Doppler return properties. For both hardbody models, the laser sweep routine developed by Evans is employed. Chapter IV presents the basic pertinent aspects of the Doppler phenomenon and discusses the Doppler measurement model.

1.3.2 Alternative Scan Techniques. Alternative scan techniques to detect the hardbody are pursued as a secondary objective. The present sweep method is primarily an evaluation tool for the one-state, hardbody center-of-mass filter. Although effective, the sweep action is

admittedly not efficient, since it requires extra computer frame time. (The sweep is performed at each update). In addition, future research involving active illumination may address more dynamic target trajectories, jinking maneuvers, multiple hotspots, and decoy identification. For these reasons, the scan time must be minimal.

Detection techniques considered include sinusoidal and conical scan patterns. Once the target is detected, it can be actively followed by the laser radar in a special tracking mode where the hardbody is continuously illuminated. The method of scanning and tracking must be governed by practical concerns, such as the power availability to the scan/tracking device and choice of appropriate wavelength considerations.

1.3.3 Performance Evaluation. With the Doppler phenomenon modeled as a form of measurement data, the augmented six-state filter's [5,6] performance is evaluated against the truth model (composed of two target states - the actual result of accurate 3-d trajectory simulation and projection onto the FLIR plane, six atmospheric jitter states, four vibration states, and two pogo states). Truth model speckle return measurements to the one-state offset filter is modified to exhibit the hardbody bias that appears with solid propellant rocket motors [2,3]. The results are compared to the previous findings of Evan's [6] research. Initial testing, with the laser sweep technique and the binary rectangular hardbody model, is conducted without the pogo and vibration states. Further evaluation includes permutations of these disturbances "switched on and off" in the truth model. In addition, sensitivity analyses of specific Doppler parameters, such as laser wavelength, angular resolution, signal-to-noise ratio, and probability-of-miss, are conducted.

The combination of Doppler and speckle measurements may enhance center-of-mass estimates. This configuration is explored and evaluated in the same fashion outlined above.

1.4 Thesis Overview

This chapter described the AFIT-developed tracking system that employs a Kalman filter, a passive FLIR sensor, and active illumination of the hardbody. A review of the prior research was provided. Chapter II gives a mathematical summary of the linear Kalman filter and relates it to the Kalman filter/correlator algorithm and the Multiple Model Adaptive Algorithm (MMAF). Chapter III describes the Doppler phenomenon aspects that are relevant to the control viewpoint of this thesis and also provides a brief technical description of the alternative detection techniques considered for this study. The AFIT tracking scenario is presented in Chapter IV. Chapters V and VI discuss the truth model and filter models, respectively. Chapter VII provides the performance analysis, and Chapter VIII presents the final conclusions and recommendations for further study.

II. The Kalman Filter Algorithm

2.1 Introduction

The process of estimating the target position, velocity, plume/hardbody interface, and other variables of interest is accomplished by the Kalman filter. The Kalman filter accounts for the uncertainties associated with the tracking system parameters and external environment, and provides an optimal solution under the basic assumptions that the system is linear (or linearized) and is driven by white Gaussian noise. By optimally combining measurements, dynamic characteristics, and *a priori* knowledge of the statistical properties of the system and measuring devices, the Kalman filter produces optimal state estimates conditioned on the history of measurements received. The *a priori* statistics of the mean and covariance provided to the filter as initial state conditions are defined by:

$$E\{\hat{x}(t_0)\} = \hat{x}_0 \quad (2-1)$$

$$E\{[\hat{x}(t_0) - \hat{x}_0][\hat{x}(t_0) - \hat{x}_0]^T\} = P, \quad (2-2)$$

where the notation $\hat{(\)}$ indicates an estimated value, and $E\{ \}$ is the expectation, or ensemble average, of the possible outcomes. The Kalman filter receives measurements at a prescribed sample rate and propagates the state conditioned upon the measurement time history $Z(t)$, given as:

$$\mathbf{Z}(t_i) = \begin{bmatrix} z(t_1) \\ \vdots \\ z(t_i) \end{bmatrix} \quad (2-3)$$

where $z(t_i)$ is the measurement data available at sample time (t_i). Then the conditional mean and covariance of the state variables are given by:

$$\hat{\mathbf{x}}(t_i) = F^i \mathbf{x}(t_1) | \mathbf{Z}(t_i) = \mathbf{Z}_i \quad (2-4)$$

$$\mathbf{P}(t_i) = E\{[\mathbf{x}(t_i) - \hat{\mathbf{x}}(t_i)][\mathbf{x}(t_i) - \hat{\mathbf{x}}(t_i)]^T | \mathbf{Z}(t_i) = \mathbf{Z}_i\} \quad (2-5)$$

where \mathbf{Z}_i is a specific realization (observed set of values) of the measurement history $\mathbf{Z}(t_i)$.

For this thesis, the linear Kalman filter is employed to serve two independent functions: the estimation of the target plume intensity centroid's position and velocity (performed by the six-state FLIR filter), and the estimation of the hardbody center-of-mass. Offset azimuth and elevation "pseudo-measurements" for the linear FLIR filter are produced from an enhanced correlator algorithm that compares the FLIR image to an optically processed template [36]. Two different configurations of the center-of-mass estimators (a one-state and a two-state Modified Maximum A Posteriori, or MAP, Multiple Model Adaptive Filter) operate autonomously from the FLIR filter.

A benign target trajectory is used to obtain an initial "look" into the ability of the Doppler phenomenon to define the plume/hardbody interface. Explicit knowledge of where the plume/hardbody interface occurs will allow for locating and tracking the hardbody center-of-mass.

As will be seen in Chapter V, the dynamics associated with the Doppler returns permit the use of a linear Kalman filter.

The following sections present the basic mathematical forms of the linear Kalman filter and the Multiple Model Adaptive Filter (MMAF) algorithms. Due to the benign target dynamics and the preliminary nature of this research, the filter development is constrained to the linear Kalman filter. However, this linear FLIR Kalman filter, which receives the offset "pseudo-measurements" from the enhanced correlator, is shown to be an element in the MMAF structure developed in previous AFIT research [12,14,33,40,41]. Thus, the MMAF is presented to offer an encompassing perspective of the AFIT adaptive tracking system, although this thesis does not explicitly develop such an MMAF algorithm. The interested reader is referred to Maybeck's *Stochastic Models, Estimation, and Control, Vol. 1 and Vol. 2*, for a rigorous development of the Kalman Filter theory and MMAF algorithm.

2.2 Linear Kalman Filter

Prior to implementing the Kalman filter a mathematical model of the system dynamics must be developed and measurements must be available. A system is generally modeled with a set of linear state differential equations of the form:

$$\dot{x}(t) = F(t)x(t) + B(t)u(t) + G(t)w(t) \quad (2-6)$$

where

- $F(t)$ = homogeneous state dynamics matrix
- $x(t)$ = vector of states of interest
- $B(t)$ = control input matrix
- $u(t)$ = deterministic control input vector

- $G(t)$ = driving noise input matrix
 $w(t)$ = white Gaussian driving noise vector

The mean of the white Gaussian driving noise vector is:

$$E\{w(t)\} = 0 \quad (2-7)$$

and the noise strength is $Q(t)$:

$$E\{w(t)w(t + \tau)^T\} = Q(t)\delta(\tau) \quad (2-8)$$

The equivalent discrete-time system model of Equation (2-6) is needed to implement the algorithm on a digital computer. The general form of the discrete-time state space form (denoted by the d subscript) of that model is given by:

$$x(t_{i+1}) = \Phi(t_{i+1}, t_i)x(t_i) + B_d(t_i)u(t_i) + w_d(t_i) \quad (2-9)$$

where

$\Phi(t_{i+1}, t_i)$ = the $n \times n$ system state transition matrix that satisfies the differential equation and initial condition:

$$\frac{d[\Phi(t, t_o)]}{dt} = F(t)\Phi(t, t_o) \quad (2-10)$$

$$\Phi(t_o, t_o) = I \quad (2-11)$$

and where

- $x(t_i)$ = discrete-time vector of states of interest
 $B_d(t_i)$ = discrete-time control input matrix
 $u(t_i)$ = discrete-time deterministic control input vector
 $w_d(t_i)$ = discrete-time independent, white Gaussian noise process with mean and covariance statistics defined as:

$$E\{w_d(t_i)\} = \mathbf{0} \quad (2-12)$$

$$E\{w_d(t_i)w_d^T(t_j)\} = \begin{cases} Q_d(t_i) & t_i = t_j \\ \mathbf{0} & t_i \neq t_j \end{cases} \quad (2-13)$$

with

$$Q_d(t_i) = \int_{t_i}^{t_{i+1}} \Phi(t_{i+1}, \tau) G(\tau) Q(\tau) G^T(\tau) \Phi^T(t_{i+1}, \tau) d\tau \quad (2-14)$$

The Kalman filter incorporates measurement information from external measuring devices to improve its estimate of a desired state. The discrete-time (sampled data) measurement model is of the form:

$$z(t_i) = H(t_i)x(t_i) + v(t_i) \quad (2-15)$$

where

- $z(t_i)$ = m-dimensional measurement vector at sample time t_i
- $H(t_i)$ = state observation matrix
- $x(t_i)$ = vector of states of interest
- $v(t_i)$ = white Gaussian measurement noise

The discrete white Gaussian measurement noise v is independent of both $x(t_0)$ and w for all time, and has a mean and covariance, R , given by:

$$E\{v(t_i)\} = \mathbf{0} \quad (2-16)$$

$$E\{v(t_i)v^T(t_j)\} = \begin{cases} R(t_i) & t_i = t_j \\ \mathbf{0} & t_i \neq t_j \end{cases} \quad (2-17)$$

The Kalman filter propagates the state conditional mean and its covariance from the instant in time immediately following the most recent measurement update, t_i^+ , to the instant in time immediately preceding the next measurement update, t_{i+1}^- , by numerical integration of the following equations:

$$\dot{\hat{x}}(t/t_i) = F(t)\hat{x}(t/t_i) \quad (2-18)$$

$$\dot{P}(t/t_i) = F(t)P(t/t_i) + P(t/t_i)F^T(t) + G(t)Q(t)G^T(t) \quad (2-19)$$

where the notation $\hat{x}(t/t_i)$ denotes optimal estimates of x at time t , conditioned on measurements through time t_i , and with initial conditions:

$$\hat{x}(t_i/t_i) = \hat{x}(t_i^+) \quad (2-20)$$

$$P(t_i/t_i) = P(t_i^+) \quad (2-21)$$

where $\hat{x}(t_i^+)$ and $P(t_i^+)$ are the results of the previous measurement update cycle. At time t_0 , \hat{x}_0 and P_0 from Equations (2-1) and (2-2) are used to initialize the first propagation.

That update cycle when a measurement becomes available at time t_i is based on the following update equations:

$$K(t_i) = P(t_i^-)H^T(t_i)[H(t_i)P(t_i^-)H^T(t_i) + R(t_i)]^{-1} \quad (2-22)$$

$$\hat{x}(t_i^+) = \hat{x}(t_i^-) + K(t_i)[z(t_i) - H(t_i)\hat{x}(t_i^-)] \quad (2-23)$$

$$P(t_i^+) = P(t_i^-) - K(t_i)H(t_i)P(t_i^-) \quad (2-24)$$

where $K(t_i)$ is the time-varying Kalman filter gain matrix that assigns "weights" to the new

information (consisting of the difference between the actual measurement and the filter's estimate of the measurement, $H(t_i)\hat{x}(t_i)$, as seen in Equation (2-23)) based on known measurement noise statistics and filter-computed covariances.

2.3 Multiple Model Adaptive algorithm

The optimality of the state estimator is dependent upon complete knowledge of the parameters that define the best model for system dynamics, output relations, and statistical description of uncertainties [18]. For Kalman filter tracking applications, maximum performance is achieved when the parameters of the filter dynamics model match the parameters of the target being tracked. Often, the parameters are known only with some uncertainty and may exhibit time-varying characteristics (such as in the case of maneuvering targets with changing acceleration levels). Thus, there is a need to devise a method that produces optimum state estimates despite the incomplete *a priori* knowledge of parameter statistics, and provides the estimates in an adaptive, on-line fashion. The multiple model adaptive filter (MMAF) satisfies these requirements [18].

To implement the MMAF algorithm, it becomes necessary to discretize the parameter space by the judicious choice of discrete values that are representatively dispersed throughout the continuous range of possible values. For the tracking problem at hand, a target can display K different discrete sets of dynamic maneuvers corresponding to one of K discrete values of acceleration vectors. As previously shown in Figure 1.1, a Kalman filter is then designed for each choice of parameter value, resulting in a bank of K separate elemental filters.

Let a denote the vector of uncertain parameters in a given linear state model for a

dynamic system. A system model would be represented by the following time-invariant, first-order, stochastic differential equation:

$$\dot{x}(t) = F(a)x(t) + B(a)u(t) + G(a)w(t) \quad (2-25)$$

with noise corrupted, discrete-time measurements given by:

$$z(t_i) = H(a)x(t_i) + v(t_i) \quad (2-26)$$

where

- $x(t)$ = n -dimensional system state vector
- $u(t)$ = r -dimensional deterministic control vector
- $w(t)$ = s -dimensional white, Gaussian, zero-mean noise vector process of strength $Q(a)$
- $z(t_i)$ = m -dimensional measurement vector
- $v(t_i)$ = m -dimensional discrete-time white, Gaussian, zero-mean noise vector process of covariance $R(a)$
- $F(a)$ = $n \times n$ system plant matrix
- $B(a)$ = $n \times r$ input distribution matrix
- $G(a)$ = $n \times s$ noise distribution matrix
- $H(a)$ = $m \times n$ matrix relating measurement to states

The parameter vector, a , is discretized into a set of K finite vector values, a_1, a_2, \dots, a_K , and associated with each a_k is a different system model of the form given by Equations (2-25) and (2-26). Each elemental Kalman filter, tuned for a specific a_k , produces a state estimate which is weighed appropriately using the hypothesis conditional probability $p_k(t_i)$ to produce the state estimate $\hat{x}_{mmof}(t_i)$ as a probabilistically weighted sum, where:

$$p_k(t_i) = \frac{f_{z(t_i)|a, Z(t_{i-1})}(z_i | a_k, Z_{i-1}) p_k(t_{i-1})}{\sum_{j=1}^K f_{z(t_i)|a, Z(t_{i-1})}(z_i | a_j, Z_{i-1}) p_j(t_{i-1})} \quad (2-27)$$

$$f_{z(t_i)|a, z(t_{i-1})}(z_i | a_k, Z_{i-1}) = \frac{\exp\{\cdot\}}{(2\pi)^{m/2} |A_k(t_i)|^{1/2}} \quad (2-28)$$

$$\{\cdot\} = \left\{ -\frac{1}{2} r_k^T(t_i) A_k^{-1}(t_i) r_k(t_i) \right\}$$

with

$$A_k(t_i) = k\text{th filter's computed residual covariance}$$

$$= H_k(t_i) P_k(t_i) H_k^T(t_i) + R_k(t_i)$$

$$r_k(t_i) = k\text{th filter's residual}$$

$$= [z(t_i) - H_k(t_i) \hat{x}_k(t_i)]$$

$$a_k = \text{parameter value assumed in the } k\text{th filter}$$

$$P_k(t_i) = k\text{th filter's computed state error covariance before}$$

$$\text{incorporating the measurement at time } t_i$$

$$Z(t_{i-1}) = \text{measurement history up to time } t_{i-1}$$

The residual of the k th elemental Kalman filter, that best matches the current target dynamics associated with the parameter value a_k , is expected to be smaller than the residuals of the other mismatched filters. The hypothesis conditional probability given by Equation (2-27) with index corresponding to the "correct" filter will then be the largest among the other conditional probabilities, thus assigning the most weight to the "correct" state estimate. This algorithm performs well if each elemental filter is optimally tuned for best performance for a specific target scenario, causing its residual to be distinguishable from those of the mismatched filters. It is also important not to add excessive amounts of pseudonoise to compensate for model inadequacies, since this tends to mask the distinction between good and bad models [17]. If the quadratic forms within the exponentials of Equation (2-28) are consistently of the same magnitude, then Equation (2-27) will result in the growth of the p_k associated with the filter with the smallest value of $|A_k|$. The values of $|A_k|$ are independent not only of the residuals, but also of the

"correctness" of the K models, and so the result would be totally erroneous [18]. Therefore, the scalar denominator of the exponential in Equation (2-28) might be removed in the final implementation of the algorithm.

The output of the MMAF algorithm is the probabilistic weighted average of the elemental filter's estimates given by:

$$\hat{x}_{mmaf}(t_i^+) = \sum_{k=1}^K p_k(t_i) \hat{x}_k(t_i^+) \quad (2-29)$$

The conditional covariance matrix for the MMAF is computed as:

$$P_{mmaf}(t_i^+) = \sum_{k=1}^K p_k(t_i) [P_k(t_i^+) + \mathcal{J}_k(t_i^+) \mathcal{J}_k^T(t_i^+)] \quad (2-30)$$

where

$$\mathcal{J}_k(t_i^+) = \hat{x}_k(t_i^+) - \hat{x}_{mmaf}(t_i^+)$$

$$p_k = k\text{th filter's conditional hypothesis probability}$$

$$P_k(t_i^+) = k\text{th filter's state error covariance matrix after incorporating the measurement at time } t_i$$

Since the values of $p_k(t_i)$ and $\hat{x}_{mmaf}(t_i^+)$ depend upon the discrete measurements taken through time t_i , $P_{mmaf}(t_i^+)$ cannot be precomputed as in the case for the elemental filters. However, Equation (2-30) need not be computed for the on-line filter algorithm.

The calculated probabilities of Equation (2-23) should involve an artificial lower bound [12,18,32]. This lower bound will prevent a mismatched filter's hypothesis conditional probability from converging to (essentially) zero. If a filter's p_k should reach zero, it will remain zero for all

time, as can be seen from the iterative nature of Equation (2-27). This effectively removes that filter from the bank and degrades the responsiveness of the MMAF to future changes of the parameter values. If some future target dynamic scenario matched the model for which the p_k was locked onto zero, that elemental filter's estimate would not be appropriately weighted and the MMAF estimate would be in error. In previous work, Tobin [41] established a lower bound of .001 for $p_k(t_i)$.

2.4 Summary

This chapter presented the mathematical models of the linear Kalman filter and the MMAF algorithm. The linear Kalman filter is an optimal estimator and constitutes an elemental filter in the MMAF structure used for the AFIT adaptive tracking system. The MMAF is an adaptive algorithm that optimally combines the estimates of individual Kalman filters that are tuned for a specific parameter value. This preliminary research of locating the hardbody via Doppler measurements utilizes linear hardbody center-of-mass Kalman filters that function autonomously from the six-state FLIR Kalman filter. The enhanced correlator that produces the offset "pseudo-measurements" as a result of comparing the FLIR image to an optical processed template is presented in Chapter V's discussion of the filter measurement models.

III. Simulation Space

3.1 Introduction

Simulation of the tracking scenario, which encompasses the target trajectory, the FLIR sensor operation, and the low-energy laser illumination of the missile hardbody and the generation of the speckle return and Doppler measurements, is performed on a digital computer. A 3-dimensional "simulation space" is generated wherein a target plume is propagated along a realistic trajectory. Several coordinate frames in the simulation space provide the means of mathematically projecting the target plume's infrared image and velocity vector onto the two-dimensional FLIR image plane [10,11,32]. In addition, these frames are utilized to project a representation of the hardbody center-of-mass, as well as to define the start and orientation of the low-energy laser scan for generating speckle and Doppler measurements [5,6]. This chapter describes the different coordinate frames of the simulation space and cover the process of pointing the FLIR sensor at the target during tracking.

3.2 Coordinate Frames

As shown in Figure 3.1, three primary coordinate frames are defined in the simulation space: a system inertial reference frame, a target reference frame, and an α - β - r reference frame. Each of these reference frames is described in the following paragraphs.

3.2.1 Inertial Reference Frame. The inertial reference frame is a North-Up-East (NUE) frame wherein the target flight trajectory occurs.

Origin: location of the FLIR sensor

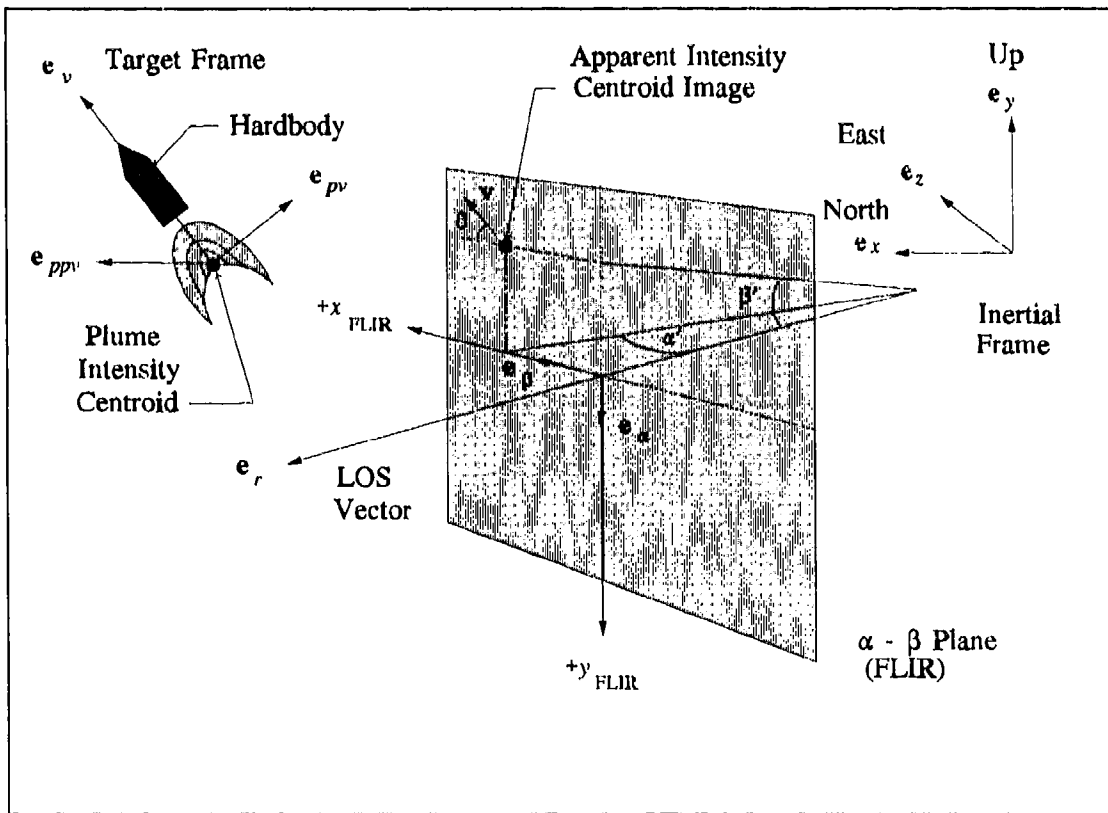


Figure 3.1 Three Primary Coordinate Frames in Simulation Space

- Axes: e_x - due north, tangent to the earth's surface, defines zero azimuth
 e_y - inertial "up" with respect to flat earth approximation
 e_z - vector completing right-hand coordinate set, defines 90° azimuth

Note: The azimuth angle (α) is measured eastward from e_x . The elevation angle (β) is measured "up" from the horizontal plane defined by e_x and e_z .

3.2.2 *Target Plume Reference Frame.* This frame is located at the target plume with one of its unit vectors co-linear with the target's velocity vector.

- Origin: plume intensity centroid
 Axes: e_v - along the true velocity vector

e_{pv} - out the right side of the target, orthogonal to both e_r and the LOS vector

e_{pvv} - vector completing the right-hand coordinate set

Note: v - along the velocity vector

p_v - perpendicular to the velocity vector

p_{vv} - perpendicular to both v and p_v

3.2.3 α - β - r Reference Frame. The α - β - r reference frame is defined by the azimuth angle α' and the elevation angle β' measured with respect to the FLIR line-of-sight (LOS) vector c_r . The true azimuth α and the true elevation β are referenced from true north and the horizon. This frame is used to project the target's position and velocity onto the FLIR plane.

Origin: plume intensity centroid

Axes: e_r , coincident with the true sensor-to-target LOS vector

e_α and e_β define a plane perpendicular to e_r , rotated from inertial e_x and e_y by the azimuth angle (α) and elevation angle (β)

There are three special coordinate frames associated with the α - β - r reference frame: the α - β (FLIR) plane, the absolute α - β - r reference frame, and the trans-FLIR plane.

3.2.3.1 α - β (FLIR Image) Plane. The FLIR plane is used to obtain the measurements of the target plume position and is the reference frame for the geometrically derived velocity vector components of the target's intensity centroid. The FLIR plane is defined by the e_α and e_β unit vectors, with the LOS vector (orthogonal to the FLIR plane) representing the pointing orientation of the FLIR sensor, and the high and low-energy laser. Note the orientation of the $+y_{FLIR}$ axis in Figure 3.1, which allows the LOS vector to be positive towards the target when it

is considered the third member of a right-handed set of coordinates as defined by the unit vectors

$$\mathbf{e}_\beta = \mathbf{e}_\alpha \times \mathbf{e}_r.$$

Due to the large distance to the target (approximately 2,000 kilometers), small angle approximations are invoked, allowing the "pseudo" azimuth and elevation angles, α' and β' , to be linearly proportional to the x and y cartesian coordinates in the FLIR plane. The x and y coordinates are measured in pixels (a pixel of linear length corresponds to 15 μ radians of arc) and will provide a means of evaluating the performance of the Kalman filter associated with tracking the intensity centroid of the target.

3.2.3.2 Absolute α - β - r Reference Frame. The absolute α - β - r reference frame is fixed in inertial space at the *initial* α - β - r coordinates of the target. This coordinate system defines the initial pointing direction of the FLIR LOS vector \mathbf{e}_r , and is also used to define the true and filter estimated target positions and velocity components on the FLIR plane.

3.2.3.3 Trans-FLIR Plane. This plane is defined as the result of translating the center of the FLIR FOV to the true center-of-mass of the missile hardbody. The frame is used to determine the x_{FLIR} and y_{FLIR} coordinate errors of the hardbody center-of-mass filter's estimates, for performance analysis purposes.

3.2.3.4 ALT/ACT Plane. This plane, shown in Figure 3.2, is a rotation of the trans-FLIR plane by the true orientation angle θ , formed by the target trajectory with respect to the FLIR coordinate plane. It is used to determine the along-track and across-track components of the tracking error mean and covariance of the hardbody center-of-mass estimates [6].

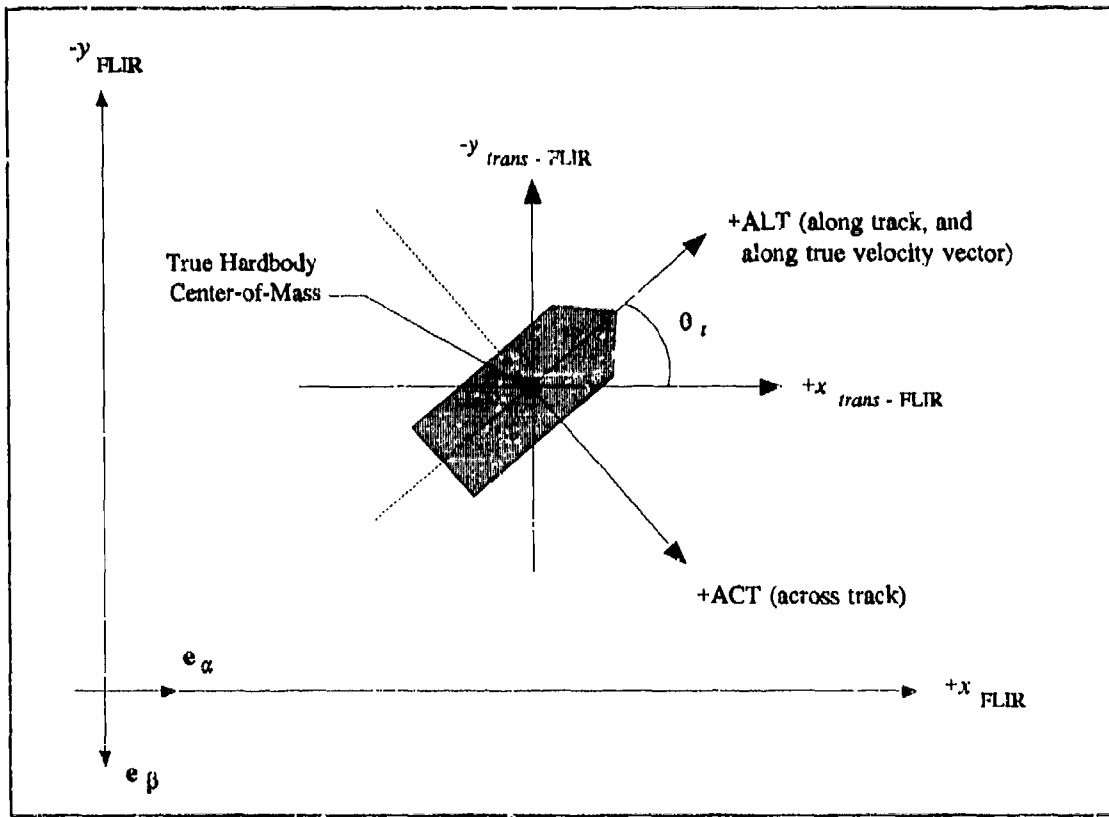


Figure 3.2 FLIR Plane, Trans-FLIR Plane, and ALT-ACT Plane

3.3 FLIR Image Plane

All dynamic events associated with the target plume intensity "pattern" or "function," and the active illumination of the missile hardbody in 3-dimensional inertial space are projected onto the 2-dimensional FLIR image plane. The measurements generated as a result of IR detection by the FLIR sensor are provided to the enhanced correlator algorithm, which produces "pseudo-measurements" to the FLIR Kalman filter to update its state estimates. For the missile hardbody, low-energy laser-generated measurements of the offset distance relative to the plume intensity centroid are geometrically projected onto the FLIR image plane. Thus, the FLIR image plane is the realm in which the performance of the Kalman filter is evaluated. Also note that it is a natural

plane for such evaluation of a laser weapon, since pointing angle errors are critical and range is not. This section introduces the FLIR Field-Of-View (FOV) "tracking window," and discusses the construction and projection of the target models.

3.3.1 FLIR Field-Of-View. The FLIR FOV, shown in Figure 3.3, consists of an 8 x 8 pixel sub-array (in the FLIR sensor 300 x 500 pixel array) which provides sensed information as a function of the varying intensity of the plume IR image and the background and internal FLIR noise. Based upon this information, the position estimates from the six-state FLIR Kalman filter serve to center the centroid of the plume IR image in the FOV. Since the low-energy laser is boresighted with the FOV, the FLIR filter position and velocity estimates of the intensity centroid define the origin and orientation of the laser scan to "paint" the hardbody. The errors of the FLIR filter's estimate of the centroid position and velocity, and the hardbody center-of-mass filter's estimate of offset, are expressed in units of "pixels." These errors become meaningful through a pixel proportionality constant, k_p equal to 15 μ radians/pixel [35]. With this constant, 1 pixel corresponds to approximately 30 meters for a range of 2,000 kilometers.

3.3.2 Target Models on the FLIR Plane. The difference of two Gaussian intensity functions creates a planform that models the hotspot of the plume target on the FLIR plane [35], as shown in Figure 3.3. The "trailing" function is subtracted from the "leading" function to construct a suitable approximation of empirically observed plume intensity profiles. The missile hardbody is not sensed by the FLIR sensor. However, it is geometrically projected onto the FLIR plane as a rectangle, located an offset distance from the plume centroid along the target's velocity vector. Since the FLIR sensor can only detect the IR intensity shape function of the plume, the

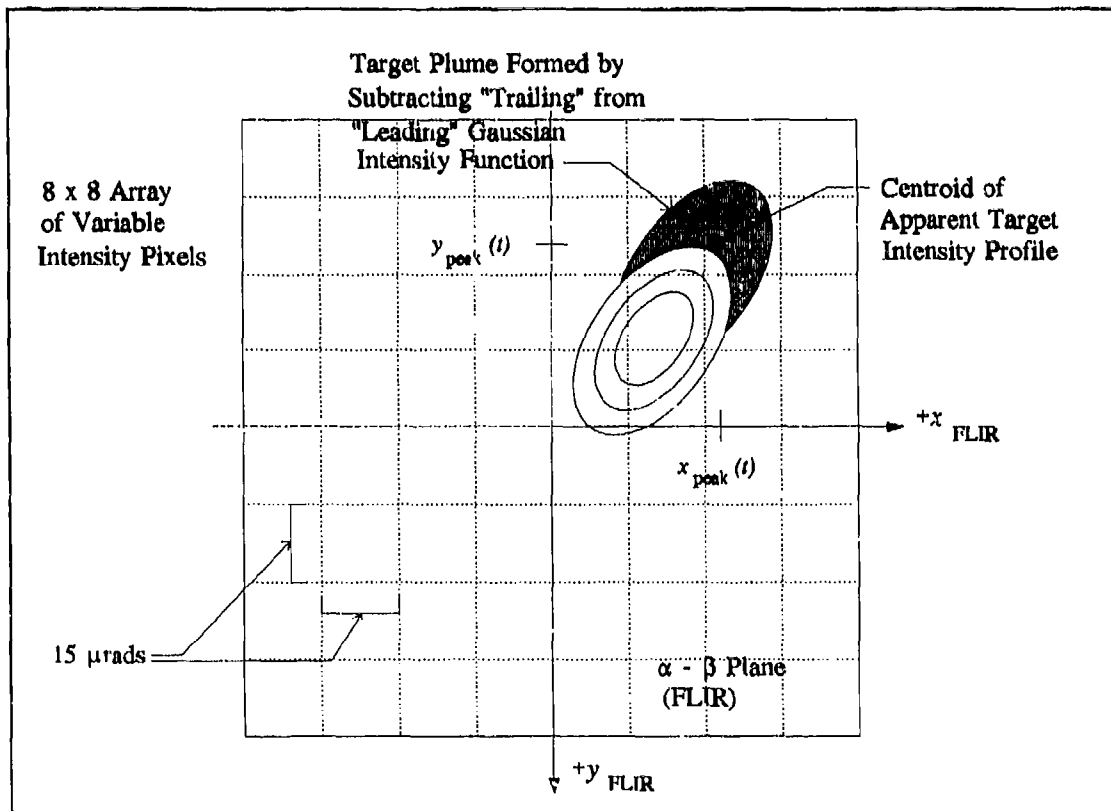


Figure 3.3 Target Plume Image in 8 x 8 FLIR Field-of-View (FOV)

remainder of this discussion emphasizes the intensity centroid model. More about the hardbody model will be presented in Chapter IV.

3.3.2.1 *Target Plume Model on the FLIR Plane.* The radiated energy from each intensity function is represented as a bivariate Gaussian distribution with elliptical constant intensity contours. Each of the two bivariate Gaussian intensity functions is given by [35]:

$$I [x, y, x_{peak}(t), y_{peak}(t)] = I_{max} \exp[-0.5 (\Delta x \Delta y) P^{-1} (\Delta x \Delta y)^T] \quad (3-1)$$

where

$\Delta x = (x - x_{peak})\cos\theta_t + (y - y_{peak})\sin\theta_t$, measured along the ALT axis of Figure 3.2

$\Delta y = (y - y_{peak})\cos\theta_t - (x - x_{peak})\sin\theta_t$, measured along the ACT axis of Figure 3.2

$\theta_t =$ true target orientation angle between the projection of the velocity vector and the x -axis in the FLIR plane; see Figure 3.2

$x, y =$ coordinate axes on the $\alpha - \beta$ plane

$x_{peak}, y_{peak} =$ peak intensity coordinates of the single Gaussian intensity function

$I_{max} =$ maximum intensity function

$\mathbf{P} =$ 2 x 2 target dispersion matrix whose eigenvalues (σ_v^2 and σ_{pv}^2) define the dispersion of the elliptical constant intensity contours

Figure 3.4 illustrates the spatial relationship between the two intensity functions along the target e_x axis. The displacement values are based on the assumption that the dispersion of the exhaust plume in the e_{pv} direction (normal to both e_x and the LOS vector) is approximately 2.0 times the diameter of the missile [35]. With the dimensions of the hardbody chosen as 40 meters long and 3 meters in diameter, the centroid of the first intensity function is located 65 meters behind the hardbody center-of-mass. The placement of the first centroid simulates the composite centroid of the exhaust plume being close to the missile exhaust nozzle, whereas the position of the second centroid enables one to simulate different plume shapes. The second, "trailing" centroid is arbitrarily located 110 meters from the center-of-mass and the defined spatial relationship remain fixed in the target frame during the simulation (should the difference between the two Gaussian intensity functions become negative, the simulation clips the difference to zero). Any external forces acting on the missile other than thrust and gravity are assumed negligible, which thus yields an assumed zero sideslip angle as well as zero angle of attack. These assumptions allow the semi-

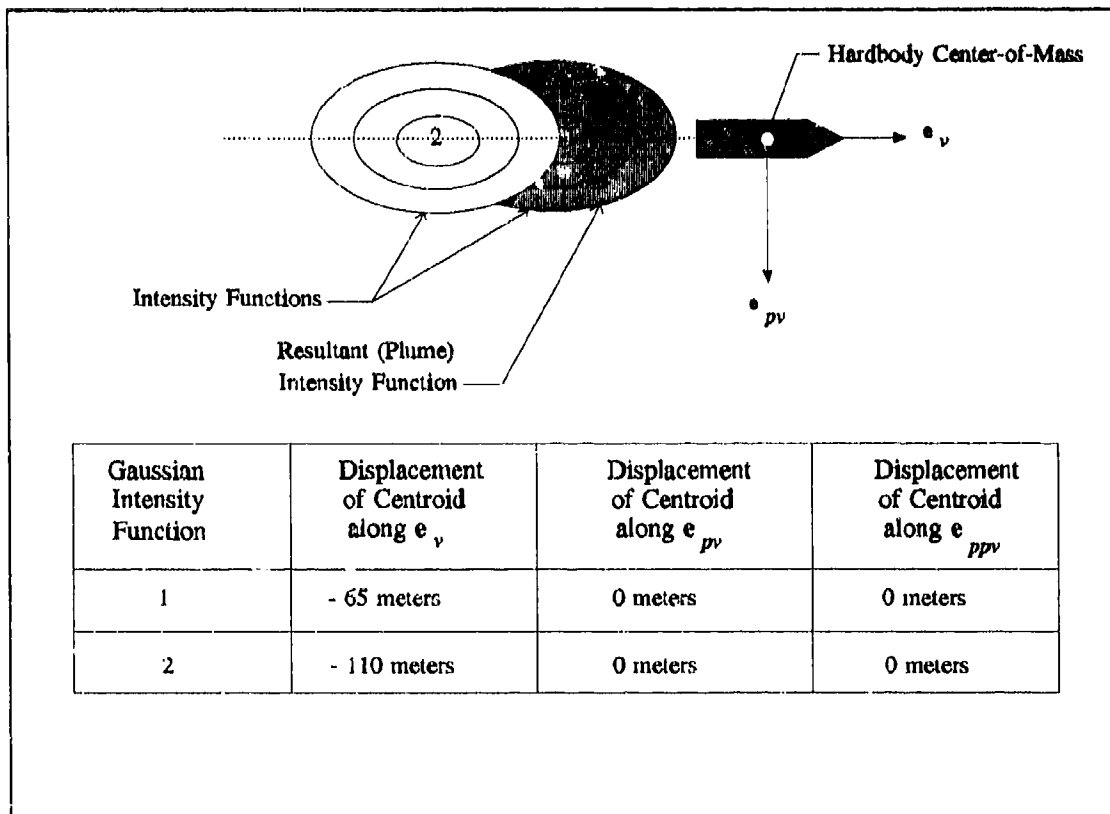


Figure 3.4 Spatial Relationship of Target Plume Gaussian Intensity Functions

major axes of the elliptical constant-intensity contours to be aligned with the projection of the target's velocity vector onto the FLIR image plane, and provides a simplified simulation geometry while retaining the essential features of the trajectory simulation.

3.3.2.2 Target Plume Projection onto the FLIR Plane. As the target plume is propagated through inertial space, the output of the FLIR pixels is simulated by projecting the two intensity functions onto the FLIR plane. The geometry of the projection is shown in Figure 3.5. The "reference target image" is oriented on the FLIR plane to correspond to the largest apparent planform (i.e., with its velocity vector orthogonal to the LOS vector) at a given initial reference range, r_o . As seen in Figure 3.6, the target intensity image is defined by the dispersion along the

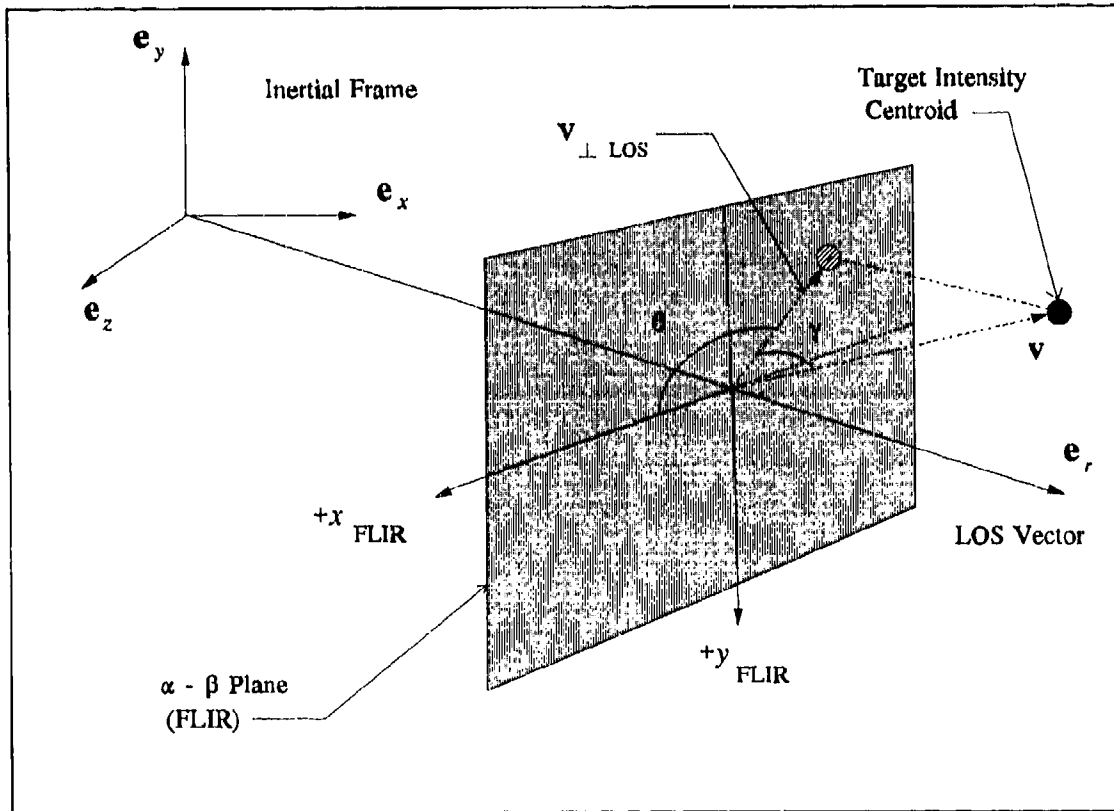


Figure 3.5 Target Plume Intensity Centroid Projection Geometry

principle axes of the two Gaussian intensity functions, given by:

$$\sigma_{pv} = \sigma_{pvo} \left(\frac{r_o}{r} \right) \quad (3-2)$$

$$\begin{aligned} \sigma_v &= \left(\frac{r_o}{r} \right) \left[\sigma_{pvo} + (\sigma_{vo} - \sigma_{pvo}) \cos \gamma \right] \\ &= \sigma_{pv} \left[1 + \frac{v_{\perp \text{ LOS}}}{v} (AR - 1) \right] \end{aligned} \quad (3-3)$$

where

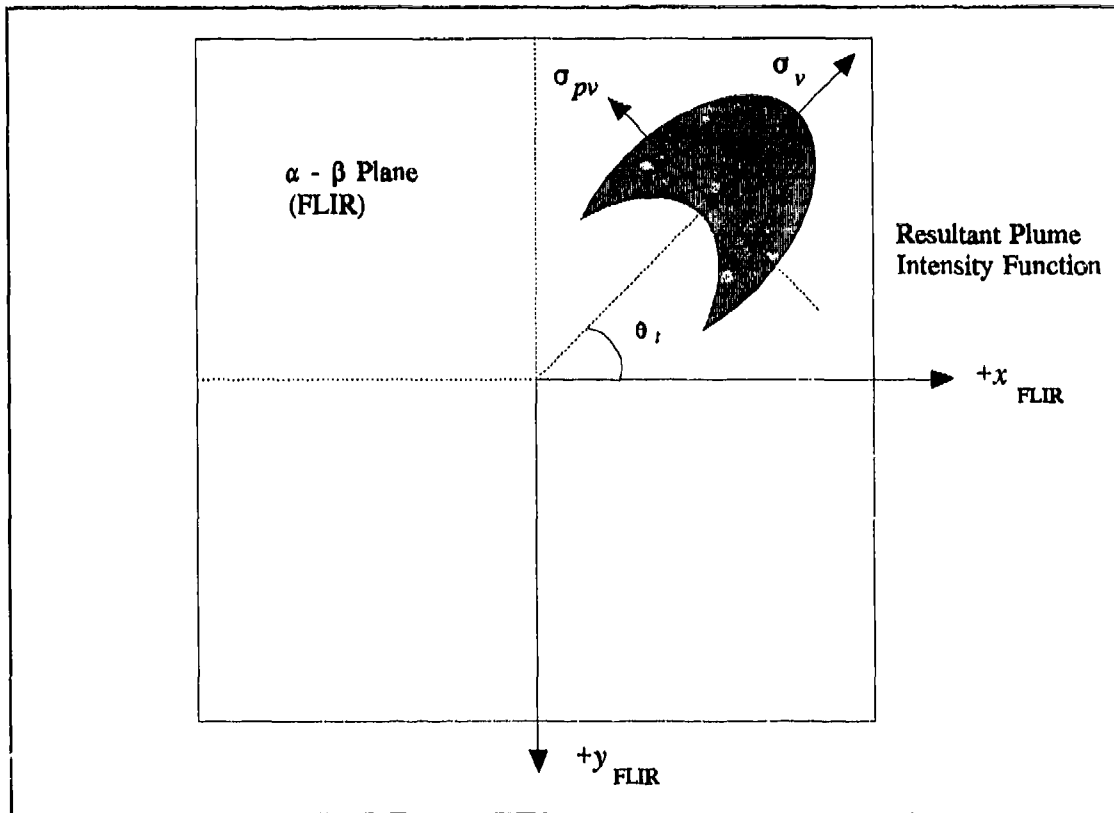


Figure 3.6 Intensity Centroid Dispersion Axes in FLIR Plane

- $\sigma_{v_0}, \sigma_{p_{v_0}}$ = the initial dispersions of the target intensity functions along e_v and e_{p_v} in the target frame of the reference image
- σ_v, σ_{p_v} = the current dispersions of the target image
- r_0 = initial sensor-to-target range of the reference image
- r = current sensor-to-target range
- \mathbf{v} = initial velocity vector of the target
- v = magnitude of \mathbf{v}
- $\mathbf{v}_{\perp LOS}$ = projection of \mathbf{v} on the $\alpha - \beta$ plane (FLIR); i.e., the component of \mathbf{v} perpendicular to the LOS vector
- $v_{\perp LOS}$ = magnitude of $\mathbf{v}_{\perp LOS}$

$$v_{\perp LOS} = \sqrt{\alpha^2 + \beta^2} \quad (3-4)$$

- γ = target aspect angle between v and the $\alpha - \beta$ plane (FLIR)
- θ = angle between $v_{\perp LOS}$ and $+x_{FLIR}$
- AR = σ_{vo}/σ_{pvo} : aspect ratio of the reference image

Referring back to Figure 3.4, the location of each intensity function, or "hotspot," is initialized as a displacement from the hardbody center-of-mass. The intensity functions are oriented in the FLIR plane via the true target orientation angle θ . The relative positions of the two intensity functions in the FLIR plane vary in response to the change in target aspect angle γ (of Figure 3.5), while the spatial relationship of the hotspots remains the same in the three-dimensional target frame. If the plume pogo forcing input is applied, the hotspots do not remain fixed in the target frame, causing the composite image centroid to oscillate along the velocity vector and produce additional perturbations to the hotspot image in the FLIR plane [35].

3.3.2.3 Target Plume Velocity Projection onto the FLIR Plane. The general discrete-time equation that models the target dynamics is given by:

$$x(t_{i+1}) = \Phi(t_{i+1}, t_i)x(t_i) + B_d(t_i)u(t_i) + G_d(t_i)w_d(t_i) \quad (3-5)$$

where

- $\Phi(t_{i+1}, t_i)$ = the system state transition matrix
- $x(t_i)$ = discrete-time vector of states of interest
- $B_d(t_i)$ = discrete-time control input matrix
- $u(t_i)$ = discrete-time deterministic control input vector
- $G_d(t_i)$ = discrete-time driving noise input matrix

$w_d(t)$ = discrete-time, zero-mean, white Gaussian noise process with independent components and covariance Q_d

Based on the geometry shown previously in Figure 3.5, the projection of the target's inertial velocity vector onto the FLIR image plane is the deterministic input vector given by [10]:

$$u_{id}(t) = [\dot{\alpha}'(t) \quad \dot{\beta}'(t)]^T \quad (3-6)$$

where

$u_{id}(t)$ = true target deterministic input vector
 $\dot{\alpha}'(t)$ = target azimuth rate in the FLIR plane
 $\dot{\beta}'(t)$ = target elevation rate in the FLIR plane

As seen in the inertial frame diagrams of Figure 3.7, the azimuth angle can be defined as:

$$\alpha(t) = \arctan \left[\frac{z(t)}{x(t)} \right] \quad (3-7)$$

Taking the time derivative of Equation (3-7) and noting that the sensor-to-target range is large so that $\dot{\alpha}'(t) = \dot{\alpha}(t)$, the azimuth velocity in the FLIR plane is given by:

$$\dot{\alpha}'(t) = \dot{\alpha}(t) = \frac{x(t)v_z(t) - z(t)v_x(t)}{x^2(t) + z^2(t)} \quad (3-8)$$

where

v_x, v_z = components of the target's inertial velocity in the e_x and e_z directions

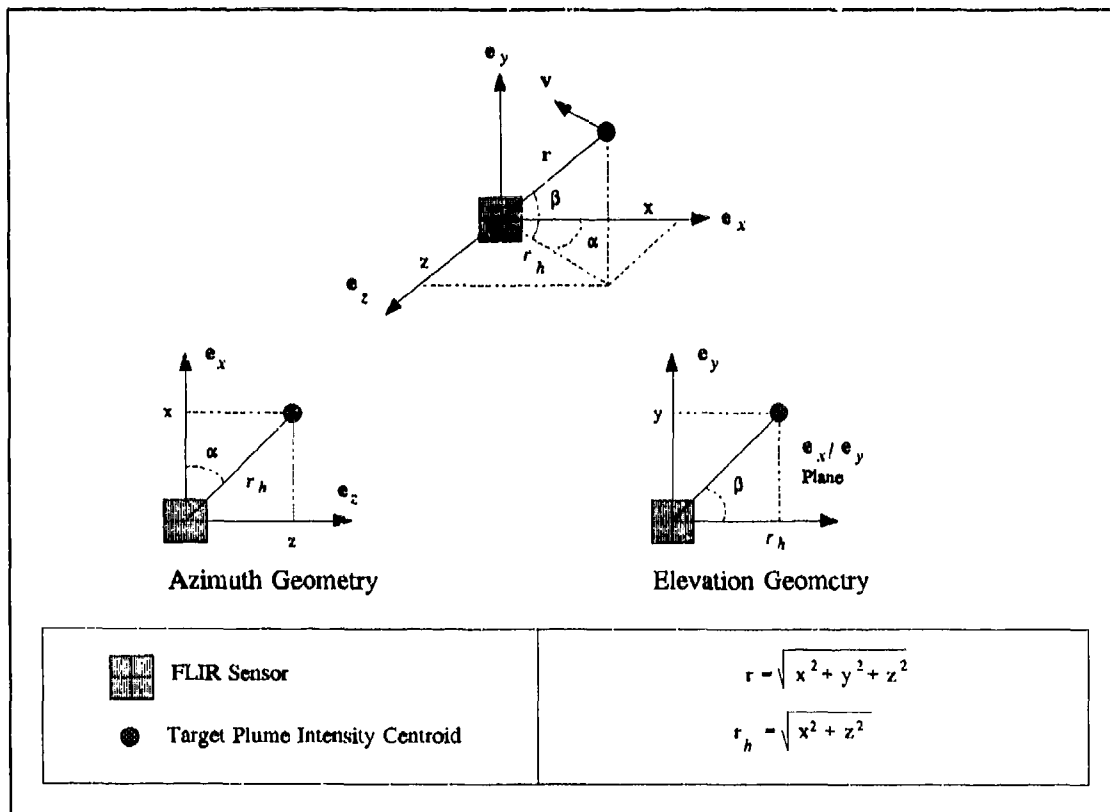


Figure 3.7 Inertial Velocity FLIR Plane Projection Geometry

Similarly, the elevation velocity in the FLIR plane is given by:

$$\dot{\beta}(t) = \dot{\beta}(t) = \frac{r_h(t)v_y(t) - y(t)\dot{r}_h(t)}{r^2(t)} \quad (3-9)$$

where

- v_y = component of the target's inertial velocity in the e_y direction
- r_h = horizontal projection of the sensor-to-target range, with its time derivative expressed as:

$$\dot{r}_h(t) = \frac{x(t)v_z(t) + z(t)v_x(t)}{r_h(t)} \quad (3-10)$$

3.4 FLIR Sensor Pointing Controller

The Kalman filter's propagated estimates of the intensity centroid's position dictate the necessary change in azimuth and elevation the FLIR sensor should undergo over the next sample period to center the hotspot on the FLIR FOV plane at the next measurement sample time. Ideally, these positional estimates are fed as commands to a pointing controller that physically implements the directional changes within one sample period (1/30 sec). However, the activation and execution of these commands will not be perfect due to the lag dynamics inherent in the controller, and the resultant mis-positioning of the hotspot may be interpreted by the filter as target motion, causing inaccurate estimates of future states.

Whether or not to include the controller lag dynamics in the simulation was the subject of a previous thesis [32]. It was found that the apparent target motion caused by the lag dynamics are interpreted by the filter as atmospheric jitter, implying a degree of robustness on the part of the filter to track a target. Moreover, the degradation in tracking performance due to the dynamic lag was found not to be of primary importance. Thus, the controller is modeled as lag-free in this research.

3.5 Summary

This chapter described the three main coordinate frames used in the simulation to establish the target plume on the FLIR image plane: 1) the 3-dimensional inertial reference frame, in which the target plume is propagated along its trajectory, 2) the target reference frame, used to define the axes of the target plume, and 3) the $\alpha - \beta - r$ frame, used to define the apparent image of the target plume's intensity centroid on the FLIR FOV. The model of the target plume was pictured

as a planform resulting from the difference of two Gaussian intensity functions with elliptical constant-intensity contours. The missile hardbody is not detected by the FLIR sensor, but is projected on the FLIR image plane as a rectangle that lies along the velocity vector. More will be said about the hardbody and measurements of its displacement from the plume centroid in the next chapter. The spatial displacement of the two intensity functions, relative to the hardbody, remains fixed in the target frame during the simulation. Plume pogo is invoked by oscillating the composite centroid along the plume's velocity vector. The position and velocity of the intensity centroid is projected onto the FLIR image plane using the geometric relationships between the three main frames. The trans-FLIR plane and the ALT-ACT plane are used to identify the missile hardbody center-of-mass, as will be seen in the next chapter. The FLIR sensor controller is modeled as lag-free since the filter interprets the lag dynamics-induced motion of the intensity centroid as atmospheric jitter, and previous research has demonstrated that ignoring this effect still yields viable performance evaluations.

IV. Truth Model

4.1 Introduction

A "truth model" represents the designer's best mathematical interpretation of the real-world dynamics as applicable to the system of interest. Such a model is the product of extensive data analysis, shaping filter design and validation in order to be confident that it adequately represents the real world, since the performance evaluation and systematic design procedure is totally dependent upon this assumption [17]. In many cases, the complete description of true system behavior may require an infinite-dimensional state model. Of course, for computational and simulation purposes, the number of truth model states must be of finite dimensionality, yet capture the dominant characteristics of system behavior. The Kalman filter is developed by systematically reducing the truth model to form the filter design model, and the resulting filter is constantly evaluated against the full-state model to ensure performance specifications are satisfied.

The dynamics of the target intensity centroid's image on the FLIR detector plane are a result of true target motion, atmospheric jitter due to distorted infrared wavefronts, bending/vibration of the optical hardware, and pogo effects of the plume's oscillations. The truth model is composed of the following fourteen states [12,27,35]:

- 2 target dynamic states
- 6 atmospheric states
- 4 mechanical bending states
- 2 pogo oscillation states

These dynamics are represented as changes of the image intensity centroid in the FLIR plane, with the centroid components x_c and y_c being measured in pixels from the center of the FOV in the x and y FLIR plane directions. Referring to Figure 4.1, the position of the target image at any one time is given by:

$$x_c = x_d + x_a + x_b + x_p \cos \theta_t \quad (4-1)$$

$$y_c = y_d + y_a + y_b - x_p \sin \theta_t \quad (4-2)$$

where

x_c, y_c = target image intensity centroid coordinates

x_d, y_d = coordinate deviation due to target dynamics

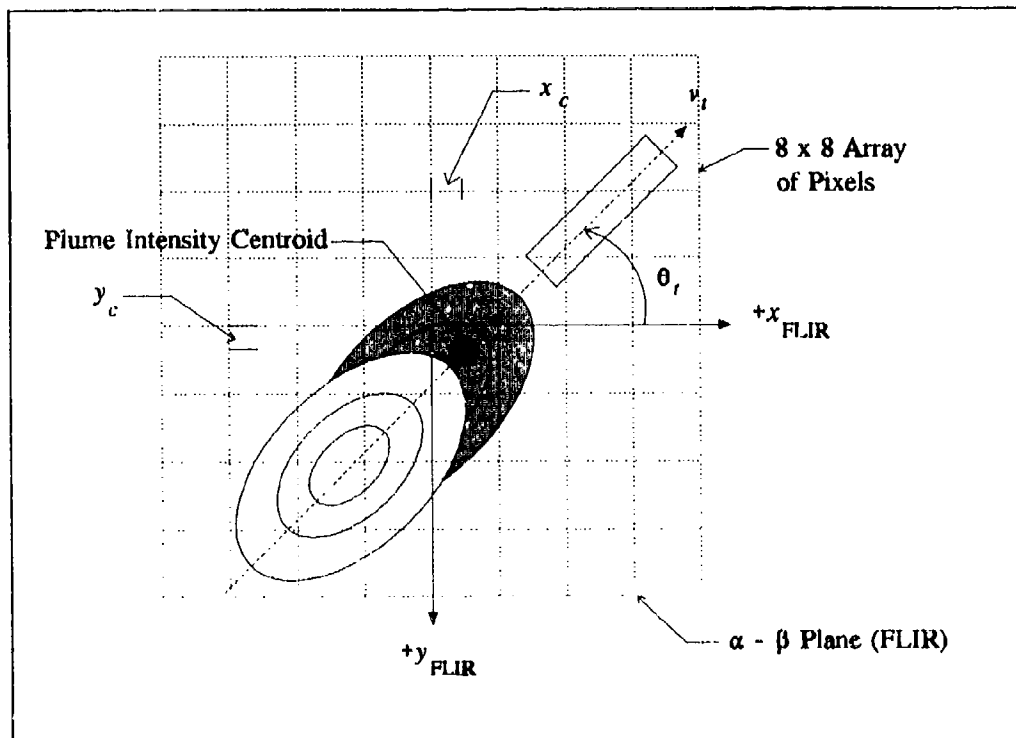


Figure 4.1 Plume Intensity Function Position on FLIR Image Plane

- x_a, y_a = coordinate deviation due to atmospheric jitter
- x_b, y_b = coordinate deviation due to bending/vibration of optical hardware
- x_p = coordinate deviation due to pogo oscillations along the velocity vector direction
- θ_t = true target orientation angle

Note that Equation (4-2) has a minus sign before the resolved pogo component, due to the coordinate definition of the FLIR coordinate frame. The states $x_a, x_b, x_d, x_p, y_a, y_b,$ and y_d comprise the output states which are extracted from an overall state model in the form of fourteen coupled scalar stochastic differential equations. The states x_d and y_d are each modeled by first-order differential equations; $x_b, y_b,$ and x_p are each modeled by second-order differential equations; and x_a and y_a are each modeled with third-order differential equations. These differential equations, when in space-state format, comprise the dynamics portion of the FLIR tracker truth model.

This chapter presents the dynamics model, the models of measurements that provide the Kalman filter periodic updates, and the initial conditions of the truth model equations and target trajectories. Some of the discussion is taken from Evans' thesis with minor modifications.

4.2 Dynamics Model

The fourteen-state model state vector is described by a first-order, stochastic differential equation given by:

$$\dot{x}_t(t) = F_t x_t(t) + B_t u_t(t) + G_t w_t(t) \quad (4-3)$$

where

- F_t = 14 x 14 time-invariant truth model plant matrix
- $x_t(t)$ = 14-dimensional truth model state vector

- $B_t = 14 \times 2$ time-invariant truth model control distribution matrix
 $u_t(t) = 2$ -dimensional deterministic input vector
 $G_t = 14 \times 14$ noise distribution matrix ($G_t = I$)
 $w_t(t) = 14$ -dimensional, white Gaussian noise process with mean and covariance kernel statistics:

$$\begin{aligned}
 E\{w_t(t)\} &= \mathbf{0} \\
 E\{w_t(t)w_t^T(t + \tau)\} &= Q_t\delta(t)
 \end{aligned}
 \tag{4-4}$$

To simulate the target dynamics model on a digital computer, the following equivalent discrete-time solution to Equation (4-3) is given by:

$$x_t(t_{i+1}) = \Phi_t(t_{i+1}, t_i)x_t(t_i) + B_{td}u_{td}(t_i) + G_{td}w_{td}(t_i)
 \tag{4-5}$$

where the state transition matrix $\Phi_t(t, t_i)$ is the solution to the differential equation:

$$\frac{d\Phi_t(t, t_i)}{dt} = F_t\Phi_t(t, t_i)
 \tag{4-6}$$

with the initial condition: $\Phi_t(t_i, t_i) = I$, (note that, for constant F_t , $\Phi_t(t, t_i)$ can be expressed as $\Phi_t(t-t_i)$) and

- $x_t(t_i) = 14$ -dimensional discrete-time truth model state vector
 $B_{td} = 14 \times 2$ discrete-time truth model control distribution matrix
 $u_{td}(t_i) = 2$ -dimensional discrete-time input vector
 $G_{td} = 14 \times 14$ discrete-time noise distribution matrix, ($G_{td} = I$)
 $w_{td}(t_i) = 12$ -dimensional discrete time, white Gaussian noise process with mean and covariance statistics:

$$E\{w_{id}(t)\} = \mathbf{0} \quad (4-7)$$

$$E\{w_{id}(t_i)w_{id}^T(t_i)\} = \mathbf{Q}_{id} = \int_{t_i}^{t_{i+1}} \Phi_i(t_{i+1} - \tau) \mathbf{G}_i \mathbf{Q}_i \mathbf{G}_i^T \Phi_i^T(t_{i+1} - \tau) d\tau \quad (4-8)$$

where \mathbf{Q}_i is defined in Equation (4-4). The discrete-time input distribution matrix \mathbf{B}_{id} is defined as:

$$\mathbf{B}_{id} = \int_{t_i}^{t_{i+1}} \Phi_i(t_{i+1} - \tau) \mathbf{B}_i d\tau \quad (4-9)$$

Note that this computation assumes $\mathbf{u}_i(t)$ is constant over each sample period: $\mathbf{u}_i(t) = \mathbf{u}_{id}(t_i)$ for all $t \in [t_i, t_{i+1})$.

The fourteen states of the discrete-time truth model are defined in the x and y coordinate axes of the FLIR plane as:

x_{FLIR}	y_{FLIR}
1 target state	1 target state
3 atmospheric states	3 atmospheric states
2 bending/vibration states	2 bending/vibration states
2 plume pogo states	

where the plume pogo states are in neither the x_{FLIR} nor y_{FLIR} direction. These states are augmented into the truth model state vector:

$$x_i = \begin{bmatrix} x_d \\ \dots \\ x_a \\ \dots \\ x_b \\ \dots \\ x_p \end{bmatrix} \quad (4-10)$$

where

- x_d = 2-dimensional target dynamics state vector
- x_a = 6-dimensional atmospheric state vector
- x_b = 4-dimensional bending/vibration state vector
- x_p = 2-dimensional plume pogo state vector

The 14 x 14 discrete-time truth model state transition matrix Φ_i is given by:

$$\Phi_i = \begin{bmatrix} \Phi_d & \mathbf{0} & \mathbf{0} & \mathbf{0} \\ \dots & \dots & \dots & \dots \\ \mathbf{0} & \Phi_a & \mathbf{0} & \mathbf{0} \\ \dots & \dots & \dots & \dots \\ \mathbf{0} & \mathbf{0} & \Phi_b & \mathbf{0} \\ \dots & \dots & \dots & \dots \\ \mathbf{0} & \mathbf{0} & \mathbf{0} & \Phi_p \end{bmatrix} \quad (4-11)$$

where the partitions correspond to the dimensionality of the states defined above. The 14 x 2 discrete-time truth model distribution matrix B_{td} is given by:

$$B_{td} = \begin{bmatrix} B_{td} \\ \dots \\ \mathbf{0} \end{bmatrix} \quad (4-12)$$

where B_{dd} is a 2×2 discrete-time control distribution matrix. The 14-dimensional discrete-time truth model white Gaussian noise process w_{id} is given by:

$$w_{id} = \begin{bmatrix} 0 \\ \dots \\ w_{da} \\ \dots \\ w_{db} \\ \dots \\ w_{dp} \end{bmatrix} \quad (4-13)$$

where

- $w_{da}(t_i)$ = 6-dimensional discrete-time, white Gaussian noise related to atmospheric jitter states
- $w_{db}(t_i)$ = 4-dimensional discrete-time, white Gaussian noise related to bending states
- $w_{dp}(t_i)$ = 2-dimensional discrete-time, white Gaussian noise related to plume pogo states

The block diagonal form of Equation (4-5), as seen in Equations (4-10) through (4-13), allows the models for target dynamics, atmospheric jitter, bending/vibration, and plume pogo to be presented separately. The following sections discuss each of the discrete state models which form the stochastic discrete-time truth model.

4.2.1 Target Model State Description. As depicted in Figure 4.2, the α - β plane (FLIR image plane) is coincident with the FLIR sensor FOV, and perpendicular to the LOS vector e_r . In the simulation, the 3-dimensional target dynamics are projected onto the FLIR image plane, and the position components of the target's intensity centroid are obtained from the azimuth and elevation displacement angles (α' and β' , respectively). Since the target distance is simulated

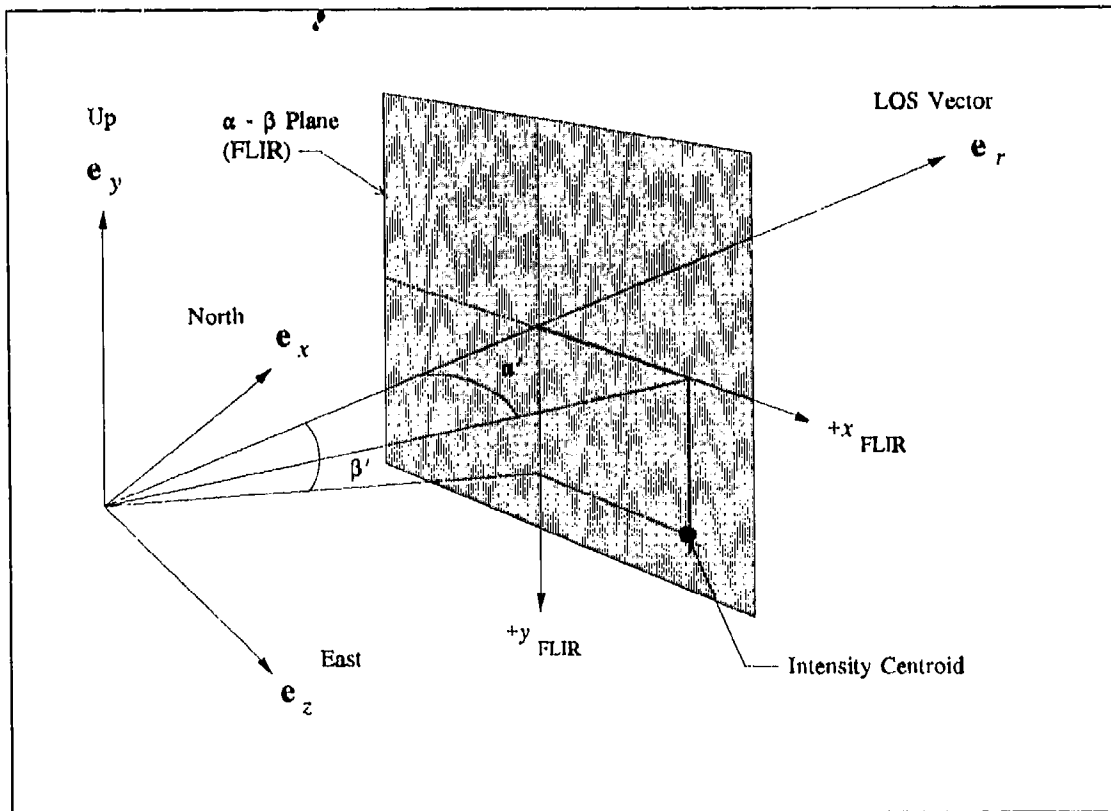


Figure 4.2 Target Centroid Image on α - β Plane with "Pseudo" Angles

as 2,000 kilometers, small angle approximations are used measuring the angle displacements in the cartesian coordinate system of the FLIR image plane. These "pseudo" angles, α' and β' , are referenced from the current LOS vector and measured in microradians. Note that the unusual orientation of the $+y_{FLIR}$ axis in Figure 4.2 allows the positive z axis to be in the positive e_z direction (by the right-hand rule).

The linear translational coordinates, x_c and y_c of Equations (4-1) and (4-2), locate the target intensity function on the FLIR plane and are measured in pixels of displacement from the center of the FLIR FOV. The angular and linear measurements are related by the pixel

proportionality constant k_p , which is the angular FOV of a single pixel. Presently, the value of k_p is approximately 15 microradians per pixel for long range targets [5,35].

The derivation of the state space model of the target dynamics assumes that the azimuth and elevation rates ($\dot{\alpha}$ and $\dot{\beta}$, respectively) remain essentially constant over each sample period Δt . Then the discrete-time target dynamics model is:

$$x_d(t_{i+1}) = x_d(t_i) + \frac{(\dot{\alpha}')(\Delta t)}{k_p} \quad (4-14)$$

$$y_d(t_{i+1}) = y_d(t_i) - \frac{(\dot{\beta}')(\Delta t)}{k_p} \quad (4-15)$$

Arranging these equations in state space form yields:

$$\tilde{x}_d(t_{i+1}) = \Phi_d(t_{i+1}, t_i) \tilde{x}_d(t_i) + B_d u_d(t_i) \quad (4-16)$$

$$\begin{bmatrix} x_d(t_{i+1}) \\ y_d(t_{i+1}) \end{bmatrix} = \begin{bmatrix} 1 & 0 \\ 0 & 1 \end{bmatrix} \begin{bmatrix} x_d(t_i) \\ y_d(t_i) \end{bmatrix} + \begin{bmatrix} \frac{\Delta t}{k_p} & 0 \\ 0 & -\frac{\Delta t}{k_p} \end{bmatrix} \begin{bmatrix} \dot{\alpha}'(t_i) \\ \dot{\beta}'(t_i) \end{bmatrix} \quad (4-17)$$

where

$\dot{\alpha}'(t_i) = d\alpha'/dt$, measured in microradians/second and constant over the time interval Δt

$\dot{\beta}'(t_i) = d\beta'/dt$, measured in microradians/second and constant over the time interval Δt

$\Delta t =$ sample time interval, $t_{i+1} - t_i$

$k_p =$ pixel proportionality constant (15 microradians/pixel)

Using these relationships in block form of the overall truth model, by inspection of Equation (4-11), the upper left block is:

$$\Phi_d = \begin{bmatrix} 1 & 0 \\ 0 & 1 \end{bmatrix} \quad (4-18)$$

and the upper block of Equation (4-12) is:

$$B_{dd} = \begin{bmatrix} \frac{\Delta t}{k_p} & 0 \\ 0 & -\frac{\Delta t}{k_p} \end{bmatrix} \quad (4-19)$$

and the input vector in Equation (4-5) is given by:

$$u_{td} = \begin{bmatrix} \dot{\alpha}'(t_i) \\ \dot{\beta}'(t_i) \end{bmatrix} \quad (4-20)$$

The minus sign of the lower right term in Equation (4-19) is due to the difference in the y axis orientation between the inertial coordinate frame and the FLIR coordinate plane.

The two target dynamic states of Equation (4-10) are used to propagate the missile along its trajectory. The formulation of the truth model target dynamics states in deterministic state space form has two advantages. First, Equation (4-17) can be substituted back into Equation (4-5) to form a single augmented vector differential equation that defines the truth model. Second, the

state space form allows the addition of white (or time-correlated) noise to Equation (4-17), if a stochastic, rather than a deterministic dynamics model, is desired.

4.2.2 Atmospheric Jitter Model. The model for the translational displacement of the intensity function due to atmospheric disturbances, is based on a study by The Analytic Sciences Corporation [27]. Using power spectral density characteristics, the atmospheric jitter phenomenon in each FLIR plane axis direction can be modeled as the output of a third-order shaping filter driven by white Gaussian noise [27]. The Laplace domain representation of the shaping filter transfer function is given by:

$$\frac{x_a(s)}{w_a(s)} = \frac{K_a \omega_1 \omega_2^2}{(s + \omega_1)(s + \omega_2)^2} \quad (4-21)$$

- x_a = output of shaping filter (x_{FLIR} direction)
- w_a = zero-mean, scalar, unit-strength white Gaussian noise
- K_a = gain, adjusted for desired atmospheric jitter rms value
- ω_1 = break frequency, 14.14 radians/second
- ω_2 = double-pole break frequency, 659.5 radians/second

The atmospheric jitter effects can be modeled similarly in the y_{FLIR} direction, wherein y_a would be the output of an identical shaping filter defined in Equation (4-21). The two shaping filters are assumed to be independent of each other and can thus be augmented to form a six-state model. The linear stochastic differential equation that describes the atmospheric jitter is given by:

$$\dot{\hat{x}}_a(t) = F_a \hat{x}_a(t) + G_a w_a(t) \quad (4-22)$$

where

- $F_a = 6 \times 6$ time-invariant atmospheric jitter plant matrix
- $x_a(t) = 6$ -dimensional atmospheric jitter state vector
- $G_a = 6 \times 2$ noise distribution matrix
- $w_a(t) = 6$ -dimensional, independent, zero mean white Gaussian noise with unit strength and independent components described as:

$$E(w_a(t_i)) = 0$$

$$E(w_a(t_i)w_a^T(t_j)) = Q_a \delta(\tau) = \begin{bmatrix} 1 & 0 \\ 0 & 1 \end{bmatrix} \delta(\tau) \quad (4-23)$$

The six atmospheric states in the state vector correspond to the low frequency pole and the higher frequency double pole in the x_{FLIR} and the y_{FLIR} directions. The atmospheric jitter plant matrix is defined in Jordan Canonical form as:

$$F_a = \begin{bmatrix} -\omega_1 & 0 & 0 & 0 & 0 & 0 \\ 0 & -\omega_2 & 1 & 0 & 0 & 0 \\ 0 & 0 & -\omega_2 & 0 & 0 & 0 \\ 0 & 0 & 0 & -\omega_1 & 0 & 0 \\ 0 & 0 & 0 & 0 & -\omega_2 & 1 \\ 0 & 0 & 0 & 0 & 0 & -\omega_2 \end{bmatrix} \quad (4-24)$$

The noise distribution matrix G_a is:

$$G_a = \begin{bmatrix} \frac{K_a \omega_1 \omega_2^2}{(\omega_1 - \omega_2)^2} & 0 \\ -\frac{K_a \omega_1 \omega_2^2}{(\omega_1 - \omega_2)^2} & 0 \\ \frac{K_a \omega_1 \omega_2^2}{(\omega_1 - \omega_2)^2} & 0 \\ 0 & \frac{K_a \omega_1 \omega_2^2}{(\omega_1 - \omega_2)^2} \\ 0 & -\frac{K_a \omega_1 \omega_2^2}{(\omega_1 - \omega_2)^2} \\ 0 & \frac{K_a \omega_1 \omega_2^2}{(\omega_1 - \omega_2)^2} \end{bmatrix} \quad (4-25)$$

The equivalent discrete-time model for Equation (4-22) is of the form:

$$x_a(t_{i+1}) = \Phi(t_{i+1}, t_i) x_a(t_i) + w_{da}(t_i) \quad (4-26)$$

The augmented six-state state transition matrix derived from the time-invariant plant matrix of Equation (4-24) is [27]:

$$\Phi_a(\Delta t) = \begin{bmatrix} \Phi_{a11} & 0 & 0 & 0 & 0 & 0 \\ 0 & \Phi_{a22} & \Phi_{a23} & 0 & 0 & 0 \\ 0 & 0 & \Phi_{a33} & 0 & 0 & 0 \\ 0 & 0 & 0 & \Phi_{a44} & 0 & 0 \\ 0 & 0 & 0 & 0 & \Phi_{a55} & \Phi_{a56} \\ 0 & 0 & 0 & 0 & 0 & \Phi_{a66} \end{bmatrix} \quad (4-27)$$

where

$$\begin{aligned}
 \Phi_{a11} &= \Phi_{a44} = \exp(-\omega_1 \Delta t) \\
 \Phi_{a22} &= \Phi_{a55} = \exp(-\omega_2 \Delta t) \\
 \Phi_{a23} &= \Phi_{a56} = \Delta t \exp(-\omega_2 \Delta t) \\
 \Phi_{a33} &= \Phi_{a66} = \exp(-\omega_2 \Delta t) \\
 \Delta t &= \text{sample time interval, } t_{i+1} - t_i
 \end{aligned}$$

The 6-dimensional, zero-mean, discrete-time, white, Gaussian noise $w_{da}(t_i)$ has statistics defined as:

$$\begin{aligned}
 E\{w_{da}(t_i)\} &= \mathbf{0} \\
 E\{w_{da}(t_i)w_{da}^T(t_i)\} &= \mathbf{Q}_{da} = \int_{t_i}^{t_{i+1}} \Phi_a(t_{i+1}-\tau) \mathbf{G}_a \mathbf{Q}_a \mathbf{G}_a^T \Phi_a^T(t_{i+1}-\tau) d\tau
 \end{aligned} \tag{4-28}$$

4.2.3 Bending/Vibration Model. The mechanical bending states were added to the truth model to account for the vibrational effects in the FLIR data that occur when the sensor is mounted on a moving, non-rigid optical platform [12]. Based on tests at the AWFL (now Phillips Laboratory), it was concluded in previous research [12] that bending effects in both the x_{FLIR} and y_{FLIR} directions can be represented by a second order shaping filter, driven by white Gaussian noise. The Laplace domain transfer function for the bending model is:

$$\frac{x_b(s)}{w_b(s)} = \frac{K_b \omega_{nb}^2}{s^2 + 2\zeta_b \omega_{nb} s + \omega_{nb}^2} \tag{4-29}$$

where

- x_b = FLIR plane positional offset (x_{FLIR} direction) due to mechanical bending disturbance
- w_b = zero-mean, unit strength, white Gaussian noise

- K_b = gain adjustment to obtain desired rms bending output,
 ($K_b^2 = 5 \times 10^{-13} \text{rad}^4/\text{sec}^4$)
 ζ_b = damping coefficient, equal to 0.15
 ω_{nb} = undamped natural frequency for bending, ($\omega = \pi \text{ rad/sec}$)

The FLIR plane positional offset in the y_{FLIR} direction, y_b , is identically modeled with the shaping filter defined in Equation (4-29). The two shaping filters are assumed to be independent of each other and can thus be augmented to form a four-state model. The linear stochastic differential equation that describes the bending/vibration is given by:

$$\dot{x}_b(t) = F_b x_b(t) + G_b w_b(t) \quad (4-30)$$

where

- F_b = 4 x 4 time-invariant bending plant matrix
 $x_b(t)$ = 4-dimensional bending state vector
 G_b = 4 x 2 noise distribution matrix
 $w_b(t)$ = 2-dimensional, white Gaussian noise process with unit strength components that are independent of each other:

$$\begin{aligned}
 E\{w_b(t)\} &= \mathbf{0} \\
 E\{w_b(t)w_b^T(t+\tau)\} &= Q_b \delta(\tau) = \begin{bmatrix} 1 & 0 \\ 0 & 1 \end{bmatrix} \delta(\tau)
 \end{aligned} \quad (4-31)$$

The bending/vibration plant matrix is defined as:

$$F_b = \begin{bmatrix} 0 & 1 & 0 & 0 \\ -\omega_{nb}^2 & -2\zeta_b \omega_{nb} & 0 & 0 \\ 0 & 0 & 0 & 1 \\ 0 & 0 & -\omega_{nb}^2 & -2\zeta_b \omega_{nb} \end{bmatrix} \quad (4-32)$$

The noise distribution matrix G_b is:

$$G_b = \begin{bmatrix} 0 & 0 \\ \omega_{nb}^2 k_p & 0 \\ 0 & 0 \\ 0 & \omega_{nb}^2 k_p \end{bmatrix} \quad (4-33)$$

(Note that k_p is the pixel proportionality constant.)

The equivalent discrete-time model for Equation (4-30) is of the form:

$$x_b(t_{i+1}) = \Phi(t_{i+1}, t_i) x_b(t_i) + w_{db}(t_i) \quad (4-34)$$

where

$$\Phi_b(\Delta t) = \begin{bmatrix} \Phi_{b11} & \Phi_{b12} & 0 & 0 \\ \Phi_{b21} & \Phi_{b22} & 0 & 0 \\ 0 & 0 & \Phi_{b33} & \Phi_{b34} \\ 0 & 0 & \Phi_{b43} & \Phi_{b44} \end{bmatrix} \quad (4-35)$$

and

$$\Phi_{b11} = \Phi_{b33} = \exp(-\sigma_b \Delta t) [\cos(\omega_b \Delta t) + (\sigma_b / \omega_b) \sin(\omega_b \Delta t)]$$

$$\Phi_{b12} = \Phi_{b34} = \exp(-\sigma_b \Delta t) [(1/\sigma_b) \sin(\omega_b \Delta t)]$$

$$\Phi_{b21} = \Phi_{b43} = \exp(-\sigma_b \Delta t) [-1 - (\sigma_b / \omega_b)^2 \sin(\omega_b \Delta t)]$$

$$\Phi_{b22} = \Phi_{b44} = \exp(-\sigma_b \Delta t) [\cos(\omega_b \Delta t) - (\sigma_b / \omega_b) \sin(\omega_b \Delta t)]$$

$\Delta t =$ sample time interval, $t_{i+1} - t_i$

$\sigma_b =$ real part of the root of the characteristic equation in Equation (4-29),
($\sigma_b = 0.47124$ second⁻¹)

$\omega_b =$ imaginary part of the root of the characteristic equation in Equation (4-29),
($\omega_b = 3.10605$ radians/second)

The 4-dimensional, discrete-time, white Gaussian noise process vector $w_{db}(t_i)$ has mean and covariance statistics:

$$\begin{aligned} E\{w_{db}(t_i)\} &= \mathbf{0} \\ E\{w_{db}(t_i)w_{db}^T(t_i)\} &= \mathbf{Q}_{db} = \int_{t_i}^{t_{i+1}} \Phi_b(t_{i+1}-\tau) \mathbf{G}_b \mathbf{Q}_b \mathbf{G}_b^T \Phi_b^T(t_{i+1}-\tau) d\tau \end{aligned} \quad (4-36)$$

4.2.4 Plume Pogo Model. To account for the oscillatory nature of a typical missile plume in the boost phase, a plume pogo model was developed [35]. A second-order Gauss-Markov model was generated using physical insight, and visual observation of the pogo phenomenon. The model allows for the study of the amplitude and frequency characteristics of the oscillatory nature of the plume, and of the effect upon tracking a missile using a Kalman filter.

The transfer function of the plume pogo model is described in the Laplace domain as:

$$\frac{x_p(s)}{w_p(s)} = \frac{K_p \omega_{np}^2}{s^2 + 2\zeta_p \omega_{np} s + \omega_{np}^2} \quad (4-37)$$

where

$x_p =$ plume pogo shaping filter output along the direction of the velocity vector

$w_p =$ zero-mean, unit strength, white Gaussian noise

- ζ_p = assumed damping coefficient, ($\zeta = 0.05$)
 ω_{np} = nominal undamped natural frequency for pogo; assumed range is 0.1 - 10 hertz, with a nominal value of 1.0 Hertz
 K_p = gain adjustment to obtain desired rms pogo amplitude determined by [35]:

$$K_p = 2\sigma_p \sqrt{\frac{\zeta_p}{\omega_{np}}} \quad (4-38)$$

where

σ_p = desired rms pogo along the velocity vector

The linear stochastic differential equation that describes the plume pogo is given in state space form as:

$$\dot{x}(t) = \begin{bmatrix} 0 & 1 \\ -\omega_{np}^2 & -2\zeta_p \omega_{np} \end{bmatrix} x_p(t) + \begin{bmatrix} 0 \\ K_p \omega_{np}^2 \end{bmatrix} w_p(t) \quad (4-39)$$

where

$x_p(t)$ = 2-dimensional pogo state vector

$w_p(t)$ = 1-dimensional zero-mean, white Gaussian noise with statistics:

$$\begin{aligned} E\{w_p(t)\} &= 0 \\ E\{w_p(t)w_p(t+\tau)\} &= Q_p \delta(t-\tau); \quad Q_p = 1 \end{aligned} \quad (4-40)$$

The equivalent discrete-time model for Equation (4-38) is of the form:

$$x_p(t_{i+1}) = \Phi(t_{i+1}, t_i) x_p(t_i) + w_{dp}(t_i) \quad (4-41)$$

$$\mathbf{x}_p(t_{i,1}) = \begin{bmatrix} \Phi_{p11}(\Delta t) & \Phi_{p12}(\Delta t) \\ \Phi_{p21}(\Delta t) & \Phi_{p22}(\Delta t) \end{bmatrix} \mathbf{x}_p(t_i) + \mathbf{w}_{dp}(t_i) \quad (4-42)$$

where

$$\begin{aligned} \Phi_{p11}(\Delta t) &= \frac{1}{\sqrt{1-\zeta_p^2}} \exp(-\zeta_p \omega_{np} \Delta t) \sin \left[\omega_{np} \sqrt{1-\zeta_p^2} \Delta t + \arctan \left(\frac{\sqrt{1-\zeta_p^2}}{\zeta_p} \right) \right] \\ \Phi_{p12}(\Delta t) &= \frac{-\omega_{np}}{\sqrt{1-\zeta_p^2}} \exp(-\zeta_p \omega_{np} \Delta t) \sin \left(\omega_{np} \sqrt{1-\zeta_p^2} \Delta t \right) \\ \Phi_{p21}(\Delta t) &= \frac{-\omega_{np}}{\sqrt{1-\zeta_p^2}} \exp(-\zeta_p \omega_{np} \Delta t) \sin \left(\omega_{np} \sqrt{1-\zeta_p^2} \Delta t \right) \\ \Phi_{p22}(\Delta t) &= \frac{1}{\sqrt{1-\zeta_p^2}} \exp(-\zeta_p \omega_{np} \Delta t) \sin \left[\omega_{np} \sqrt{1-\zeta_p^2} \Delta t + \arctan \left(\frac{\sqrt{1-\zeta_p^2}}{-\zeta_p} \right) + \pi \right] \end{aligned} \quad (4-43)$$

The 2-dimensional, discrete time, white Gaussian noise process $\mathbf{w}_{dp}(t_i)$ has mean and covariance statistics:

$$\begin{aligned} E\{\mathbf{w}_{dp}(t_i)\} &= \mathbf{0} \\ E\{\mathbf{w}_{dp}(t_i)\mathbf{w}_{dp}^T(t_i)\} &= \mathbf{Q}_{dp} = \int_{t_i}^{t_{i+1}} \Phi_p(t_{i+1}-\tau) \mathbf{G}_p \mathbf{Q}_p \mathbf{G}_p^T \Phi_p^T(t_{i+1}-\tau) d\tau \end{aligned} \quad (4-44)$$

The 2-dimensional pogo state vector defines the position of the plume image intensity centroid and its velocity along the longitudinal axis of the missile. For the simulation, it is assumed that the velocity vector lies coincident with the longitudinal axis of the hardbody. As shown in Figure 4.3, the plume oscillates about an equilibrium point also located on the longitudinal axis. This equilibrium point is defined by the initial positions of the two intensity

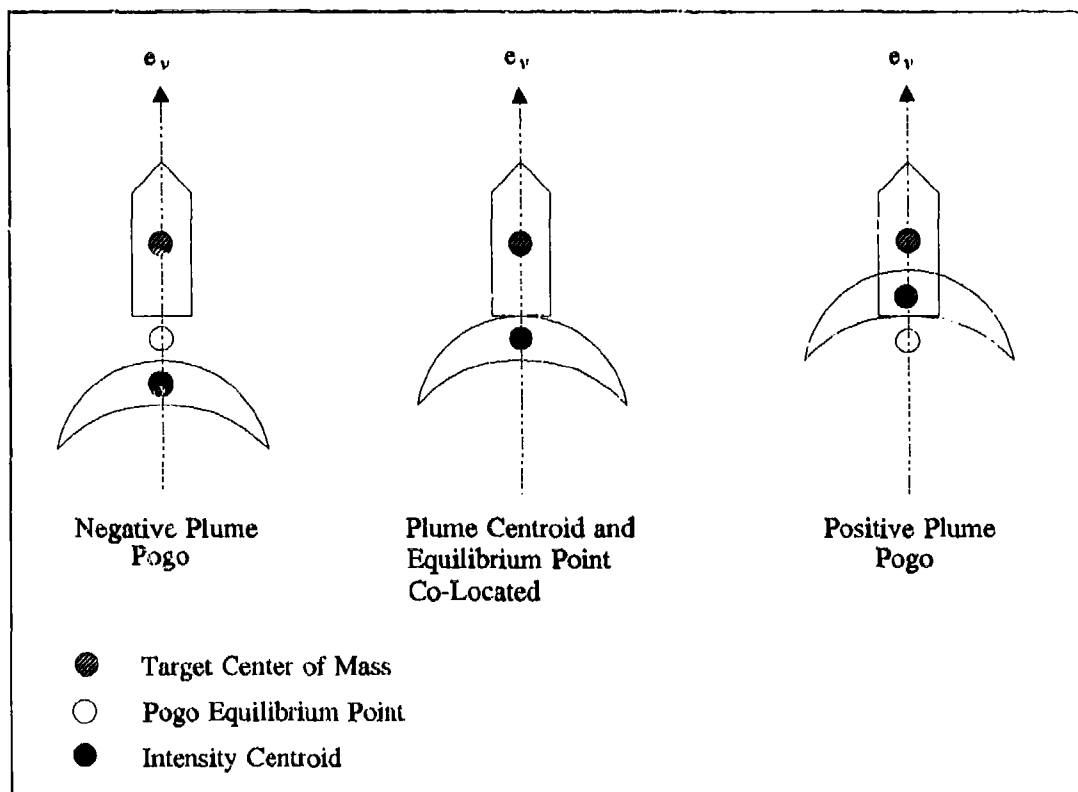


Figure 4.3 Plume Pogo Oscillation

functions in the target coordinate frame (to be discussed in Section 4.3.1), and remains equidistant from the hardbody center-of-mass throughout the simulation (the spatial relationship of the intensity functions can be seen in Figure 3.4). The crescent-shaped plume represents one of many equal-intensity contour lines of the actual plume. The angle of attack and sideslip angle of the missile are also assumed negligible, and have zero values for the simulation [35].

4.3 Measurement Models

In real-world applications, physical sensors provide the measurements that are used by the Kalman filter to update its state estimates. In the simulation, the measurement models generate discrete-time measurements for the filters used in this thesis. These measurements are corrupted

by simulations of sensor inaccuracies or measurement noise, with characteristics that are determined from prior knowledge and/or physical insight of the sensor's limitations. Two distinct types of measurements are modeled: first, "psuedo-measurements" are generated by an enhanced correlator algorithm from raw FLIR data [36] to the six-state FLIR filter to update its position and velocity estimates of the target plume centroid. Second, low-energy laser return measurements of the hardbody are produced and furnished to independent center-of-mass filters. Use of the latter type of measurements will allow one to explore the feasibility of the Doppler return in discerning the plume/hardbody interface, as well as observe the effect of the plume's speckle reflectance upon the hardbody's speckle return. For these reasons, this research is motivated to study three separate, independent center-of-mass filters: a one-state filter that receives Doppler return measurements, a one-state filter that accepts speckle return measurements, and a two-state filter that processes both speckle and Doppler return measurements. These center-of-mass filters will be discussed in detail in Chapter V.

The scenario for the center-of-mass measurement begins with the FLIR filter's estimate of the intensity centroid's position. The plume of a ballistic missile in boost phase is tracked using FLIR sensor measurements. The FLIR sensor measurements alone cannot provide any information regarding the hardbody, for it only senses the plume's IR radiation. The "psuedo-measurements" derived from the FLIR measurements and enhanced correlator are input to a linear Kalman filter which estimates the position and velocity of the plume's intensity centroid. Using the estimated intensity centroid position as a starting point, a low-energy laser is then scanned along the velocity vector to obtain a reflection from the hardbody. Once the low-energy laser scan illuminates the hardbody, information regarding the dimensions of the hardbody is obtained based upon distinct low-energy laser returns of the plume/hardbody and the space-background/hardbody

interfaces. An offset distance from the plume intensity centroid is calculated to pinpoint the hardbody center-of-mass and is provided as the measurement to the one-state center-of-mass filter for its update. If no laser reflection occurs, the one-state-filter continues to propagate its state estimate.

Eden's [5] research revealed that, for long ranges, jitter in the filter-estimated intensity centroid position resulted in a 15-20% rate of laser reflection from the hardbody. This low rate hampered efforts to assess the performance of the one-state center-of-mass filter, and consequently, a sweep of the low-energy laser scan about the velocity vector was created by Evans [6]. The laser sweep, although not an efficient method of illuminating the hardbody, substantially increases the rate of reflection returns and improves the estimate of the hardbody center-of-mass.

The two measurement models, one which simulates the 8 x 8 FLIR sensor array and one which simulates the low-energy laser reflection returns, are discussed in subsections 4.3.1 and 4.3.2. An introduction to the basic concepts of the Doppler phenomenon and the Doppler Measurement Model are presented in subsection 4.3.3.

4.3.1 FLIR Model. The FLIR sensor model is composed of an 8 x 8 pixel array "tracking window" extracted from the total array of 300 x 500 pixels. The missile plume is projected onto the FLIR focal plane, with its characteristic crescent-shaped intensity function formed as the difference of two bivariate Gaussian intensity functions, as shown in Figure 4.4. This model depends upon knowledge of several parameters: the size of the major and minor axis of the elliptical contours of each bivariate Gaussian function, and the orientation of the principal axis in the FLIR image plane. The target intensity function obtained from evaluating the resulting non-Gaussian intensity function is corrupted by spatially correlated and temporally uncorrelated

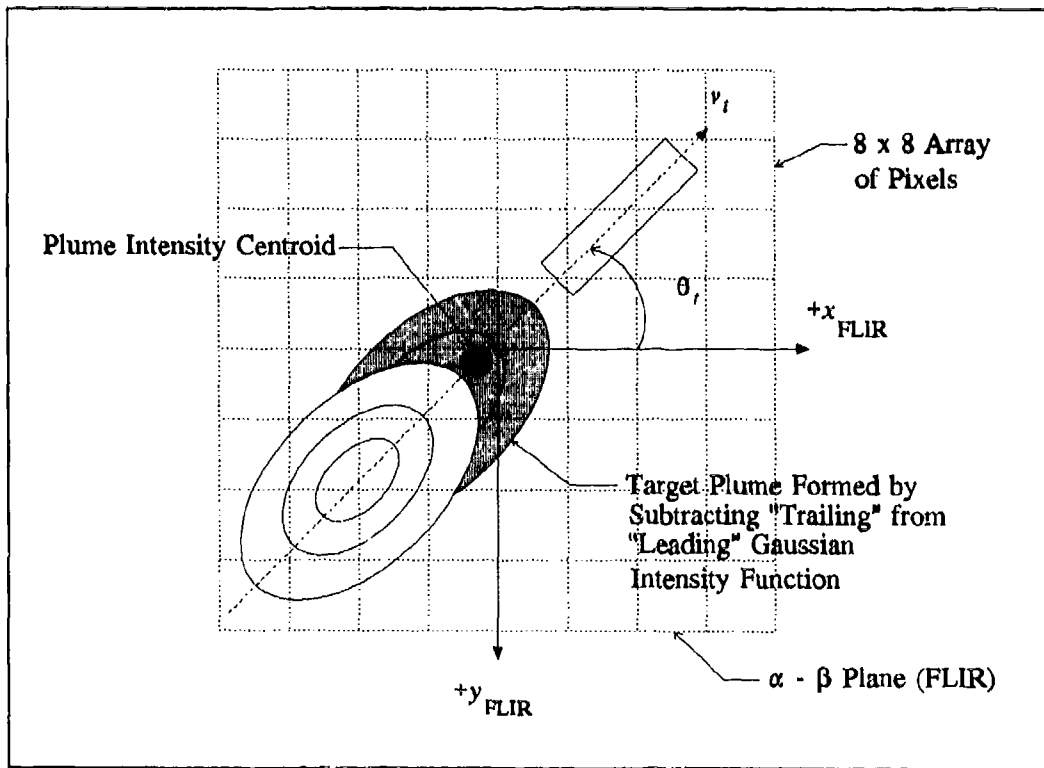


Figure 4.4 Composite Plume Intensity Function on FLIR Plane

background and internal FLIR noise according to models of actual data taken from a FLIR sensor looking at various backgrounds [33].

For each pixel in the FLIR FOV (the 8 x 8 array "tracking window"), the target's intensity function, correlated background noise, and FLIR internal noise are added together to produce an intensity measurement. For the 8 rows and 8 columns of the FOV, the intensity measurement corresponding to the pixel in the j^{th} row and k^{th} column at sampling time t_i is given by:

$$\begin{aligned}
 z_{jk}(t_i) = & \frac{1}{A_p} \int_{\text{pixel}_{jk}} \{ I_1[x, y, x_{\text{peak1}}(t_i), y_{\text{peak1}}(t_i)] \\
 & - I_2[x, y, x_{\text{peak2}}(t_i), y_{\text{peak2}}(t_i)] \} dx dy \\
 & + n_{jk}(t_i) + b_{jk}(t_i)
 \end{aligned}
 \tag{4-45}$$

where

- $z_{jk}(t_i)$ = output of pixel in the j^{th} row and k^{th} column
- A_p = area of one pixel
- I_1, I_2 = intensity function of first and second Gaussian intensity function respectively of Figure 4.4
- x, y = coordinates of any point within pixel jk
- x_{peak1}, y_{peak1} = coordinates of maximum point of first Gaussian intensity function
- x_{peak2}, y_{peak2} = coordinates of maximum point of second Gaussian intensity function
- $n_{jk}(t_i)$ = effect of internal FLIR sensor noise on jk^{th} pixel
- $b_{jk}(t_i)$ = effect of spatially correlated background noise on jk^{th} pixel

The sensor error, $n_{jk}(t_i)$, is the result of thermal noise and dark current in the IR detectors (pixels). This error is assumed to be both temporally and spatially uncorrelated [35].

The background noise, $b_{jk}(t_i)$, was observed in the FLIR data by AWFL personnel during a tracking operation [10]. It is represented as a spatially correlated noise with radial symmetry, with a correlation that decays exponentially. Harnly and Jensen [10] concluded that spatial correlation can be depicted as a correlation distance of approximately two pixels in the FLIR plane, and simulated this by maintaining non-zero correlation coefficients between each pixel and its two closest neighbors symmetrically in all directions. In that two-pixel distance, the correlation decays exponentially to one-tenth of its peak value.

The generation of spatially correlated white Gaussian noises is accomplished by allowing non-zero cross correlations between the measurement noises, $b_{jk}(t_i)$, associated with each of the 64 pixels from the 8 x 8 pixel FLIR FOV. The correlated measurement noise in Equation (4-45) is given as:

$b(t_i)$ = 64-dimensional vector of spatially correlated noise with statistics:

$$\begin{aligned} E\{b(t_i)\} &= \mathbf{0} \\ E\{b(t_i)b^T(t_j)\} &= R\delta_{ij} \end{aligned} \quad (4-46)$$

where R is a 64 x 64 measurement noise covariance matrix. This matrix describes the spatial correlation between pixels, and is given by [10]:

$$R = \sigma_R^2 \begin{bmatrix} 1 & r_{1,2} & r_{1,3} & \dots & r_{1,64} \\ r_{2,1} & 1 & r_{2,3} & \dots & r_{2,64} \\ r_{3,1} & r_{3,2} & 1 & \dots & r_{3,64} \\ \vdots & \vdots & \vdots & \vdots & \vdots \\ r_{64,1} & r_{64,2} & r_{64,3} & \dots & 1 \end{bmatrix} \quad (4-47)$$

where σ_R^2 is the variance of each scalar noise and the correlation coefficients $r_{j,k}$ are evaluated to reflect the radially symmetric, exponentially decaying pattern. The spatially correlated background noise $b(t_i)$ is simulated as:

$$b(t_i) = \sqrt[{}^c]{R} b'(t_i) \quad (4-48)$$

where

$\sqrt[{}^c]{}$ = Cholesky square root

$b'(t_i)$ = 64-dimensional vector of readily simulated discrete, independent white Gaussian noise with statistics:

$$\begin{aligned} E\{b'(t_i)\} &= \mathbf{0} \\ E\{b'(t_i)b'^T(t_j)\} &= I\delta_{ij} \end{aligned} \quad (4-49)$$

4.3.2 Low-Energy Laser Speckle Reflection Model. The low-energy speckle reflection model evolved through the work accomplished by Eden and Evans. The model makes no attempt to simulate the detailed physical phenomena associated with the speckle return of the reflected laser from the plume or hardbody. Rather, the model simulates the reflectivity information from the hardbody speckle return which would be derived by speckle detection circuitry. This research into the applicability of the Doppler return to discern the missile hardbody from the plume is a continuation of the laser speckle reflection model and hardbody center-of-mass development by Eden and Evans [5,6]. It is motivated by some shortcomings of speckle measurement information, and the same perspective of modeling the information derivable from such measurements, rather than the detailed phenomenology and physics of such measurements, shall be pursued.

The low-energy laser speckle reflection model simulates a measurement to the one-state center-of-mass Kalman filter for estimating the offset distance from the plume intensity centroid along the vehicle's FLIR image plane velocity vector. The first attempt to model the laser speckle return consisted of the hardbody designed as a rectangle with a binary-valued reflectivity function, which provided a binary indication of the hardbody whenever successful interception by the laser beam occurred [5]. With this model, speckle reflection information was equally obtained over the entire vehicle. This was followed by an enhanced, 3-dimensional, reflectivity model which accounted for the realistic distribution of the laser speckle return according to the curvature and aspect angle of the hardbody [6]. The 3-dimensional model is employed for this research since the Doppler return is also a function of reflectivity [38,39,44]. The following subsections discuss the development of Evans' 3-dimensional Hardbody Reflectivity Model and introduce the Plume Reflectance Model.

4.3.2.1 The Hardbody Reflectivity Model. The 3-dimensional reflectivity model was developed by Evans [6] based upon his analysis of empirical data, shown in Figure 4.5, obtained from the 6585th Test Group, Holloman AFB, New Mexico [7]. The data illustrates the return power (expressed in decibels-square meters) as a function of radar cross section (RCS) from a 20 x 249 inch cylinder with hemispherical endcaps as it was rotated longitudinally in the plane of the radar source. (RCS is defined as the projected area of a metal sphere which would return the same echo signal as the target, had the sphere been substituted for the target [38].) Note the peak values at 90° and 270°, where the cylinder was orthogonal to the line of sight, and the sharp dropoff in reflection as the angle deviates from that orthogonal condition. The reflectivity model, shown relative to the FLIR image plane in Figure 4.6, modifies the previous rectangular model to include 29 discrete-weighted line segments along the length of the model. Two functions define the hardbody reflectivity model: the cross-sectional function and the longitudinal function.

Each discrete-weighted line represents a cross-sectional reflectivity function which duplicates the data in Figure 4.5. The reflectivity function models the curvature by defining the strength of the reflected signal at each discrete line, where the amplitude of the reflected signal is highest along the missile centerline and discretely tapers towards the hardbody sides in 0.1 meter increments. The discrete implementation of the cross-sectional reflectivity function for the simulation is shown in Figure 4.7. Note the peak reflection of the cross-sectional reflectivity function's center is represented by an arbitrary value of 50 units of reflection magnitude [6]. The remaining line segments are scaled according to the empirical data of Figure 4.5. The reflectivity function also yields zero reflection for those portions of the original rectangle far from the missile centerline, so the effective reflective area of the hardbody is less than that of the binary model.

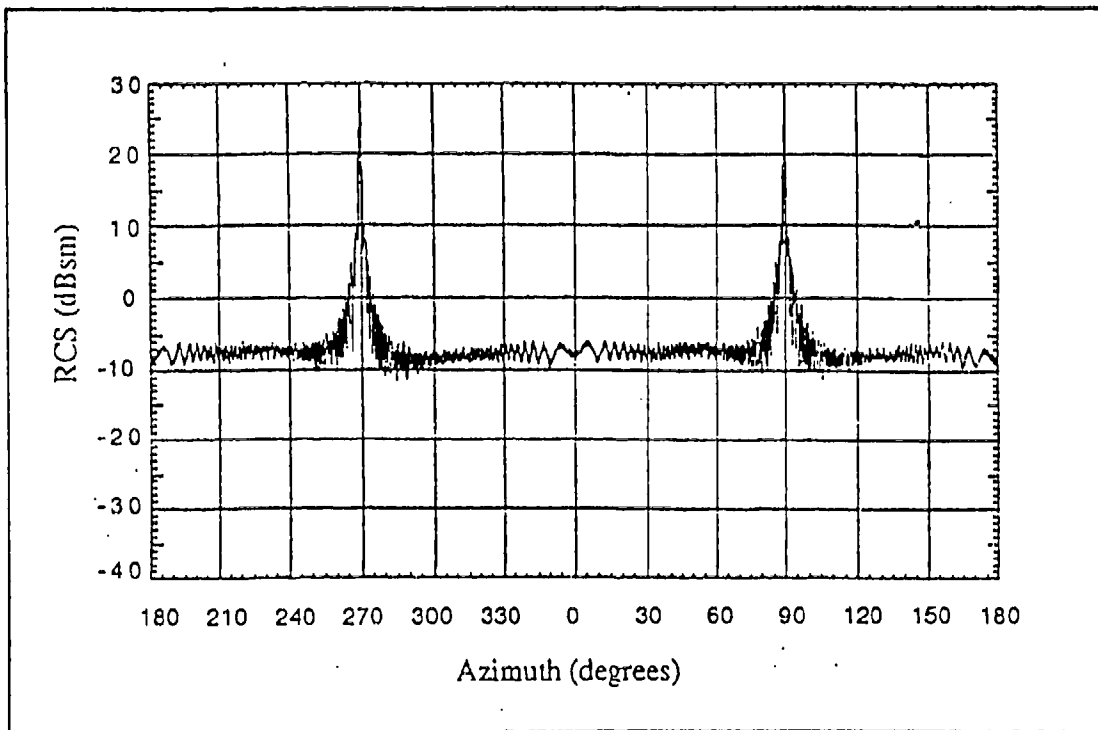


Figure 4.5 Empirical Radar Reflection Data of Cylinder [7]

The angle γ , defined as the angle between the inertial velocity vector and the FLIR plane, is utilized by the longitudinal reflectivity function to provide a scaling factor of the total reflection function if the missile centerline is oriented other than normal to the FLIR plane. Similar to the cross-sectional reflectivity function, the longitudinal function assigns a scaling factor to the reflected signal based upon the angular aspect of the target velocity.

Another factor in determining the received speckle reflection is the sensitivity level of the low-energy laser sensor. This sensitivity is represented in the simulation as a threshold limit below which the low-energy laser sensor cannot detect the reflection return. To illustrate the function of the sensor sensitivity factor, consider the hardbody at an aspect angle γ , relative to the FLIR image plane. In this orientation, the maximum amount of reflection is obtained in the

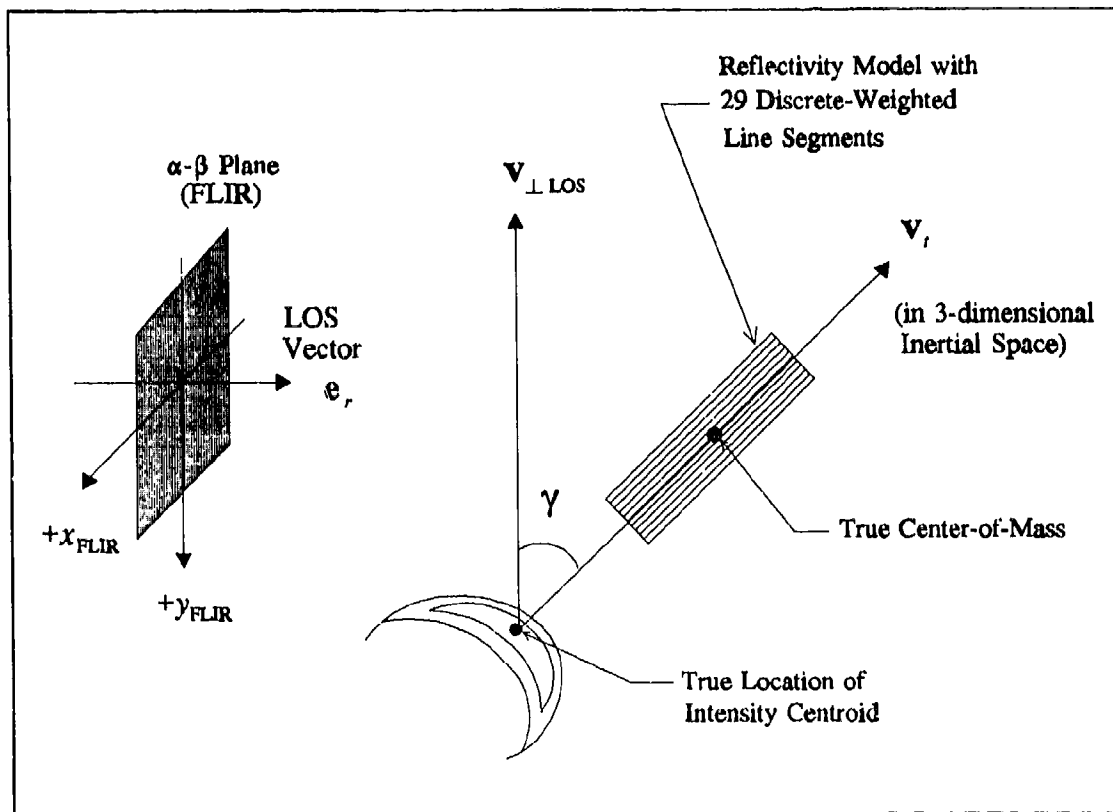


Figure 4.6 3-d Hardbody Reflectivity Model Relative to FLIR Image Plane

simulation by multiplying the peak reflection value (50 units of magnitude) by an appropriate scaling factor [6]. Let the sensor sensitivity factor be defined as some function of the threshold, $\mu(\cdot)$, and the resultant magnitude of reflection be defined as m_r . If (\cdot) is less than m_r , the reflective output is clipped to zero. Therefore, $\mu(\cdot)$ represents the sensor's ability to discern a target's return signal [6].

The total reflectivity function is given by [6]:

$$R_T = \sum_{i=1}^n \mu[A_i F(\gamma)] \quad (4-50)$$

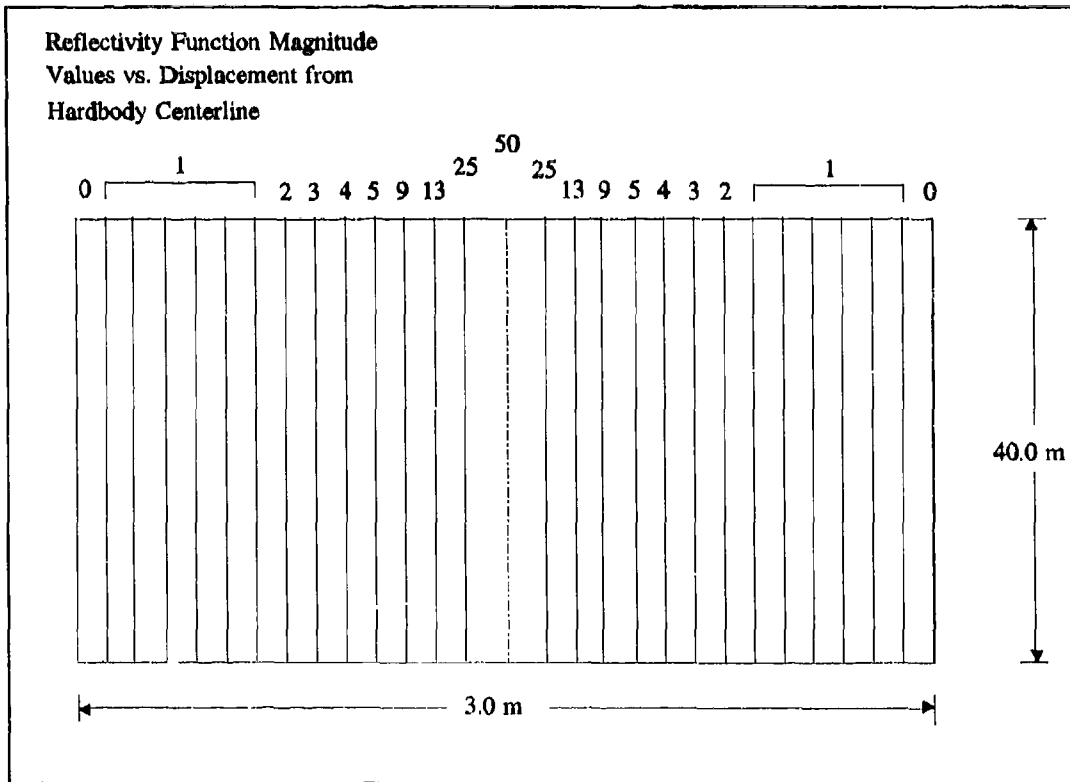


Figure 4.7 Discrete Implementation of Cross-Sectional Reflectivity Function [6]

where

R_T = total reflectivity received by the low energy sensor

n = number of line segments crossed by laser scan

$\mu(\cdot)$ = sensitivity threshold function of low-energy sensor:

$$\mu(m_r) = \begin{cases} m_r, & \text{if } m_r \geq \text{threshold} \\ 0 & \text{if } m_r < \text{threshold} \end{cases}$$

A_i = cross-sectional reflectivity function reflection amplitude of the i^{th} discrete line segment

$F(\gamma)$ = longitudinal reflectivity function, where γ is the angle between target v and the α - β plane

As the hardbody traverses along its trajectory in 3-dimensional inertial space, the projection of its motion onto the 2-dimensional FLIR image plane generates the corresponding propagation of the first two states in the truth model. Similarly, to simulate the center-of-mass measurements in terms of FLIR plane variables, the hardbody model is also projected onto the 2-dimensional FLIR plane. Referring to Figure 4.8, the geometry for projection is described by:

$$ML_{FLIR} = ML_{Actual} \cos \gamma \quad (4-51)$$

where

ML_{FLIR} = FLIR plane projection of missile length

ML_{Actual} = true missile length in pixels

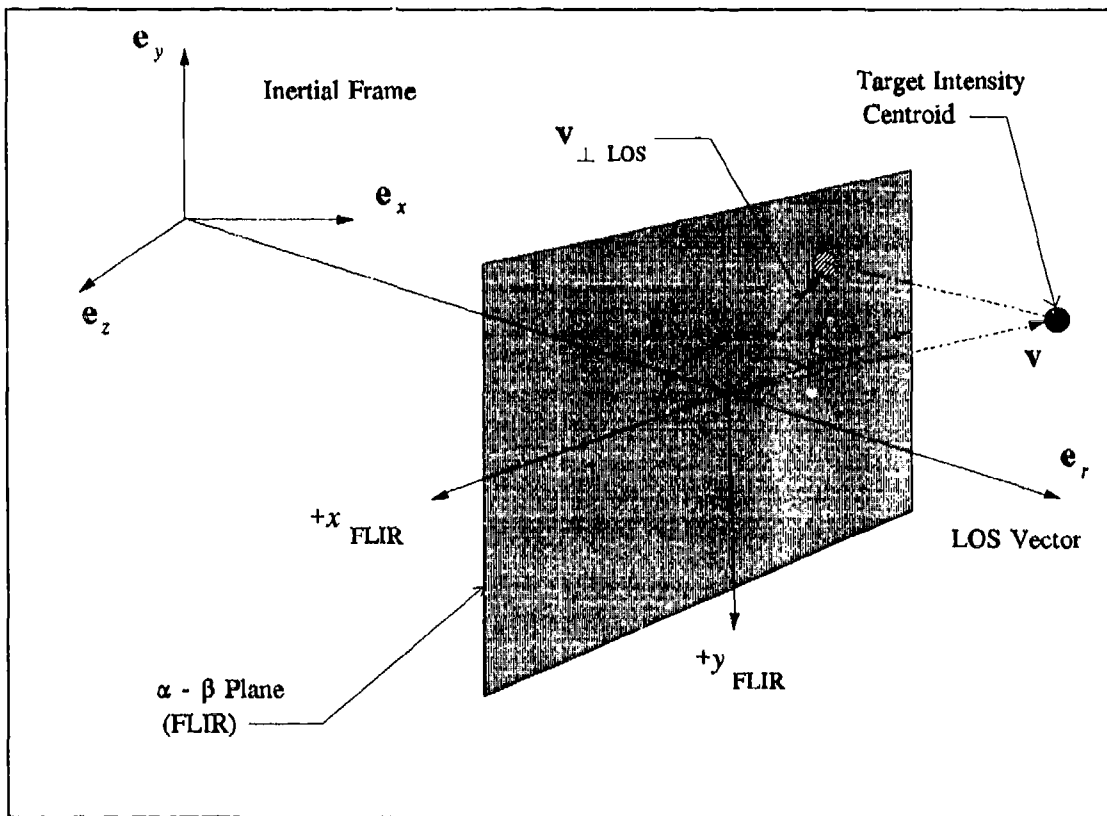


Figure 4.8 Projection Geometry onto FLIR Image Plane

γ = angle between v_t (velocity vector of the target) and the FLIR plane

Since the missile is cylindrical, the projection of the missile diameter onto the FLIR plane is equal to its diameter. Once the projection is accomplished, the hardbody is located on the FLIR plane by offsetting the hardbody's center from the truth model intensity centroid by ML_{FLIR} of Equation (4-51) along the truth model velocity vector.

The subtended arc of the low-power laser beam is simulated as a rectangle with the smaller side represented as the finite width of a dithered laser beam after it has traveled 2000 kilometers. Shown in Figure 4.9 are the ideal conditions for the laser scan. (Generally, the filter estimates of the intensity centroid position, the orientation angle, and the velocity vector are not equal to the truth model values.) One end of the long centerline of laser scan rectangle is located at the estimated intensity centroid, positioned at the center of the FLIR FOV. The other end of the laser scan rectangle is taken as three times the truth model offset distance between the intensity centroid and the hardbody center-of-mass ($3 \times 87.5 = 262.5$ meters or 8.75 pixels) to ensure the laser scan is long enough to intercept the hardbody, despite the effects of "pogo". The second endpoint of the laser rectangle along its centerline is given as:

$$\begin{aligned}x_p &= x_c + L \cos \theta_f \\y_p &= y_c - L \sin \theta_f\end{aligned}\tag{4-52}$$

where

- x_p, y_p = the FLIR plane coordinates of the second end of the centerline of the laser rectangle
- x_c, y_c = the FLIR plane intensity centroid coordinates
- L = length of the laser rectangle

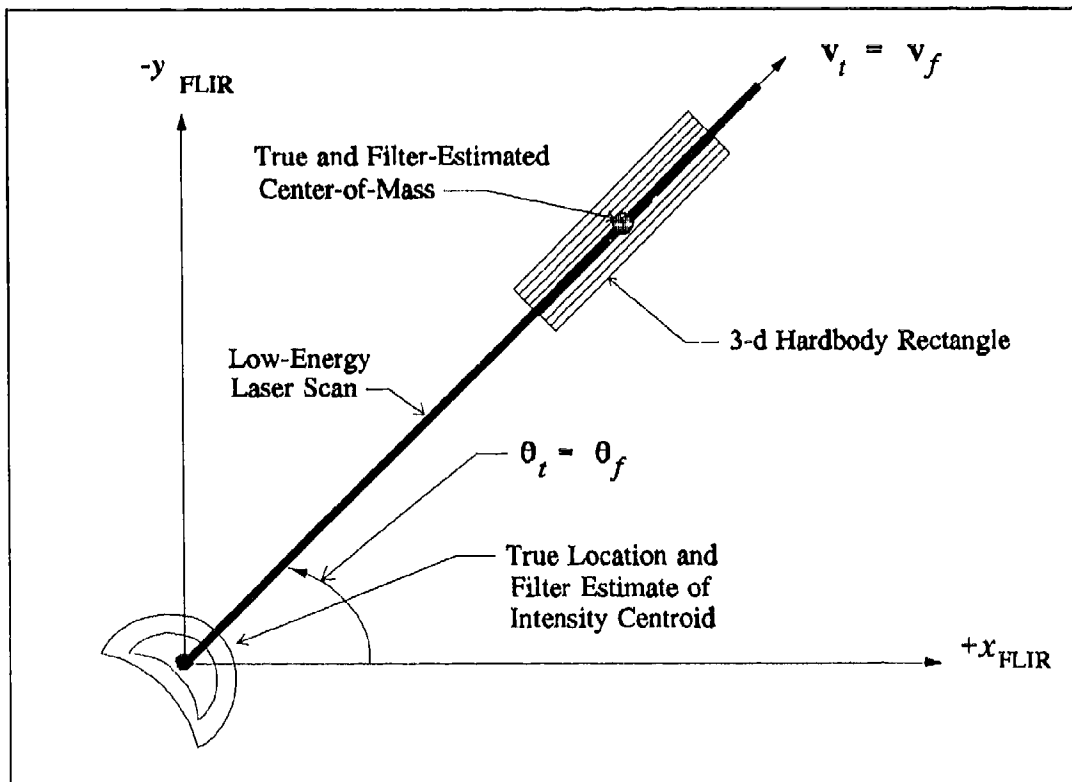


Figure 4.9 Ideal Low-Energy Laser Scan

θ_f = six-state (FLIR) filter estimate of velocity orientation angle

As mentioned earlier, the FLIR filter's imprecise centering of the intensity centroid caused inadequate hardbody illumination rates by the laser scan. (The estimated velocity vector, and thus the estimated orientation angle, θ_f , were estimated precisely, however.) As a result, an *ad hoc* sweep routine was developed, shown in Figure 4.10, that offsets the initial laser scan clockwise from the estimated velocity vector. The laser scans are swept counterclockwise in order to assure illumination of the entire body. Evans found that, without pogo, a 30° offset was required, and 35° with pogo applied [6].

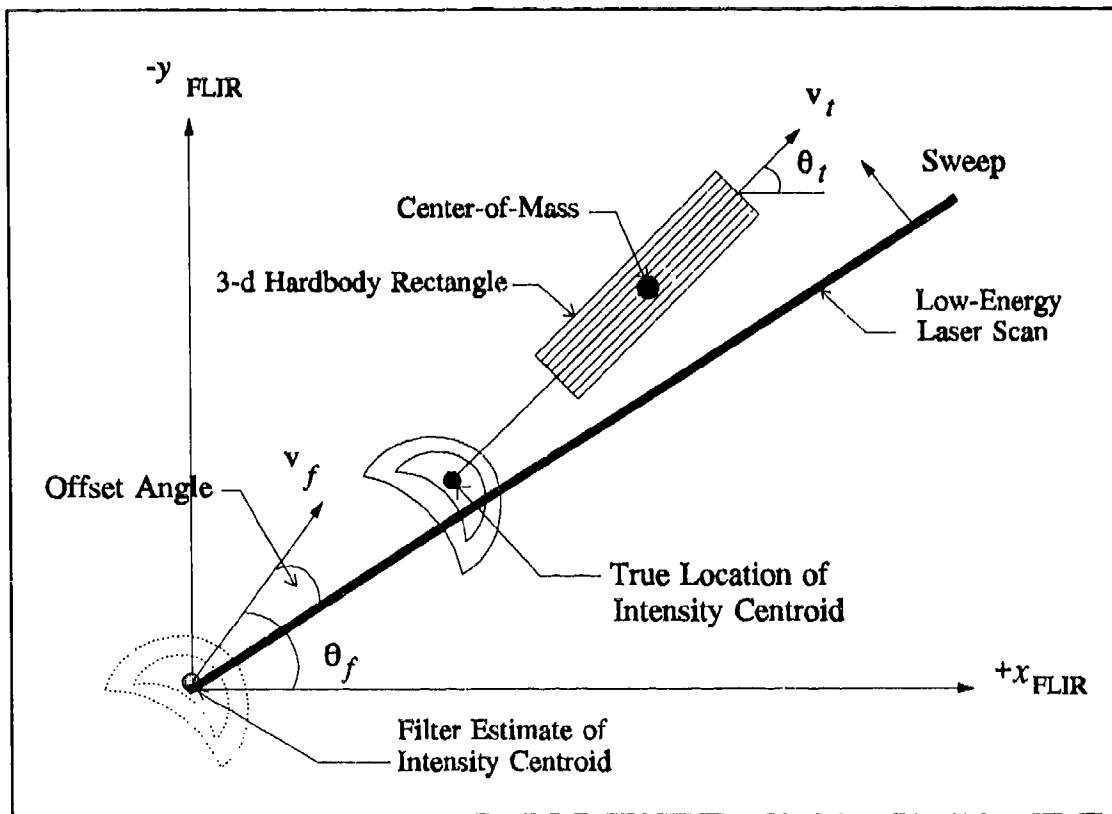


Figure 4.10 Sweep Technique of Laser Scan

4.3.2.2 *Plume Reflectance Model.* Prior to this research, the concept of illuminating the missile hardbody with a low-energy laser and analyzing the speckle return (also called backscatter radiation) was predicated upon the assumption that the missile plume would not possess any backscatter properties or possess a speckle return similar to the hardbody's, when illuminated by a low-energy laser. The laser scan travels along the intensity centroid's velocity vector until a speckle return is received, signifying the start of the metallic hardbody. The scan continues along the hardbody until no backscatter exists, signaling the end of the hardbody, and thus information is provided to calculate the center-of-mass. However, recent experimental data confirms the

presence of plume reflectance from solid-propellant rocket motors [2,30] which significantly alters the previous conception.

Experimental programs at the Arnold Engineering and Development Center (AEDC), in Tennessee, have observed and measured laser backscatter radiation from the exhaust plume of a solid-propellant rocket motor [30]. The measurements of the plume's backscatter radiation were found to be on the same order of magnitude and comparable to that of a hardbody [2], due to aluminum particles and other substances in the plume. During the STARLAB flight experiment, which collected plume data under actual flight conditions, a rocket booster and its exhaust plume were "painted" by a low energy laser. Video recordings of the flight experiment showed the randomized appearance and low-frequency oscillation of the plume's reflectance [2,3]. The existence of plume reflectance creates an ambiguity that impedes the precision tracking necessary to define the plume/hardbody interface.

The purpose of the newly devised plume reflectance model is to simulate the presence of plume backscatter radiation and its effect upon the offset measurement. Figure 4.11 depicts the reflectance from both the plume and hardbody, as observed in the STARLAB flight experiment. From the viewpoint of the speckle return sensor, the plume reflectance has the effect of elongating the apparent missile hardbody. The plume reflectance model simulates the hardbody elongation by applying a bias to the offset measurement in the direction of the elongation, defined as in the opposite direction of the estimated velocity vector. In the simulation, the model first receives the offset measurement as determined by the low-energy speckle reflection model. The biased measurement, $x_{offsetbias}$, is formed by converting the bias into pixels, projecting it onto the FLIR plane, and subtracting it from the original offset measurement. The biased offset measurement is

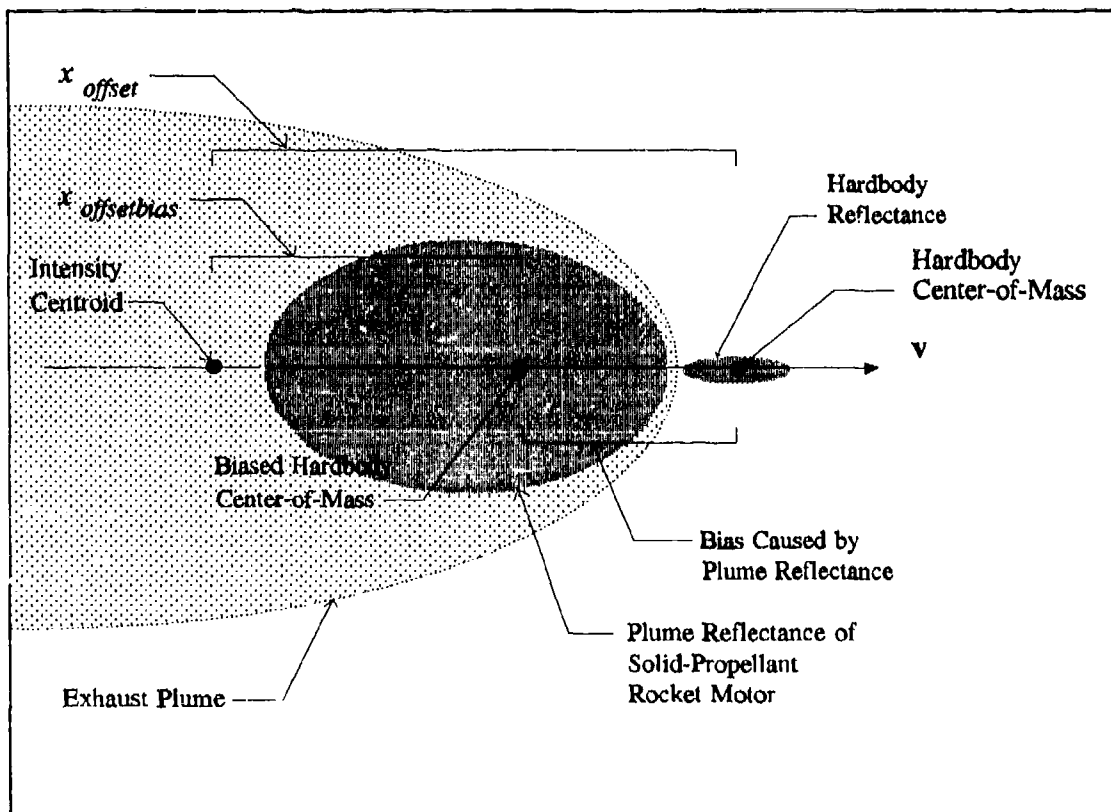


Figure 4.11 Biased Offset Measurement Caused by Plume Reflectance

then provided to the one-state center-of-mass filter for its update. The plume reflectance model is given by:

$$x_{offsetbias} = x_{offset} - \left(\frac{b}{Rk_p} \right) \cos\gamma \quad (4-53)$$

where

- $x_{offsetbias}$ = biased offset measurement due to plume speckle reflectance
- x_{offset} = offset measurement from the low-energy reflectivity model, without plume speckle reflectance effect
- b = bias value
- R = range

- k_p = pixel proportionality constant (15 μ rads/pixel)
 γ = angle between 3-dimensional inertial space velocity vector and the FLIR image plane

The randomized nature of the plume's reflectance is modeled as a percentage of time that appearance of the bias occurs. A random number generator, of uniform density output, provides the logic to turn the bias "on and off" according to the percentage selected. In correspondence with Phillips Laboratory personnel, a bias of approximately 25-30 meters with an appearance percentage of 90 - 95% was observed during the STARLAB flight experiment [3].

4.3.3 The Doppler Measurement Model. The Doppler measurement model simulates the offset measurements that are obtained by exploiting the differences between hardbody and plume-induced Doppler returns. As with the laser speckle return research of Eden and Evans, the modeling of the actual physical properties of the Doppler phenomenon will not be attempted. Instead, modeling efforts will entail simulating the information that would be available from Doppler detection circuits as measurement data for the Kalman filter. The following subsections briefly introduce and describe the basic concepts of the Doppler phenomenon, as applicable to the properties of the hardbody and plume-induced Doppler returns. The treatment of the Doppler phenomenon is not intended to be rigorous and reflects the level of understanding necessary to appreciate the manner with which the Doppler returns are employed to generate an offset measurement relative to the intensity centroid. For a rigorous development of the Doppler phenomenon, the interested reader is referred to *Principles and Practice of Laser-Doppler Anemometry* by Durst, F., A. Melling, and J. H. Whitelaw [4], and *The Doppler Effect* by Gill, T. P. [9].

4.3.3.1 The Doppler Effect. The Doppler effect has been well researched since Christian J. Doppler published his work on the subject [9]. The phenomenon is employed in numerous areas ranging from radar moving target indicators to police speeding traps and weather reporting. Many define the Doppler effect as a shift in the frequency of a wave radiated, reflected, or received by an object in motion [38,39]. From a radar, Doppler shifts are produced by the relative motion between the radar and the target. The radar may be a pulsed, coherent laser beam that propagates the electromagnetic energy to "paint" the target of interest. If the target is in motion and illuminated by a low-energy laser, the returned signal (or backscatter) is represented as a time-delayed, Doppler-shifted version of the transmitted signal, wherein the amount Doppler shift is proportional to the reflecting target's range rate relative to the laser transmitter [38,39]. A continuous transmitted signal is given as:

$$E_t = E_o \cos(2\pi f_o t) \quad (4-54)$$

For this transmitted signal, the echo signal from a moving target will be [38]:

$$E_r = k E_o \cos[2\pi(f_o \pm f_d)t + \phi] \quad (4-55)$$

where

- E_o = amplitude of transmitted signal
- E_r = reflected signal
- k = an attenuation constant that represents losses incurred during propagation
- f_d = Doppler frequency shift
- f_o = transmitted frequency
- ϕ = a phase shift, dependent upon the range of detection

Figure 4.12 shows the frequency spectrum of the echo signal, shifted from the transmitted frequency, f_o , by the Doppler shift, f_d , given by [38]:

$$\pm f_d = \pm \frac{2v_r}{\lambda} = \pm \frac{2v_r f_o}{c} \quad (4-56)$$

where

v_r = relative velocity of target with respect to transmitter

λ = transmitted wavelength

c = velocity of propagation (3×10^8 m/s)

The relative velocity, v_r , is expressed as:

$$v_r = v \sin \gamma \quad (4-57)$$

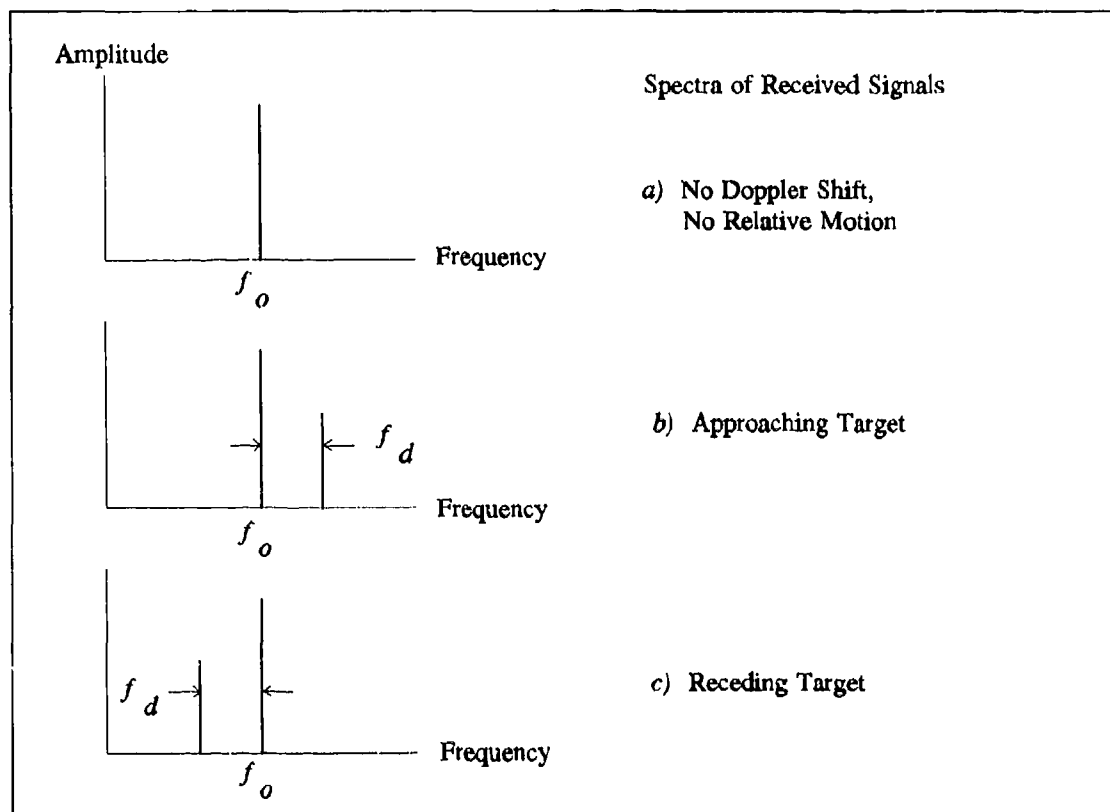


Figure 4.12 Spectra of Received Signals [38]

where

- v = target velocity in 3-dimensional inertial space
- γ = angle between the target trajectory and plane perpendicular to the laser LOS (i.e., FLIR plane); see Figure 4.8

The plus sign associated with the Doppler frequency shift applies if the distance between target and transmitter is decreasing (approaching target), and conversely, the minus sign applies if the distance is increasing (receding target).

As shown in Figure 4.12, the frequency spectrum of a continuous reflected sinusoidal signal appears as a straight vertical line. The scenario proposed by the Phillips Laboratory calls for a pulsed and coherent laser beam to illuminate a ballistic boosting target [3]. Both these laser properties have an impact upon the nature of the returned spectrum.

For illustration purposes, Figure 4.13 shows a train of independent pulses having a pulse width (PW) of 0.001 seconds and a constant pulse repetition frequency (PRF), along with its associated frequency spectrum. Because the pulses are "on" a fraction of the time, the amplitude of the frequency spectrum decreases but is still centered at f_o . The total power is in fact distributed over a band of frequencies extending from 1000 Hz below f_o to 1000 Hz above it, for a null-to-null bandwidth of 2 KHz. The bandwidth (i.e. spectrum spread), is inversely proportional to the pulse width and is given by [39]:

$$BW_{nn} = \frac{2}{\tau} \quad (4-58)$$

where

- BW_{nn} = null-to-null bandwidth
- τ = pulse width (sec)

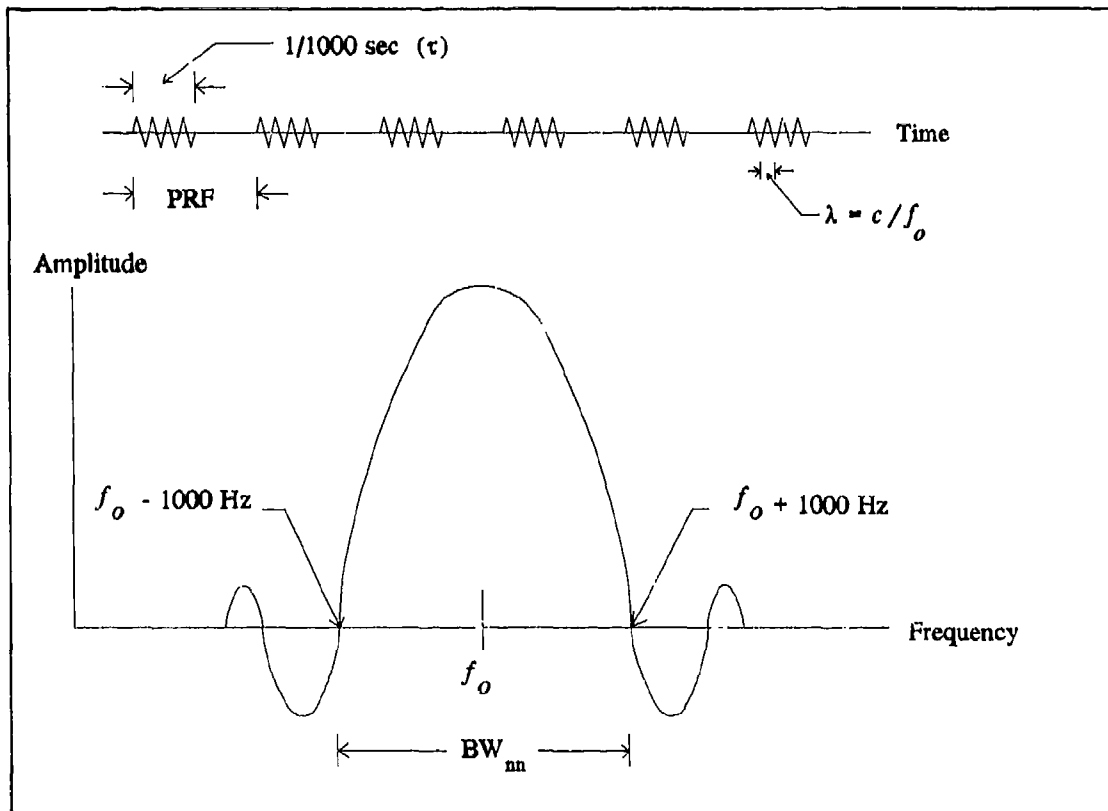


Figure 4.13 Pulsed Signal Frequency Spectrum [39]

By coherence is meant a consistency, or continuity, in the phase of a signal from one pulse to the next [39]. The term ϕ in Equation (4-55) represents the phase shift which is a function of the range during detection. Figure 4.14 illustrates the difference between the frequency spectrum of a coherent signal and a non-coherent signal. With non-coherent transmission, the signal's central spectral lobe is spread over a band of frequencies. In contrast, the spectrum associated with coherent transmission shows the signal appearing at many points. Its spectrum, in fact, consists of a series of evenly spaced lines, wherein the interval between the spectral lines equals $(1/\text{PRF})$ [39]. Further comparison reveals that the coherent frequency spectrum is stronger (higher amplitude) than the non-coherent signal because the energy has been

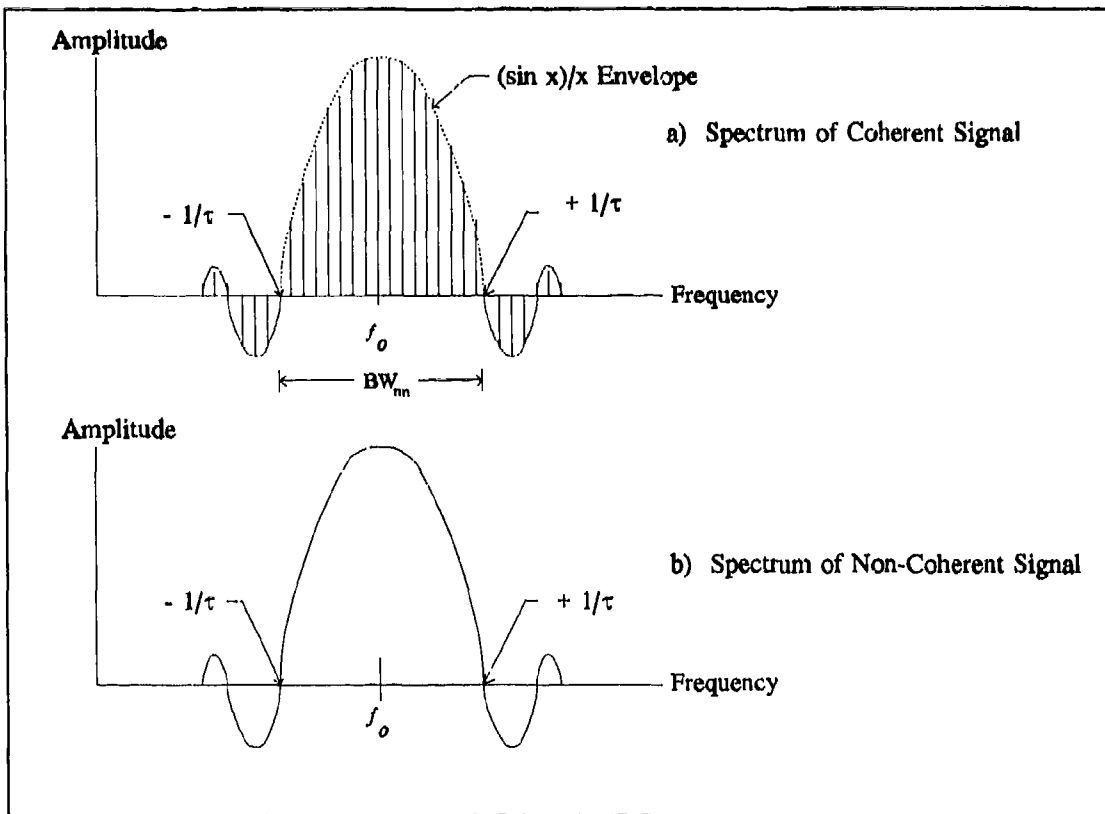


Figure 4.14 Spectra of Coherent and Non-Coherent Pulsed Signals [39]

concentrated into a few narrow lines. In addition, the envelope within which these lines fit has the same shape ($[\sin x]/x$) and the same null-to-null BW ($2/\tau$) as the spectrum of the non-coherent signal.

4.3.3.2 Hardbody Doppler Return. At a range of 2000 kilometers, the missile hardbody can be defined as a smooth, dense single point target. Any rotational motion of the hardbody about its longitudinal axis is assumed much less than the hardbody's velocity, and is considered negligible. It is further assumed that the target hardbody's velocity remains constant over the duration of a transmitted pulse. With such a target, the spectrum of the return will have a

bandwidth that closely approximates $(2/\tau)$, and centered about the Doppler-shifted frequency corresponding to the range rate.

4.3.3.3 Plume Doppler Return. The case of the exhaust plume can be represented as the situation where numerous point targets are imaged. The plume can be described as a randomly distributed array of point targets which are dispersed in range and velocity. The plume particulates are small (submicron in size), nonspherical and nonhomogeneous, and their size and spatial distribution vary strongly with the radial distance from the plume axis [16,26,45]. Typically, larger particles are concentrated near the plume's symmetry axis, and in contrast to the hardbody, the numerous exhaust plume particles exhibit numerous velocity orientations over the duration of a laser pulse.

When the laser beam illuminates an infinite number of point targets, the superposition of each particle's backscatter radiation within the laser beamwidth will form the resultant return [44,45]. Thus, the Doppler frequency spectrum will be quite broad, due to the numerous Doppler shifts of the numerous plume particulate velocities [3,16,26]. This Doppler spreading of spectral lines arises from the fact that backscatter from a particulate will be shifted in frequency in a manner depending on the approach or recession of the particulate. The plume experimental programs at AEDC have observed and measured plume Doppler reflectance frequency spectrums with null-to-null BWs of 2 - 5 GHz [28]. This sharply contrasts the hardbody-induced return whose spectrum null-to-null BW equals $2/\tau$, with an order of magnitude in MHz. However, one other significant difference exists between the hardbody and plume-induced Doppler returns.

Generally, the velocity of the plume will be oriented 180 degrees from the hardbody's velocity [3,16,26]. This is shown in Figure 4.15(a), where the respective Doppler frequency shifts

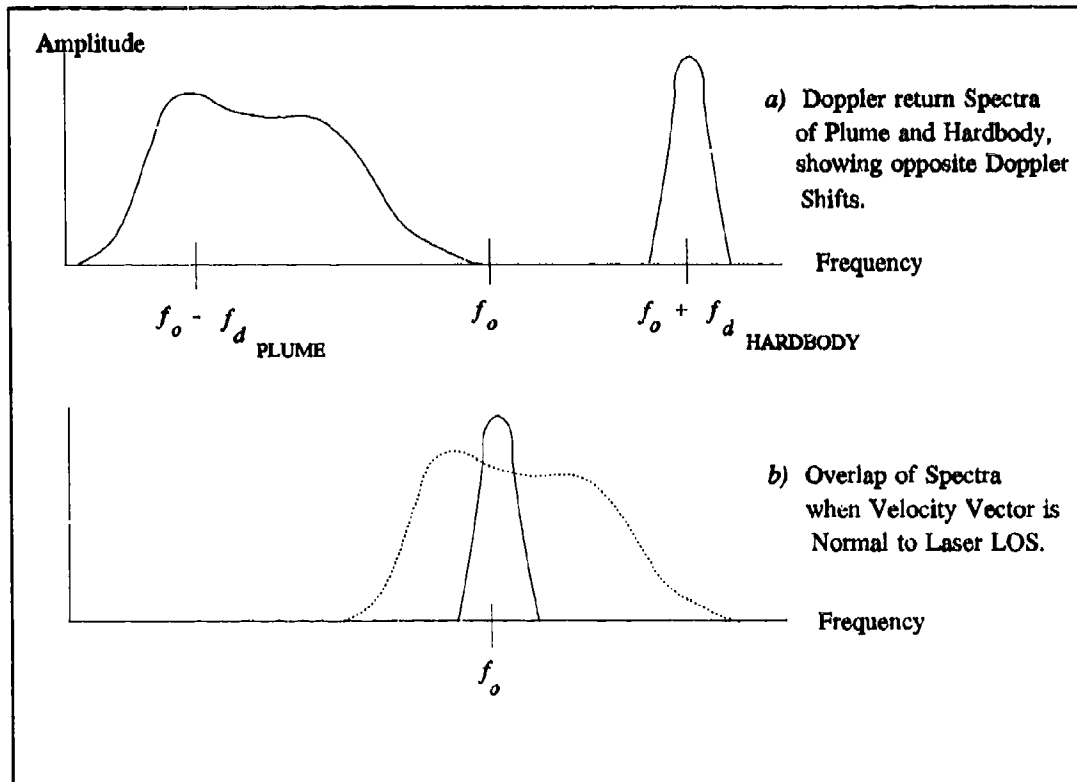


Figure 4.15 Spectra of Plume and Hardbody-Induced Doppler Returns

will always be opposite in sign. A majority of the observed plume particles would have a relative radial velocity towards the tracker and the resultant return would have a negative Doppler frequency shift. Conversely, the hardbody as shown is receding from the tracker and will thus exhibit a positive Doppler frequency shift. Hence, by exploiting the two differences in plume and hardbody-induced Doppler returns, precise tracking and definition of the plume/hardbody interface can be realized.

However, the angle γ , of which the relative velocity v , is a function, has an impact upon the discernibility between the plume and the hardbody-induced Doppler shifts. Referring to Equation (4-57), as γ approaches 0° , where the plume and hardbody velocity vectors become

orthogonal to the LOS vector, the radial velocity relative to the tracker approaches nil and no Doppler shift is produced. Figure 4.15(b) shows that, under these circumstances, the return spectra of the plume and hardbody converge towards the transmitted frequency and eventually overlap, obscuring most of the hardbody-induced Doppler return. This imperfect ability to detect the hardbody spectrum, as distinct from the plume spectrum, will be addressed in the next section which develops the Doppler measurement model.

The measurement modeling approach taken by this thesis is to consider the Doppler return of the hardbody significantly distinctive from that of the plume. The Doppler detector must be designed to filter out the broader plume return and only pass the hardbody return, a function achievable with a Doppler matched filter design [26,38]. This vital concept signifies that the Doppler truth measurement model can neglect the plume's Doppler return and solely simulate the hardbody-induced Doppler return. Although there may be instances of no apparent distinction between the plume and hardbody spectra, these occurrences will be embodied in a probability-of-miss parameter (P_m), to be discussed later.

Since Doppler information is obtainable from backscatter radiation, which includes the speckle return [38,39], the 3-d hardbody reflectivity model is utilized in this modeling approach. However, in contrast to the laser speckle return measurement model, the biasing effect caused by the plume's reflectance is no longer applicable and is not incorporated in the Doppler measurement model. As a result, the center-of-mass measurement and offset measurement generated by the Doppler measurement model will simulate the true offset measurement, x_{offset} , for the one-state filter (or two-state filter to estimate both offset and bias in the speckle measurement, if both types of measurements are used).

4.3.3.4 Doppler Measurement Noises. In a study sponsored by the Phillips Laboratory, Dr. Paul McManamon investigated feasible and implementable wavelengths to illuminate the plume and hardbody, while meeting the space tracking scenario requirements [16]. His choice of wavelengths, based upon ranges, power requirements, hardbody temperatures, and tracking accuracies, range from 0.53 to 15 μm . For this study, the following wavelengths were selected for a sensitivity analysis: 0.53, 1.06, 2.01, 4.00, 6.00, 8.00, and 10.5 μm . The tracking inaccuracies associated with these wavelengths are adopted in the Doppler measurement model to corrupt the offset measurements realistically.

The tracking accuracy for a laser beam is a function of the amount of power, or amplitude, of the return signal. The return signal, in turn, is dependent upon several variables, among which are the target's radar cross section (RCS) and the location of the target in the laser beam [16,38,39]. A target ideally located in the center of the laser beam reflects the maximum return signal (i.e., optimum SNR). If the target falls off to the side of the beam's center, then less energy hits the target. The degree of tracking accuracy then becomes a question of, how far off to the side can a target be to reflect the signal at an acceptable level?

Dr. McManamon addresses this issue [16] by first defining the acceptable beam diffraction limit as the angle within the 3db power points of the laser beam. He defines the diffraction limit as:

$$\theta_{3db} = 1.08 \frac{\lambda}{d} \quad (4-59)$$

where

θ_{3db} = half angle defined from beam center to half-power points, in radians

- λ = wavelength, in meters
- d = radar aperture, in meters

One then determines the acceptable level of signal loss within the θ_{3db} limits. In Dr. McManamon's assessment, a 10% loss can be tolerated, and he determined that this loss is reflected by decreasing the diffraction limit by a factor of 2.667 [16]. Equation (4-53) becomes:

$$\theta_B = \frac{\theta_{3db}}{2.667} \quad (4-60)$$

where

- θ_B = allowed diffraction limit for 10% signal loss

The measurement noise for the Doppler Measurement Model thus consists of the tracking angle errors, in pixels, as a function of the diffraction limited beam and acceptable signal-to-noise ratio (SNR). Inasmuch as SNR is a design parameter, this study includes the following values of SNR for the sensitivity analysis: 10, 8, 6, and 4. The relationship is given as [16,26]:

$$\theta_T = \frac{\theta_B}{3\sqrt{\text{SNR}}} \frac{1}{k_p} \quad (4-61)$$

where

- θ_T = rms tracking angle errors in pixels
- θ_B = beam diffraction limit
- SNR = signal-to-noise ratio
- k_p = pixel proportionality constant, 15 μ rad/pixel

In addition to providing the offset measurement, the Doppler measurement model also simulates a return signal probability-of-miss, P_m . The probability-of-miss encompasses two cases: first, the probability-of-miss takes into account the situation in which the hardbody is illuminated by the low-energy laser, but the return is not detected due to attenuation of the returning signal as it propagates the 2000 kilometer range, beam-bending as a result of atmospheric distortions (the intended location of the laser scan should have illuminated the target, but bending of the beam resulted in no intersection with the target); or due to signal losses (i.e., high sensor sensitivity threshold; refer to Section 4.3.2.1) within the receiving equipment. Secondly, in Equation (4-51), it was shown that the relative velocity is a function of γ , such that no Doppler shift occurs if the target's velocity is normal to the transmitter's LOS. Hence, as shown in Figure 4.15, as γ approaches 0° , both the broadened plume-induced Doppler spectrum and hardbody-induced spectrum will converge and overlap. The two spectra will become more indistinguishable, perhaps rendering detection of the hardbody's Doppler return impossible.

The simulation of the probability-of-miss is similar to the technique employed by the plume reflectance model. A random number generator, with a uniformly distributed output, also provides the logic to turn the hardbody laser backscatter "on and off." Figure 4.16 shows the detection characteristic for a known signal. The graph presents a set of parametric curves that give the probability-of-detection, P_d , as functions of peak signal-to-noise ratio (SNR) for various values of probability-of-false alarm, P_{fa} . P_{fa} is defined as falsely indicating the presence of a return signal when none exists [38]. Both P_d and P_{fa} are specified by the system requirements; the radar designer computes the probability-of-false alarm and, from Figure 4.16, determines the minimum detectable signal. A range of 70 - 99 percent probability-of-detection is representative of current Doppler detection equipment capabilities with the tracking scenario [26]. Since $P_m = (1.0 - P_d)$,

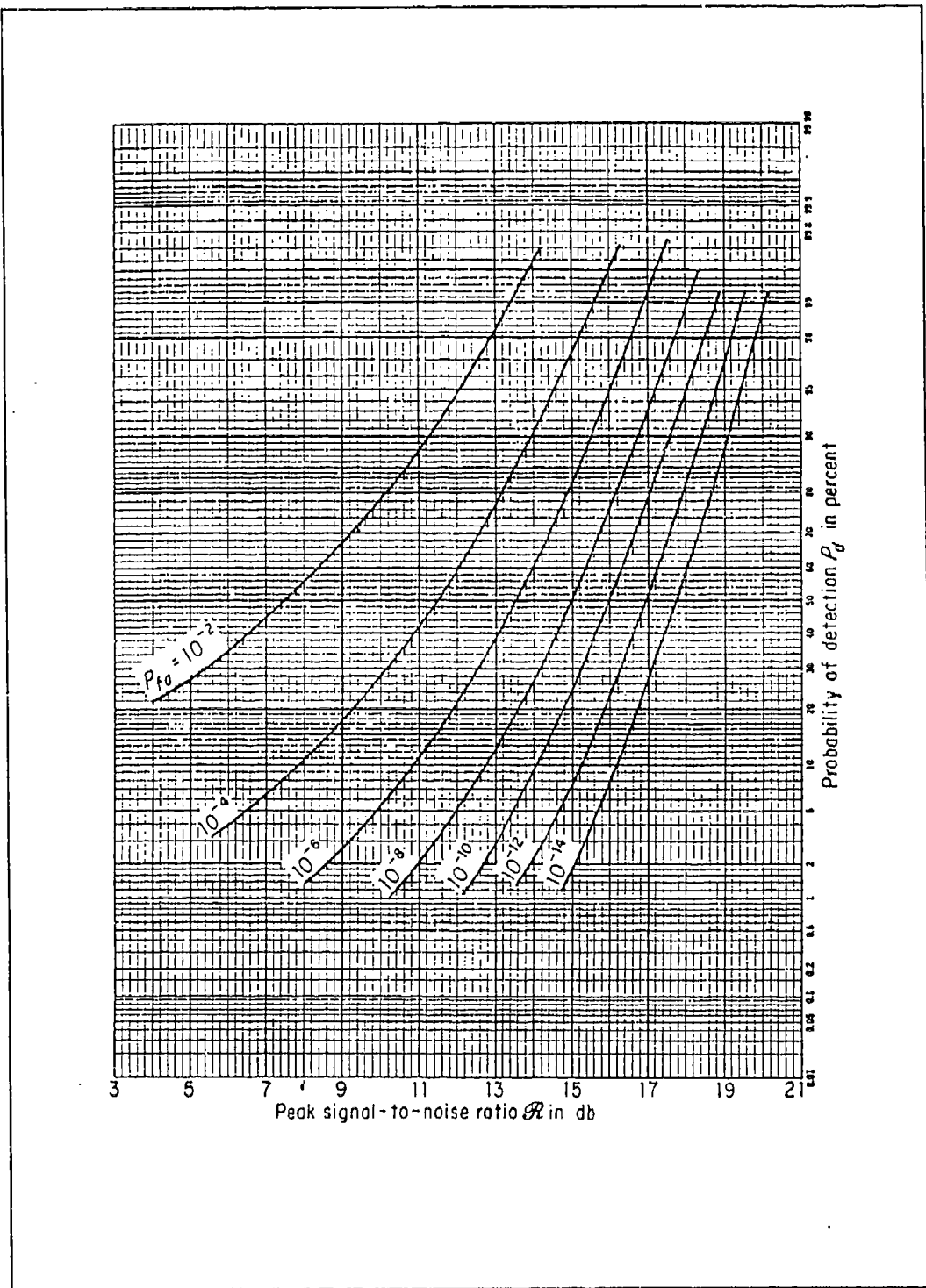


Figure 4.16 Detection Characteristics [38]

a performance sensitivity analysis will be performed for probability-of-miss values of 0.0, 0.01, 0.02, 0.03, 0.04, 0.05, 0.10, 0.20, and 0.30.

4.4 *Truth Model Parameters*

The discussions in the previous sections introduced some of the truth model parameters used in the simulation. The purpose of this section is to provide a consolidated listing of the parameters and initial conditions of the truth model.

4.4.1 Target Trajectory Initial Conditions. The initial conditions of the target inertial position, velocity, and velocity vector orientation angle, θ , are as follows:

$$\begin{aligned}e_x &= 27,000 \text{ meters} \\e_y &= 100,000 \text{ meters} \\e_z &= 2,000,000 \text{ meters} \\v_x &= -2500 \text{ meters/sec} \\v_y &= 4330 \text{ meters/sec} \\v_z &= 0 \text{ meters/sec} \\\theta &= 60^\circ\end{aligned}$$

4.4.2 Target Model, Dimensions, and Orientation. The target plume consists of a crescent-shaped intensity function formed from the difference of two bivariate Gaussian intensity functions. Each Gaussian function is modeled with elliptical constant-intensity loci with an aspect ratio of 1.5, and a semi-minor axis of one. For this thesis, Evans' 3-dimensional reflectivity model is used to model the hardbody. The hardbody length is 40 meters (1.33 pixels) and 3 meters (0.1 pixels) wide. The offset distance of the hardbody center-of-mass from the intensity centroid is 87.5 meters (2.92 pixels), a carryover from the previous thesis. For the simulation, the

intensity centroid and the hardbody longitudinal axis are aligned with the velocity vector, and the hardbody has zero sideslip and zero angle-of-attack.

4.4.3 Intensity Functions. The two Gaussian bivariate intensity functions are centered at 65 and 110 meters behind the missile. Each intensity function has a maximum intensity value of 20 intensity units.

4.4.4 Atmospheric Jitter. The variance and mean squared value for the atmospheric jitter in both FLIR directions is 0.2 pixels².

4.4.5 Bending/Vibration. From Equation (4-29), the values for the second-order bending/vibration model are as follows:

$$\begin{aligned}K_b^2 &= 5 \times 10^{-13} \text{ rad}^4/\text{sec}^4 \\ \zeta_b &= 0.15 \\ \omega_{nb} &= \pi \text{ rad/sec}\end{aligned}$$

4.4.6 Plume Pogo Characteristics. The size of the plume is on the order of 30 times the diameter of the missile at the altitudes of interest. The values below represent values of pogo oscillation as determined in previous research [35].

$$\begin{aligned}\text{pogo oscillation} &= 0.1 - 10 \text{ Hz (nominal is 1 Hz)} \\ \text{pogo rms} &= 33.6 \text{ meters (1.12 pixels)}\end{aligned}$$

4.4.7 Spatially Correlated Background Noise. The rms value of v_{jk} , the summed effect of the spatially correlated background noise b_{jk} and the FLIR sensor noise n_{jk} , of Equation (4-45), equals one. This produces a SNR of 20.

4.4.8 Low-Energy Laser Speckle Return Measurement Dimensions. The low-energy scan is represented as a rectangle at the hardbody target. The scan length is 262.5 meters (8.75 pixels), which is three times the true model center-of-mass offset distance, and the scan width is 0.1 meters. The measurement noise associated with the speckle return was obtained by taking 1% of the hardbody's length, and converting to pixels, giving a variance of 0.000178 pixels² [6].

4.4.9 Plume Reflectance Model. From correspondence with Phillips Laboratory personnel [3], the bias utilized by the plume reflectance model is approximately 25 - 30 meters and appears 90 - 95% while the plume is illuminated during the boost phase. For the simulation, nominal values for the bias and rate of appearance are set at 25 meters and 90%, respectively.

4.4.10 Low-Energy Doppler Return Measurement Dimensions. The Doppler measurement noise rms tracking errors are functions of wavelength, radar aperture, and SNR. From Dr. McManamon's study [16] and with agreement from the Phillips Laboratory, the wavelength values of .53 μ m, 1.06 μ m, 2.01 μ m, 4 μ m, 6 μ m, 8 μ m, and 10.5 μ m, with SNR values of 10, 8, 6, and 4, and P_m values of 0.0, 0.01, 0.02, 0.03, 0.04, 0.05, 0.10, 0.20, and 0.30 are utilized in a sensitivity analysis. The radar aperture (d of Equation (5-29) of .5 meters is used as a constant.

4.4.11 Hardbody Reflectivity Measurement Model. The function $\mu(\cdot)$, in Equation (4-50), represents the sensitivity threshold of the low-energy laser return sensor. The threshold must be less than the magnitude of reflection, m , (scaled according to the aspect angle γ), to detect the return from the hardbody. In the simulation, the value of the threshold is set to 0.0.

4.5 Summary

This chapter presented the mathematical description of the truth model. The truth model consists of 14 states: 2 deterministic target trajectory states, 6 stochastic atmospheric jitter states, four stochastic bending/vibration states, and two stochastic pogo states. The infrared target plume model is formed from the difference of two bivariate Gaussian functions. The FLIR measurements are corrupted by spatially and temporally uncorrelated FLIR sensor noise, and spatially correlated and temporally uncorrelated background noise. The low-energy measurement models, which provide an offset measurement from the intensity centroid to the hardbody center-of-mass, consist of the plume reflectance model, the 3-dimensional hardbody reflectivity model, and the Doppler measurement model. The plume reflectance model simulates the elongation of the apparent hardbody in the speckle measurement data due to the simultaneous hardbody and plume speckle return. The 3-dimensional hardbody reflectivity model provides realistic backscatter that is a function of the hardbody's curvature and aspect angle. The Doppler measurement model also utilizes the backscatter information from the 3-dimensional reflectivity model and corrupts that information with rms angle tracking errors associated with a particular wavelength, radar aperture, and SNR.

V. Filter Models

5.1 Introduction

The Kalman filter dynamics model is a reduced-order and simplified version of the truth model. The decrease in the number of states results in a more viable and implementable filter algorithm when computational processing time and memory storage may be limited. However, the state reduction must be accomplished in a purposeful manner such that the dominant behavior of the truth model is preserved.

For this research, the FLIR filter receives measurements from the FLIR sensor to update its state estimates, and subsequently propagates these estimates to the next sample time. Since the FLIR filter's one-sample-period-ahead predictions are used as commands for the FLIR sensor controller to center the target on the FLIR image plane at the next measurement sample time, the accuracy and reliability of the FLIR filter's state estimates are essential to maintain lock on the target plume and to track it precisely..

This chapter discusses the four linear Kalman filters utilized for this study. First, a six-state FLIR filter, a development from previous theses [5,35], uses an enhanced correlator [36] to process FLIR measurements. The six-state FLIR filter presented here also defines an elemental Kalman filter within the MMAF structure (Chapter II). Second is a one-state filter that estimates the hardbody center-of-mass location relative to the target IR image center of intensity. A low-energy laser is scanned along the FLIR filter's estimated velocity vector from the estimated center

of intensity and the received speckle return is used to generate an offset measurement from the target plume intensity centroid to the hardbody center-of-mass, to be used as the input measurement for this second filter [5,6]. Third is a one-state center-of-mass filter that similarly uses a low-energy laser scan, but instead receives measurements processed from the Doppler return of the plume and the hardbody. Fourth is an alternative to either of the two previous filters: a two-state center-of-mass filter, in a modified MAP MMAF structure, that utilizes the offset measurements generated from both the speckle and the Doppler returns. The latter two filters are relevant to the primary objectives of this thesis. Presented in the following sections are the dynamics and measurement models for each filter, as well as the enhanced correlator algorithm.

5.2 Six-State FLIR Filter

This study and the two previous theses on locating and tracking the missile hardbody [5,6] all employ the six-state FLIR filter that has been developed by AFIT students over thirteen years of research [5,13,27,29,35,36]. The filter consists of two target plume position states, two target plume velocity states, and two atmospheric jitter position states. A six-state FLIR filter as such provides estimates for the plume intensity centroid's position and velocity, separated from the atmospheric jitter effects. The resulting estimates are used to track and maintain lock on the target plume, and additionally to define the origin and orientation of the low-energy scan. The following subsections cover the FLIR filter dynamics model and the FLIR measurement model.

5.2.1 Dynamics Model. The six-state FLIR Kalman filter is based upon the state vector:

$$x_f = \begin{bmatrix} x_1 \\ x_2 \\ x_3 \\ x_4 \\ x_5 \\ x_6 \end{bmatrix} = \begin{bmatrix} x_d \\ y_d \\ v_x \\ v_y \\ x_a \\ y_a \end{bmatrix} \quad (5-1)$$

where

x_d = x component of centroid position (azimuth), relative to center of FOV

y_d = y component of centroid position (elevation), relative to center of FOV

v_x = x component of centroid velocity

v_y = y component of centroid velocity

x_a = x component of atmospheric jitter

y_a = y component of atmospheric jitter

Each state in Equation (5-1) is coordinatized in the α - β (FLIR) plane of Section 3.2.3.1. The target velocity is represented as an exponentially time-correlated first order Gauss-Markov process [5,35]. A comparison between the filter model presented here and the fourteen-state truth model earlier described in Section 4.2 reveals the extent of state reduction. Note that the atmospheric jitter model has been reduced from the six states defined in the truth model in Section 4.2.2 to two states. The effect of the higher frequency double pole in each FLIR axis direction was negligible and was intentionally disregarded to reduce the filter order [33]. Furthermore, the bending/vibration states defined in Section 4.2.3 are similarly excluded since past research found no significant degradation in filter performance without these states [12]. Lastly, the pogo states defined in Section 4.2.4 are not at all modeled in the filter for this research.

The following time-invariant, linear stochastic differential equation describes the six-state

FLIR filter model:

$$\dot{x}_f(t) = F_f x_f(t) + G_f w_f(t) \quad (5-2)$$

where

- F_f = 6 x 6 time-invariant system matrix
- $x_f(t)$ = 6-dimensional filter state vector
- G_f = 6 x 4 time-invariant noise distribution matrix
- $w_f(t)$ = 4-dimensional, white Gaussian noise process with independent components, and mean and covariance kernel statistics:

$$\begin{aligned} E\{w_f(t)\} &= \mathbf{0} \\ E\{w_f(t)w_f^T(t + \tau)\} &= Q_f \delta(\tau) \end{aligned} \quad (5-3)$$

The time-invariant system matrix F_f is given by:

$$F_f = \begin{bmatrix} 0 & 0 & 1 & 0 & 0 & 0 \\ 0 & 0 & 0 & 1 & 0 & 0 \\ 0 & 0 & -\frac{1}{\tau_x} & 0 & 0 & 0 \\ 0 & 0 & 0 & -\frac{1}{\tau_y} & 0 & 0 \\ 0 & 0 & 0 & 0 & -\frac{1}{\tau_{ax}} & 0 \\ 0 & 0 & 0 & 0 & 0 & -\frac{1}{\tau_{ay}} \end{bmatrix} \quad (5-4)$$

The noise distribution matrix G_f is:

$$\mathbf{G}_f = \begin{bmatrix} 0 & 0 & 0 & 0 \\ 0 & 0 & 0 & 0 \\ 1 & 0 & 0 & 0 \\ 0 & 1 & 0 & 0 \\ 0 & 0 & 1 & 0 \\ 0 & 0 & 0 & 1 \end{bmatrix} \quad (5-5)$$

The strength of the white Gaussian noise w_f , given by \mathbf{Q}_f , is:

$$\mathbf{Q}_f = \begin{bmatrix} \frac{2\sigma_x^2}{\tau_x} & 0 & 0 & 0 \\ 0 & \frac{2\sigma_y^2}{\tau_y} & 0 & 0 \\ 0 & 0 & \frac{2\sigma_{ax}^2}{\tau_{ax}} & 0 \\ 0 & 0 & 0 & \frac{2\sigma_{ay}^2}{\tau_{ay}} \end{bmatrix} \quad (5-6)$$

where

- τ_x, τ_y = correlation times for the intensity centroid x and y velocities
- τ_{ax}, τ_{ay} = correlation time for the atmospheric jitter process in the x and y directions
- σ_x^2, σ_y^2 = variance and mean-squared value for the intensity centroid x and y velocities
- $\sigma_{ax}^2, \sigma_{ay}^2$ = variance and mean-squared value for the atmospheric jitter position process

The filter state estimate and error covariance matrix are propagated forward to the next measurement update using the following discrete-time filter propagation equations [17]:

$$\hat{\mathbf{x}}_f(t_{i+1}^-) = \Phi_f(\Delta t)\hat{\mathbf{x}}_f(t_i^+) \quad (5-7)$$

$$P_f(t_{i+1}^-) = \Phi_f(\Delta t)P_f(t_i^+) \Phi_f^T(\Delta t) + Q_{df} \quad (5-8)$$

where

$\hat{x}_f(t_i)$ = filter estimate of the 6-dimensional state vector

$\Phi_f(\Delta t)$ = 6 x 6 time-invariant state transition matrix for propagation over the sample period: $\Delta t = t_{i+1} - t_i$

$P_f(t_i)$ = 6 x 6 filter covariance matrix

(t_i^-) = time instant before FLIR measurement is incorporated into the estimate at time t_i

(t_i^+) = time instant after FLIR measurement is incorporated into the estimate at time t_i

Q_{df} = 6 x 6 filter dynamics noise covariance given by:

$$Q_{df} = \int_{t_i}^{t_{i+1}} \Phi_f(t_{i+1}-\tau) G_f Q_f G_f^T \Phi_f^T(t_{i+1}-\tau) d\tau \quad (5-9)$$

The time invariant state transition matrix $\Phi_f(\Delta t)$ is given by:

$$\Phi_f(\Delta t) = \begin{bmatrix} 1 & 0 & \Phi_{13} & 0 & 0 & 0 \\ 0 & 1 & 0 & \Phi_{24} & 0 & 0 \\ 0 & 0 & \Phi_{33} & 0 & 0 & 0 \\ 0 & 0 & 0 & \Phi_{44} & 0 & 0 \\ 0 & 0 & 0 & 0 & \Phi_{55} & 0 \\ 0 & 0 & 0 & 0 & 0 & \Phi_{66} \end{bmatrix} \quad (5-10)$$

where

$$\begin{aligned}
\Phi_{13} &= \tau_x \left[1 - \exp\left(-\frac{(\Delta t)}{\tau_x}\right) \right] \\
\Phi_{24} &= \tau_y \left[1 - \exp\left(-\frac{(\Delta t)}{\tau_y}\right) \right] \\
\Phi_{33} &= \exp\left(-\frac{(\Delta t)}{\tau_x}\right) \\
\Phi_{44} &= \exp\left(-\frac{(\Delta t)}{\tau_y}\right) \\
\Phi_{55} &= \exp\left(-\frac{(\Delta t)}{\tau_{ax}}\right) \\
\Phi_{66} &= \exp\left(-\frac{(\Delta t)}{\tau_{ay}}\right)
\end{aligned}
\tag{5-11}$$

The filter dynamics noise covariance Q_{df} is given by:

$$Q_{df} = \begin{bmatrix} q_{df11} & 0 & q_{df13} & 0 & 0 & 0 \\ 0 & q_{df22} & 0 & q_{df24} & 0 & 0 \\ q_{df31} & 0 & q_{df33} & 0 & 0 & 0 \\ 0 & q_{df42} & 0 & q_{df44} & 0 & 0 \\ 0 & 0 & 0 & 0 & q_{df55} & 0 \\ 0 & 0 & 0 & 0 & 0 & q_{df66} \end{bmatrix}
\tag{5-12}$$

where

$$\begin{aligned}
q_{df11} &= 2\sigma_x^2\tau_x \left\{ (\Delta t) - 2\tau_x \left[1 - \exp\left(-\frac{(\Delta t)}{\tau_x}\right) \right] + \frac{\tau_x}{2} \left[1 - \exp\left(-\frac{2(\Delta t)}{\tau_x}\right) \right] \right\} \\
q_{df22} &= 2\sigma_y^2\tau_y \left\{ (\Delta t) - 2\tau_y \left[1 - \exp\left(-\frac{(\Delta t)}{\tau_y}\right) \right] + \frac{\tau_y}{2} \left[1 - \exp\left(-\frac{2(\Delta t)}{\tau_y}\right) \right] \right\} \\
q_{df13} &= 2\sigma_x^2 \left\{ 2\tau_x \left[1 - \exp\left(-\frac{(\Delta t)}{\tau_x}\right) \right] - \frac{\tau_x}{2} \left[1 - \exp\left(-\frac{2(\Delta t)}{\tau_x}\right) \right] \right\} \\
q_{df24} &= 2\sigma_y^2 \left\{ 2\tau_y \left[1 - \exp\left(-\frac{(\Delta t)}{\tau_y}\right) \right] - \frac{\tau_y}{2} \left[1 - \exp\left(-\frac{2(\Delta t)}{\tau_y}\right) \right] \right\} \\
q_{df31} &= q_{df13} \\
q_{df33} &= \sigma_x^2 \left[1 - \exp\left(-\frac{2(\Delta t)}{\tau_x}\right) \right] \\
q_{df42} &= q_{df24} \\
q_{df44} &= \sigma_y^2 \left[1 - \exp\left(-\frac{2(\Delta t)}{\tau_y}\right) \right] \\
q_{df55} &= \sigma_{ax}^2 \left[1 - \exp\left(-\frac{2(\Delta t)}{\tau_{ax}}}\right) \right] \\
q_{df66} &= \sigma_{ay}^2 \left[1 - \exp\left(-\frac{2(\Delta t)}{\tau_{ay}}}\right) \right]
\end{aligned} \tag{5-13}$$

The propagated intensity centroid position estimates $\hat{x}_1(t_{i+1})$ and $\hat{x}_2(t_{i+1})$ are applied as control signals to the FLIR pointing controller (Section 3.4). These estimates prescribe the required change in azimuth and elevation that the FLIR pointing controller should execute over the next sample period to center the hotspot image on the FLIR FOV plane at the next measurement sample time.

5.2.2 FLIR Measurement Model. Measurements of the intensity centroid's position are generated by an enhanced correlator algorithm, shown in Figure 5.1, developed by Rogers [36]. Unlike the standard correlator tracker that correlates the current FLIR data frame with the previous data frame, this enhanced correlator algorithm correlates the current FLIR data frame with a template that represents an estimate of the target plume's intensity function. "Pseudo-measurements" of the centroid's position offsets are produced by this correlator; they are linear in the states of the filter, and this tracker therefore uses a linear Kalman filter. The following discussion of the processes within the enhanced correlator algorithm that are used to treat the FLIR sensor data is reproduced from the previous thesis [6] with some modifications.

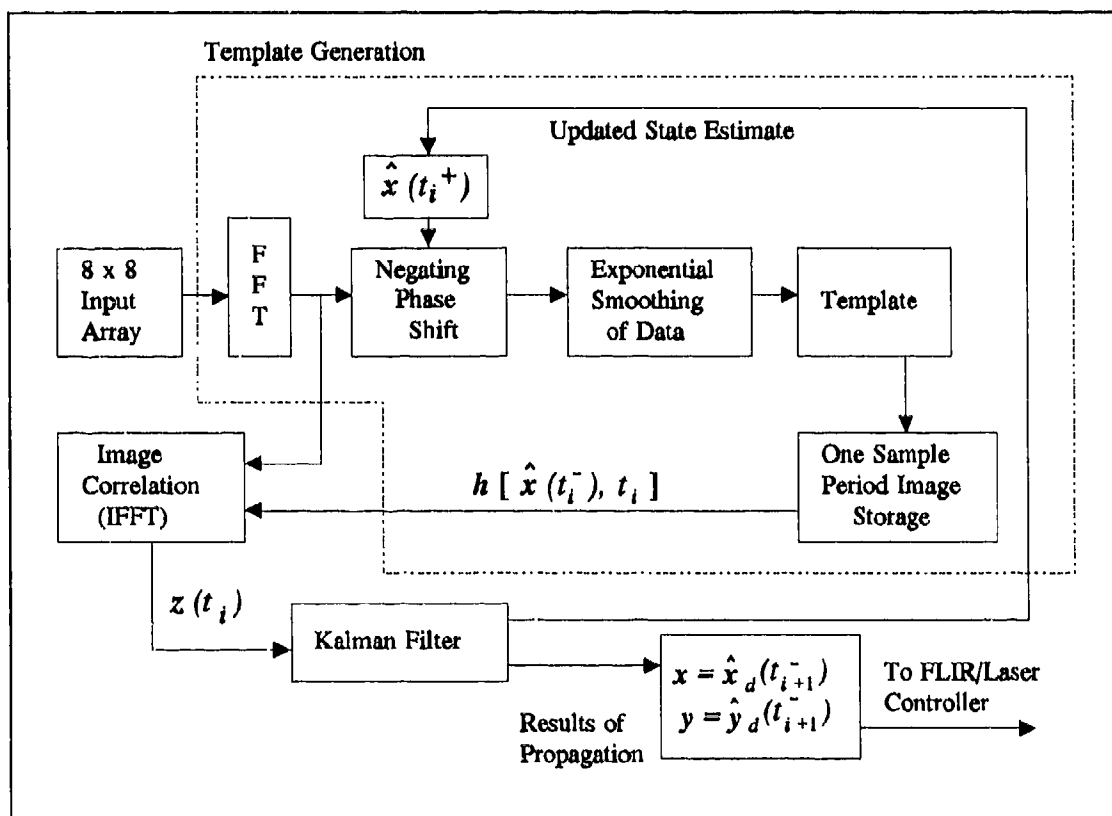


Figure 5.1 Linear Kalman Filter/Enhanced Correlator Algorithm

5.2.2.1 Enhanced Correlator Algorithm. The algorithm presented here was developed as an alternative to an earlier 64-dimensional, non-linear measurement model of Equation (4-39). Previously, an extended Kalman filter processed raw FLIR measurement data from a standard FLIR sensor, with no correlation algorithm utilized at all [27]. With the enhanced correlator algorithm, a linear Kalman filter is employed since the output measurements from the correlation algorithm are 2-dimensional position measurements that are linear functions of the states to be estimated. This configuration outperformed the extended Kalman filter and further provided a reduction in computational loading. The "enhancement" occurs in the following manner [36]:

1. The most current FLIR data is correlated with a template (which is an estimate of the target's intensity function), instead of with the previous FLIR data frame.
2. Instead of outputting the peak of the correlation function, a technique known as "thresholding" is used along with a simple center-of-mass computation. The enhanced correlator outputs the center-of-mass of the portion of the correlation function that is greater than some predetermined lower bound. Consequently, the enhanced correlator has no difficulty distinguishing global peaks from local peaks, as do many conventional "peak-finding" correlation algorithms.
3. The FLIR/laser pointing commands are generated via the Kalman filter propagation cycle instead of by the "raw measurement" output of a standard correlation algorithm.
5. The Kalman filter estimate, $\hat{x}(t_i^+)$, is used to center the template, so that the offsets seen in the enhanced correlator algorithm should be smaller than those visible in the

conventional correlator. This increases the amount of "overlap" between the actual FLIR data and the stored template, and thus improves performance.

Referring back to Figure 5.1, the enhanced correlation algorithm uses the 8 x 8 array of target intensities obtained by the FLIR measurement, to establish a 64-element shape function from the target plume intensity profile (Section 4.3.1). The intensity functions are centered on the FLIR plane by translational shifts using centroid offset estimates from $\hat{x}(t_i^+)$, using the "shifting property" of the Fourier Transform, where negating phase shifts are applied in the spatial frequency domain to accomplish a translational shift in the original domain. Rather than perform the difficult correlation in the time domain, the Fourier domain allows one to apply straightforward multiplication to implement the "translational shift" of the intensity functions and eventual correlation with the template. Exponential smoothing is then used to average the result with previously centered images to yield an updated template. The current FLIR data is then correlated against the template of the previously stored shape function that has been centered on the FLIR image plane. The outputs of the algorithm are two linear offsets, x_c and y_c as shown in Equations (4-1) and (4-2), that yield the highest correlation of the current data with the template. These "pseudo-measurements" are then fed to the linear FLIR Kalman filter for its update. The filter provides the updated estimate, $\hat{x}(t_i^+)$, used to center the FLIR intensity profile to be included in the template generation for the next measurement.

5.2.2.2 Template Generation. The template reconstructs the shape, size, and location of the intensity centroid using the raw noise-corrupted FLIR measurements. The template generation begins with an input of a FLIR frame of data to the enhanced correlator algorithm of Figure 5.1. Using the "shifting" property of the fast Fourier transform (FFT), which states that a translational

shift in the spatial domain is equivalent to a linear phase shift in the frequency domain, the phase shift is computed by:

$$F\{g(x - x_{shft}, y - y_{shft})\} = G(f_x, f_y) \exp\{-j2\pi(f_x \cdot x_{shft} + f_y \cdot y_{shft})\} \quad (5-14)$$

where

$$\begin{aligned} F\{\cdot\} &= \text{Fourier transform operator} \\ g(x,y) &= \text{2-dimensional spatial data array} \\ G(f_x, f_y) &= F\{g(x,y)\} \\ f_x, f_y &= \text{spatial frequencies} \end{aligned}$$

The Fourier transform is implemented in the simulation software using the Cooley-Tukey algorithm [36]. The target plume intensity shape function is "centered on the FLIR plane" by phase shifting the transformed function an amount equal to:

$$\begin{aligned} x_{shft}(t_i) &= \hat{x}_d(t_i') + \hat{x}_a(t_i') \\ y_{shft}(t_i) &= \hat{y}_d(t_i') + \hat{y}_a(t_i') \end{aligned} \quad (5-15)$$

where $\hat{x}_d, \hat{y}_d, \hat{x}_a, \hat{y}_a$ are the state estimates defined in Equation (5-1). Once the data is centered on the FLIR plane, it is incorporated into an updated template for the next sample period. In the simulation, the Kalman filter's first update cycle is bypassed to form the initial template.

The template is generated by averaging the N most recent centered intensity functions observed by the FLIR sensor. The averaging process tends to accentuate the target intensity function and attenuate the corrupting background and FLIR noises. The memory size N is chosen according to how rapidly the shape functions change, i.e., highly dynamic intensity functions

require small values of N , while slowly varying functions use large N values. Typically, a true finite memory averager would require a large computer memory [18]. However, the enhanced correlator algorithm circumvents the memory storage issue by incorporating an "exponential smoothing" technique to approximate the averaging. This technique has properties similar to finite memory averaging, but with the advantage of requiring only the storage of a single FLIR frame of data. The template is maintained by the exponential smoothing algorithm given by:

$$\hat{I}(t_i) = \gamma I(t_i) + (1 - \gamma)\hat{I}(t_{i-1}) \quad (5-16)$$

where

- $\hat{I}(t_i)$ = "smoothed estimate" (template) of the target's intensity function
- $I(t_i)$ = "raw" intensity function from the current FLIR data frame
- γ = smoothing constant: $0 < \gamma \leq 1$

The smoothing constant γ is comparable to the value selected for N . From Equation (5-16), it can be seen that large values of γ emphasize the current data frame and correspond to small values of N . Based on previous studies [14,40], a smoothing constant of $\gamma = 0.1$ is used for this thesis.

A reinitialization algorithm is used once after the first ten sample periods (although it could be called periodically thereafter as well, in actual implementation). Once the template is computed, its centroid is calculated and shifted to the center of field of view for the template, thus eliminating any biases. It is this template which is now stored and correlated with the next FLIR data to produce the "pseudo-measurements."

5.2.2.3 "Pseudo-Measurements". The template serves as the best estimate of the shape of the target plume intensity function prior to receiving a new FLIR data frame. The cross-

correlation of the incoming FLIR data with the template provides the position offsets from the center of the FOV to the centroid of the target intensity image. The cross-correlation is computed by taking the inverse fast Fourier transform (IFFT) of the equation [36]:

$$F\{g(x,y) * I(x,y)\} = G(f_x, f_y)L^*(f_x, f_y) \quad (5-17)$$

where

$$\begin{aligned} F\{\cdot\} &= \text{Fourier transform operator} \\ g(x,y) &= \text{measured target intensity function of the current FLIR data frame} \\ I(x,y) &= \text{expected target plume intensity function (i.e., template)} \\ g(x,y) * I(x,y) &= \text{cross-correlation of } g(x,y) \text{ and } I(x,y) \\ G(f_x, f_y) &= F\{g(x,y)\} \\ L^*(f_x, f_y) &= \text{complex conjugate of } F\{I(x,y)\} \end{aligned}$$

After the IFFT is accomplished, the values of the correlation function, $g(x,y) * I(x,y)$, are modified such that any value less than 0.3 of the function's maximum value is set to zero [14,32]. This "thresholding" technique is used to eliminate false peaks in the correlation function that occur due to noise and other effects. As shown earlier in Figure 5.1, the output of the image correlation is the offset of the "thresholded" FLIR intensity centroid from the center of the FLIR FOV. This offset is assumed to be the result of the summed effects of target dynamics, atmospheric jitter, and measurement noise. The x - and y -components of the offsets are the pseudo-measurements provided to the FLIR Kalman filter, and are expressed in terms of Equation (5-1) as:

$$\begin{aligned} x_{offset} &= x_d + x_a + v_{f1} \\ y_{offset} &= y_d + y_a + v_{f2} \end{aligned} \quad (5-18)$$

These two measurements can be represented in state form as:

$$z(t_i) = H_f x_f(t_i) + v_f(t_i) \quad (5-19)$$

where

$$z(t_i) = [x_{offset}(t_i), y_{offset}(t_i)]^T$$

$$H_f = 2 \times 6 \text{ measurement matrix}$$

$$x_f(t_i) = \text{state vector of Equation (5-1)}$$

$$v_f(t_i) = \text{2-dimensional, discrete-time, white Gaussian measurement noise with statistics:}$$

$$E\{v(t_i)\} = \mathbf{0}$$

$$E\{v(t_i)v^T(t_j)\} = \begin{cases} \mathbf{R} & t_i = t_j \\ \mathbf{0} & t_i \neq t_j \end{cases} \quad (5-20)$$

The FLIR measurement matrix H_f is given by:

$$H_f = \begin{bmatrix} 1 & 0 & 0 & 0 & 1 & 0 \\ 0 & 1 & 0 & 0 & 0 & 1 \end{bmatrix} \quad (5-21)$$

The measurement noise $v_f(t_i)$ represents the combined corrupting effects of the spatially correlated background noise, the FLIR sensor noise (Section 4.3.1), and the errors due to the FFT/IFFT processes. The covariance matrix R_f (with units of pixels²) associated with this error is given by [10,29,36]:

$$R_f = \begin{bmatrix} 0.00363 & 0 \\ 0 & 0.00598 \end{bmatrix} \quad (5-22)$$

Since the pseudo-measurements are linear, a linear Kalman filter is utilized where the update cycle is defined by the equations [17]:

$$\begin{aligned} K(t_i) &= P_f(t_i^-) H_f^T [H_f P_f(t_i^-) H_f^T + R_f]^{-1} \\ \hat{x}_f(t_i^+) &= \hat{x}_f(t_i^-) + K(t_i) [z(t_i) - H_f \hat{x}_f(t_i^-)] \\ P_f(t_i^+) &= P_f(t_i^-) - K(t_i) H_f P_f(t_i^-) \end{aligned} \quad (5-23)$$

where

- $K(t)$ = 6 x 2 filter gain matrix
- $P_f(t)$ = 6 x 6 filter covariance matrix
- H_f = 2 x 6 measurement matrix; Equation (5-21)
- R_f = 2 x 2 measurement noise covariance matrix; Equation (5-22)
- $\hat{x}_f(t)$ = 6-dimensional estimated state vector; Equation (5-1)
- $z(t)$ = 2-dimensional measurement vector; Equation (5-19)
- (t_i^-) = time instant immediately before measurements are incorporated at time t_i
- (t_i^+) = time instant immediately after measurements are incorporated at time t_i

5.2.3 Filter Parameters. This section provides a consolidated reference of the parameters used in the simulation. Presented below are definitions of the modeling parameters, initial conditions, and tuning parameters for the six-state FLIR filter employed in this research.

5.2.3.1 *Modeling Values.* The filter target dynamics correlation time constants τ_x and τ_y , in Section 5.2.1, are both equal to 8.5 seconds and represent a missile target with benign dynamics. The atmospheric correlation time constants τ_{ax} and τ_{ay} are both set equal to 0.0707 seconds in the simulation [6].

5.2.3.2 *Initial Conditions.* Since initial acquisition characteristics of the FLIR filter have been explored in the past [41], emphasis is placed upon the tracking problem, rather than acquisition and tracking. Thus, taken from previous research [5,6], the filter is artificially initialized to zero error for the position and velocity states of Equation (5-1). The position states x_1 and x_2 are initialized with the target plume intensity centroid centered in the FLIR FOV. The velocity states x_3 and x_4 are initialized in accordance with the target's initial trajectory conditions as defined in Section 4.5.1. Both atmospheric states x_5 and x_6 are initialized to zero.

The initial state covariance matrix $P(t_0)$ is:

$$P(t_0) = \begin{bmatrix} 10 & 0 & 0 & 0 & 0 & 0 \\ 0 & 10 & 0 & 0 & 0 & 0 \\ 0 & 0 & 2000 & 0 & 0 & 0 \\ 0 & 0 & 0 & 2000 & 0 & 0 \\ 0 & 0 & 0 & 0 & .2 & 0 \\ 0 & 0 & 0 & 0 & 0 & .2 \end{bmatrix} \quad (5-24)$$

where the units of the covariance associated with the position states x_1 and x_2 and the atmospheric states x_5 and x_6 are pixels², and those of the velocity states x_3 and x_4 are expressed in pixels²/seconds² [6].

The measurement covariance matrix R_f was established empirically in past research [23,36]. R_f (with units of pixels²) is given by:

$$R_f = \begin{bmatrix} 0.00363 & 0 \\ 0 & 0.00598 \end{bmatrix} \quad (5-25)$$

5.2.3.3 Tuning Values. Both filter dynamic variances σ_x^2 and σ_y^2 , in Section 5.2.1, are equal to 800 pixels²/seconds² with or without plume pogo applied to the intensity centroid. Both atmospheric variances σ_{ax}^2 and σ_{ay}^2 are equal to 0.2 pixels² in accordance with the truth model (Section 4.4.4) [6].

5.3 Hardbody Center-of-Mass Filters

Parallel to the two previous theses [5,6], the primary objective of this research is the precise tracking of the missile hardbody and determination of its center-of-mass location. The basic premise underlying the dynamics modeling efforts is that the center-of-mass is located at an offset distance relative to the intensity centroid. The offset distance is oriented angularly using the FLIR filter estimated intensity centroid's velocity in the FLIR image plane [5]. Figure 5.2 illustrates the geometry of estimating the offset distance and the dependence of the center-of-mass filters upon the FLIR filter's estimates of the position and velocity of the intensity centroid. (Note that Figure 5.2 depicts the ideal situation; in general, the filter estimates of the centroid position, velocity, and the orientation angle are not equal to the truth model values.) Originating at the intensity centroid's estimated position, a low-energy laser is scanned along the estimated velocity vector. The reflections of the low-energy scan generate a measurement of the offset distance, to be utilized as aimpoint information for the high-energy laser.

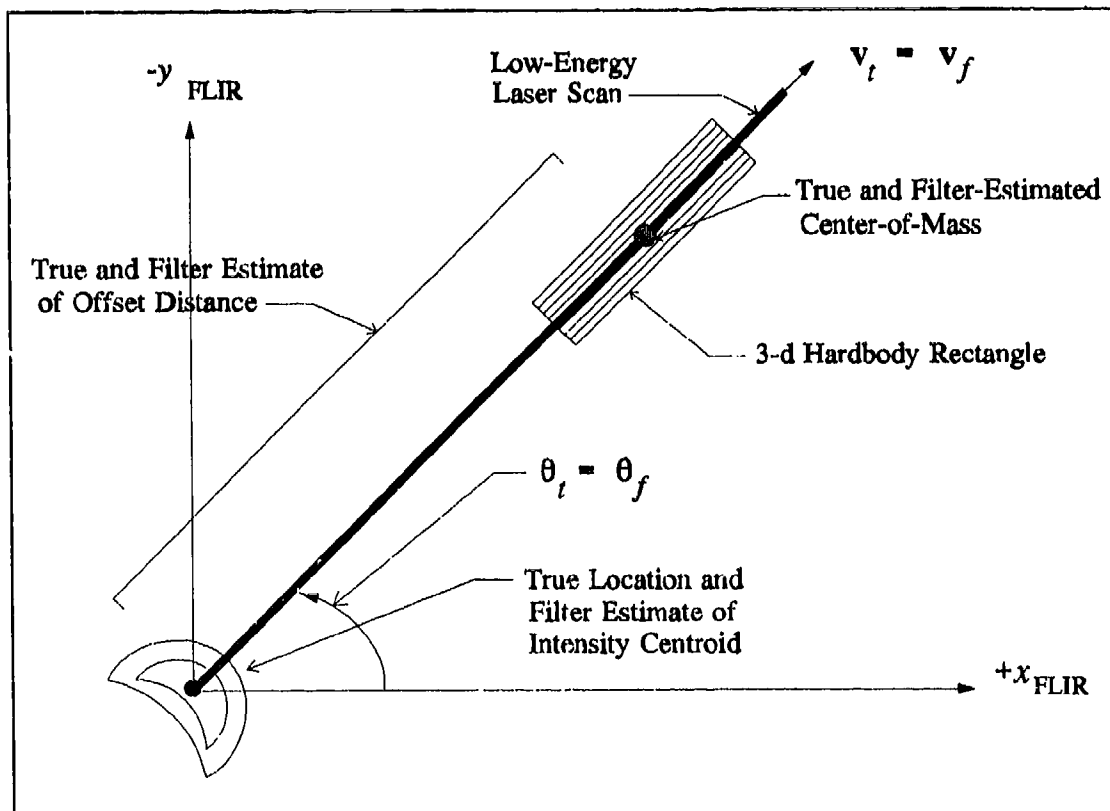


Figure 5.2 Filter Estimate of Offset Distance (Ideal Conditions)

Except for the dependence upon the FLIR filter's estimated intensity centroid position and velocity, the center-of-mass filters function autonomously; the FLIR filter has no knowledge of the existence of the center-of-mass filter. Eden [5] developed a one-state center-of-mass filter that processed measurements derived from the speckle return of the plume/hardbody interface. Evans [6] followed with an eight-state filter, composed of the six-state FLIR filter augmented with two states that represent the x and y components of the offset distance. Again, the augmented partition of the eight-state filter is independent of the FLIR partition, except for its reliance on information regarding the intensity centroid's position and velocity vector. Evans compared the performance of the hardbody center-of-mass estimates between the eight-state filter and the six-state FLIR/one-

state center-of-mass filter configuration and found that both performed equally well. He concluded the one-state center-of-mass filter performs sufficiently well for the given benign trajectory and has the advantage of requiring less computer processing time [6].

This thesis differs from Eden's and Evans' work by using the Doppler return, instead of the speckle return, of the low-energy scan to discern the plume/hardbody interface. This approach is driven by the need for a more meticulous discrimination of the plume/hardbody interface since there is evidence of speckle return emanating from the plume of a solid-propellant rocket due to the presence of aluminum and other metallic particulates (Section 4.3.2.2). Measurements of the plume's speckle return were determined to be on the same order of magnitude as that of the hardbody [2,34] and, under these conditions, the precise definition of the plume/hardbody interface becomes ambiguous and degrades the ability to locate the hardbody center-of-mass. Eden's one-state filter, that processes measurements of the offset distance as derived from the laser speckle return, is evaluated to determine the extent of performance degradation caused by the plume's reflectance (this phenomenon was not simulated in either Eden's or Evans' work).

To investigate the feasibility of employing Doppler returns, two center-of-mass filter configurations are utilized in this study. First, the identical dynamics model of Eden's one-state filter will be used to process measurements of the offset distance as acquired from the plume and hardbody-induced Doppler returns. Second, a two-state center-of-mass filter in a modified Maximum a Posteriori (MAP) Multiple Model Adaptive Filter (MMAF) structure is developed to accept measurements generated from both laser speckle and Doppler returns.

The following subsections begin by presenting the dynamics of the one-state filter and includes separate discussions on the speckle and Doppler measurement models. Next, the two-state MAP MMAF center-of-mass filter that employs both measurement models is described.

5.3.1 One-State Center-of-Mass Filter Dynamics Model. The offset between the intensity centroid and the hardbody center-of-mass is represented as a bias. This bias is modeled as a simple integrator, with driving pseudo-noise for filter tuning purposes. The single-state representation of the linear, time-invariant, stochastic differential equation is given by:

$$\dot{x}_f = F_f x_f(t) + G_f w_f(t) \quad (5-26)$$

where

- $F_f = 0$
- $x_f(t) =$ state representing offset distance between missile center-of-mass and FLIR image plane intensity centroid
- $G_f =$ time-invariant noise distribution matrix, equal to unity
- $w_f(t) =$ white Gaussian noise process, independent of the noise processes of the six-state filter, with mean and covariance kernel statistics:

$$\begin{aligned} E\{w_f(t)\} &= 0 \\ E\{w_f(t)w_f(t + \tau)\} &= Q_f \delta(\tau) \end{aligned} \quad (5-27)$$

The scalar discrete-time representation of the filter propagation Equations (5-7) and (5-8) is:

$$\hat{x}_f(t_{i+1}) = \Phi_f(\Delta t) \hat{x}_f(t_i) \quad (5-28)$$

$$P_f(t_{i+1}) = \Phi_f(\Delta t) P_f(t_i) \Phi_f^T(\Delta t) + Q_{df} \quad (5-29)$$

where

- $\hat{x}_f(t_i)$ = filter estimate of the 1-dimensional state vector
 $\Phi_f(\Delta t)$ = time-invariant state transition matrix, equal to unity, for propagation over the sample period: $\Delta t = t_{i+1} - t_i$
 $P_f(t_i)$ = 1 x 1 filter covariance matrix
 (t_i^-) = time instant before FLIR measurement is incorporated into the estimate at time t_i
 (t_i^+) = time instant after FLIR measurement is incorporated into the estimate at time t_i
 Q_{df} = filter dynamics noise variance given by:

$$Q_{df} = \int_{t_i}^{t_{i+1}} \Phi_f(t_{i+1} - \tau) G_f Q_f G_f^T \Phi_f^T(t_{i+1} - \tau) d\tau \quad (5-30)$$

where $Q_{df} = Q_f \Delta t$ since $G_f = \Phi_f = 1$. The transposes that appear in Equations (5-29) and (5-30) are not really necessary since all quantities are scalar, but they are retained for convenience.

5.3.1.1 Speckle Reflectance Measurement Model. This model is included in this study to observe the effects caused by the low-energy laser speckle return of the plume (Section 4.3.2.2) upon the center-of-mass estimates. If the speckle reflection of both the hardbody and plume is received by a low-energy laser sensor, a noise corrupted measurement of the offset distance, further biased by the plume's reflectance, is provided to the one-state filter (Equation (4-47)). The discrete-time measurement model is given by:

$$z(t_i) = H_f x_f(t_i) + v_f(t_i) \quad (5-31)$$

where

- $z(t_i)$ = biased measurement of the offset distance (Equation (4-47))
 H_f = measurement matrix, equal to unity

$x_f(t_i)$ = center-of-mass offset state
 $v_f(t_i)$ = discrete-time, white Gaussian measurement noise with statistics:

$$\begin{aligned}
 E\{v(t_i)\} &= 0 \\
 E\{v(t_i)v(t_j)\} &= \begin{cases} R_f & t_i = t_j \\ 0 & t_i \neq t_j \end{cases}
 \end{aligned}
 \tag{5-32}$$

where $R_f = R$, (true measurement variance) = 0.000178 pixels² (Section 4.4.8) [6].

5.3.1.2 Doppler Measurement Model. In contrast with the speckle measurement model, this model provides a measurement based upon the low-energy laser Doppler return of the hardbody. The significant dissimilarities between the plume and hardbody-induced Doppler returns can be exploited to discern the plume/hardbody interface (Section 4.3.3.2) precisely, and provide information regarding the location of the hardbody. The low-energy laser measurement is provided to the one-state filter whenever the laser intercepts the hardbody, and the hardbody-induced (and plume-induced) Doppler return is received by Doppler return sensor equipment. The resulting measurement to be provided to the filter is a noise-corrupted offset distance between the FLIR filter's estimate of the intensity centroid and the computed center-of-mass. The discrete-time measurement model is given by:

$$z(t_i) = H_f x_f(t_i) + v_f(t_i) \tag{5-33}$$

where

$z(t_i)$ = measurement of the offset distance
 H_f = measurement matrix, equal to unity
 $x_f(t_i)$ = center-of-mass offset state

$v_f(t_i)$ = discrete-time, white Gaussian measurement noise with statistics:

$$\begin{aligned} E\{v(t_i)\} &= 0 \\ E\{v(t_i)v(t_j)\} &= \begin{cases} R_f & t_i = t_j \\ 0 & t_i \neq t_j \end{cases} \end{aligned} \quad (5-34)$$

where $R_f = R$, (true Doppler measurement variance), a function of low-energy laser wavelength, radar aperture, and signal-to-noise ratio (Section 4.3.3.4). Since both measurement models are linear, the one-state filter processes the measurements using a linear update cycle defined by the scalar version of Equation (5-23).

5.3.2 Two-State Modified MAP MMAF. For this research, a 2-state modified MAP MMAF structure is developed to capitalize on both the speckle and Doppler reflections of the low-energy laser scan. There are three advantages to this endeavor: first, this filter benefits from both measurements, and all available information regarding the location of the hardbody's center-of-mass is provided to the filter at each update cycle. Second, as the hardbody's aspect angle γ approaches 0° (normal to the Doppler transmitter's LOS), the plume-induced Doppler spectrum converges with that of the hardbody (as in Figure 4.14), rendering detection of the hardbody-induced Doppler return difficult (Section 4.3.3.2). Nevertheless, the low-energy laser speckle returns continue to provide measurements under these conditions, and can compensate for the temporary loss of Doppler information. Third, should either the speckle return or Doppler return sensing circuitry/equipment malfunction, the availability of both measurements establishes a level of redundancy that ensures the tracking system remains operational, albeit with some degradation in performance.

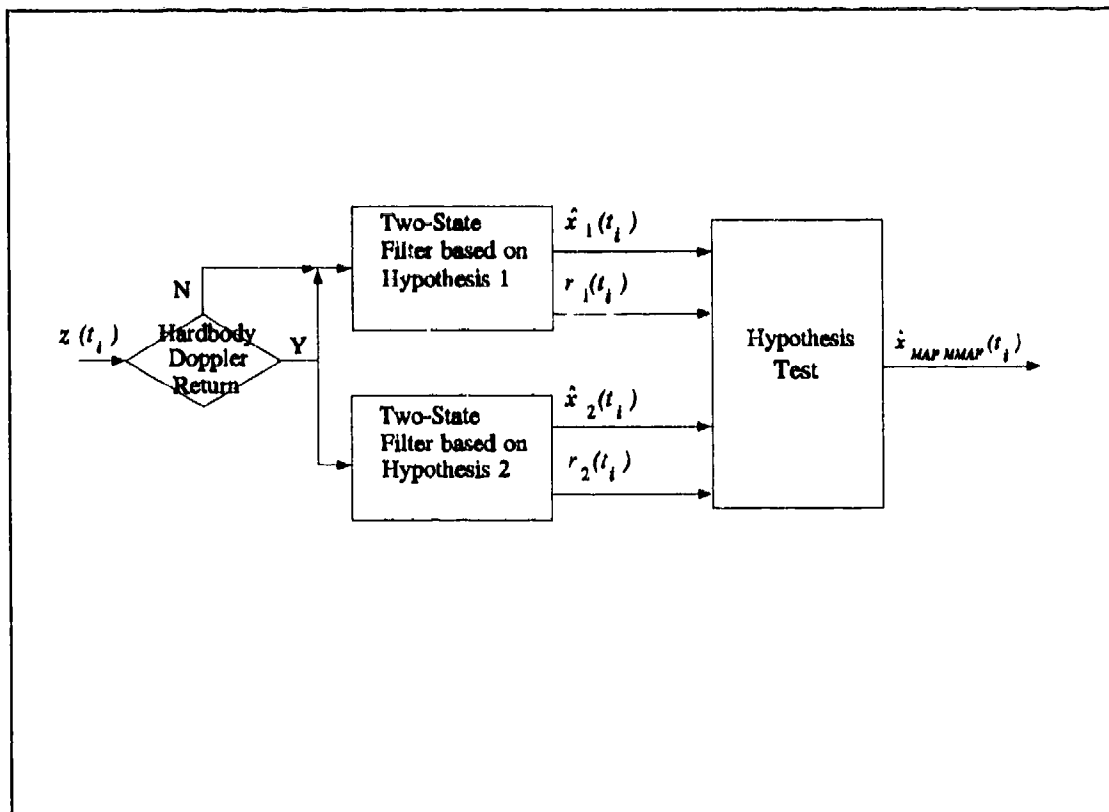


Figure 5.3 Two-State Modified MAP MMAF Structure

Figure 5.3 shows the modified MAP MMAF structure with a decision block followed by two elemental filters. Each elemental filter is composed of two states: one state that represents the offset distance from the FLIR image intensity centroid to the hardbody's center-of-mass; and one state that represents the bias caused by the plume's speckle reflectance (Section 4.3.2.2). The role of the decision block is to ascertain the presence of the hardbody-induced Doppler return in the measurements for each sample time. If the hardbody Doppler return is detectable, the measurements are provided to the two elemental filters that are based upon two hypothesis: 1) the bias caused by the plume's speckle reflectance exists in the measurement, and 2) the bias does not exist in the measurement.

The two hypotheses capture the intermittent appearance of the plume's speckle reflectance. As mentioned in Section 4.3.2.2, the plume's speckle reflectance was observed to occur 90% of the time during the boost phase, which implies that the bias is not included in the speckle measurement 10% of the time. To validate either hypothesis, the residuals of the elemental filters are monitored and compared to each other. The state estimate associated with the "best" residual (meaning the smaller of the two) would have the highest probability of being associated with the correct hypothesis, and thus of being the optimal state estimate for the given sample time.

The estimation process could have been handled as well by a Bayesian MMAF, in which the state vector estimate of each elemental filter is weighed appropriately using a hypothesis conditional probability to produce the state estimate, $\hat{x}_{mmaf}(t_i)$, as a probabilistically weighted sum (Section 2.3). Nonetheless, it was felt that the respective residuals would be sufficient and distinctive enough to verify their respective hypotheses, and the appropriate $\hat{x}_{map\ mmaf}(t_i)$ would be selected. In addition, the modified MAP MMAF is simple, requires minimal computational processing, and is therefore easy to implement. Hence, a decision was made to pursue the modified MAP MMAF structure [20].

If the hardbody-induced Doppler return is not detectable, the measurement is provided to the elemental filter based upon the first hypothesis. This allows the speckle return measurement to continue when the hardbody Doppler return ceases to be distinct from the plume's (Section 4.3.3.2) and a Doppler return measurement cannot be generated. With the first hypothesis, it is anticipated that the bias would exist in the speckle return measurements, due to the high rate of appearance of the plume's speckle reflectance. This bias is not separately observable based only on speckle measurements, so the most recent bias estimate is retained until such time that Doppler

measurements resume. The following subsections discuss the 2-state modified MAP MMAF dynamics model, and measurement model, and it also covers the adaptive algorithm.

5.3.2.1 Two-State Dynamics Model. The two states, one offset distance state and one bias state, are each represented as the output of simple integrators driven by white Gaussian pseudo-noise for tuning purposes. The linear, time-invariant, stochastic differential equation for this model is given by:

$$\dot{\mathbf{x}}_f = \mathbf{F}_f \mathbf{x}_f(t) + \mathbf{G}_f \mathbf{w}_f(t) \quad (5-35)$$

where

- $\mathbf{F}_f = \mathbf{0}$
- $\mathbf{x}_f(t)$ = 2-dimensional state vector
- $\mathbf{G}_f = 2 \times 2$ time-invariant noise distribution matrix equal to \mathbf{I}
- $\mathbf{w}_f(t)$ = 2-dimensional independent, white Gaussian noise process with mean and covariance statistics:

$$\begin{aligned} E\{\mathbf{w}_f(t)\} &= \mathbf{0} \\ E\{\mathbf{w}_f(t)\mathbf{w}_f^T(t + \tau)\} &= \mathbf{Q}_f \delta(\tau) \end{aligned} \quad (5-36)$$

The time-invariant, discrete-time representation of the filter propagation Equations (5-7) and (5-8) is:

$$\hat{\mathbf{x}}_f(t_{i+1}^-) = \Phi_f(\Delta t) \hat{\mathbf{x}}_f(t_i^+) \quad (5-37)$$

$$\mathbf{P}_f(t_{i+1}^-) = \Phi_f(\Delta t) \mathbf{P}_f(t_i^+) \Phi_f^T(\Delta t) + \mathbf{Q}_{df} \quad (5-38)$$

where

- $\hat{\mathbf{x}}_f(t_i)$ = modified MAP MMAF estimate of the 2-dimensional state vector

$\Phi_f(\Delta t)$ = 2 x 2 time-invariant state transition matrix, equal to I , for propagation over the sample period: $\Delta t = t_{i+1} - t_i$

$P_f(t_i)$ = 2 x 2 filter covariance matrix

(t_i^-) = time instant before measurement is incorporated into the estimate at time t_i

(t_i^+) = time instant after measurement is incorporated into the estimate at time t_i

Q_{df} = filter dynamics noise covariance given by:

$$Q_{df} = \int_{t_i}^{t_{i+1}} \Phi_f(t_{i+1}-\tau) G_f Q_f G_f' \Phi_f^T(t_{i+1}-\tau) d\tau \quad (5-39)$$

where $Q_{df} = Q_f \Delta t$ since $G_f = \Phi_f = I$.

5.3.2.2 Measurement Model. When the low-energy laser intercepts the hardbody, noise-corrupted measurements derived from both Doppler return and speckle return are provided to the two-state modified MAP MMAF. While the Doppler return provides measurements of the offset distance from the FLIR image intensity centroid to the hardbody-of-mass, the measurements acquired from the speckle return generally consist of the offset distance with the bias caused by the plume's speckle reflectance.

Let s denote a vector of uncertain parameters in the measurement. The discrete-time measurement model is given by:

$$z(t_i) = H(s)_f x_f(t_i) + v_f(t_i) \quad (5-40)$$

where

$z(t_i)$ = 2-dimensional hardbody center-of-mass measurement

$H(s)_f$ = 2 x 2 measurement distribution matrix

$x_f(t_i)$ = 2-dimensional state vector

$v_f(t_i)$ = 2 x 2 discrete-time, white Gaussian measurement noise with statistics:

$$E\{v(t_i)\} = \mathbf{0}$$

$$E\{v(t_i)v^T(t_j)\} = \begin{cases} \mathbf{R} & t_i = t_j \\ \mathbf{0} & t_i \neq t_j \end{cases} \quad (5-41)$$

The measurement distribution matrix, $\mathbf{H}(s)_f$, is given by:

$$\mathbf{H}(s)_f = \begin{bmatrix} \mathbf{H}_{speckle} \\ \dots\dots\dots \\ 1 \quad 0 \end{bmatrix} \quad (5-42)$$

where

$\mathbf{H}_{speckle}$ = 1 x 2 partition, adaptively configured according to the presumed quality of the scalar speckle measurement

Figure 5.4 diagrams the algorithm for adaptively defining the $\mathbf{H}_{speckle}$ partition and shows two paths that branch from the "Detectable Hardbody Doppler Return" decision block. Each path corresponds to the two events mentioned earlier - the intermittent nature of the plume's speckle reflectance (right path), and the loss of hardbody-induced Doppler returns (left path). The right path of the algorithm is contingent upon two hypotheses: 1) the bias caused by the plume's speckle reflectance exists, and 2) the bias does not exist. The right path of the algorithm operates sequentially in the following manner:

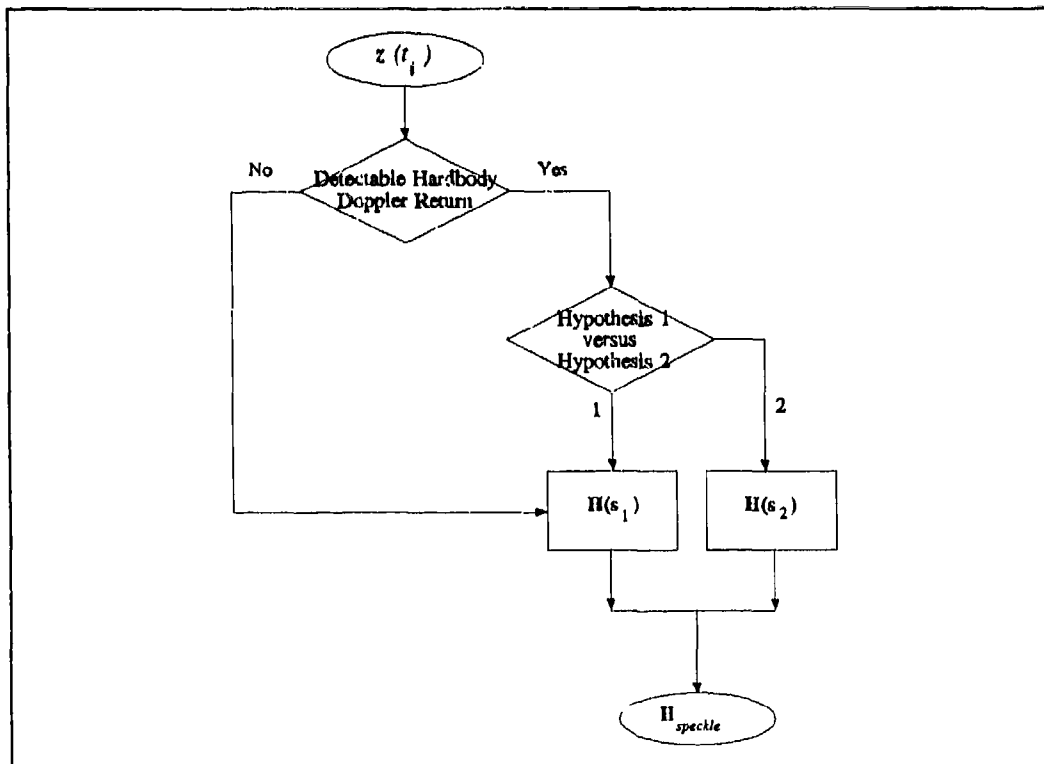


Figure 5.4 Modified MAP MMAF Algorithm

1. Under the first hypothesis, the measurement is provided to the filter according to the model:

$$z_f(t_i) = H(s_1)_f x_f(t_i) + v_f \quad (5-43)$$

The discrete-time, scalar representation of Equation (5-43) is given by:

$$\begin{bmatrix} z_{f1}(t_i) \\ z_{f2}(t_i) \end{bmatrix} = \begin{bmatrix} 1 & -1 \\ \dots\dots\dots \\ 1 & 0 \end{bmatrix} \begin{bmatrix} x_{f1}(t_i) \\ x_{f2}(t_i) \end{bmatrix} + \begin{bmatrix} v_{f1} \\ v_{f2} \end{bmatrix} \quad (5-44)$$

where

$z_{f1}(t_i)$ = noise-corrupted speckle return measurement

$z_{f2}(t_i)$ = noise-corrupted Doppler return measurement

- $x_{p1}(t_i)$ = center-of-mass offset distance state
- $x_{p2}(t_i)$ = bias state
- $v_{p1}(t_i)$ = discrete, white Gaussian measurement noise associated with the speckle measurement
- $v_{p2}(t_i)$ = discrete, white Gaussian measurement noise associated with the Doppler measurement

Note that the $H_{(speckle)}$ partition is shown as [1 -1] to signify the bias caused by the plume's speckle reflectance is in the opposite direction of the hardbody's velocity vector.

The residual, r_1 , is then calculated as [17]:

$$r_1(t_i) = z_f(t_i) - H(s_1)_f \hat{x}_f(t_i^-) \quad (5-45)$$

where

r_1 = residual formed from the elemental filter based on the first hypothesis

2. Similarly, the measurement is provided simultaneously to the elemental filter under the second hypothesis (that no bias exists in the measurement) according to the following model:

$$z_f(t_i) = H(s_2)_f x_f(t_i) + v_f \quad (5-46)$$

The detailed representation of Equation (5-46) is given by:

$$\begin{bmatrix} z_{f1}(t_i) \\ z_{f2}(t_i) \end{bmatrix} = \begin{bmatrix} 1 & 0 \\ \dots\dots\dots & \\ 1 & 0 \end{bmatrix} \begin{bmatrix} x_{f1}(t_i) \\ x_{f2}(t_i) \end{bmatrix} + \begin{bmatrix} v_{f1} \\ v_{f2} \end{bmatrix} \quad (5-47)$$

with the $H_{speckle}$ partition shown as [1 0]. The residual, r_2 , is then calculated as:

$$r_2(t_i) = z_f(t_i) - H(s_2) \hat{x}_f(t_i) \quad (5-48)$$

where

r_2 = residual formed in the elemental filter based on the second hypothesis

- Each residual r_i is a 2-dimensional vector with the first scalar component directly associated with the hypothesis testing. The detailed representation of Equation (5-48) for the residual, r_i , is given by:

$$\begin{bmatrix} r_{i1}(t_i) \\ r_{i2}(t_i) \end{bmatrix} = \begin{bmatrix} z_{f1}(t_i) \\ z_{f2}(t_i) \end{bmatrix} - \begin{bmatrix} H_{speckle} \\ \dots\dots\dots \\ 1 \quad 0 \end{bmatrix} \begin{bmatrix} \hat{x}_{r1}(t_i) \\ \hat{x}_{f2}(t_i) \end{bmatrix} \quad (5-49)$$

where the component r_{i1} is given by:

$$r_{i1}(t_i) = z_{f1}(t_i) - H_{speckle} \hat{x}_f(t_i) \quad (5-50)$$

Thus, the scalar components r_{i1} of the residuals r_1 and r_2 are compared, whereby the "best" residual (i.e., the smaller of the two r_{i1} components) determines which associated elemental filter has the highest probability to provide the correct state estimate at a given time.

The left path of the algorithm allows the reception of speckle return measurements to continue during the loss of distinct hardbody Doppler returns. The measurement is provided to the elemental filter based upon the first hypothesis with the assumption that the measurement

contains the bias. Thus, the $H_{speckle}$ partition is configured as [1 -1] to accept the speckle return measurement of the offset distance, assuming that it has the bias.

5.3.3 Filter Parameters. In the preceding discussions, parameters were introduced for the filter dynamics and measurement models. This section consolidates and defines the initial conditions and tuning parameters for the hardbody center-of-mass filters used in this research.

5.3.3.1 One-State Filter with Speckle Return Measurements: Initial Conditions. Based on previous research [5,6], the offset distance from the FLIR image intensity centroid to the hardbody center-of-mass is initialized to one pixel. The initial state variance $P(t_0)$ is equal to 0.2 pixels², and the measurement variance is equal to the true measurement variance, 0.00178 pixels².

5.3.3.2 One-State Filter with Speckle Return Measurements: Tuning Values. From Evans [6], the filter dynamics noise variance Q_{df} is equal to 0.7 pixels².

5.3.3.3 One-State Filter with Doppler Return Measurements: Initial Conditions. The values of the initial offset distance and initial state variance, $P(t_0)$, are carried forward from Evan's thesis: 1 pixel and 0.2 pixels², respectively [6]. The measurement variance, R_f , is equal to the true measurement variance and is a function of the low-energy laser wavelength, SNR, and aperture diameter of the transmitter (Section 4.3.3.4). The filter measurement variance is given by:

$$R_f = R_t = \left[\frac{\theta_b}{3k_p \sqrt{\text{SNR}}} \right]^2 \quad (5-51)$$

where

R_f = filter measurement variance

R_t = true measurement variance

- θ_B = beam diffraction limit (Equation (4-54))
- k_p = pixel proportionality constant, 15 μ rad/pixel (Section 4.2.1)
- SNR = signal-to-noise ratio

5.3.3.4 *One-State Filter with Doppler Return Measurements: Tuning Values.* The filter dynamics noise variance Q_{df} is equal to 0.7 pixels², based upon Evans' research [6].

5.3.3.5 *Two-State Modified MAP MMAF: Initial Conditions.* The initial offset distance is retained at one pixel, and the initial bias is again set at one pixel. Thus, the initial states $x(t_0)$ is given by:

$$x_f(t_0) = \begin{bmatrix} 1.0 \\ 1.0 \end{bmatrix} \quad (5-52)$$

The initial state covariance matrix, $P(t_0)$, is given as:

$$P(t_0) = \begin{bmatrix} 0.2 & 0.0 \\ 0.0 & 0.2 \end{bmatrix} \quad (5-53)$$

with units of pixels². The measurement variance matrix, R_f , is given by:

$$R_f = \begin{bmatrix} 0.00178 & 0.0 \\ 0.0 & R_{f22} \end{bmatrix} \quad (5-54)$$

where R_{22} is equal to the Doppler measurement variance of Equation (5-49).

5.3.3.6 *Two-State Modified MAP MMAF: Tuning Values.* The performance plots that resulted from tuning the two-state modified MAP MMAF are shown in Appendix D. For the initial tuning values, the filter dynamics noise variances were set equal to the values mentioned in Sections 5.3.3.2 and 5.3.3.4 for each one-state filter. The covariance of the discrete-time white Gaussian dynamics driving noise, given by Q_{df} , is:

$$Q_{df} = \begin{bmatrix} q_{df11} & 0.0 \\ 0.0 & q_{df22} \end{bmatrix} \quad (5-55)$$

where

q_{df11} = offset dynamics noise variance

q_{df22} = bias dynamics noise variance

From Figure D.1, it can be seen that these original tuning values were overly conservative. The variances were gradually decreased by an order of magnitude until the overall time histories of actual rms errors and the filter computed rms error matched well [17]. Table 5.1 lists the statistics

Table 5.1 Two-State Modified MAP MMAF Tuning Statistics

q_{df11}	q_{df22}	True Error Mean(t_i)	True Error Mean(t_i^+)	True Error $1\sigma(t_i)$	True Error $1\sigma(t_i^+)$
0.7	0.7	0.33329E-4	-0.18450E-4	0.14906E+0	0.32113E-2
0.07	0.07	0.33747E-4	-0.18576E-4	0.14905E+0	0.32121E-2
0.007	0.0007	0.35241E-4	-0.18108E-4	0.14897E+0	0.31975E-2
0.01	0.001	0.34722E-4	-0.17817E-4	0.14900E+0	0.31980E-2
0.03	0.001	0.33822E-4	-0.18678E-4	0.14904E+0	0.31945E-2

that were achieved from 5 sets of tuning values. Decreasing the dynamics noise strengths q_{d11} and q_{d22} produced negligible differences in performance; however, the last entry was chosen based upon its performance plot in Figure D.25.

From Equation (5-54), the two-state modified MAP MMAF dynamics noise covariance \mathbf{Q}_{df} , in units of pixels², is given by:

$$\mathbf{Q}_{df} = \begin{bmatrix} 0.03 & 0.0 \\ 0.0 & 0.001 \end{bmatrix} \quad (5-56)$$

5.4 Summary

Four linear Kalman filters are used for this research to investigate the feasibility of employing measurements derived from low-energy laser reflections to locate and track the missile hardbody center-of-mass. The previously developed six-state FLIR filter [5,8,10,11,12,14,27,29, 32,33,35,36, 37,40,41] processes "pseudo-measurements" from an enhanced correlator algorithm and produces position and velocity estimates of the FLIR image target plume intensity centroid. The position and velocity estimates provide the reference position and angular orientation for the low-energy scan. The one-state center-of-mass filter [5] that receives measurements from the low-energy speckle returns, is examined to analyze the effects caused by the speckle reflectance of a solid-propellant motor's exhaust plume. This study adopts the one-state center-of-mass filter's dynamics model to receive the alternative Doppler return measurements. A two-state center-of-mass modified MAP MMAF is developed to capitalize on the available speckle and Doppler returns. The two-state modified MAP MMAF yields several advantages over using just Doppler

(or just speckle) measurements: the use of all available measurement information, compensation for the loss of hardbody-induced Doppler returns by using speckle returns, and measurement redundancy in the event of speckle or Doppler sensor equipment failure.

VI. Procedures and Results

6.1 Introduction

This chapter presents the results of carrying out the research objectives cited in Chapter I. The individual performances of two configurations of hardbody center-of-mass Doppler return filters (the one-state and the two-state Modified MAP MMAF respectively) is evaluated by conducting a sensitivity analysis with respect to three parameters (see Sections 4.3.3.4 and 4.4.10): low-energy laser wavelength, signal-to-noise ratio (SNR), and probability-of-miss (P_m). Each filter is subjected to all the possible combinations of all the respective variations of these three parameters.

Time allotted did not allow the pursuit of two secondary objectives since the sensitivity analysis generated a vast amount of data. Thus the alternative scan techniques are not explored, nor is the implementation of the pogo phenomenon achieved. All simulation runs, however, employ Evans [6] 3-dimensional hardbody model along with the laser sweep routine, as described in Section 4.3.2.1.

Each simulation run consists of 10 Monte Carlo runs over a 10 second period of the target's trajectory. The collection of the statistics of the actual errors (mean and standard deviation) and the filter-computed error standard deviation is given in Appendix A. Performance plots, statistical results, and tabular data are presented in the appendices, and are referred to throughout this chapter. Note that, in the plots of Appendices C, D, E, and F, the collection of the error statistics begin at the second sample time. The purpose for the one-sample delay is to

form the template for the enhanced correlator algorithm with the first set of FLIR data (Section 5.2.2.2). Consequently, most of the plots exhibit no initial transient behavior that would result from the initial conditions given to the center-of-mass filters (Sections 5.3.3.1, 5.3.3., and 5.3.3.5 define the initial conditions). However, depending on the circumstances imposed by the values of wavelength, SNR, and P_m , other plots may display an initial non-zero mean error; these are the cases that exhibit slower initial transients. This is seen to occur particularly in Appendix F. For practical purposes, only the performance plots for a selected parameter set which adequately illustrate significant trends are contained in the appendices. Similarly, the tabular data shown in this chapter are not all inclusive. However, the statistical results and tables in the appendices reflect all data gathered for this research. A description and explanation of the statistical plots can be found in Appendix B.

The analysis and performance evaluation of all the center-of-mass filters is based upon their behavior and sensitivity to changes in the parameters. The performance indicators are the RMS errors obtained at t_i^- and t_i^+ . For time t_i , the RMS error is calculated as:

$$E_{RMS}(t_i) = \sqrt{\bar{e}^2(t_i) + \sigma_e^2(t_i)} \quad (6-1)$$

where

$$\begin{aligned} E_{RMS}(t_i) &= \text{RMS error} \\ \bar{e}(t_i) &= \text{mean error} \\ \sigma_e(t_i) &= \text{error standard deviation} \end{aligned}$$

However, the mean errors t_i^- and t_i^+ of the upcoming tabular data are insignificant as compared to the 1σ values and would therefore have negligible impact upon the RMS error calculations.

Thus, the standard deviations at t_i^- and t_i^+ can therefore become gauges of the trends in the RMS errors. Furthermore, the error standard deviations at t_i^- are deemed critical since they describe how well the filter propagates its offset distance estimates, which are used as control signals for the FLIR sensor controller (Section 3.4); these ultimately determine the tracker pointing accuracy.

The following sections discuss the results of each filter used for this study. The one-state center-of-mass filter with only speckle return measurements is first evaluated to observe the effects from the plume's speckle reflectance. The subsequent sections discuss the results and trends observed from the sensitivity analysis accomplished on both the one-state center-of-mass filter with Doppler return measurements and the two-state center-of-mass modified MAP MMAF using both speckle and Doppler return measurements. Finally, the resulting error statistics are compiled in order to compare the two Doppler filters' performances.

6.2 One-State Filter with Speckle Return Measurements

As mentioned in Section 4.3.2.2, the plume's speckle reflectance was observed to cause an offset bias aftward of about 25-30 meters, appearing 90 - 95% of the time in the measurements. For the simulation, the nominal values for the bias and appearance rate were set at 25 meters (equal to 0.833 pixels) and 90%, respectively. It was anticipated that the additional bias would be apparent in the errors. The filter error statistics (in units of pixels and meters) are shown in Table 6.1, and the statistical plots are shown in Figures 6.1 through 6.3. Although Table 6.1 presents 5 significant figures, in actuality, the first 3 digits are significant. The values shown represent the time-averaged statistics over ten Monte Carlo runs. (This is also true of Tables 6.4 through 6.7, and the tables in Appendix H.) Note, in Table 6.1, the substantial increase of the 1σ values, in meters, over a propagation sample period. Figure 6.1 shows the true rms errors versus the filter

Table 6.1 Offset Distance Statistics of One-State Speckle Return Filter

Offset distance	mean(t_i)	mean(t_i^+)	$1\sigma(t_i)$	$1\sigma(t_i^+)$
pixels	-0.7489	-0.7499	0.26857	0.19545
meters	-22.467	-22.497	8.0571	5.8635

computed rms errors, while Figures 6.2 and 6.3 show the true mean errors \pm the error standard deviations. (Plots, such as in Figure 6.1, are included to demonstrate that good tuning is achieved, whereas plots such as those in Figures 6.2 and 6.3 show the resulting performance of the filter. A further explanation of the plot symbology is given in Appendix B.) The results do show an inclination of the filter's offset measurements towards the bias. Attempts to tune the filter by increasing the dynamics driving noise strength had no significant impact upon the performance. Figure 6.3 shows that the 90% occurrence rate of bias due to plume speckle produced interesting results in the offset errors at t_i^+ . Note, that if the bias were to occur 100% of the time, the plots of Figures 6.2 and 6.3 would exhibit a mean error of .833 pixels (25 meters). Each of the unbiased measurements (occurring 10% of the time) causes a quantized jump in mean and 1σ , where the quantization is directly attributed to using a 10-run Monte Carlo analysis, i.e., the quantizations correspond to 0 "good" measurements out of 10 runs of measurements for each t_i ; 1 "good" out of 10; 2 "good" out of 10, etc.

6.3 One-State Filter with Doppler Return Measurements

The primary purpose of this study was directed by the testing of the one-state filter that is provided with Doppler return measurements of the offset distance rather than speckle return

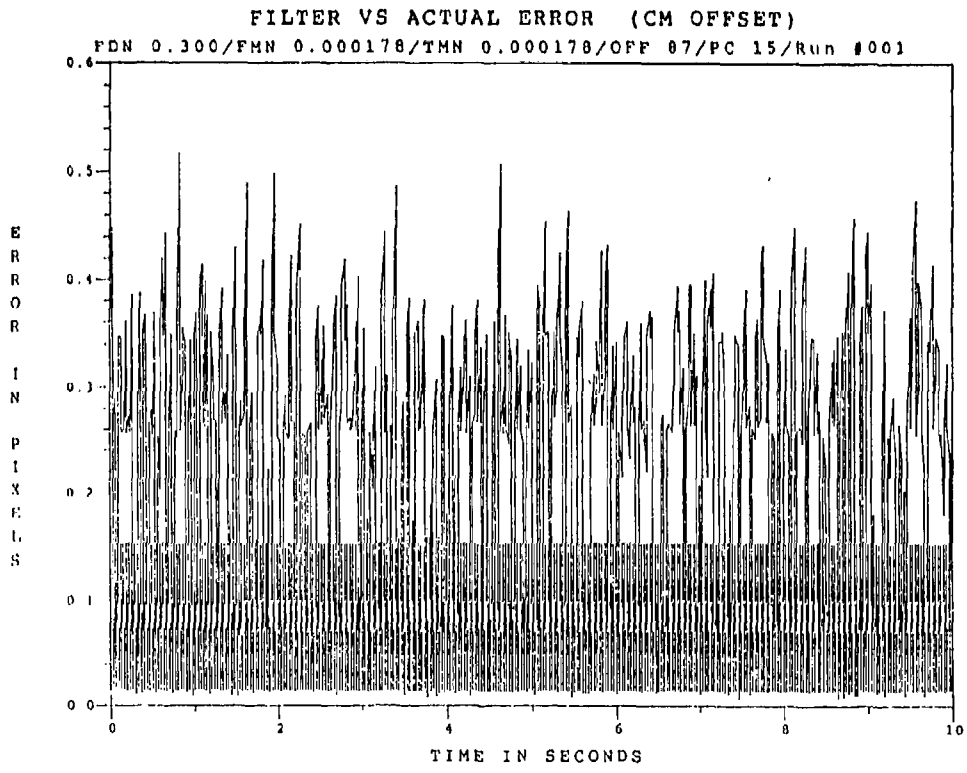


Figure 6.1 One-State Speckle Return Filter Biased Offset Error

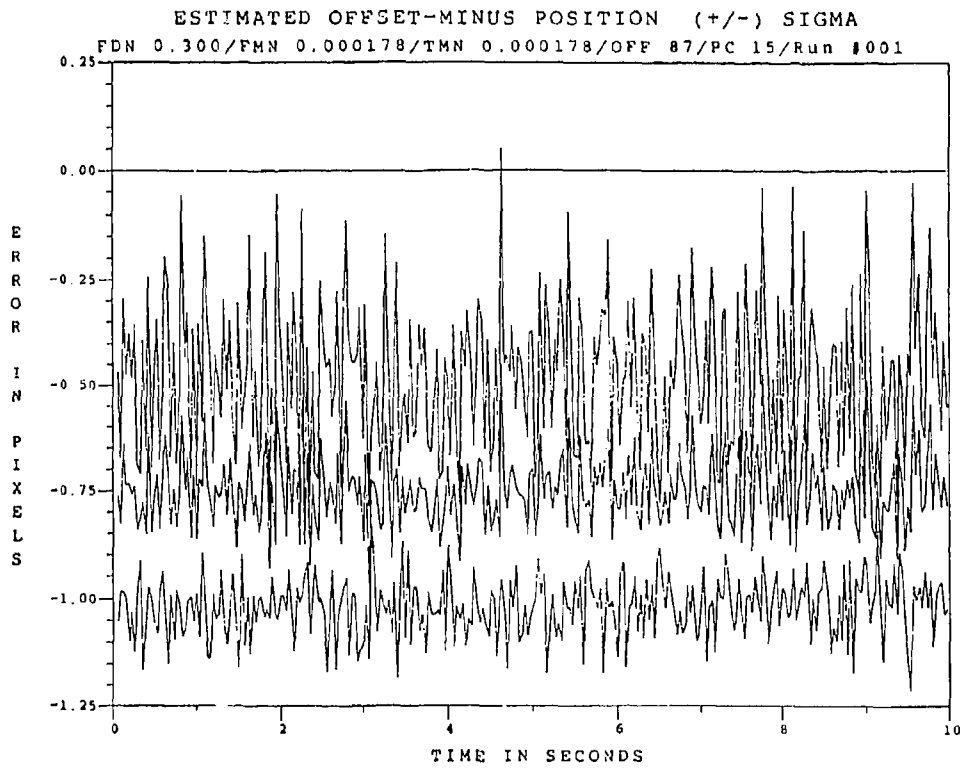


Figure 6.2 One-State Speckle Return Filter Biased Offset Error at t_i

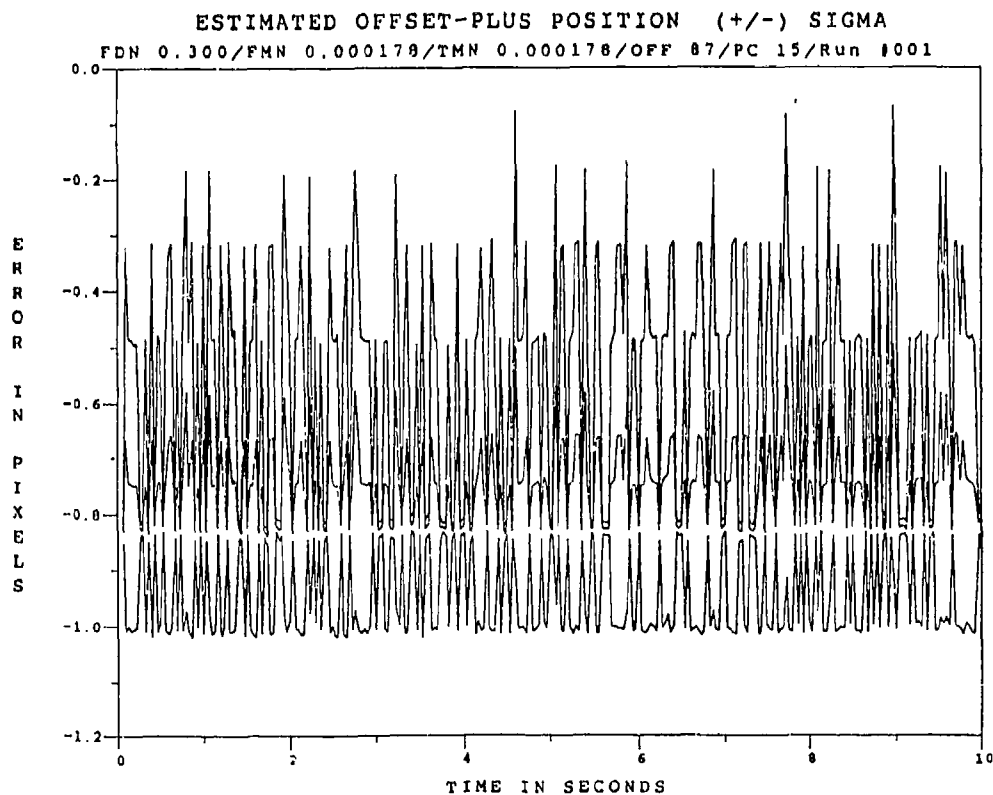


Figure 6.3. One-State Speckle Return Filter Biased Offset Error at t_i^+

measurements. The filter is analyzed with variations in three parameters that influenced the quality of the Doppler return measurements. Table 6.2 lists the three parameters and their variations that are explored. Although the dynamics model for the one-state filter is identical to what was developed by Eden [5] and Evans [6], a fundamental difference between the speckle return and Doppler return is the variance associated with the measurement noise. Referring to Section 4.3.3.4 and Equations (4-53) through (4-55), Table 6.3 lists the assorted measurement noise variances associated with given values of wavelength and SNR. In comparison with the speckle return measurement noise variance equal to $0.000178 \text{ pixels}^2$ [6], the shortest wavelength exhibits an order of magnitude decrease in the values of measurement noise, especially with the higher values of SNR. Furthermore, a *significantly* more precise measurement should be

Table 6.2 Values of Parameter Variations

λ	SNR	P_m
0.53 μm	10	0.00
1.06 μm	8	0.01
2.01 μm	6	0.02
4.00 μm	4	0.03
6.00 μm		0.04
8.00 μm		0.05
10.5 μm		0.10
		0.20
		0.30

Table 6.3 Measurement Noise Variances for Transmitted Wavelength and SNR

λ	SNR	Measurement Noise Variance, pixels ²
0.53 μm	10	0.0000091
	4	0.0000227
2.01 μm	10	0.0001308
	4	0.0003272
10.5 μm	10	0.0035700
	4	0.0089280

realizable for a SNR of 4 with a wavelength of 0.53 μm . Thus, at the shorter wavelengths, improved error statistics, as compared to the one-state speckle return filter, were expected using Doppler return measurements. However, it remained to be seen how much impact the probability-of-miss parameter would have upon the filter's estimates.

The statistical performance plots for the one-state filter are contained in Appendix C. To limit the size of the appendices, only a chosen set of plots (identified with wavelengths 0.53 μm , 2.01 μm , and 10.5 μm ; SNRs 10 and 4; and P_m of 0.0, 0.05, and 0.30) are shown to illustrate the significant statistical trends.

In general, the plots show that the filter's performance is relatively stable through all variations of parameters. The filter obviously becomes less efficient and attains higher RMS errors as λ increases or SNR decreases (which result in an increase in the measurement noise variance). However, the average of the offset errors consistently converge about zero mean; note that the mean is consistently much smaller than the standard deviation. Following the variations in P_m shows that the filter tolerates the intermittent absence of Doppler return measurements and performs well for P_m up to 0.05. Figures C.1.5, C.2.5, C.3.5, C.4.5, C.5.5, and C.6.5 show negligible differences in the offset error mean $\pm 1\sigma$ values at t_i for P_m equal to 0.05. Figures C.1.6, C.2.6, C.3.6, C.4.6 depict the offset errors mean $\pm 1\sigma$ values at t_i^* and show how the filter recovers quickly when a measurement is received. It is noted that, as P_m increases, the plots of the offset error mean $\pm 1\sigma$ at t_i^* , do exhibit less efficiency, implying a sensitivity to variations of P_m . This is illustrated by comparing Figures C.1.1, C.1.2, and C.1.3 with Figures C.1.4 through C.1.9. Note that the plots in the latter group of figures show large transients, while plots in the first group, (associated with P_m equal to zero) do not. The cause of these transients is therefore

attributed to the combination of the initial condition (set arbitrarily to 1 pixel) and the absence of measurements, averaged over the ten Monte Carlo runs.

At t_i^- , the filter's performance remains consistent, as opposed to the sensitivity of the error standard deviations at time t_i^+ to parameter variations; this indicates that the filter's propagated estimates maintain a degree of insensitivity to variations within the parameter set. This insensitivity of the standard deviation at t_i^- can be attributed to the propagation errors which dominate the performance characteristics. Table 6.4 lists a subset of the error statistics for the one-state Doppler return filter. One can examine the mean errors at t_i^- and t_i^+ and notice their erratic performance (although still centered about zero mean, i.e., of much smaller magnitude than the standard deviation) in contrast to the systematic behavior of the 1σ values at t_i^- and t_i^+ . It is apparent that the 1σ values at t_i^- are relatively stable, whereas those at t_i^+ increase with increasing λ and P_m , and decreasing SNR. To compare the one-state Doppler filter to the one-state speckle return filter of the previous thesis, Table 6.5 lists the error statistics Evans [6] achieved without including the effects of the plume's speckle reflectance. Clearly, with the shorter wavelengths, the one-state Doppler return filter achieved better values of 1σ at t_i^- throughout the SNR and P_m range as compared to the one-state speckle return filter. Furthermore, the one-state Doppler filter performance is undoubtedly superior when Table 6.4 is also compared with Table 6.1, which properly reflects the impact of the plume speckle bias on the one-state speckle filter (whereas Table 6.5 artificially does not).

Table 6.4 One-State Doppler Filter Error Statistics (in Pixels)

$\lambda, \mu\text{m}$	SNR	P_m	$\text{mean}(t_i^-)$	$\text{mean}(t_i^+)$	$1\sigma(t_i^-)$	$1\sigma(t_i^+)$
.53	10	0.0	-.30391E-4	.15079E-3	.14402E+0	.28674E-2
		.01	.13520E-3	.14715E-2	.14436E+0	.12484E-1
		.02	-.55185E-3	.16988E-2	.14479E+0	.18428E-1
		.03	-.85223E-3	.94931E-3	.14461E+0	.29420E-1
		.04	-.44544E-3	.85601E-4	.14509E+0	.36668E-1
		.05	.27581E-3	.64996E-3	.14478E+0	.39320E-1
		.10	.44882E-3	.50387E-3	.14477E+0	.70834E-1
		.20	.31482E-2	.39645E-2	.14495E+0	.11249E+0
		.30	.30750E-2	.32894E-2	.14520E+0	.12629E+0
			4	0.0	.51095E-4	.23792E-3
.01	-.68101E-4			.15506E-2	.14437E+0	.14030E-1
.02	-.48477E-3			.17917E-2	.14485E+0	.19918E-1
.03	-.78556E-3			.10110E-2	.14457E+0	.30657E-1
.04	-.58538E-3			.14446E-3	.14507E+0	.37841E-1
.05	.46723E-5			.38337E-3	.14528E+0	.43738E-1
.10	.49465E-3			.53090E-3	.14477E+0	.71501E-1
.20	.31985E-2			.40154E-2	.14501E+0	.11270E+0
.30	.31100E-2			.33113E-2	.14521E+0	.12634E+0
2.01	10			0.0	.36007E-3	.56858E-3
		.01	.18846E-3	.18493E-2	.14439E+0	.19898E-1
		.02	-.23438E-3	.21442E-2	.14510E+0	.25584E-1
		.03	-.53112E-3	.12396E-2	.14440E+0	.35400E-1
		.04	-.14913E-3	.37758E-3	.14500E+0	.42347E-1
		.05	.30485E-3	.65790E-3	.14549E+0	.47879E-1
		.10	.66959E-3	.64378E-3	.14476E+0	.74103E-1
		.20	.33901E-2	.42120E-2	.14529E+0	.11359E+0
		.30	.32428E-2	.33960E-2	.14528E+0	.12665E+0

$\lambda, \mu\text{m}$	SNR	P_m	$\text{mean}(t_i^-)$	$\text{mean}(t_i^+)$	$1\sigma(t_i^-)$	$1\sigma(t_i^+)$
	4	0.0	.66680E-3	.89720E-3	.14401E+0	.17082E-1
		.01	.44352E-3	.21331E-2	.14444E+0	.25713E-1
		.02	.17095E-4	.24826E-2	.14535E+0	.31197E-1
		.03	-.27951E-3	.14609E-2	.14426E+0	.40153E-1
		.04	.92439E-4	.60917E-3	.14495E+0	.46868E-1
		.05	.60920E-3	.93585E-3	.14569E+0	.52037E-1
		.10	.84940E-3	.77198E-3	.14478E+0	.76803E-1
		.20	.35800E-2	.44078E-2	.14560E+0	.11463E+0
		.30	.33720E-2	.34791E-2	.14543E+0	.12712E+0
10.5	10	0.0	.26115E-2	.29295E-2	.14534E+0	.53274E-1
		.01	.20358E-2	.36996E-2	.14583E+0	.59557E-1
		.02	.16022E-2	.43570E-2	.14770E+0	.63928E-1
		.03	.13037E-2	.27672E-2	.14480E+0	.68595E-1
		.04	.16703E-2	.20807E-2	.14594E+0	.74279E-1
		.05	.25731E-2	.27723E-2	.14776E+0	.77298E-1
		.10	.20497E-2	.18295E-2	.14653E+0	.95123E-1
		.20	.47999E-2	.57305E-2	.14890E+0	.12380E+0
		.30	.42102E-2	.41334E-2	.14854E+0	.13309E+0
	4	0.0	.42651E-2	.45982E-2	.14876E+0	.78044E-1
		.01	.33884E-2	.48892E-2	.14910E+0	.82539E-1
		.02	.29406E-2	.57096E-2	.15147E+0	.86402E-1
		.03	.26006E-2	.38282E-2	.14766E+0	.88773E-1
		.04	.30215E-2	.32559E-2	.14908E+0	.94020E-1
		.05	.42458E-2	.43537E-2	.15119E+0	.95596E-1
		.10	.30541E-2	.28026E-2	.15063E+0	.11036E+0
		.20	.58285E-2	.69039E-2	.15386E+0	.13345E+0
		.30	.49931E-2	.48497E-2	.15375E+0	.14073E+0

Table 6.5 One-State Speckle Return Filter Statistics Without Plume Reflectance (in Pixels) [6]

mean (t_i^-)	mean (t_i^+)	1σ (t_i^-)	1σ (t_i^+)
0.67629E-3	0.66146E-3	0.14964	0.12666E-1

6.4 Two-State Modified MAP MMAF

The algorithm for the two-state Modified MAP MMAF allows the speckle return measurements to be taken every sample period, to aid the estimation process especially whenever the hardbody-induced Doppler return becomes undetectable (Section 5.3.2). The circumstances that cause an indistinguishable hardbody-induced Doppler return are embodied in the probability-of-miss (P_m) parameter. However, there is a second category of events that requires investigation, namely, the instances where the low-energy laser return is not received (either due to bending or attenuation of the returning signal as it propagates the 2000 km range, or due to signal losses within the receiving equipment). Consequently, under these conditions, neither speckle nor Doppler return measurements are generated and the filter merely continues to propagate its most recent estimates.

To accommodate the two preceding categories, the sensitivity analysis for the two-state Modified MAP MMAF is conducted under two case conditions. Case 1 encompasses the complete loss of the low-energy laser return signal and neither measurement is provided at the specific sample time. In Case 2, the speckle return measurements are provided continuously during instances of undetectable hardbody-induced Doppler return. Appendices E and F contain the respective statistical plots for Cases 1 and 2, respectively. For a given set of parameters, the plots portray the filter's performance in estimating the offset distance state and the bias state

caused by the plume's speckle reflectance. The plots of the bias estimation errors are included simply for completeness. The discussion and comparison of filter performance focuses upon the offset estimation errors, which are of importance to this research.

6.4.1 Case 1: The Loss of Both Returns. As mentioned in Section 5.3.2, the measurements provided to the two-state Modified MAP MMAF generally consist of the hardbody-induced Doppler return and the hardbody-induced speckle return which is biased 90% of the time by the plume's speckle reflectance. This case not only considers the loss of both returns, but also provides the opportunity to observe the effectiveness of the filter's adaptiveness once the measurements resume (Section 5.3.2.2), i.e., the estimate associated with the filter which provides the "best" residual is selected as being most the most probabilistically correct for the given sample time.

The plots in Appendix E reveal those instances in which the filter produced the wrong estimate. Such is the case in Figure E.1.3, where the 1σ values at t_i^+ occasionally expand, or "spike." Evidently, the wrong choice of "best" residual was made at those times when the magnitude of the measurement noises caused the less precise hypothesis to be favored. However, it is significant to note the filter's immediate recovery once subsequent measurements are received. Referring to Figure E.1.2, the 1σ values at t_i^- (which indicate the quality of the control signals for the FLIR sensor controller) appear stable and well-behaved. Figures E.1.7 through E.1.12 illustrate the impact of invoking the probability-of-miss. Although the 1σ values at t_i^- remain relatively unchanged, the 1σ values at t_i^+ are more erratic, a behavior attributed to the combination of incorrect state estimates and the propagation of state estimates when measurements are not available. With P_m equal to 0.30, the filter's performance degrades notably, as seen in Figures

E.1.13 through E.1.18. The same pattern is noticeable for λ equal to 2.01 μm , as seen in Figures E.3.1 through E.3.18.

For the longer wavelengths, the filter's performance becomes sensitive to increases in P_m , as illustrated in Figures E.5.1 through E.6.18 with λ equal to 10.5 μm . To refer back to Table 6.3, the measurement noise variance of the 10.5 μm Doppler return is now two orders of magnitude greater than the variance for λ equal to 0.53 μm . In addition, the 10.5 μm Doppler return measurement noise variance is also greater than the speckle return measurement variance. In Figure E.5.3, note the different characteristics in the σ values. The recovery from a wrong estimate is no longer a "spike" with a quick return, but extended periods of expansion. As Figures E.6.14 and E.6.15 show, the filter's performance further degrades with an increase in P_m to a point where the filter successively generates incorrect state estimates. This behavior is brought about by the increase in measurement noise and P_m such that the correctness of the two hypothesis become less discernible in the residual characteristics.

The extent of this deterioration can be seen in Table 6.6, which lists the true offset error statistics for Case 1. Similar to the one-state Doppler filter, the true mean errors of Table 6.6 are not systematic and offer little insight into the filter's performance; they are very small compared to the standard deviation, as seen in the previous case. Nonetheless, trends can again be observed in the 1σ values at t_i^- and t_i^+ . The pattern of these values confirm that the filter performs well with the shorter wavelengths. Note that, while the values for 1σ at t_i^- remain relatively stable, the 1σ values at t_i^+ grow methodically with an increase in λ and P_m , along with a decrease in SNR. At λ equal to 10.5 μm , the filter's performance becomes unacceptable.

Table 6.6 Two-State Modified MAP MMAF Offset Error Statistics for Case 1 (in Pixels)

$\lambda, \mu\text{m}$	SNR	P_m	$\text{mean}(t_i^-)$	$\text{mean}(t_i^+)$	$1\sigma(t_i^-)$	$1\sigma(t_i^+)$
.53	10	0.0	.33822E-4	-.18678E-4	.14904E+0	.31945E-2
		.01	-.39903E-3	.32547E-3	.14932E+0	.12852E-1
		.02	-.89191E-3	.43935E-3	.14954E+0	.18845E-1
		.03	-.12107E-2	-.24677E-3	.14989E+0	.30205E-1
		.04	-.69277E-3	-.97808E-3	.14988E+0	.37895E-1
		.05	-.13571E-3	-.38331E-3	.15000E+0	.44448E-1
		.10	.27966E-3	-.35659E-3	.15038E+0	.72172E-1
		.20	.15996E-2	.20021E-2	.15063E+0	.11733E+0
		.30	.13357E-2	.16175E-2	.15053E+0	.13116E+0
	4	0.0	-.13042E-5	-.52716E-4	.14895E+0	.41866E-2
		.01	-.47029E-3	.25518E-3	.14927E+0	.13865E-1
		.02	-.94834E-3	.37101E-3	.14949E+0	.19772E-1
		.03	-.12849E-2	-.34905E-3	.14986E+0	.31022E-1
		.04	-.81988E-3	-.11022E-2	.14972E+0	.38708E-1
		.05	-.23537E-3	-.49898E-3	.14983E+0	.45154E-1
		.10	.21631E-3	-.43852E-3	.15030E+0	.72594E-1
		.20	.15713E-2	.19594E-2	.15054E+0	.11738E+0
		.30	.12517E-2	.15399E-2	.15044E+0	.13112E+0
2.01	10	0.0	-.45957E-3	-.49394E-3	.14870E+0	.12443E-1
		.01	-.12408E-2	-.23504E-2	.14747E+0	.20557E-1
		.02	-.69788E-3	-.20630E-2	.14232E+0	.26077E-1
		.03	-.10382E-2	-.89523E-3	.14823E+0	.37409E-1
		.04	-.49185E-3	-.13671E-2	.14797E+0	.45259E-1
		.05	.19771E-3	.37456E-3	.14733E+0	.49297E-1
		.10	-.17522E-2	-.12557E-2	.15180E+0	.76836E-1
		.20	.87361E-3	.87518E-3	.15014E+0	.10868E+0
		.30	.18422E-1	.18320E-1	.15178E+0	.13459E+0

$\lambda, \mu\text{m}$	SNR	P_m	$\text{mean}(t_f^-)$	$\text{mean}(t_f^+)$	$1\sigma(t_f^-)$	$1\sigma(t_f^+)$
	4	0.0	-.32932E-2	-.31397E-2	.14971E+0	.22819E-1
		.01	-.33141E-2	-.32291E-2	.15189E+0	.32314E-1
		.02	-.98558E-3	-.13796E-2	.14561E+0	.31069E-1
		.03	-.40762E-2	-.42124E-2	.15748E+0	.51092E-1
		.04	-.32898E-3	.11863E-2	.13978E+0	.46989E-1
		.05	.50116E-3	-.10566E-2	.14657E+0	.53971E-1
		.10	-.25768E-2	-.31636E-2	.14960E+0	.75933E-1
		.20	-.15304E-2	-.22255E-2	.14749E+0	.10642E+0
		.30	.19264E-2	.31013E-2	.14733E+0	.12655E+0
10.5	10	0.0	-.21071E-1	-.20738E-1	.18448E+0	.84377E-1
		.01	-.16689E-1	-.15960E-1	.17880E+0	.84557E-1
		.02	-.20723E-1	-.18649E-1	.18634E+0	.97423E-1
		.03	-.17178E-1	-.16382E-1	.17808E+0	.93890E-1
		.04	-.29128E-1	-.29388E-1	.19848E+0	.13033E+0
		.05	-.26703E-1	-.27624E-1	.19660E+0	.13089E+0
		.10	-.26909E-1	-.27012E-1	.19716E+0	.14193E+0
		.20	-.26618E-1	-.26112E-1	.20074E+0	.17841E+0
		.30	-.35108E-1	-.34632E-1	.21324E+0	.20015E+0
	4	0.0	-.23786E-1	-.23439E-1	.19198E+0	.99170E-1
		.01	-.16894E-1	-.16176E-1	.18136E+0	.92106E-1
		.02	-.21026E-1	-.18947E-1	.18884E+0	.10353E+0
		.03	-.17262E-1	-.16431E-1	.18008E+0	.99596E-1
		.04	-.32105E-1	-.32382E-1	.20460E+0	.14033E+0
		.05	-.47341E-1	-.47771E-1	.23468E+0	.18452E+0
		.10	-.28458E-1	-.28269E-1	.20094E+0	.14764E+0
		.20	-.30184E-1	-.29689E-1	.20984E+0	.18882E+0
		.30	-.35536E-1	-.35092E-1	.21675E+0	.20395E+0

6.4.2 *Case 2: Continuously Available Speckle Returns.* As mentioned earlier, the two-state Modified MAP MMAF in this case functions with the P_m parameter exclusively affecting the Doppler return (the hardbody-induced Doppler return becomes indistinguishable from that of the plume). Under these circumstances, the filter operates under the assumption that the bias caused by the plume's speckle reflectance is in the speckle return measurement (Section 5.3.2.2). Even though this is true only 90% of the time, the bias cannot be actively estimated when the Doppler measurement is unavailable (due to the inherent observability problem with only the speckle measurement). Therefore, the most recent bias value is assumed to persist in all speckle measurements until Doppler measurements return and active bias estimation can resume. As the plots in Appendix F show, the filter's performance is almost similar to Case 1. Figures F.5.1 through F.6.10 show the same pattern of extended periods of incorrect estimates as compared to Figures E.5.1 through E.5.10. However, the figures for Case 2 in Appendix F.4 begin to exhibit longer transient times before reaching a steady state. This initial behavior occurs in Case 2 since the configuration of the measurement distribution matrix is forced to include the bias state whenever the Doppler return is undetectable, thus providing more opportunities to select the wrong hypothesis (Section 5.3.2.2). However, there is some improvement in the estimates, which can be credited to the constant availability of the speckle return measurements. For instance, comparing Figure E.6.9 with F.6.9 (the results of these plots are actually not acceptable, but they clearly illustrate the improvement gained by having continuous speckle return measurements) shows that Case 2's performance does not deteriorate as much as Case 1's. Although a longer initial transient is seen for Case 2 (Figure F.6.9), one can note the smaller values of σ and the better recovery ability. This better performance is confirmed by comparing Table 6.7 to Table 6.6 and noting the improvement in the 1σ values.

Table 6.7 Two-State Modified MAP MMAF Offset Error Statistics for Case 2 (in Pixels)

$\lambda, \mu\text{m}$	SNR	P_m	$\text{mean}(t_i^-)$	$\text{mean}(t_i^+)$	$1\sigma(t_i^-)$	$1\sigma(t_i^+)$
.53	10	0.0	0.33822E-4	-0.18678E-4	0.14904E+0	0.31945E-2
		.01	-0.10650E-3	-0.25523E-3	0.14831E+0	0.53584E-2
		.02	0.27202E-3	0.11516E-3	0.14269E+0	0.79514E-2
		.03	-0.43156E-3	-0.16704E-3	0.14806E+0	0.13082E-1
		.04	-0.37338E-3	-0.14840E-3	0.14744E+0	0.15582E-1
		.05	-0.11909E-3	0.20641E-4	0.14750E+0	0.19875E-1
		.10	-0.11103E-2	-0.11407E-2	0.15249E+0	0.34393E-1
		.20	0.56603E-4	0.27481E-3	0.14906E+0	0.52569E-1
		.30	-0.44194E-3	-0.32322E-3	0.14890E+0	0.72982E-1
	4	0.0	-0.42414E-3	-0.33754E-3	0.14842E+0	0.56773E-2
		.01	-0.91824E-3	-0.57512E-3	0.14887E+0	0.82736E-2
		.02	0.43942E-3	0.38938E-3	0.14511E+0	0.10417E-1
		.03	-0.12666E-2	-0.12221E-2	0.15557E+0	0.17398E-1
		.04	0.41729E-3	0.92052E-3	0.13861E+0	0.16539E-1
		.05	0.58756E-4	0.18977E-3	0.14590E+0	0.21870E-1
		.10	-0.21232E-2	-0.17971E-2	0.14866E+0	0.34161E-1
		.20	-0.26346E-2	-0.26733E-2	0.14541E+0	0.52123E-1
		.30	-0.13965E-2	-0.12422E-2	0.14380E+0	0.73377E-1
2.01	10	0.0	-0.45957E-3	-0.49394E-3	0.14870E+0	0.12443E-1
		.01	-0.86927E-3	-0.10156E-2	0.14819E+0	0.15144E-1
		.02	-0.10440E-2	-0.12024E-2	0.14232E+0	0.17888E-1
		.03	-0.18569E-2	-0.16089E-2	0.14759E+0	0.22171E-1
		.04	-0.12858E-2	-0.10667E-2	0.14644E+0	0.23761E-1
		.05	-0.47967E-3	-0.34617E-3	0.14755E+0	0.26227E-1
		.10	-0.30232E-2	-0.30411E-2	0.15131E+0	0.41426E-1
		.20	-0.11163E-2	-0.89814E-3	0.14899E+0	0.57322E-1
		.30	-0.21351E-2	-0.20301E-2	0.14803E+0	0.75903E-1

$\lambda, \mu\text{m}$	SNR	P_m	mean(t_i^-)	mean(t_i^+)	$1\sigma(t_i^-)$	$1\sigma(t_i^+)$
	4	0.0	-0.23257E-2	-0.22422E-2	0.15023E+0	0.22428E-1
		.01	-0.20302E-2	-0.16982E-2	0.15005E+0	0.21492E-1
		.02	-0.10081E-2	-0.10582E-2	0.14491E+0	0.23964E-1
		.03	-0.42251E-2	-0.41811E-2	0.15707E+0	0.33630E-1
		.04	-0.61153E-3	-0.11602E-3	0.13876E+0	0.27786E-1
		.05	-0.40743E-3	-0.28042E-3	0.14638E+0	0.31682E-1
		.10	-0.33908E-2	-0.31044E-2	0.14984E+0	0.43704E-1
		.20	-0.56010E-2	-0.58369E-2	0.14825E+0	0.62616E-1
		.30	-0.43593E-2	-0.41875E-2	0.14626E+0	0.79954E-1
10.5	10	0.0	-0.21071E-1	-0.20738E-1	0.18448E+0	0.84377E-1
		.01	-0.13267E-1	-0.13409E-1	0.17218E+0	0.70387E-1
		.02	-0.19407E-1	-0.19548E-1	0.17415E+0	0.83323E-1
		.03	-0.18826E-1	-0.18930E-1	0.17470E+0	0.79366E-1
		.04	-0.63974E-2	-0.62002E-2	0.15939E+0	0.57878E-1
		.05	-0.74758E-2	-0.73681E-2	0.16349E+0	0.62397E-1
		.10	-0.12305E-1	-0.12303E-1	0.16461E+0	0.76550E-1
		.20	-0.20081E-1	-0.20217E-1	0.17927E+0	0.10990E+0
		.30	-0.40824E-1	-0.40763E-1	0.21284E+0	0.16459E+0
	4	0.0	-0.23344E-1	-0.23223E-1	0.19079E+0	0.10238E+0
		.01	-0.18769E-1	-0.18477E-1	0.18358E+0	0.90538E-1
		.02	-0.16465E-1	-0.16187E-1	0.17719E+0	0.87058E-1
		.03	-0.27113E-1	-0.27153E-1	0.19645E+0	0.10856E+0
		.04	-0.28952E-1	-0.28138E-1	0.19392E+0	0.12448E+0
		.05	-0.67151E-4	0.35709E-5	0.15185E+0	0.54615E-1
		.10	-0.33658E-1	-0.33433E-1	0.20460E+0	0.13460E+0
		.20	-0.32079E-1	-0.32443E-1	0.19449E+0	0.13145E+0
		.30	-0.28231E-1	-0.27757E-1	0.18730E+0	0.13638E+0

6.5 Comparison of the One-state Filter and the Two-State Modified MAP MMAF

This section compiles and compares the performance results of the one-state Doppler filter, and Cases 1 and 2 of the two-state Modified MAP MMAF. The compiled results, contained in Appendix G, are plotted to show the sensitivity of the filters to variations in the parameters of wavelength, signal-to-noise ratio, and probability-of-miss at t_i^- and t_i^+ . Appendix G is divided into two subappendices: Appendix G.1 contains graphs that present a set of parametric curves that give RMS errors (in units of pixels) as functions of wavelength for various SNR's and for a given value of P_m , and Appendix G.2 contains graphs that show a set of parametric curves that give RMS errors as functions of wavelength, for various values of P_m and for a given value of SNR. Each figure has three graphs, arranged to present the performances of the one-state Doppler filter, and the two cases of the two-state Modified MAP MMAF, concurrently. Additionally, for each subappendix, the results at t_i^+ are presented first, followed by the results at t_i^- , to illustrate the pattern of errors that result from state estimate propagation. One should be aware of the change of scale of the RMS errors axis when transitioning from t_i^+ to t_i^- .

In Appendix G.1, one notes the general increase in RMS errors as P_m increases and/or SNR decreases at both t_i^+ and t_i^- . At t_i^+ , the parametric curves of the one-state Doppler filter appear constant, and as Figures G.1.1 through G.1.6 show, the slope of the curves decreases as P_m increases. The parametric curves for Case 1 and 2 of the two-state Modified MAP MMAF are not as structured and stray at the longer wavelengths. This irregular behavior suggests that more than ten Monte Carlo runs should be performed to smooth the data in order to reveal the patterns more adequately. In Case 1, the curves at shorter wavelengths (less than 2.01 μm) do possess some readable patterns. As P_m increases, the slope of the curves begin to decrease, and as Figures

G.1.4(b) through G.1.6(b) illustrate, the curves reacquire an increase in slope, causing a "basin" phenomenon to develop for a range of wavelengths less than $2.01 \mu\text{m}$, at P_m greater than or equal to 0.10. The occurrence of the "basin" within a region of wavelengths implies a balance between the propagation of the state estimates and the contribution of noise-corrupted speckle return measurements. With lesser values of P_m , the filter receives both Doppler and speckle return measurements more frequently. As P_m increases, an equilibrium point, within a range of wavelengths, is reached where merely propagating the state estimates is more advantageous to the filter, instead of receiving a measurement. This rationale is supported by recalling the small values of dynamics noise variance that resulted from tuning the two-state Modified MAP MMAF (Section 5.3.3.6) is now the dominant driver of the propagation errors. Also, an examination of Tables 6.4 and 6.6 shows that the inclusion of the speckle return in the measurements, along with the concurrent absence of both returns, increases the error standard deviations as compared to using Doppler measurements alone. Thus, in a region of wavelengths less than $2.01 \mu\text{m}$, the absence of measurements (corresponding to an increase in P_m) is an advantage, where it is more beneficial for the filter to rely instead on using its dynamics model to propagate the most recent state estimates. However, note that even though the "basin" occurs, the RMS errors remain larger than Case 2's.

In Figures G.1.1 through G.1.6, a comparison at the shorter wavelength region of Case 2 with Case 1 reveals a slower growth rate of RMS errors. Although the curves do not exhibit the decreasing slope or "basin" phenomenon, the RMS errors remain less than those of both Case 1 and the one-state Doppler filter. This exceptional performance can be substantiated by realizing that, unlike Case 1, the offset state estimates are continually updated by virtue of the unhindered speckle return measurements. Thus, the propagation errors do not grow as large as in Case 1, and

the improved performance of Case 2 over Case 1 shows that the filter obviously functions better with one measurement, corrupted as it may be, rather than no measurement. Based on these results, using continuous speckle return measurements can indeed compensate for the loss of the hardbody-induced Doppler return.

At t_i^- (note the change in scale compared to the case of t_i^+), the one-state Doppler filter's errors are relatively constant at the shorter wavelengths. Curves at the longer wavelengths display a tendency to spread, although the differences in errors are minuscule. In contrast, the curves of Case 1 and 2 begin to spread at wavelengths beyond 2.01 μm . Furthermore, the same "basin" pattern of Case 1 is seen in Figures G.1.8(b) through G.1.12(b). Generally, the one-measurement filter achieves the best results at t_i^- , with Case 2 of the two-measurement filter configuration slightly outperforming Case 1.

The graphs of Appendix G.2 show parametric curves that give RMS errors as functions of wavelength, for a number of values of P_m and for a given value of SNR. For the one-state Doppler filter at t_i^+ , it is evident that decreasing SNR has little effect, as compared to increasing P_m . Although the plots for Cases 1 and 2 also suggest a need for more Monte Carlo runs (as seen previously), one can also observe an insensitivity to SNR. Figures G.2.1(b) and (c) through G.2.4(b) and (c), illustrate that, at the shorter wavelengths, for SNR equal to 10, 8, 6, and 4, the RMS errors are relatively unchanged.

At t_i^- , similar insensitivity to decreases in SNR is apparent in the one-state Doppler filter, and for the shorter wavelengths of Cases 1 and 2. For a given SNR, the parametric curves of the one-state Doppler filter are nearly horizontal and concentrated at the shorter wavelengths. As the SNR decreases, the curves become slightly less dense as the wavelengths increase, which signifies

less precise measurements due to the increase in measurement noise variance. However, the relative flatness of the curves is attributed to two factors. First, as seen in Equation (4-61), the measurement noise variance is inversely proportional to the square root of the SNR value. Hence, a decrease in SNR within the given range of values invokes small increases in measurement noise variance. Second, the propagated state estimates remain accurate whenever a measurement is missing due to the elementary form and adequacy of the one-measurement filter's dynamics model. This type of insight is not as obvious in Case 1 or 2, although the divergence of the curves does imply less precise measurements, particularly when the Doppler return measurement noise variance approaches and exceeds that of the speckle return. The divergence is further compounded by the occasional wrong estimates of the two-state Modified MAP MMAF due to choice of the wrong hypothesis in the adaptive decision process. However, in the region of shorter wavelengths, Case 2 consistently displays better performance than Case 1, proving the benefit of continuously available speckle returns.

6.6 Summary

This chapter presented the results and findings of this thesis. The performance of the one-state speckle return filter was shown to exhibit the effects of the plume's speckle reflectance. As anticipated, the offset estimates were biased by a corresponding amount of plume speckle return. Graphical and tabular results of a sensitivity analysis conducted on the one-state Doppler filter and two-state Modified MAP MMAF were presented and discussed. The results were compiled and incorporated into two graphical sets of parametric curves which were utilized to compare the performances of the Doppler filters. In general, each filter's performance at t_i^+ showed a sensitivity to changes in P_m and SNR, whereas the performance at t_i^- was consistent, revealing

a degree of tolerance to the parameter variations at t_i . Although this tolerance is largely due to the propagation errors that dominate the performance characteristics, the consistent behavior at t_i signifies that the propagated control signals to the FLIR sensor controller will also be dependable. Overall, the center-of-mass filters all exhibited less sensitivity to variations in SNR values than in P_m values. In the shorter wavelengths, the two-state Modified MAP MMAF, Case 2, outperformed both Case 1 and the one-state Doppler filter. Its superior performance results from the constant update of the offset state, thus decreasing the propagation errors. The performance not only attests to the advantage of using all available measurement sources, but also confirms that the continuous speckle return is a viable backup during the loss of Doppler returns.

VII. Conclusions and Recommendations

7.1 Introduction

This chapter presents the conclusions based upon the results in Chapter 6 and suggests topics for further research. This thesis has been a feasibility study of employing Doppler for a finer discernment of a target missile plume/hardbody interface than is possible from the speckle return from a low-power laser. Presented in Section 7.2 are the conclusions derived from the sensitivity analysis conducted on the one-state Doppler filter and the two-state modified MAP MMAF. Section 7.3 covers the recommendations that arise from this study.

7.2 Conclusions

The results show the viability of utilizing Doppler return measurements with a linear Kalman filter in the estimation of the location of the missile hardbody center-of-mass. A key consideration in making the Doppler phenomenon workable in the tracking scenario is the distinct contrast between the plume and hardbody-induced Doppler spectra. Based on these differences, a model which represents offset measurements derived from the hardbody-induced Doppler return was developed. For the model, no attempt was made to simulate the actual Doppler phenomenon. Rather, the approach was based upon simulating the quality of the low-energy laser return as a function of wavelength and signal-to-noise ratio, and simulating a specified probability of no Doppler information at a given sample time due to either the plume and hardbody spectra being nondistinguishable or the low-power laser beam being distorted as to miss the intended aimpoint on the target body.

This study, in conjunction with the two previous theses [5,6], regards the location of the hardbody center-of-mass as an offset distance relative to the target plume intensity centroid on the FLIR image plane. A low-energy laser is aimed at the FLIR filter's positional estimates of the intensity centroid, and then scanned along the target's estimated velocity vector. The success of locating the hardbody is therefore dependent upon the accuracy of the FLIR filter's estimates. However, an "apparent" jitter of the intensity centroid on the FLIR image plane due to atmospheric distortions presents a major obstacle for the laser scan to intercept the hardbody and, as a result, motivated the development of a laser sweep routine [6] .

The performances of the one-state Doppler filter and the two-state Modified MAP MMAF are judged on the basis of the respective mean $\pm 1\sigma$ error plots at t_i^- and at t_i^+ (just before and just after update, respectively) shown in Appendices C (one-state Doppler filter), E (two-state: Case 1) and F (two-state: Case 2). In addition to the error plots, the actual RMS errors at t_i^- and t_i^+ , in units of pixels, are also calculated and are utilized to compare the respective performances (Appendix G). The error analysis of Chapter VI noted from tabular data that the magnitude of the true mean errors are substantially smaller than the 1σ values and are thus insignificant in the calculation of the actual RMS errors. The analysis, therefore, focused upon the quality of the standard deviations (1σ) at t_i^- as a measure of the stability and performance of the center-of-mass filters. The usefulness of this criterion is strengthened by recognizing that the estimates propagated over a sample period are used to drive the FLIR sensor pointing controller, and therefore the propagated values of standard deviations are crucial for maintaining track on the center-of-mass in order to ensure that a high-energy laser is continuously directed at the hardbody for a finite length of time. Presented below are the conclusions regarding the individual

performances of the one-state Doppler filter and the two-state Modified MAP MMAF, and the comparison of their effectiveness during the sensitivity analysis.

7.2.1 One-State Filter with Doppler Return Measurements. The one-state Doppler filter's performance was stable throughout the sensitivity analysis. The filter was tolerant to changes in wavelength of the low-power laser and SNR of the return signal, and it demonstrated an insensitivity to the intermittent absences of measurements. Under the worst conditions ($\lambda = 10.5\mu\text{m}$, $\text{SNR} = 4$, $P_m = 0.30$), the one-state filter obtained a 1σ value at t_i^- of 0.154 pixel (from Table 6.4), or a 6.8% increase of the 1σ value under the best conditions. This increase corresponds to a 0.291 meter difference between the two 1σ values. The insensitivity of the $\hat{x}(t_i)$ values is due to dominant effects of atmospheric jitter upon the propagation errors; much higher sensitivity is seen in the $\hat{x}(t_i^+)$ values.

The parametric curves of the one-state Doppler filter in Appendix G achieved nearly constant RMS errors throughout the sensitivity analysis. The best performance is observed at the shorter wavelengths, attributable to the smaller measurement noise variances associated with this range. The curves indicate that the one-state filter is more sensitive to changes in P_m than in SNR. This observation can be substantiated by noting in Equations (4-53) through (4-55) that the measurement noise variance associated with the Doppler measurement is inversely proportional to the square root of the SNR. Thus, changes in SNR within the given range of values invoke small changes in measurement quality, whereas the absence of measurements forces the filter to propagate the most recent estimates without the benefit of a current update. Moreover, the measurements may be absent over sequential sample times, and the quality of the propagated estimates is then reliant upon the adequacy of the propagation model.

7.2.2 *Two-State Modified MAP MMAF.* The two-state Modified MAP MMAF was proposed so as to take advantage of both speckle return and Doppler return measurements. The sensitivity analysis was performed on two case conditions that respectively take into account the absence of both returns or the exclusive absence of the Doppler return. In Case 1, both speckle and Doppler return measurements are missing due to events that include attenuation of the return signal as it propagates the 2000 km range, bending of the low-power laser beam such that no intercept with the hardbody is accomplished, and signal losses within the receiving equipment. Under these circumstances, the two-measurement filter merely propagates its most recent estimates. Case 2 encompasses those instances where the target's aspect angle approaches an orientation orthogonal to the LOS vector. When this occurs, the radial velocity of the plume and hardbody become nil, resulting in no Doppler shift. Consequently, the return spectra of the plume and hardbody converge and overlap each other, which makes the hardbody-induced Doppler return difficult, if not impossible, to detect. However, the availability of the speckle return measurement is not affected by the target aspect angle and, under in this situation, continues to be provided to the two-measurement filter.

It should be mentioned that the irregular nature of the RMS errors for the longer wavelengths (as seen in Appendix G) suggest the need for more Monte Carlo runs in order to pinpoint the statistics adequately in that region. Thus, conclusions about the two-state Modified MAP MMAF's performance are confined and limited to the shorter wavelengths.

7.2.2.1 *Case 1: The Loss of Both Returns.* In Appendix E, the plots corresponding to probability-of-miss P_m equal to 0.0 show that the algorithm performs well in capturing the random nature of the plume's speckle reflectance by choosing between the two hypotheses about speckle

return: plume speckle bias present or absent in the measurements. There were instances, however, where the algorithm provided the wrong estimates, generated by the filter based on the wrong hypothesis, due to the nature of individual samples of the measurement noises. Nevertheless, the filter recovered quickly and the effect of the erroneous estimates was negligible. The parametric curves were observed to develop a "basin" phenomenon at P_m greater than or equal to 0.10. The occurrence of the "basin" within a region of wavelengths implies a balance between the absence of measurements and the contribution of noise-corrupted speckle return measurements. Otherwise stated, with lesser values of P_m , the filter received both speckle and Doppler measurements at a higher rate. Tables 6.4 and 6.6 evince that including the speckle return increased the 1σ values over the results of using only Doppler return measurements. With higher values of P_m , the filter benefits from the absence of corrupted measurements, relying instead on its internal dynamics model to propagate the most recent estimates. The tabular data of Table 6.6 show that acceptable values of 1σ at t_i are achieved at the shorter wavelengths. As with the one-state filter, the graphs in Appendix G indicate the filter is more sensitive to changes in P_m than to changes in SNR.

7.2.2.2 Case 2: Continuous Speckle Returns. As discussed in Section 5.3.2, during the temporary loss of Doppler return measurements, the measurement matrix is configured to accept speckle return under the assumption the plume speckle bias is present in the measurement. This assumption is necessary since, without the Doppler return, the bias state is unobservable. Furthermore, this assumption is supported by recalling that the bias appears 90% of the time. As a result, until Doppler return measurements resume, the most recent bias state estimate is retained.

The two-state Modified MAP MMAF disclosed a better performance under Case 2 conditions. The effect of utilizing the speckle return measurements to compensate for undetectable

hardbody-induced Doppler returns is clearly beneficial, as evidenced by the data in Table 6.7 and the parametric curves of Appendix G displaying lesser RMS errors than Case 1. The parametric curves also show that the filter is tolerant of changes in SNR and, compared to the one-state Doppler filter and Case 1, is the least sensitive to fluctuations in P_m at t_i .

7.2.3 Filter Comparison. In the region of the shorter wavelengths, each filter performed well, due to the corresponding small measurement noise variance. In general, the filters exhibited more sensitivity to fluctuations in P_m than in SNR. The one-state Doppler filter has the advantage of receiving more precise measurements of only the offset distance (versus speckle measurements that are less precise and are biased 90% of the time) and, as evidenced by the nearly constant RMS errors, displayed a favorable degree of tolerance throughout the sensitivity analysis. The one disadvantage of the one-state Doppler filter is the total dependence on the Doppler return, which raises reliability concerns.

Although the specific analysis is lacking for the larger wavelengths, Case 2 of the two-state Modified MAP MMAF identified a region of wavelengths where its performance is superior to that of the one-state Doppler filter. Additionally, Case 2 has the advantage of being a dual-return measurement system, which increases its level of reliability. Furthermore, the provision of both speckle and Doppler return would enhance the filter's performance if the target missile utilizes a liquid propellant rather than a solid propellant and thus displays no significant plume reflectance. This study, in spite of its limitations, advocates the two-state Modified MAP MMAF and use of shorter wavelength low-power laser to generate the measurements, as well as further exploration on the operability of such a filter with the larger wavelengths.

7.3 Recommendations

The following are suggested topics for further study in using a linear Kalman filter to track a missile hardbody using FLIR data and Doppler and/or speckle return measurements. Some of the recommendations correspond to secondary objectives of this research which were not pursued due to time constraints. Other recommendations are made to enhance the modeling of the Doppler return and strengthen the analysis at the longer wavelengths.

7.3.1 Increased Number of Monte Carlo Runs. With the two-state Modified MAP MMAF, the irregularity of the RMS errors at the longer wavelengths suggests a need for an increased number of Monte Carlo runs. The two-state Modified MAP MMAF displayed the potential to provide equal, if not better, performance compared to that of the one-state Doppler filter in a limited range of wavelengths. Future research into the operability of the two-state Modified MAP MMAF over longer wavelengths necessitates this recommendation.

7.3.2 Plume/Hardbody Interface Doppler Return. The issue of whether the Doppler phenomenon is feasible for tracking the missile hardbody was addressed on the basis of the measurement quality for a low-energy laser reflection. Specifically, a relationship that gives RMS angle tracking errors as a function of wavelength and signal-to-noise ratio [16] was invoked to model noise-corrupted Doppler return measurements. Although documentation regarding the Doppler return characteristics of the plume is available, experimental data on the Doppler return of the plume/hardbody interface would be more valuable for modeling purposes. The data should reflect the effect upon the Doppler return as the laser beam traverses from the plume to the hardbody. This would furnish a measure of how well the interface can be discerned and this information can be coupled with the RMS angle tracking errors to develop a more realistic

measurement model. Note that the "probability-of-miss" simulated here addresses the inability to discern the difference between hardbody and plume returns under certain circumstances, but only doing so probabilistically.

7.3.3 Consolidation of Cases 1 and 2 of the Two-State Modified MAP MMAF. Since the sensitivity analyses for Cases 1 and 2 were conducted separately, the data generated can be used in a conservative sense. Should there be a need to note the performance of the two-state Modified MAP MMAF under Case 1 conditions for a P_m of 0.10 and simultaneously under Case 2 conditions for a P_m of 0.03, the reasonable approach would be to consider the performance as ranging between the results for the two cases. However, the tracking scenario may not afford the luxury of such conservativeness and may require more definite results. If so, then further research in this area should develop a model that consolidates both cases.

7.3.4 Alternative Low-Energy Scan Techniques. As with the previous thesis [6], this topic remains to be investigated. The low-energy laser sweep is one possible method to ensure that a measurement is available to the filter at each update. Although the sweep is not preferred, it does compensate for the "apparent" jitter of the intensity centroid on the FLIR image plane. Unless the FLIR filter positional estimates improve, alternate means of propagating the laser scan which are computationally more efficient than the sweep are required. Several techniques that may be explored include sinusoidal scans and circular scans along the FLIR filter estimated velocity vector.

7.3.5 Oscillation of the Plume's Speckle Reflectance. As mentioned in Section 4.3.2.2, the plume's speckle reflectance was observed to exhibit low-frequency oscillations about its longitudinal axis. This observed oscillation will have an impact on the offset distance estimates

that are realizable from the speckle return measurements. The wavering action may be simulated by a model similar to the pogo phenomenon model [35], with its own nominal amplitude and frequency values. Since the observation is germane to the two-state Modified MAP MMAF, it should be included in future studies.

7.3.6 Plume/Hardbody Interface Speckle Return. From the previous thesis [6], the measurement noise variance associated with the speckle return was determined by setting the standard deviation to 1.0% of the length of the hardbody and converting to variance in pixels² by squaring. Based upon the uncertainties of the plume's speckle reflectance, a decision was made to retain that particular value of variance for this thesis. However, future studies should incorporate relationships that give measurement noise variance as a function of wavelength and SNR similar to the Doppler return measurement noise variance. Additionally, in a manner parallel to Section 7.3.2, knowledge of the effect of the speckle return as the low-energy laser migrates over the plume/hardbody interface would enhance the speckle measurement model. Moreover, with the presence of the plume's speckle reflectance, data regarding the speckle return as it traverses from the plume to the hardbody may provide more modeling insight.

7.3.7 Bayesian Approach to the Plume Speckle Reflectance and MMAF. In this study, the speckle reflectance emanating from the plume of a solid-propellant rocket motor is set to a nominal value of 25 meters. Although sufficient for a first-cut model, the plume speckle reflectance model can be enhanced further by modeling the length of the bias as Gaussian distributed values that range from 0 to 30 meters. Moreover, a bias equal to 0 meters would represent instances of no plume speckle reflectance and would therefore reflect the bias's non-appearance percentage during boost time.

Similarly, the estimation process of the two-state MMAF may be performed in a Bayesian, rather than MAP, manner. As noted in the analysis of Chap VI and the performance plots in Appendices E and F, the two-state Modified MAP MMAF occasionally produced the wrong state estimate. When the parameters of wavelength, SNR, and P_m were varied, the instances of incorrect estimates became more frequent and successive. This is a dominant factor in the increase of the time-averaged error standard deviations. With a Bayesian MMAF, the state estimate would be a "blended", probabilistically weighed summed estimate. The instances of incorrect estimates may diminish and thus reduce the error standard deviations.

Appendix A

Data Processing Statistics Method

The performance of the Kalman filters used in this thesis is evaluated using ten Monte Carlo runs. A Monte Carlo analysis involves collecting statistical information generated from simulating samples of stochastic processes [17]. Although ten Monte Carlo runs are generally sufficient to converge to the actual statistics that would result from an infinite number of runs [6,20], the analysis of the two-state Modified MAP MMAF's performance showed a need for more than ten runs.

For the simulation, the truth model creates an environment to provide a realistic target plume representation as it propagates through inertial space. The FLIR filter attempts to track the target plume using its internal dynamics model and periodic measurements from the enhanced correlator algorithm. The truth model also simulates the location of the hardbody center-of-mass as an *a priori* offset distance from the plume's intensity centroid on the FLIR image plane. The center-of-mass filters estimate the offset distance upon acquiring low-energy laser return measurements.

After collecting N samples of truth model and filter model data for ten separate Monte Carlo runs, the true error statistics can be approximated by computing the sample mean error and error variance for the ten runs. The sample mean error and error variance are computed by:

$$\bar{E}(t_i) = \frac{1}{N} \sum_{n=1}^N [x_{truth_n}(t_i) - \hat{x}_{filter_n}(t_i)] \quad (A.1)$$

$$\sigma^2(t_i) = \frac{1}{N-1} \sum_{n=1}^N [x_{truth_n}(t_i) - \hat{x}_{filter_n}(t_i)]^2 - \frac{N}{N-1} \bar{E}^2(t_i) \quad (A.2)$$

where

- $\bar{E}(t_i)$ = sample mean of the error of interest at time t_i
- $\sigma^2(t_i)$ = sample error variance at time t_i
- $x_{truth_n}(t_i)$ = truth model value of the variable of interest at time t_i during simulation n

$\hat{x}_{filter,n}(t_i)$ = filter estimate of the variable of interest at time t_i during simulation n

N = number of Monte Carlo runs

The variable of interest for this study is the offset distance along the estimated velocity of the intensity centroid on the FLIR image plane. The performance evaluation of the center-of-mass filters and the conclusions drawn from the sensitivity analysis are based upon the error statistics of the offset distance estimates. The statistics are calculated before the measurement update at (t_i^-) and after the update at (t_i^+) . They are reduced further to obtain average scalar values over the time of the run, by temporally averaging the mean error and standard deviation (σ) time histories over the last eight seconds of the ten second simulation. The first two seconds are not used to ensure that the data reflects only steady state performance [6]. The errors are measured in units of pixels, where a pixel is 15 μ rad on a side (approximately 30 meters at a distance of 2,000 km).

Appendix B

Examples of Performance Plots

Two different types of data plots are presented in Appendices C through F to assess the performance of the center-of-mass filters employed in this thesis. The first type of plot, shown in Figure B.1, provides filter tuning information by illustrating the relationship between the actual RMS errors in the estimates of the variables of interest, committed by the filter, with the filter-computed RMS errors, i.e., the filter's own representation of its errors. The second type of plot, shown in Figure B.2, provides a measure of the tracking performance. The plot shows the sample mean filter error, averaged over the ten Monte Carlo runs, for a state or variable of interest. In addition, this type of plot displays the 1σ (standard deviation) through the mean $\pm 1\sigma$ curves that surround the mean curves, either just before a measurement is generated at t_i^- , or after a measurement is generated at t_i^+ . The offset values at t_i^- are used as control signals for the FLIR sensor controller in between measurements and are crucial for tracking the hardbody effectively. Furthermore, the quality of the 1σ values at t_i^- provides the basis for the analysis and performance evaluation of the center-of-mass filters.

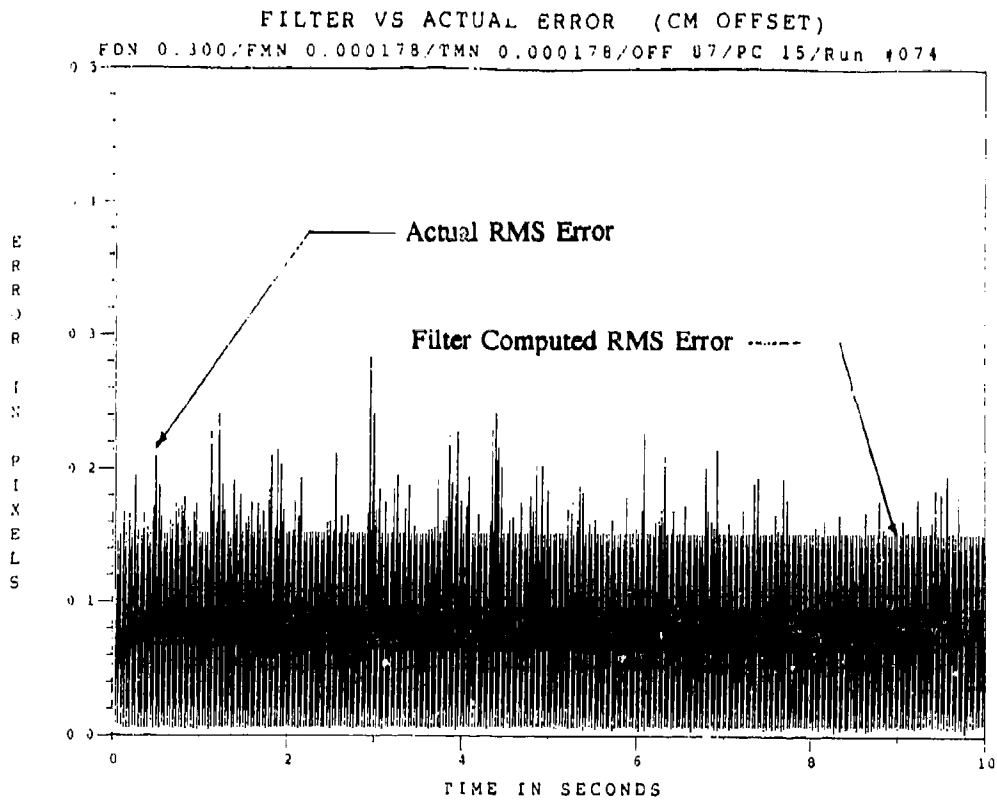


Figure B.1 Example of Time History Plot of Filter vs. Actual errors

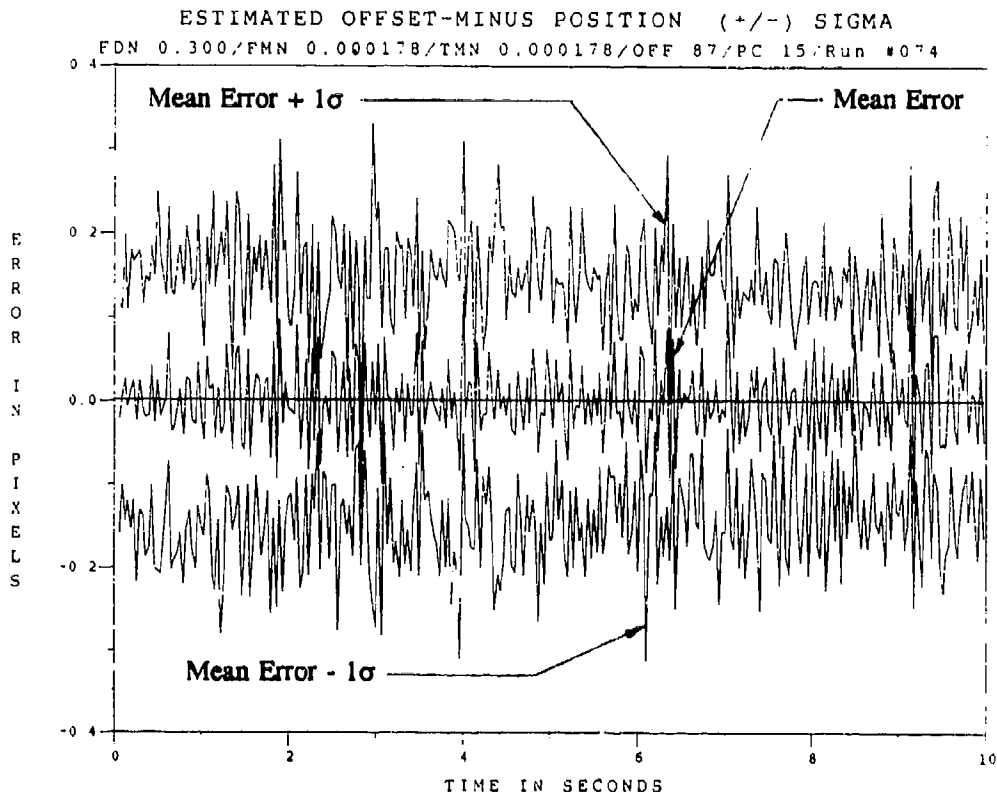


Figure B.2 Example Time History Plot of Filter Error Statistics (Mean $\pm 1\sigma$)

Appendix C

One-State Center-of-Mass Filter

with

Doppler Return Measurements

This appendix contains the true offset error plots for the one-state center-of-mass filter that receives measurements derived from low-energy laser Doppler measurements. The plots show the errors, in units of pixels, between the filter's estimated and true offset distance in the FLIR image plane. The plots represent a sample of the sensitivity analysis that was conducted with wavelength, signal-to-noise ratio, and probability-of-miss parameters. This appendix is divided into the following sub-appendices:

<u>Sub-Appendix</u>	<u>Category</u>
C.1	0.53 μm Wavelength, SNR = 10
C.2	0.53 μm Wavelength, SNR = 4
C.3	2.01 μm Wavelength, SNR = 10
C.4	2.01 μm Wavelength, SNR = 4
C.5	10.5 μm Wavelength, SNR = 10
C.6	10.5 μm Wavelength, SNR = 4

Each sub-appendix contains three sets of three plots, for a total of nine plots. Each set corresponds to a particular value of P_m equal to 0.0, 0.05, and 0.30, respectively. The three types of plots for each value of P_m show: 1) the filter-computed versus true RMS errors, 2) true mean error ± 1 sigma at t_i^- , and 3) true mean error ± 1 sigma at t_i^+ . An explanation of the plot symbology can be found in Appendix B.

Appendix C.1

One-State Center-of-Mass Filter

with

0.53 μm Doppler Return Measurements

at SNR = 10

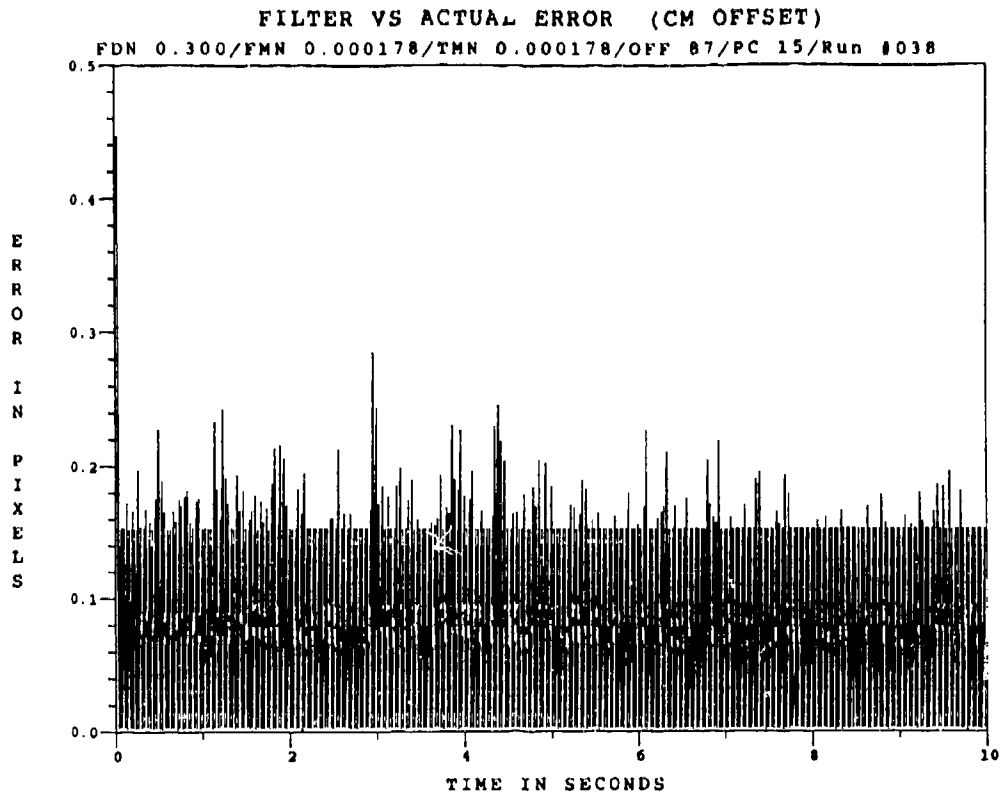


Figure C.1.1 0.53 μm Doppler Return One-State Filter Offset Error, SNR = 10, $P_m = 0.0$

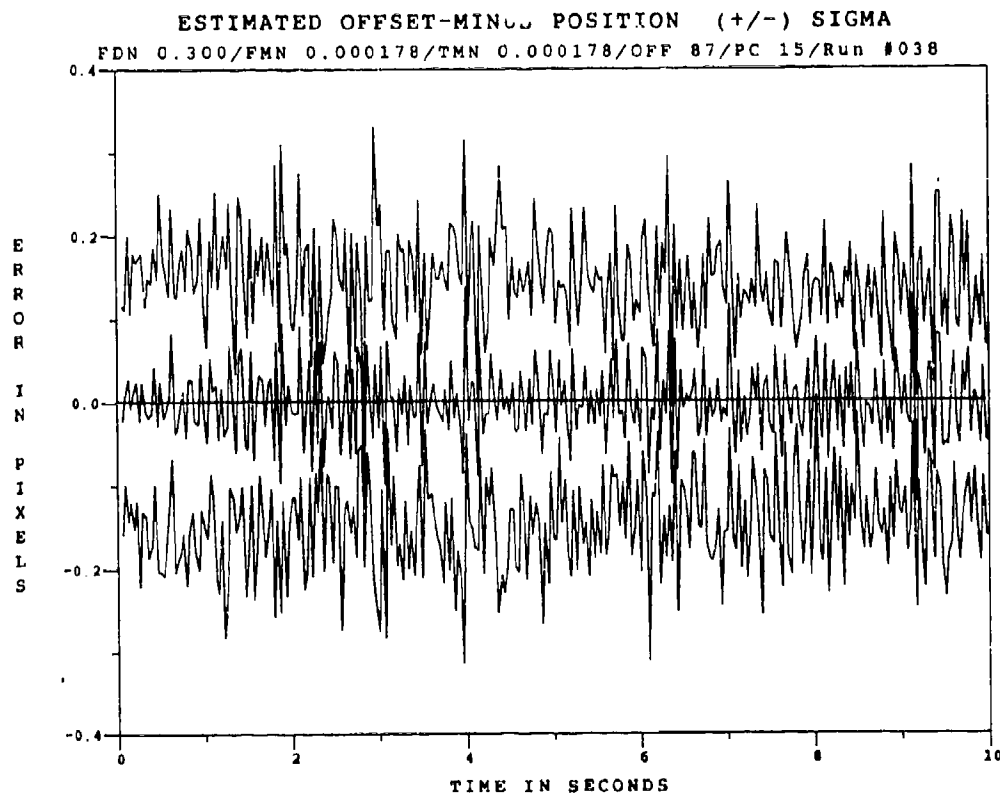


Figure C.1.2 0.53 μm Doppler Return One-State Filter Offset Error at t_i , SNR=10, $P_m = 0.0$

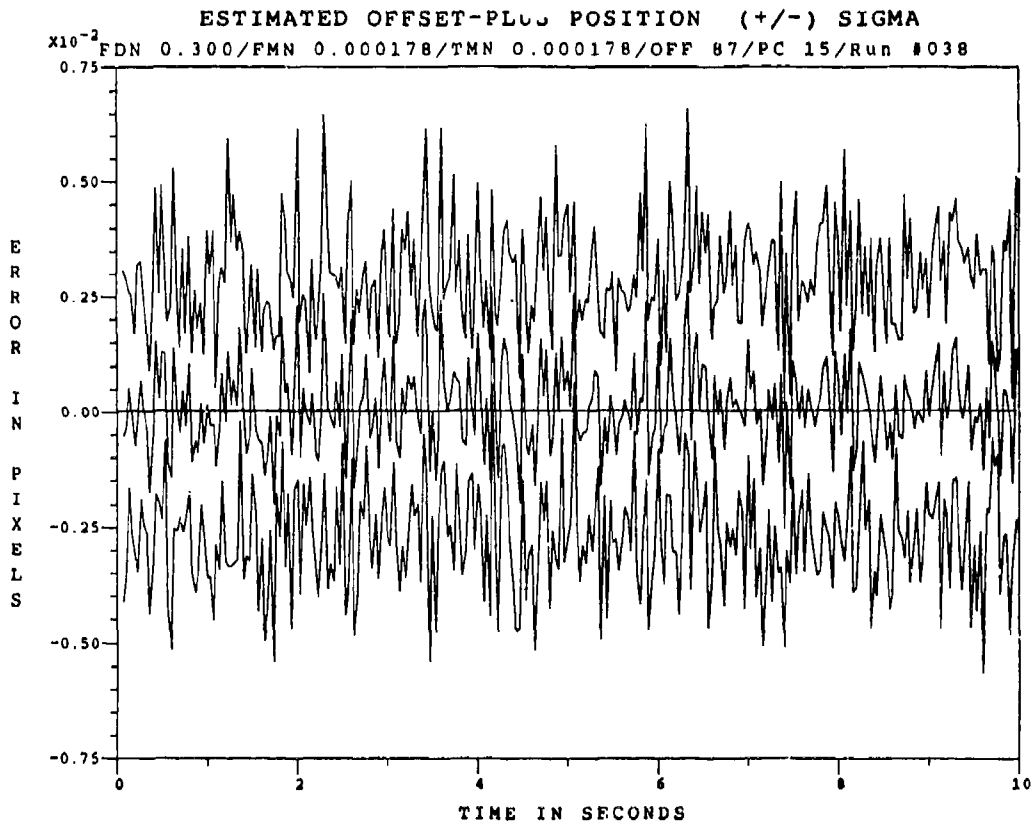


Figure C.1.3 0.53 μm Doppler Return One-State Filter: Offset Error at t_i^* , SNR=10, $P_n = 0.0$

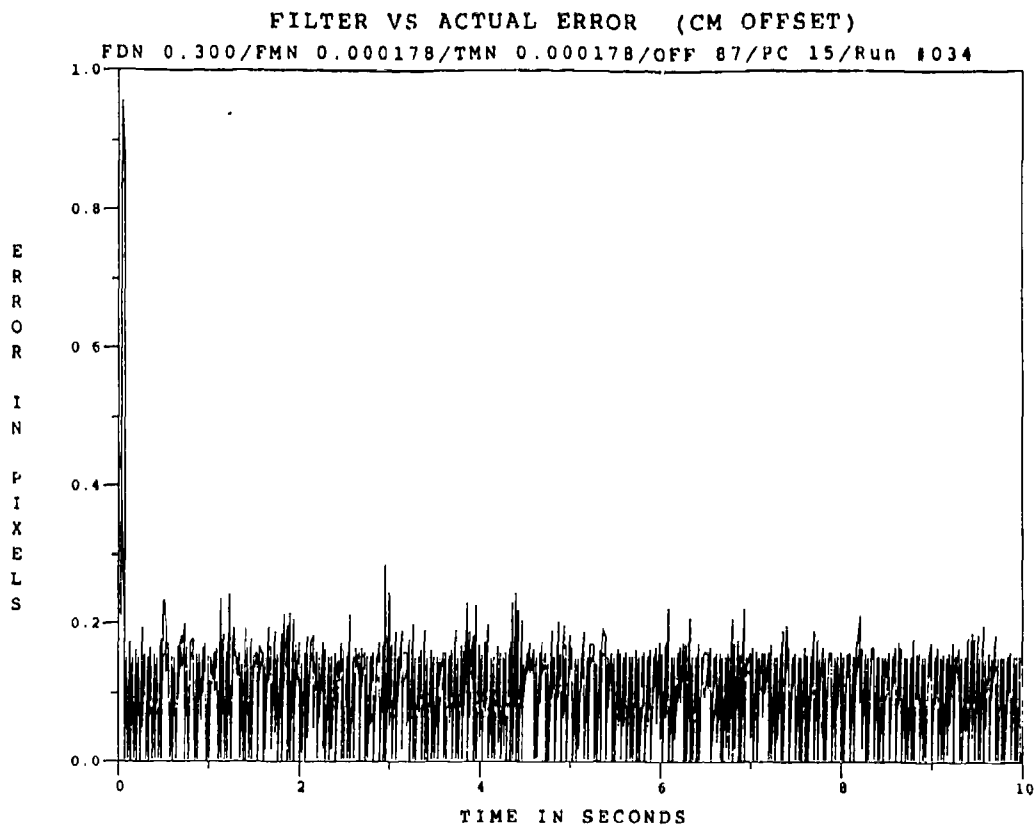


Figure C.1.4 0.53 μm Doppler Return One-State Filter Offset RMS Error, SNR=10, $P_m = 0.05$

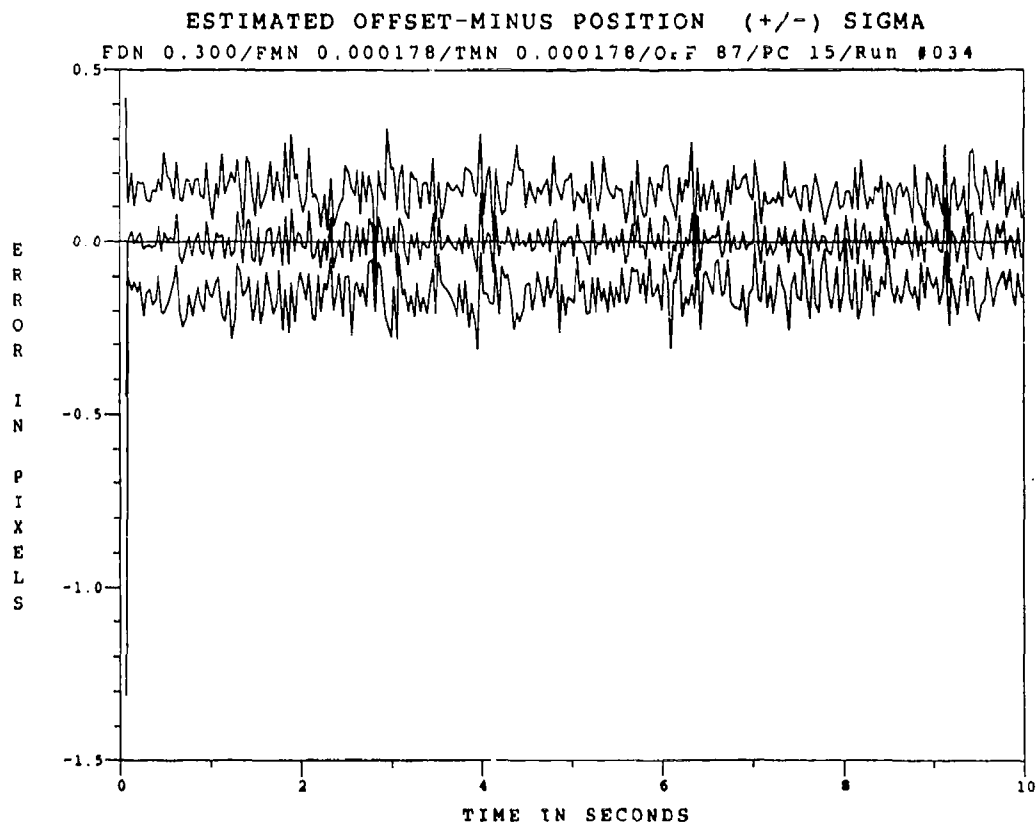


Figure C.1.5 0.53 μm Doppler Return One-State Filter Offset Error, SNR=10, $P_m = 0.05$, at t_i

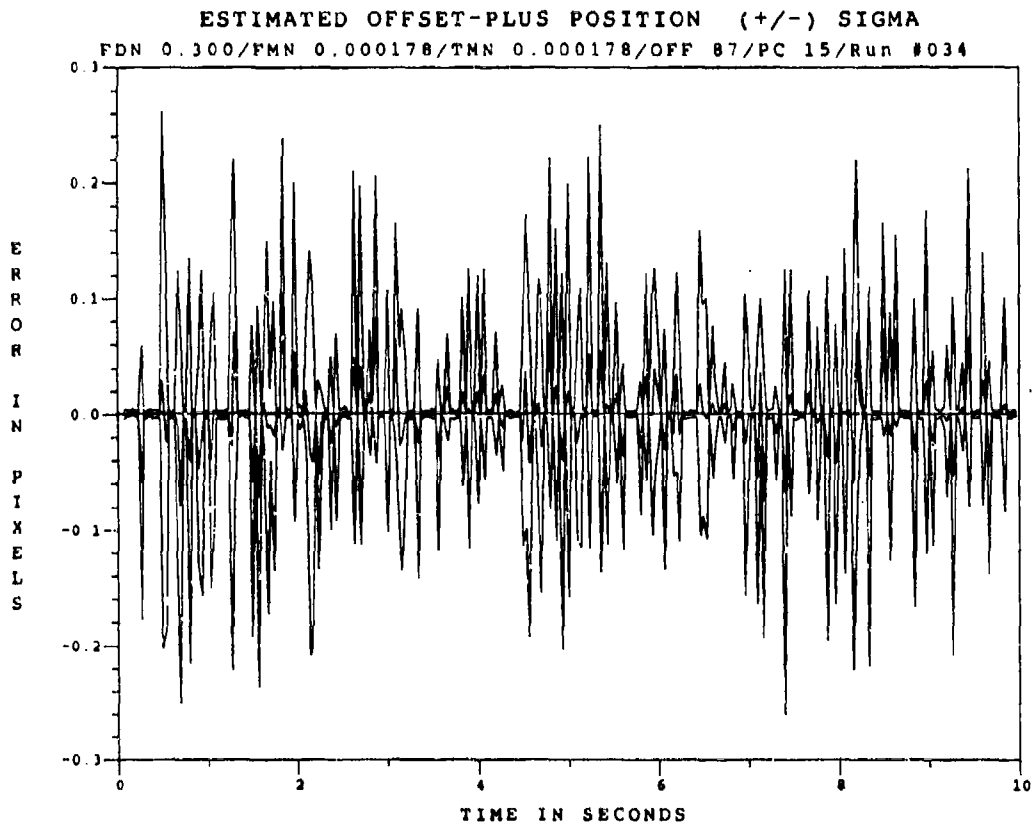


Figure C.1.6 0.53 μm Doppler Return One-State Filter Offset Error, SNR=10, $P_{\text{m}}=-0.05$, at t_1^*

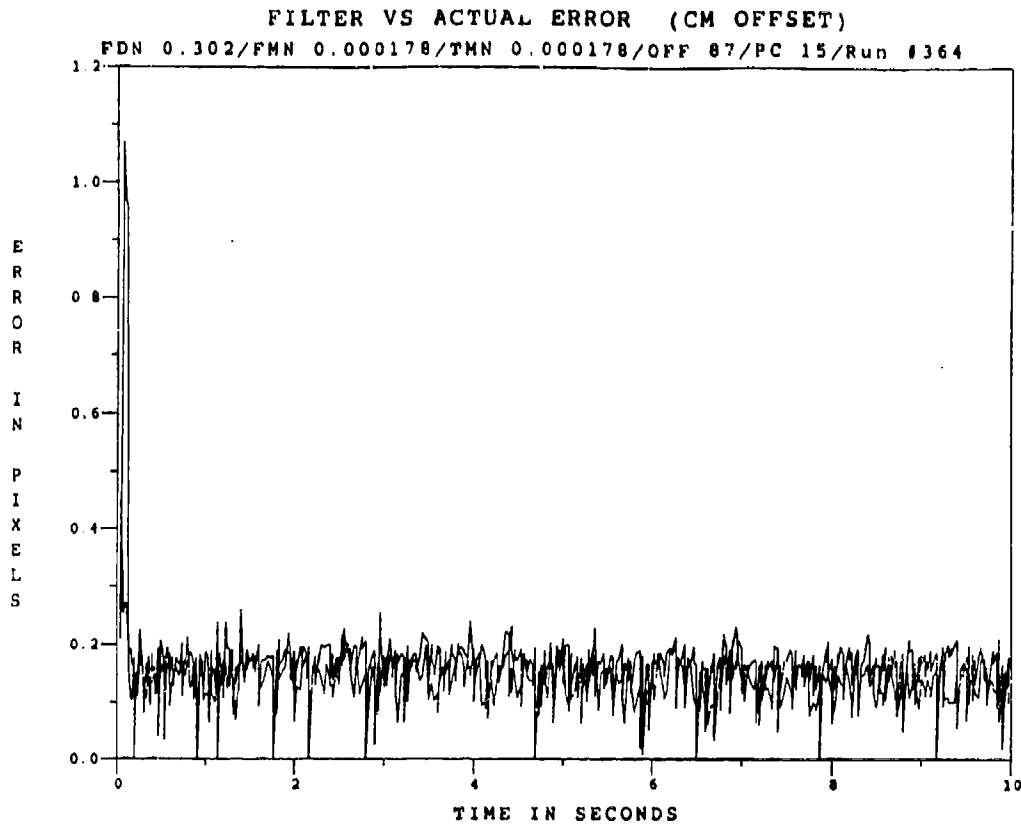


Figure C.1.7 0.53 μm Doppler Return One-State Filter Offset Error, SNR=10, $P_m = 0.30$

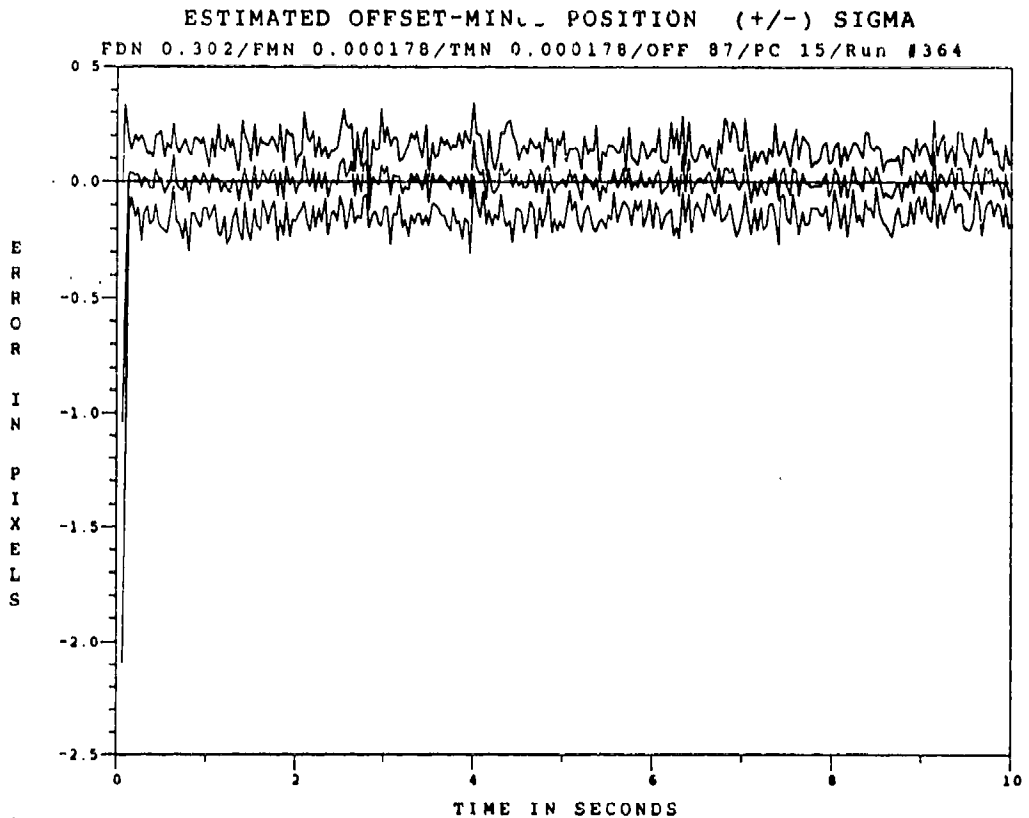


Figure C.1.8 0.53 μm Doppler Return One-State Filter Offset Error, SNR=10, $P_m = 0.30$, at t_i

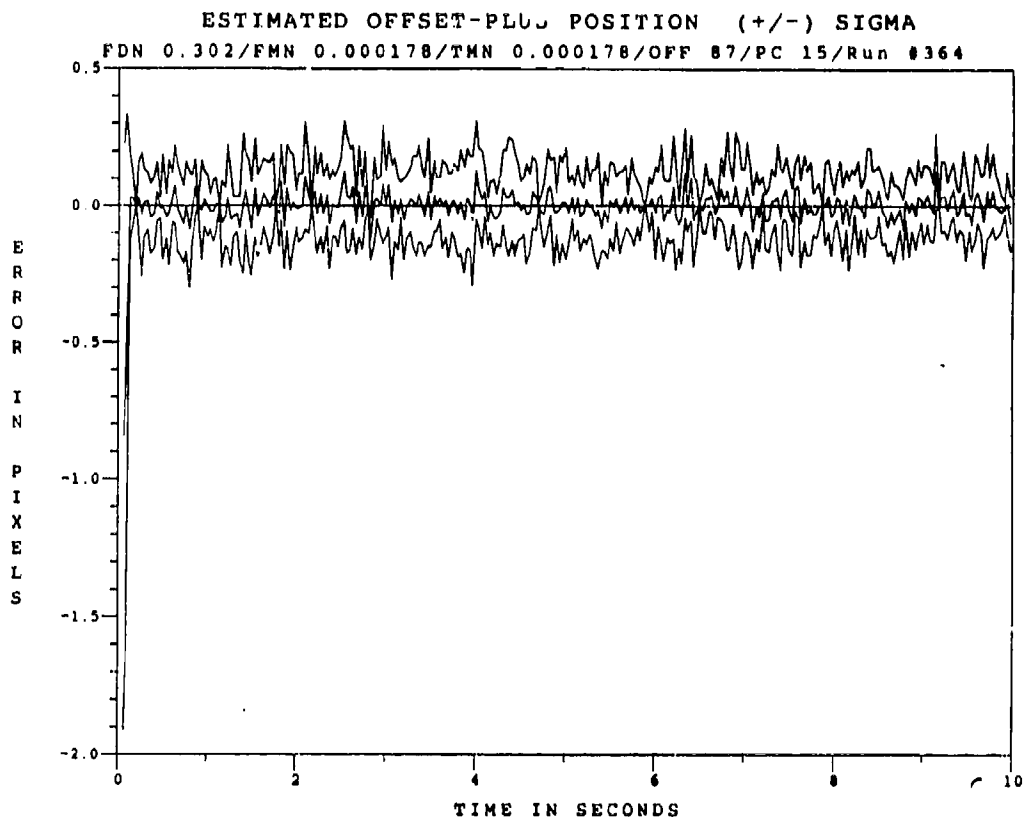


Figure C.1.9 0.53 μm Doppler Return One-State Filter Offset Error, SNR=10, $P_m = -0.30$, at t_i^*

Appendix C.2

One-State Center-of-Mass Filter

with

0.53 μm Doppler Return Measurements

at SNR = 4

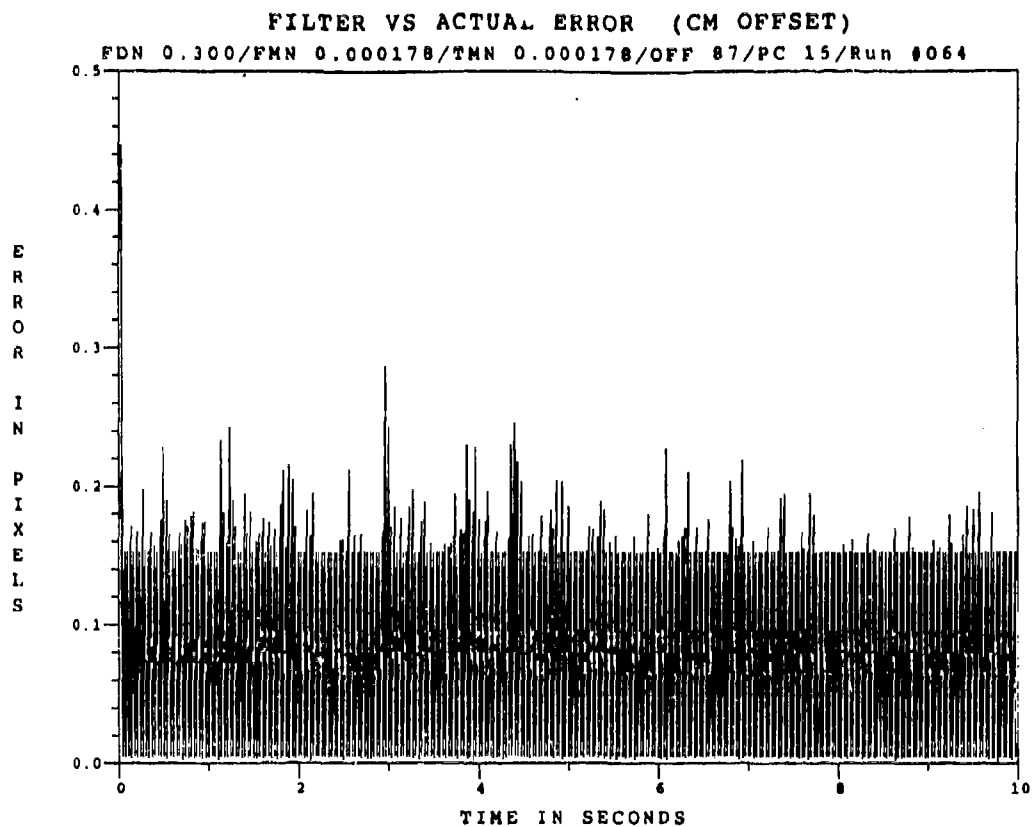


Figure C.2.1 0.53 μm Doppler Return One-State Filter Offset Error, with SNR = 4, $P_m = 0.0$

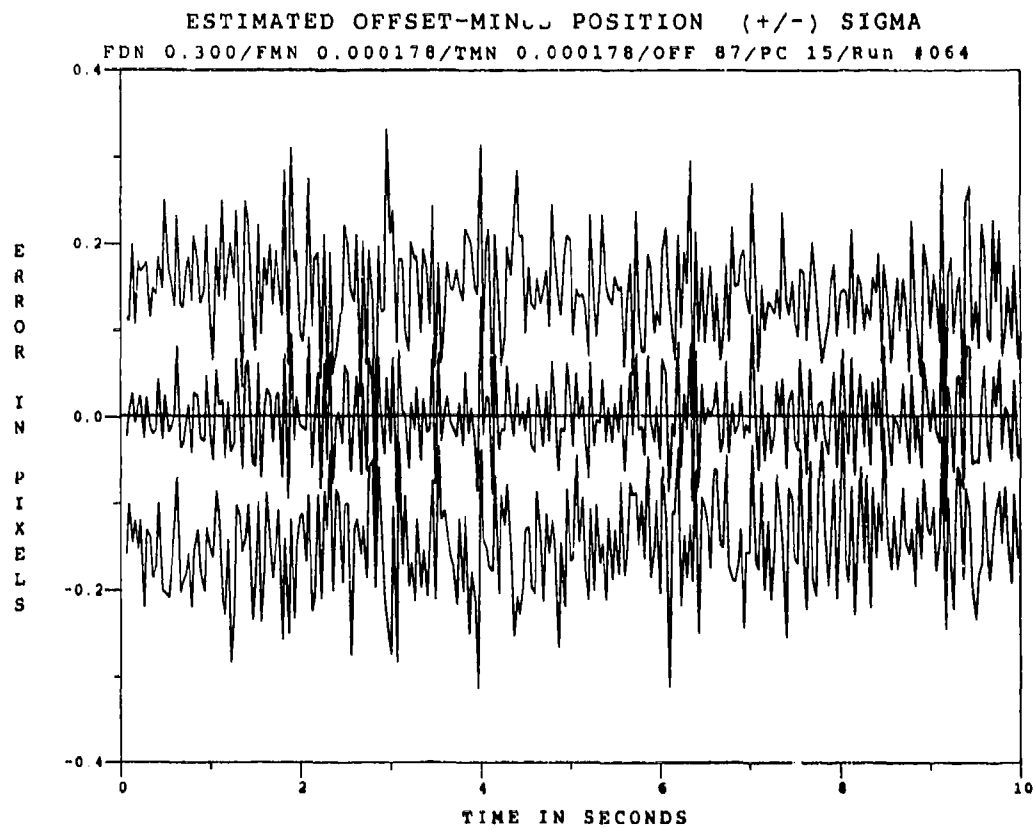


Figure C.2.2 0.53 μm Doppler Return One-State Filter Offset Error, SNR = 4, $P_m = 0.0$ at t_i

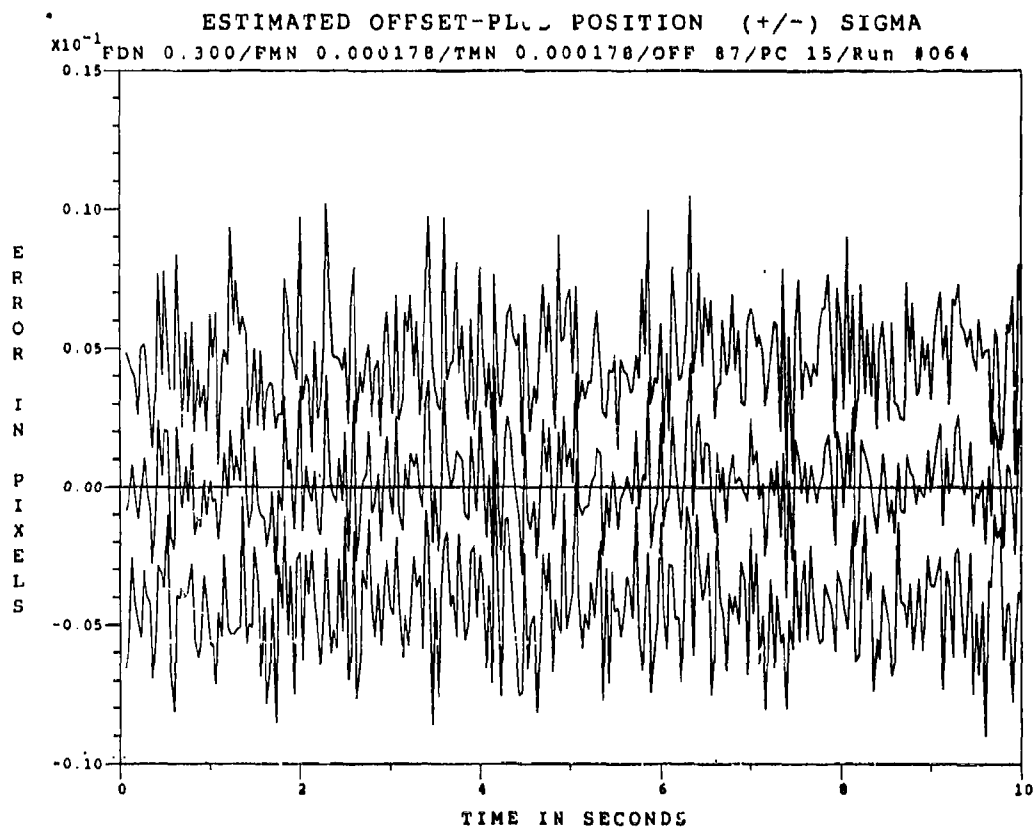


Figure C.2.3 0.53 μm Doppler Return One-State Filter Offset Error, SNR = 4, $P_m = 0.0$ at t_i^*

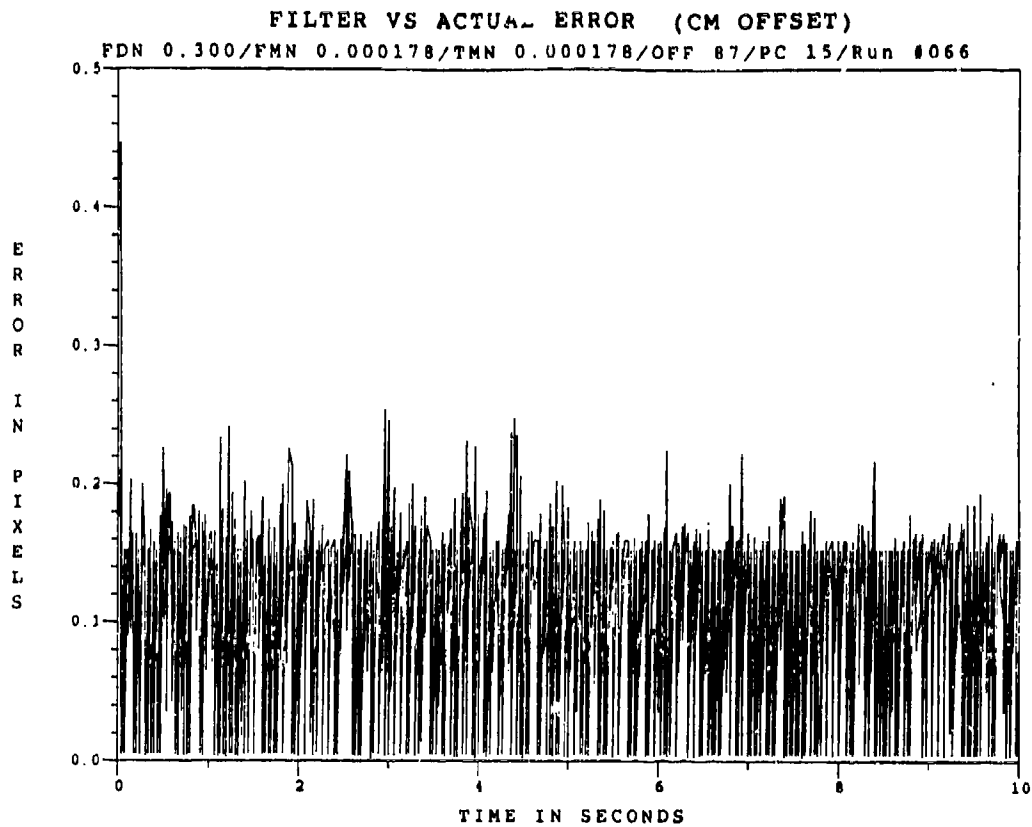


Figure C.2.4 0.53 μm Doppler Return One-State Filter Offset Error, SNR = 4, $P_m = 0.05$

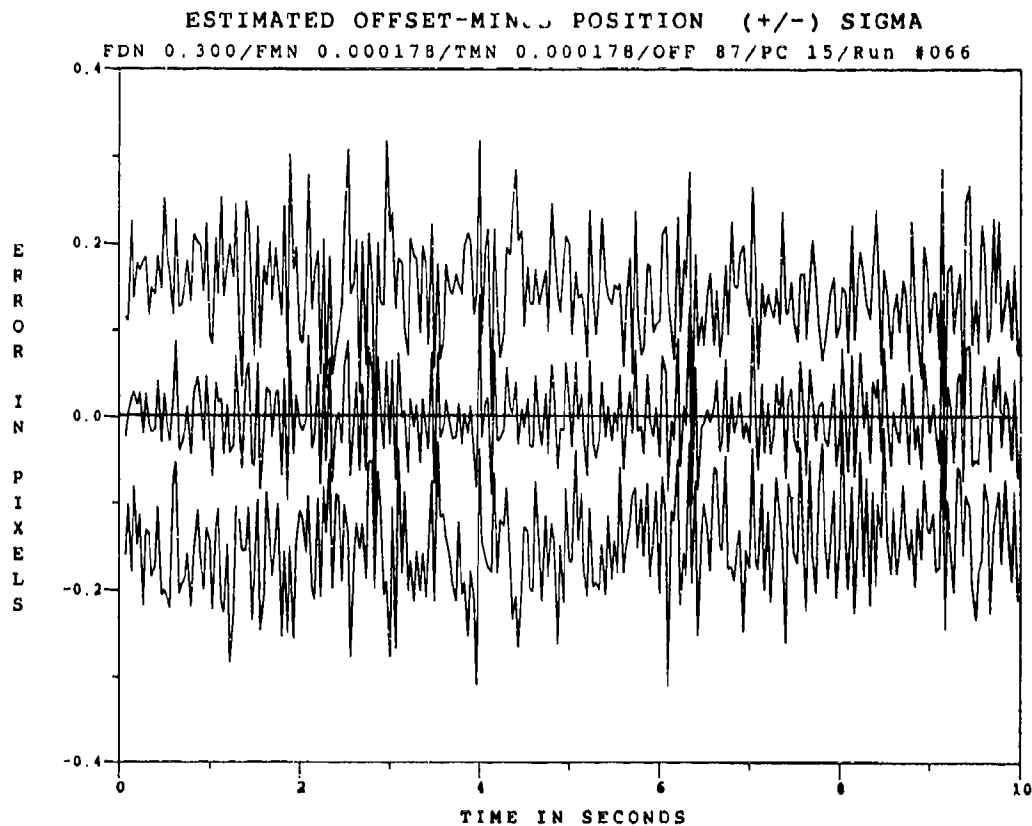


Figure C.2.5 0.53 μm Doppler Return One-State Filter Offset Error, SNR=4, $P_m = 0.05$, at t_i

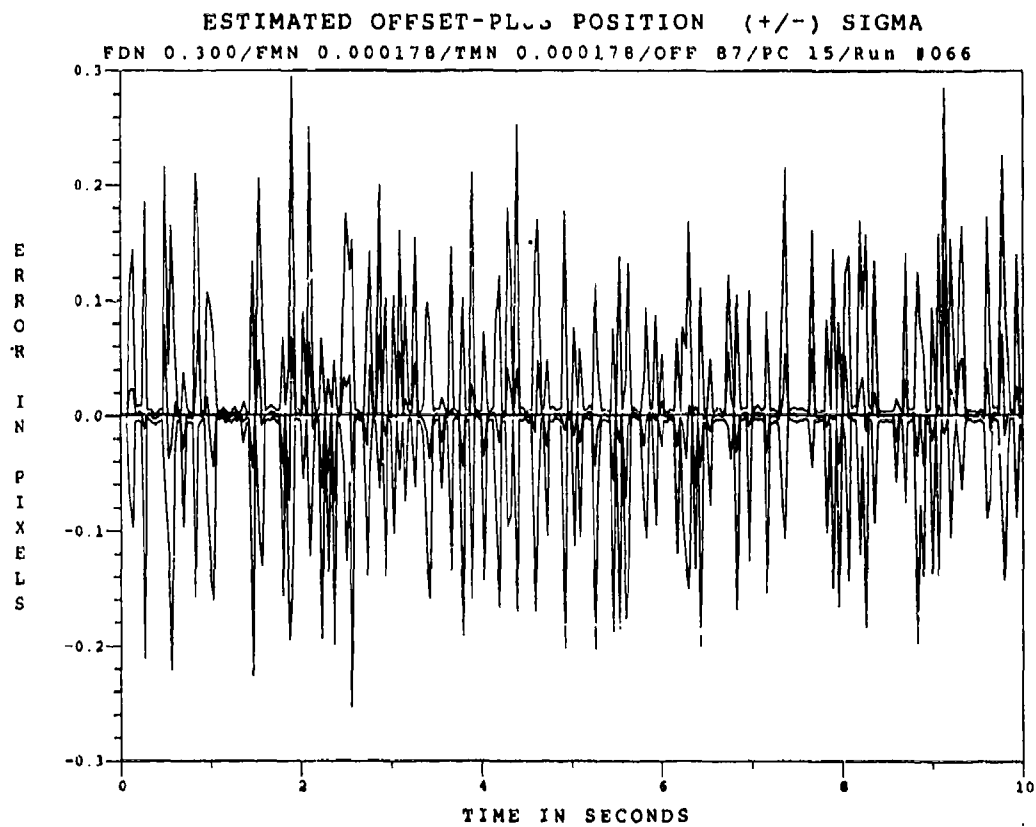


Figure C.2.6 0.53 μm Doppler Return One-State Filter Offset Error, $\text{SNR}=4$, $P_m = 0.05$, at t_i^+

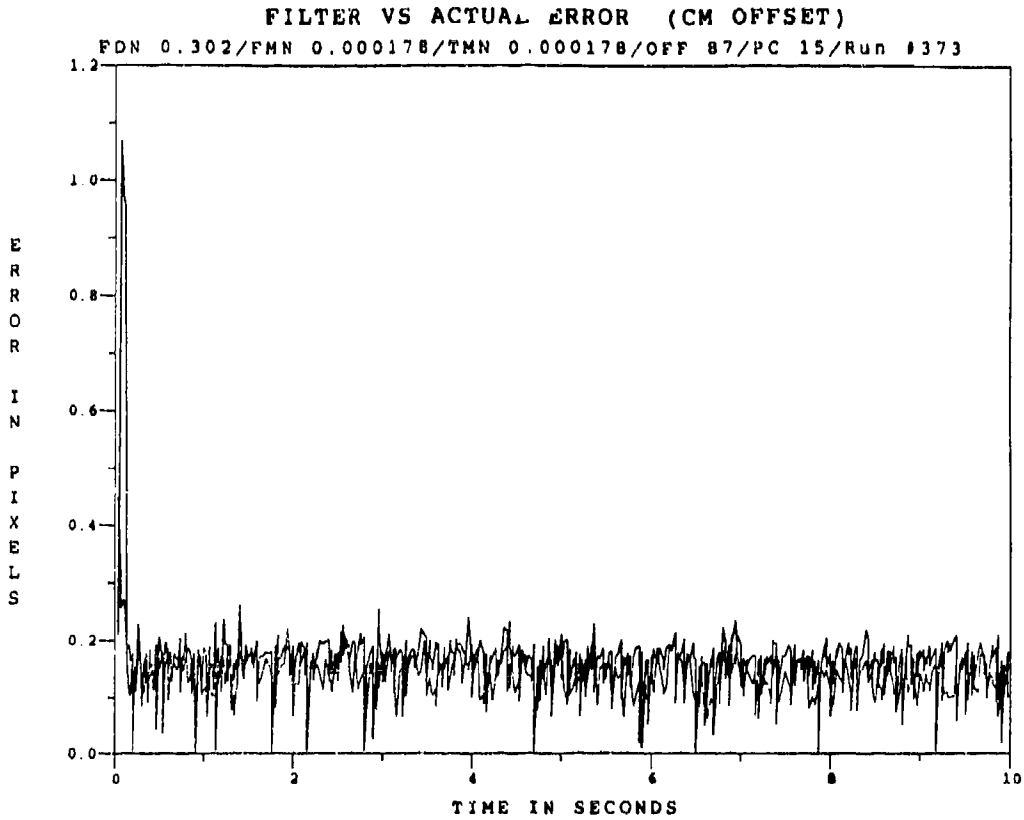


Figure C.2.7 0.53 μm Doppler Return One-State Filter Offset Error, SNR = 4, $P_m = 0.30$

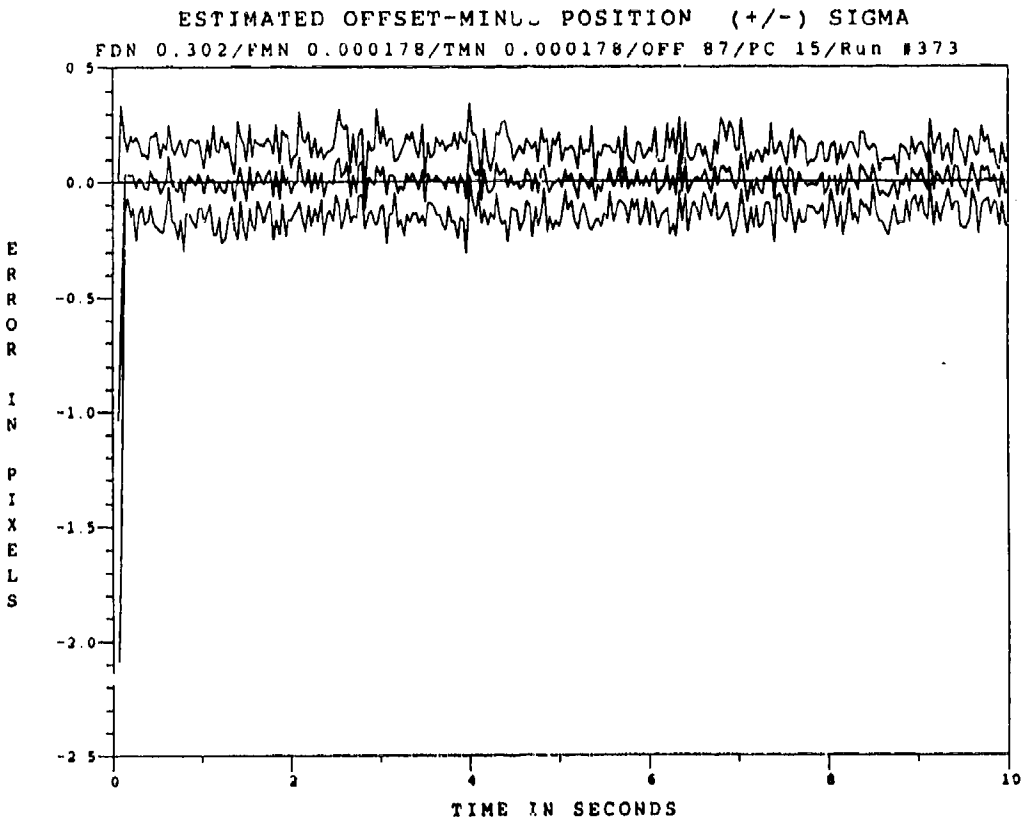


Figure C.2.8 0.53 μm Doppler Return One-State Filter Offset Error, SNR=4, $P_m = 0.30$, at t_j

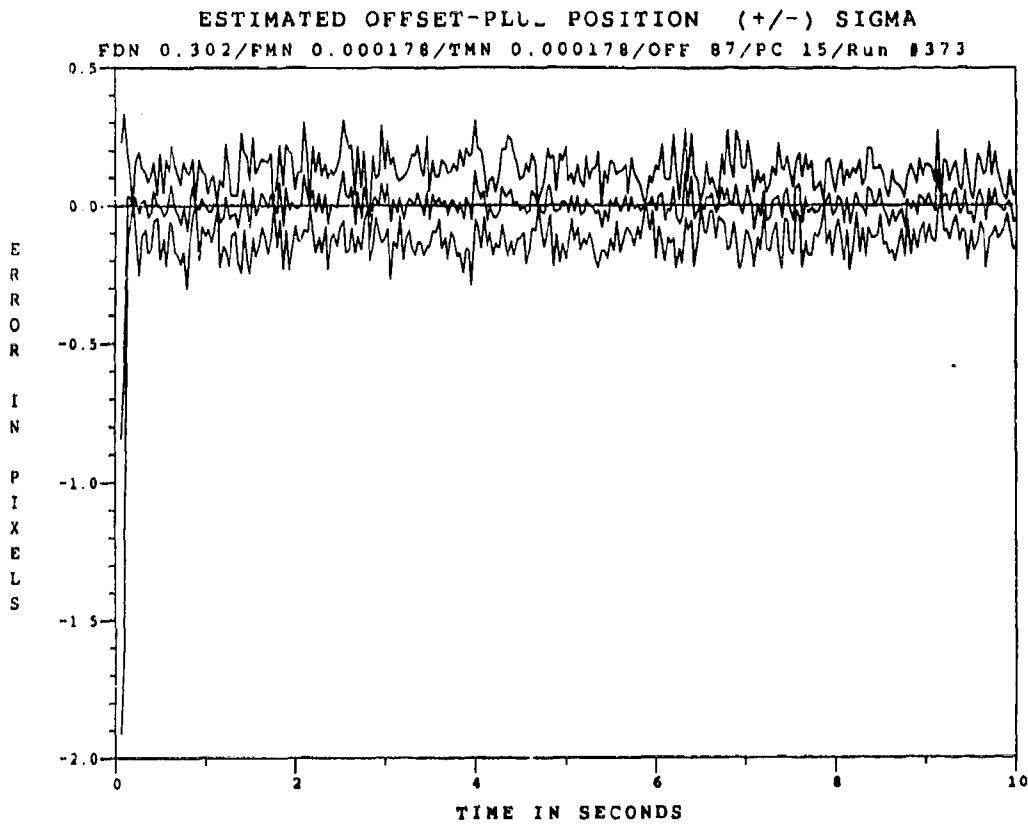


Figure C.2.9 0.53 μm Doppler Return One-State Filter Offset Error, SNR=4, $P_m = 0.30$, at t_i^+

Appendix C.3

One-State Center-of-Mass Filter

with

2.01 μm Doppler Return Measurements

at SNR = 10

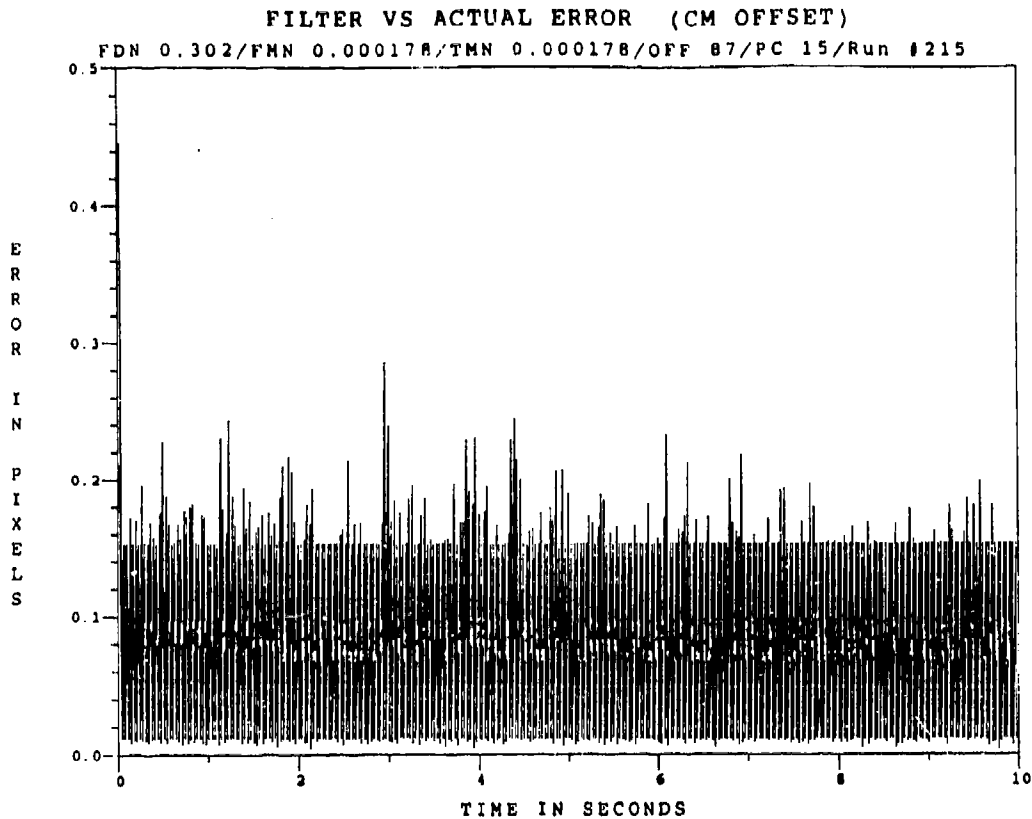


Figure C.3.1 2.01 μm Doppler Return One-State Filter Offset Error with $\text{SNR} = 10$, $P_m = 0.0$

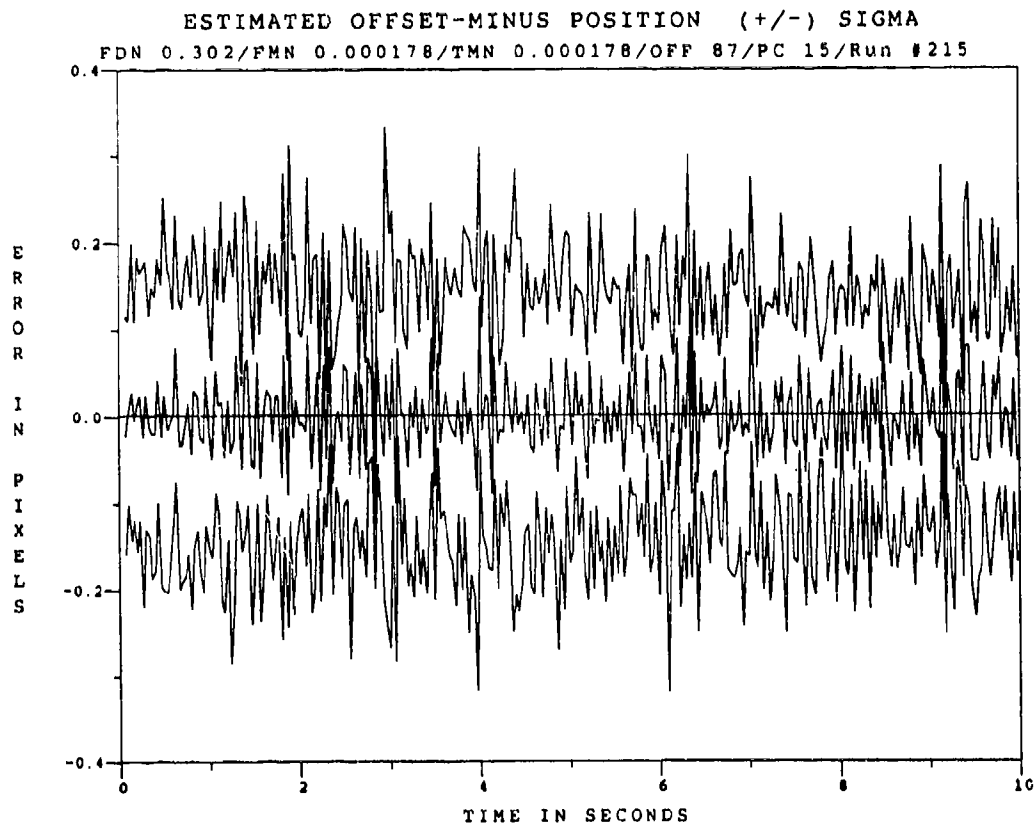


Figure C.3.2 2.01 μm Doppler Return One-State Filter Offset Error, $\text{SNR} = 10$, $P_m = 0.0$ at t_i

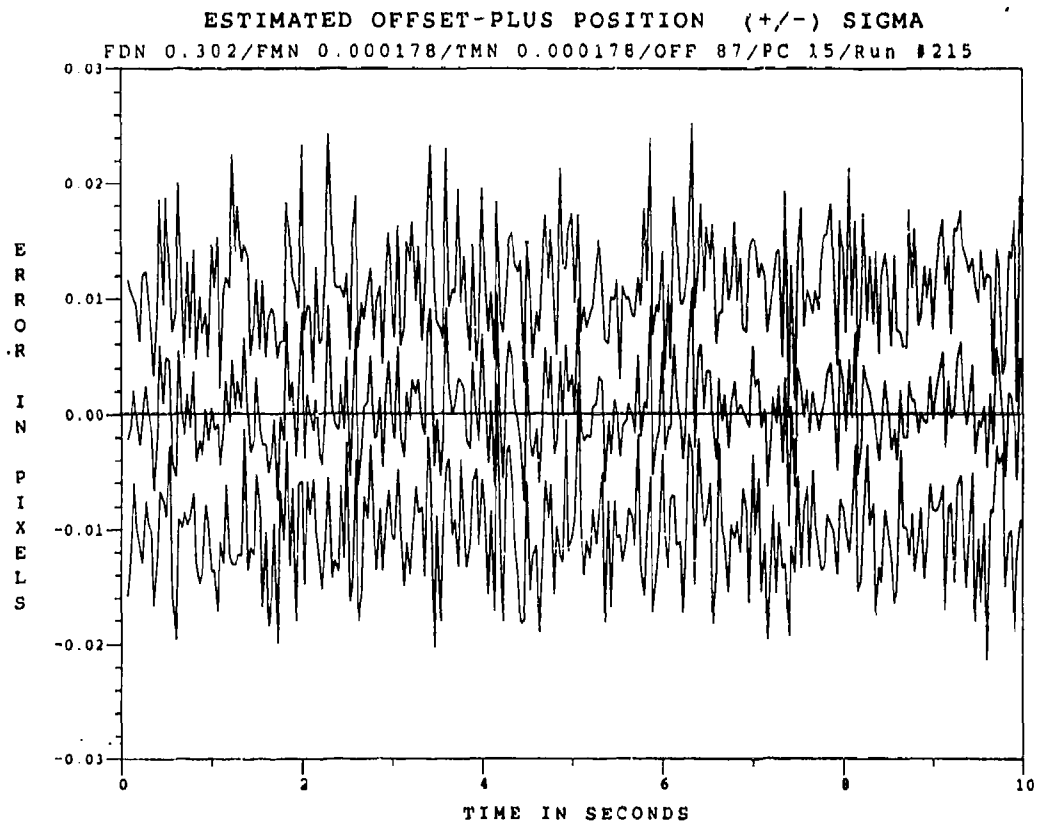


Figure C.3.3 2.01 μm Doppler Return One-State Offset Filter, with $\text{SNR} = 10$, $P_m = 0.0$ at t_i^+

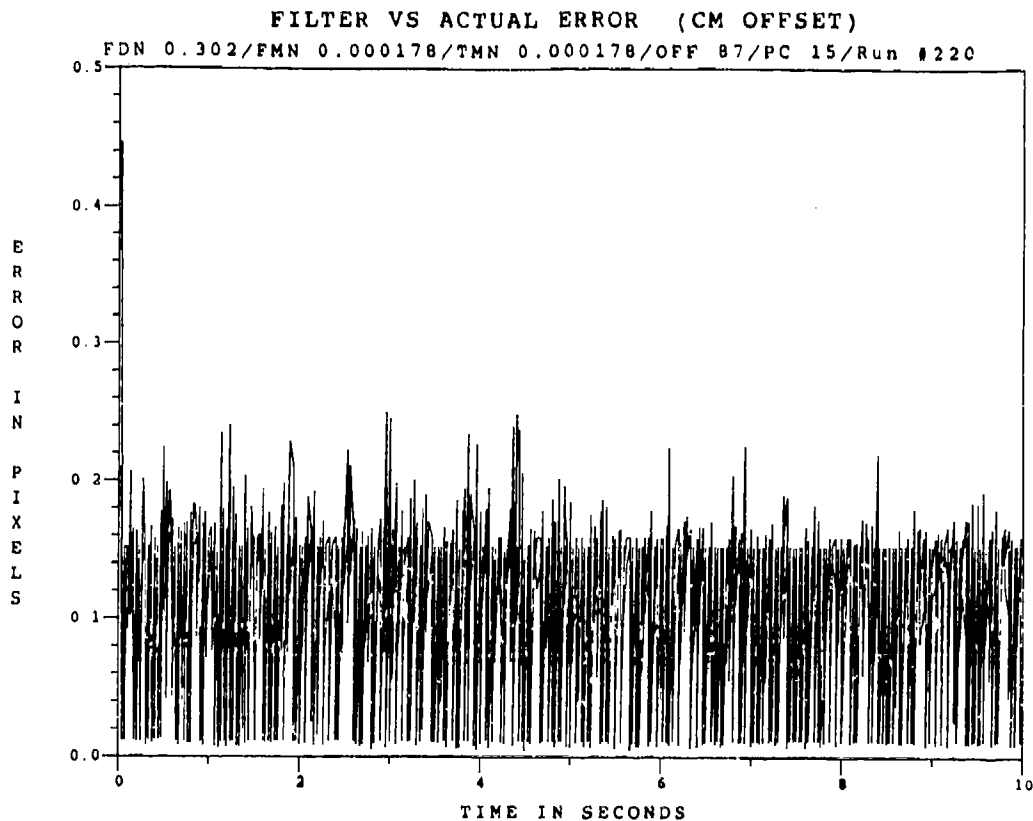


Figure C.3.4 2.01 μm Doppler Return One-State Filter Offset Error, $\text{SNR} = 10$, $P_m = 0.05$

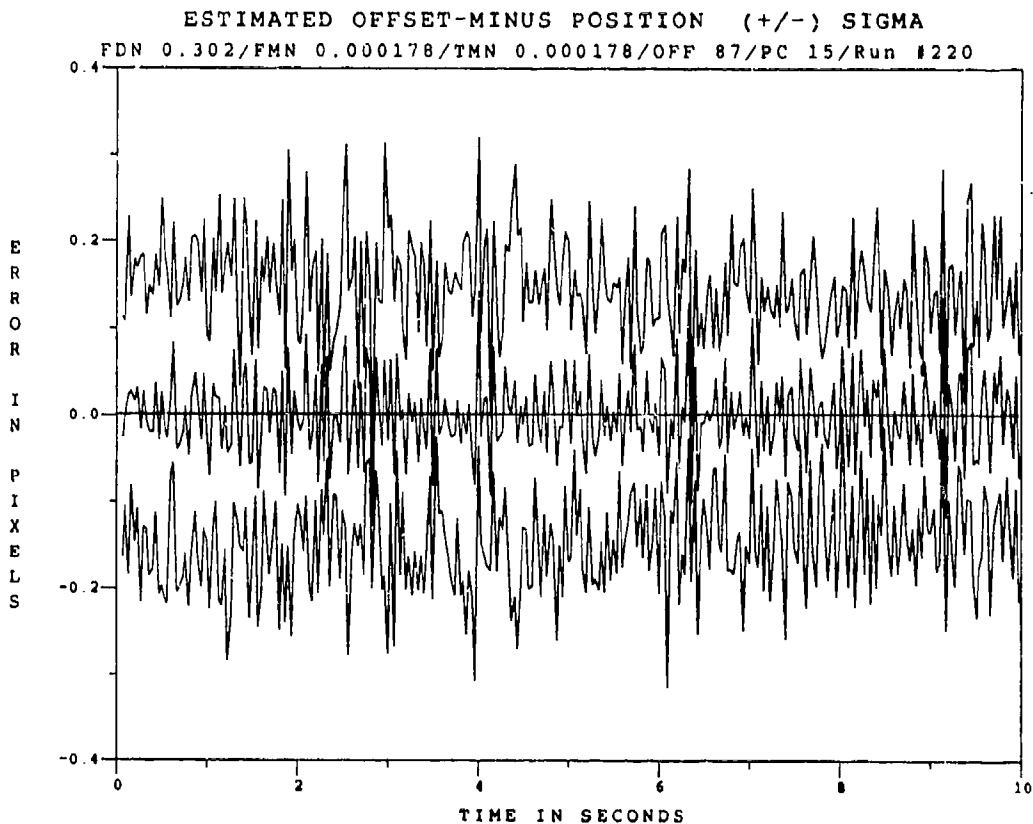


Figure C.3.5 2.01 μm Doppler Return One-State Filter Offset Error, $\text{SNR} = 10$, $P_m = 0.05$, at t_i

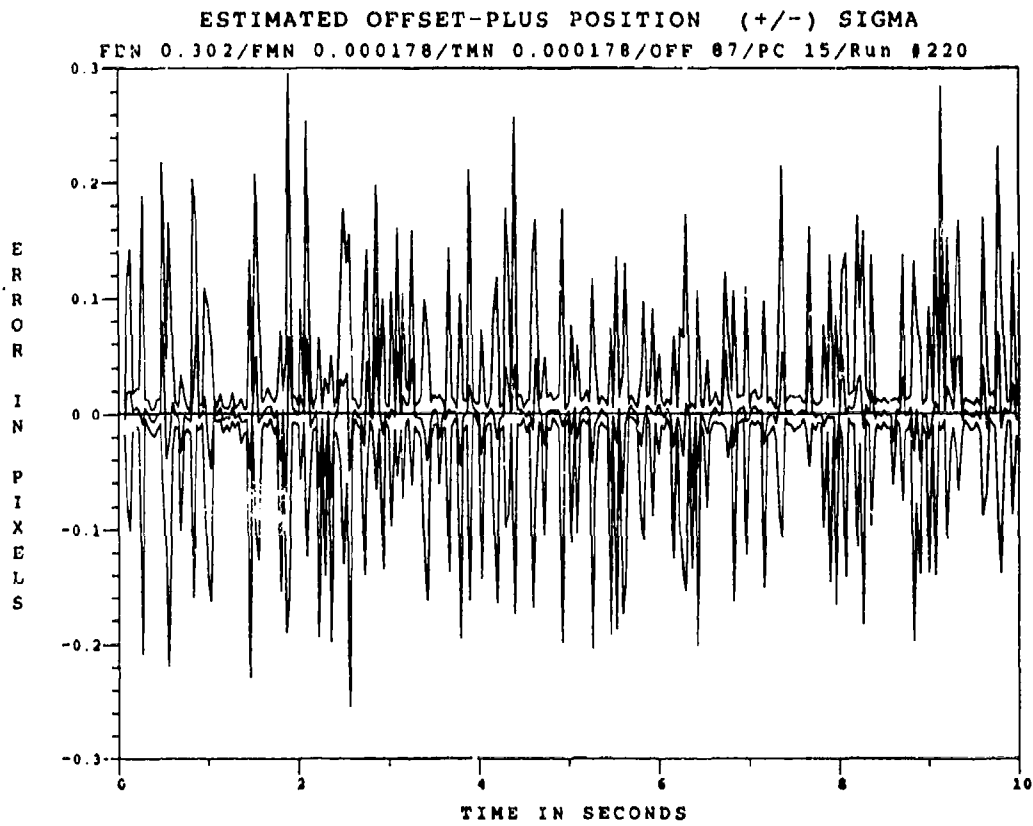


Figure C.3.6 2.01 μm Doppler Return One-State Filter Offset Error, SNR=10, $P_m=0.05$, at t_i^*

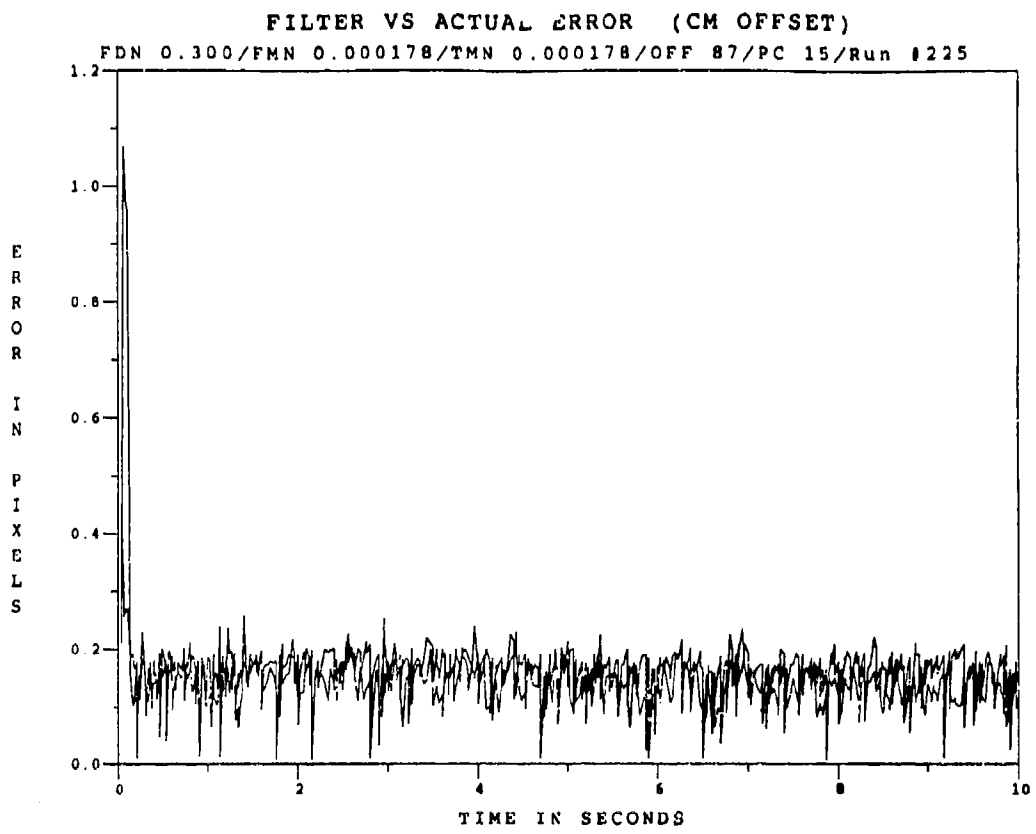


Figure C.3.7 2.01 μm Doppler Return One-State Filter Offset Error, SNR = 10, $P_m = 0.30$

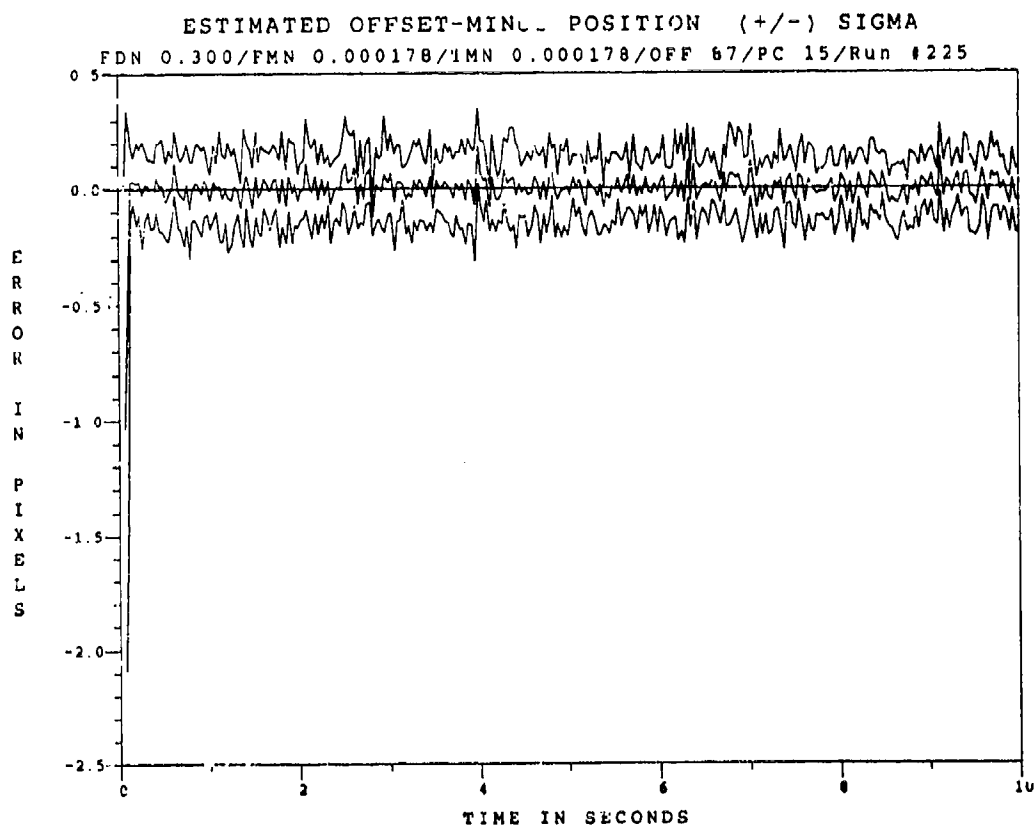


Figure C.3.8 2.01 μm Doppler Return One-State Filter Offset Error, SNR=10, $P_m = 0.30$, at t_i

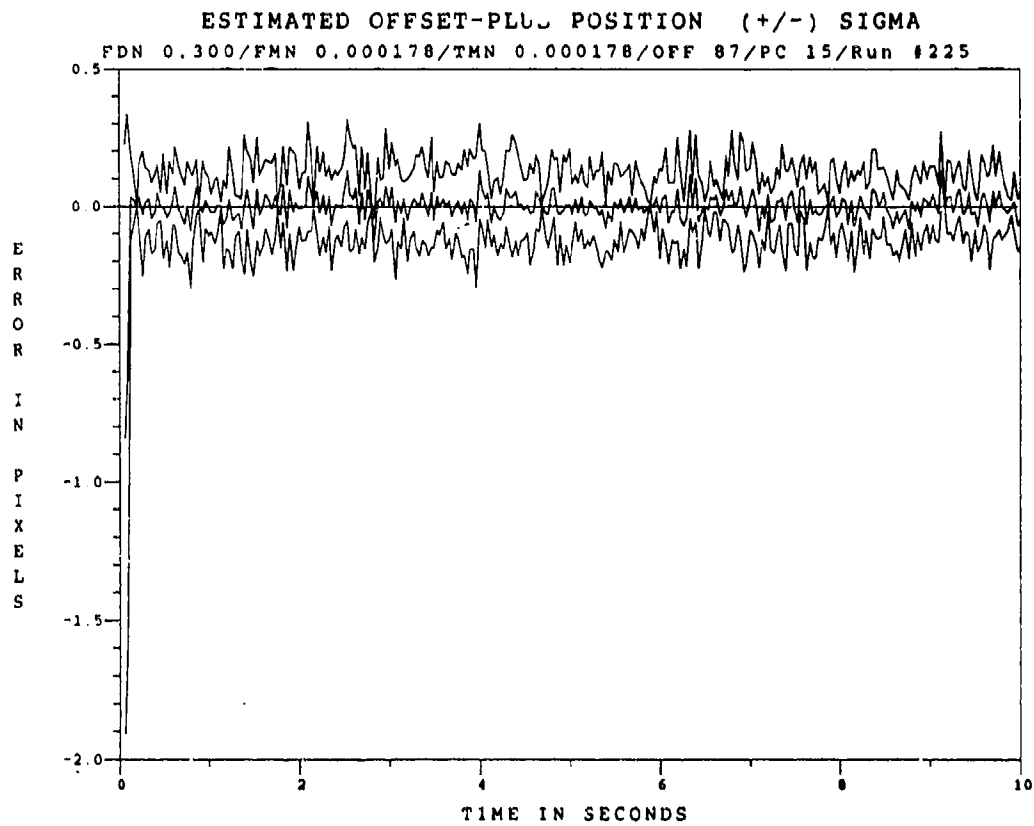


Figure C.3.9 2.01 μm Doppler Return One-State Filter Offset Error, SNR=10, $P_m = -0.30$, at t_i^*

Appendix C.4

One-State Center-of-Mass Filter

with

2.01 μm Doppler Return Measurements

at SNR = 4

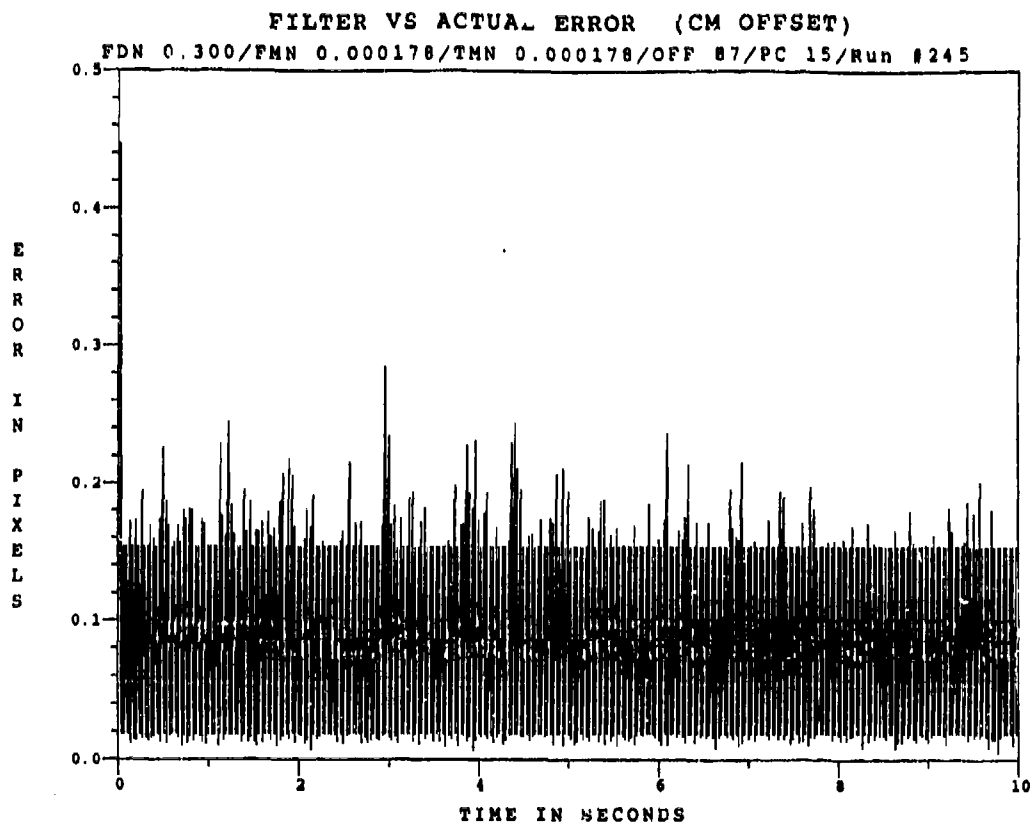


Figure C.4.1 2.01 μm Doppler Return One-State Filter Offset Error with $\text{SNR} = 4$, $P_m = 0.0$

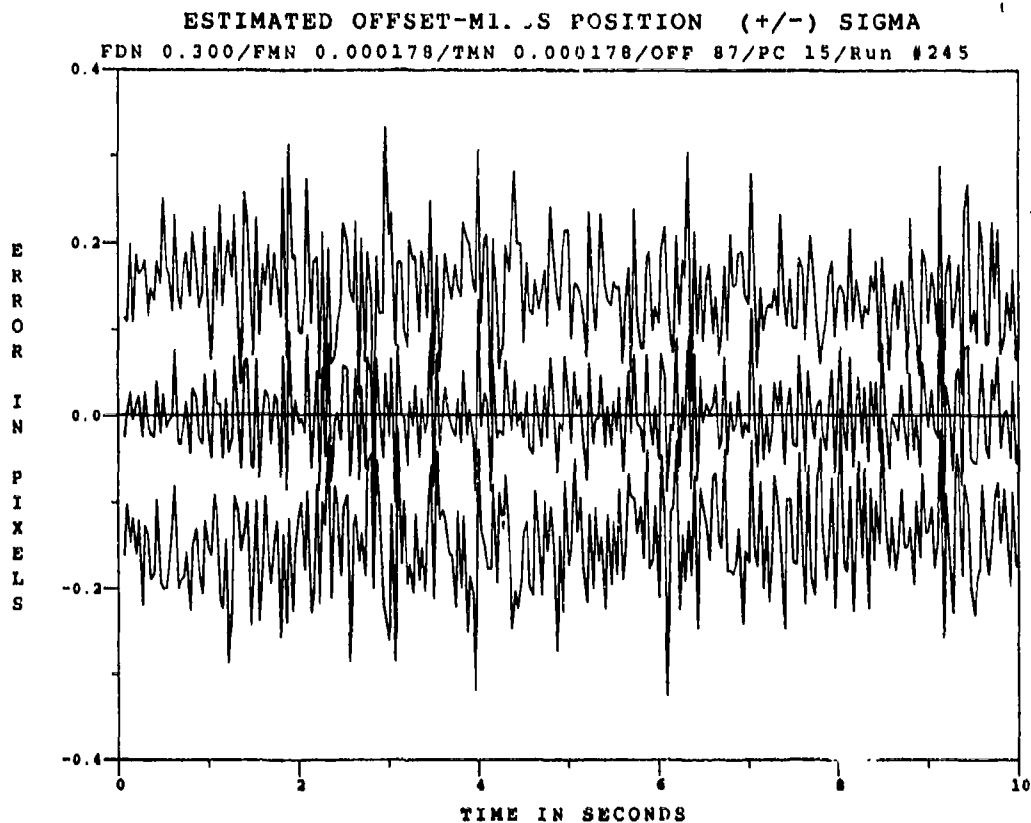


Figure C.4.2 2.01 μm Doppler Return One-State Filter Offset Error, $\text{SNR} = 4$, $P_m = 0.0$ at t_i

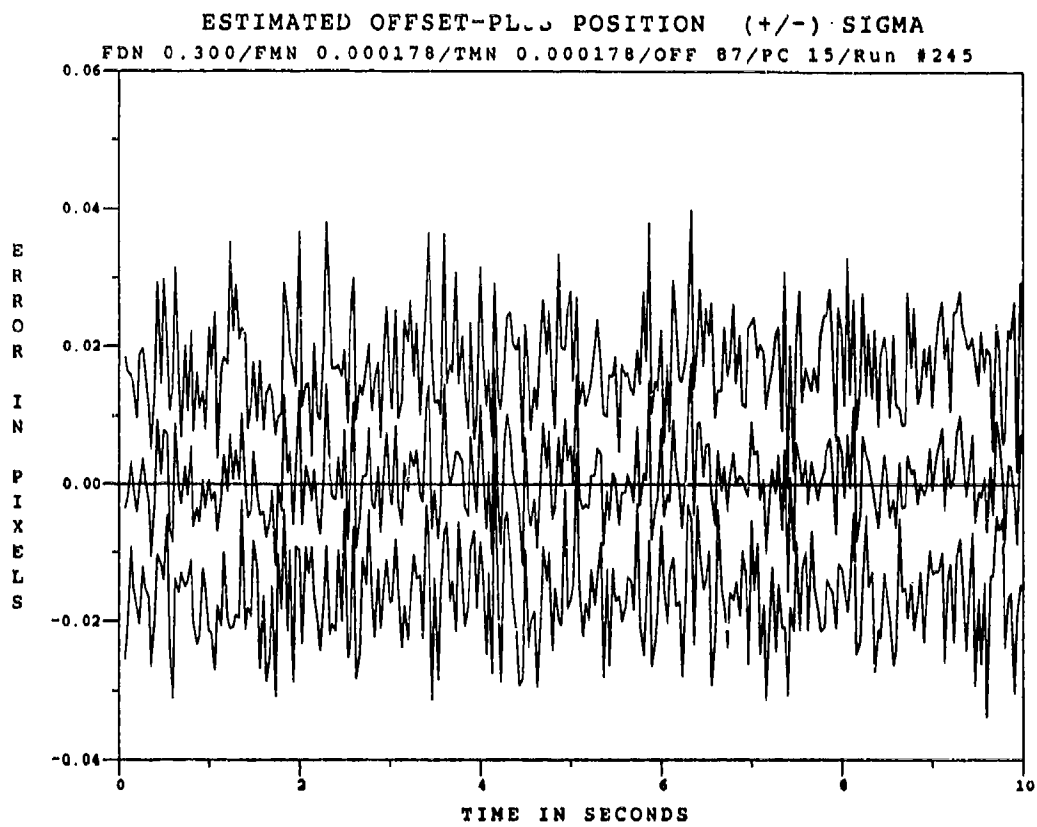


Figure C.4.3 2.01 μm Doppler Return One-State Filter Offset Error, SNR = 4, $P_m = 0.0$ at t_i^+

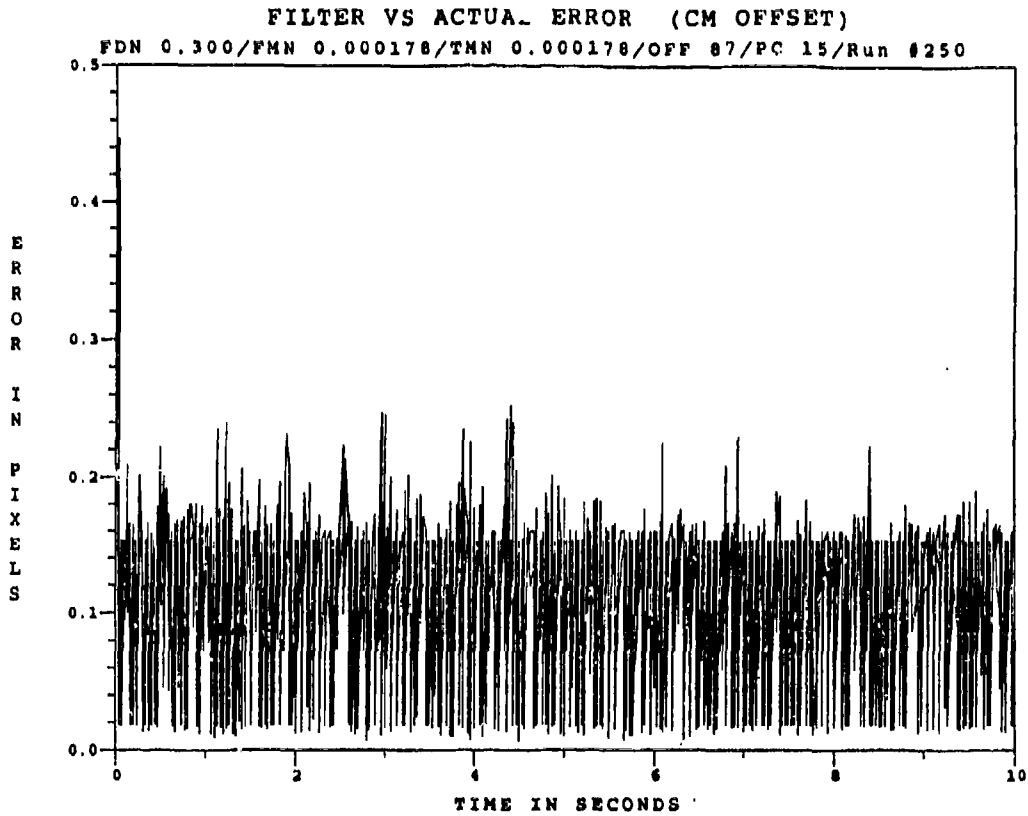


Figure C.4.4 2.01 μm Doppler Return One-State Filter Offset Error with $\text{SNR} = 4$, $P_m = 0.05$

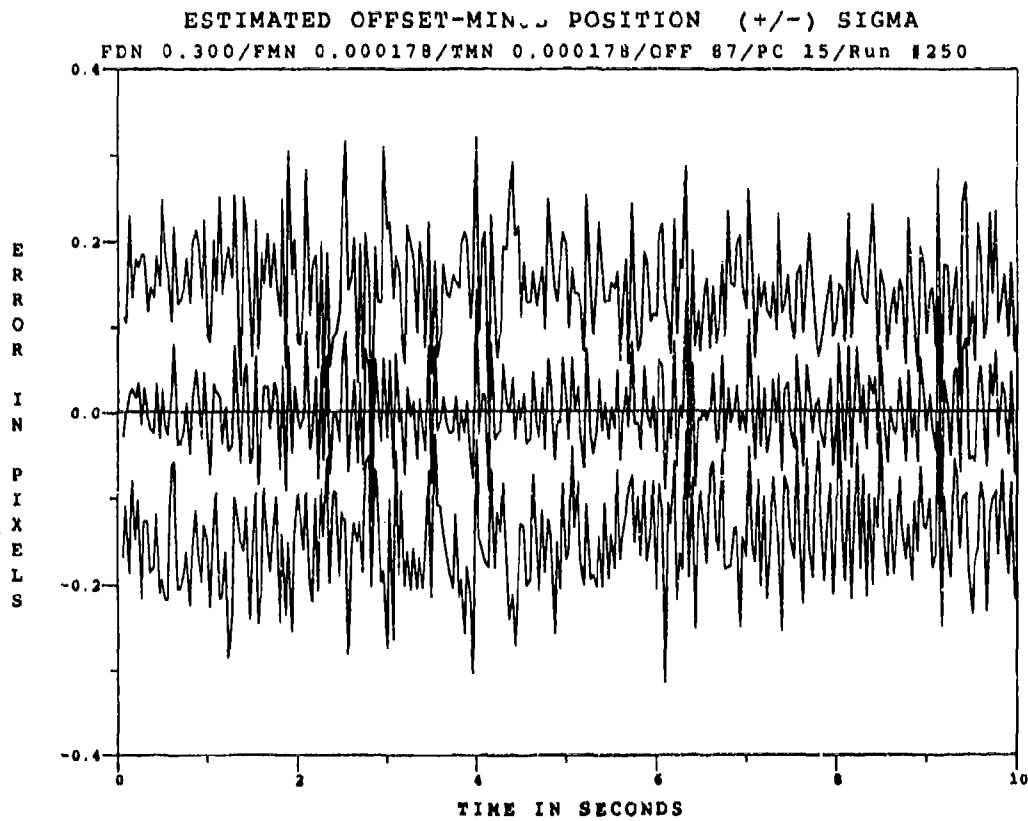


Figure C.4.5 2.01 μm Doppler Return One-State Filter Offset Error, $\text{SNR}=4$, $P_m = 0.05$, at t_j

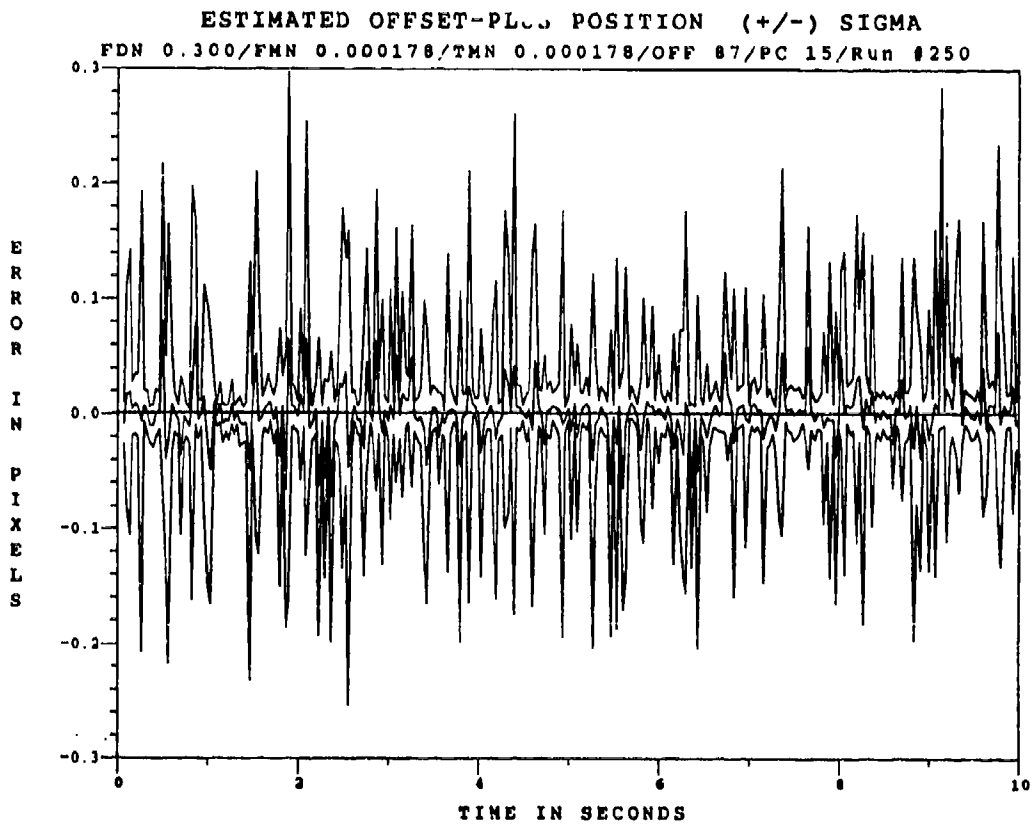


Figure C.4.6 2.01 μm Doppler Return One-State Filter Offset Error, SNR=4, $P_m = 0.05$, at t_f^*

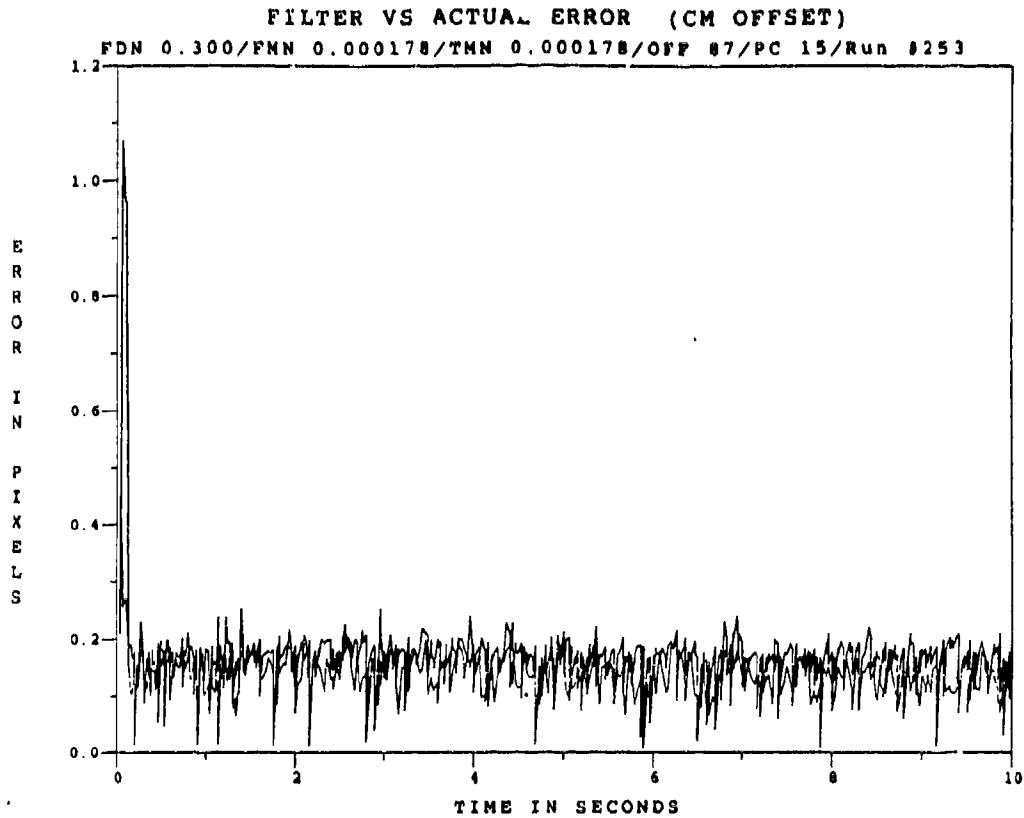


Figure C.4.7 2.01 μm Doppler Return One-State Filter Offset Error with SNR = 4, $P_m = 0.30$

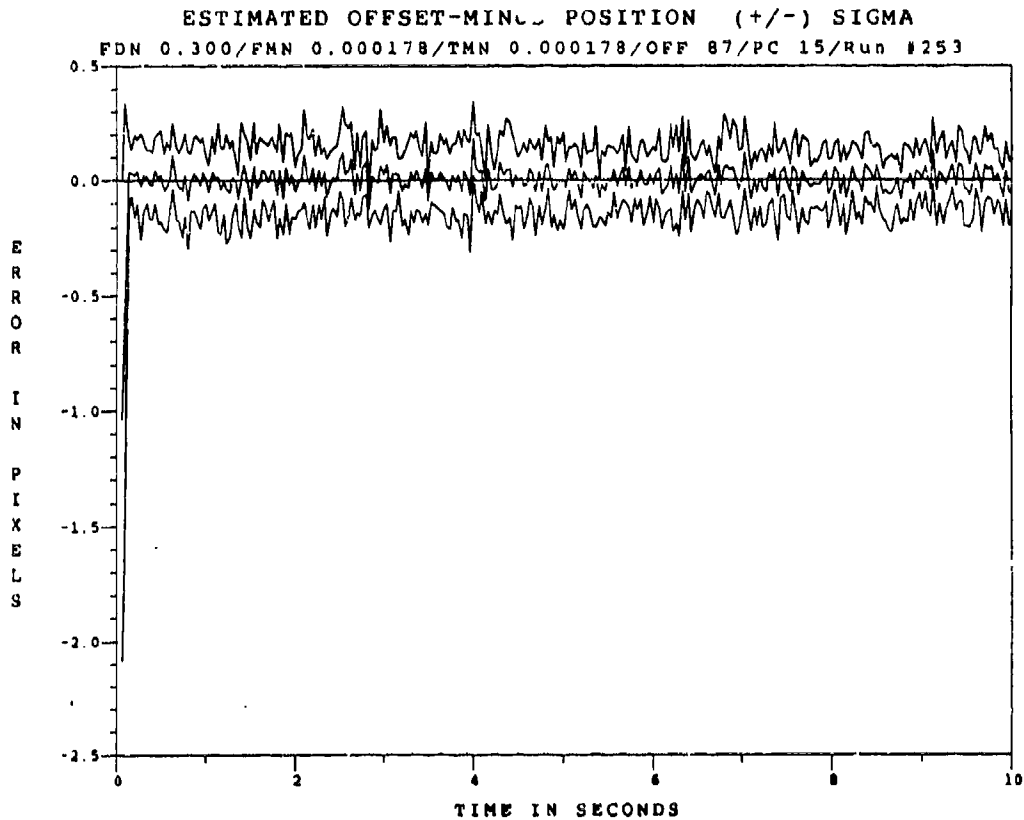


Figure C.4.8 2.01 μm Doppler Return One-State Filter Offset Error, SNR=4, $P_m = 0.30$, at t_i

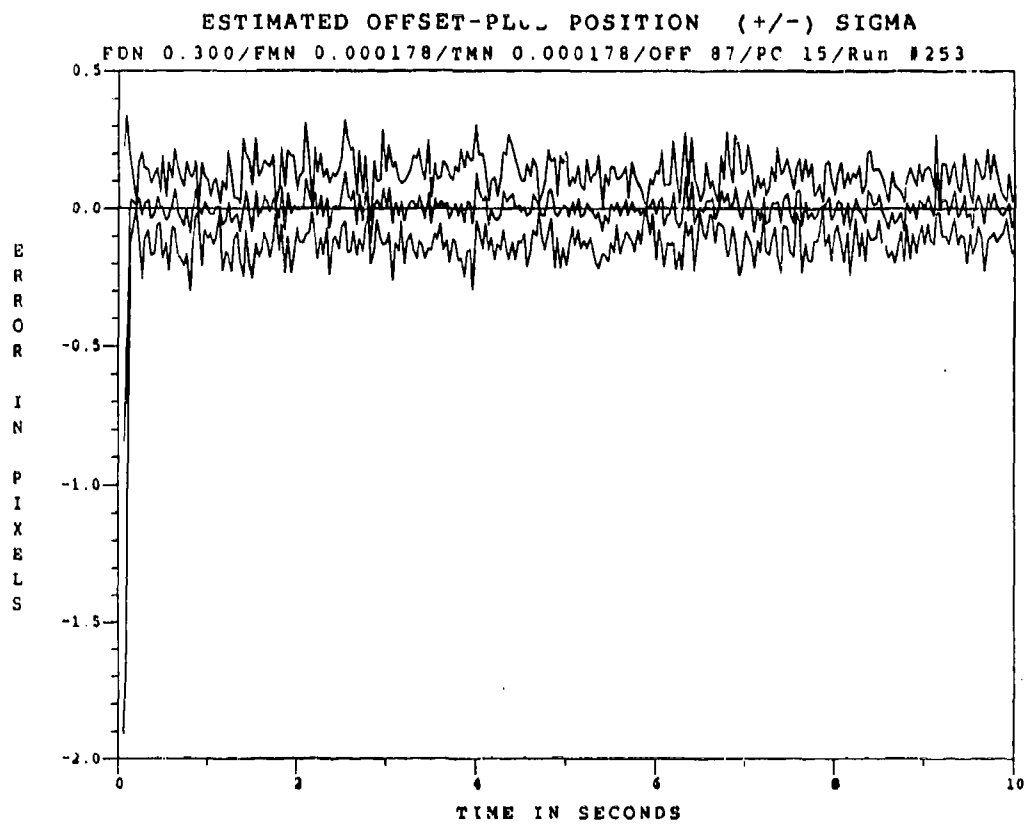


Figure C.4.9 2.01 μm Doppler Return One-State Filter Offset Error, SNR=4, $P_m = 0.30$, at t_1^*

Appendix C.5

One-State Center-of-Mass Filter

with

10.5 μm Doppler Return Measurements

at SNR = 10

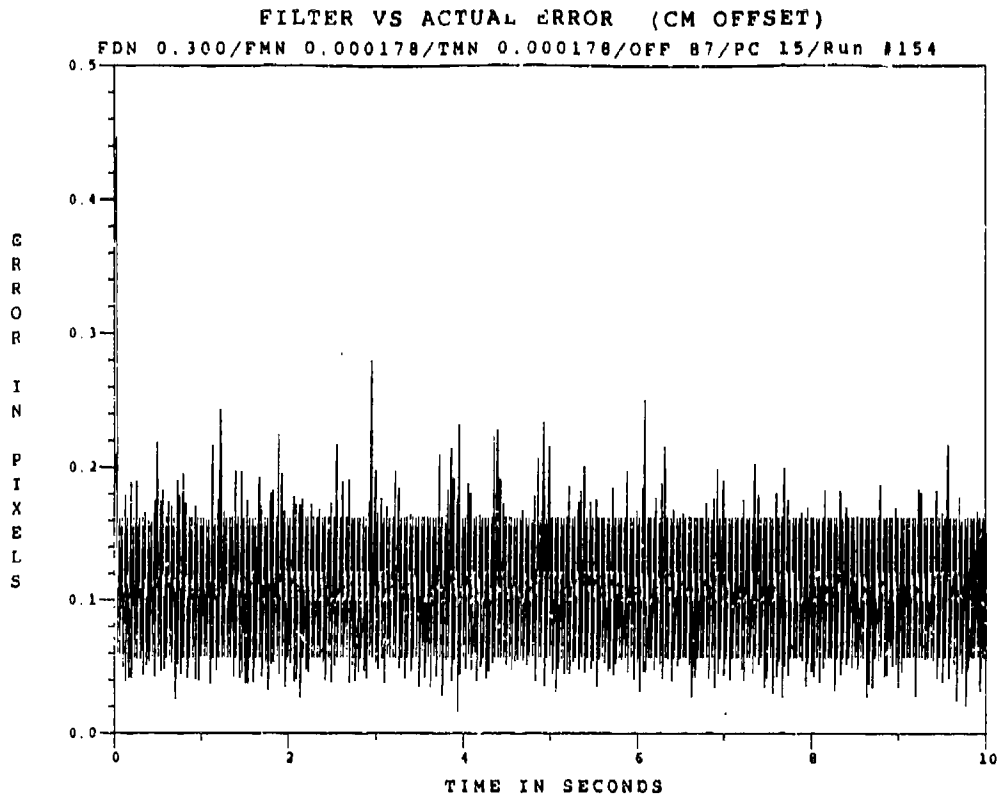


Figure C.5.1 10.5 μm Doppler Return One-State Filter Offset Error with SNR = 10, $P_m = 0.0$

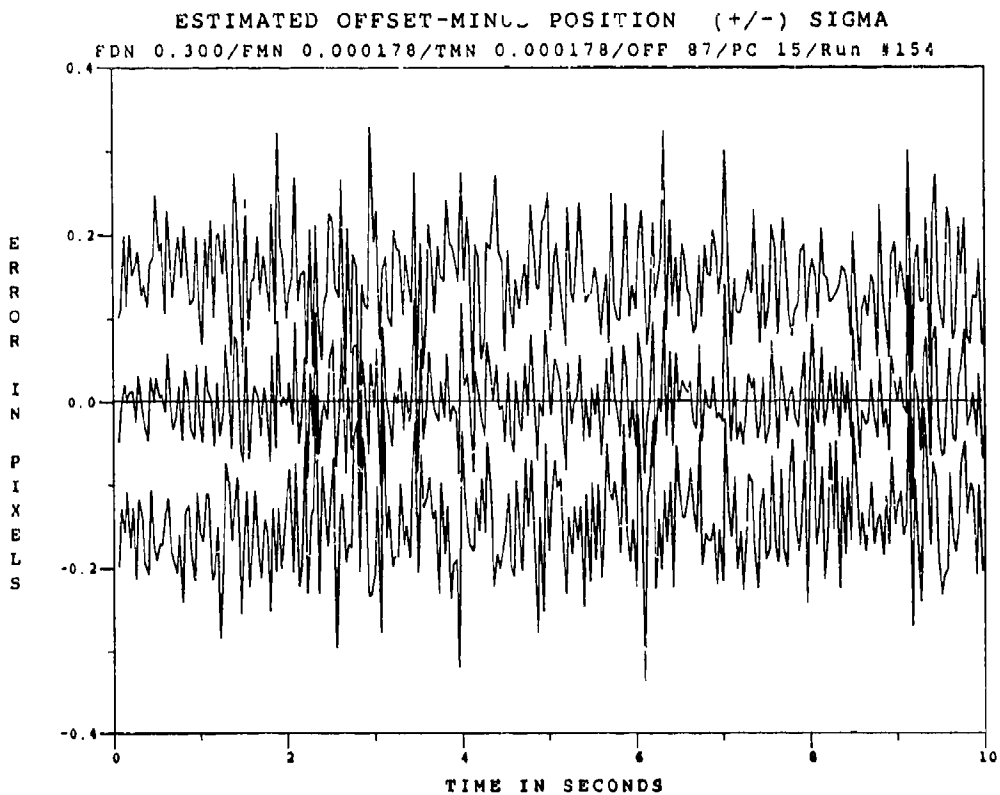


Figure C.5.2 10.5 μm Doppler Return One-State Filter Offset Error, SNR = 10, $P_m = 0.0$ at t_i

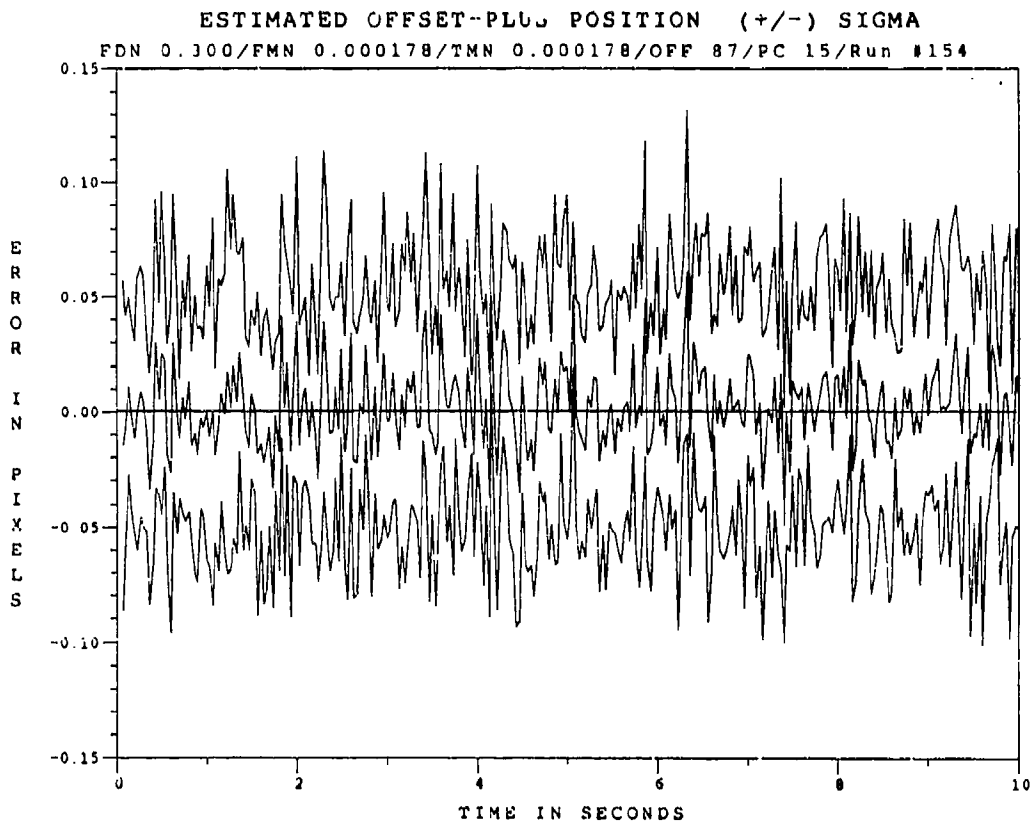


Figure C.5.3 10.5 μm Doppler Return One-State Filter Offset Error, SNR = 10, $P_{\text{off}} = 0.0$ at t_i^+

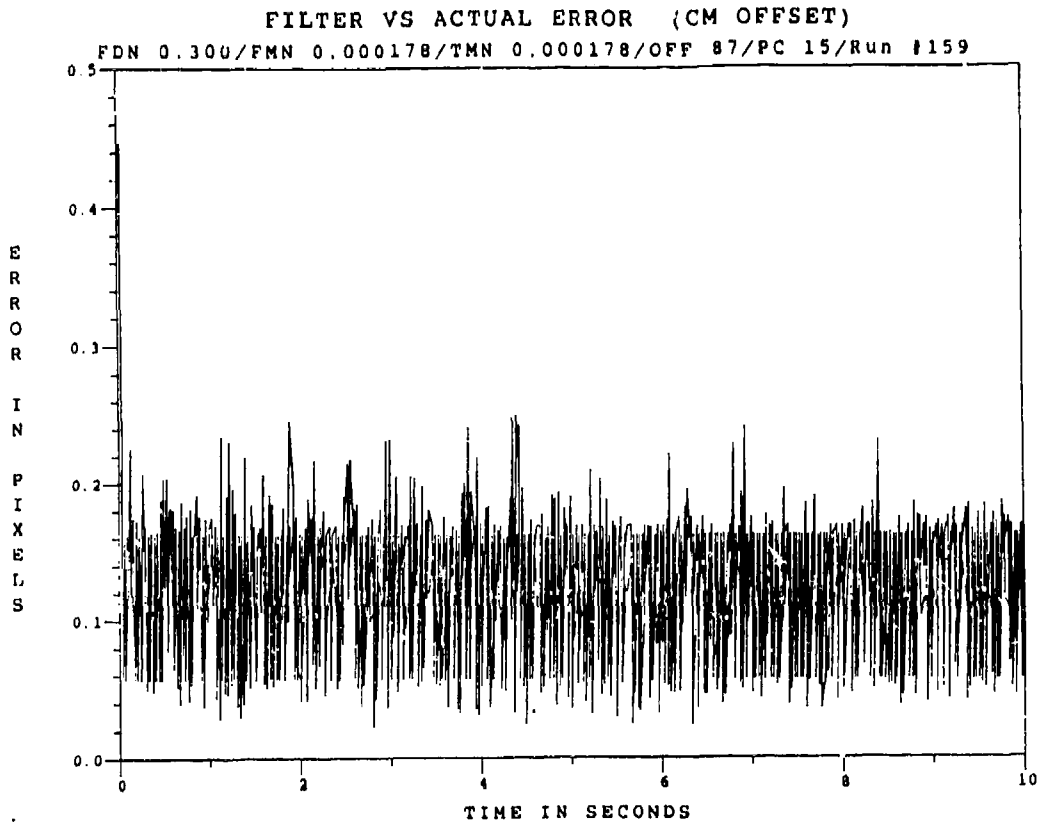


Figure C.5.4 10.5 μm Doppler Return One-State Filter Offset Error, SNR = 10, $P_m = 0.05$

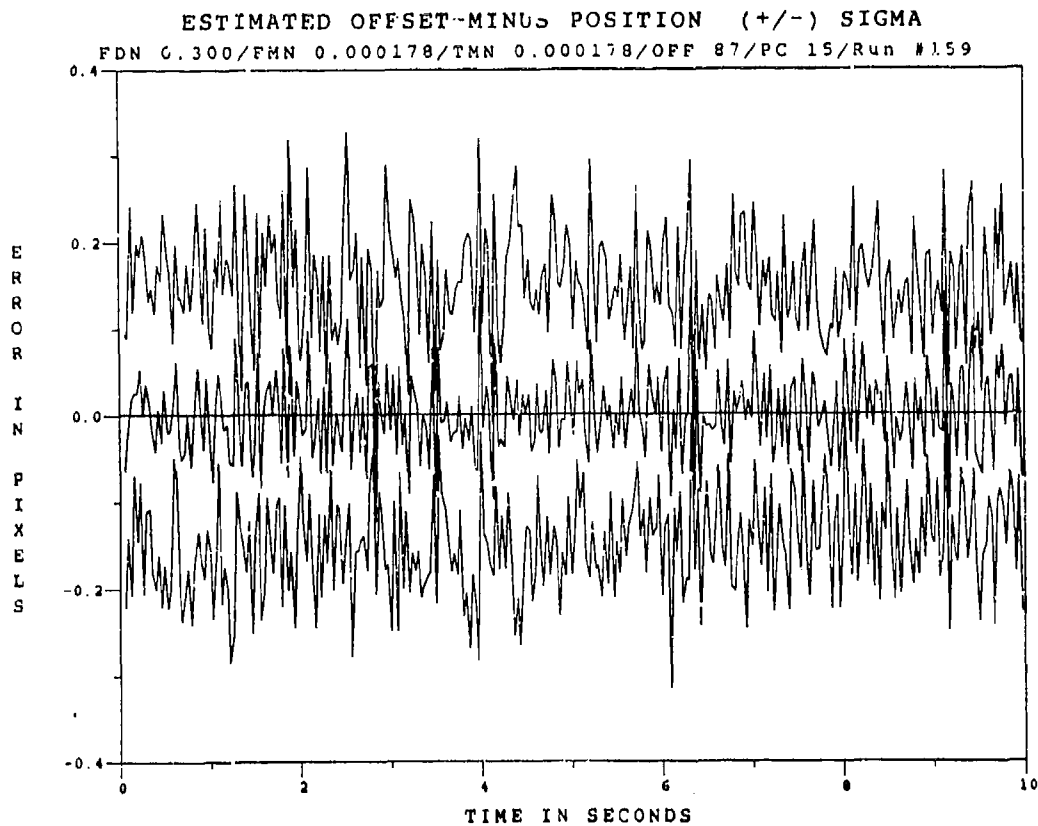


Figure C.5.5 10.5 μm Doppler Return One-State Filter Offset Error, SNR=10, $P_m = 0.05$, at t_j

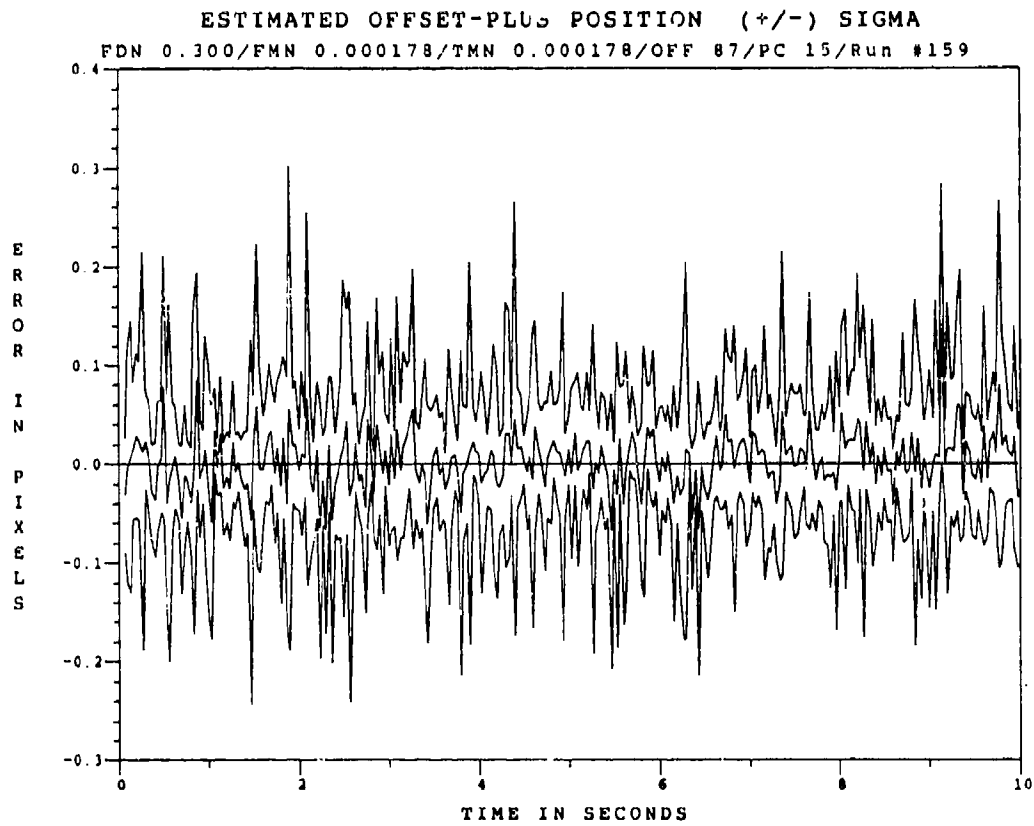


Figure C.5.6 10.5 μm Doppler Return One-State Filter Offset Error, SNR=10, $P_m = -0.05$, at t_i^+

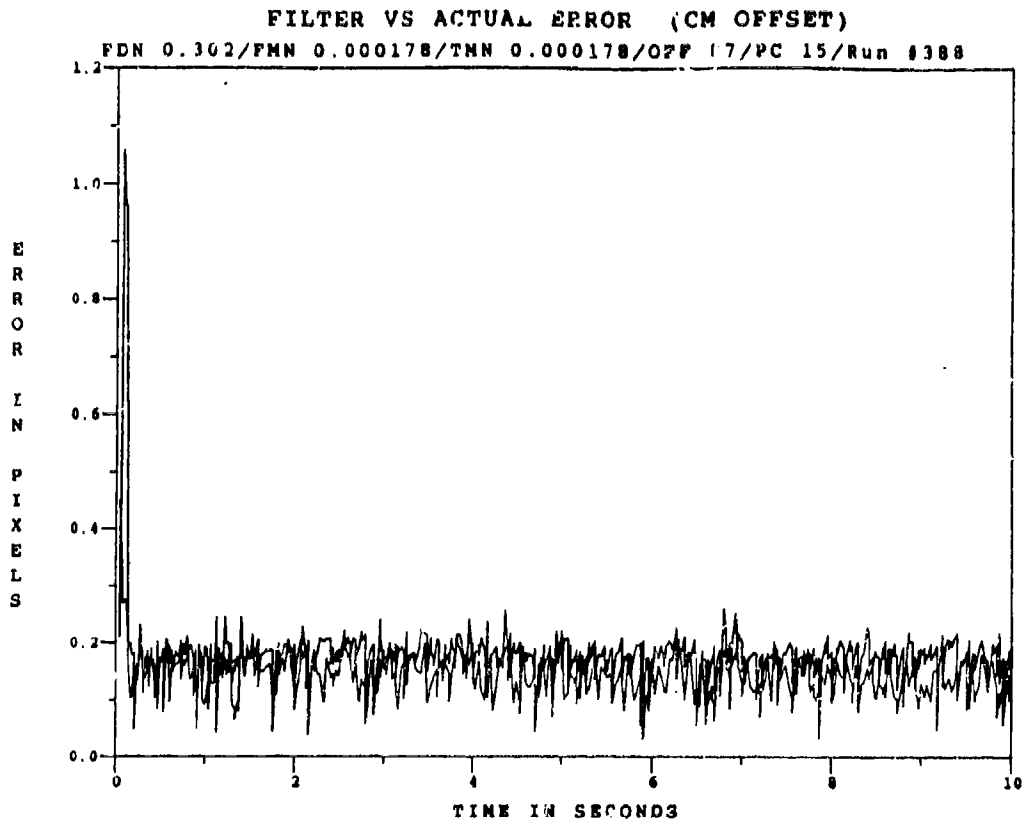


Figure C.5.7 10.5 μm Doppler Return One-State Filter Offset Error; SNR = 10, $P_m = 0.30$

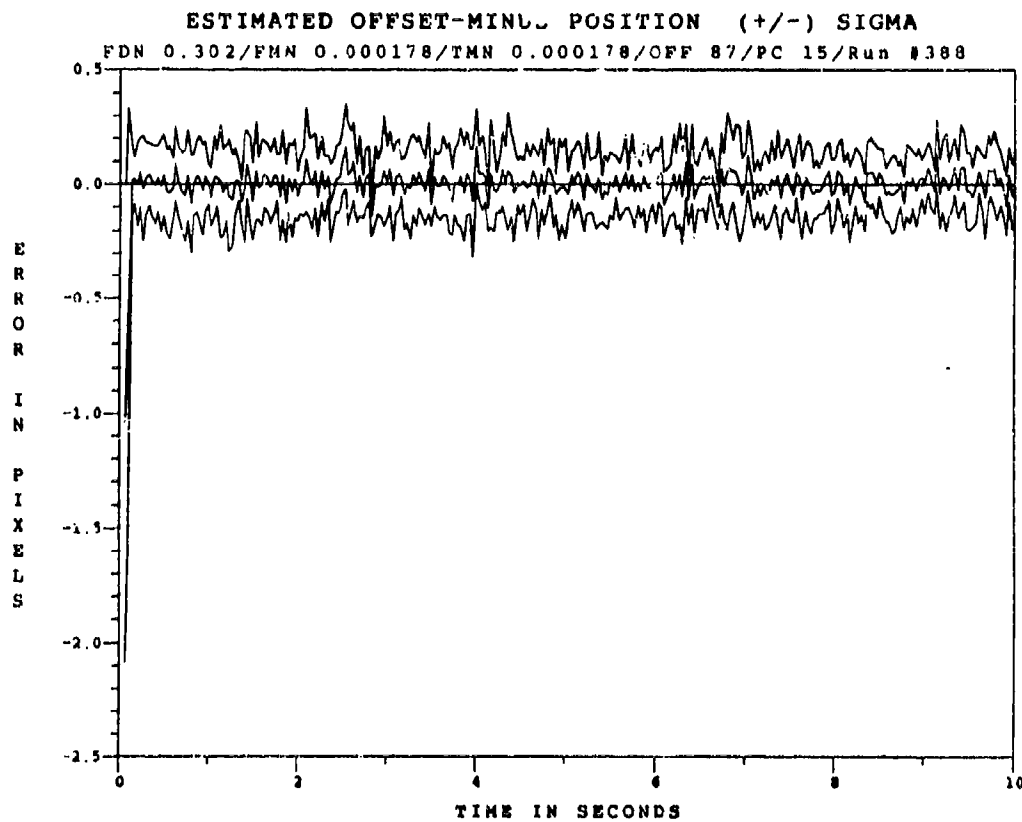


Figure C.5.8 10.5 μm Doppler Return One-State Filter Offset Error, SNR=10, $P_m = 0.30$, at t_i

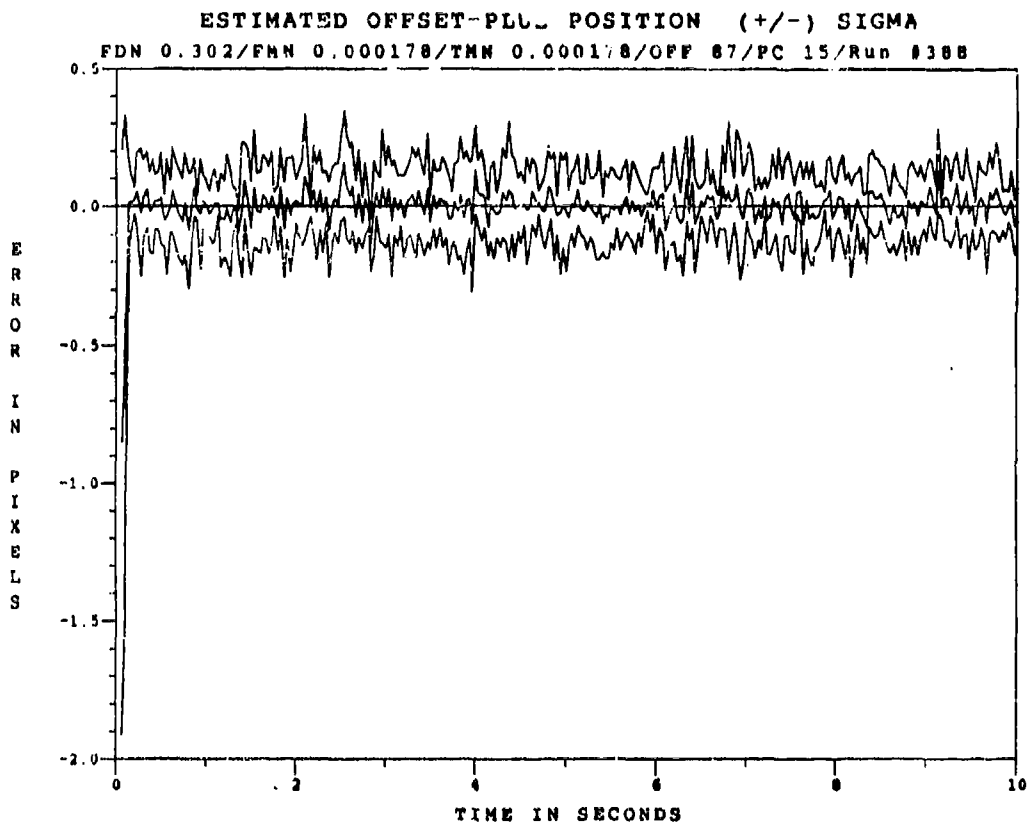


Figure C.5.9 10.5 μm Doppler Return One-State Filter Offset Error, SNR=10, $P_m = -0.30$, at t_1^*

Appendix C.6

One-State Center-of-Mass Filter

with

10.5 μm Doppler Return Measurements

at SNR = 4

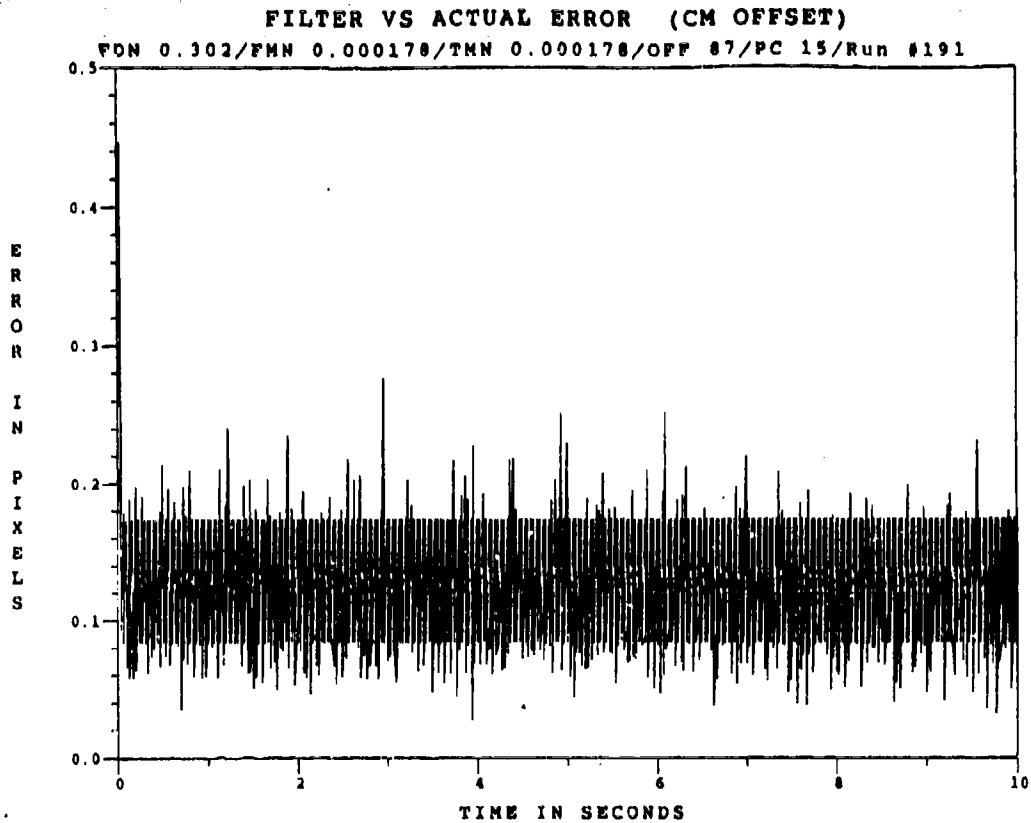


Figure C.6.1 10.5 μ m Doppler Return One-State Filter Offset Error with SNR = 4, $P_m = 0.0$

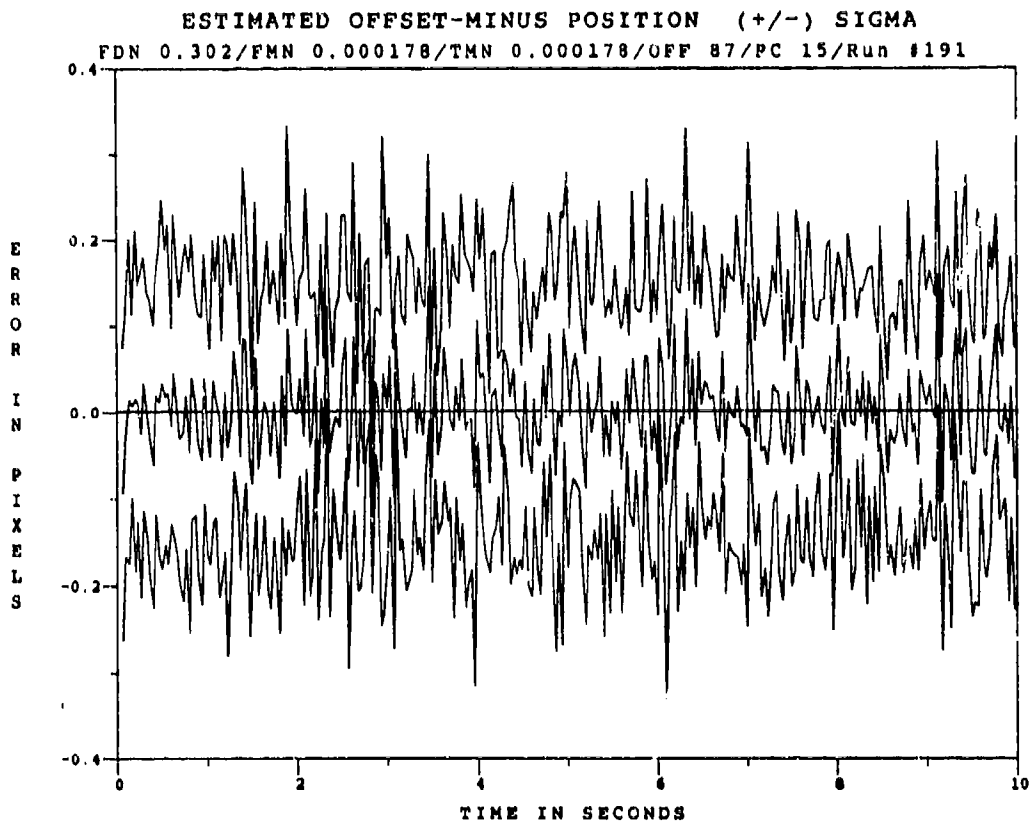


Figure C.6.2 10.5 μ m Doppler Return One-State Filter Offset Error, SNR = 4, $P_m = 0.0$ at t_i

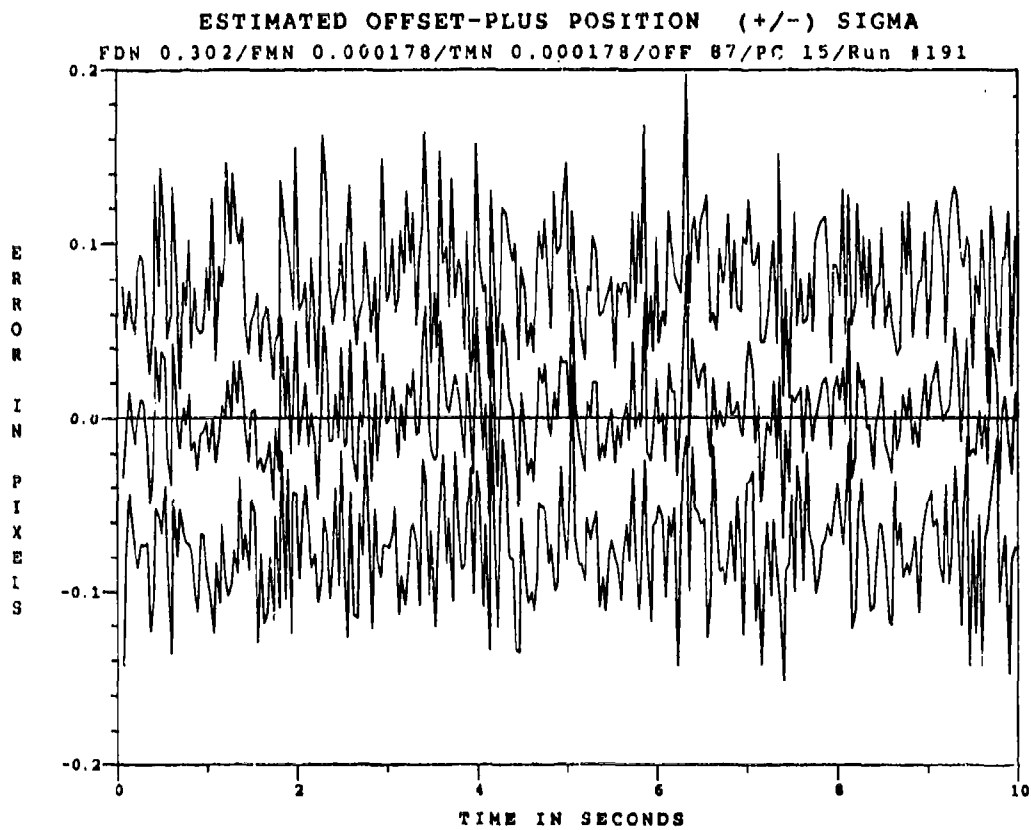


Figure C.6.3 10.5 μm Doppler Return One-State Filter Offset Error, SNR = 4, $P_m = 0.0$ at t_i^*

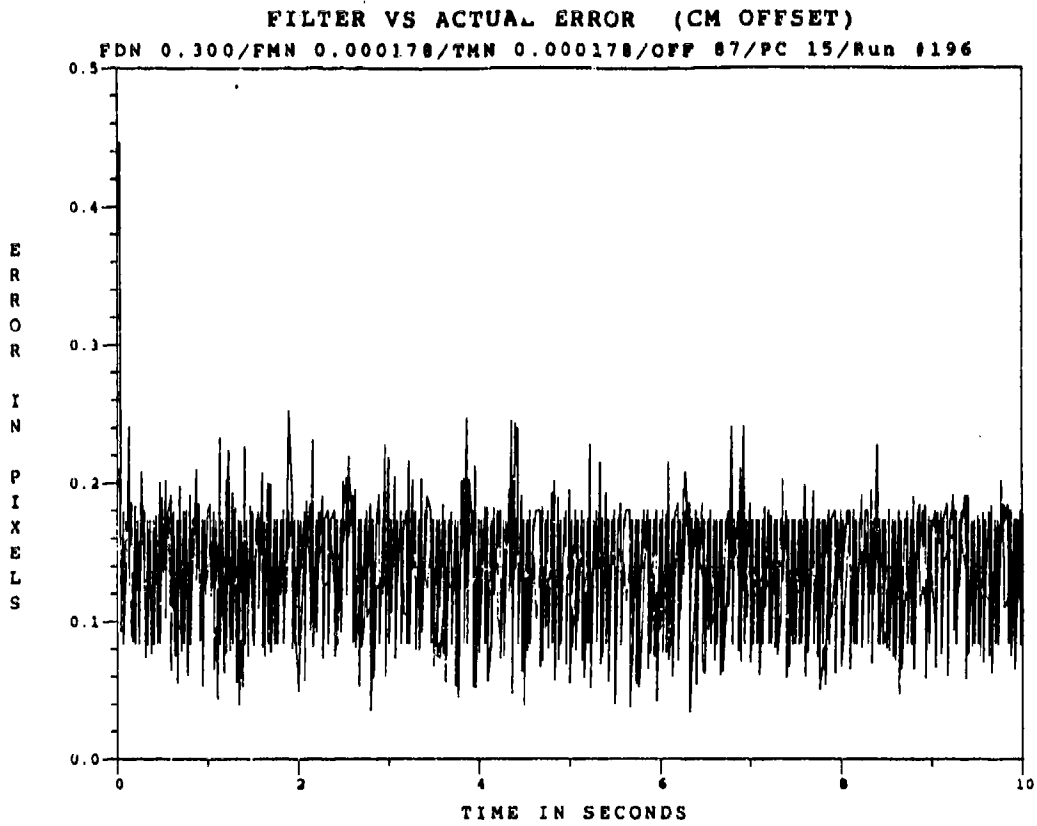


Figure C.6.4 10.5 μm Doppler Return One-State Filter Offset Error, SNR = 4, $P_m = 0.05$

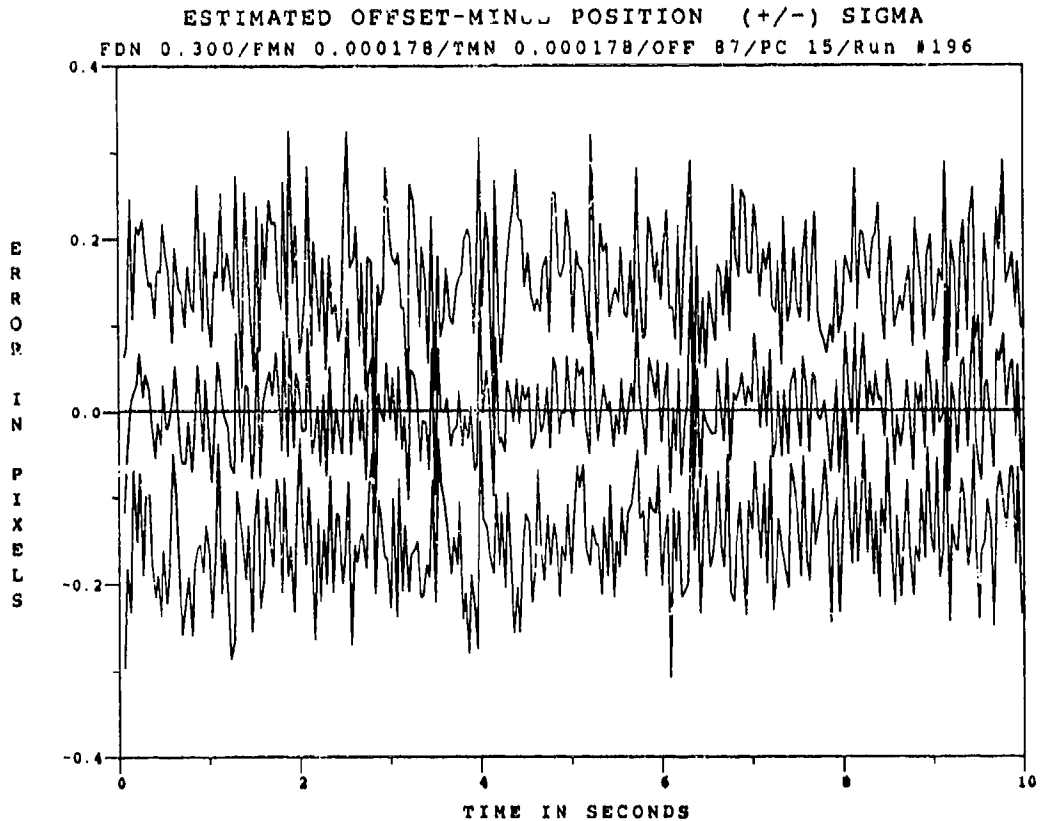


Figure C.6.5 10.5 μm Doppler Return One-State Filter Offset Error, SNR=4, $P_m = 0.05$, at t_i

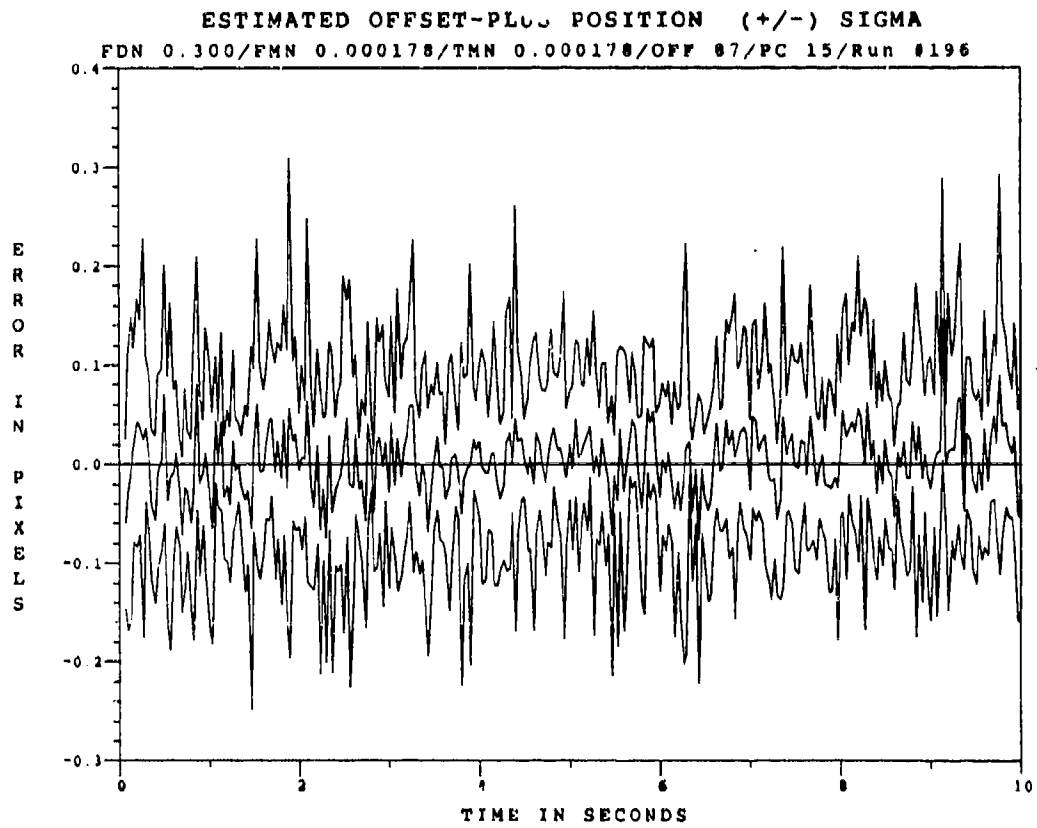


Figure C.6.6 10.5 μm Doppler Return One-State Filter Offset with $\text{SNR} = 4$, $P_m = 0.05$, at t_1^*

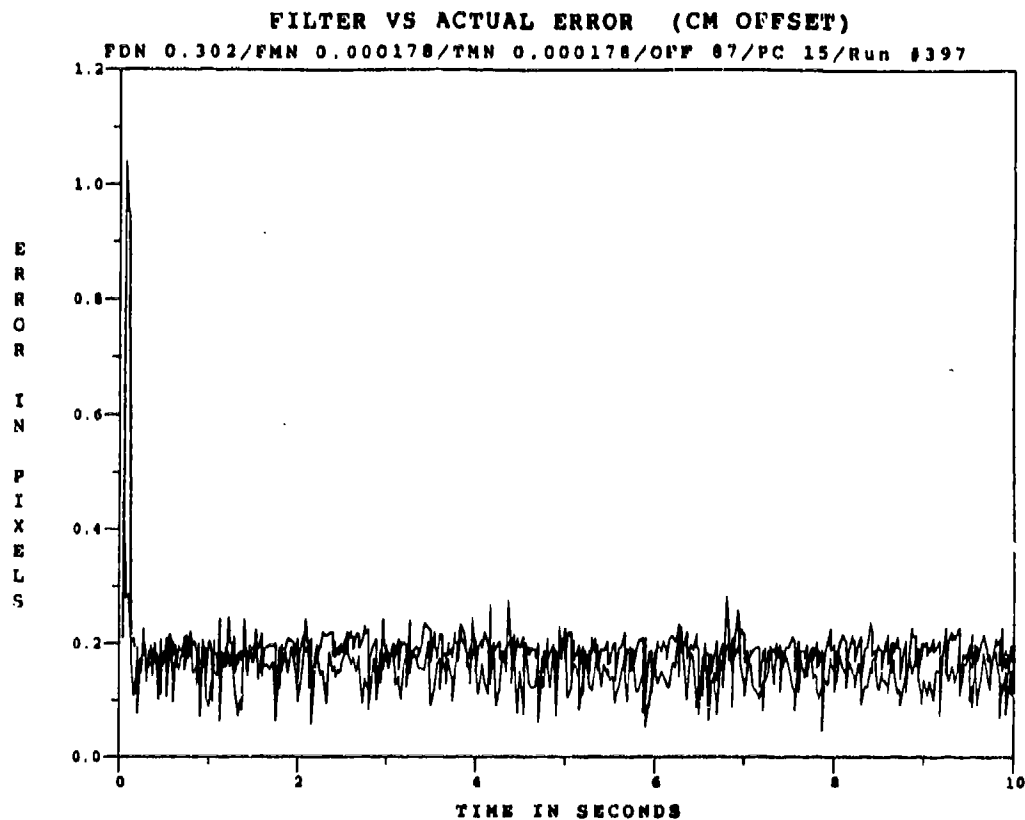


Figure C.6.7 10.5 μm Doppler Return One-State Filter Offset Error with $\text{SNR} = 4$, $P_m = 0.30$

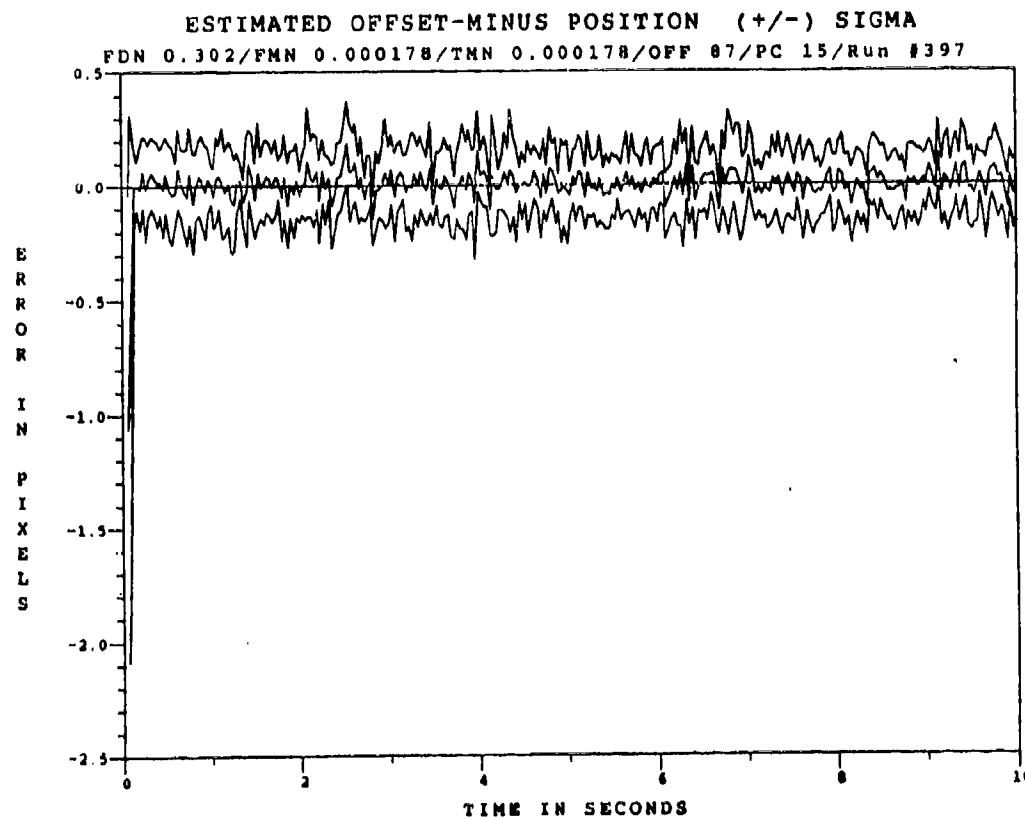


Figure C.6.8 10.5 μm Doppler Return One-State Filter Offset Error, $\text{SNR}=4$, $P_m = 0.30$, at t_i

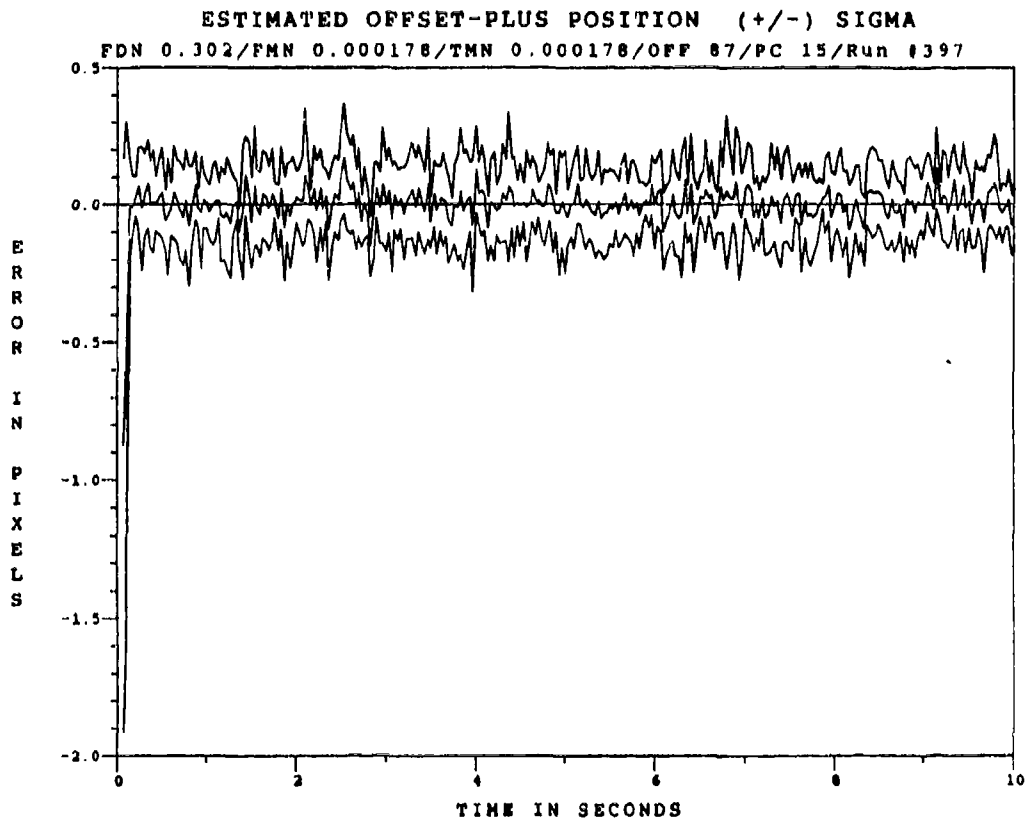


Figure C.6.9 10.5 μm Doppler Return One-State Filter Offset Error, $\text{SNR}=4$, $P_{\text{m}} = 0.30$, at t_i^*

Appendix D

Two-State Modified MAP MMAF

Tuning Runs

This appendix contains the offset error plots that resulted from 5 of the 11 tuning runs for the two-state Modified MAP MMAF. For each tuning run, there are two sets of plots that are respectively associated with the two states (the offset distance state and the plume speckle reflectance bias state). With each set, there are the two types of plots, as discussed in Appendix B. Table D.1 lists the different values for the dynamics noise variances q_{df11} and q_{df22} that were explored during the tuning efforts. For the initial tuning values, the filter dynamics variances were set equal to the values mentioned in Sections 5.3.3.2 and 5.3.3.4 for each one-state filter. The covariance of the discrete-time white Gaussian noise w_{df} , given by Q_{df} of Equation (5-39), is:

$$Q_{df} = \begin{bmatrix} q_{df11} & 0.0 \\ 0.0 & q_{df22} \end{bmatrix} \quad (D.1)$$

where

$$\begin{aligned} q_{df11} &= \text{offset dynamics noise variance} \\ q_{df22} &= \text{bias dynamics noise variance} \end{aligned}$$

From Figure D.1, it can be seen that these original tuning values were overly conservative. The variances were gradually decreased by an order of magnitude until the overall time histories of rms errors and the filter computed-rms error matched well. As seen in Table D.1, decreasing the dynamics noise strengths q_{df11} and q_{df22} produced negligible differences in performance; however, the last entry was chosen based upon its performance plot in Figure D.25.

Referring back to Equation (5-56), the two-state modified MAP MMAF dynamics noise covariance Q_{df} , in units of pixels², is given by:

$$Q_{df} = \begin{bmatrix} 0.03 & 0.0 \\ 0.0 & 0.001 \end{bmatrix} \quad (D.2)$$

Table D.1 Tuning Values for Dynamics Noise Variances (in Pixels²)

q_{a11} (pixels ²)	q_{a22} (pixels ²)	RMS errors, t_i^- (pixels)	RMS errors, t_i^+ (pixels)	Figure No.
0.7	0.7	0.1491	0.0032	D.1-6
0.7	0.07	0.1491	0.0032	D.7-12
0.7	0.007	0.1491	0.0032	NA
0.7	0.01	0.1491	0.0032	NA
.07	0.07	0.1491	0.0032	NA
0.07	0.01	0.1491	0.0032	NA
0.07	0.007	0.1491	0.0032	D.13-18
0.007	0.0007	0.1489	0.00319	D.19-24
0.01	0.001	0.1490	0.00319	NA
0.02	0.001	0.1490	0.00319	NA
0.03	0.001	0.1490	0.00319	D.25-30

FILTER VS ACTUAL ERROR (CM OFFSET)

FDN 0.300/FMN 0.000179 TMN 0.000179/OFF 87/PC 15/Run #mm3

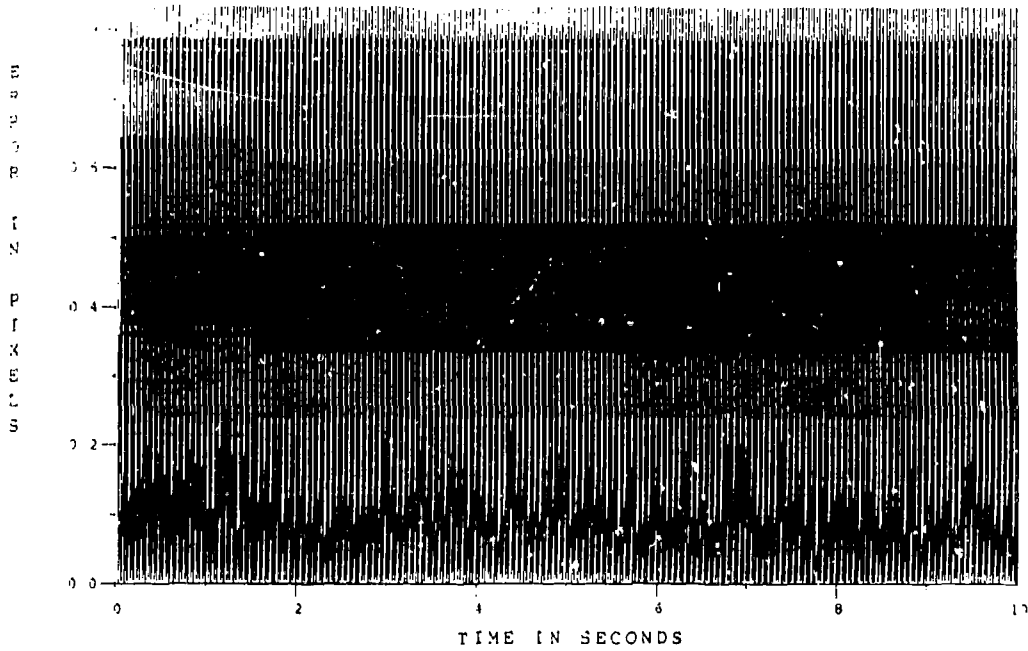


Figure D.1 Two-State Modified MAP MMAF Offset Error. $q_{\sigma 11} = 0.7$. $q_{\sigma 22} = 0.7$

ESTIMATED OFFSET-MINUS POSITION (+/-) SIGMA

FDN 0.300/FMN 0.000179 TMN 0.000179/OFF 87/PC 15/Run #mm3

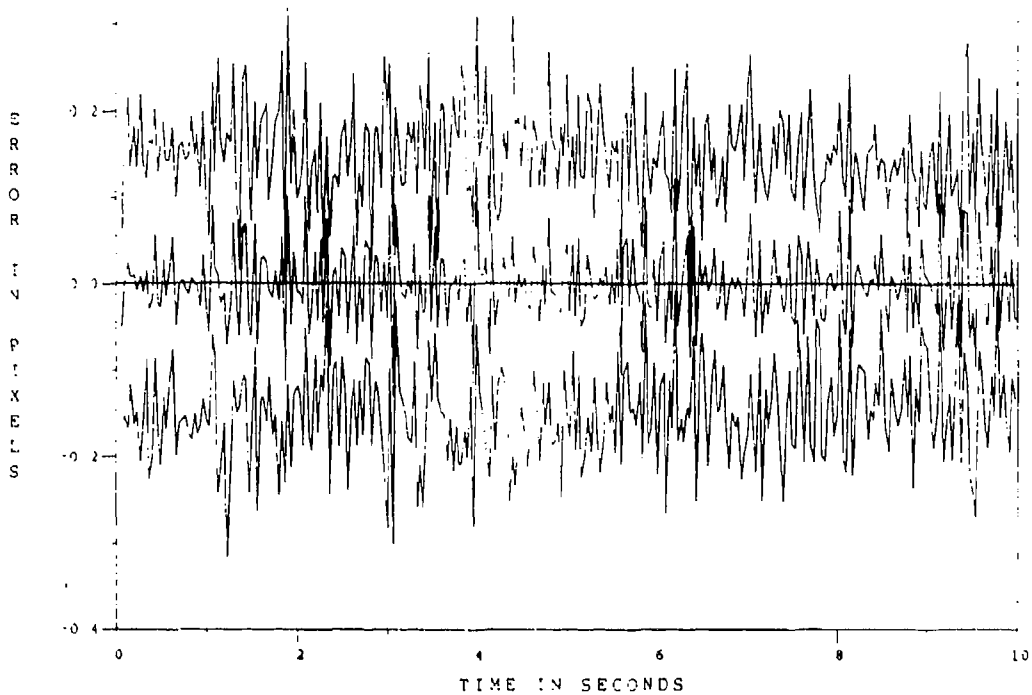


Figure D.2 Two-State Modified MAP MMAF Offset Error at t_i . $q_{\sigma 11} = 0.7$. $q_{\sigma 22} = 0.7$

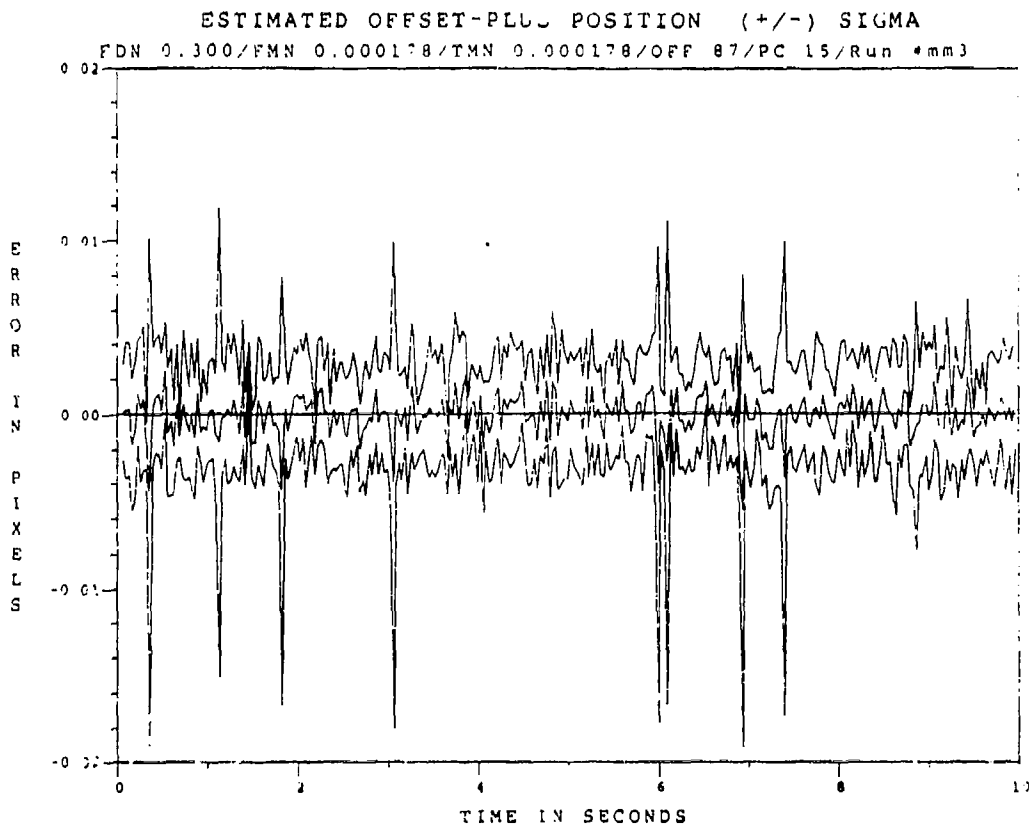


Figure D.3 Two-State Modified MAP MMAF Offset Error at t_1^+ , $q_{d11} = 0.7$, $q_{d22} = 0.7$

FILTER VS ACTUAL ERROR (BIAS)

FDN 0.000/FMN 0.000178 TMN 0.000178/OFF 97/PC 15/Run #mm3

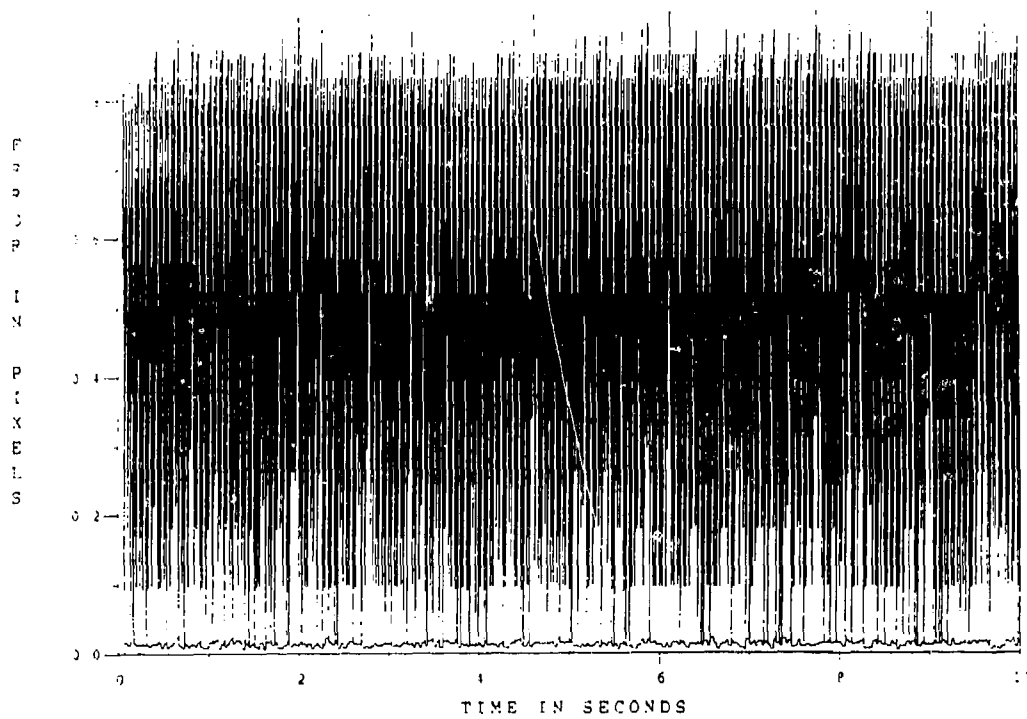


Figure D.4 Two-State Modified MAP MMAF Bias Error, $q_{af11} = 0.7$, $q_{af22} = 0.7$

ESTIMATED BIAS...INUS (+/-) SIGMA

FDN 0.000/FMN 0.000178 TMN 0.000178/OFF 97/PC 15/Run #mm3

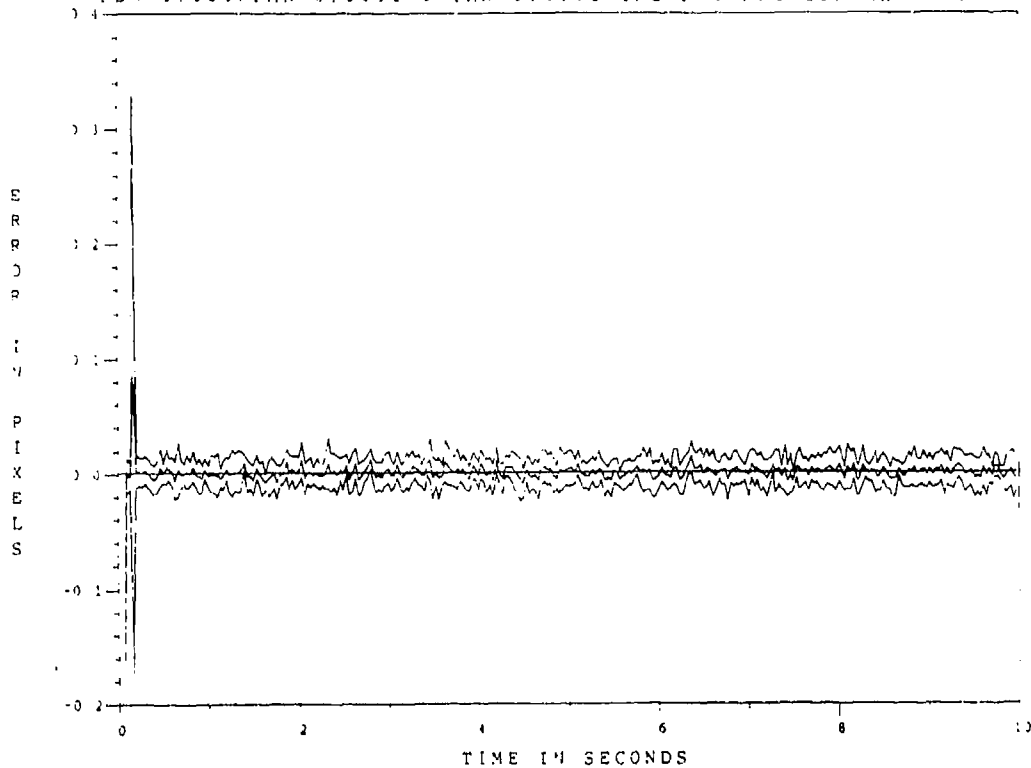


Figure D.5 Two-State Modified MAP MMAF Bias Error at t_i , $q_{af11} = 0.7$, $q_{af22} = 0.7$

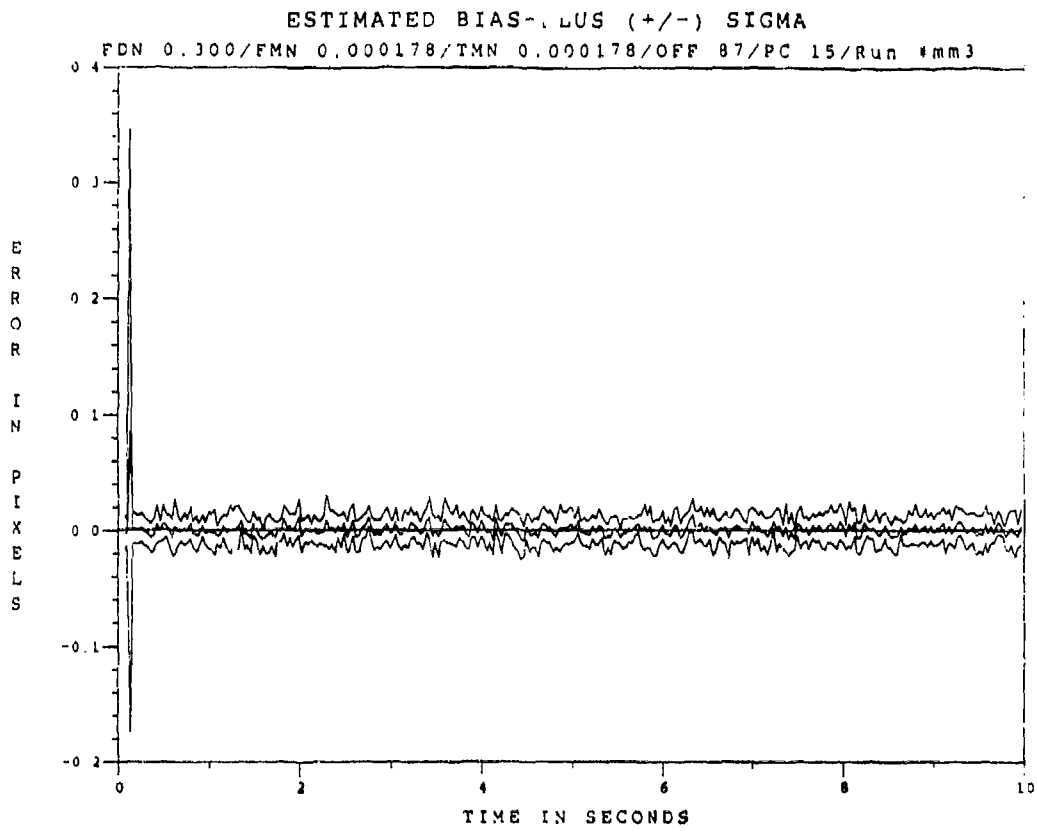


Figure D.6 Two-State Modified MAP MMAF Bias Error at t_i^* , $q_{\sigma 11} = 0.7$, $q_{\sigma 22} = 0.7$

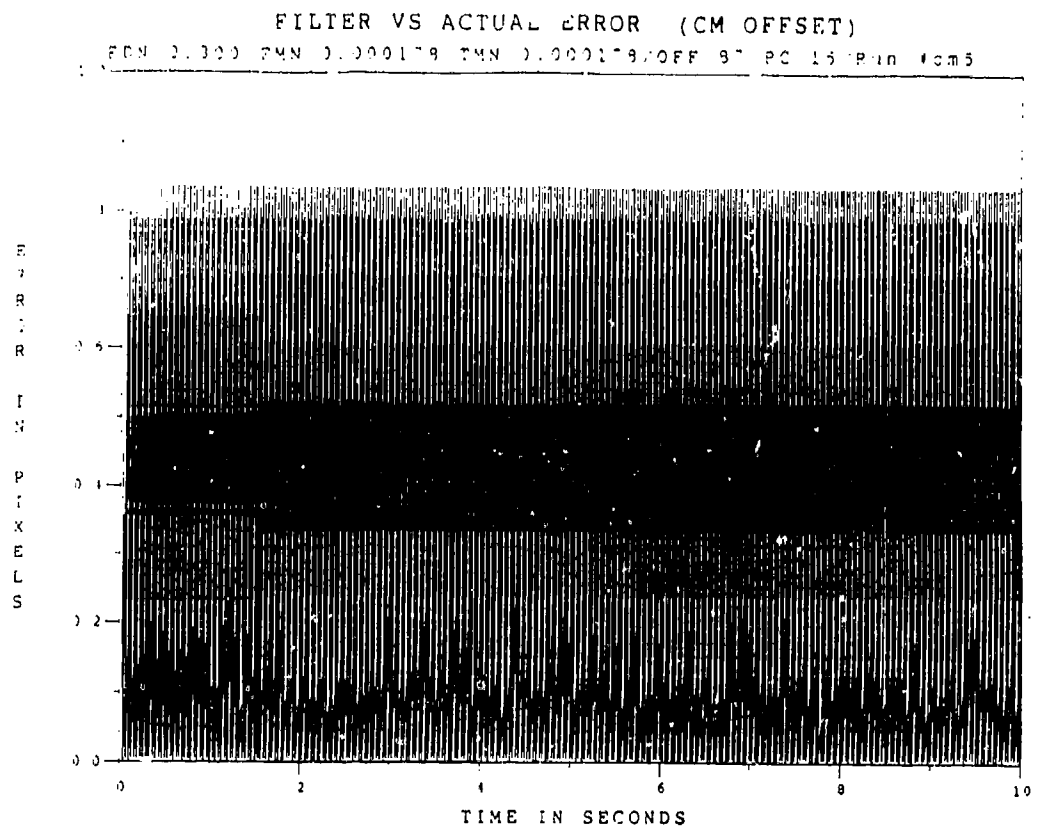


Figure D.7 Two-State Modified MAP MMAF Offset Error, $q_{af11} = 0.7, q_{af22} = 0.07$

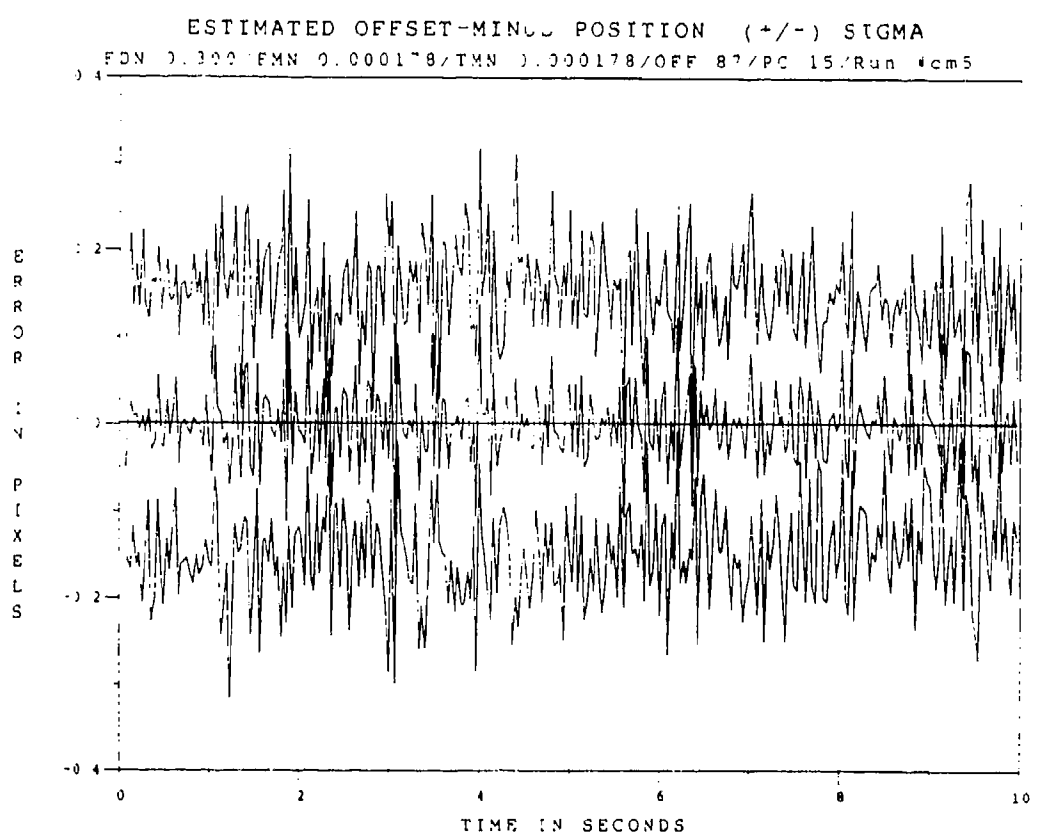


Figure D.8 Two-State Modified MAP MMAF Offset Error at $t_i, q_{af11} = 0.7, q_{af22} = 0.07$

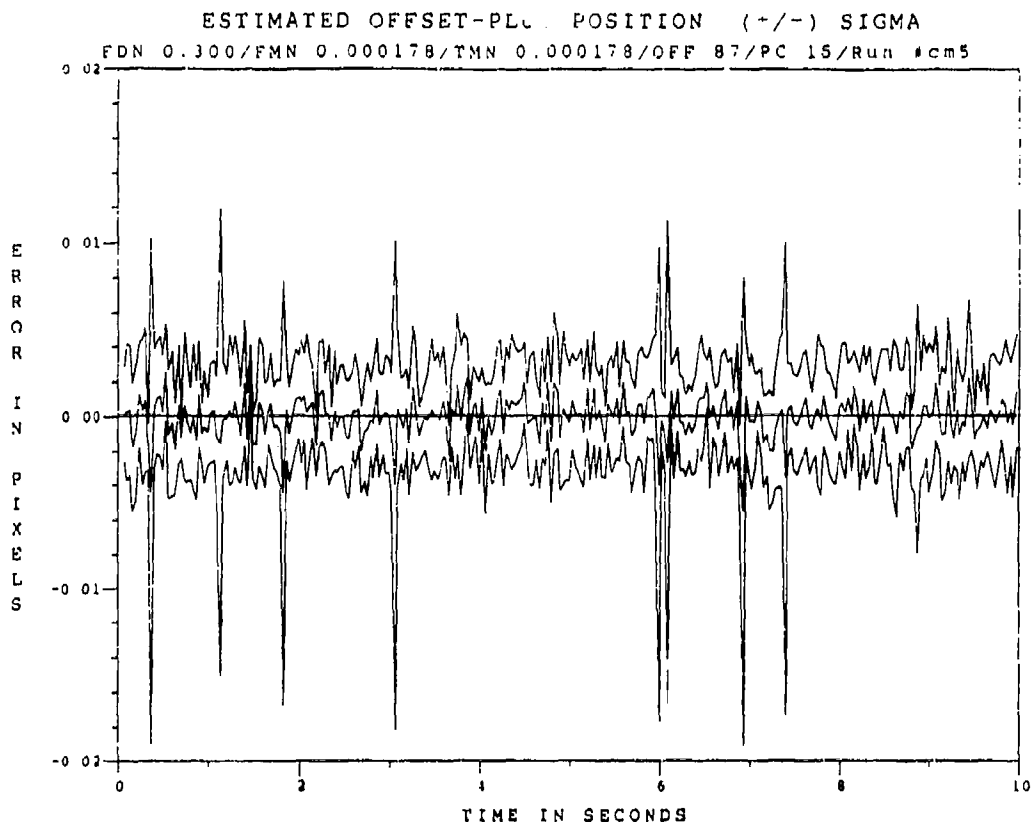


Figure D.9 Two-State Modified MAP MMAF Offset Error at t_i^* , $q_{af11} = 0.7$, $q_{af22} = 0.07$

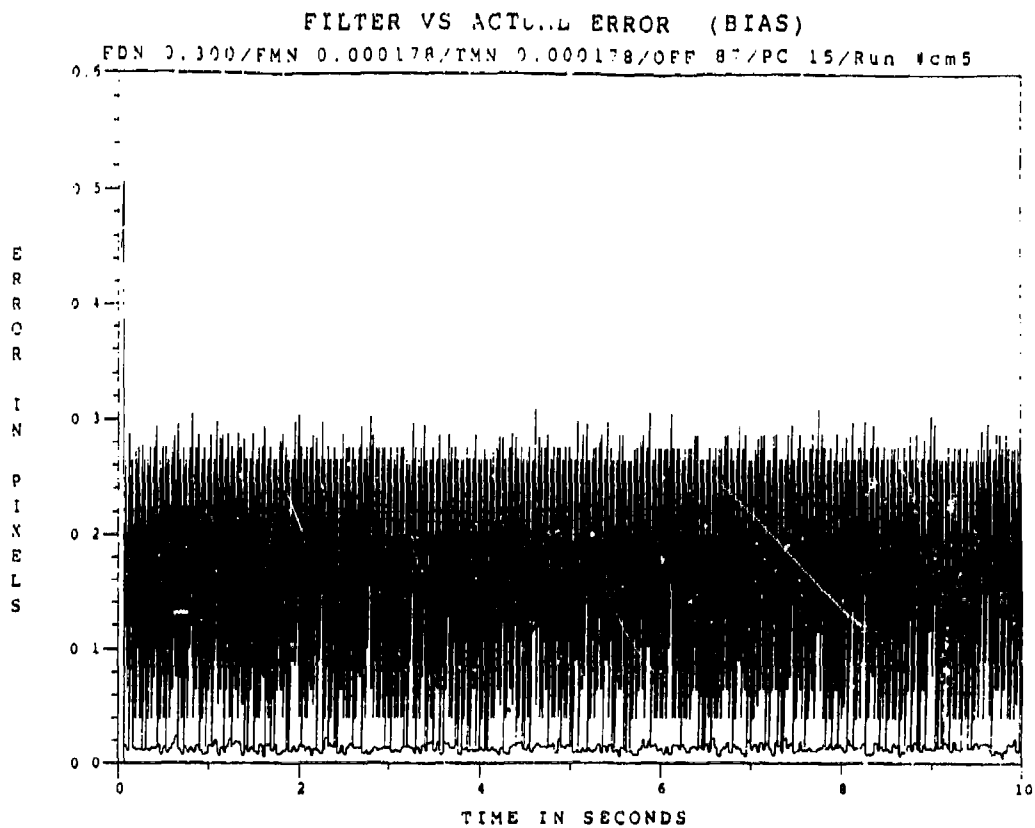


Figure D.10 Two-State Modified MAP MMAF Bias Error. $q_{\sigma 11} = 0.7$, $q_{\sigma 22} = 0.07$

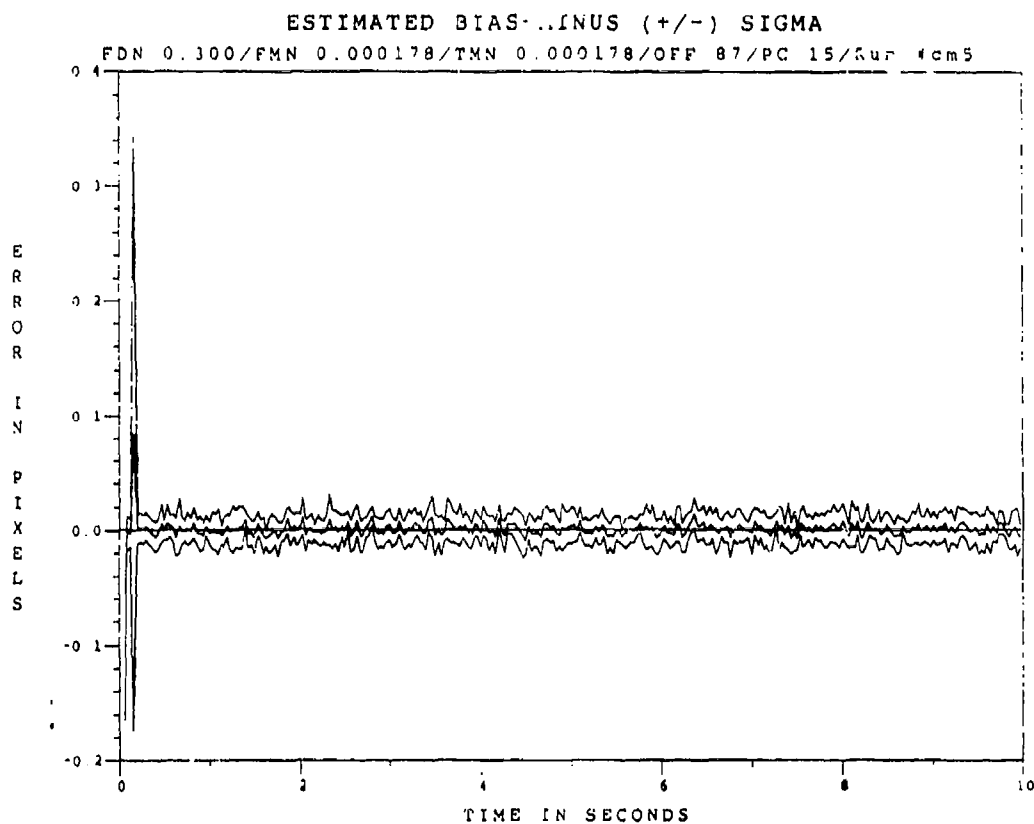


Figure D.11 Two-State Modified MAP MMAF Bias Error at t_i , $q_{\sigma 11} = 0.7$, $q_{\sigma 22} = 0.07$

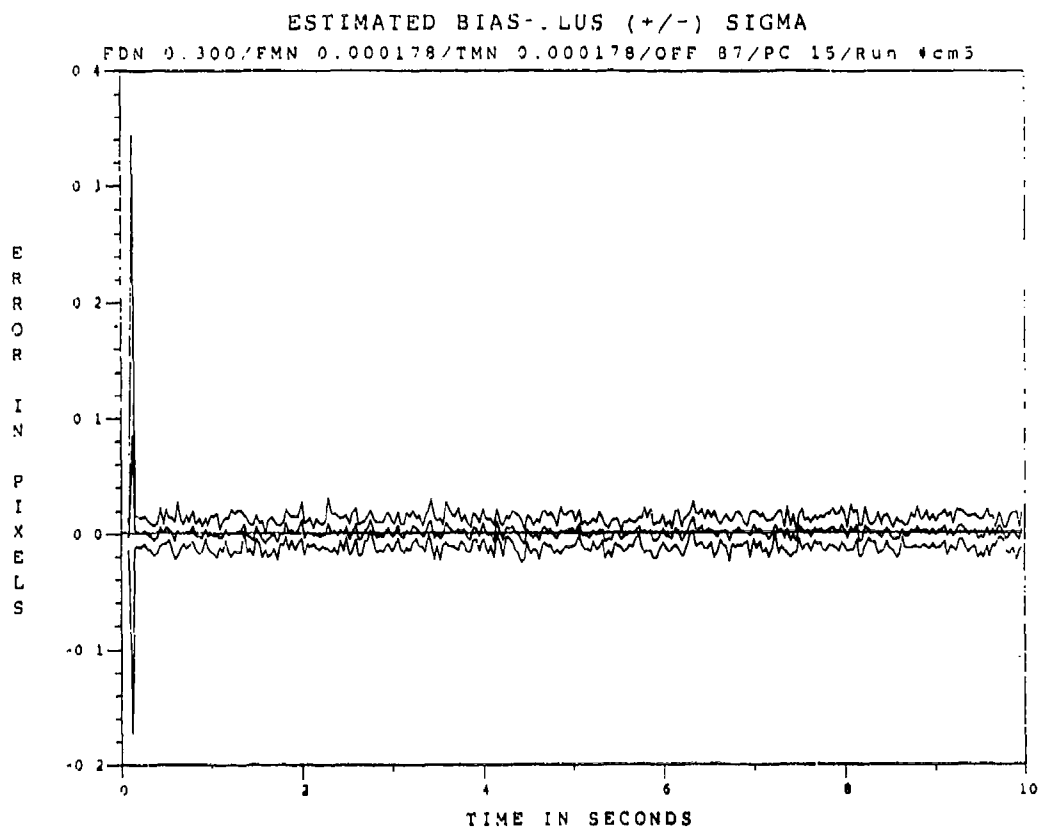


Figure D.12 Two-State Modified MAP MMAP Bias Error at t_1^* , $q_{M11} = 0.7$, $q_{M22} = 0.07$

FILTER VS ACTUAL ERROR (CM OFFSET)

FDN 0.300/FMN 0.000178/TMN 0.000178/OFF 87/PC 15/Run *cm8

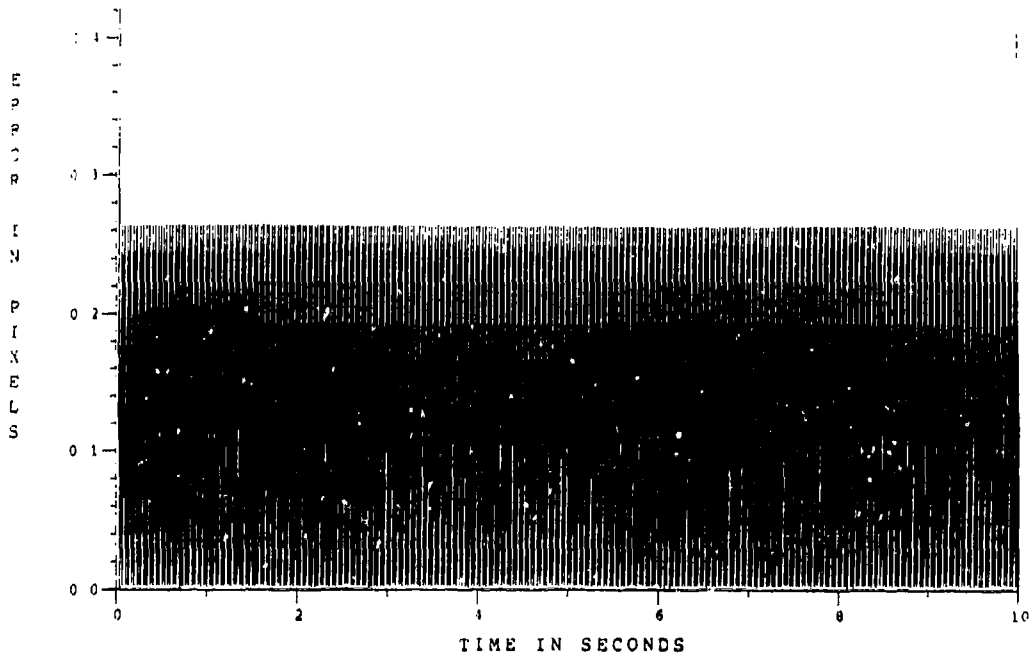


Figure D.13 Two-State Modified MAP MMAF Offset Error, $q_{af11} = 0.07$, $q_{af22} = 0.007$

ESTIMATED OFFSET-MINUT. POSITION (+/-) SIGMA

FDN 0.300/FMN 0.000178/TMN 0.000178/OFF 87/PC 15/Run *cm8

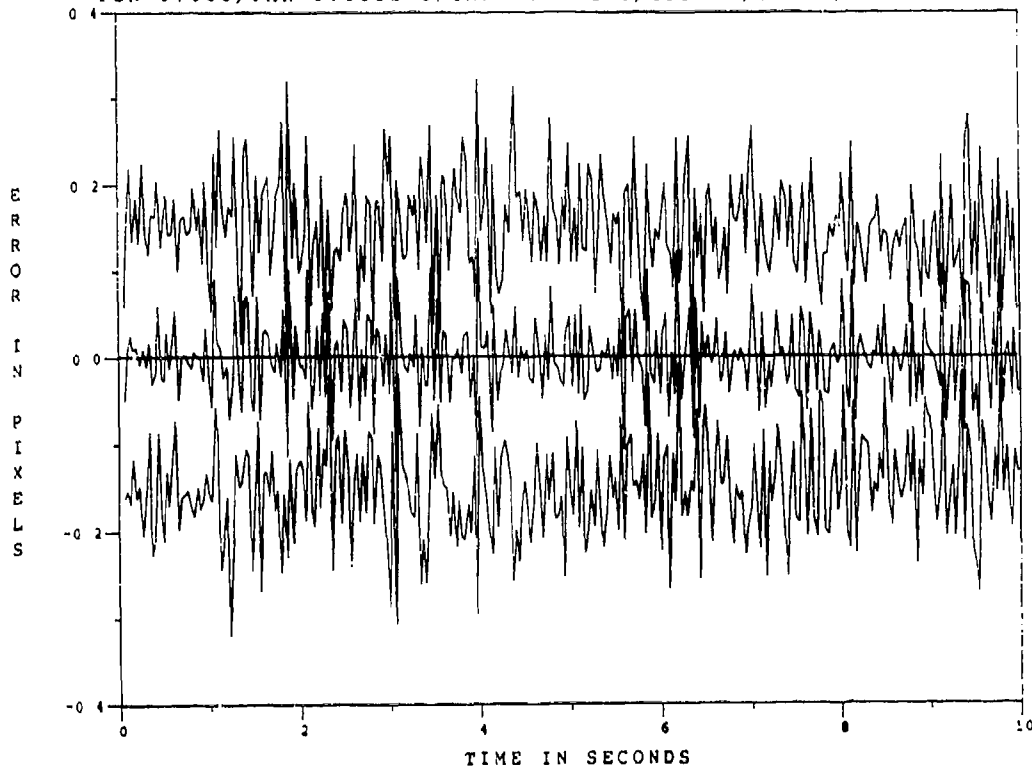


Figure D.14 Two-State Modified MAP MMAF Offset Error at t_i , $q_{af11} = 0.07$, $q_{af22} = 0.007$

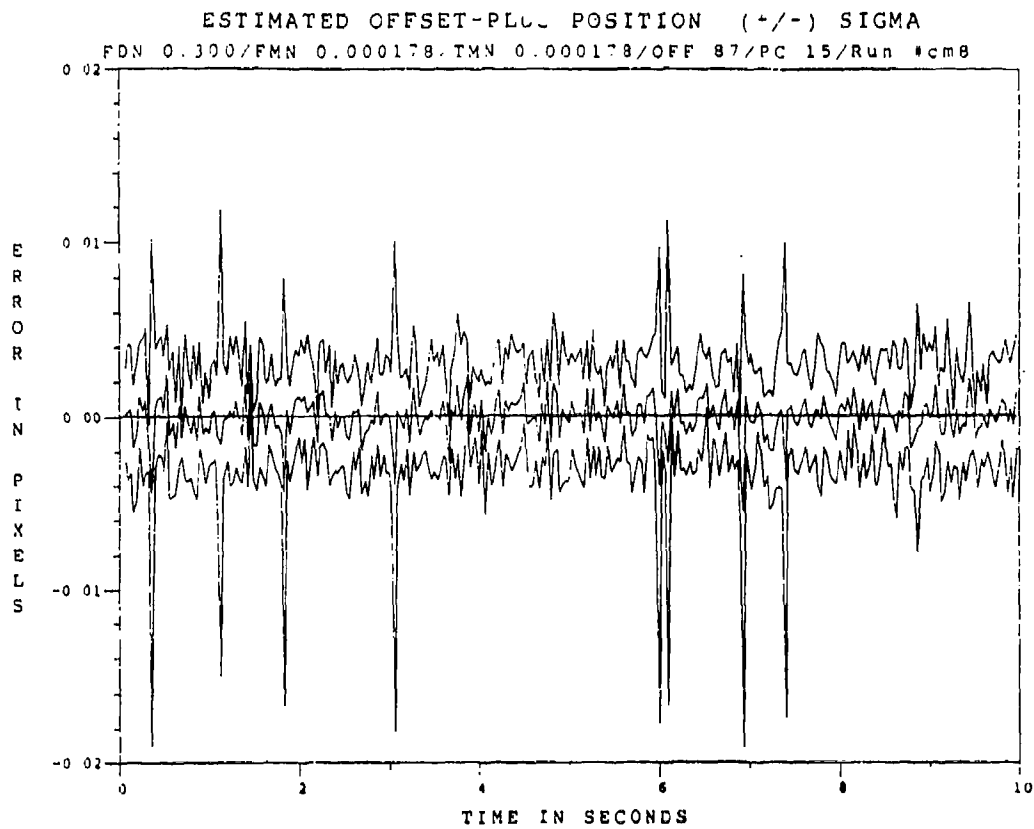


Figure D.15 Two-State Modified MAP MMAF Offset Error at t_1^* , $q_{\alpha 11} = 0.07$, $q_{\alpha 22} = 0.007$

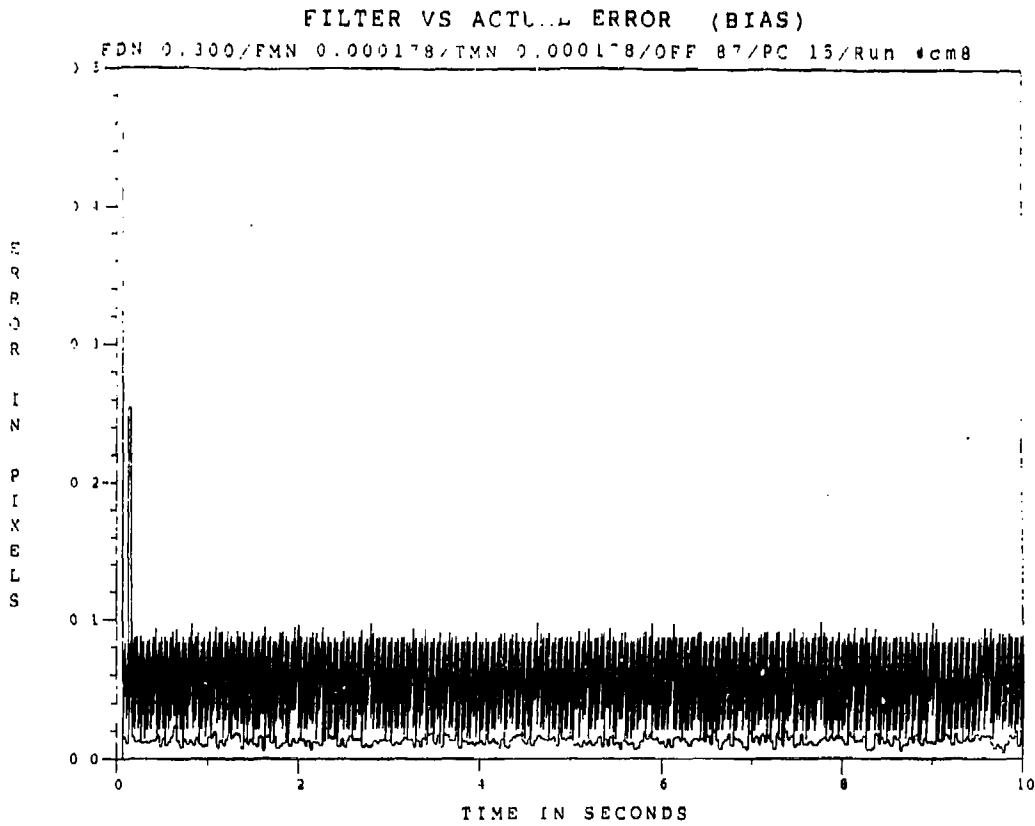


Figure D.16 Two-State Modified MAP MMAF Bias Error, $q_{d11} = 0.07$, $q_{d22} = 0.007$

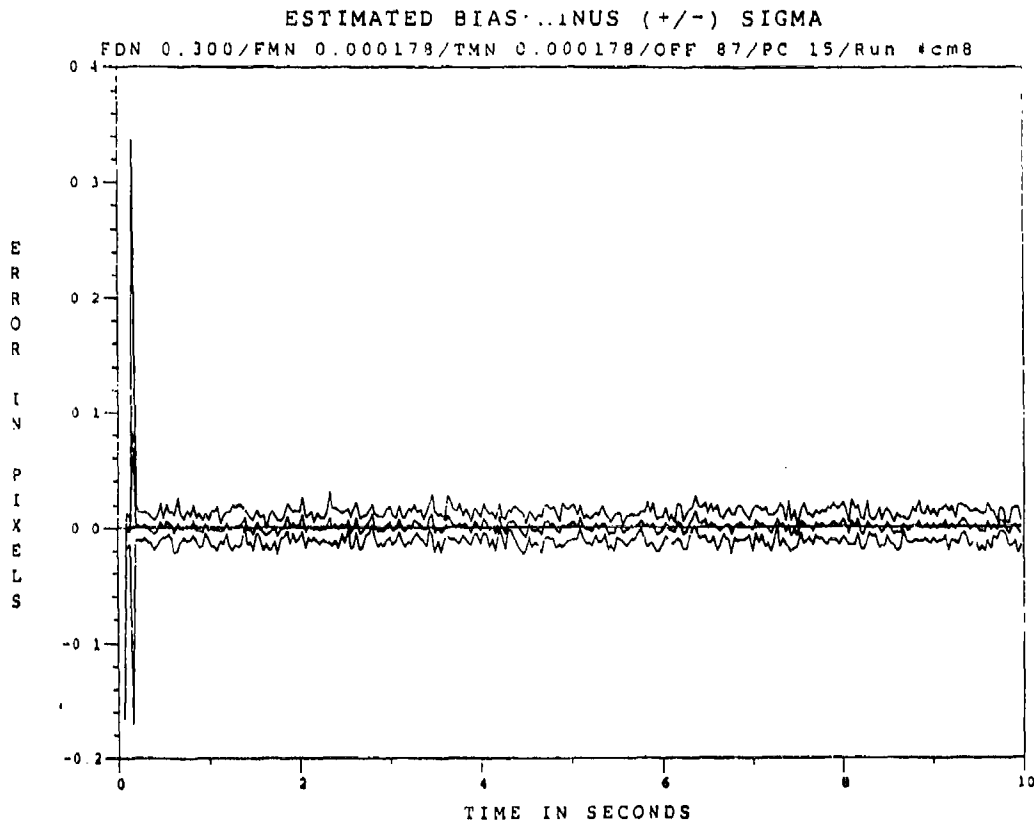


Figure D.17 Two-State Modified MAP MMAF Bias Error at t_i , $q_{d11} = 0.07$, $q_{d22} = 0.007$

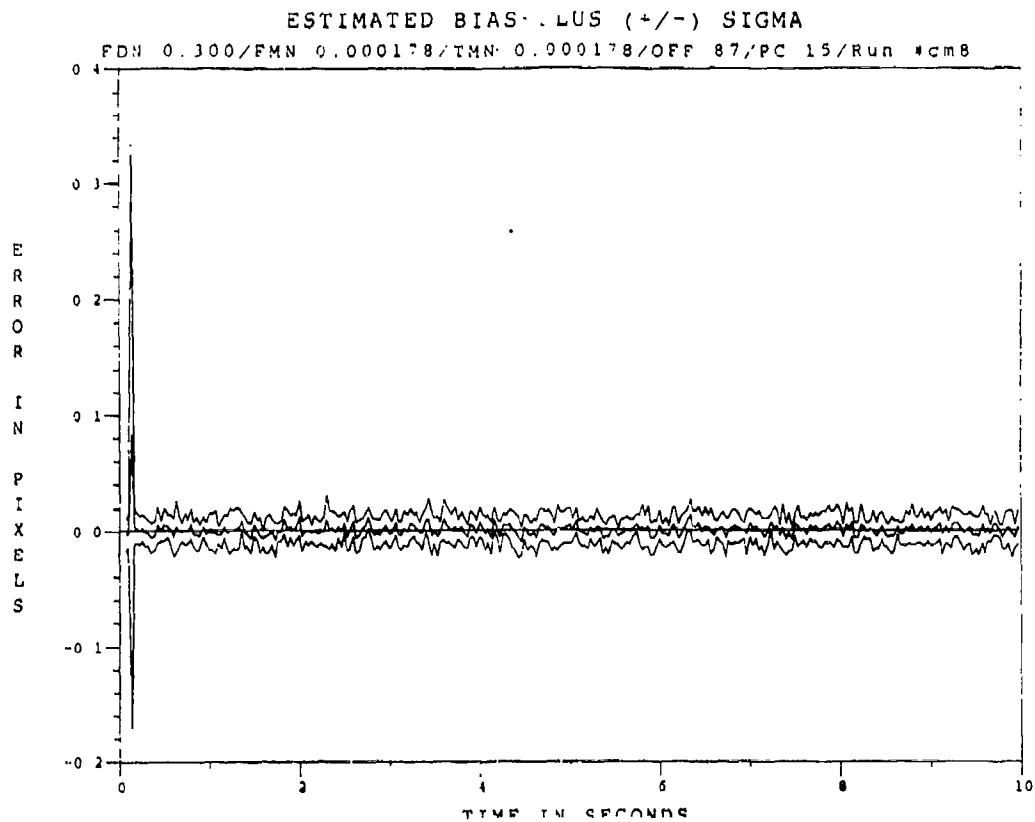


Figure D.18 Two-State Modified MAP MMAF Bias Error at t_i^* , $q_{\sigma 11} = 0.07$, $q_{\sigma 22} = 0.007$

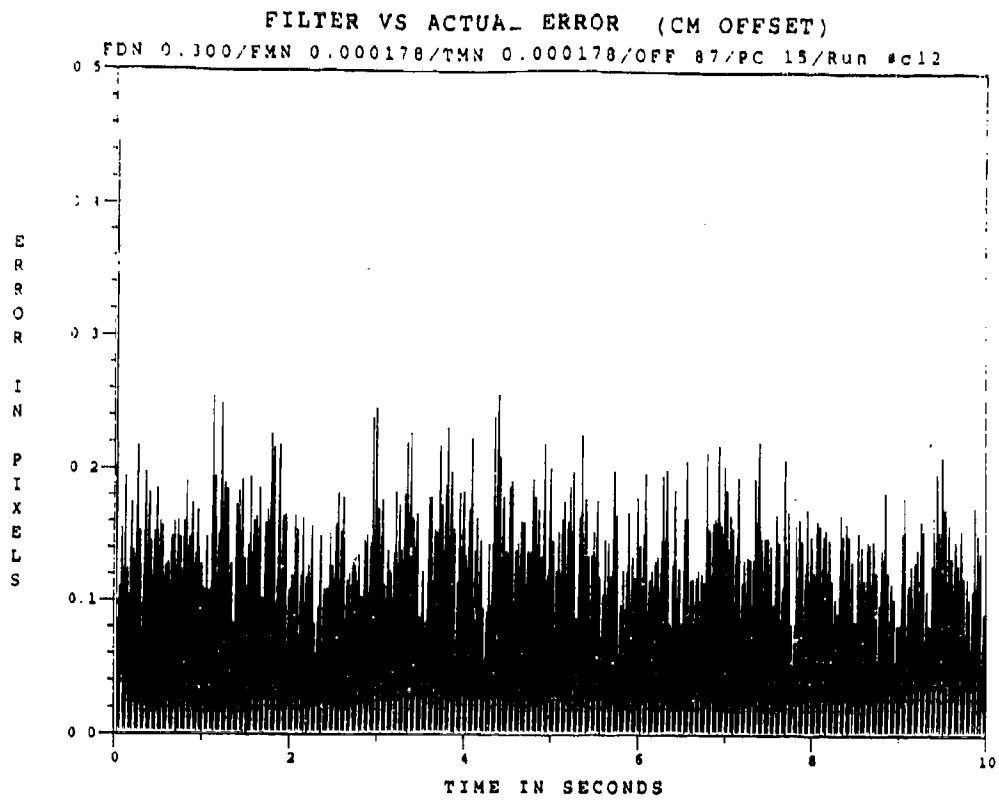


Figure D.19 Two-State Modified MAP MMAF Offset Error, $q_{\sigma 11} = 0.007$, $q_{\sigma 22} = 0.0007$

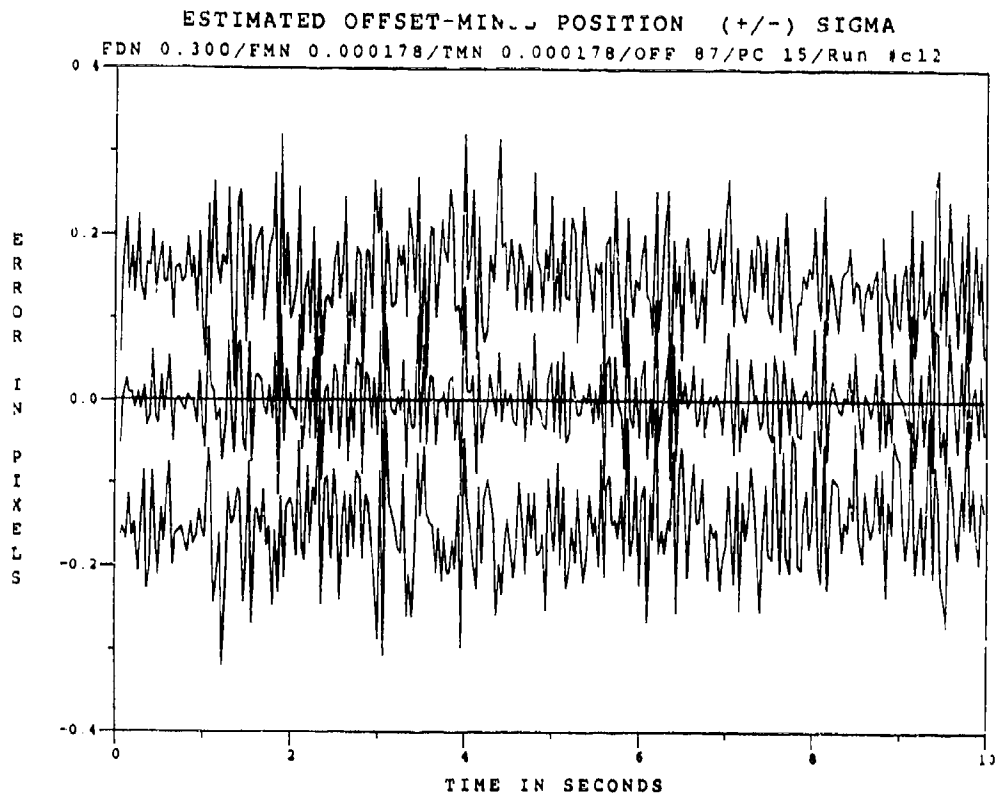


Figure D.20 Two-State Modified MAP MMAF Offset Error at t_i , $q_{\sigma 11} = 0.007$, $q_{\sigma 22} = 0.0007$

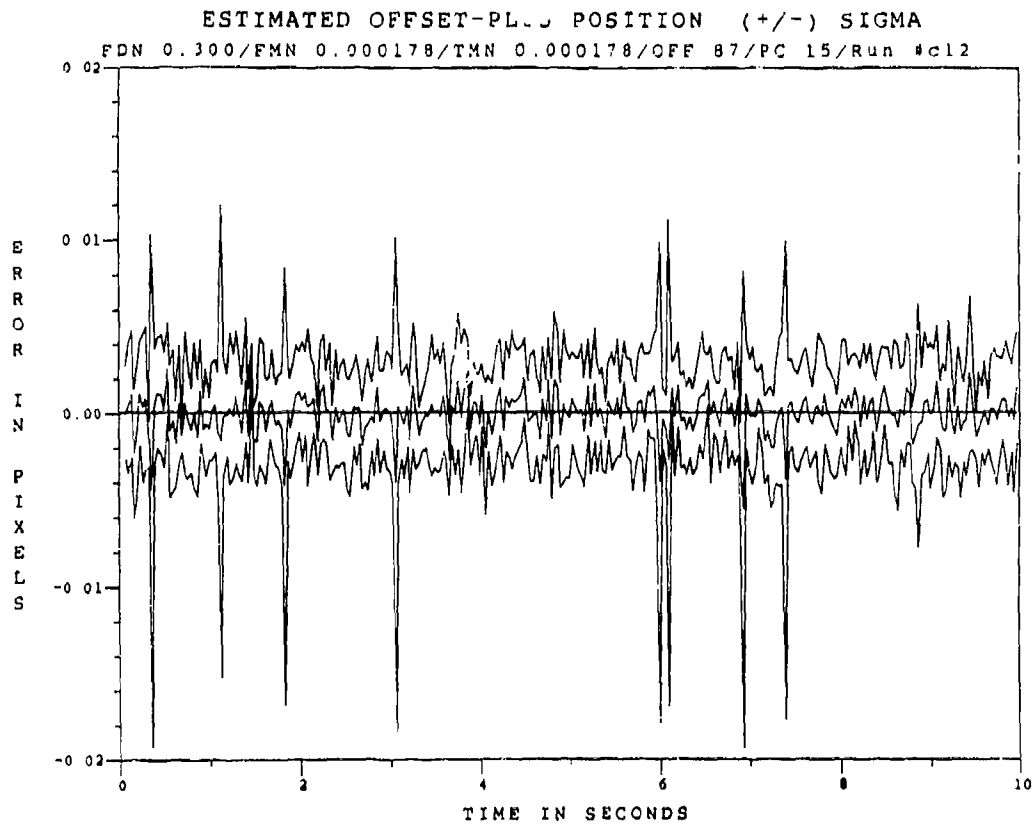


Figure D.21 Two-State Modified MAP MMAF Offset Error at $t_i^*, q_{df 11} = 0.007, q_{df 22} = 0.0007$

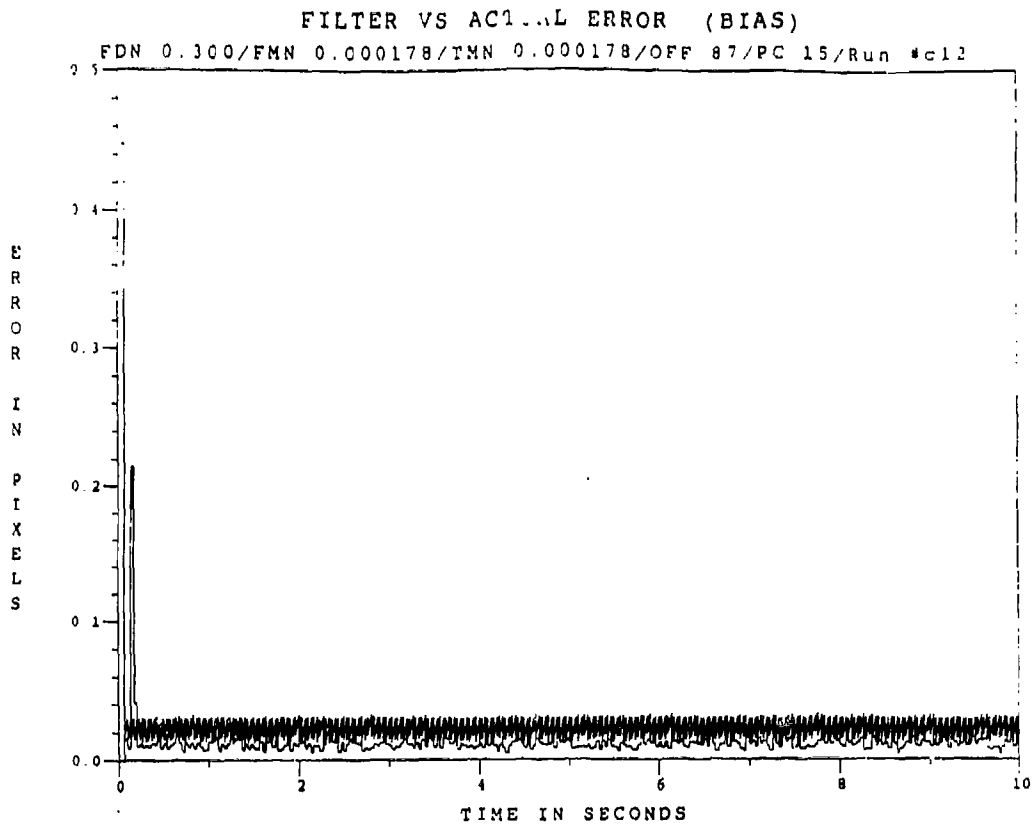


Figure D.22 Two-State Modified MAP MMAF Bias Error, $q_{d11} = 0.007$, $q_{d22} = 0.0007$

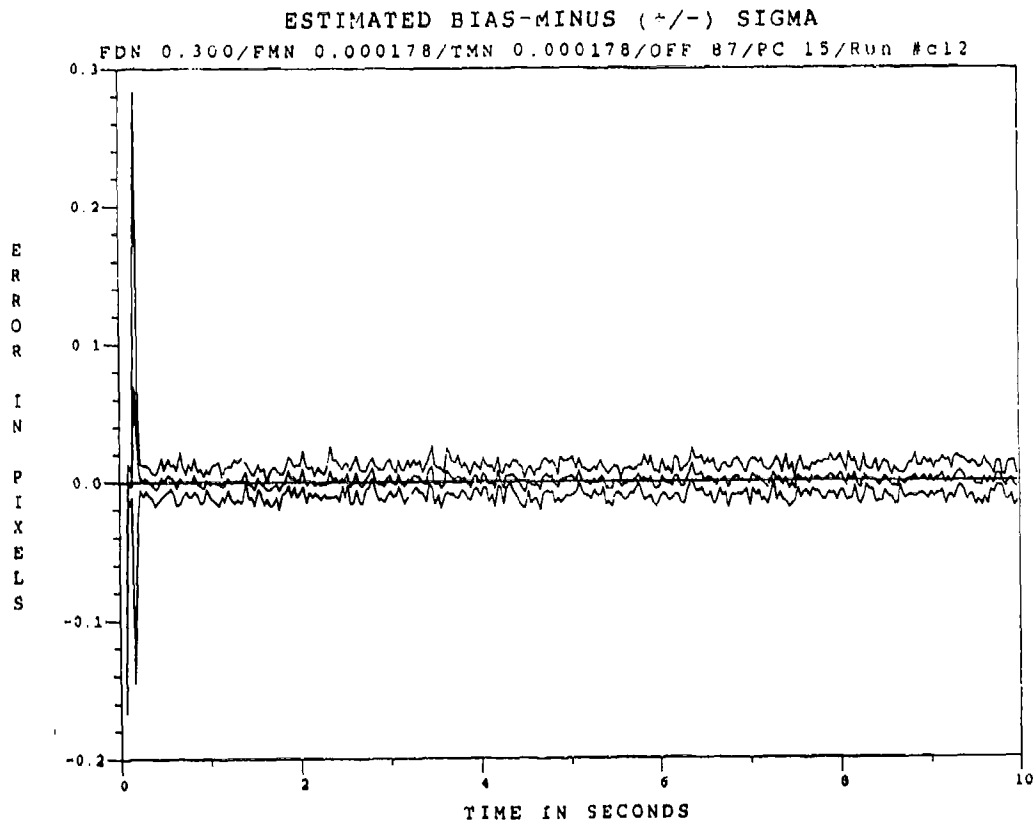


Figure D.23 Two-State Modified MAP MMAF Bias Error at t_1 , $q_{d11} = 0.007$, $q_{d22} = 0.0007$

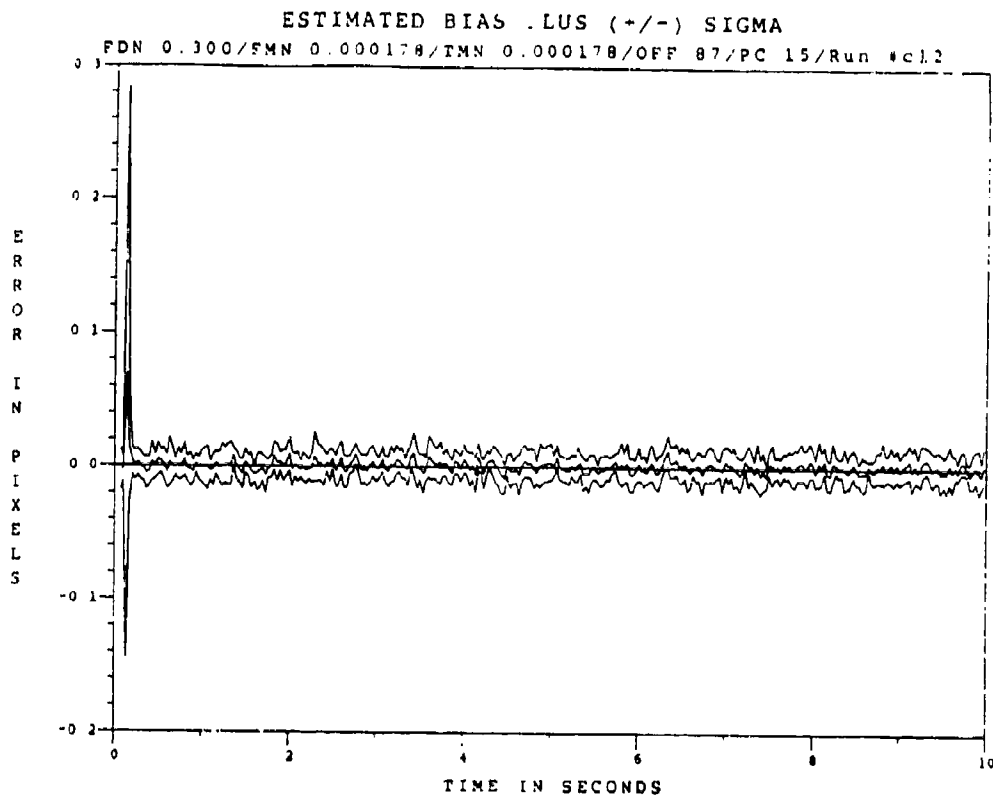


Figure D.24 Two-State Modified MAP MMAF Bias Error at t_1^* , $q_{M11} = 0.007$, $q_{M22} = 0.0007$

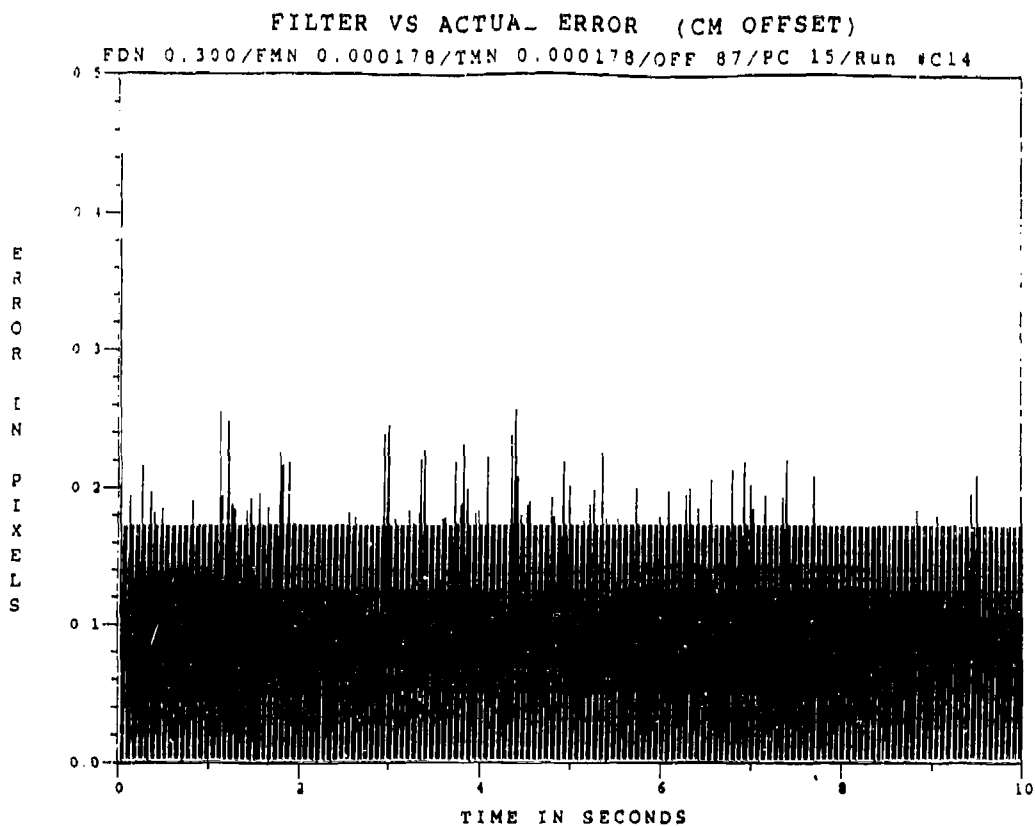


Figure D.25 Two-State Modified MAP MMAF Offset Error, $q_{\sigma 11} = 0.03$, $q_{\sigma 22} = 0.001$

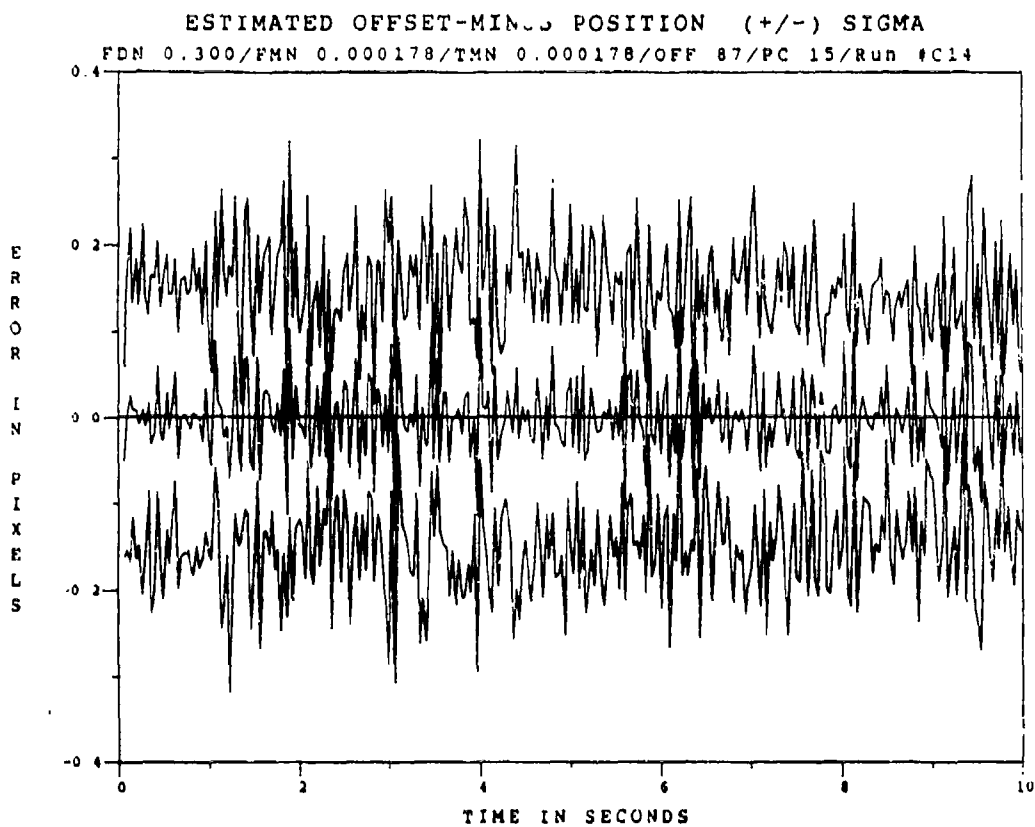


Figure D.26 Two-State Modified MAP MMAF Offset Error at t_i , $q_{\sigma 11} = 0.03$, $q_{\sigma 22} = 0.001$

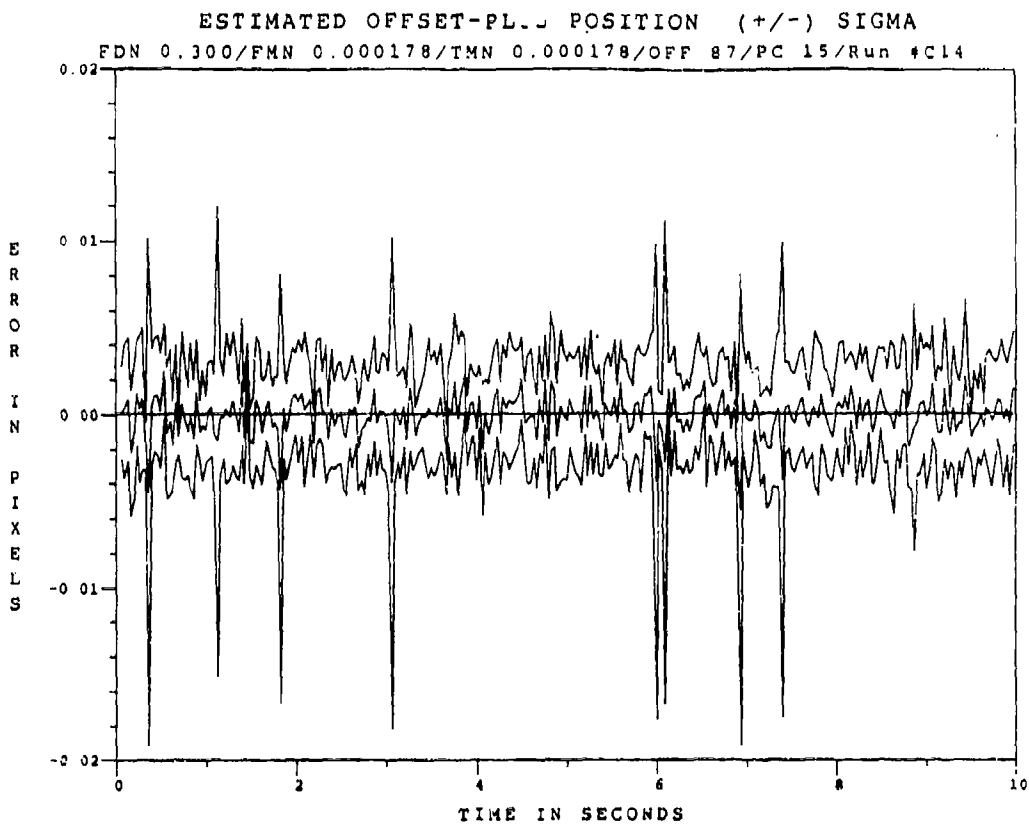


Figure D.27 Two-State Modified MAP MMAF Offset Error at r_1^* , $q_{\sigma 11} = 0.03$, $q_{\sigma 22} = 0.001$

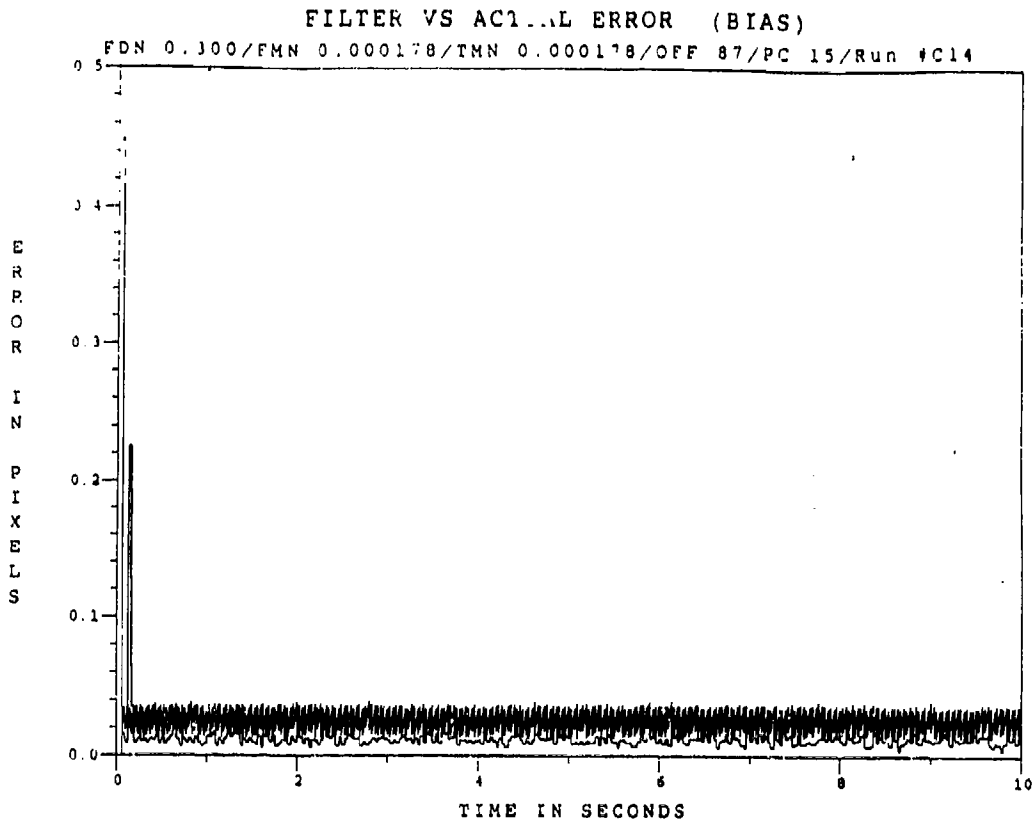


Figure D.28 Two-State Modified MAP MMAF Bias Error. $q_{d11} = 0.03$, $q_{d22} = 0.001$

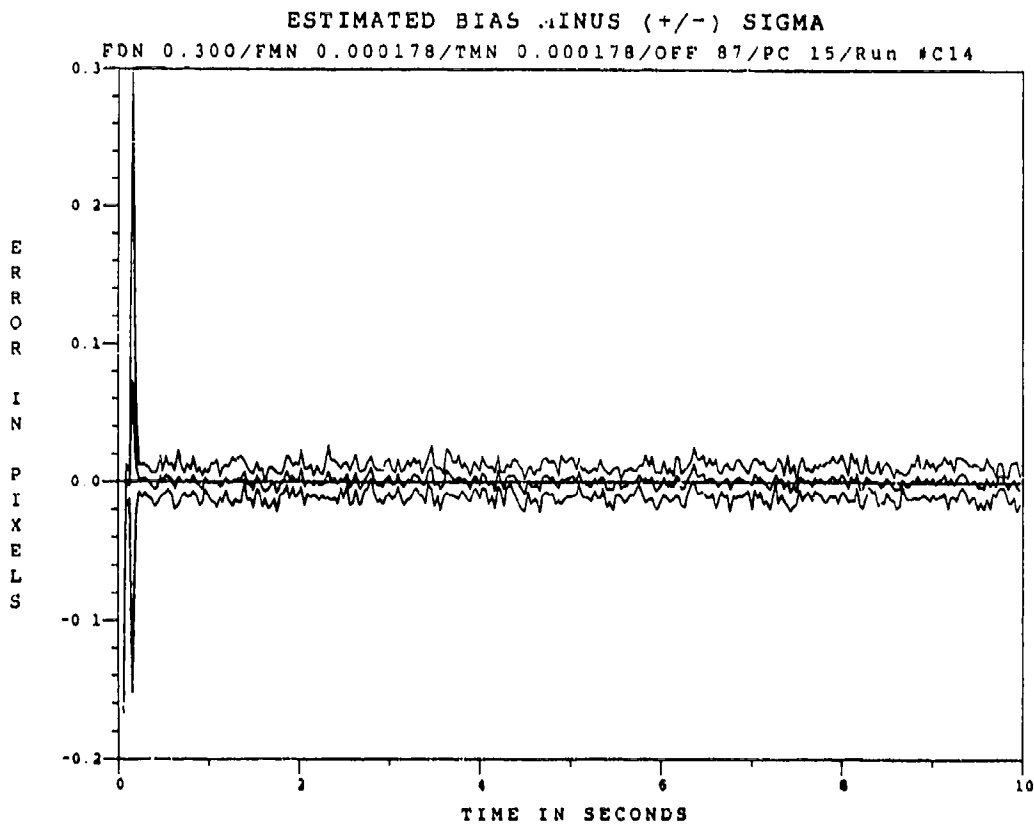


Figure D.29 Two-State Modified MAP MMAF Bias Error at t_i , $q_{d11} = 0.03$, $q_{d22} = 0.001$

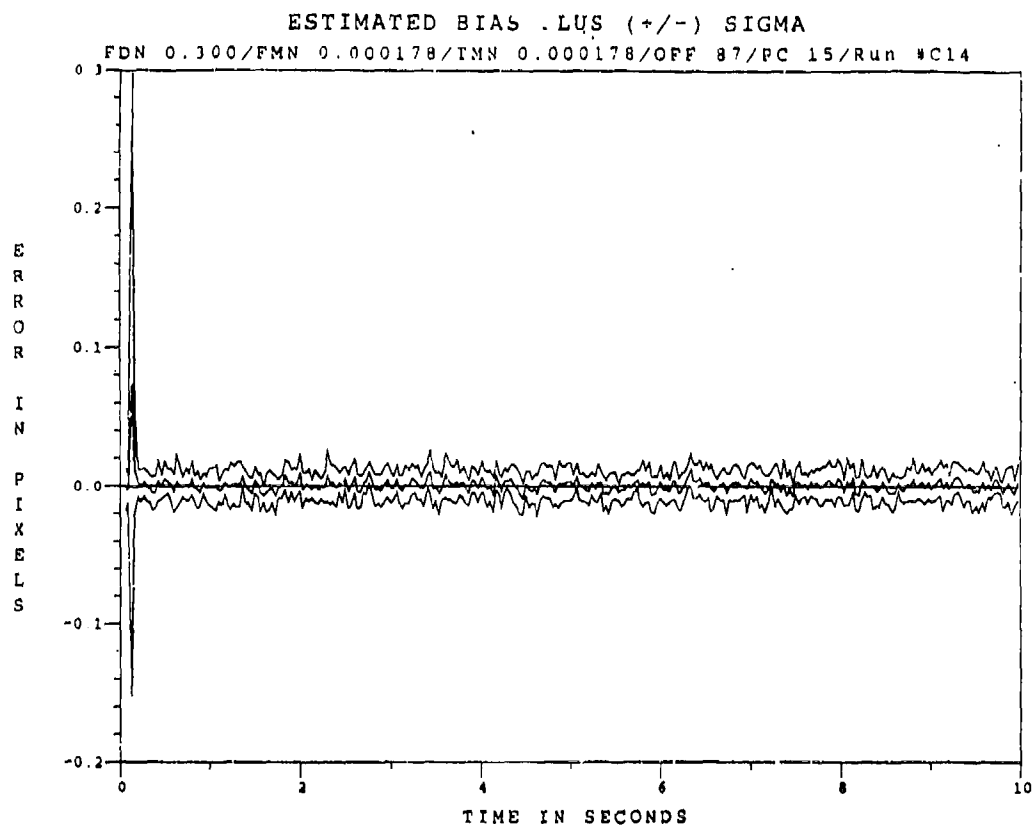


Figure D.30 Two-State Modified MAP MMAF Bias Error at t_1^* , $q_{d11} = 0.03$, $q_{d22} = 0.001$

Appendix E

Two-State Center-of-Mass

Modified MAP MMAF

Case 1

This Appendix contains the error plots of the two-state center-of-mass Modified MAP MMAF, wherein the probability-of-miss, P_m , impacts both the low-energy speckle return and Doppler return. In this case, the "miss" signifies those circumstances in which the low-energy laser return does not exist due to bending of the return signal as it propagates through the 2000 km range, or due to noises in the receiving equipment. The Appendix is divided into sub-appendices that correspond to different values of low-energy laser wavelength and SNR. Each wavelength with a given SNR, is further separated into three values of Probability-of-Miss, P_m . The plots show the relationship, in error mean ± 1 standard deviation values (in pixels), of the errors between the filter estimated and true offset distance from the intensity centroid to the hardbody center-of-mass, and errors between the filter's estimate and the true bias caused by the plume's speckle reflectance. This appendix is divided into the following sub-appendices:

<u>Sub-Appendix</u>	<u>Category</u>
E.1	0.53 μm Wavelength, SNR = 10
E.2	0.53 μm Wavelength, SNR = 4
E.3	2.01 μm Wavelength, SNR = 10
E.4	2.01 μm Wavelength, SNR = 4
E.5	10.5 μm Wavelength, SNR = 10
E.6	10.5 μm Wavelength, SNR = 4

Appendix E.1

Two-State Center-of-Mass

Modified MAP MMAF

with

0.53 μm Doppler Return Measurements

at SNR = 10

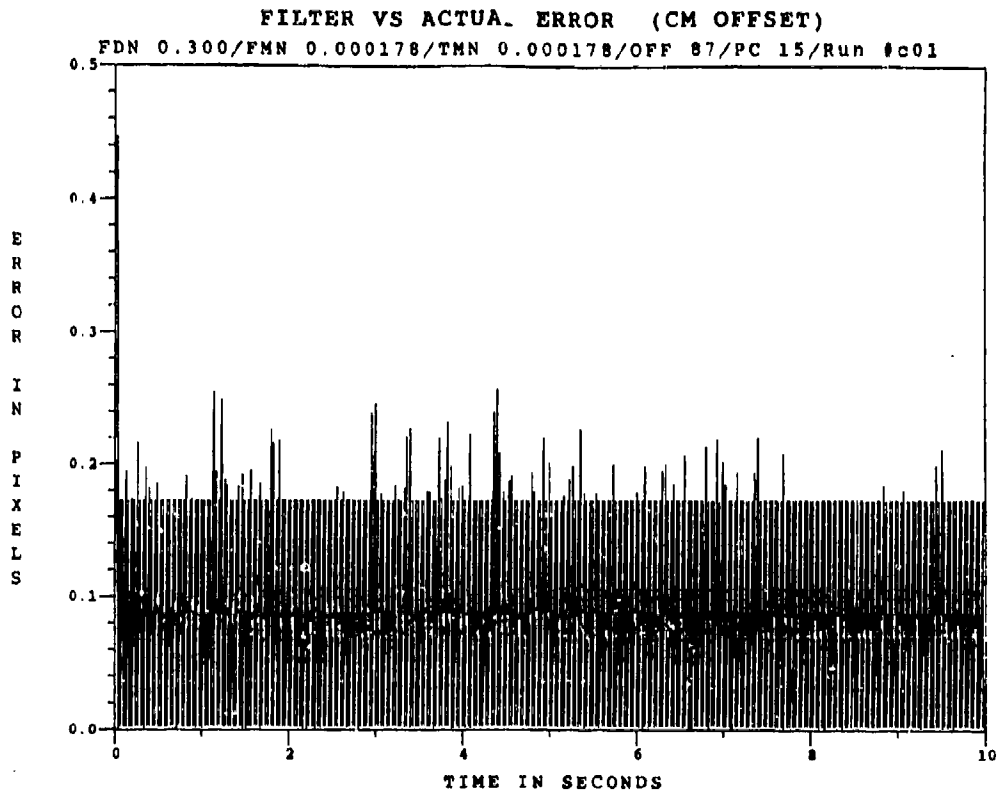


Figure E.1.1 0.53 μm Two-State Modified MAP MMAF Offset Error, SNR=10, $P_{\text{off}}=-0.0$

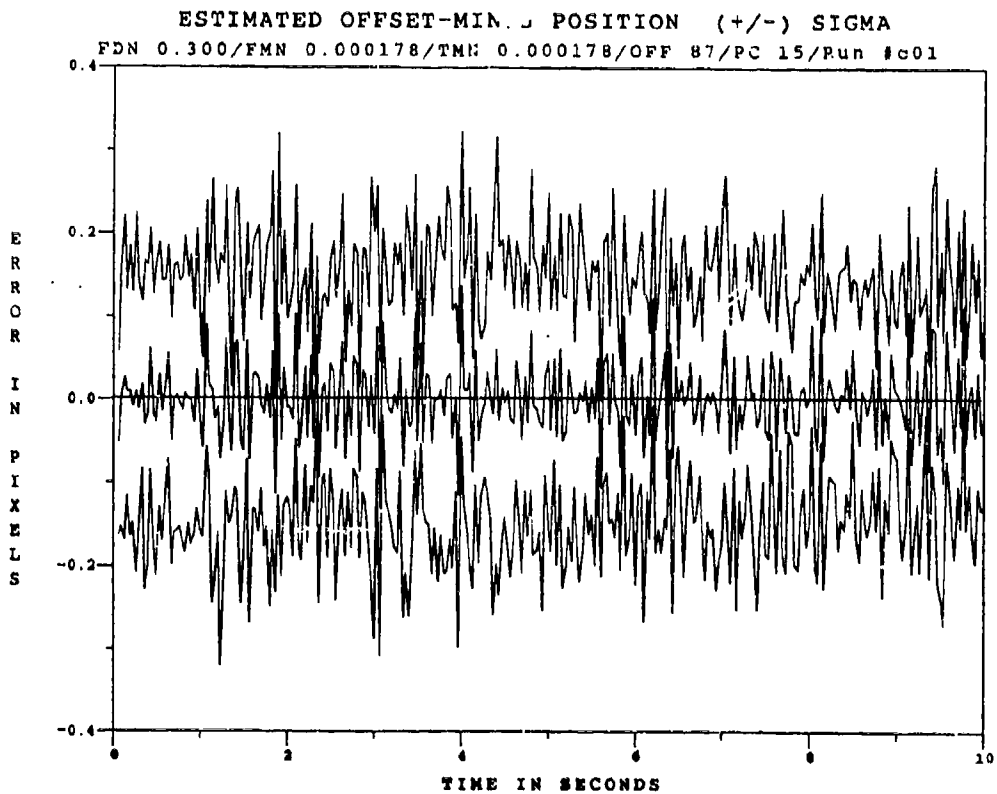


Figure E.1.2 0.53 μm Two-State Modified MAP MMAF Offset Error, SNR=10, $P_{\text{off}}=-0.0$, at t_i

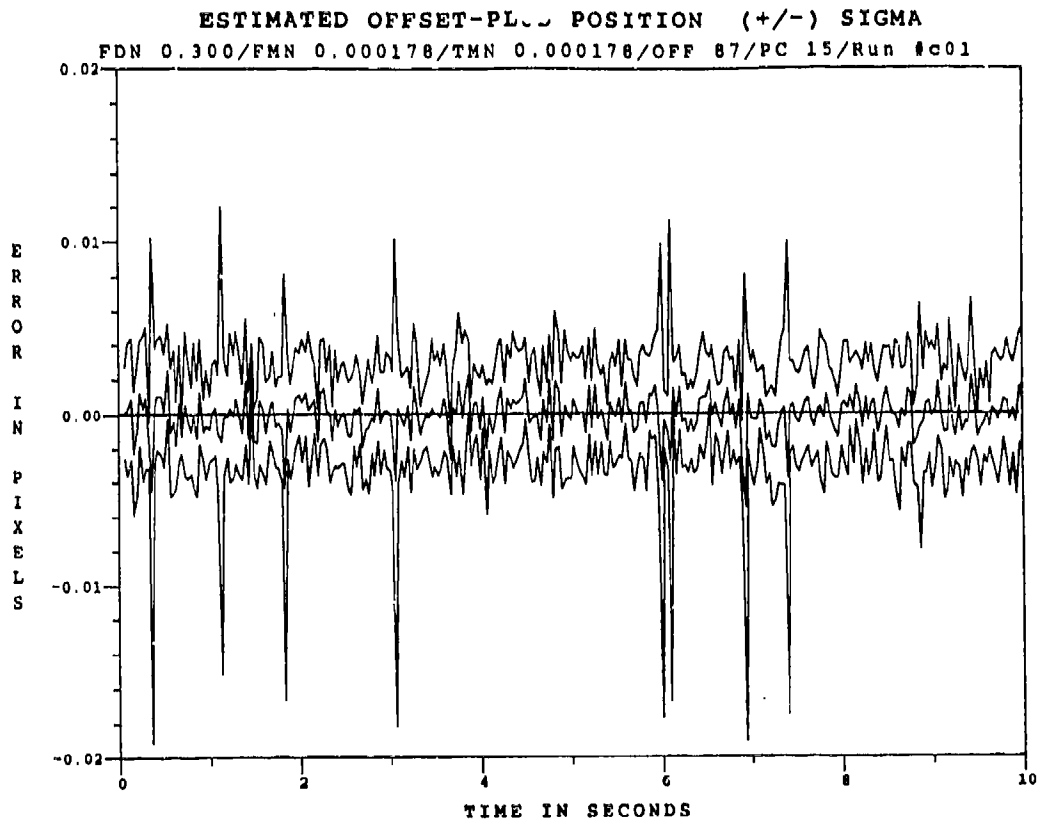


Figure E.1.3 0.53 μm Two-State Modified MAP MMAF Offset Error, SNR=10, $P_m = -0.0$, at t_i^*

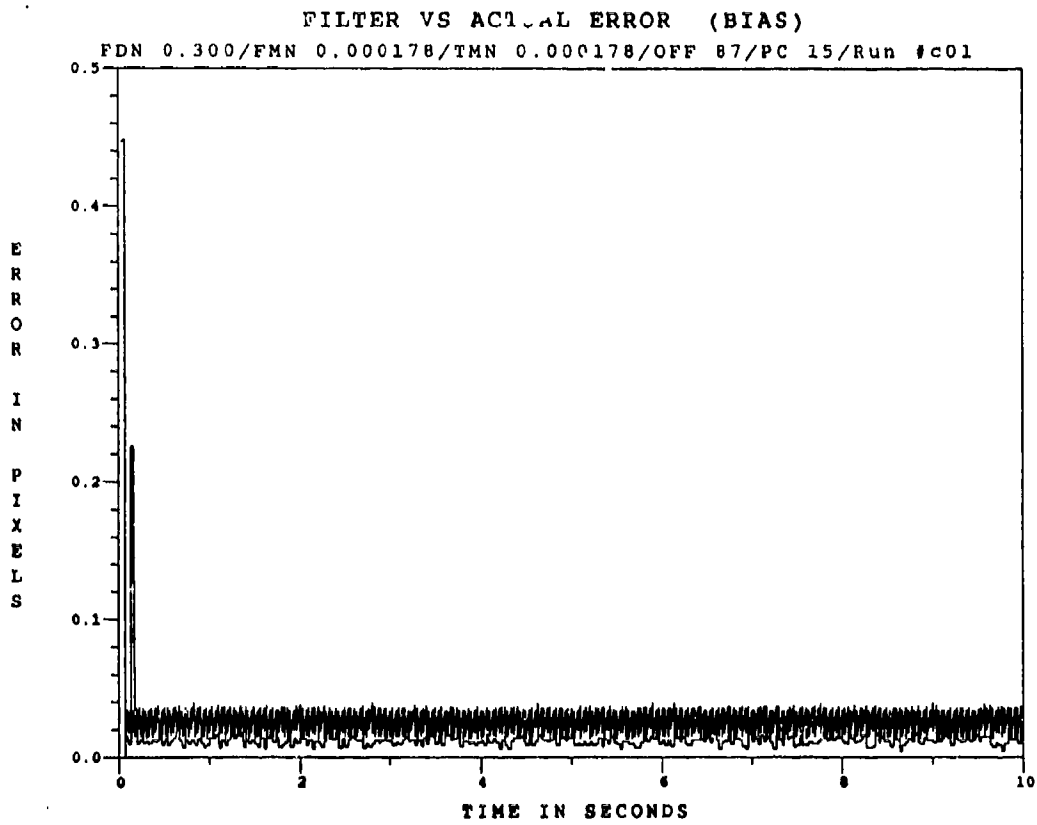


Figure E.1.4 0.53 μm Two-State Modified MAP MMAF Bias Error, SNR=10, $P_m = -0.0$

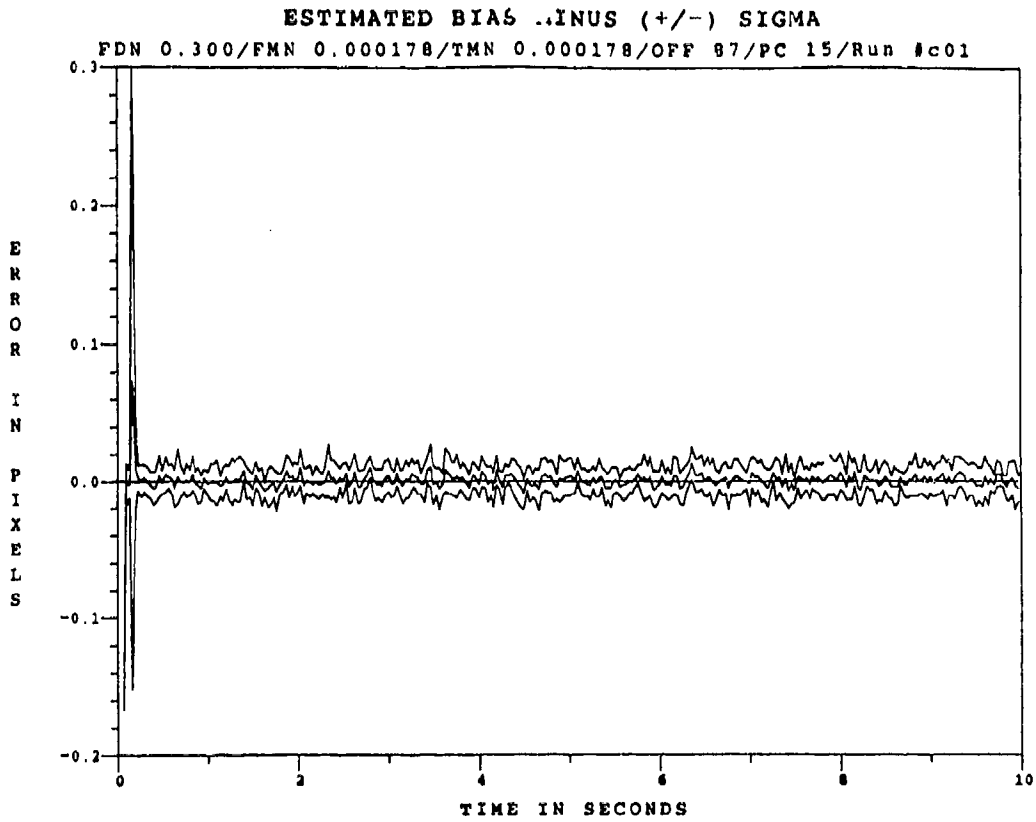


Figure E.1.5 0.53 μm Two-State Modified MAP MMAF Bias Error, SNR=10, $P_m = 0.0$, at t_i^+

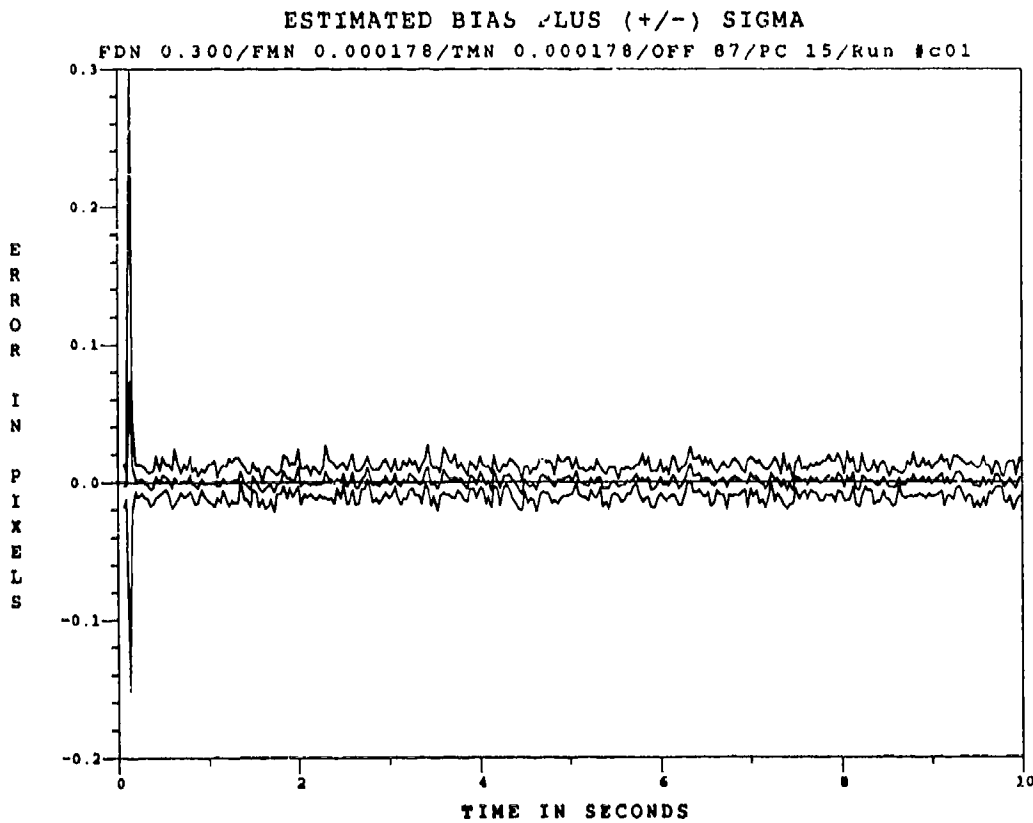


Figure E.1.6 0.53 μm Two-State Modified MAP MMAF Bias Error, SNR=10, $P_m = 0.0$, at t_i^+

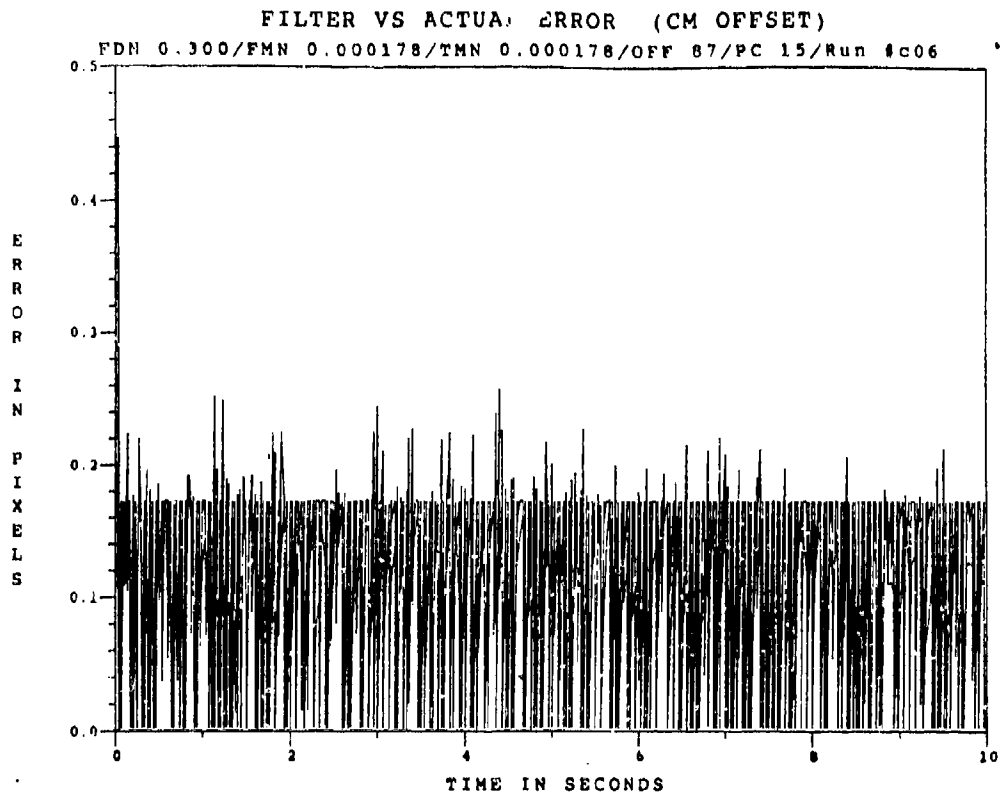


Figure E.1.7 0.53 μm Two-State Modified MAP MMAF Offset Error, SNR = 10, $P_m = 0.05$

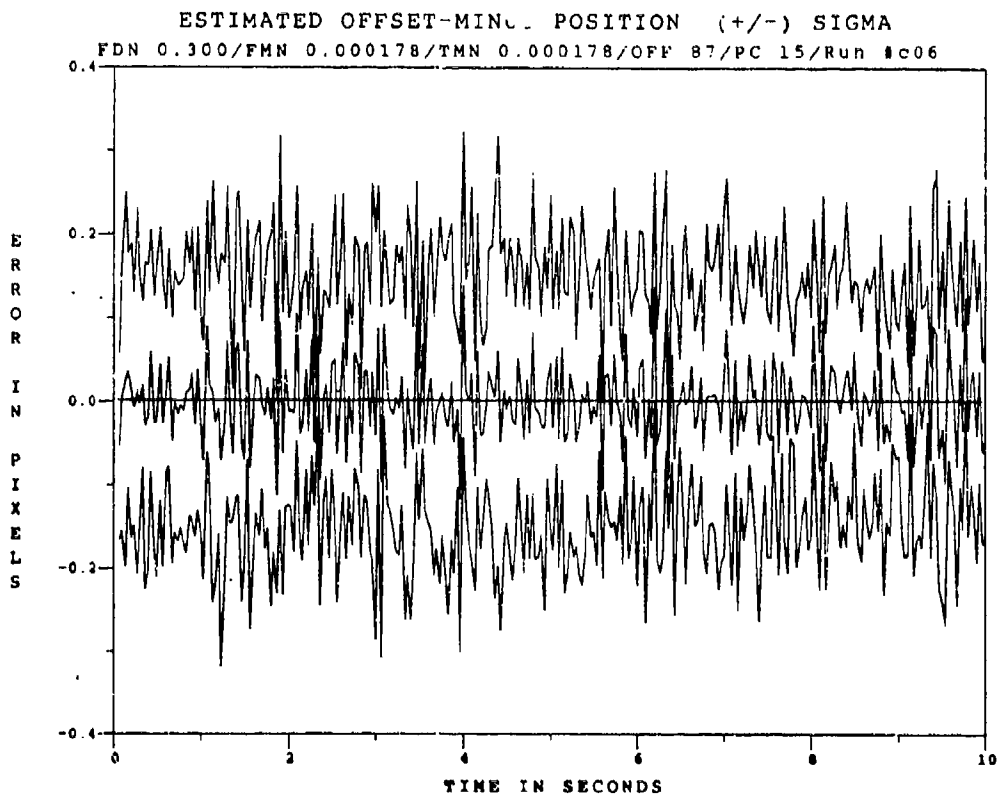


Figure E.1.8 0.53 μm Two-State Modified MAP MMAF Offset Error, SNR=10, $P_m=0.05$, at t_i

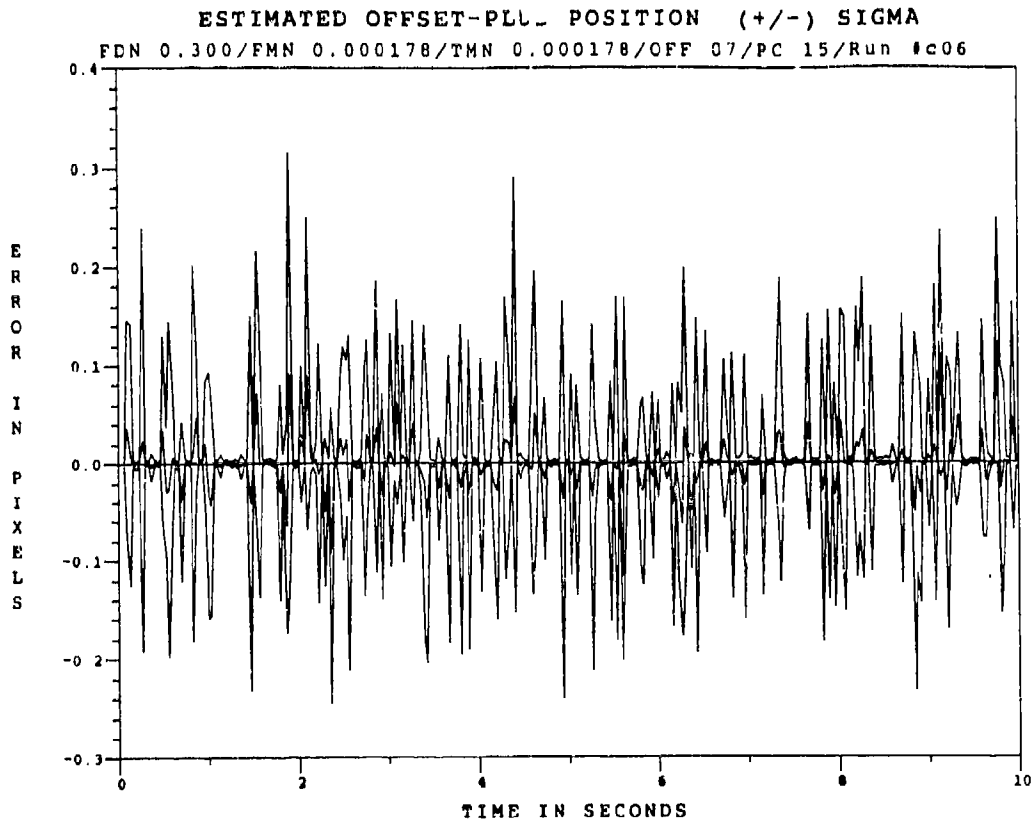


Figure E.1.9 0.53 μ m Two-State Modified MAP MMAF Offset Error, SNR=10, $P_m = 0.05$, at t_i^*

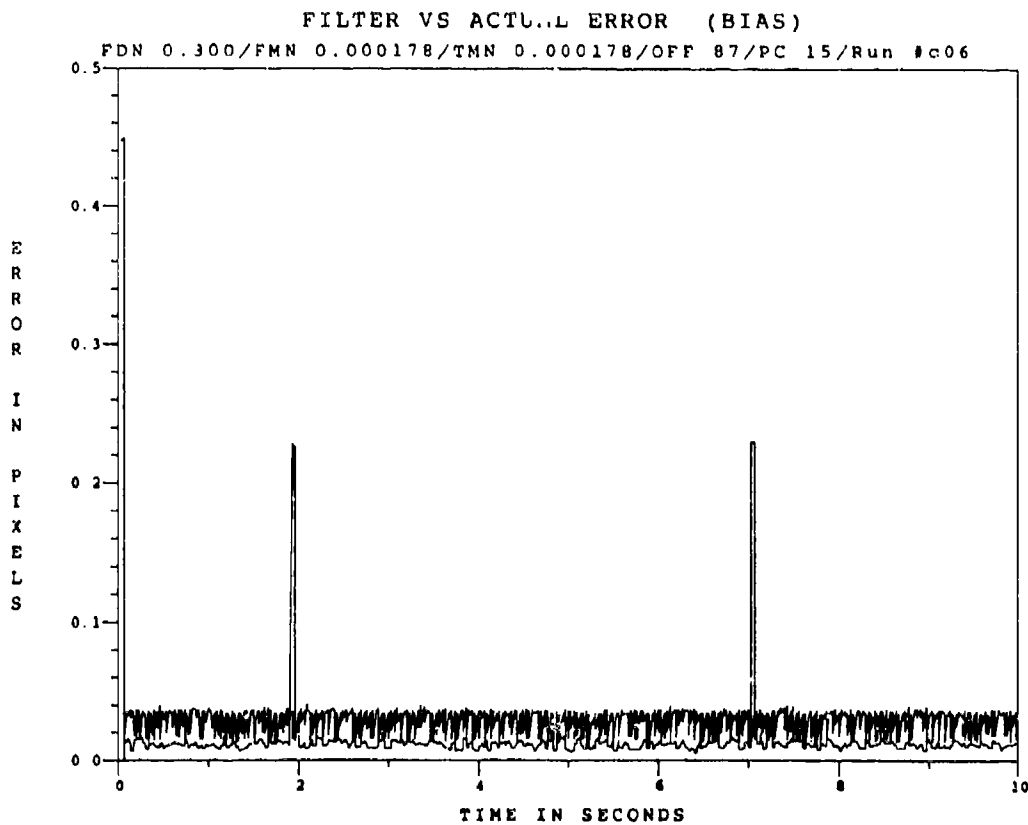


Figure E.1.10 0.53 μ m Two-State Modified MAP MMAF Bias Error, SNR = 10, $P_m = 0.05$

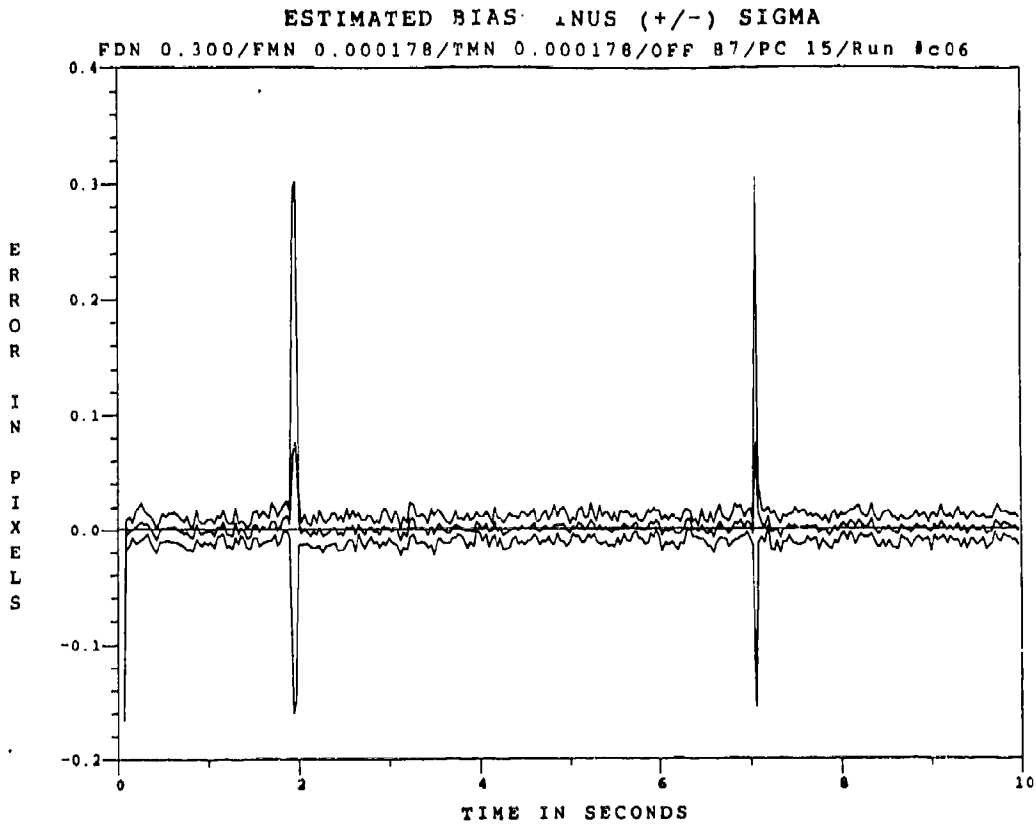


Figure E.1.11 0.53 μm Two-State Modified MAP MMAF Bias Error, SNR=10, $P_m = -0.05$, at t_i^-

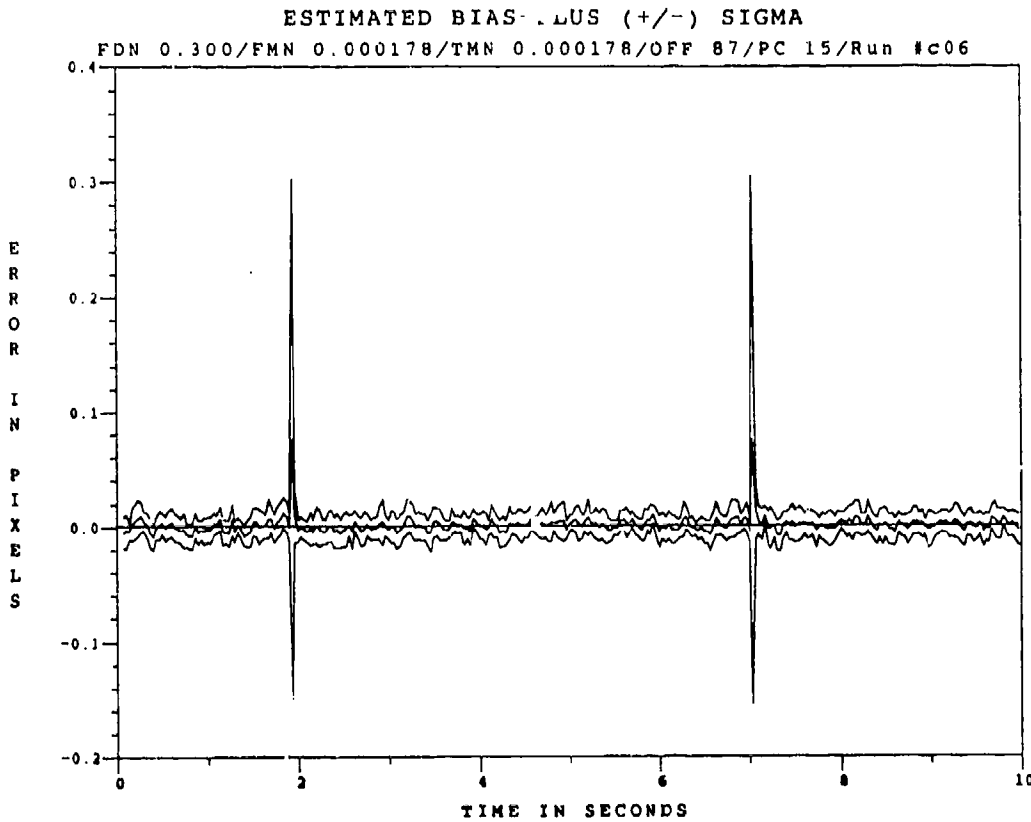


Figure E.1.12 0.53 μm Two-State Modified MAP MMAF Bias Error, SNR=10, $P_m = -0.05$, at t_i^+

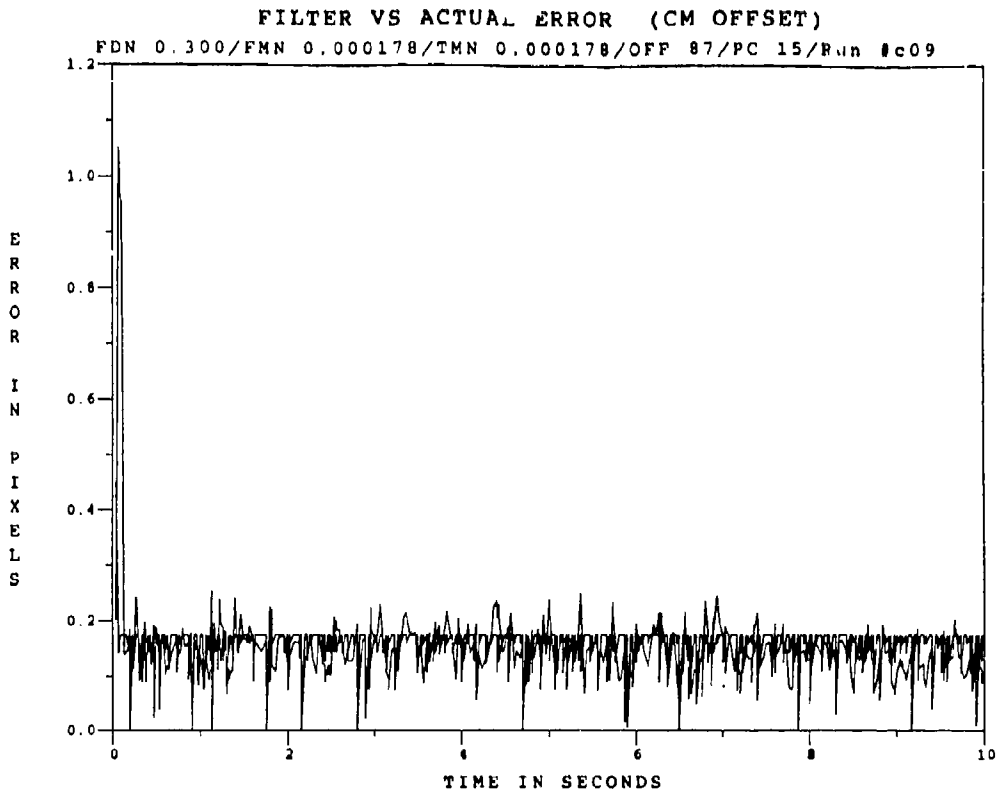


Figure E.1.13 0.53 μ m Two-State Modified MAP MMAF Offset Error, SNR = 10, $P_m = 0.30$

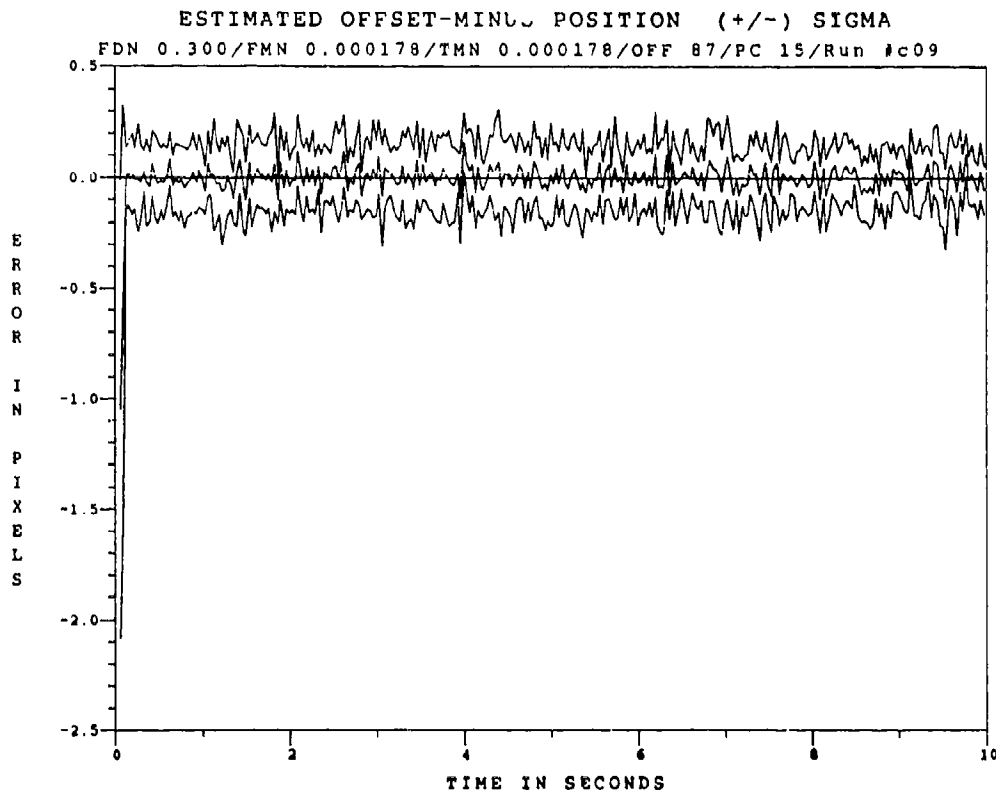


Figure E.1.14 0.53 μ m Two-State Modified MAP MMAF Offset Error, SNR=10, $P_m = 0.30$, at t_i

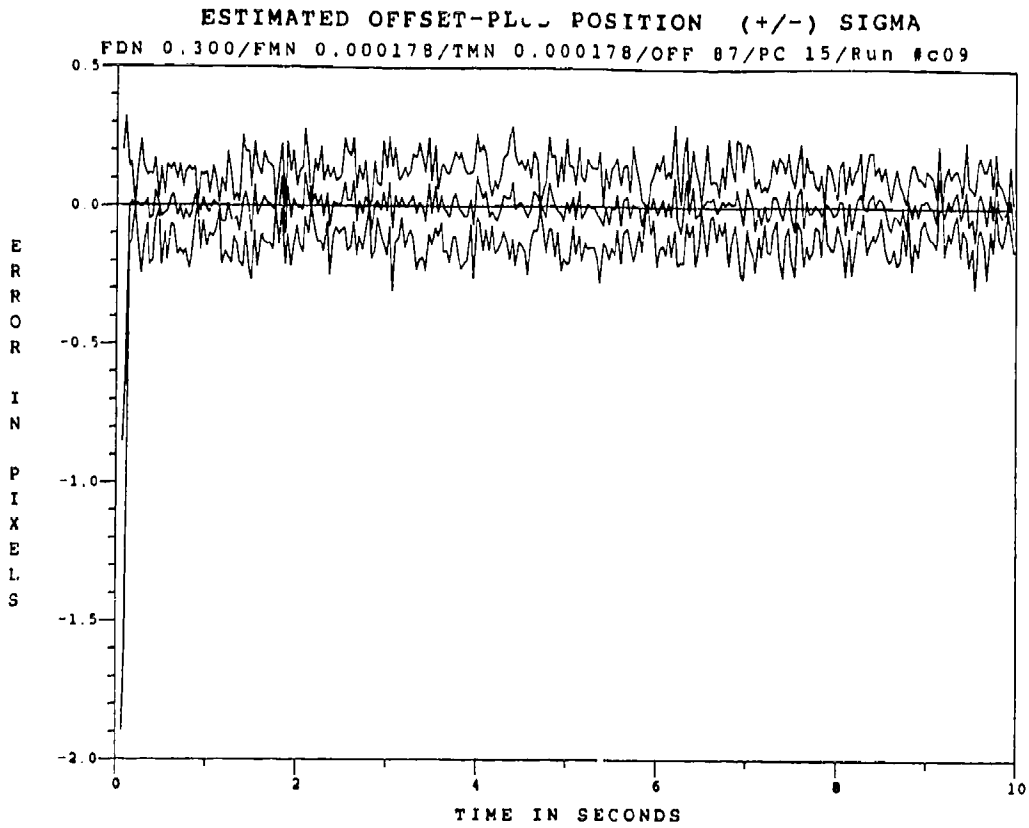


Figure E.1.15 0.53 μ m Two-State Modified MAP MMAF Offset Error, SNR=10, $P_m = -0.30$, at t_i^*

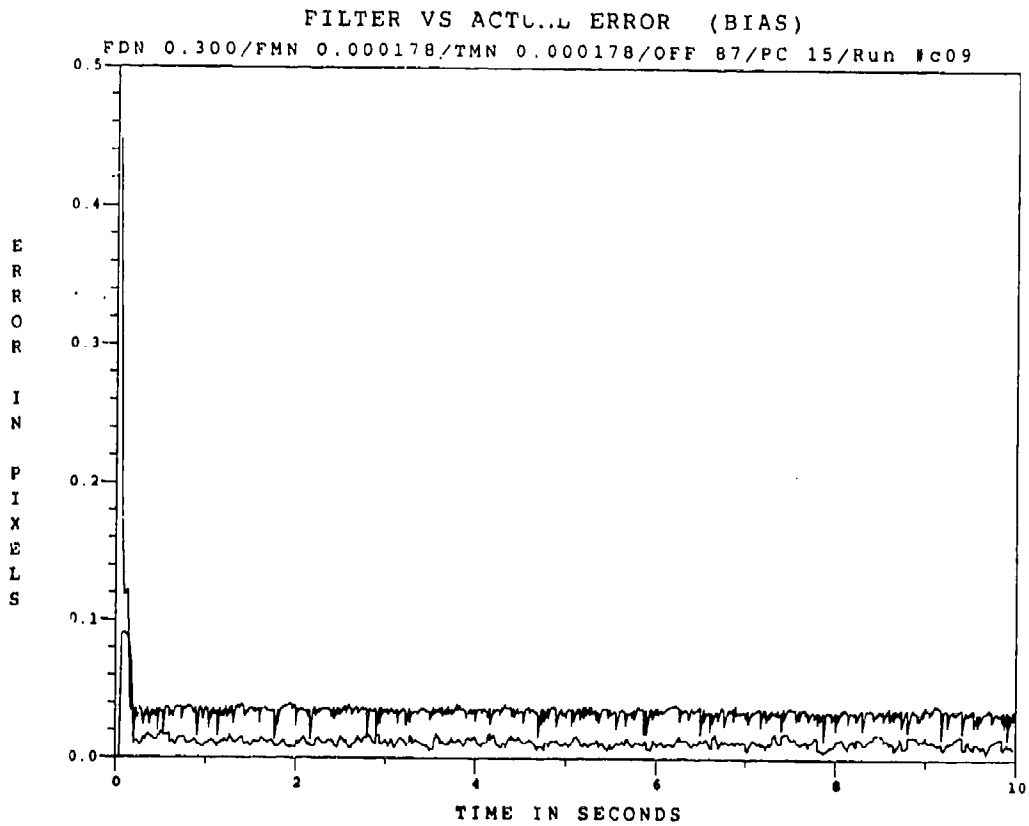


Figure E.1.16 0.53 μ m Two-State Modified MAP MMAF Bias Error, SNR = 10, $P_m = 0.30$

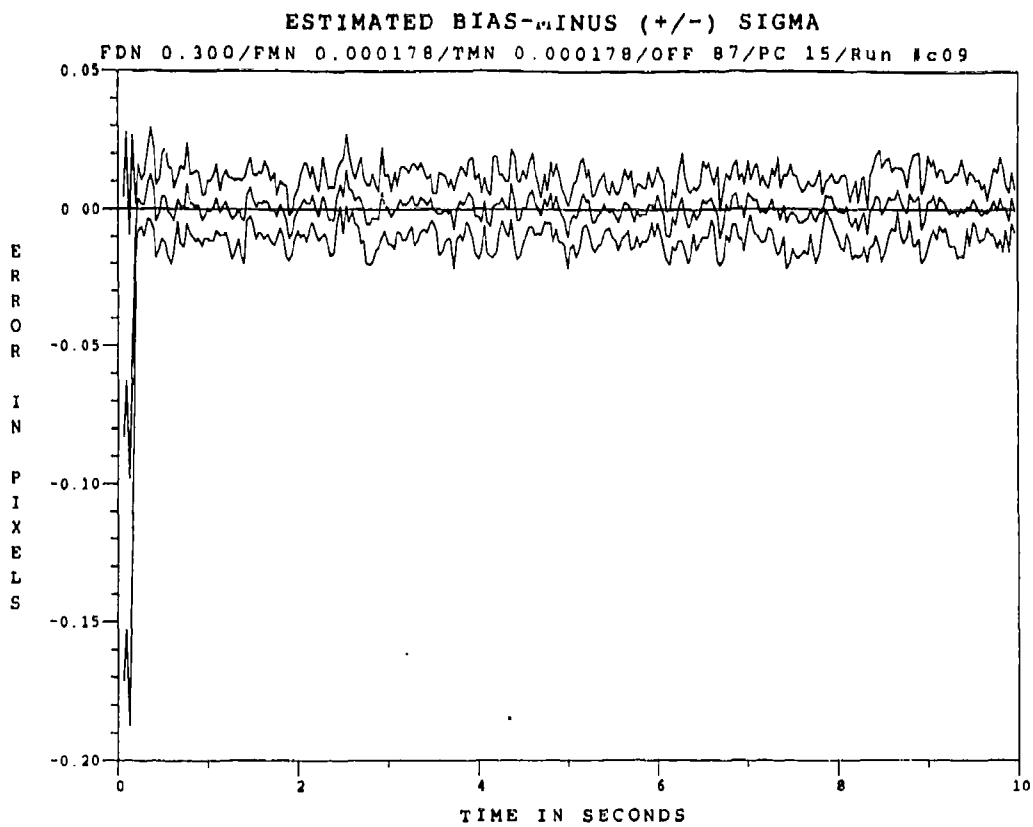


Figure E.1.17 0.53 μ m Two-State Modified MAP MMAF Bias Error, SNR=10, $P_n = -0.30$, at t_i

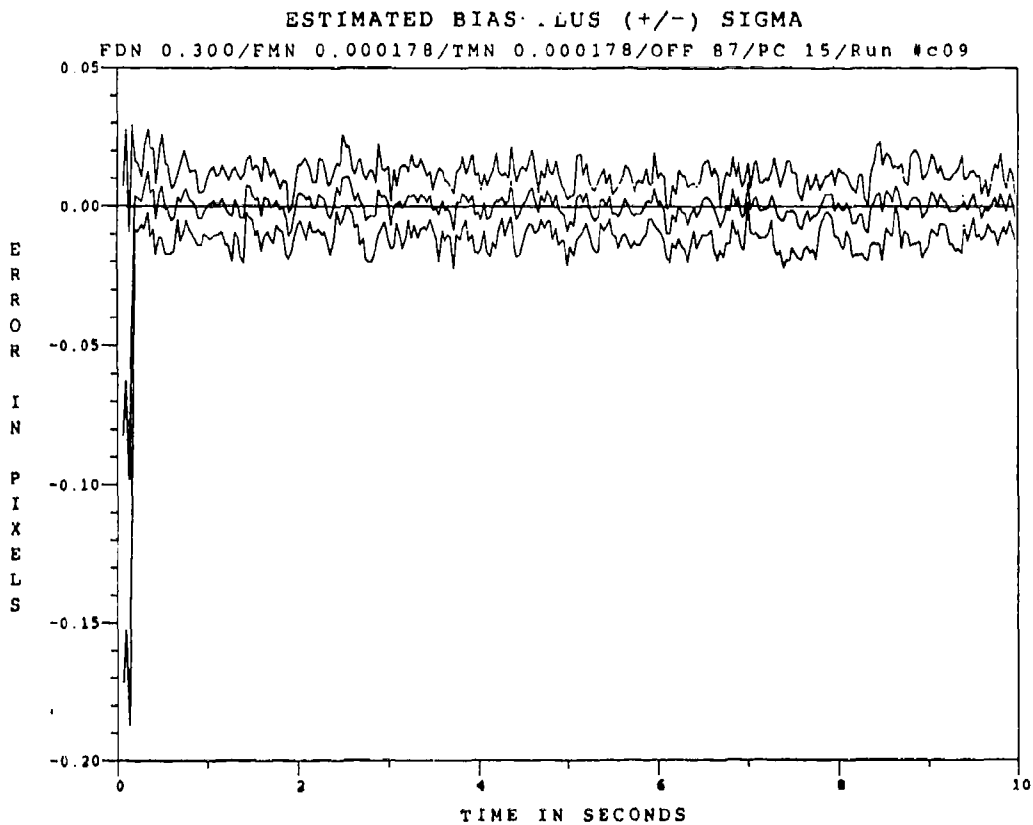


Figure E.1.18 0.53 μ m Two-State Modified MAP MMAF Bias Error, SNR=10, $P_n = -0.30$, at t_i

Appendix E.2

Two-State Center-of-Mass

Modified MAP MMAF

with

0.53 μm Doppler Return Measurements

at SNR = 4

FILTER VS ACTUAL ERROR (CM OFFSET)

FDN 0.300/FMN 0.000178/TMN 0.000178/OFF 87/PC 15/Run #c28

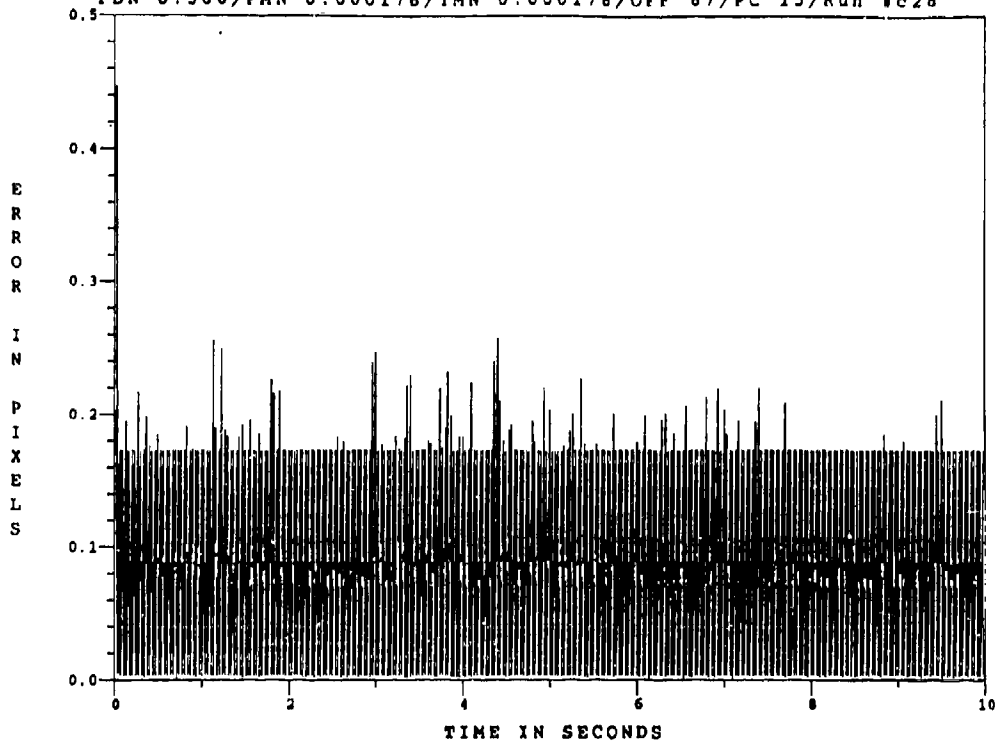


Figure E.2.1 0.53 μm Two-State Modified MAP MMAF Offset Error, SNR=4, $P_m = -0.0$

ESTIMATED OFFSET-MIN. POSITION (+/-) SIGMA

FDN 0.300/FMN 0.000178/TMN 0.000178/OFF 87/PC 15/Run #c28

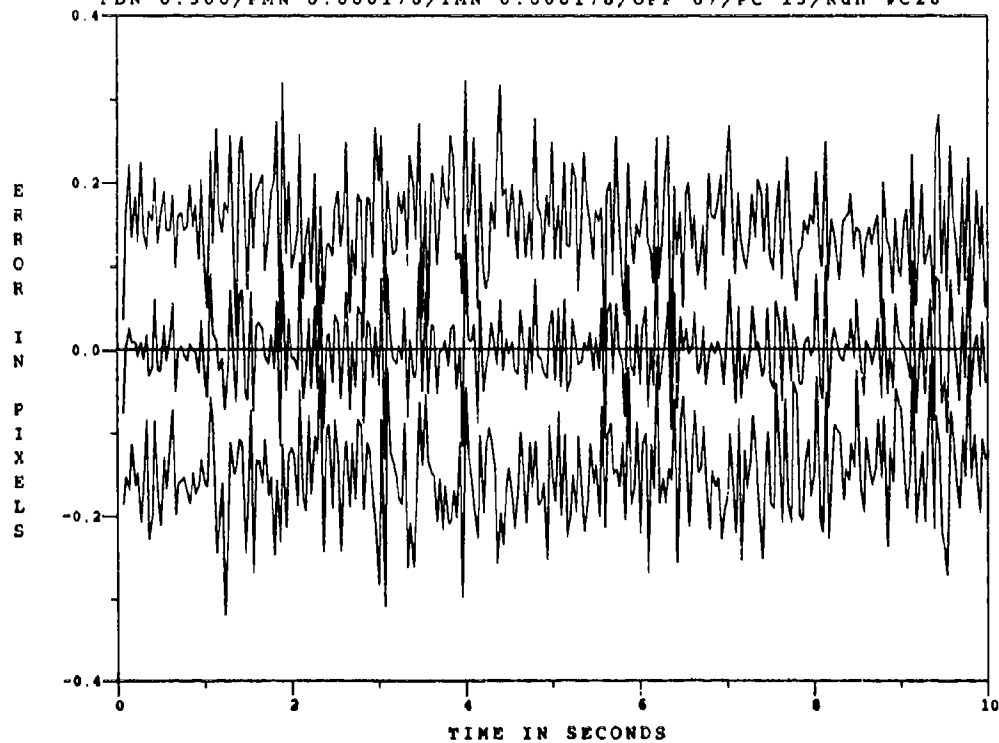


Figure E.2.2 0.53 μm Two-State Modified MAP MMAF Offset Error, SNR=4, $P_m = -0.0$, at t_i

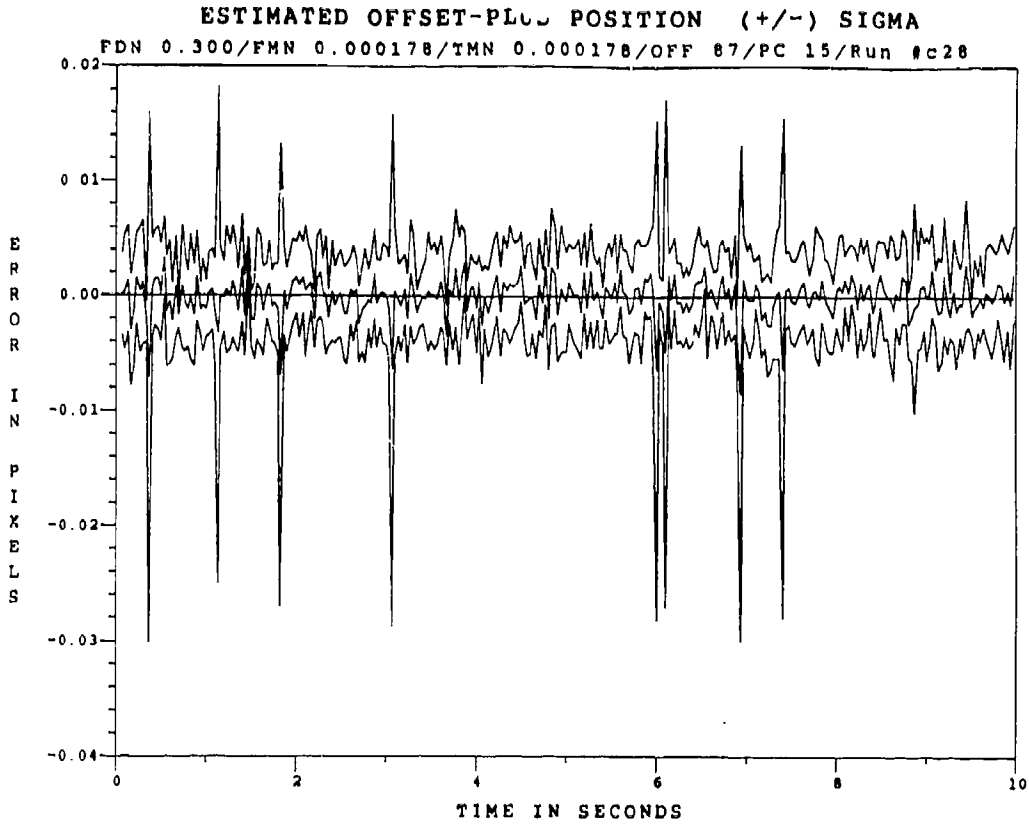


Figure E.2.3 0.53 μm Two-State Modified MAP MMAF Offset Error, SNR=4, $P_m = -0.0$, at t_i^*

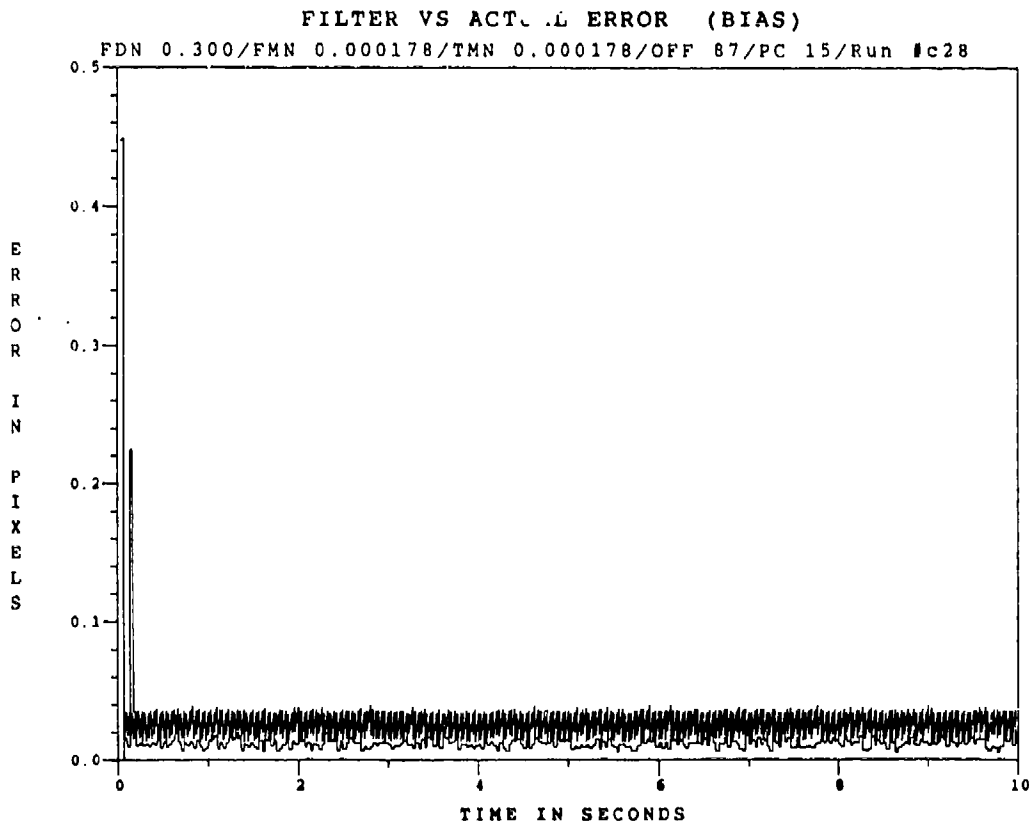


Figure E.2.4 0.53 μm Two-State Modified MAP MMAF Bias Error, SNR=4, $P_m = -0.0$

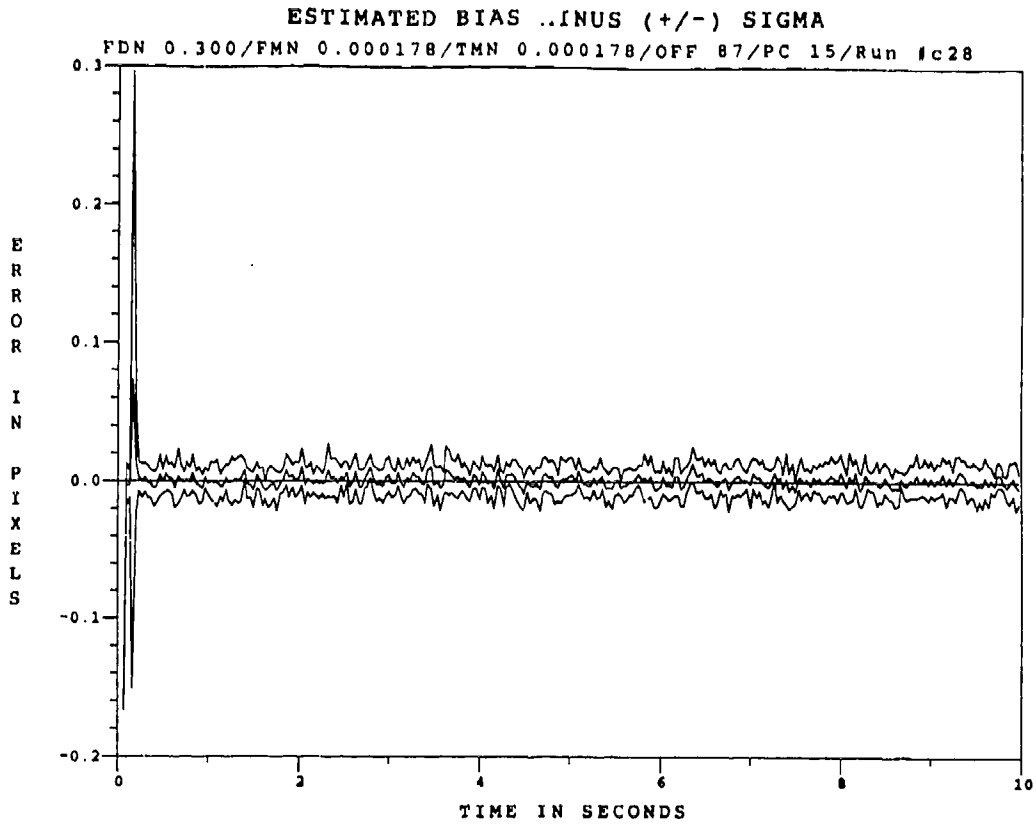


Figure E.2.5 0.53 μm Two-State Modified MAP MMAF Bias Error, SNR=4, $P_m = 0.0$, at t_i

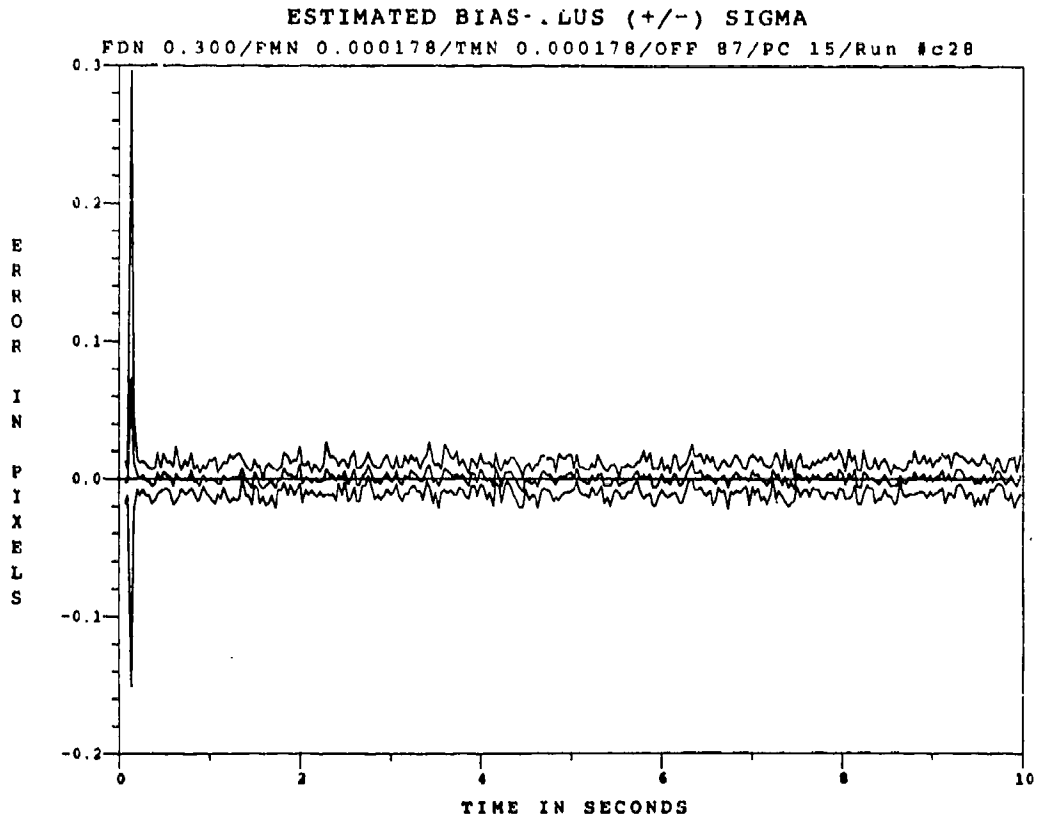


Figure E.2.6 0.53 μm Two-State Modified MAP MMAF Bias Error, SNR=4, $P_m = 0.0$, at t_i^*

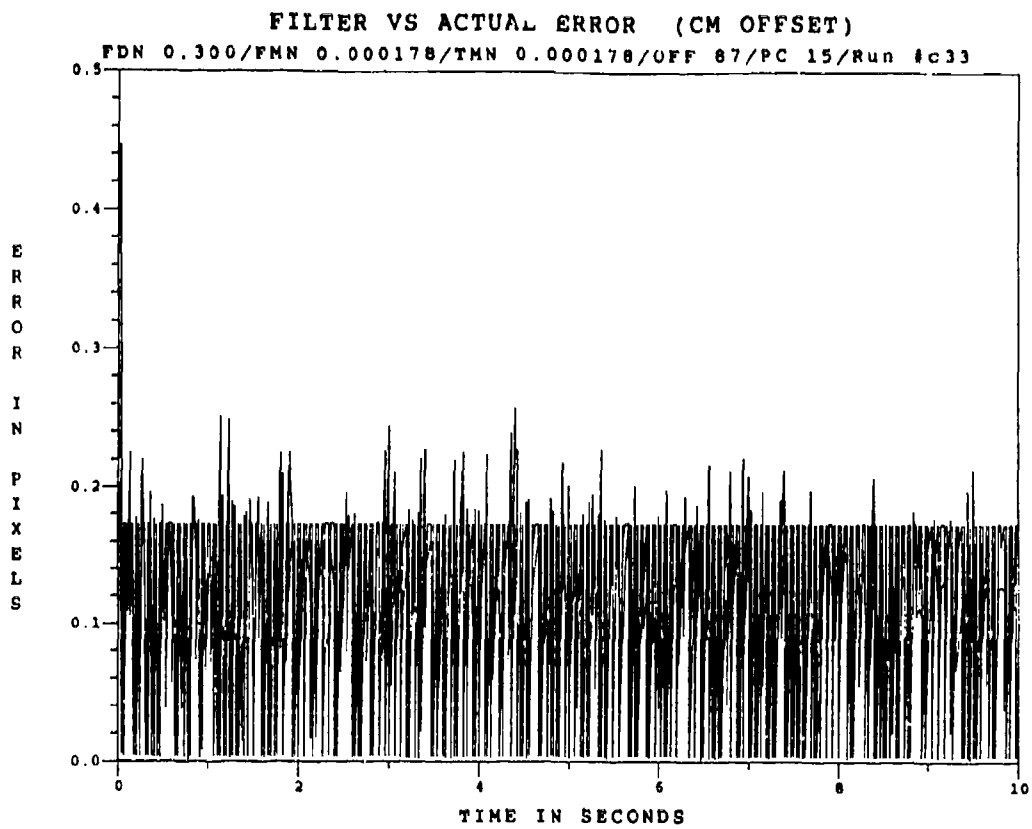


Figure E.2.7 $0.53 \mu\text{m}$ Two-State Modified MAP MMAF Offset Error, $\text{SNR} = 4$, $P_n = 0.05$

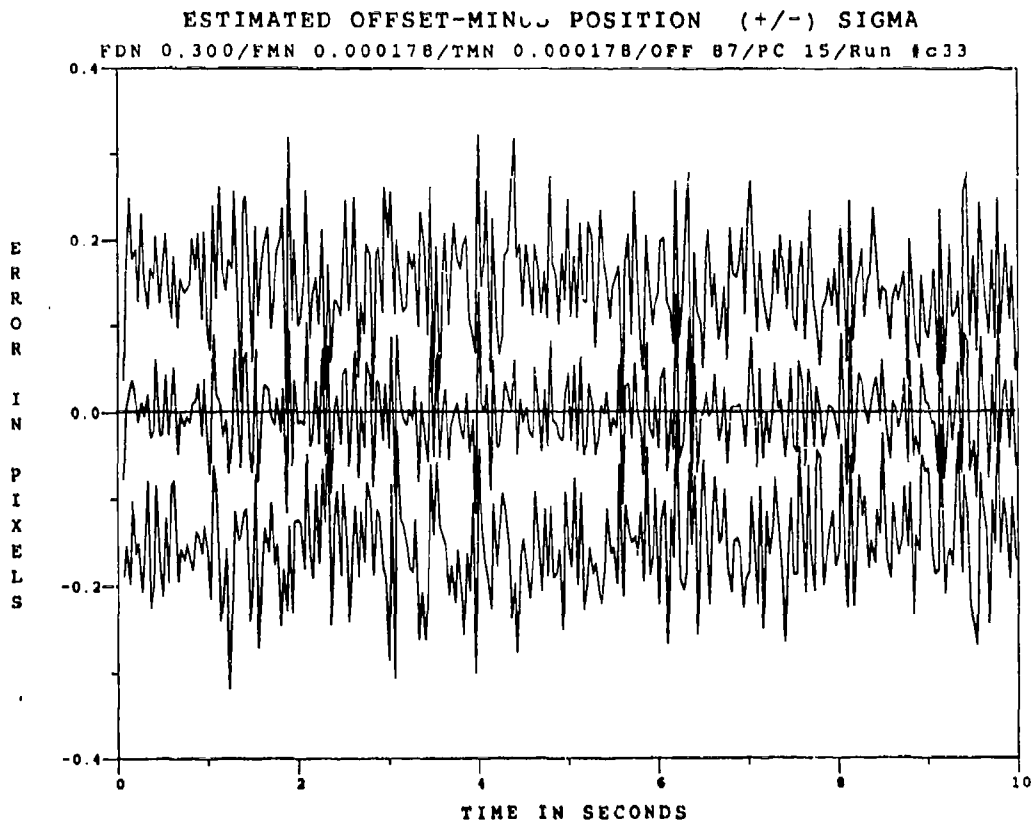


Figure E.2.8 $0.53 \mu\text{m}$ Two-State Modified MAP MMAF Offset Error, $\text{SNR} = 4$, $P_n = 0.05$, at t_i

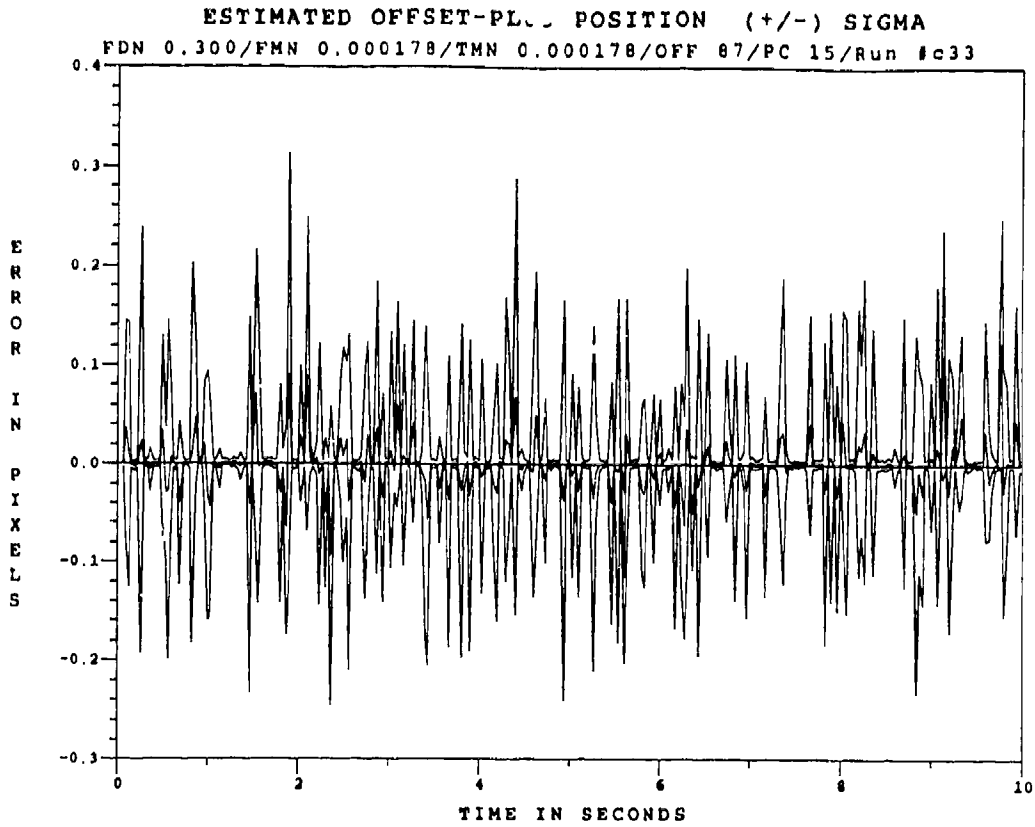


Figure E.2.9 0.53 μ m Two-State Modified MAP MMAF Offset Error, SNR=4, $P_m = 0.05$, at t_i^*

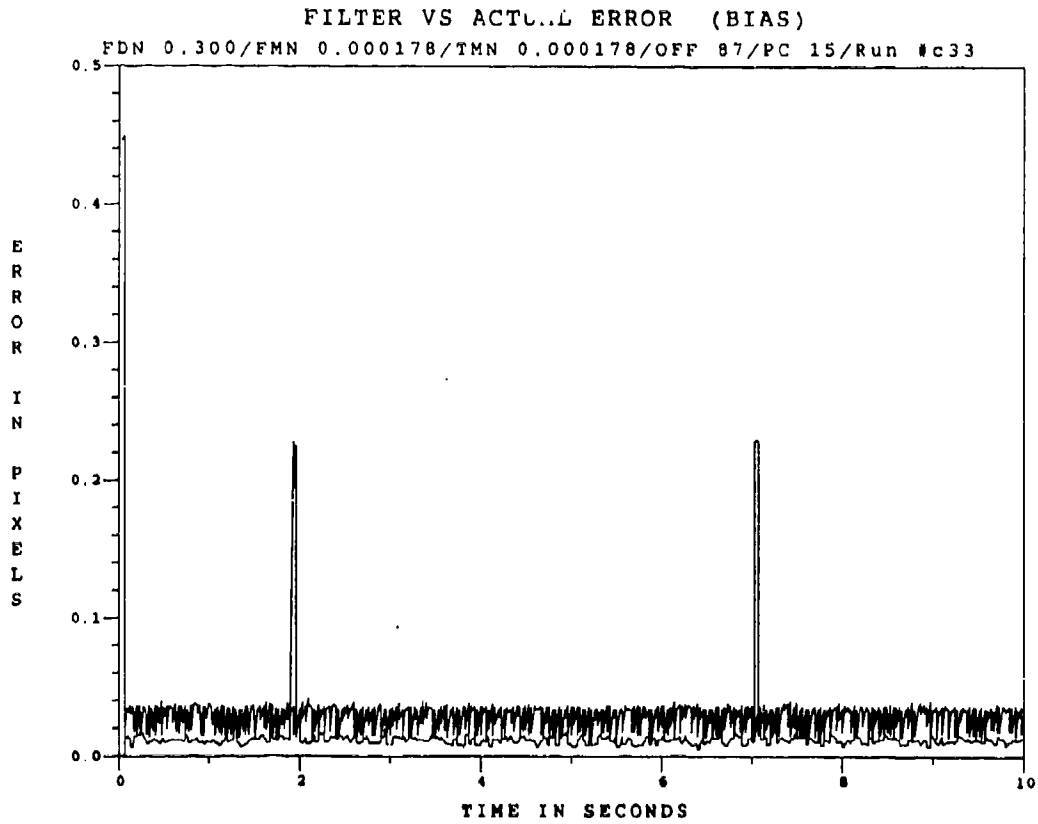


Figure E.2.10 0.53 μ m Two-State Modified MAP MMAF Bias Error, SNR = 4, $P_m = 0.05$

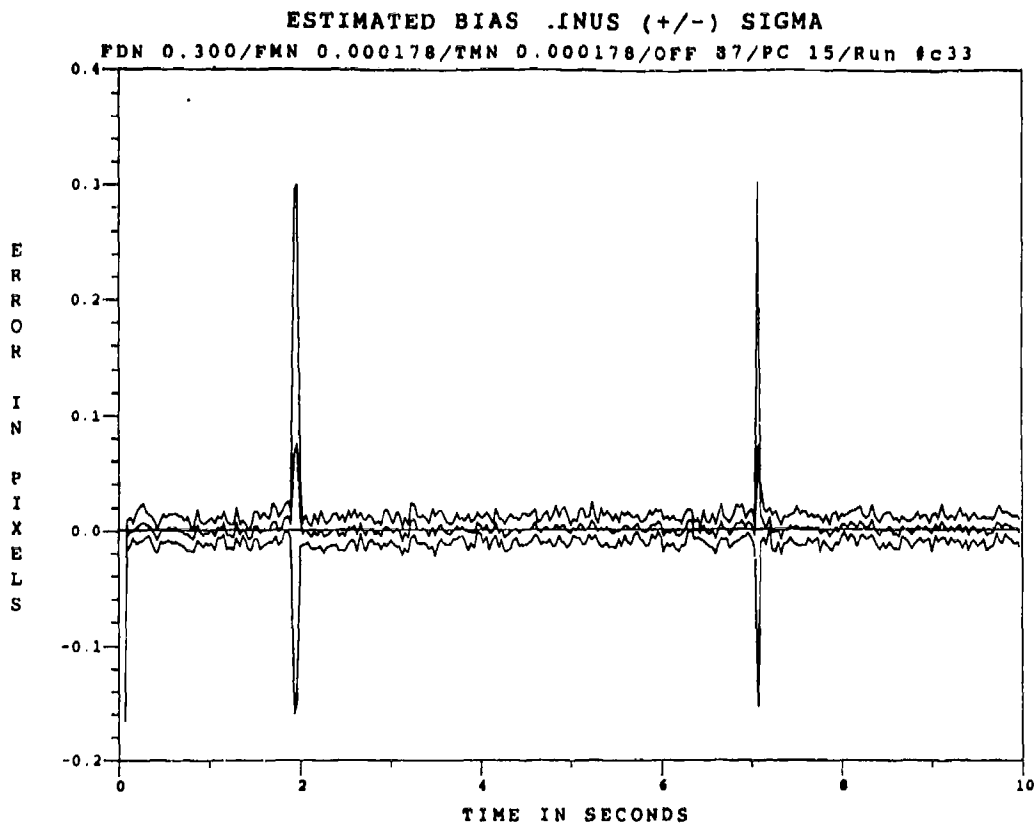


Figure E.2.11 0.53 μm Two-State Modified MAP MMAF Bias Error, SNR=4, $P_m = -0.05$, at t_i^*

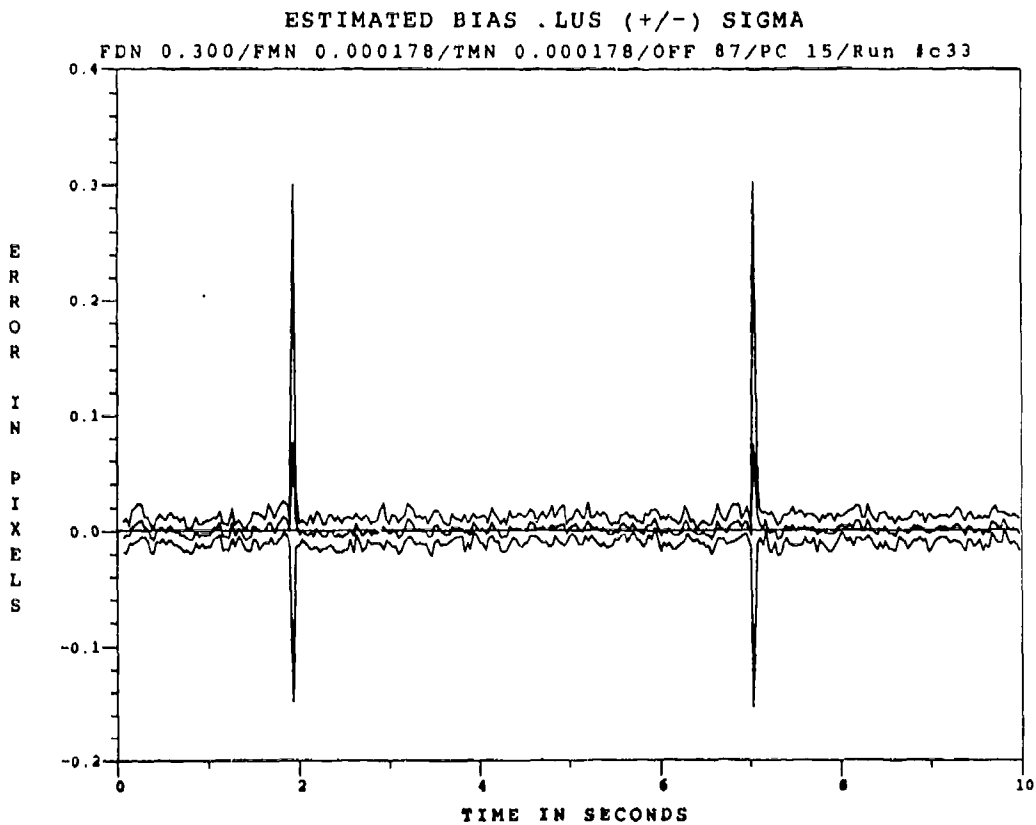


Figure E.2.12 0.53 μm Two-State Modified MAP MMAF Bias Error, SNR=4, $P_m = -0.05$, at t_i^*

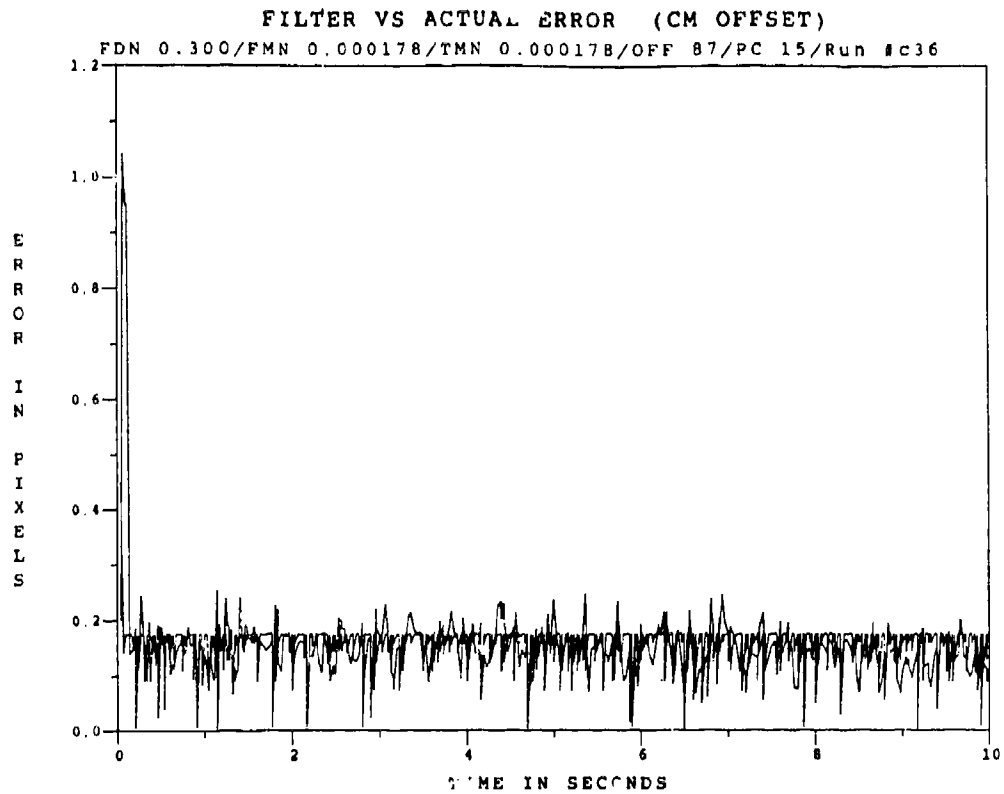


Figure E.2.13 0.53 μ m Two-State Modified MAP MMAF Offset Error, SNR = 4, $P_m = 0.30$

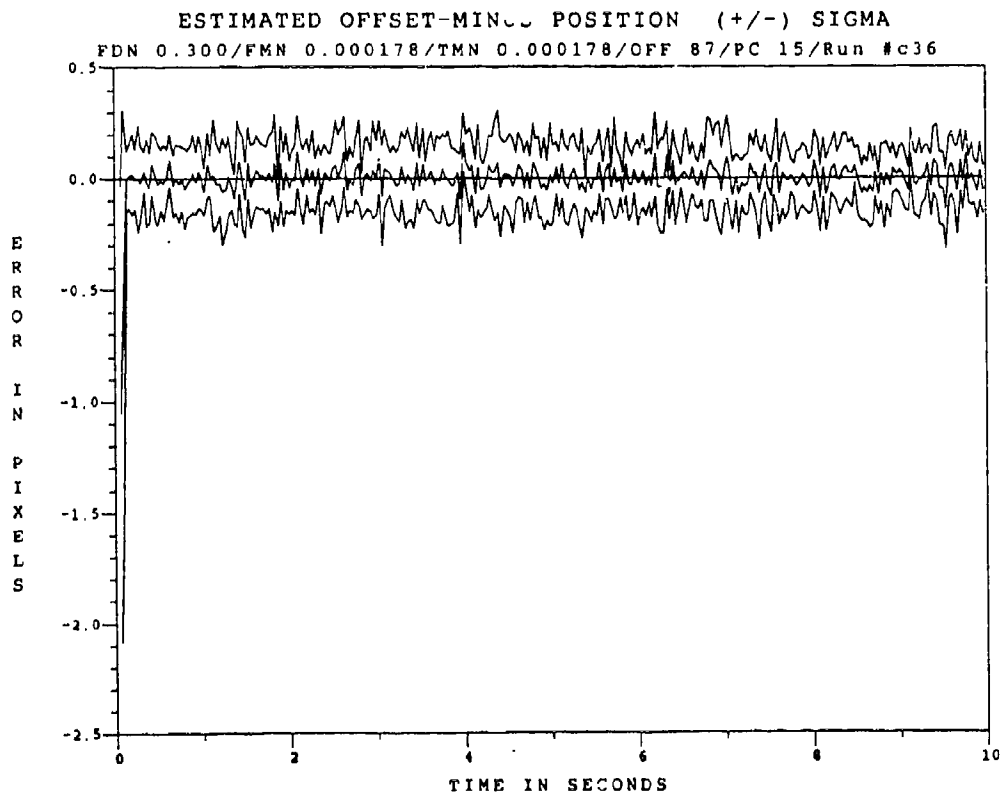


Figure E.2.14 0.53 μ m Two-State Modified MAP MMAF Offset Error, SNR=4, $P_m = 0.30$, at t_i

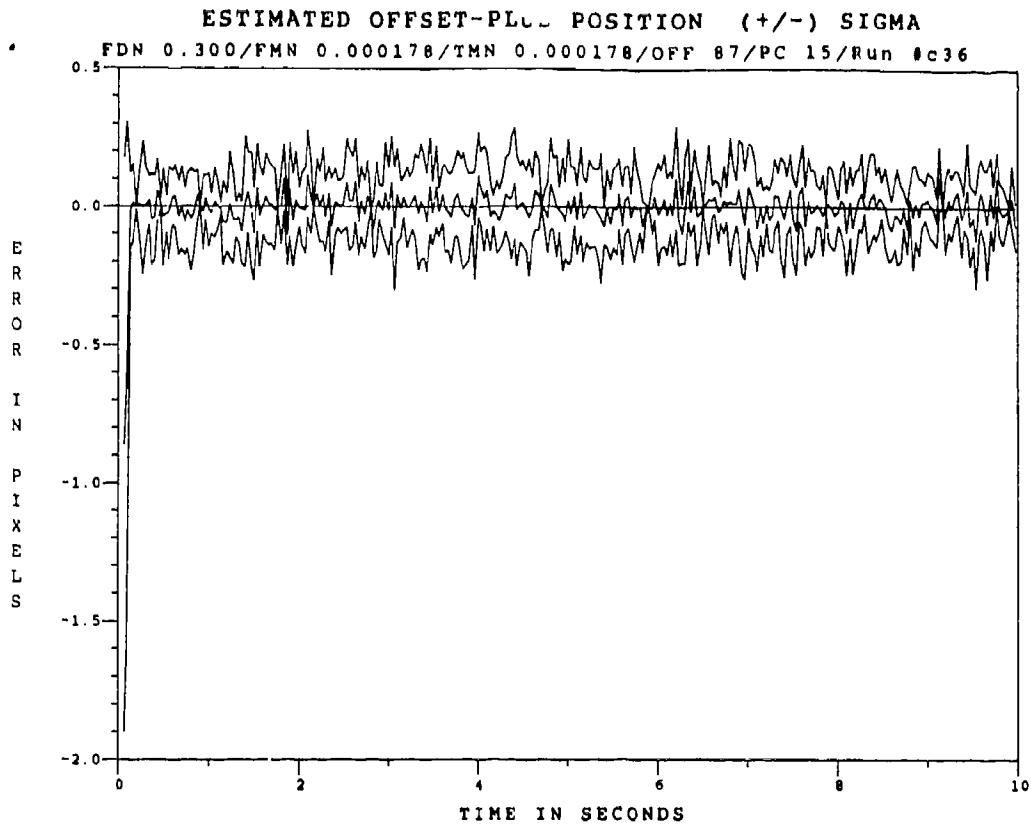


Figure E.2.15 0.53 μ m Two-State Modified MAP MMAF Offset Error, SNR=4, $P_m = -0.30$, at t_i^+

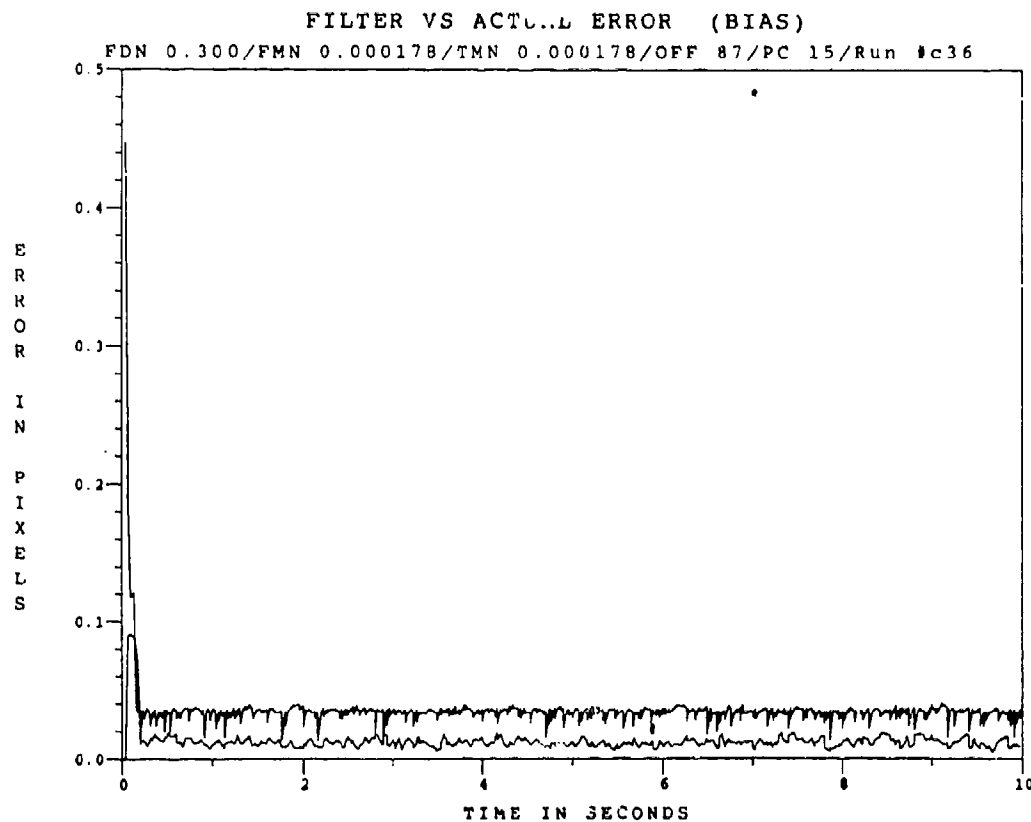


Figure E.2.16 0.53 μ m Two-State Modified MAP MMAF Bias Error, SNR = 4, $P_m = 0.30$

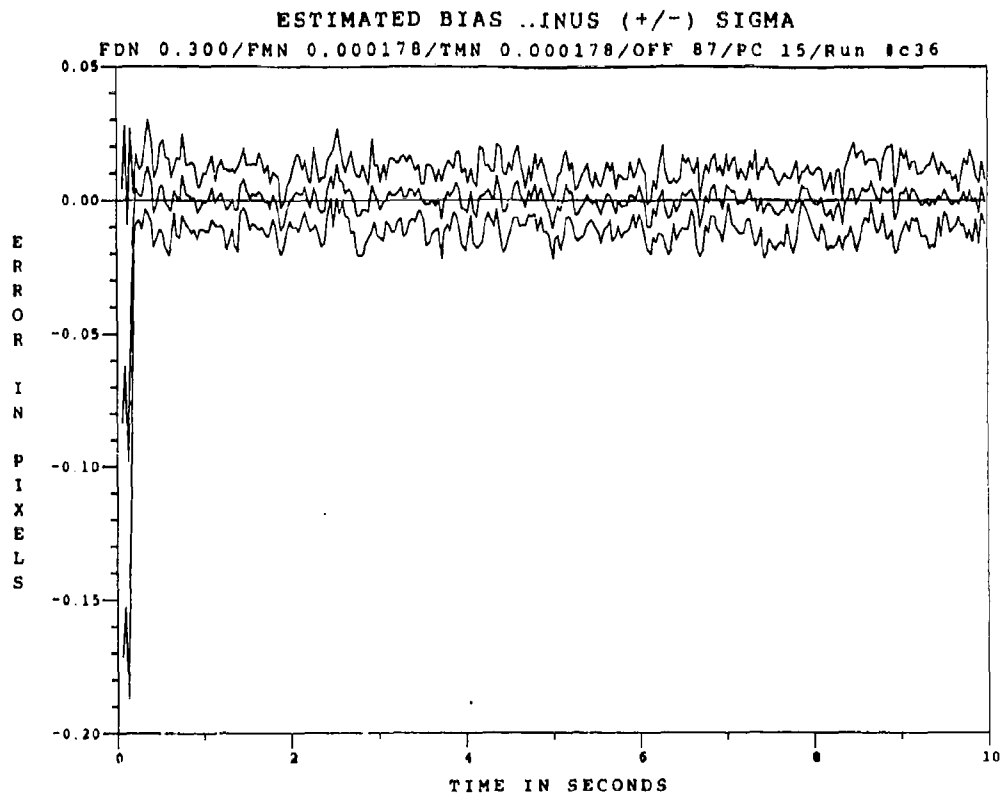


Figure E.2.17 0.53 μ m Two-State Modified MAP MMAF Bias Error, SNR=4, $P_m = -0.30$, at t_i^+

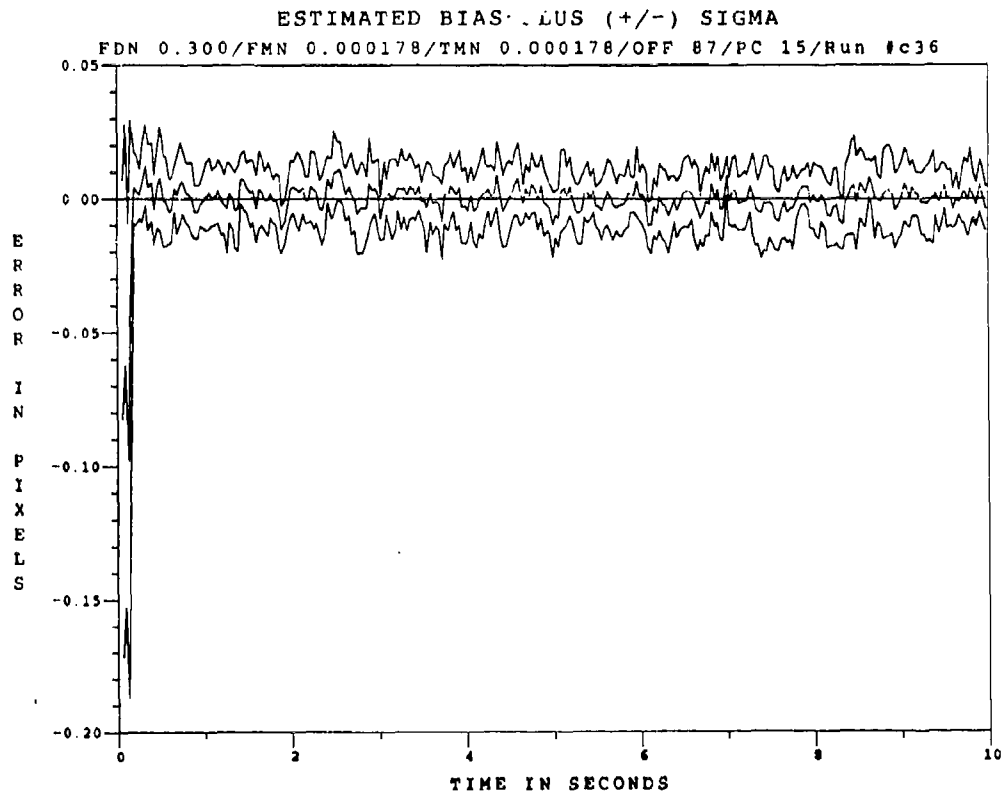


Figure E.2.18 0.53 μ m Two-State Modified MAP MMAF Bias Error, SNR=4, $P_m = -0.30$, at t_i^+

Appendix E.3

Two-State Center-of-Mass

Modified MAP MMAF

with

2.01 μm Doppler Return Measurements

at SNR = 10

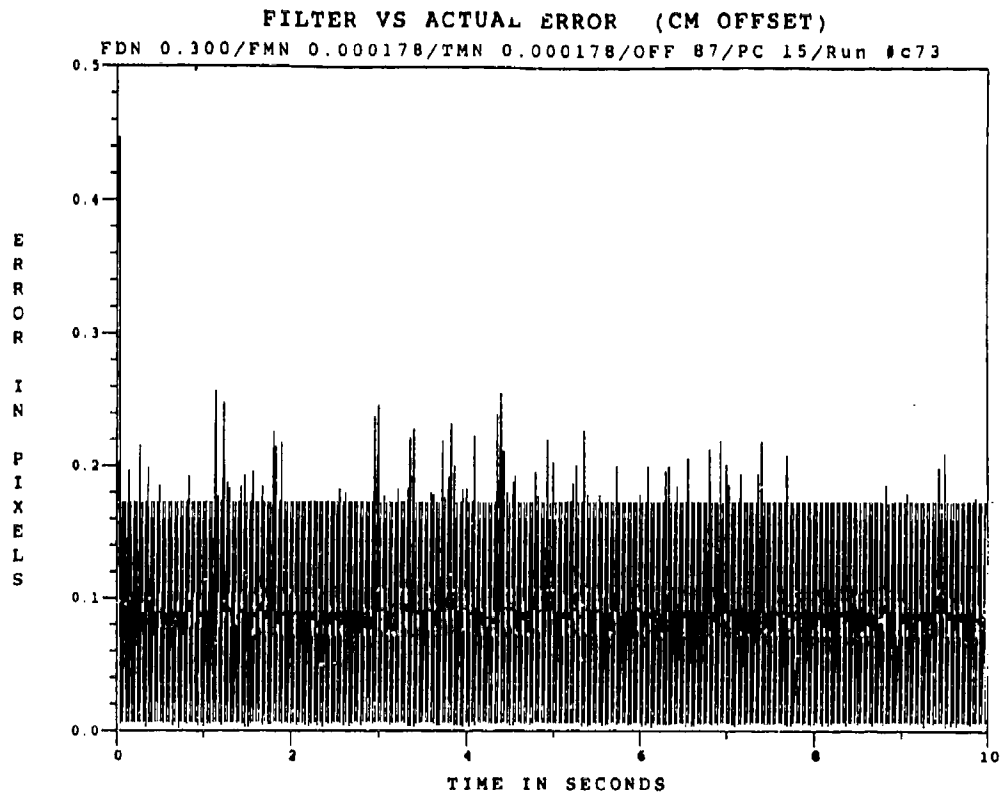


Figure E.3.1 2.01 μm Two-State Modified MAP MMAF Offset Error, SNR=10, $P_m = 0.0$

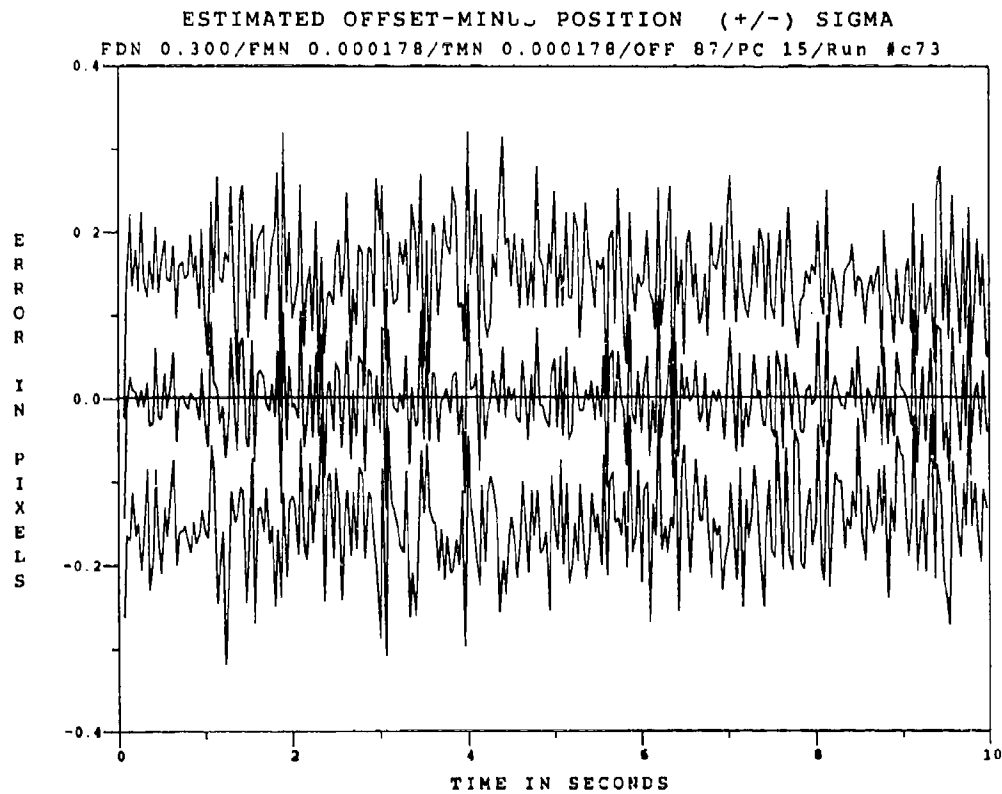


Figure E.3.2 2.01 μm Two-State Modified MAP MMAF Offset Error, SNR=10, $P_m = 0.0$, at t_i

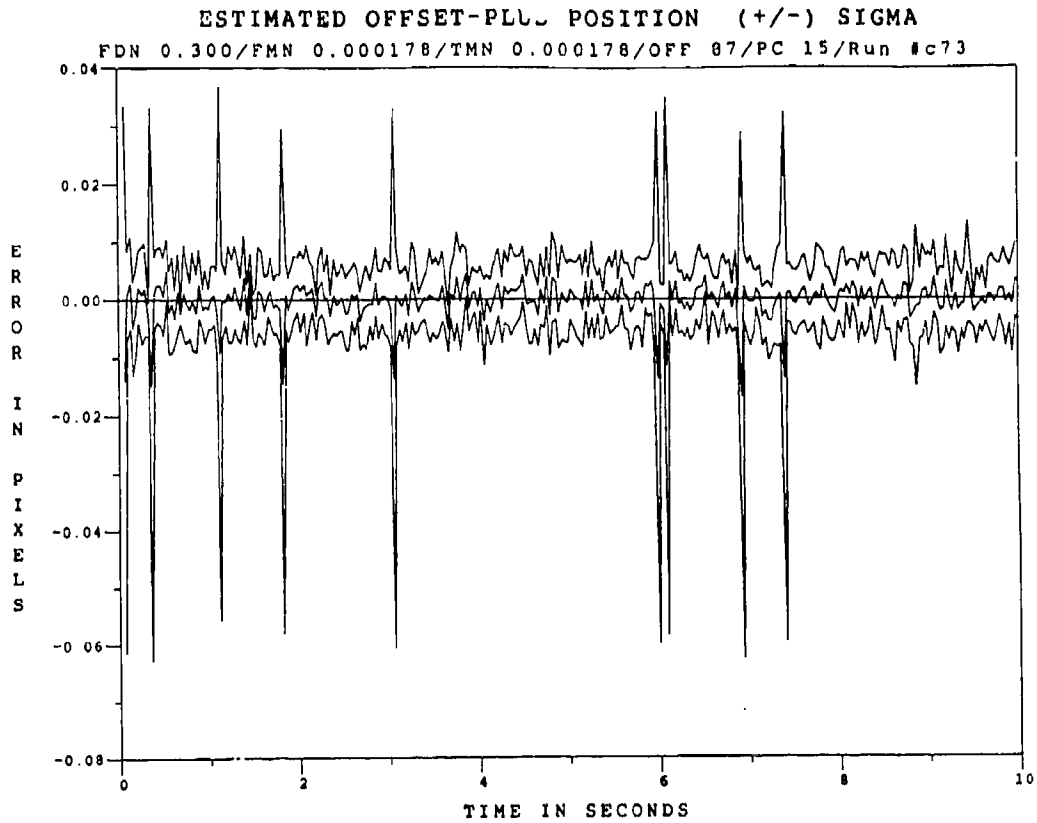


Figure E.3.3 2.01 μm Two-State Modified MAP MMAF Offset Error, SNR=10, $P_m = 0.0$, at t_i^+

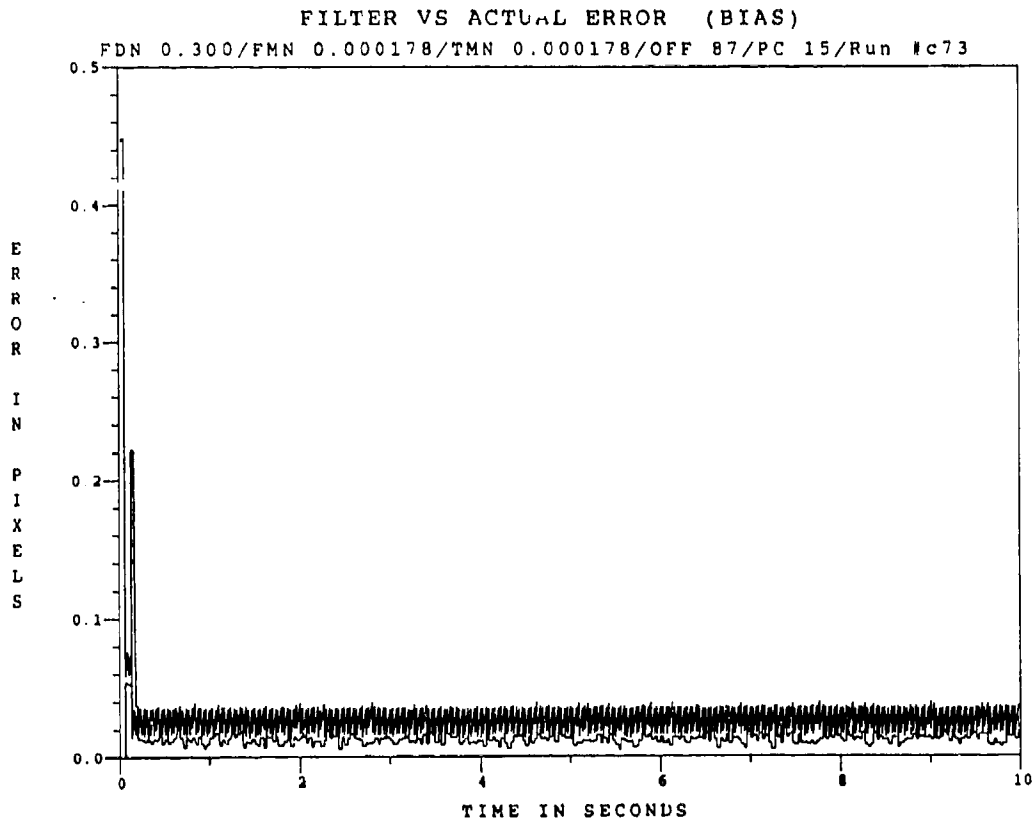


Figure E.3.4 2.01 μm Two-State Modified MAP MMAF Bias Error, SNR=10, $P_m = 0.0$

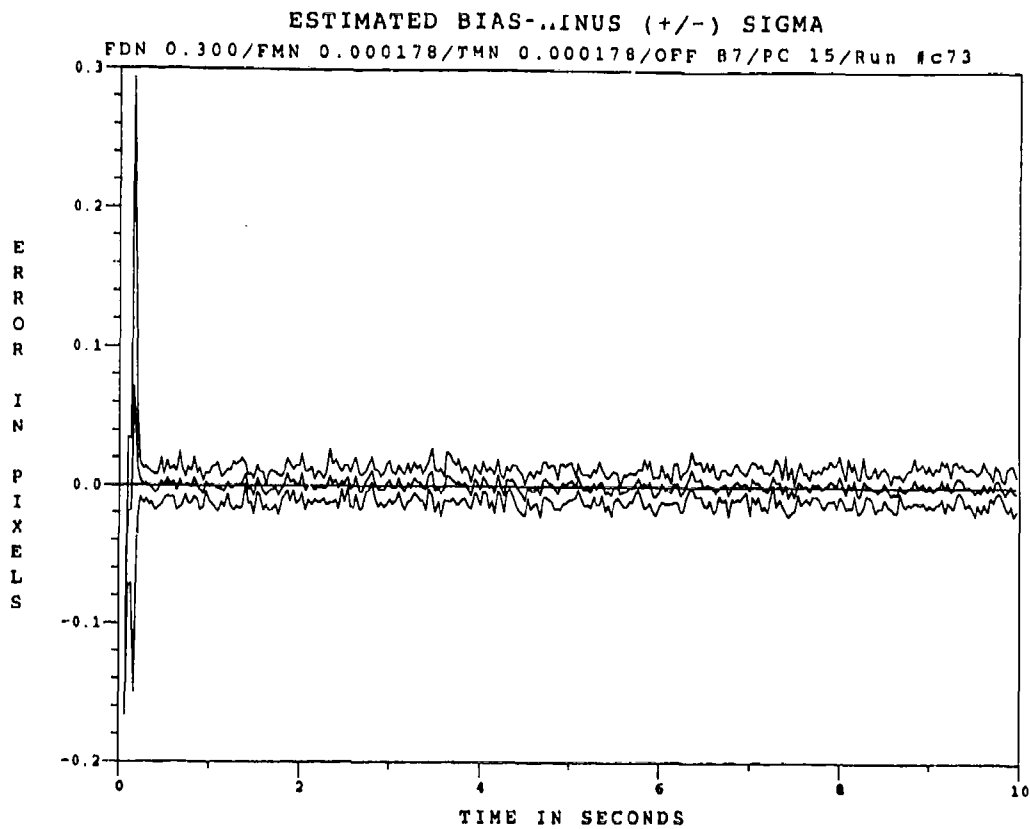


Figure E.3.5 2.01 μm Two-State Modified MAP MMAF Bias Error, SNR=10, $P_m = -0.0$, at t_i^*

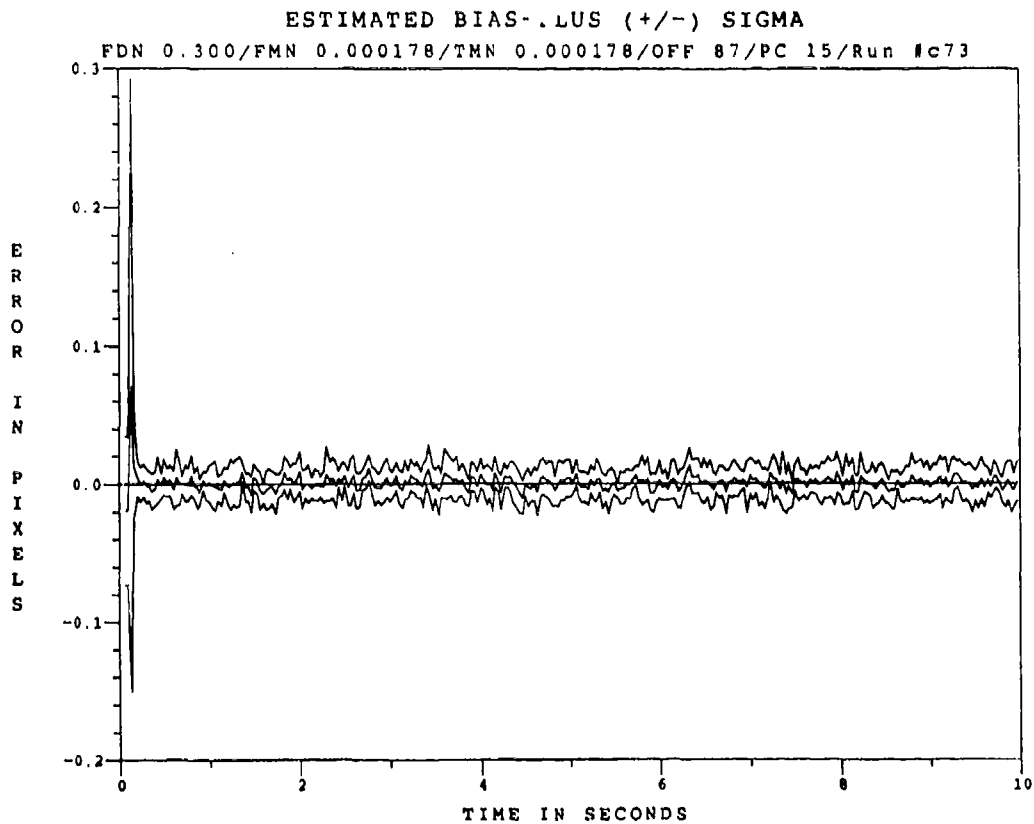


Figure E.3.6 2.01 μm Two-State Modified MAP MMAF Bias Error, SNR=10, $P_m = -0.0$, at t_i^*

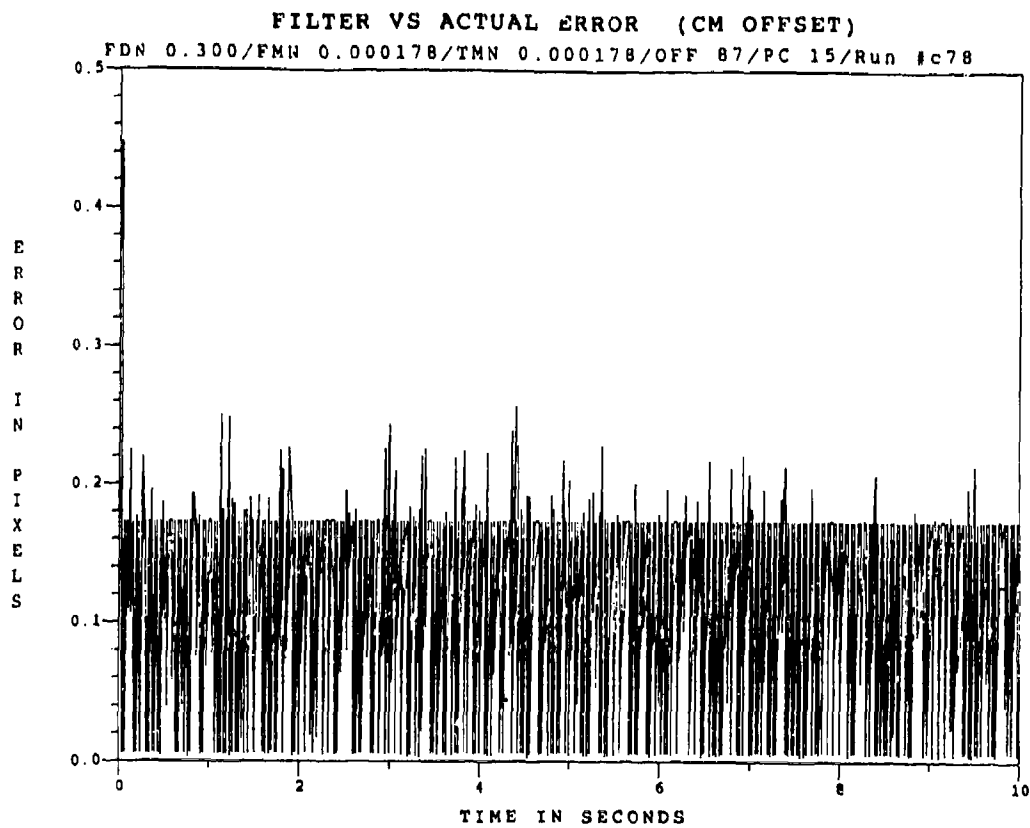


Figure E.3.7 2.01 μm Two-State Modified MAP MMAF Offset Error, SNR = 10, $P_m = 0.05$

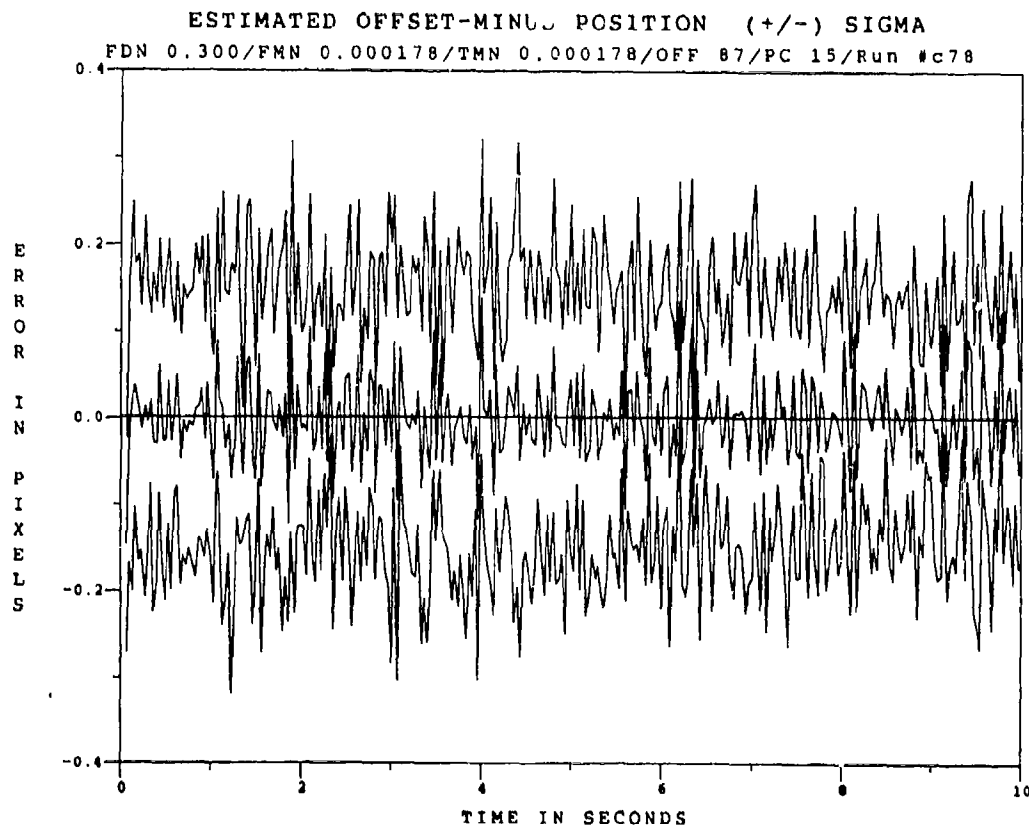


Figure E.3.8 2.01 μm Two-State Modified MAP MMAF Offset Error, SNR=10, $P_m = 0.05$, at t_i

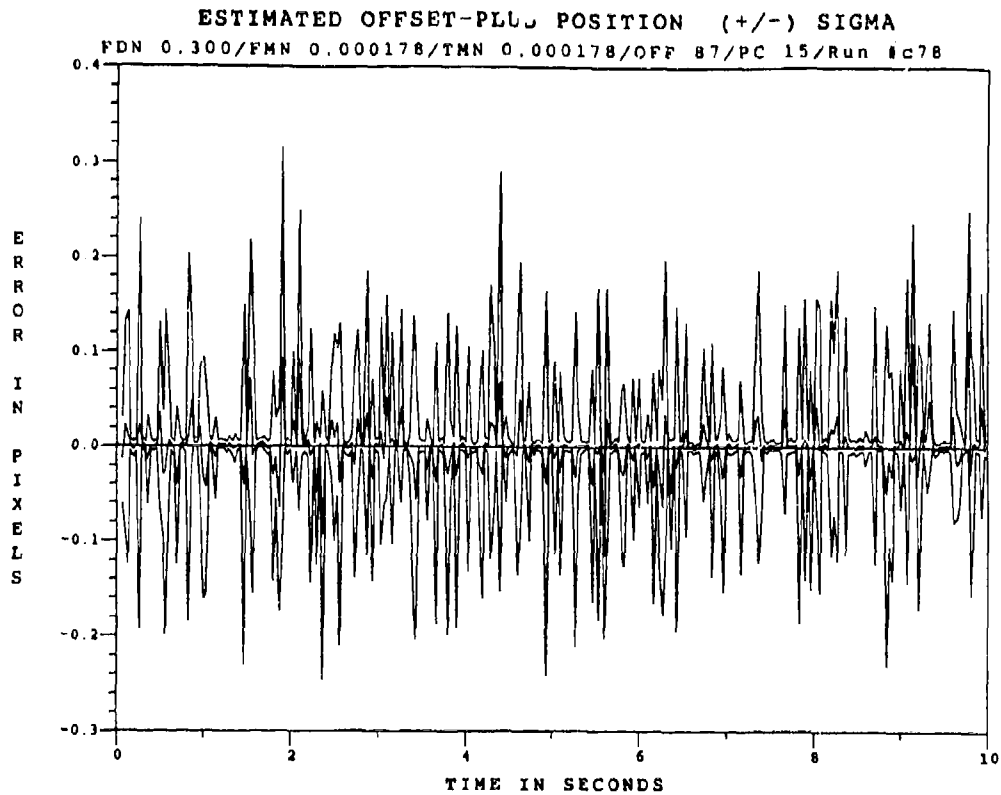


Figure E.3.9 2.01 μ m Two-State Modified MAP MMAF Offset Error, SNR=10, $P_m = -0.05$, at t_1^+

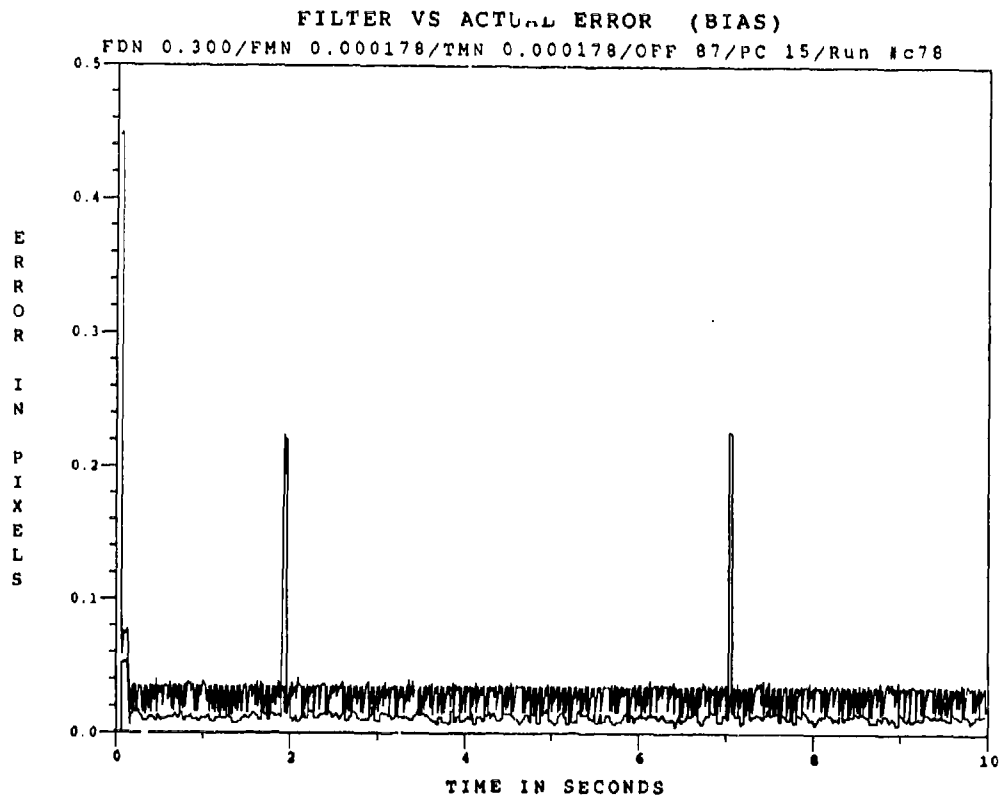


Figure E.3.10 2.01 μ m Two-State Modified MAP MMAF Bias Error, SNR = 10, $P_m = 0.05$

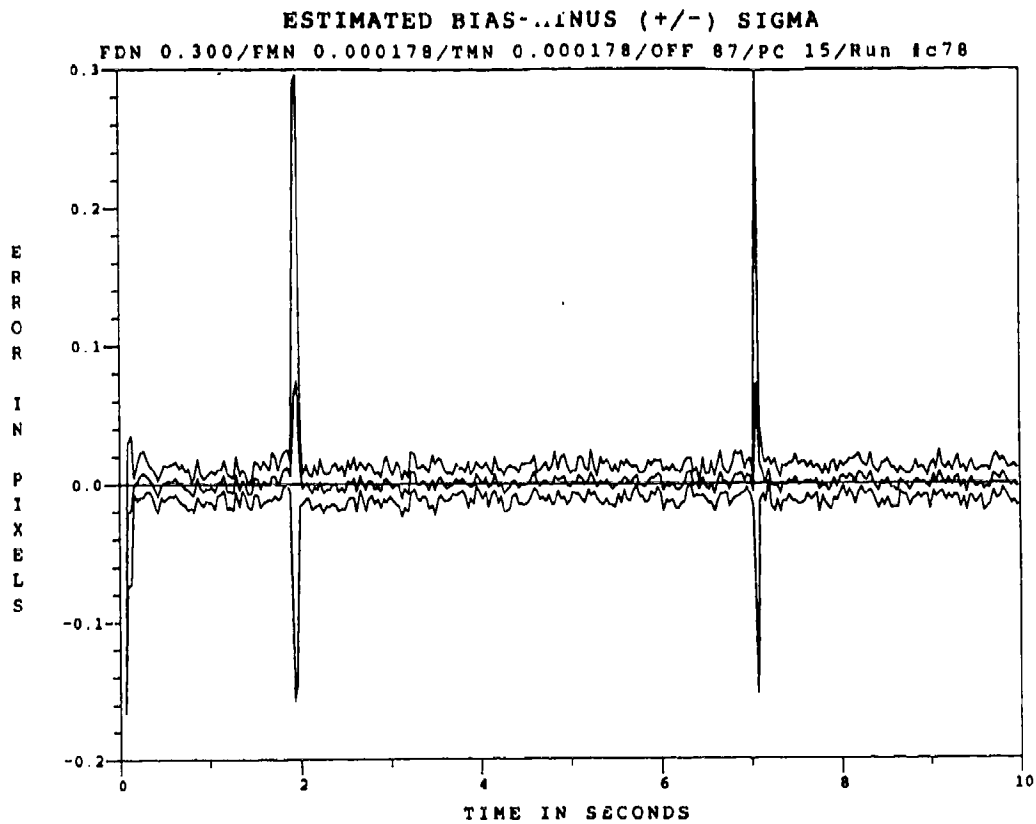


Figure E.3.11 2.01 μm Two-State Modified MAP MMAF Bias Error, SNR=10, $P_m = 0.05$, at t_i^*

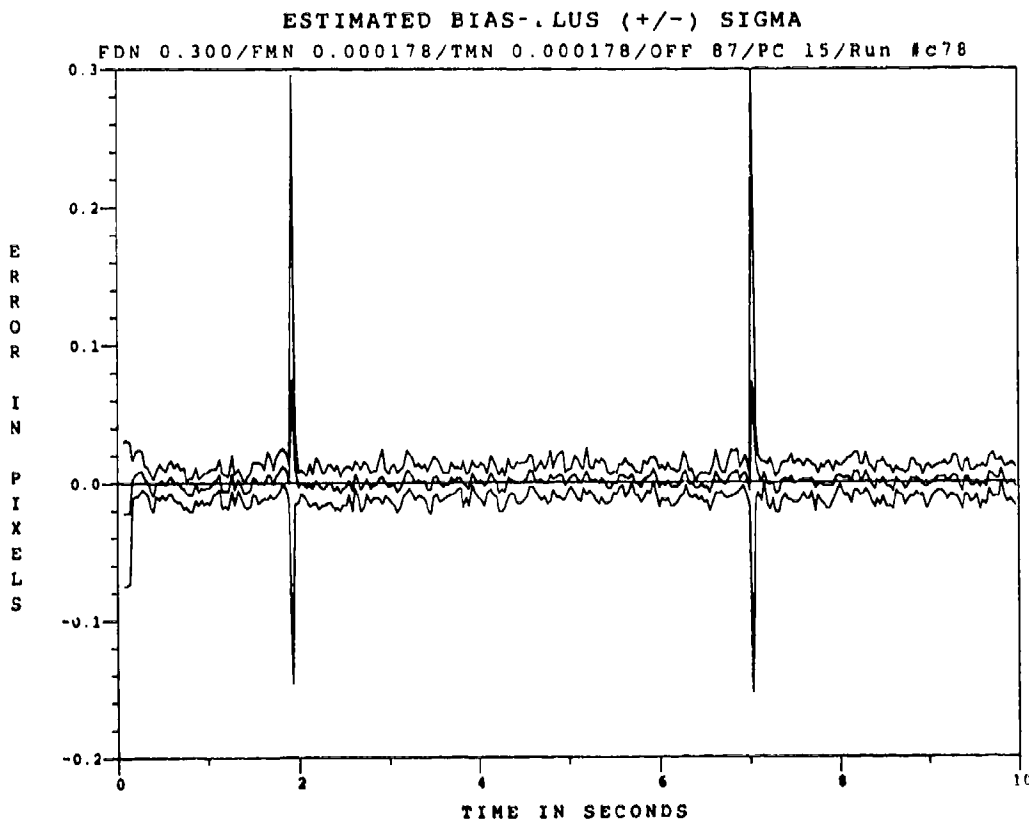


Figure E.3.12 2.01 μm Two-State Modified MAP MMAF Bias Error, SNR=10, $P_m = 0.05$, at t_i^*

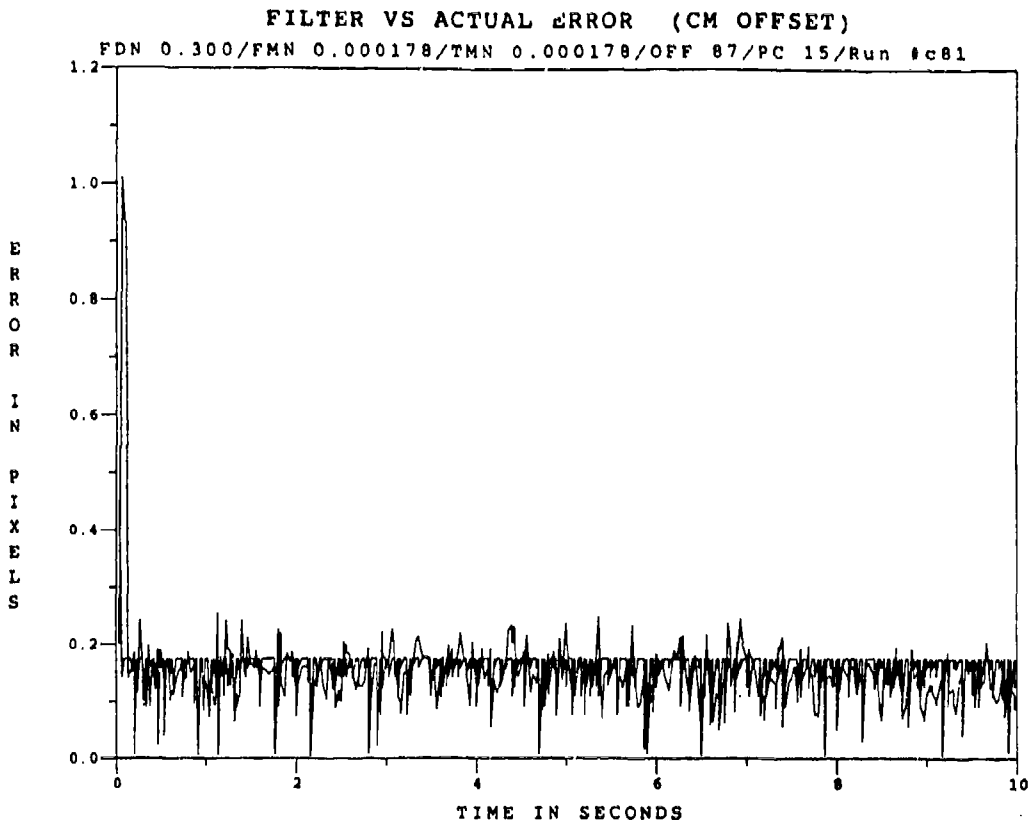


Figure E.3.13 2.01 μm Two-State Modified MAP MMAF Offset Error, SNR = 10, $P_m = 0.30$

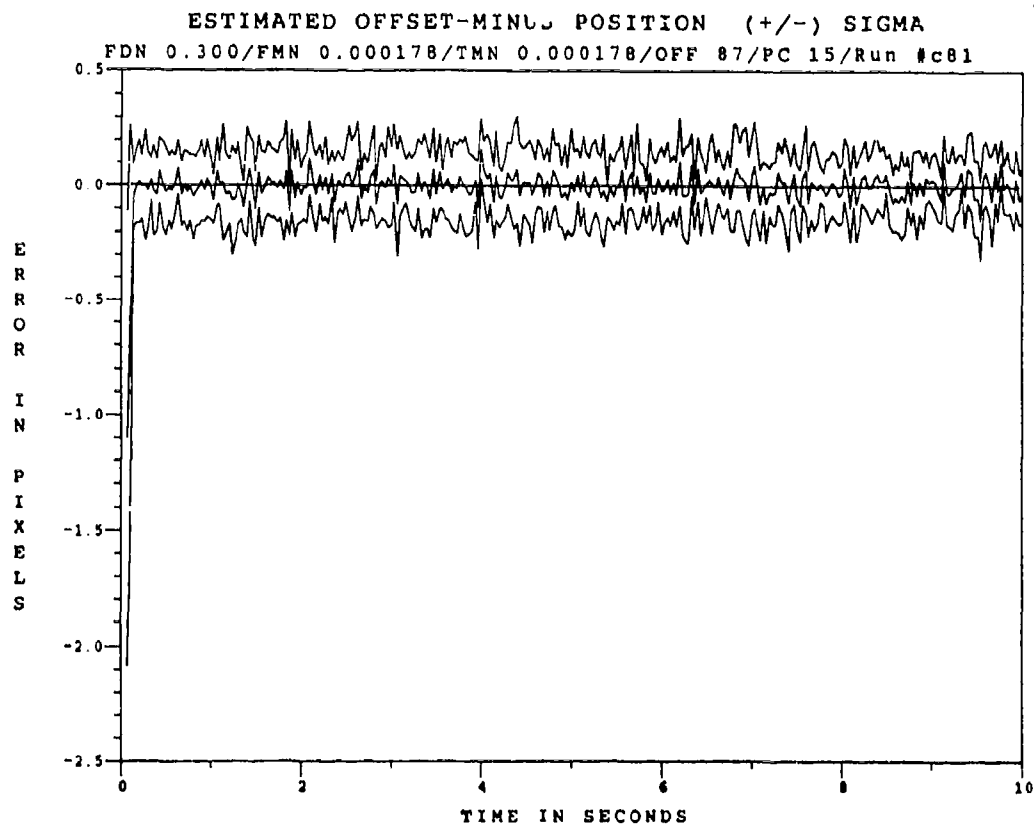


Figure E.3.14 2.01 μm Two-State Modified MAP MMAF Offset Error, SNR=10, $P_m=0.30$, at t_i

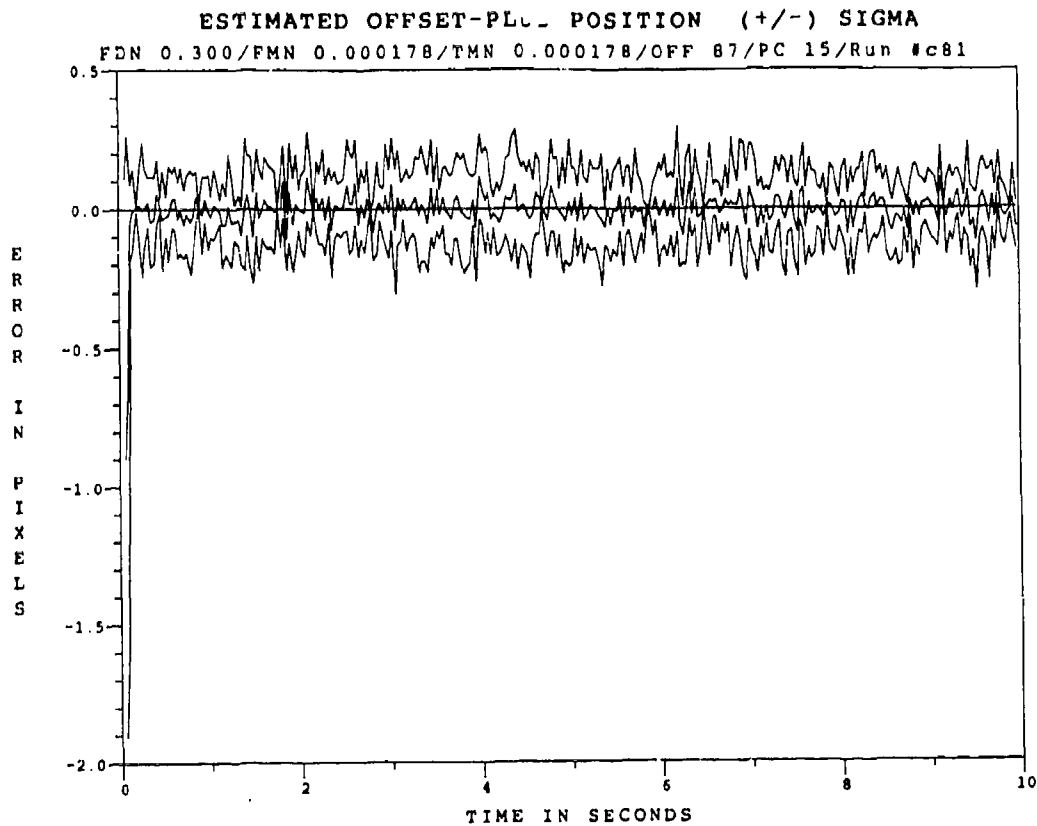


Figure E.3.15 2.01 μ m Two-State Modified MAP MMAF Offset Error, SNR=10, $P_m = -0.30$, at t_i^*

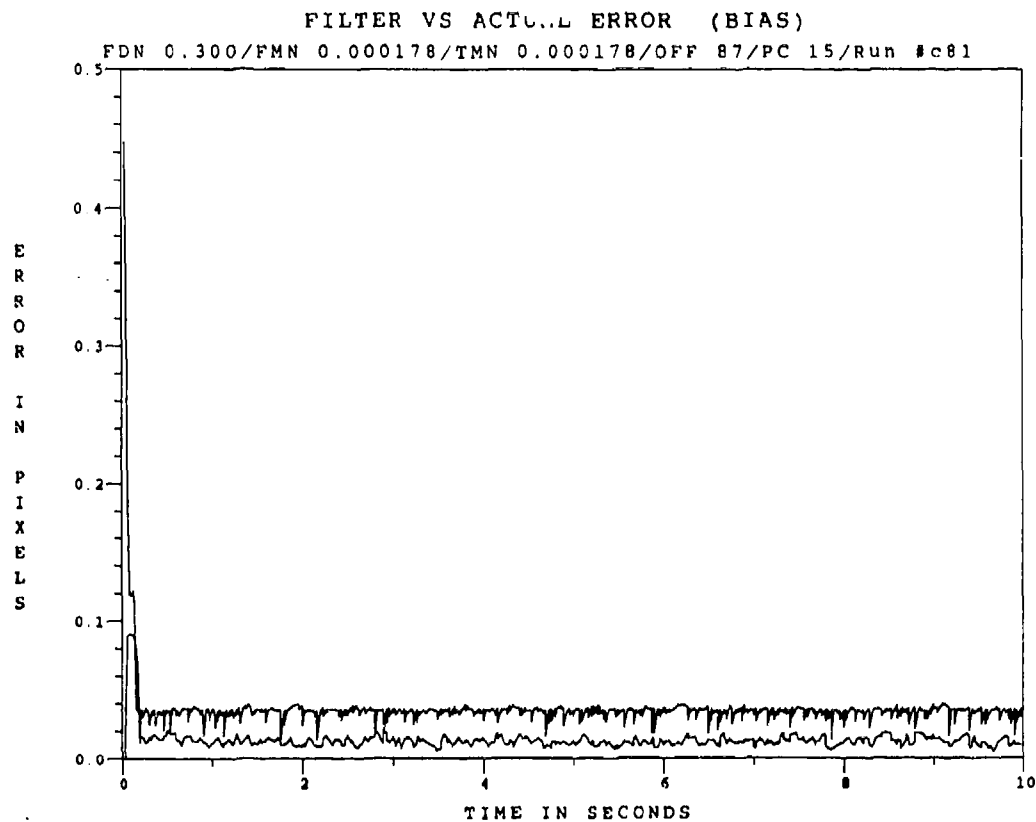


Figure E.3.16 2.01 μ m Two-State Modified MAP MMAF Bias Error, SNR = 10, $P_m = -0.30$

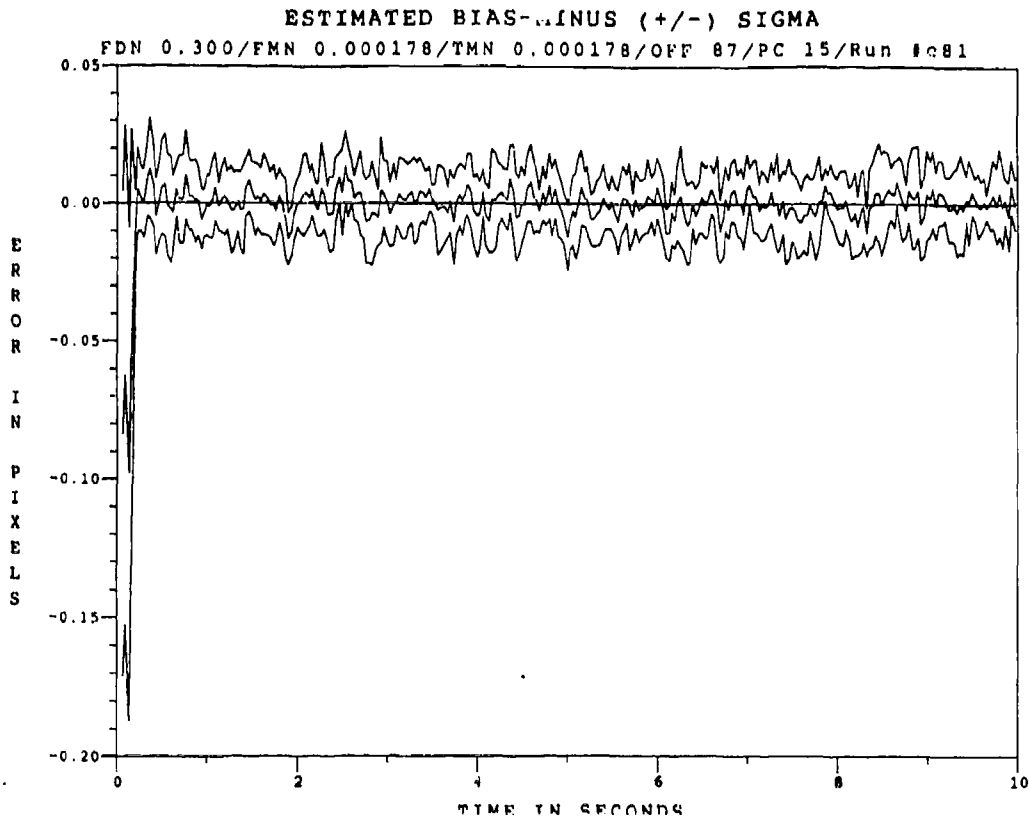


Figure E.3.17 2.01 μ m Two-State Modified MAP MMAF Bias Error, SNR=10, $P_w = -0.30$, at t_i^+

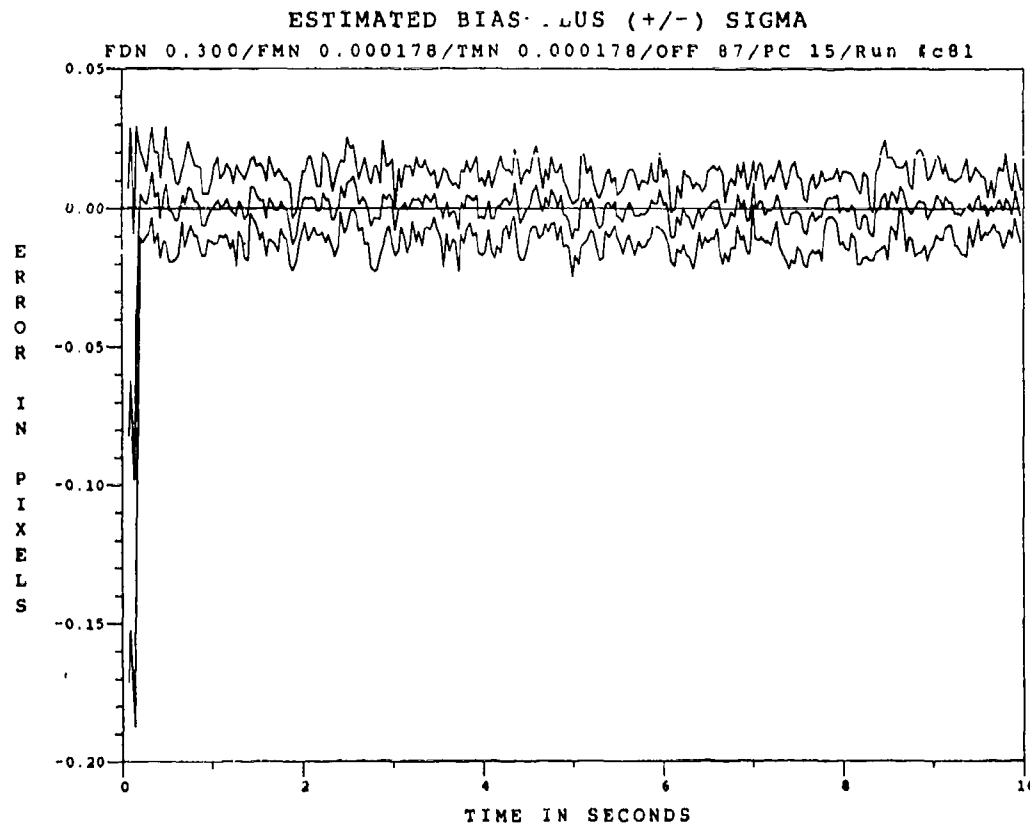


Figure E.3.18 2.01 μ m Two-State Modified MAP MMAF Bias Error, SNR=10, $P_w = -0.30$, at t_i^+

Appendix E.4

Two-State Center-of-Mass

Modified MAP MMAF

with

2.01 μm Doppler Return Measurements

at SNR = 4

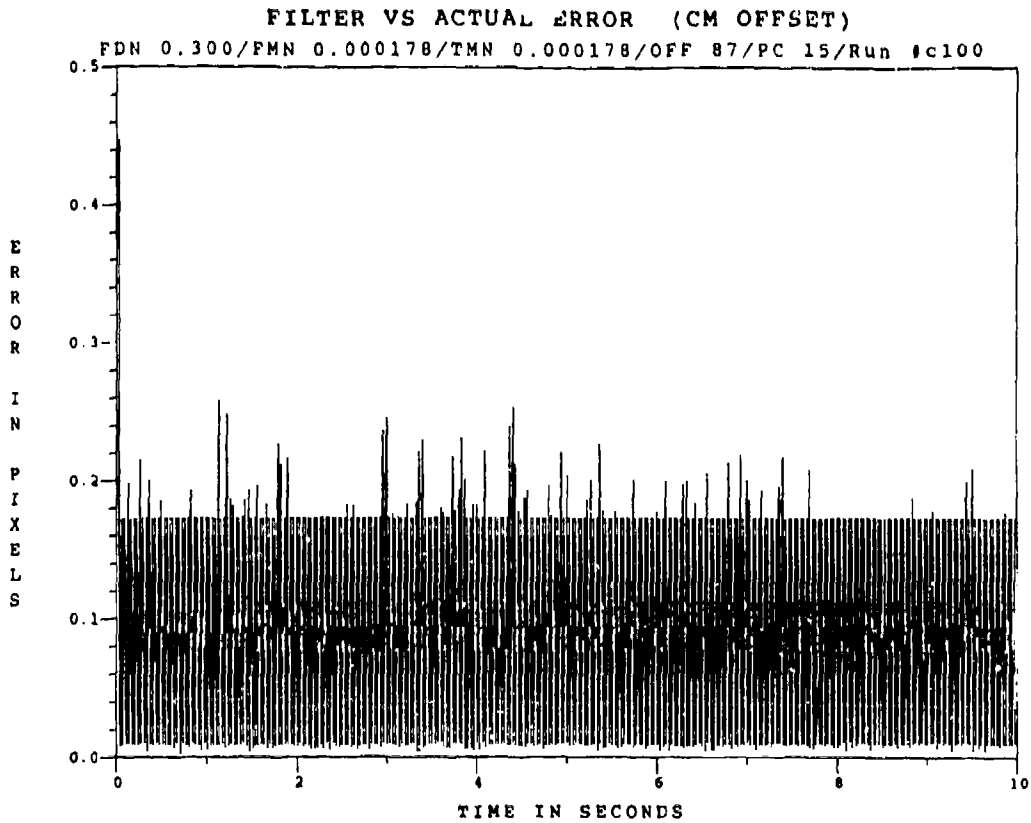


Figure E.4.1 2.01 μm Two-State Modified MAP MMAF Offset Error, SNR=4, $P_m=0.0$

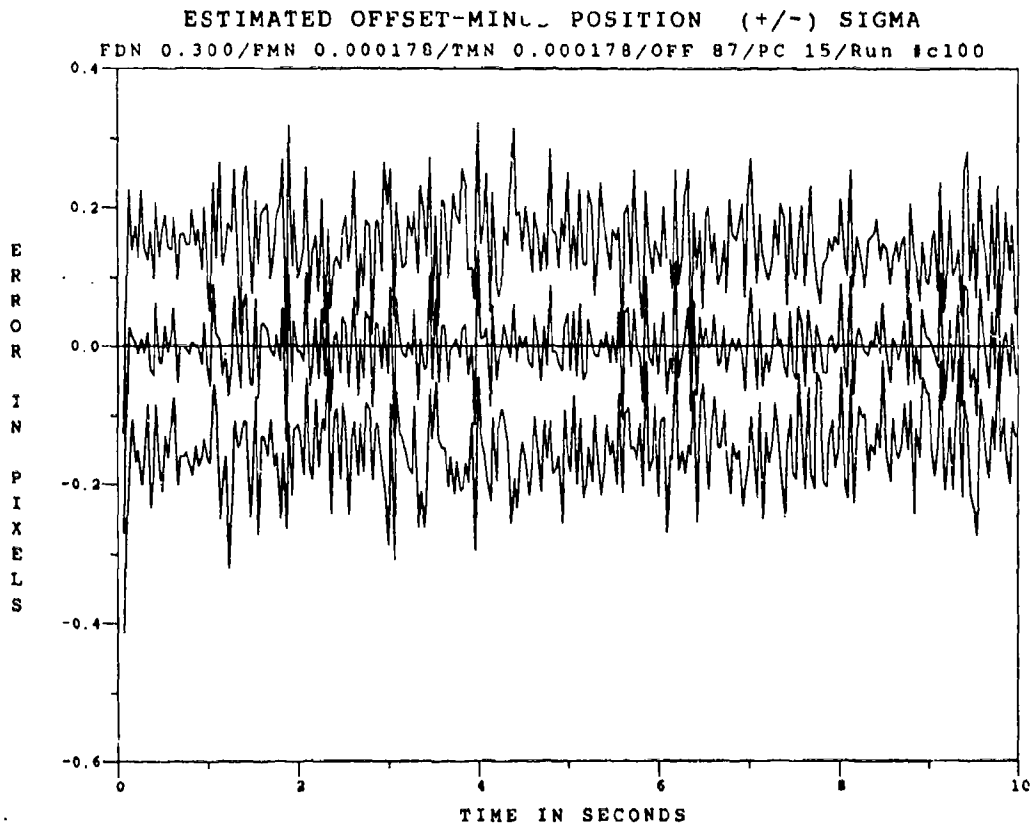


Figure E.4.2 2.01 μm Two-State Modified MAP MMAF Offset Error, SNR=4, $P_m=0.0$, at t_i

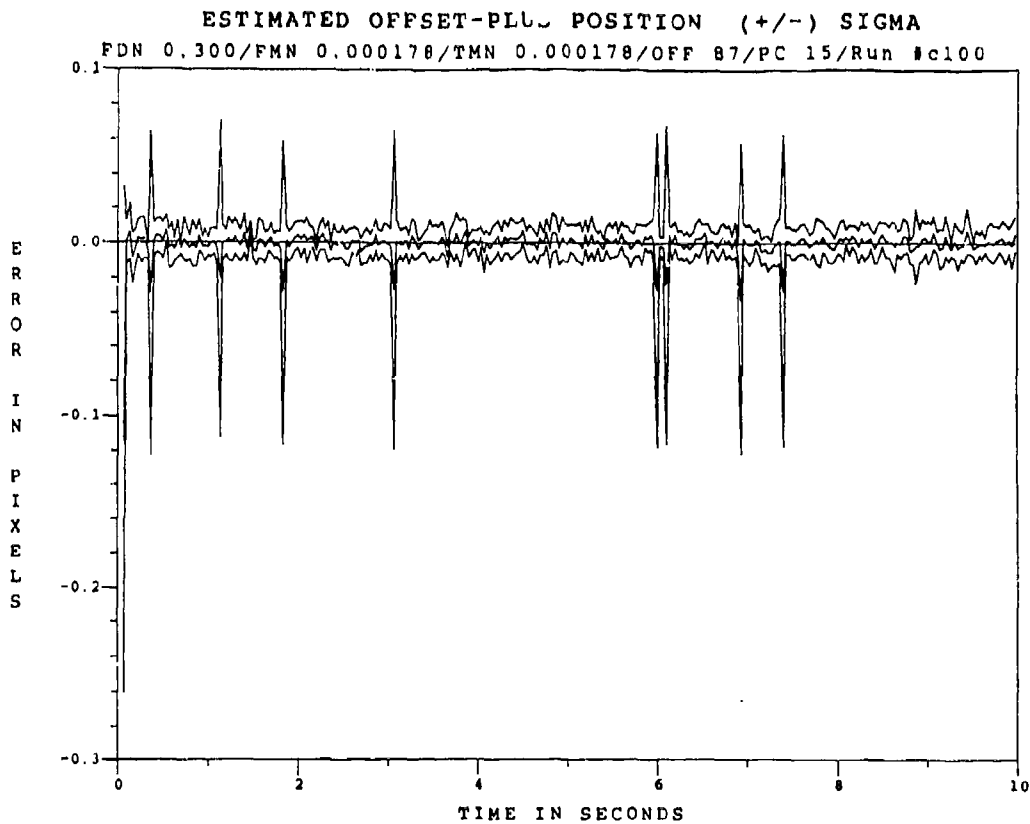


Figure E.4.3 2.01 μm Two-State Modified MAP MMAF Offset Error, SNR=4, $P_m = -0.0$, at t_i^*

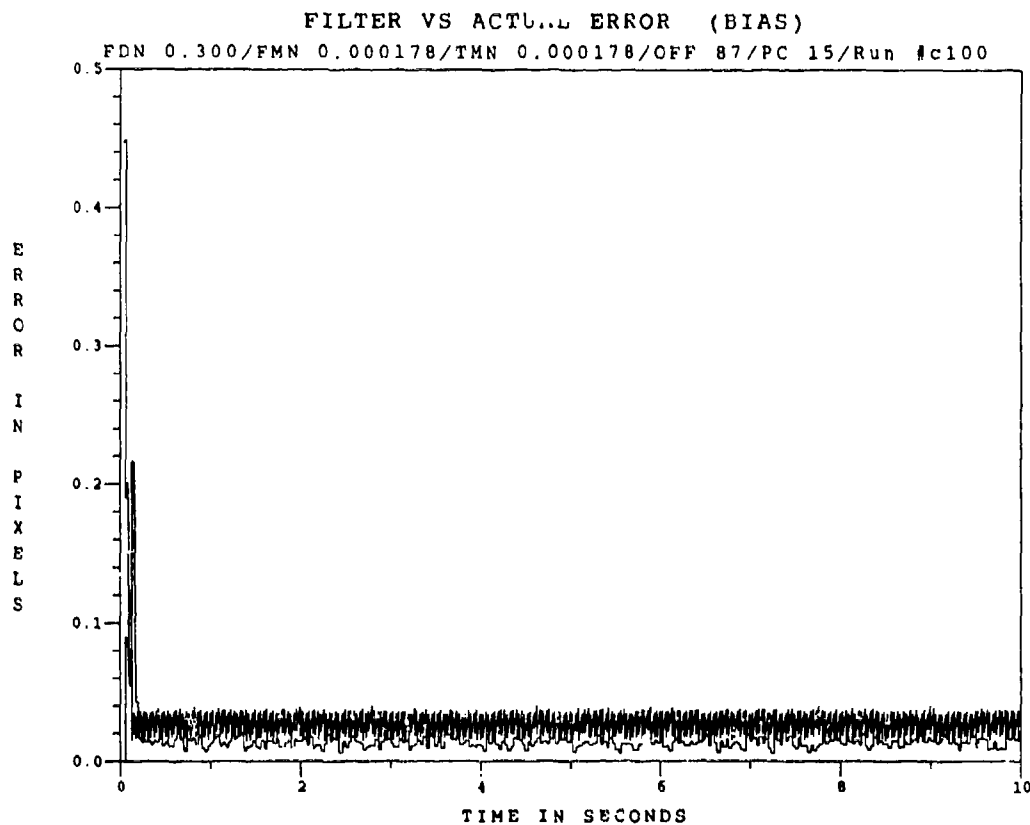


Figure E.4.4 2.01 μm Two-State Modified MAP MMAF Bias Error, SNR=4, $P_m = -0.0$

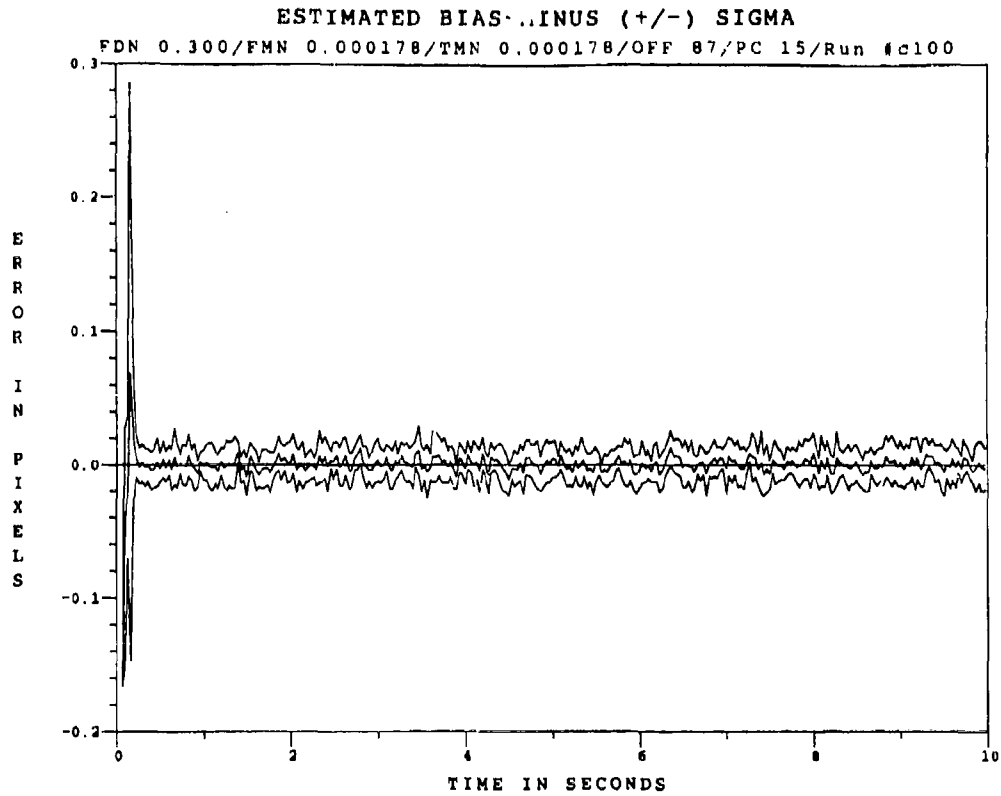


Figure E.4.5 2.01 μm Two-State Modified MAP MMAF Bias Error, SNR=4, $P_m = -0.0$, at t_i^*

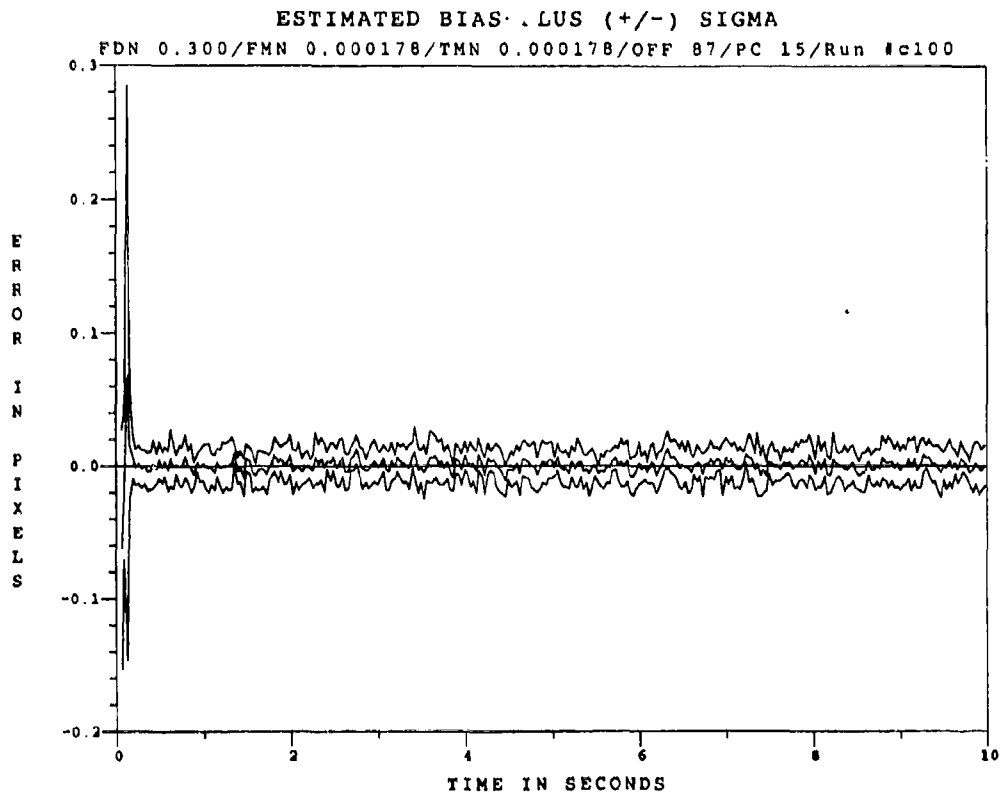


Figure E.4.6 2.01 μm Two-State Modified MAP MMAF Bias Error, SNR=4, $P_m = -0.0$, at t_i^*

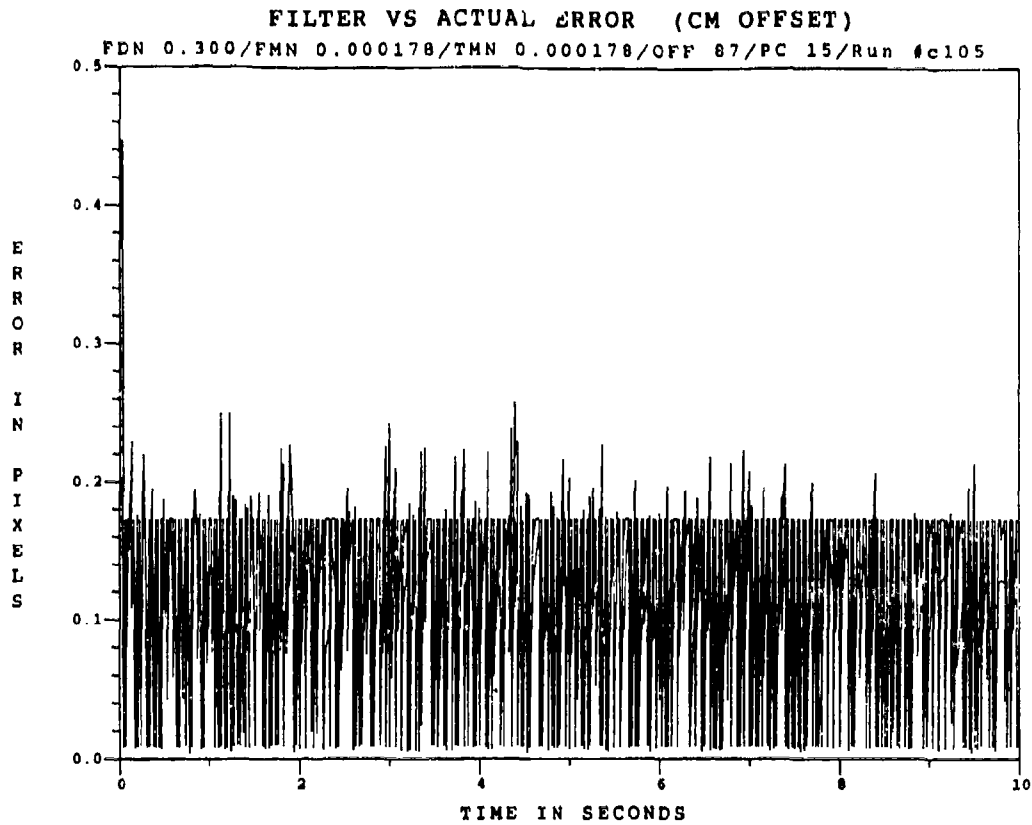


Figure E.4.7 2.01 μm Two-State Modified MAP MMAF Offset Error, SNR = 4, $P_m = 0.05$

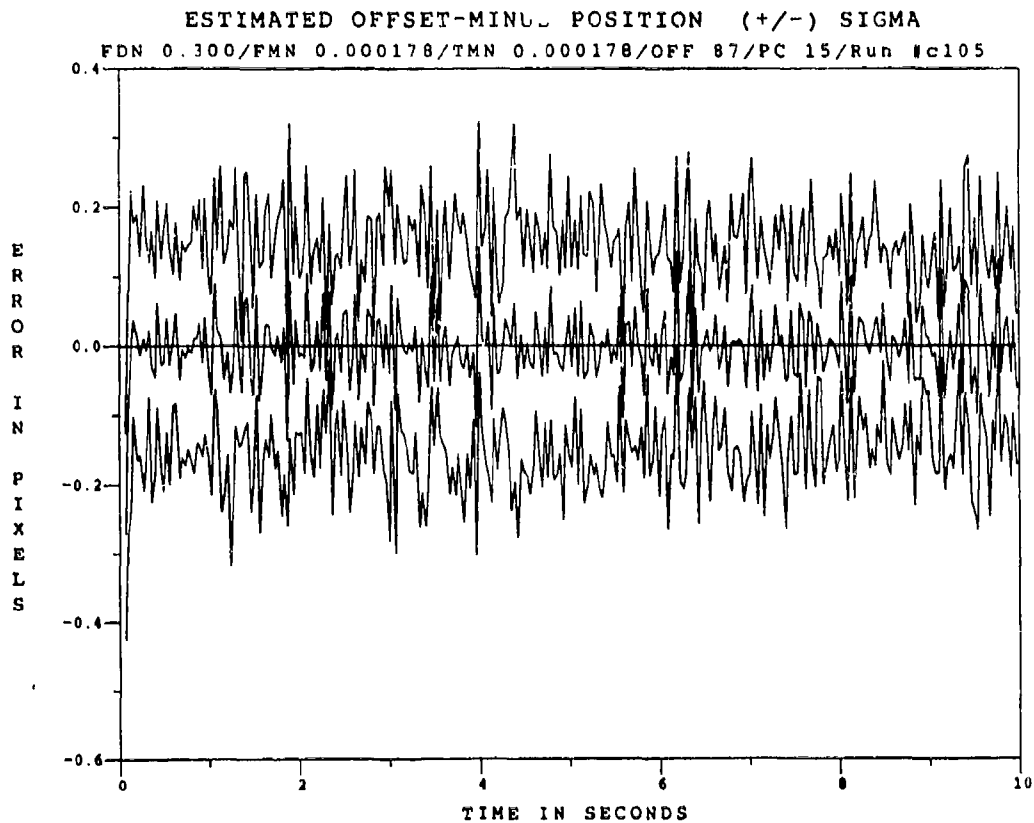


Figure E.4.8 2.01 μm Two-State Modified MAP MMAF Offset Error, SNR=4, $P_m = 0.05$, at t_i

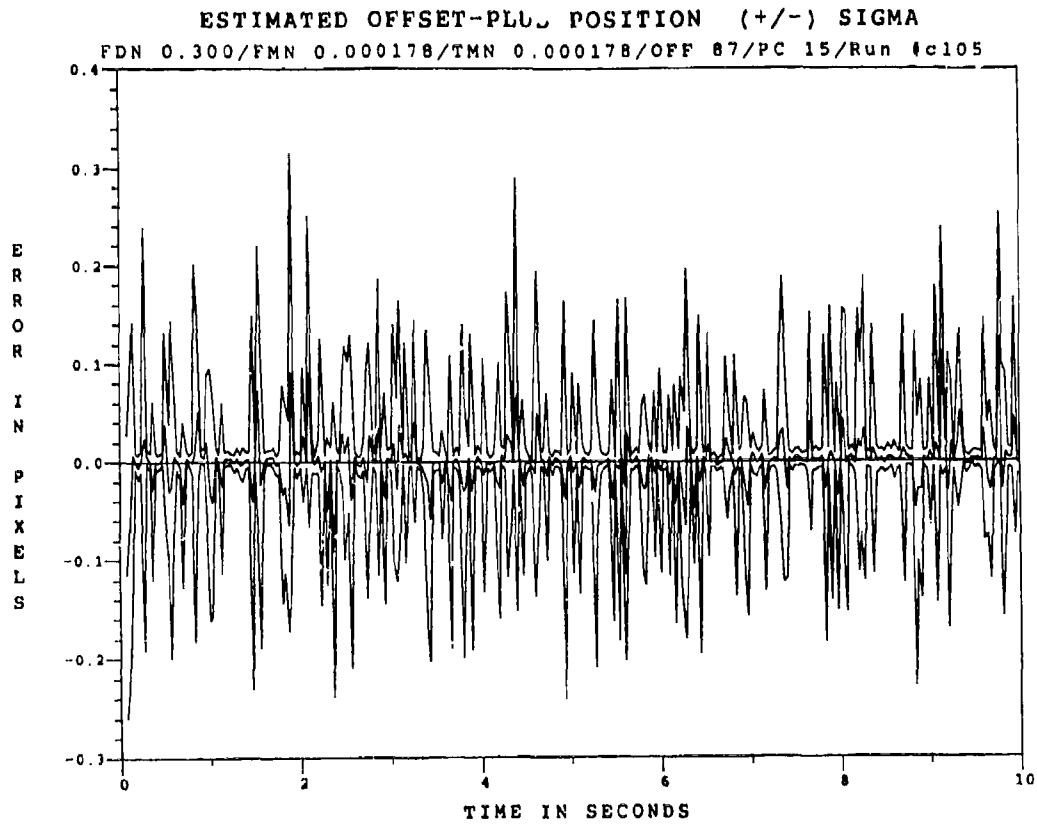


Figure E.4.9 2.01 μ m Two-State Modified MAP MMAF Offset Error, SNR=4, $P_m = -0.05$, at t_i^+

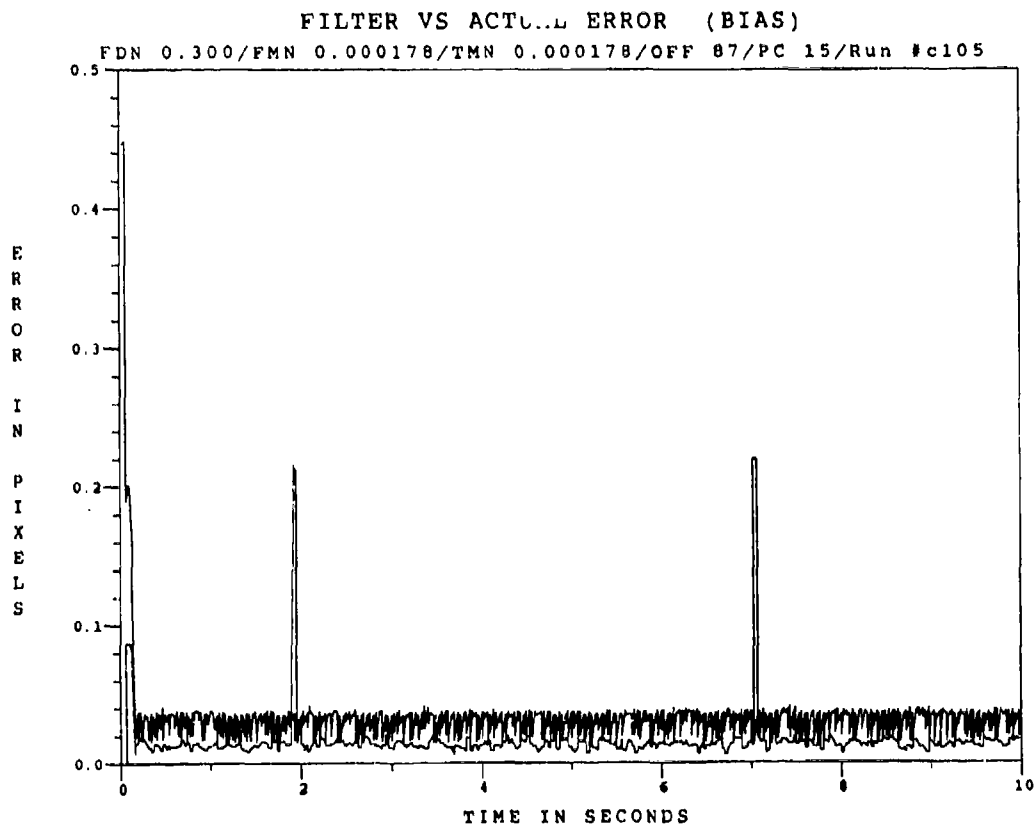


Figure E.4.10 2.01 μ m Two-State Modified MAP MMAF Bias Error, SNR = 4, $P_m = 0.05$

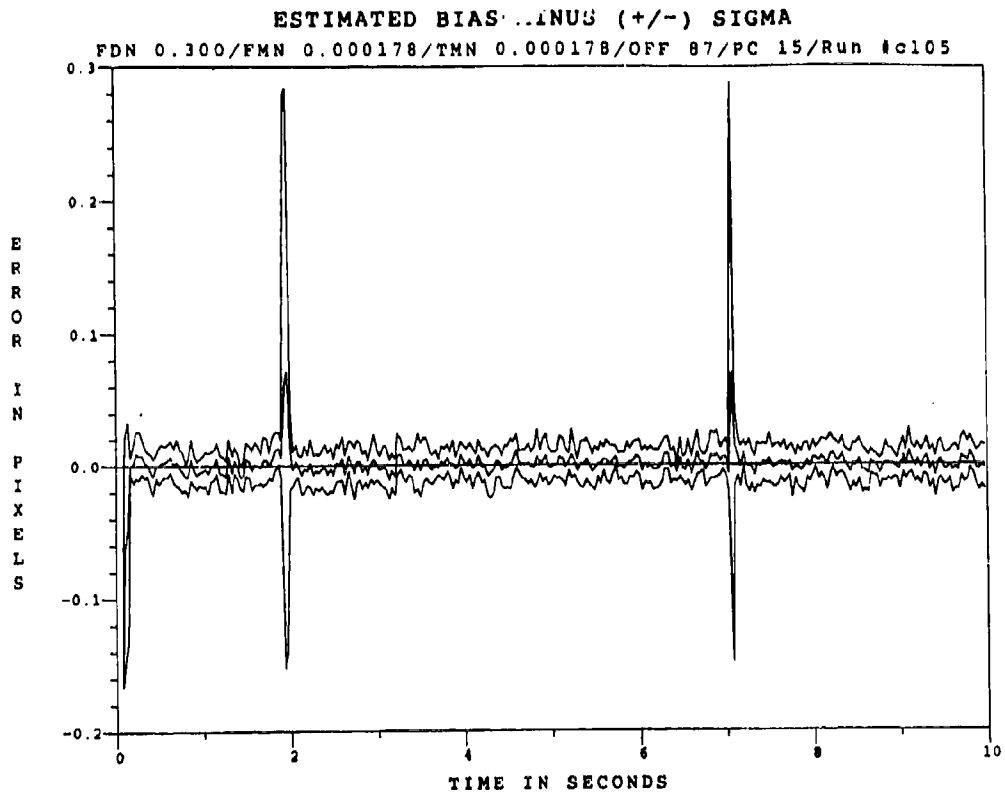


Figure E.4.11 2.01 μm Two-State Modified MAP MMAF Bias Error, SNR=4, $P_m = -0.05$, at t_i

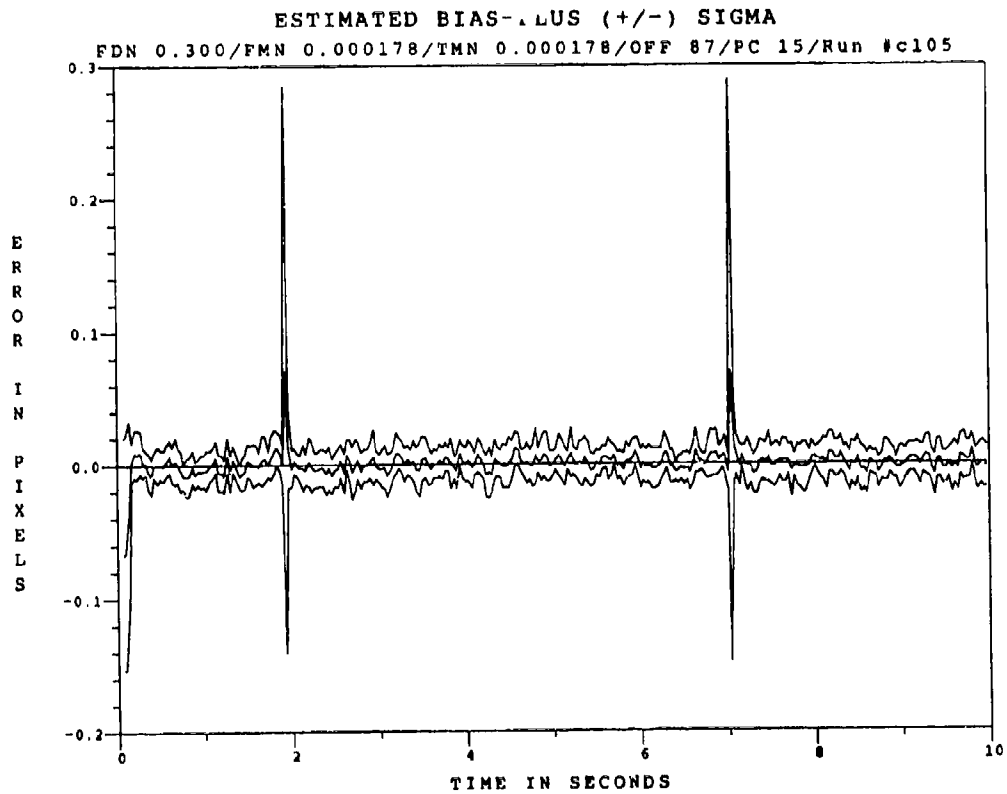


Figure E.4.12 2.01 μm Two-State Modified MAP MMAF Bias Error, SNR=4, $P_m = -0.05$, at t_i^+

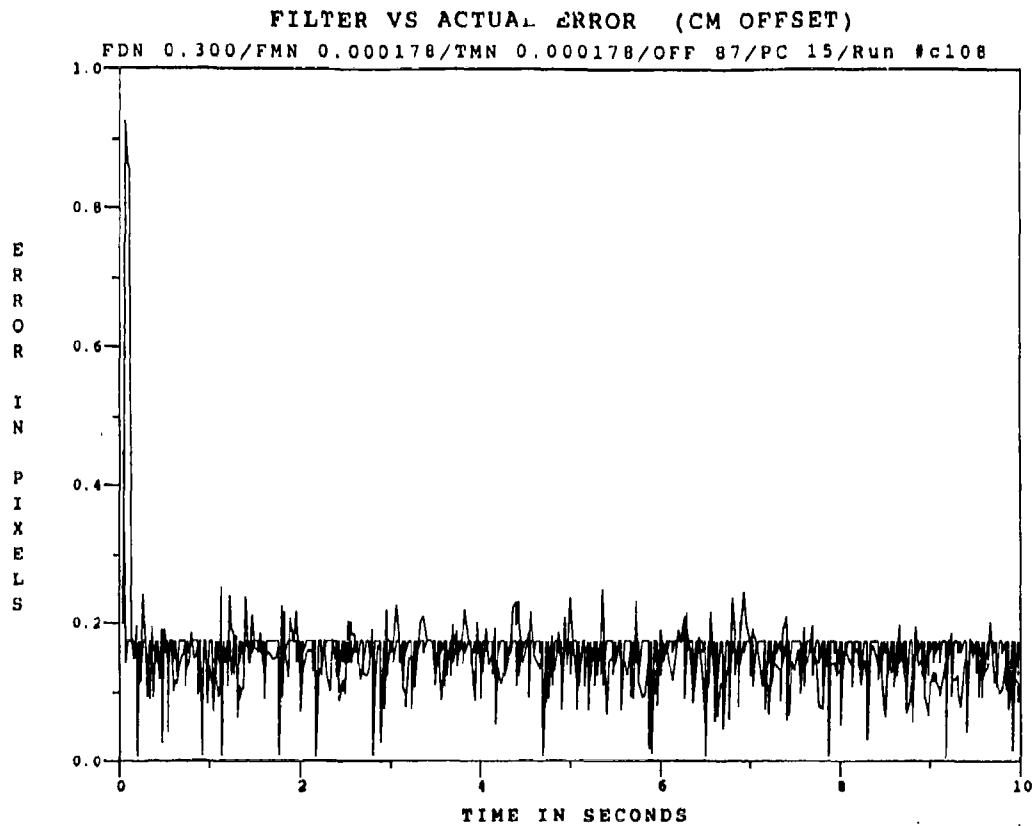


Figure E.4.13 2.01 μ m Two-State Modified MAP MMAF Offset Error, SNR = 4, $P_m = 0.30$

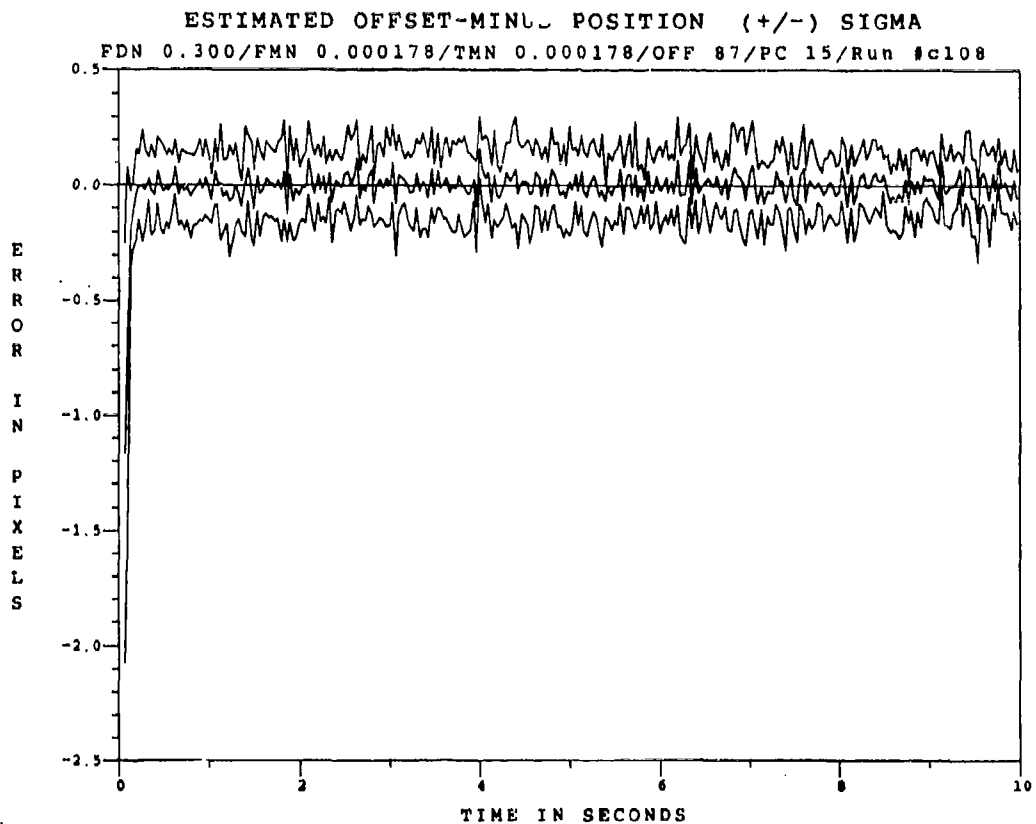


Figure E.4.14 2.01 μ m Two-State Modified MAP MMAF Offset Error, SNR=4, $P_m = 0.30$, at t_i

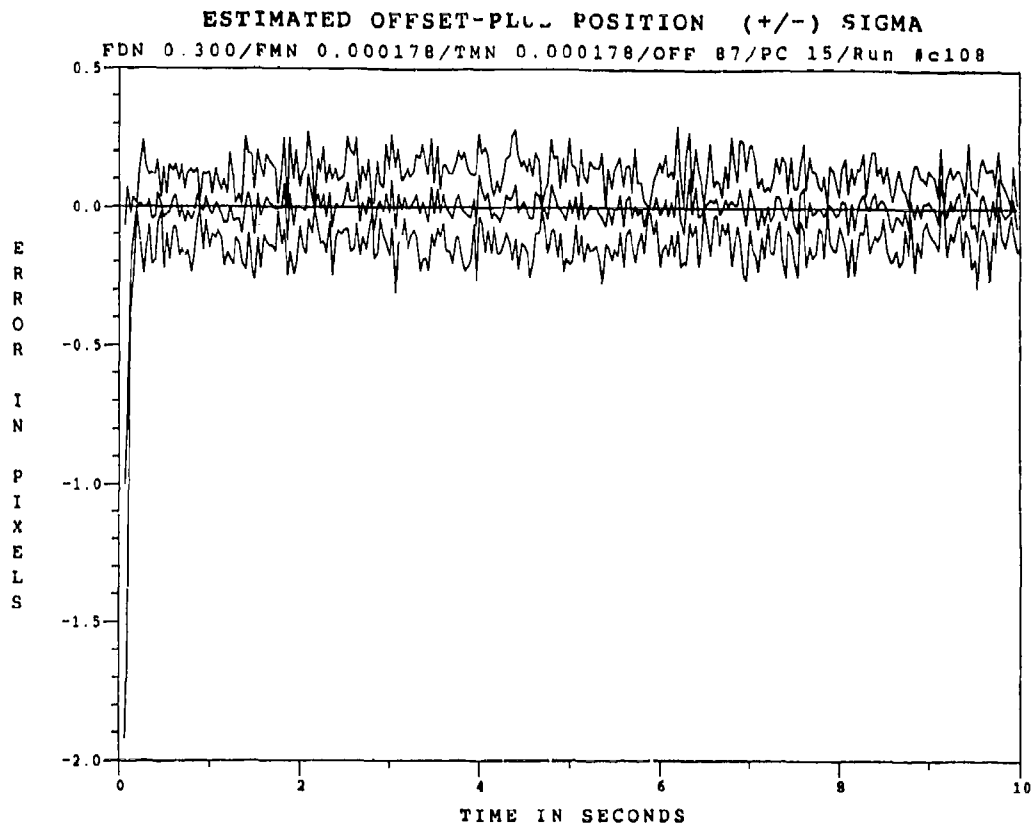


Figure E.4.15 2.01 μ m Two-State Modified MAP MMAF Offset Error, SNR=4, $P_m = -0.30$, at t_i^+

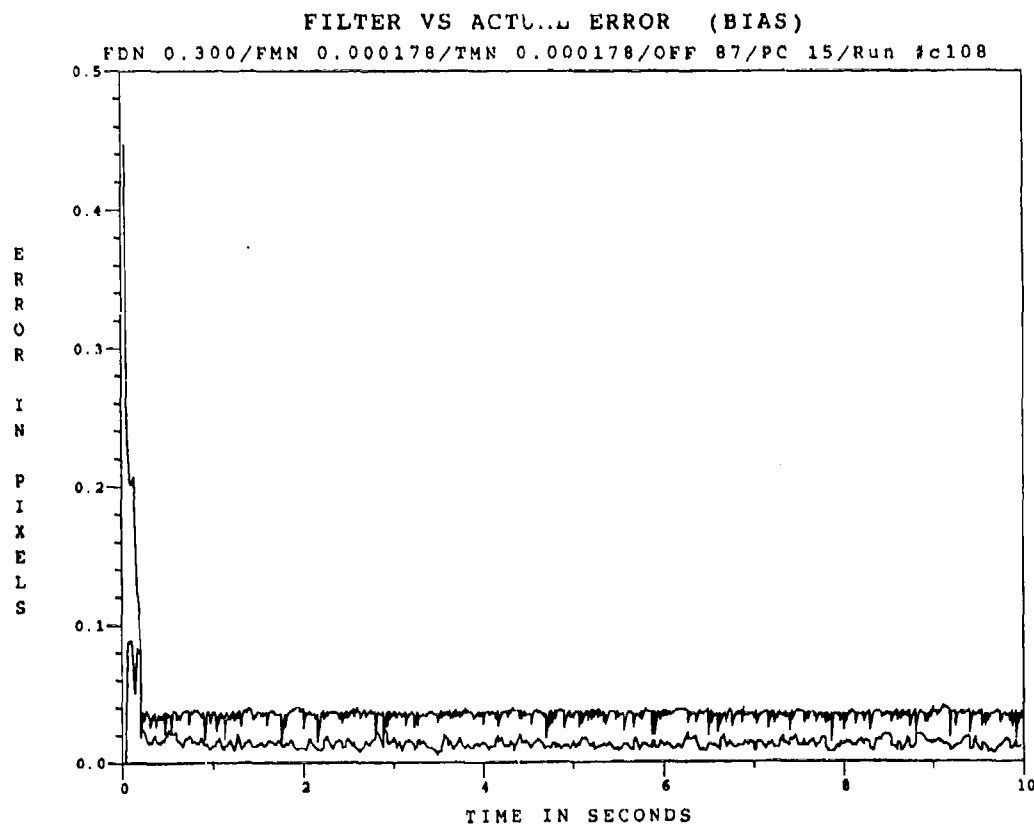


Figure E.4.16 2.01 μ m Two-State Modified MAP MMAF Bias Error, SNR = 4, $P_m = -0.30$

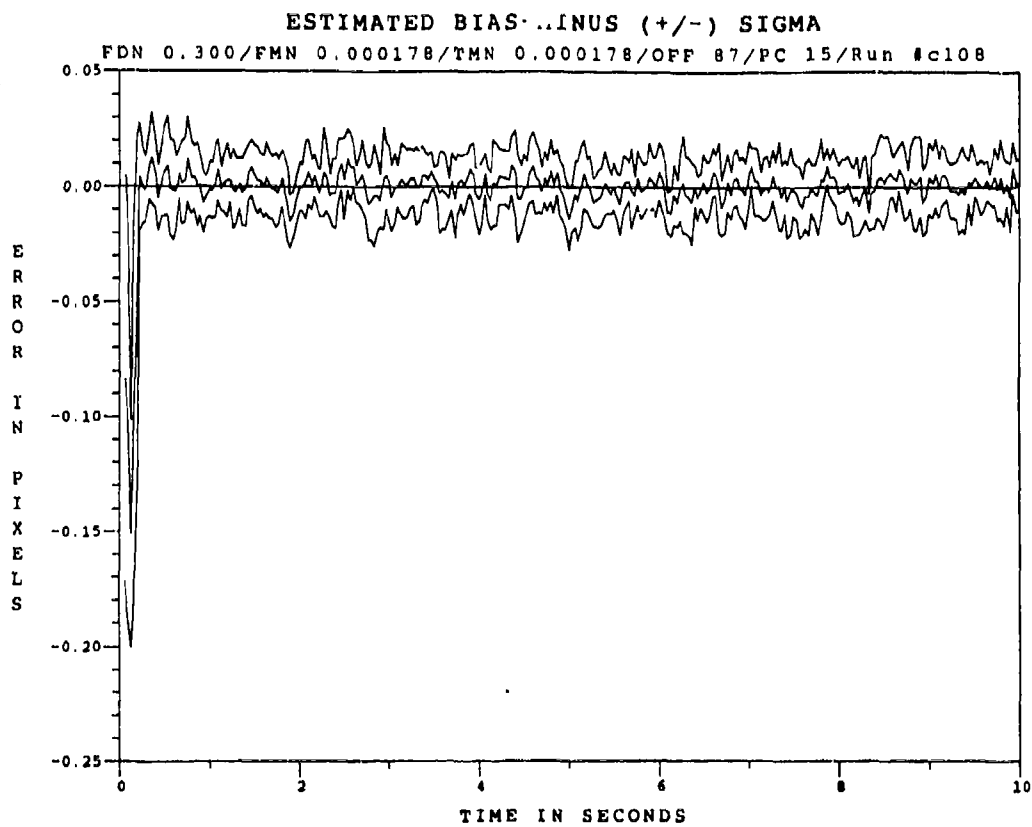


Figure E.4.17 2.01 μ m Two-State Modified MAP MMAF Bias Error, SNR=4, $P_m = -0.30$, at t_i

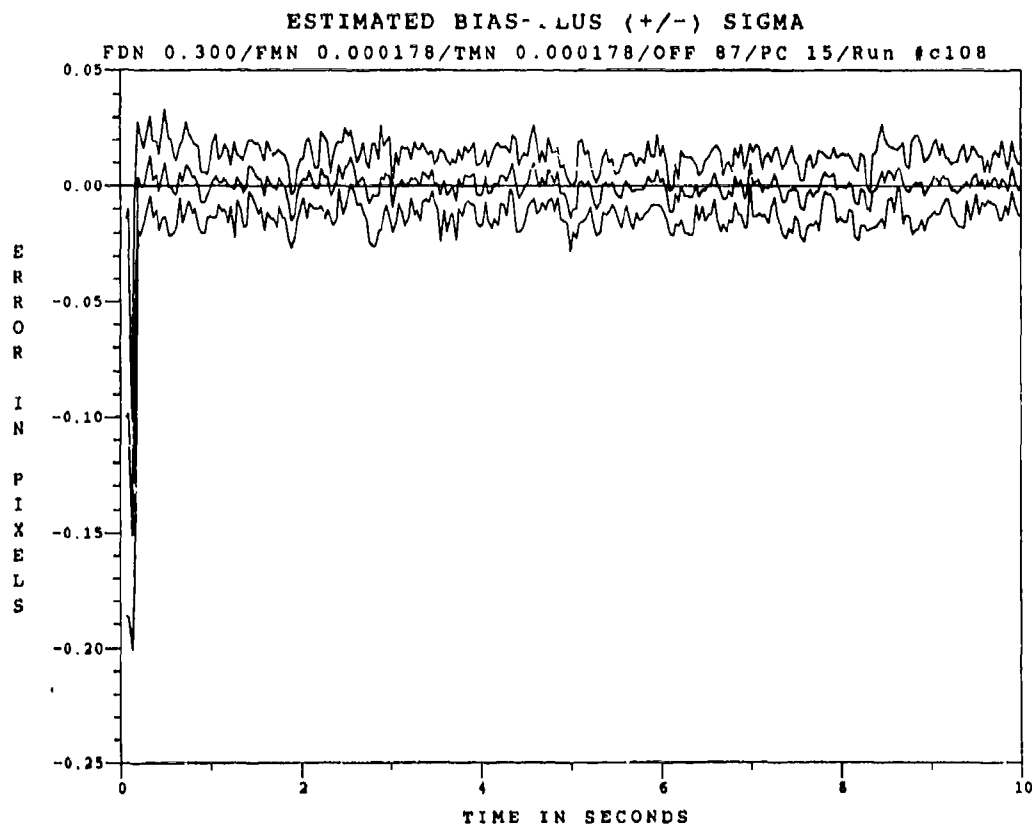


Figure E.4.18 2.01 μ m Two-State Modified MAP MMAF Bias Error, SNR=4, $P_m = -0.30$, at t_i

Appendix E.5

Two-State Center-of-Mass

Modified MAP MMAP

with

10.5 μm Doppler Return Measurements

at SNR = 10

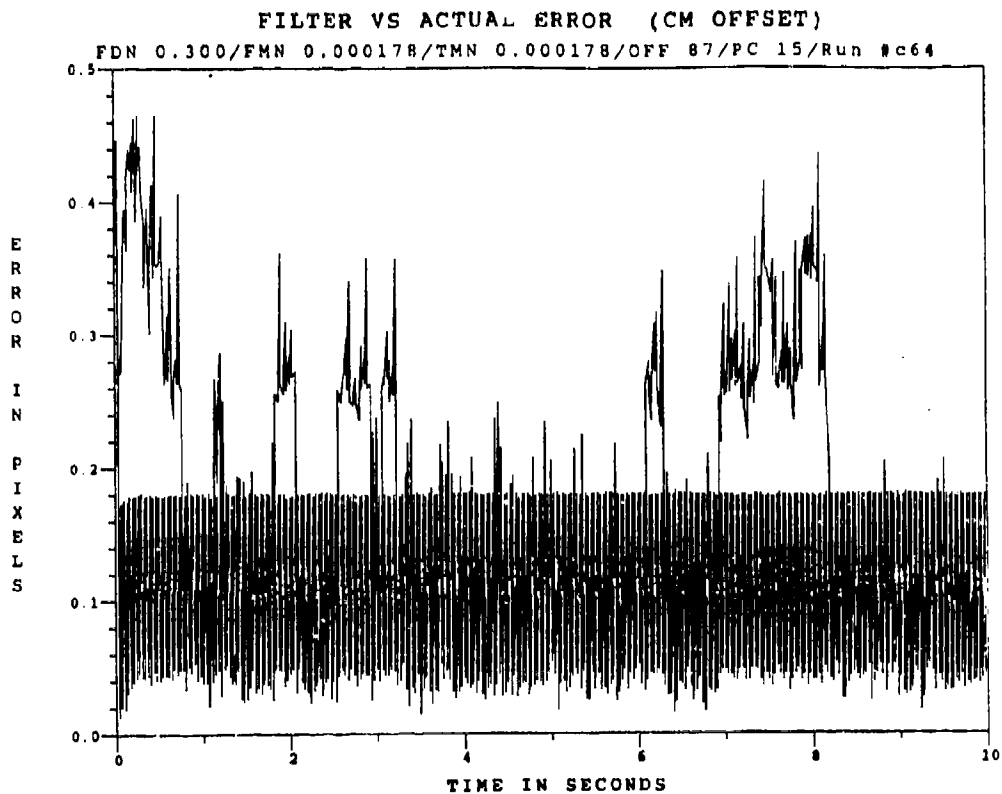


Figure E.5.1 10.5 μm Two-State Modified MAP MMAF Offset Error, SNR=10, $P_m=0.0$

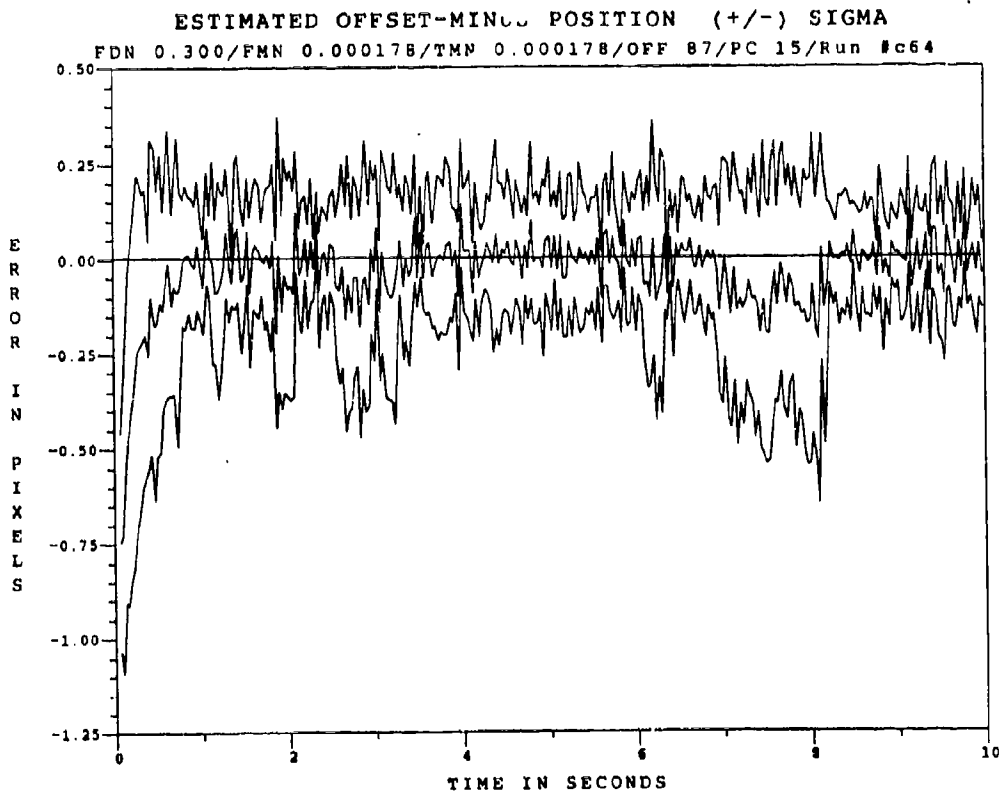


Figure E.5.2 10.5 μm Two-State Modified MAP MMAF Bias Error, SNR=10, $P_m=0.0$, at t_i

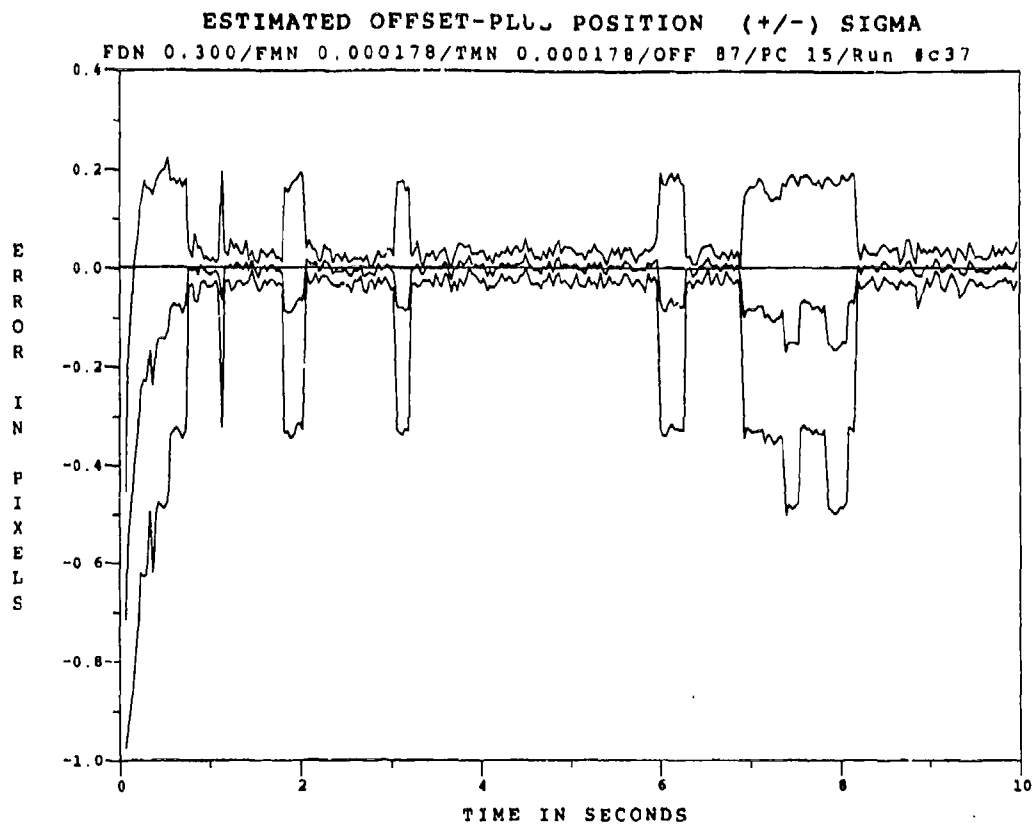


Figure E.5.3 10.5 μm Two-State Modified MAP MMAF Offset Error, SNR=10, $P_w = -0.0$, at t_0^*

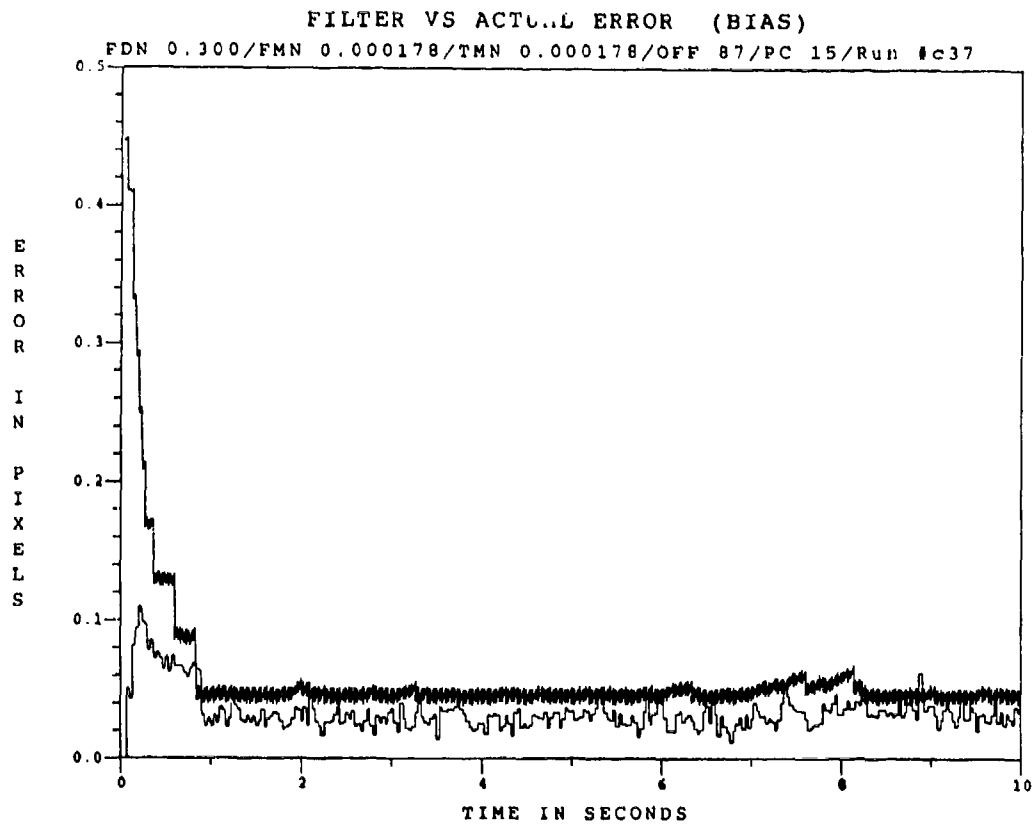


Figure E.5.4 10.5 μm Two-State Modified MAP MMAF Bias Error, SNR=10, $P_w = -0.0$

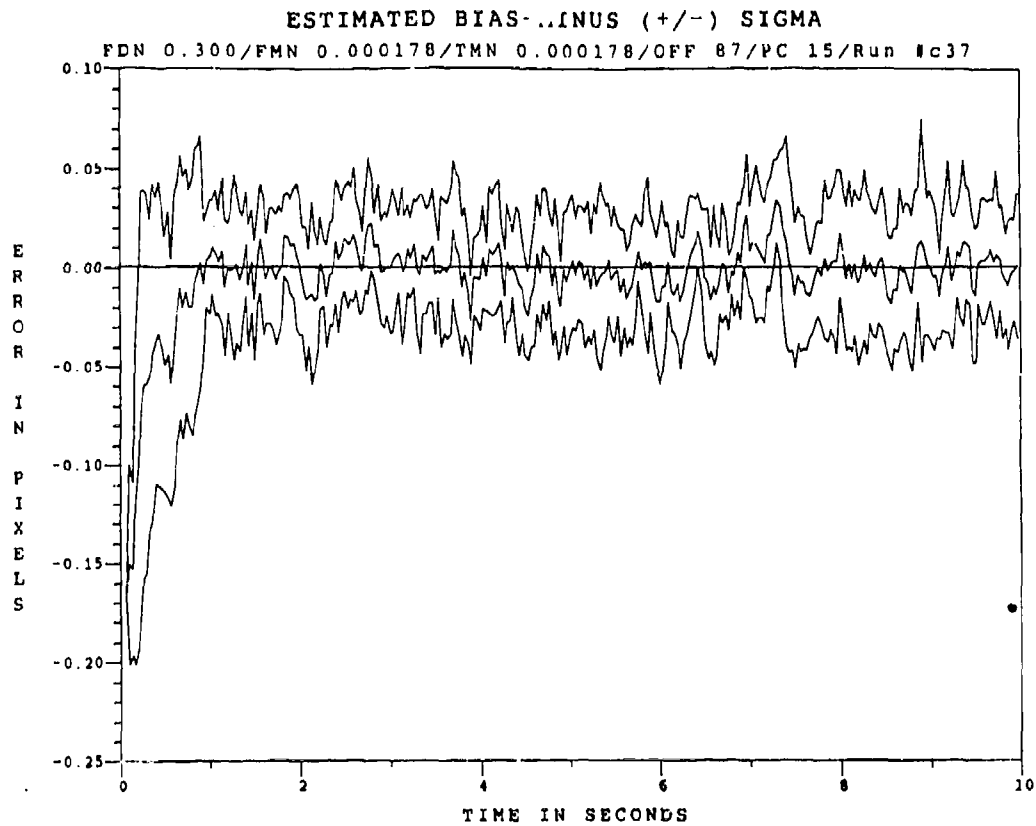


Figure E.5.5 10.5 μm Two-State Modified MAP MMAF Bias Error, SNR=10, $P_m = -0.0$, at t_i

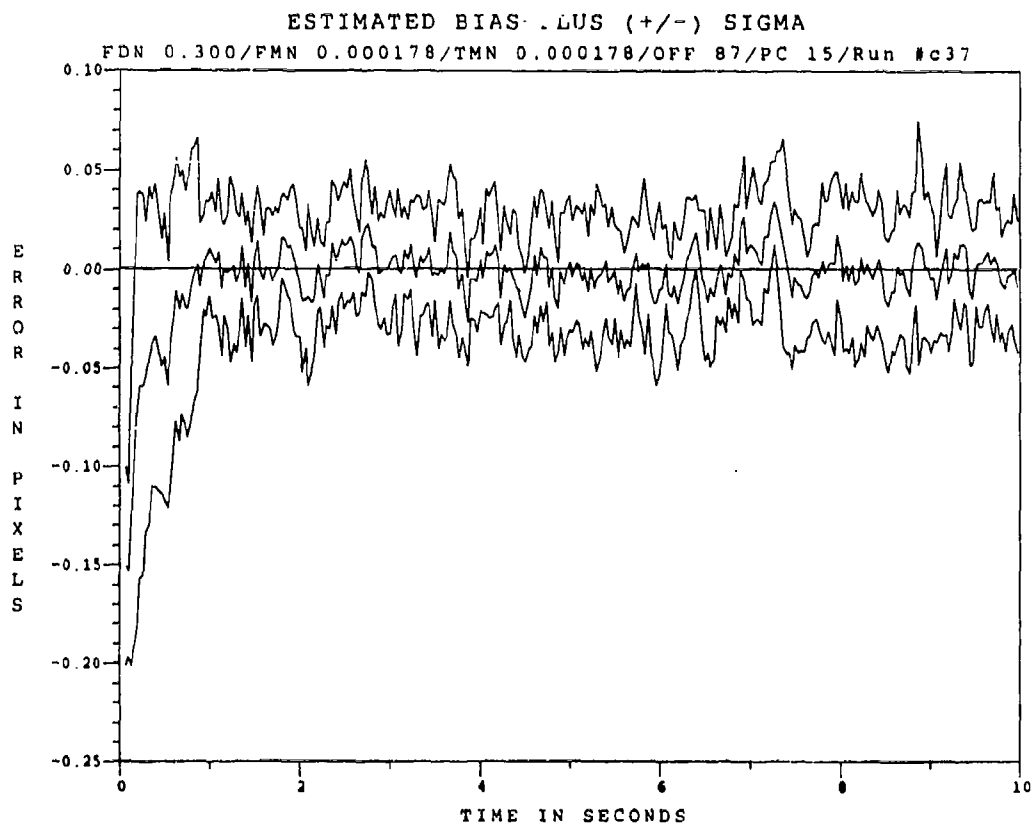


Figure E.5.6 10.5 μm Two-State Modified MAP MMAF Bias Error, SNR=10, $P_m = -0.0$, at t_i

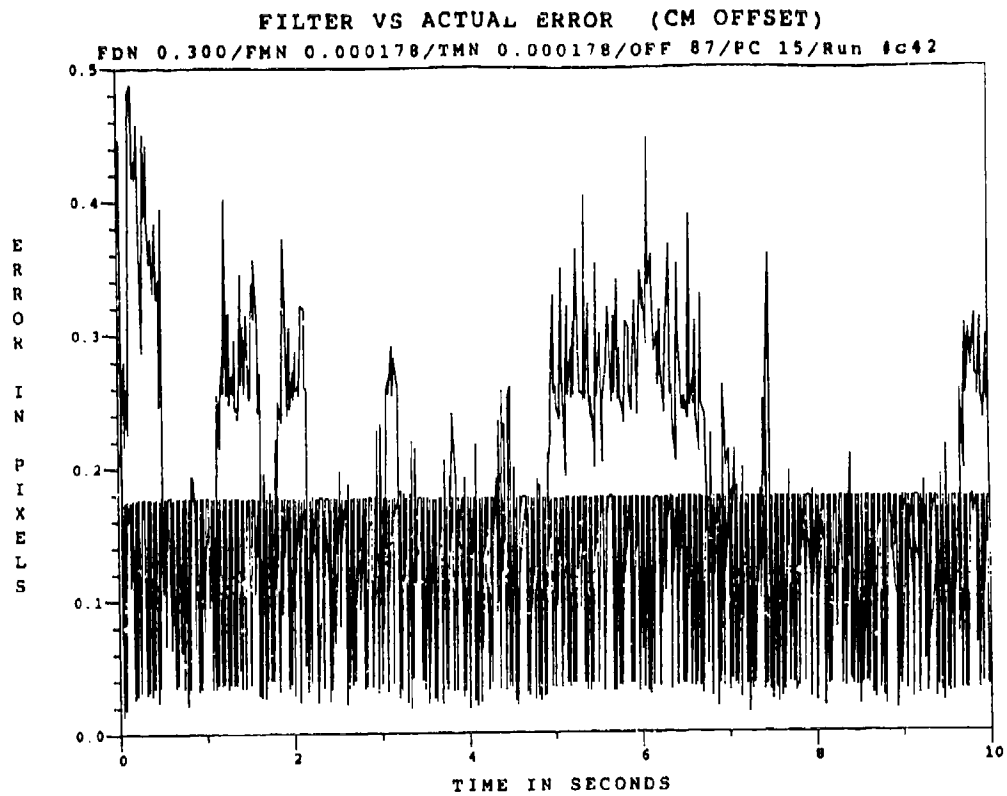


Figure E.5.7 10.5 μm Two-State Modified MAP MMAF Offset Error, SNR = 10, $P_m = 0.05$

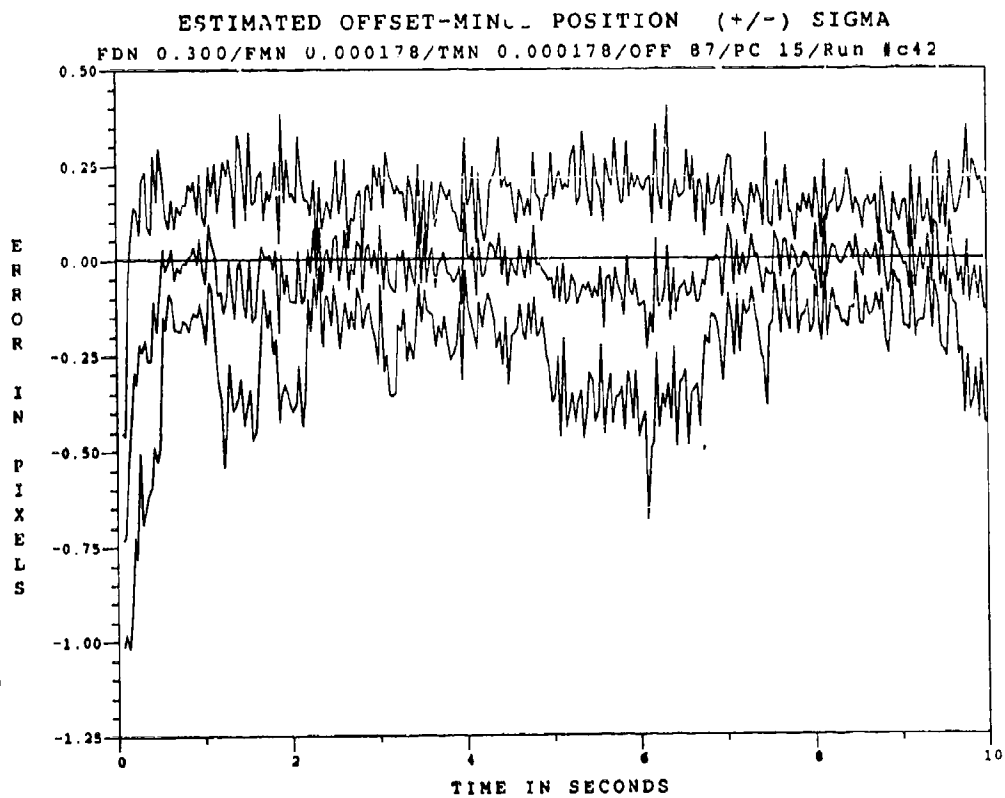


Figure E.5.8 10.5 μm Two-State Modified MAP MMAF Offset Error, SNR=10, $P_m=0.05$, at t_i

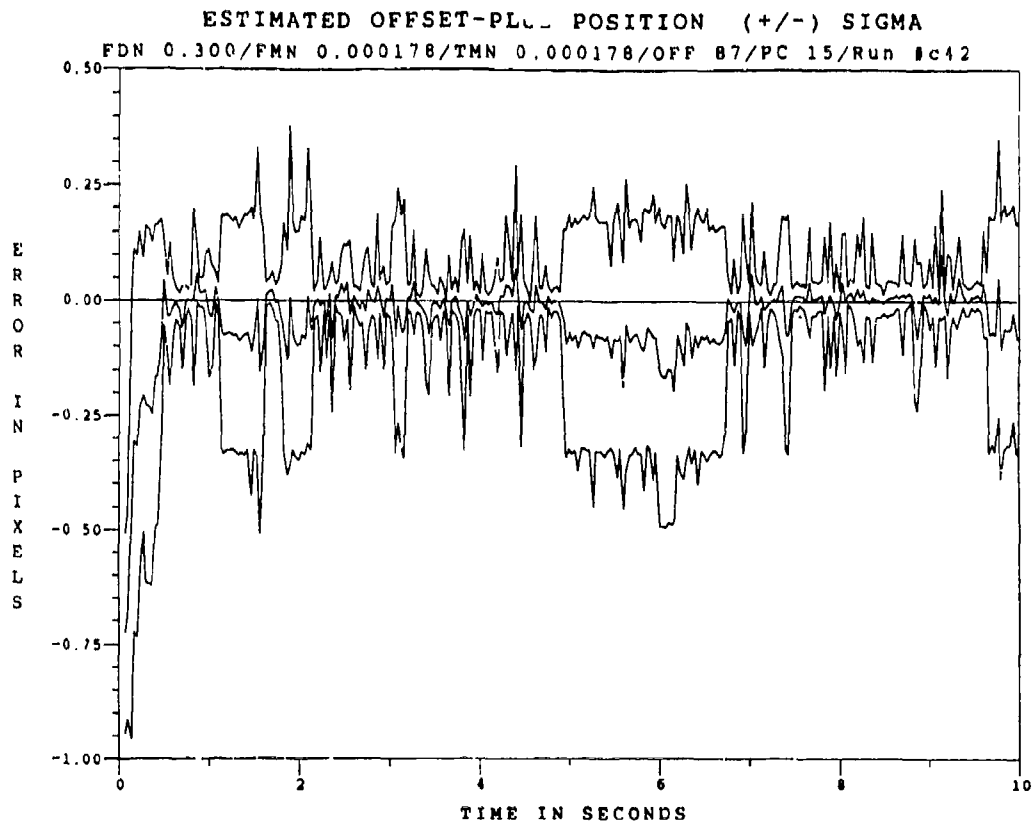


Figure E.5.9 10.5 μ m Two-State Modified MAP MMAF Offset Error, SNR=10, $P_m = 0.05$, at t_0^+

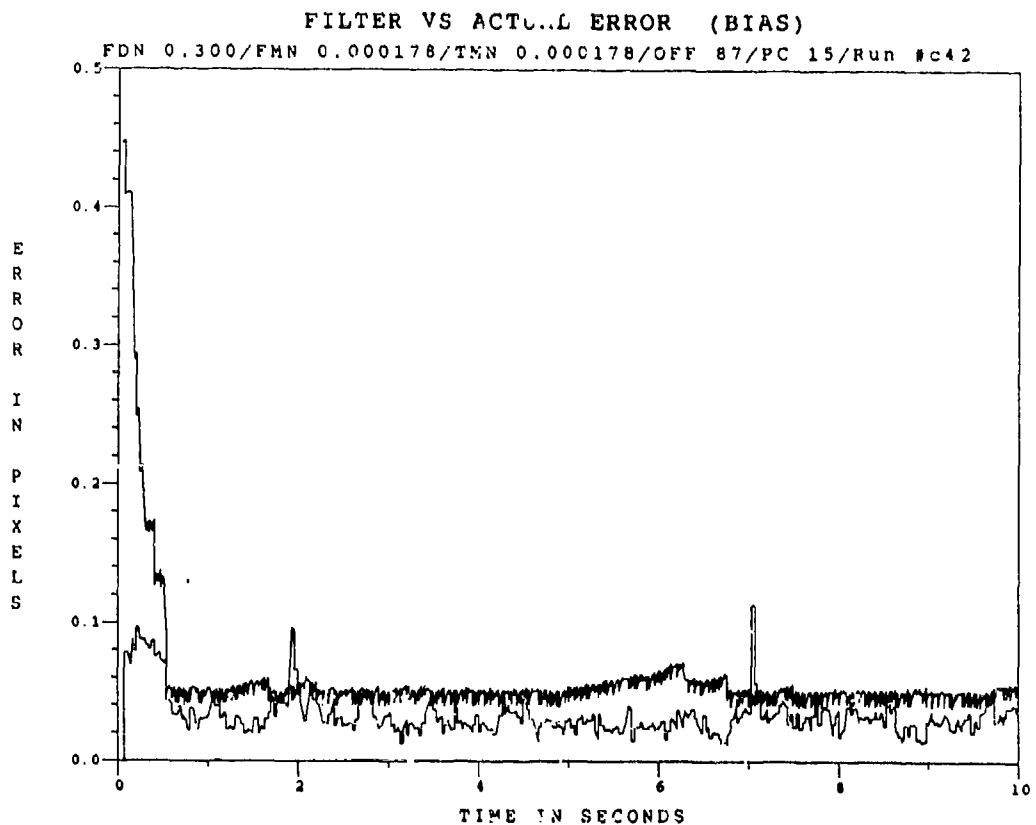


Figure E.5.10 10.5 μ m Two-State Modified MAP MMAF Bias Error, SNR = 10, $P_m = 0.05$

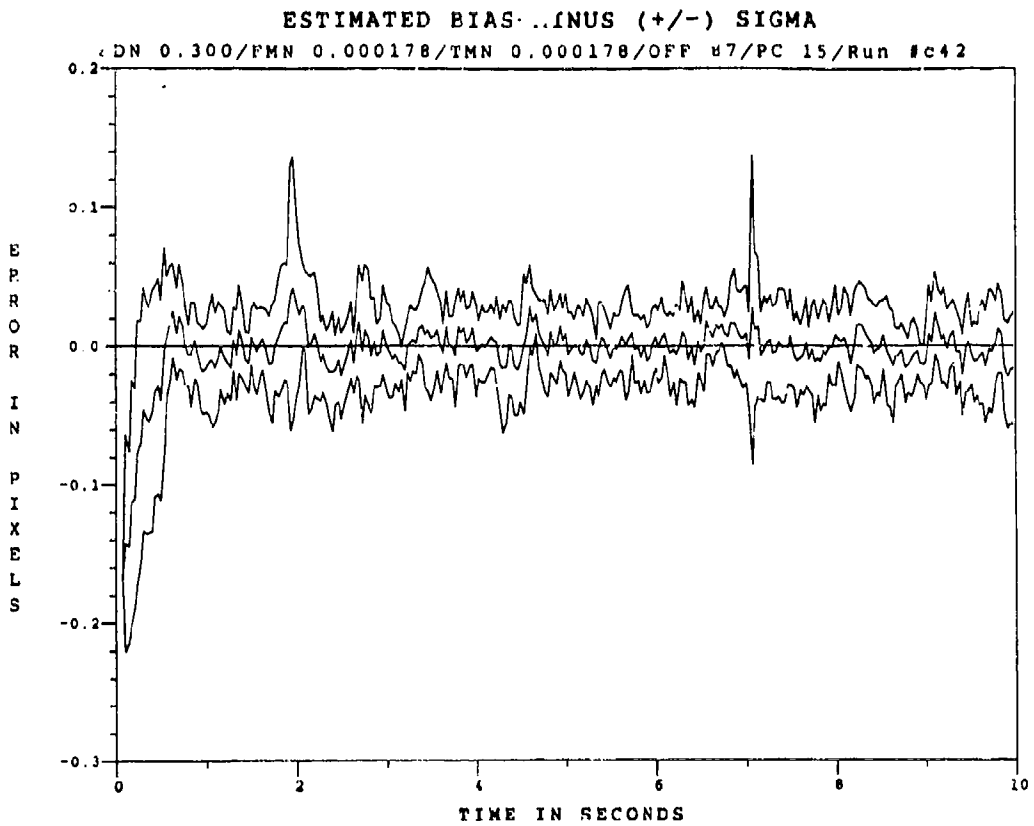


Figure E.5.11 10.5 μm Two-State Modified MAP MMAF Bias Error, SNR=10, $P_{\text{m}}=0.05$, at t_i^+

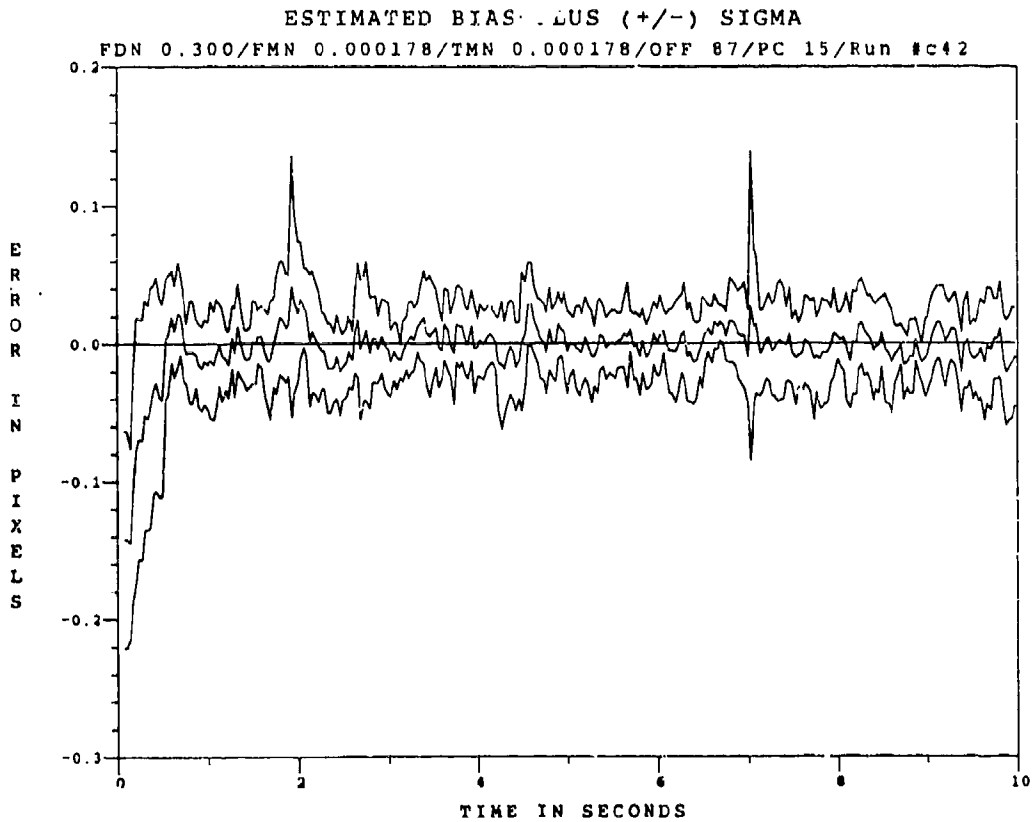


Figure E.5.12 10.5 μm Two-State Modified MAP MMAF Bias Error, SNR=10, $P_{\text{m}}=0.05$, at t_i^+

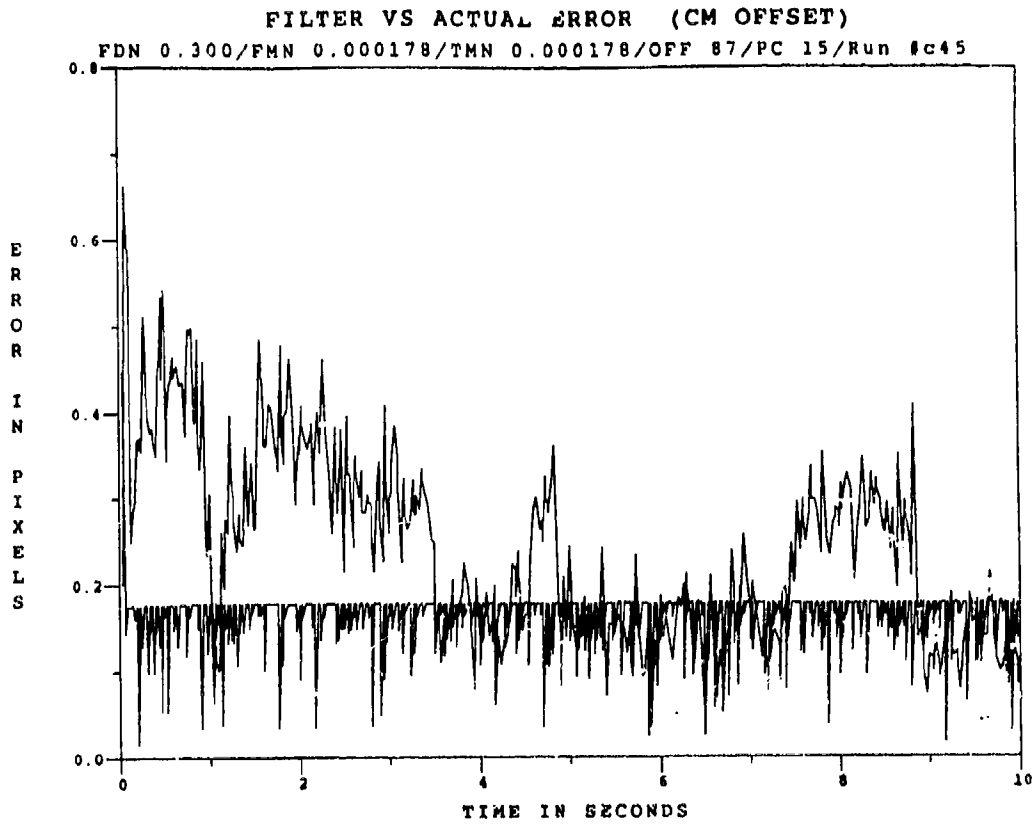


Figure E.5.13 10.5 μ m Two-State Modified MAP MMAF Offset Error, SNR = 10, $P_m = 0.30$

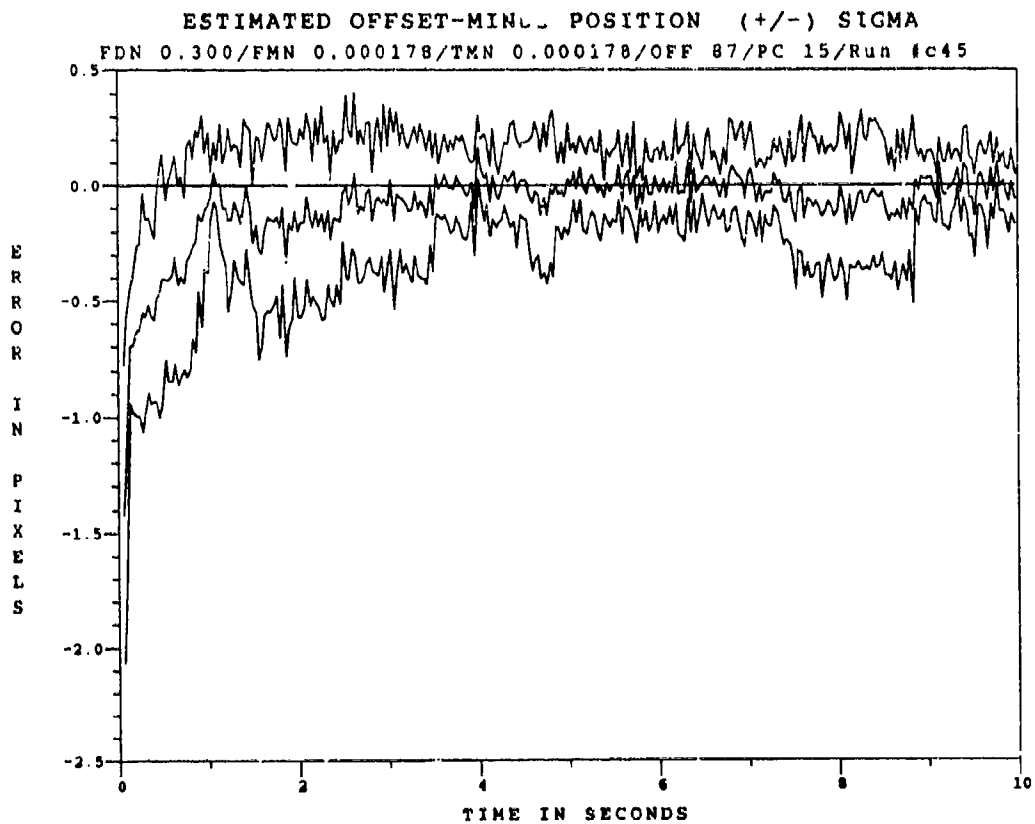


Figure E.5.14 10.5 μ m Two-State Modified MAP MMAF Offset Error, SNR=10, $P_m=0.30$, at t_i

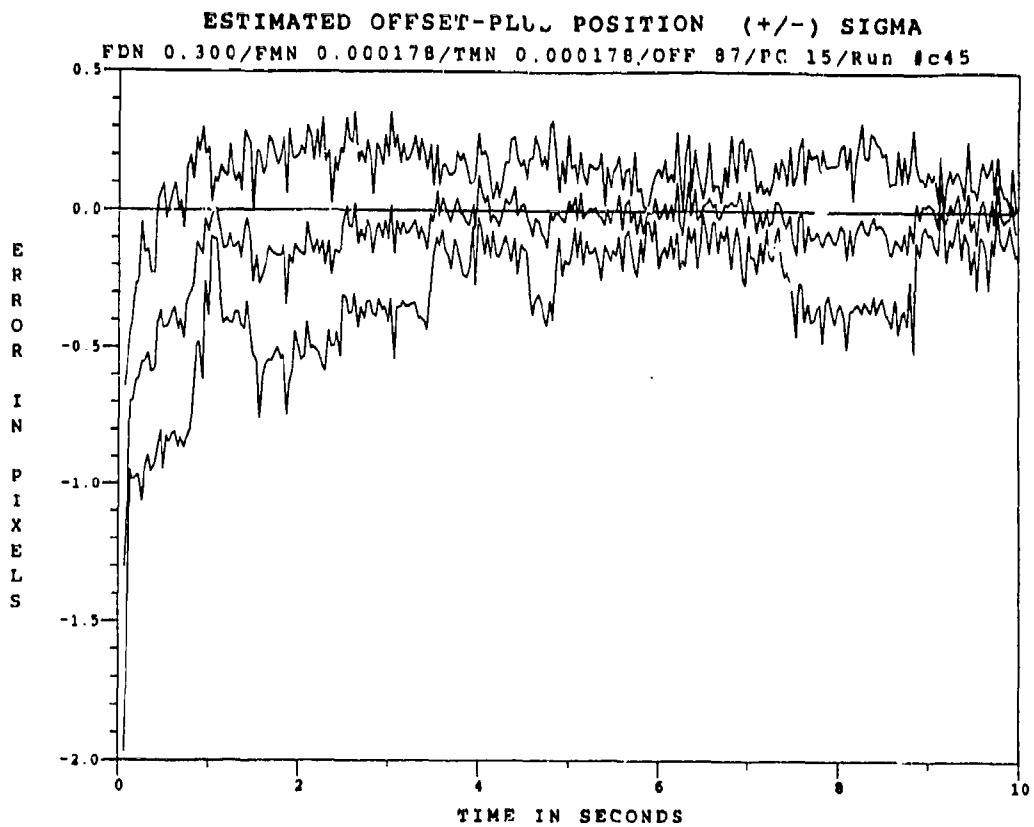


Figure E.5.15 10.5 μ m Two-State Modified MAP MMAF Offset Error, SNR=10, $P_m = -0.30$, at t_1^+

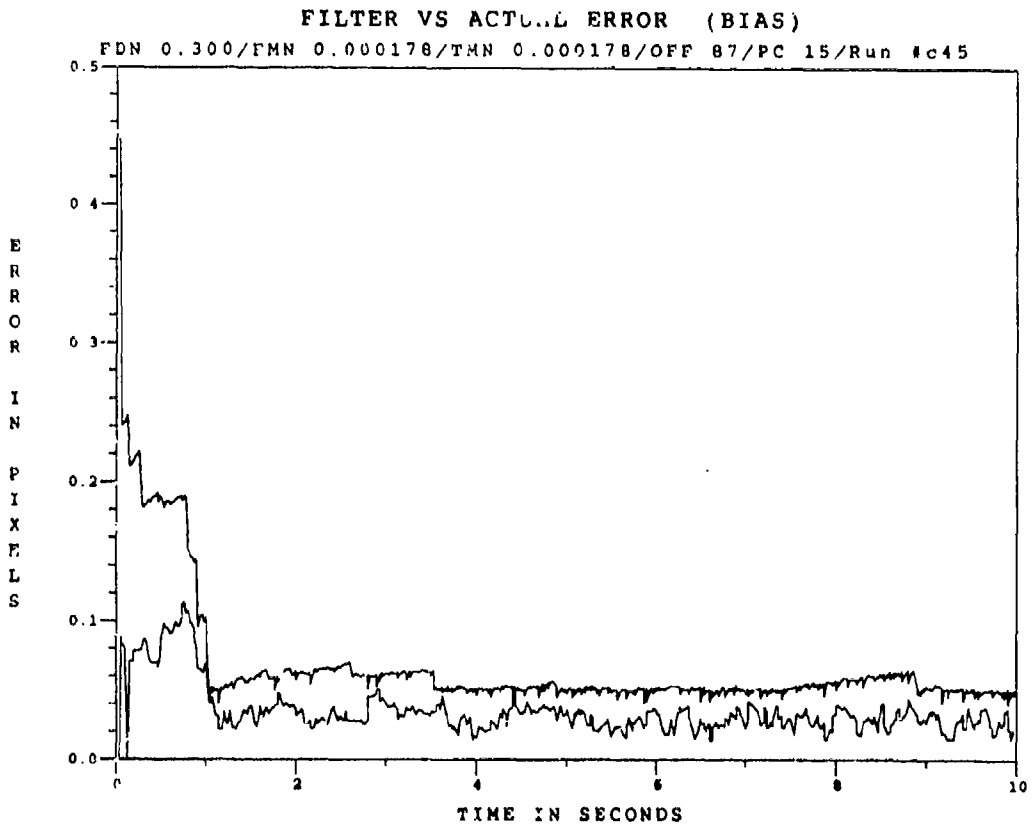


Figure E.5.16 10.5 μ m Two-State Modified MAP MMAF Bias Error, SNR = 10, $P_m = 0.30$

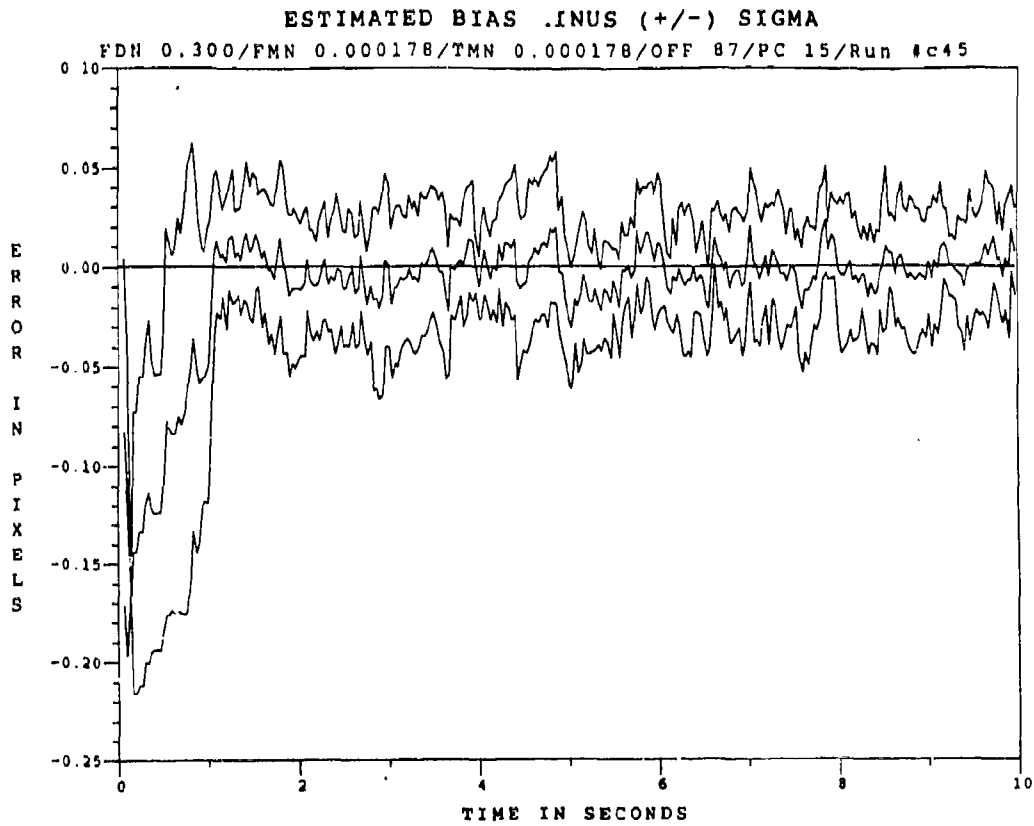


Figure E.5.17 10.5 μ m Two-State Modified MAP MMAF Bias Error, SNR=10, $P_m = -0.30$, at t_i

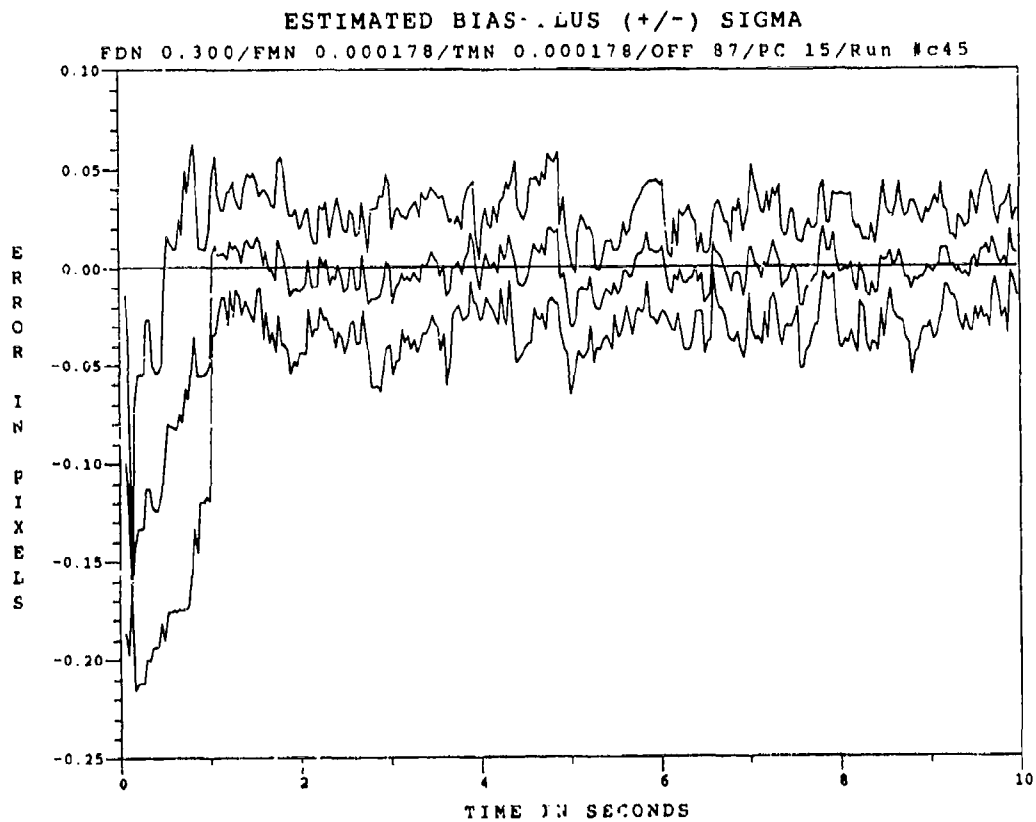


Figure E.5.18 10.5 μ m Two-State Modified MAP MMAF Bias Error, SNR=10, $P_m = -0.30$, at t_i

Appendix E.6

Two-State Center-of-Mass

Modified MAP MMAF

with

10.5 μm Doppler Return Measurements

at SNR = 4

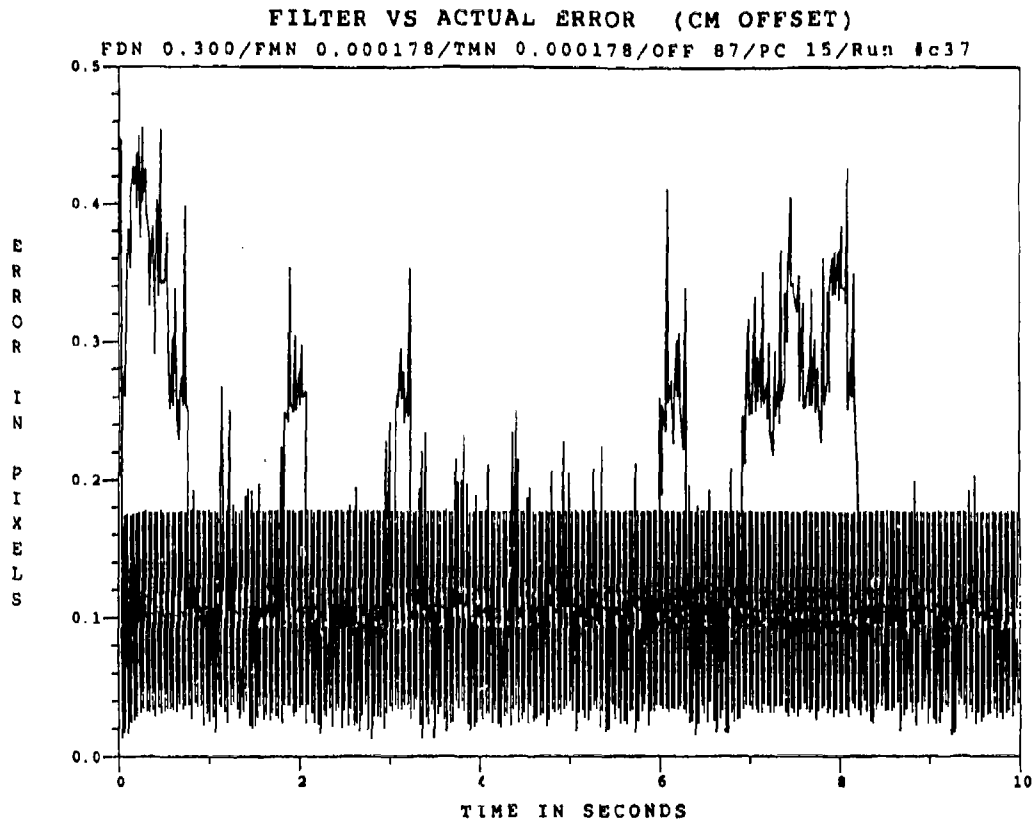


Figure E.6.1 10.5 μm Two-State Modified MAP MMAF Offset Error, SNR=4, $P_m=0.0$

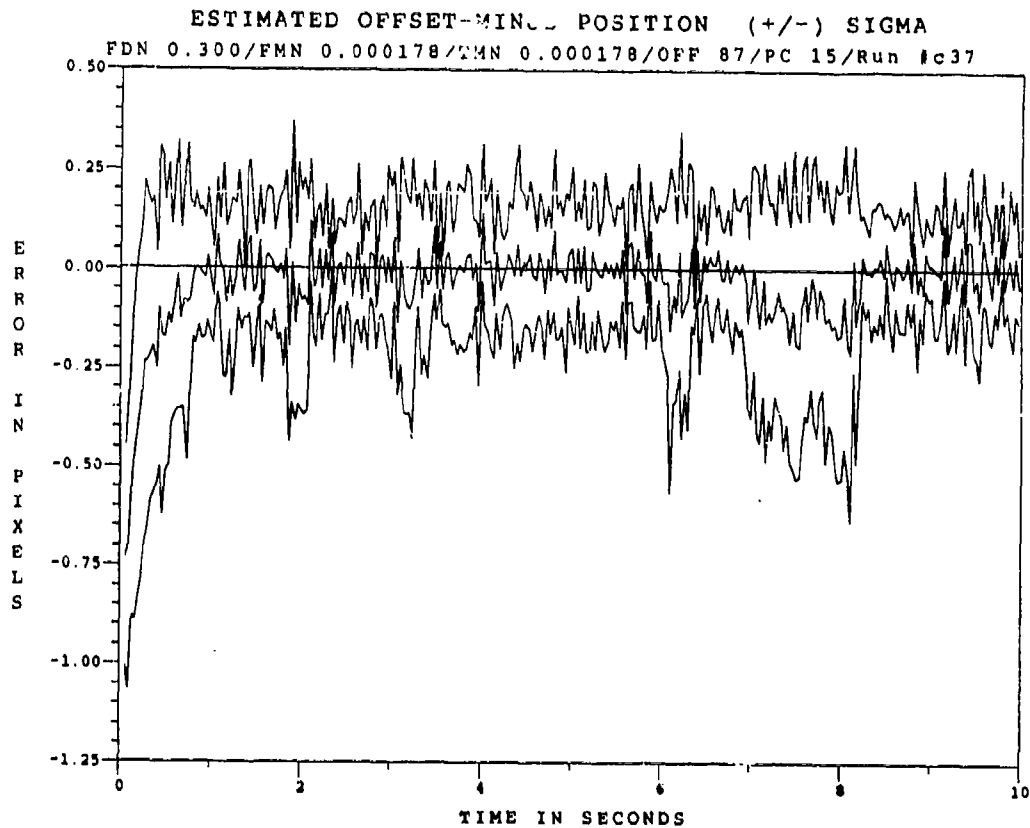


Figure E.6.2 10.5 μm Two-State Modified MAP MMAF Offset Error, SNR=4, $P_m=0.0$, at t_i

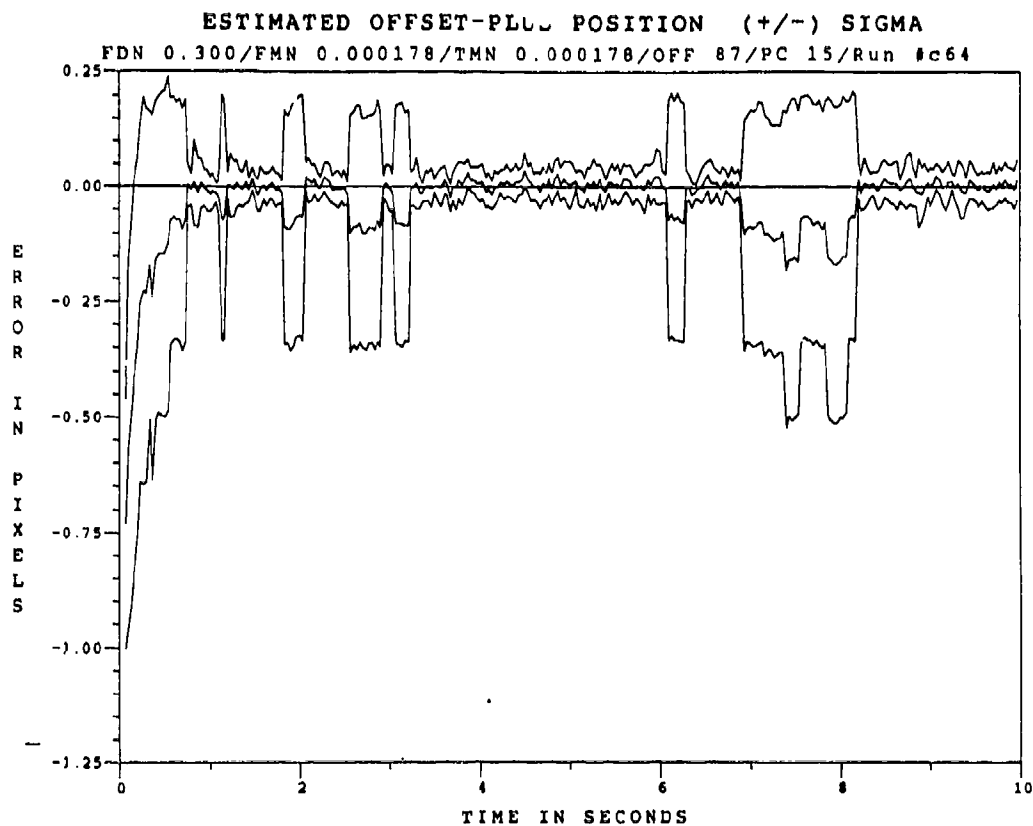


Figure E.6.3 10.5 μm Two-State Modified MAP MMAF Offset Error, SNR=4, $P_m = -0.0$, at t_i^+

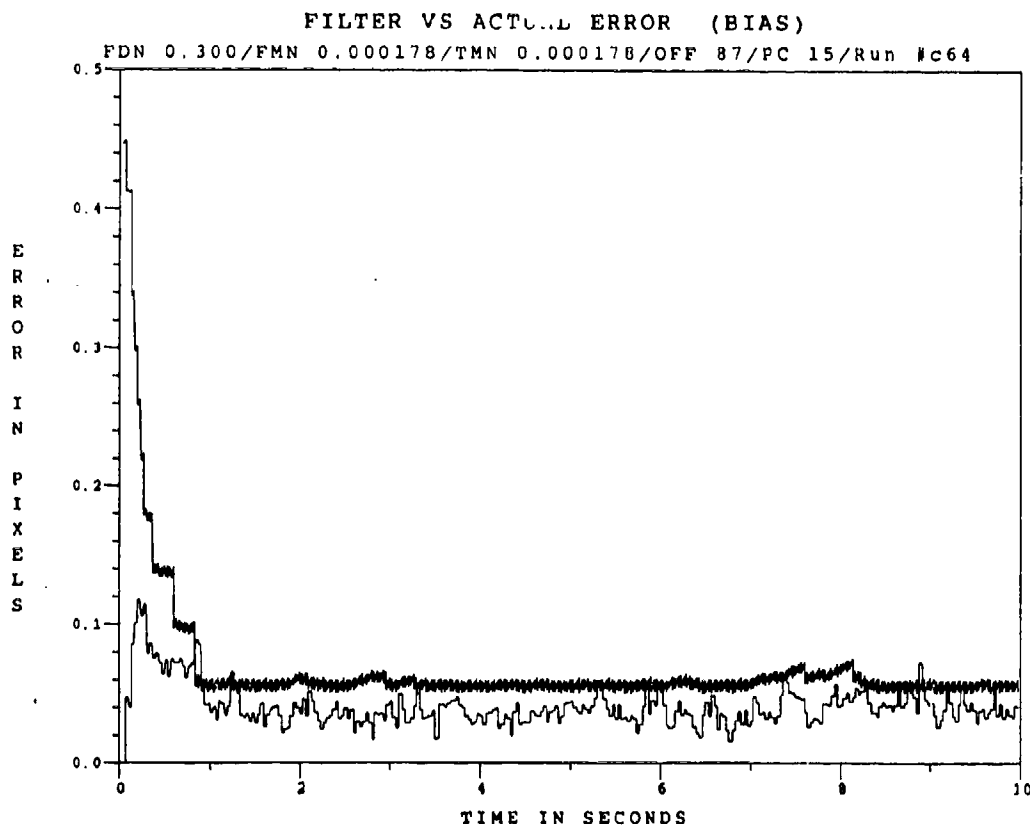


Figure E.6.4 10.5 μm Two-State Modified MAP MMAF Bias Error, SNR=4, $P_m = -0.0$

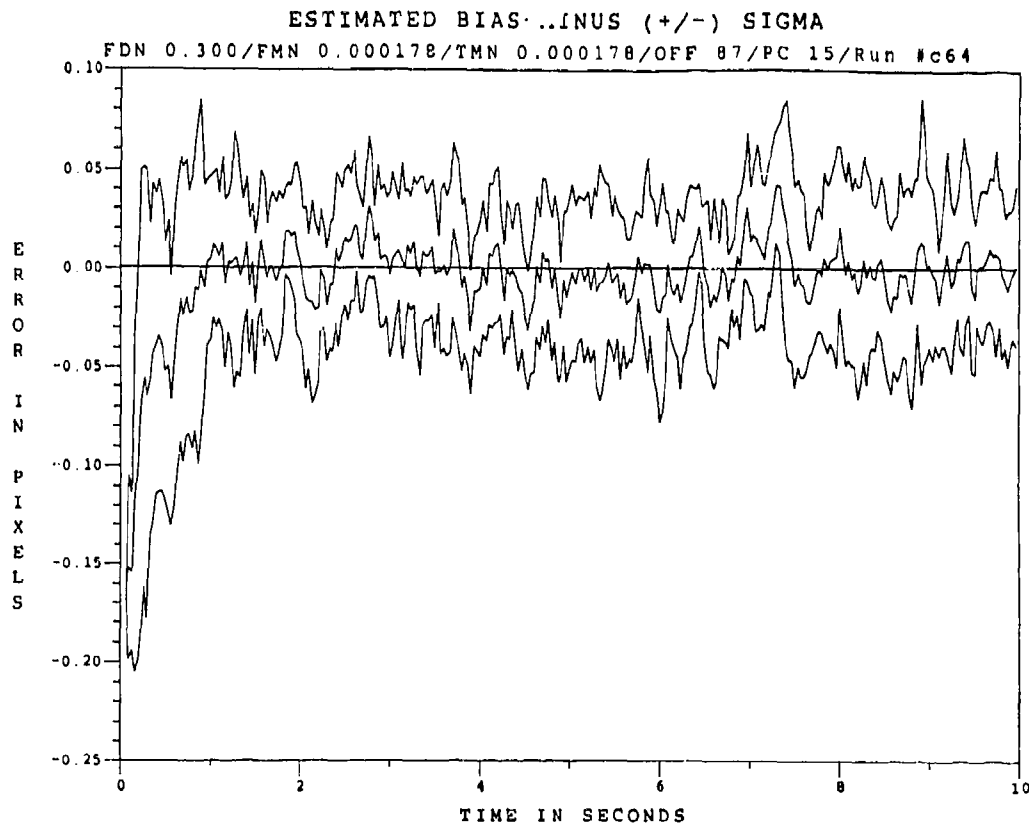


Figure E.6.5 10.5 μm Two-State Modified MAP MMAF Bias Error, SNR=4, $P_m = -0.0$, at t_i

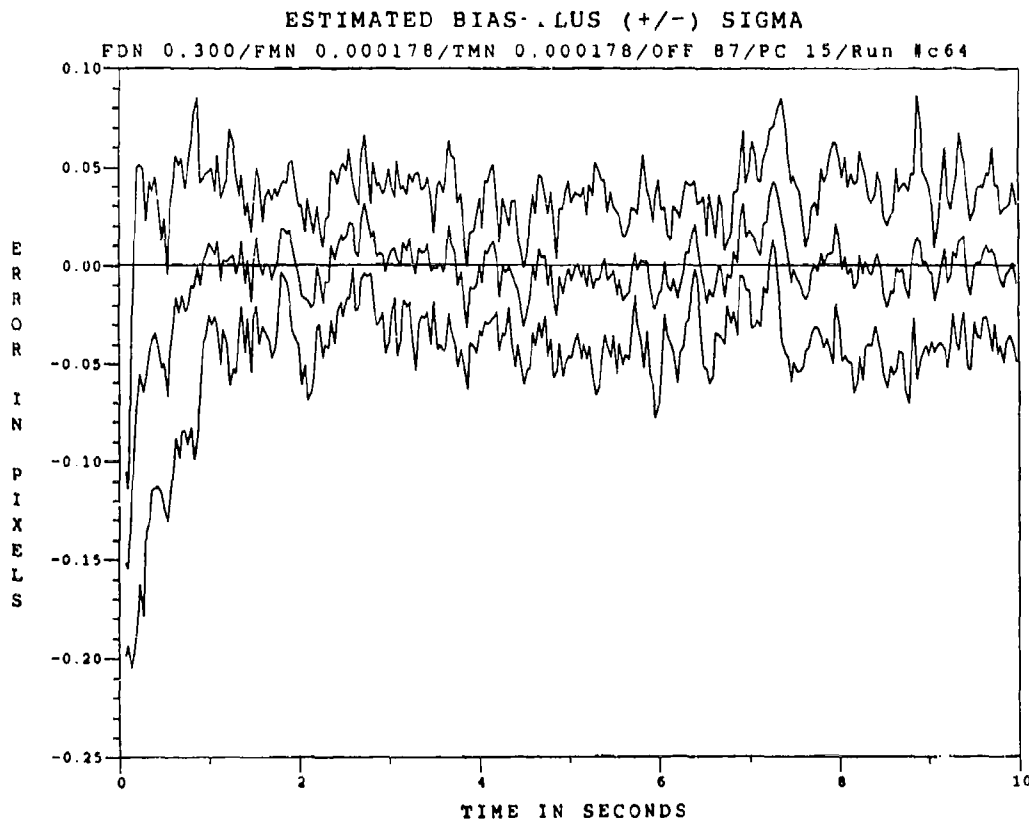


Figure E.6.6 10.5 μm Two-State Modified MAP MMAF Bias Error, SNR=4, $P_m = -0.0$, at t_i

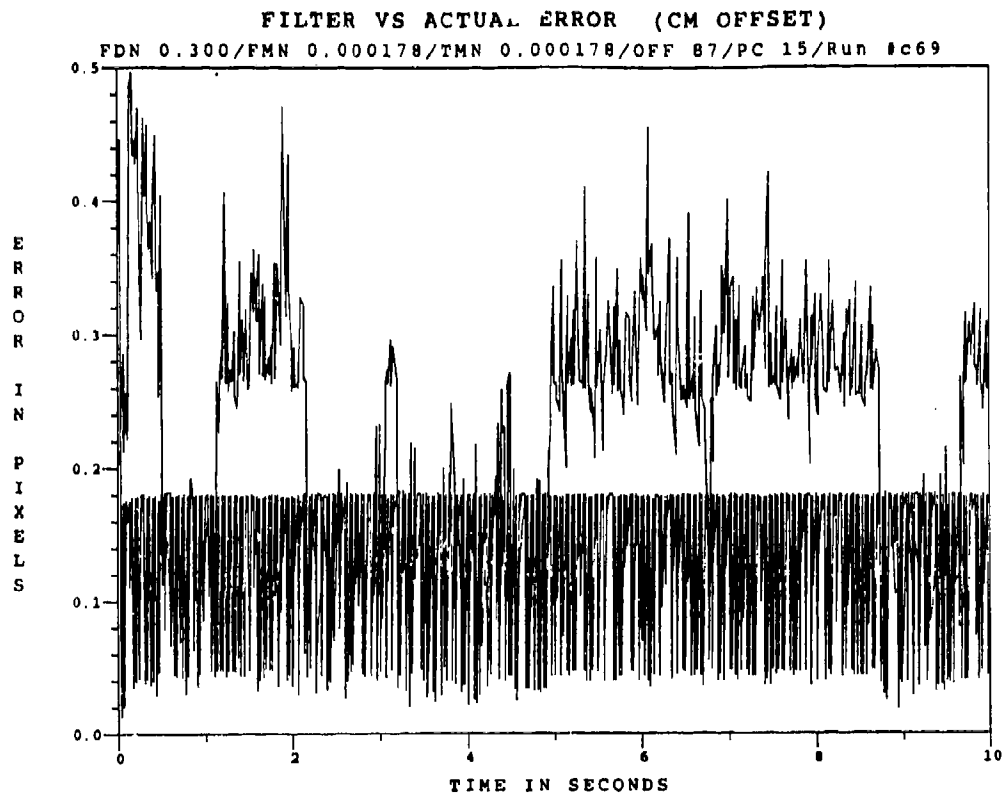


Figure E.6.7 10.5 μm Two-State Modified MAP MMAF Offset Error, SNR = 4, $P_m = 0.05$

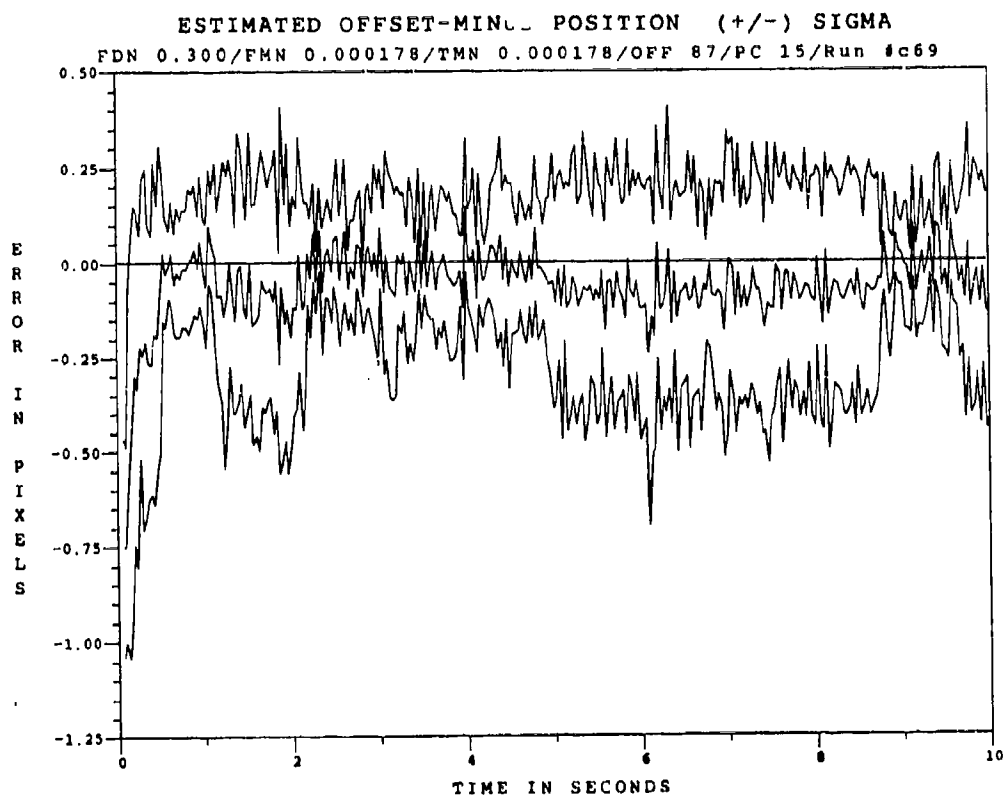


Figure E.6.8 10.5 μm Two-State Modified MAP MMAF Offset Error, SNR=4, $P_m = 0.05$, at t_i

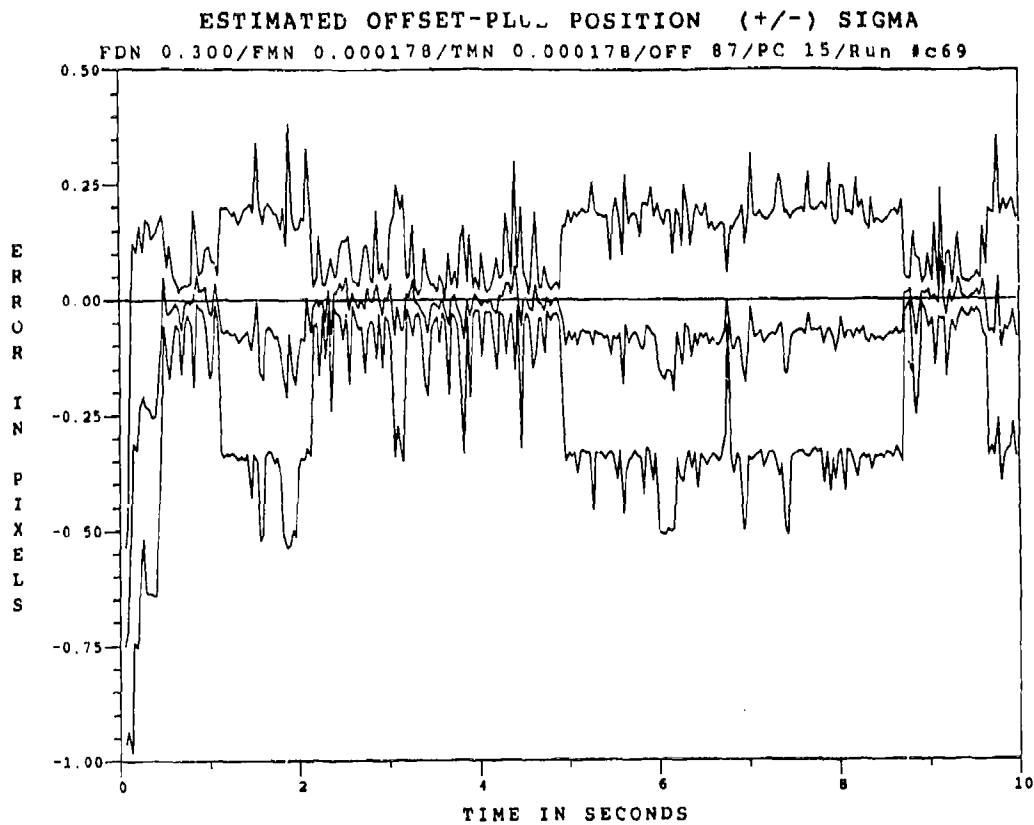


Figure E.6.9 10.5 μ m Two-State Modified MAP MMAF Offset Error, SNR=4, $P_m = 0.05$, at t_1^+

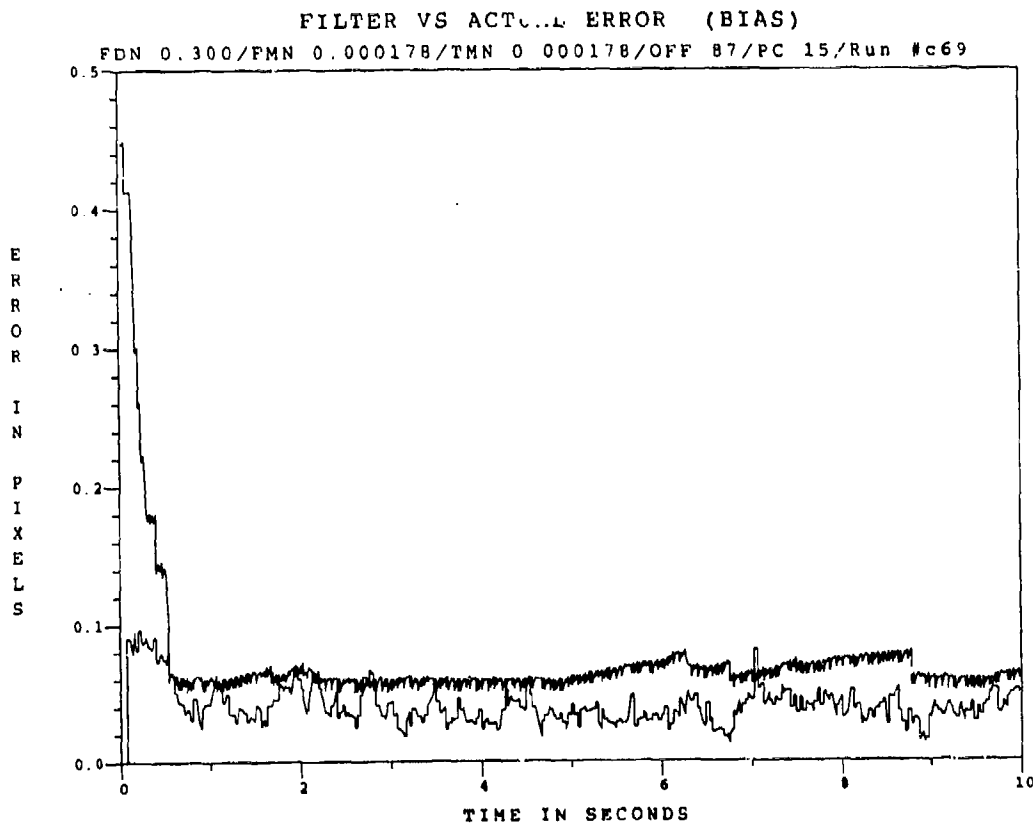


Figure E.6.10 10.5 μ m Two-State Modified MAP MMAF Bias Error, SNR = 4, $P_m = 0.05$

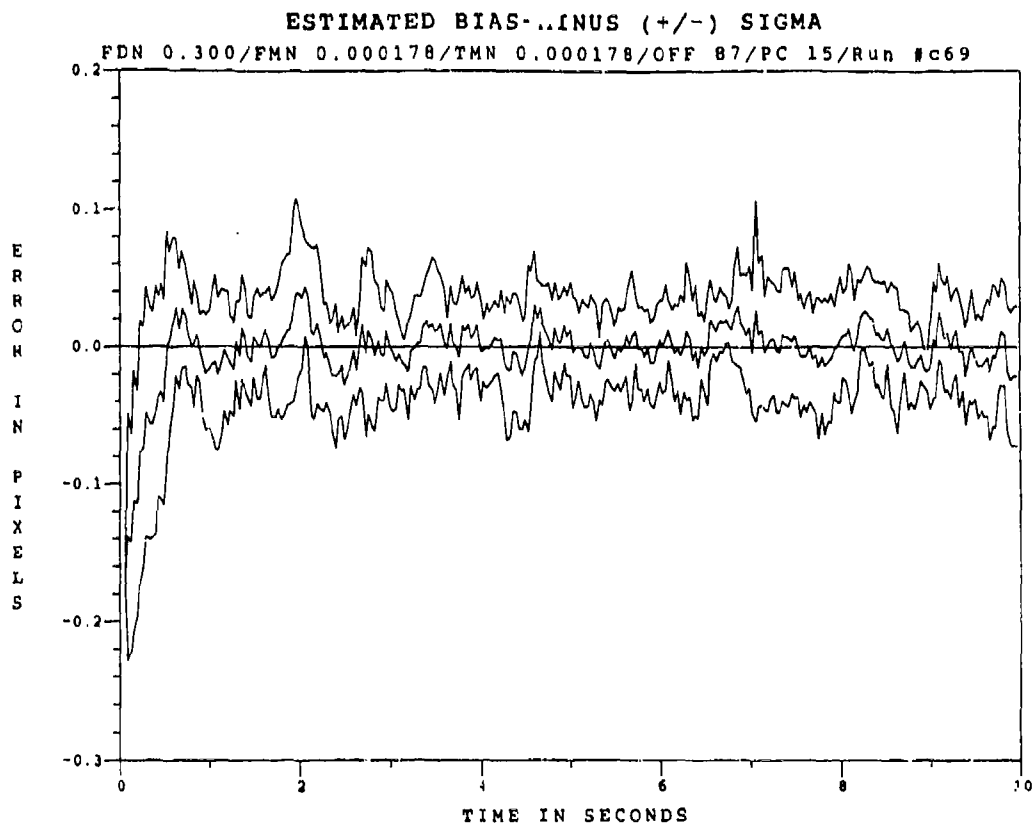


Figure E.6.11 10.5 μm Two-State Modified MAP MMAF Bias Error, SNR=4, $P_m = 0.05$, at t_i^*

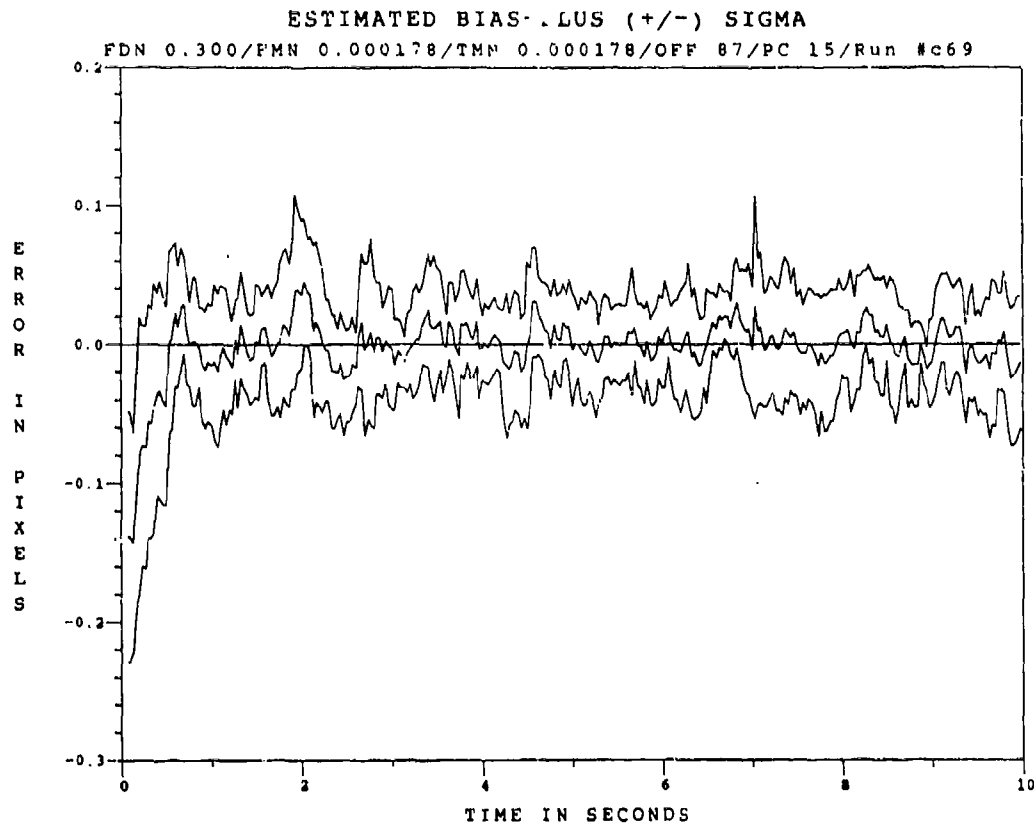


Figure E.6.12 10.5 μm Two-State Modified MAP MMAF Bias Error, SNR=4, $P_m = 0.05$, at t_i^*

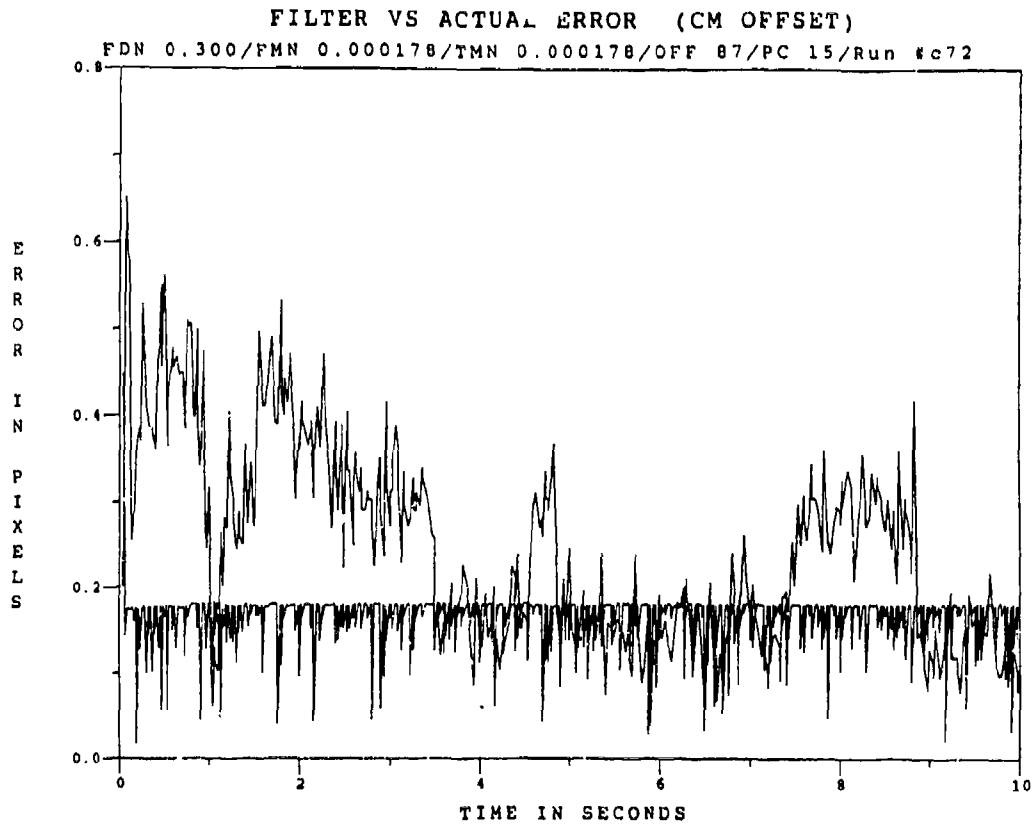


Figure E.6.13 10.5 μ m Two-State Modified MAP MMAF Offset Error, SNR = 4, $P_m = 0.30$

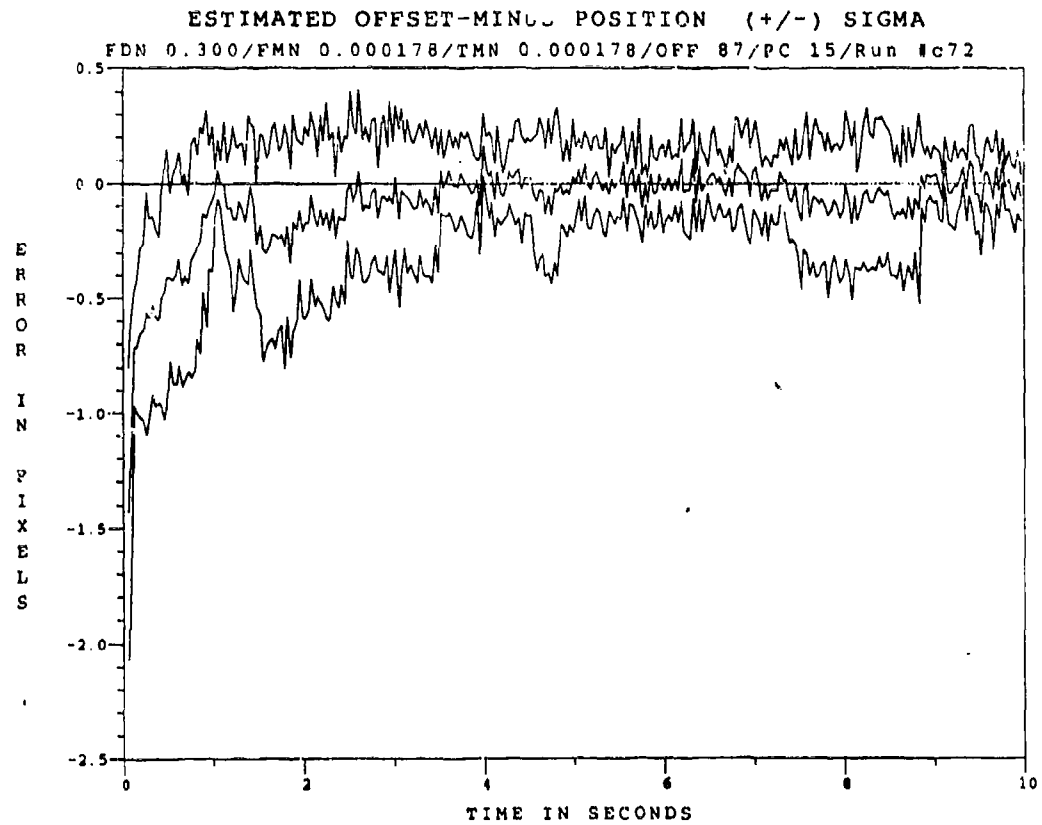


Figure E.6.14 10.5 μ m Two-State Modified MAP MMAF Offset Error, SNR=4, $P_m=0.30$, at t_i

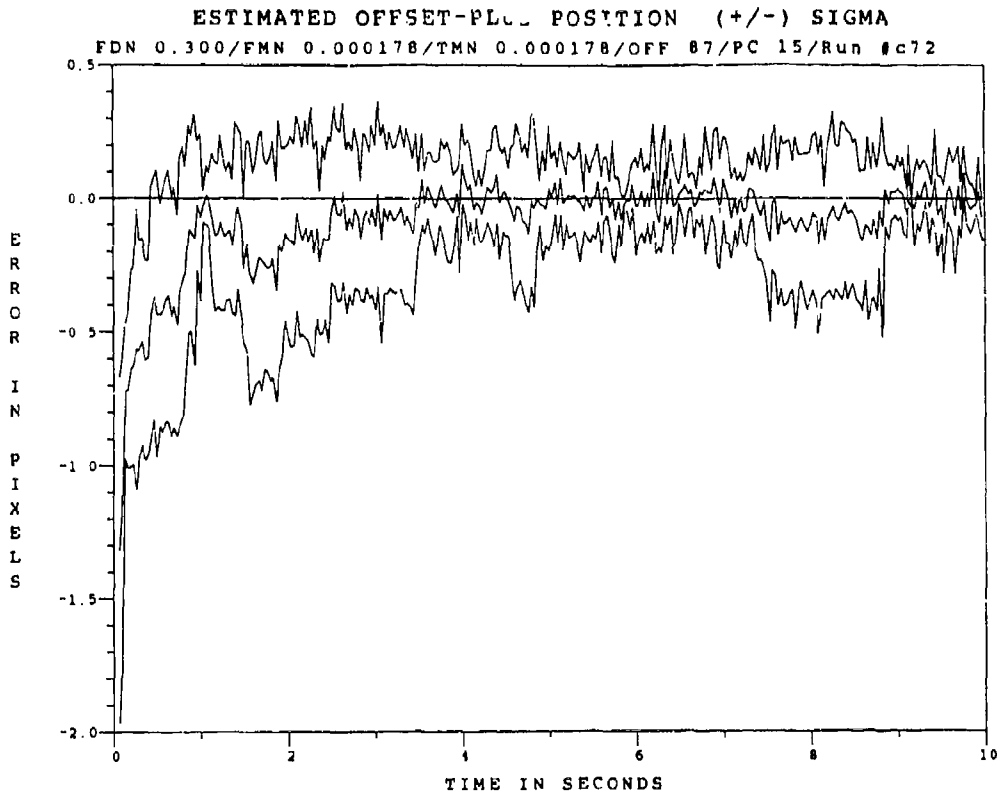


Figure E.6.15 10.5 μ m Two-State Modified MAP MMAF Offset Error, SNR=4, $P_m = -0.30$, at t_i^*

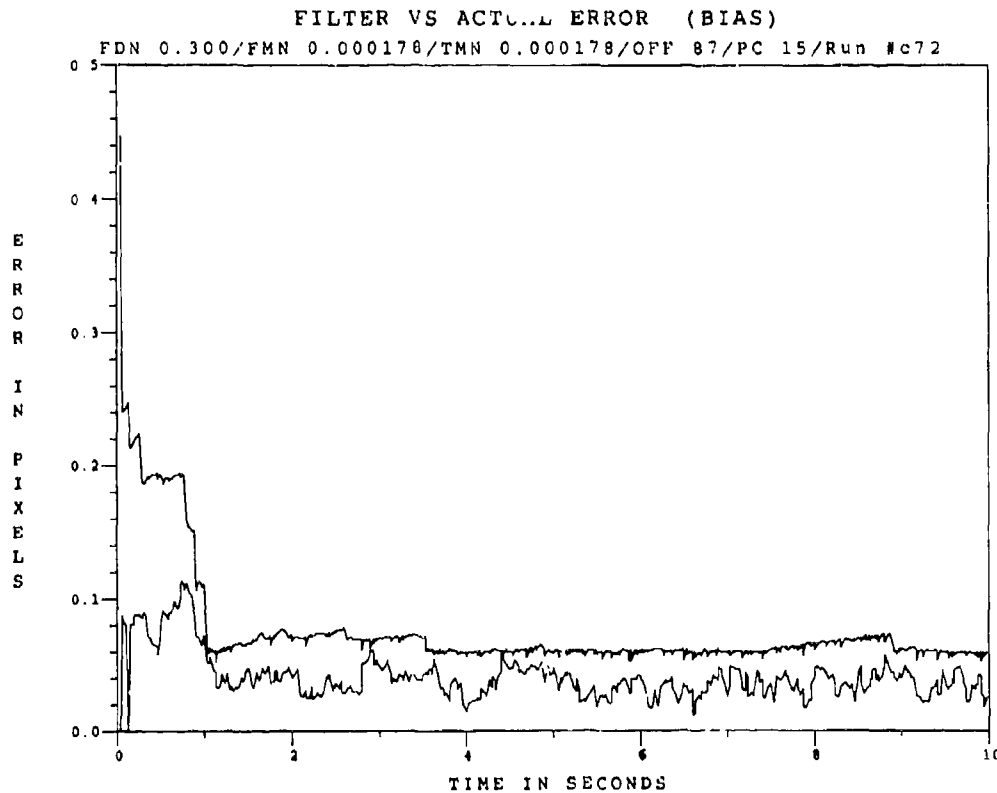


Figure E.6.16 10.5 μ m Two-State Modified MAP MMAF Bias Error, SNR = 4, $P_m = 0.30$

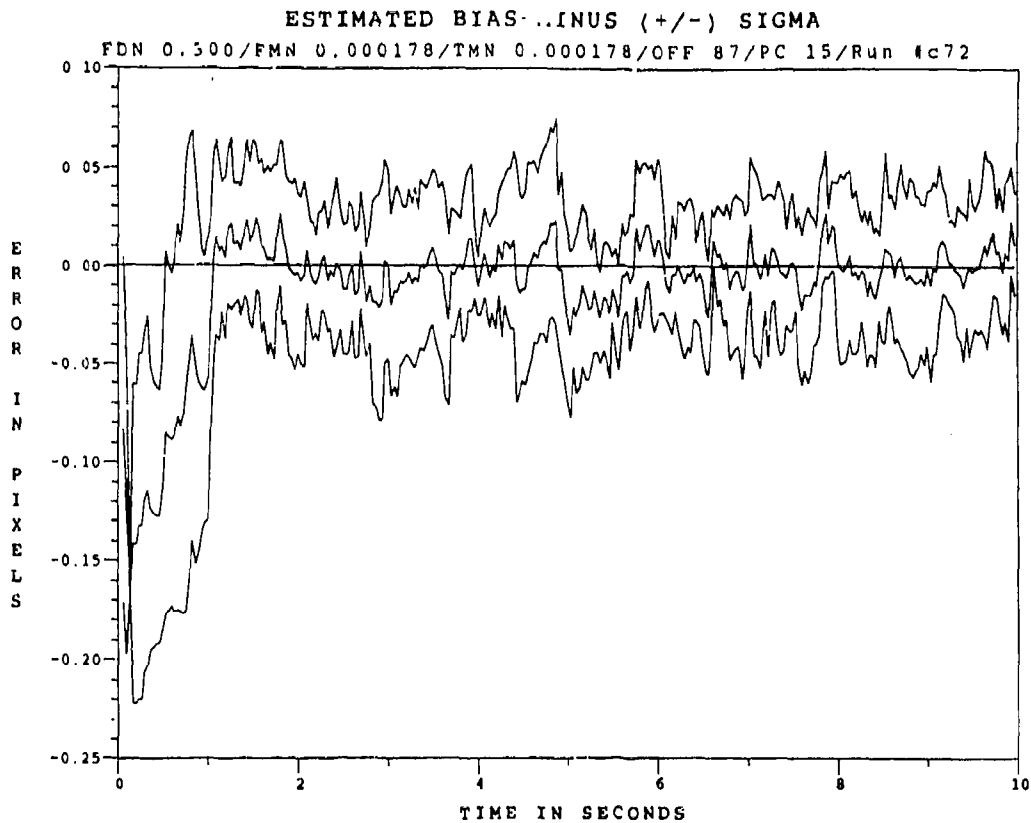


Figure E.6.17 10.5 μ m Two-State Modified MAP MMAF Bias Error, SNR=4, $P_m = -0.30$, at t_i^+

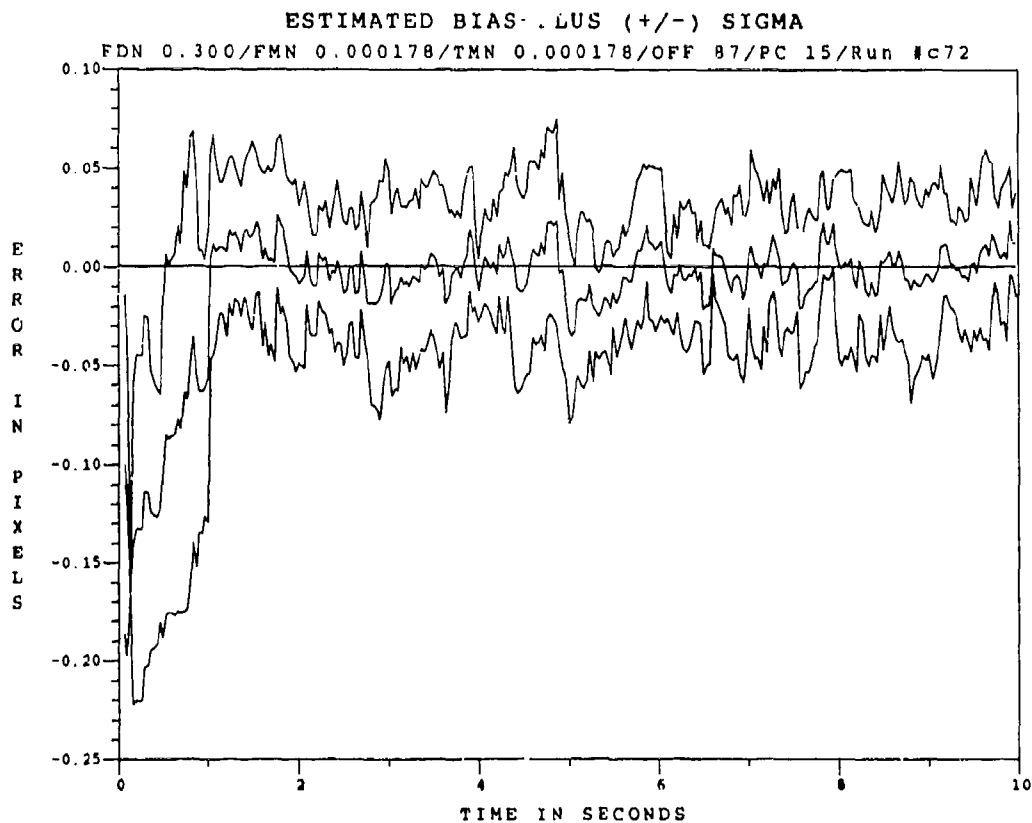


Figure E.6.18 10.5 μ m Two-State Modified MAP MMAF Bias Error, SNR=4, $P_m = -0.30$, at t_i^+

Appendix F

Two-State Center-of-Mass

Modified MAP MMAF

Case 2

This Appendix contains the error plots of the two-state center-of-mass Modified MAP MMAF, wherein the low-energy speckle return is continuously received when the hardbody-induced Doppler return is undetectable. The Appendix is divided into sub-appendices that correspond to different values of low-energy laser wavelength and SNR. Each wavelength with a given SNR, is further separated into three values of Probability-of-Miss, P_m . The plots show the error relationship, in error mean ± 1 standard deviation values (in pixels), of the true errors between the filter estimated and true offset distance from the intensity centroid to the hardbody center-of-mass, and the true errors between the filter's estimate and the true bias caused by the plume's speckle reflectance. This appendix is divided into the following sub-appendices:

<u>Sub-Appendix</u>	<u>Category</u>
F.1	0.53 μm Wavelength, SNR = 10
F.2	0.53 μm Wavelength, SNR = 4
F.3	2.01 μm Wavelength, SNR = 10
F.4	2.01 μm Wavelength, SNR = 4
F.5	10.5 μm Wavelength, SNR = 10
F.6	10.5 μm Wavelength, SNR = 4

Appendix F.1

Two-State Center-of-Mass

Modified MAP MMAP

with

0.53 μm Doppler Return Measurements

at SNR = 10

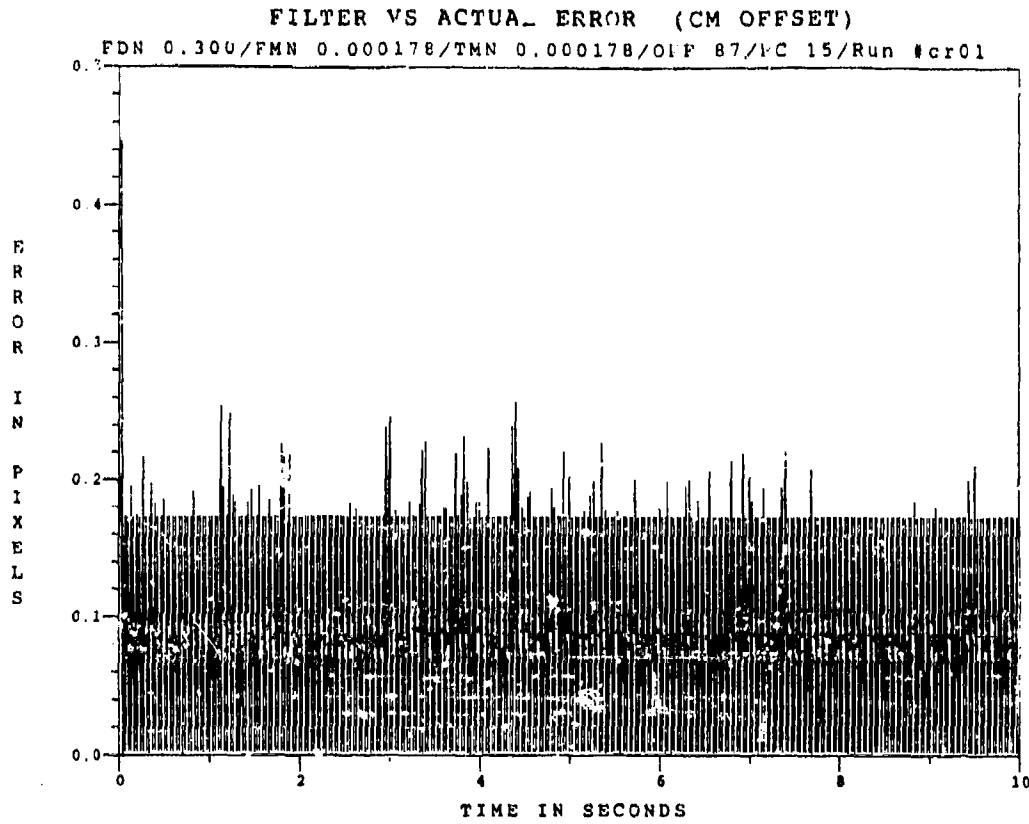


Figure F.1.1 0.53 μ m Two-State Modified MAP MMAF Offset Error, SNR=10, $P_m = 0.0$

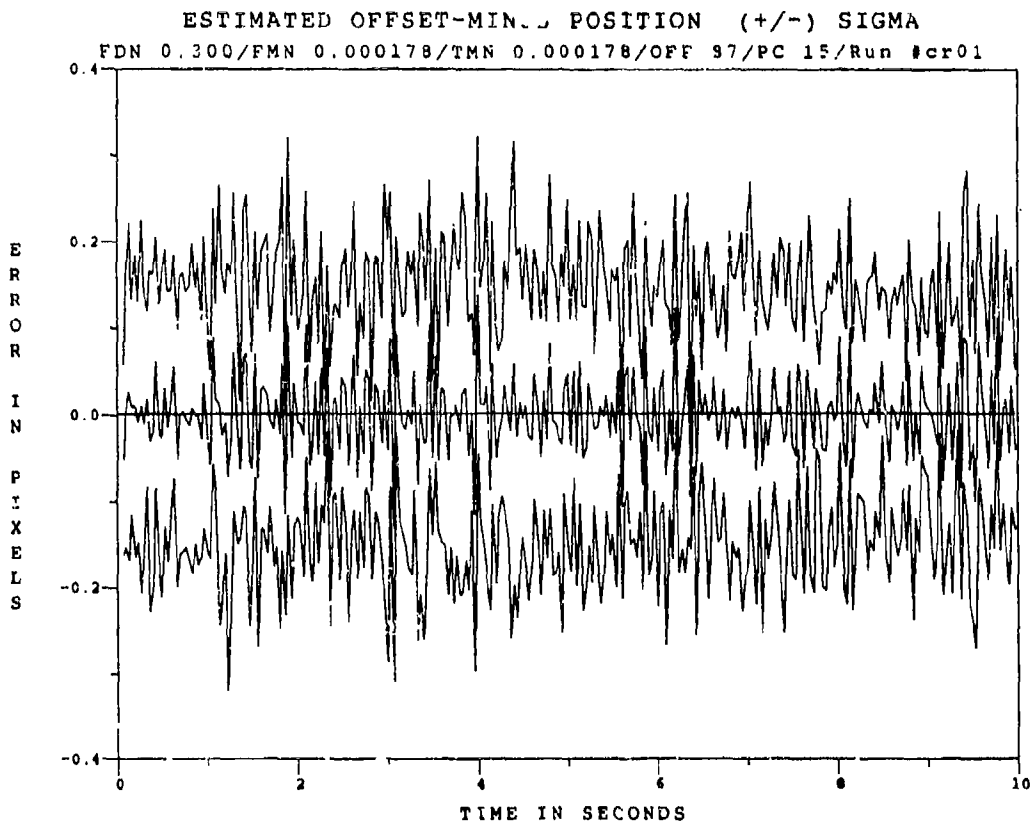


Figure F.1.2 0.53 μ m Two-State Modified MAP MMAF Bias Error, SNR=10, $P_m = 0.0$, at t_i

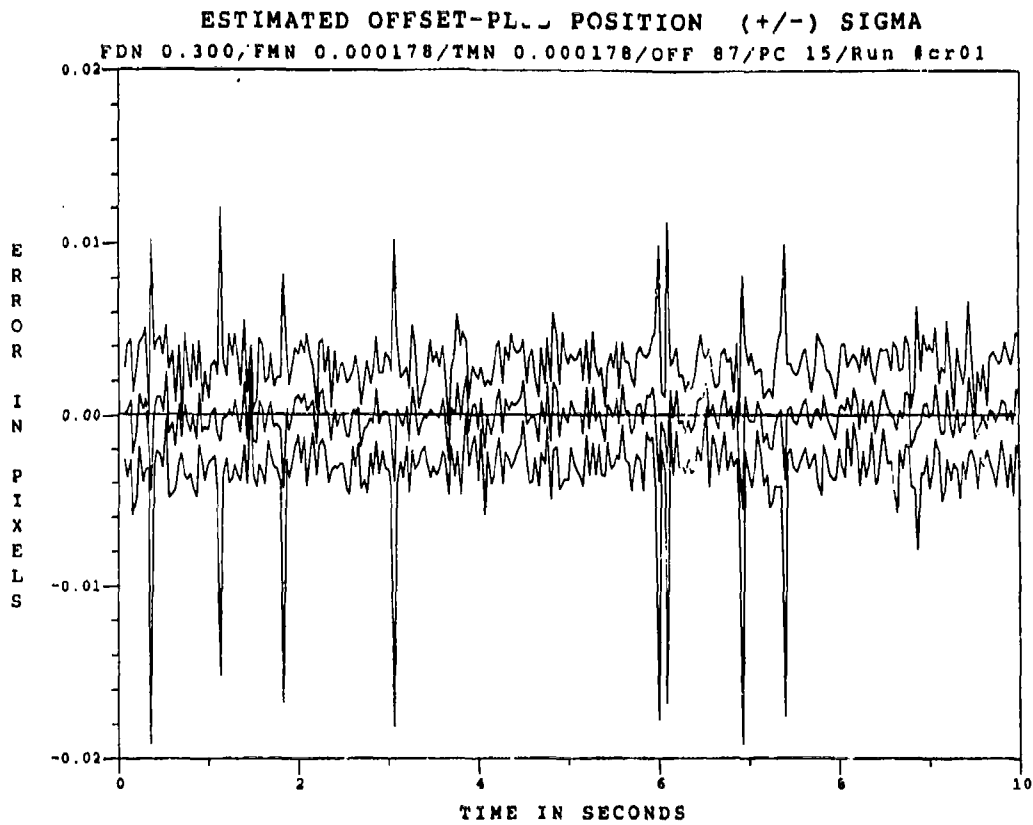


Figure F.1.3 0.53 μm Two-State Modified MAP MMAF Offset Error, SNR=10, $P_m = -0.0$, at t_i^+

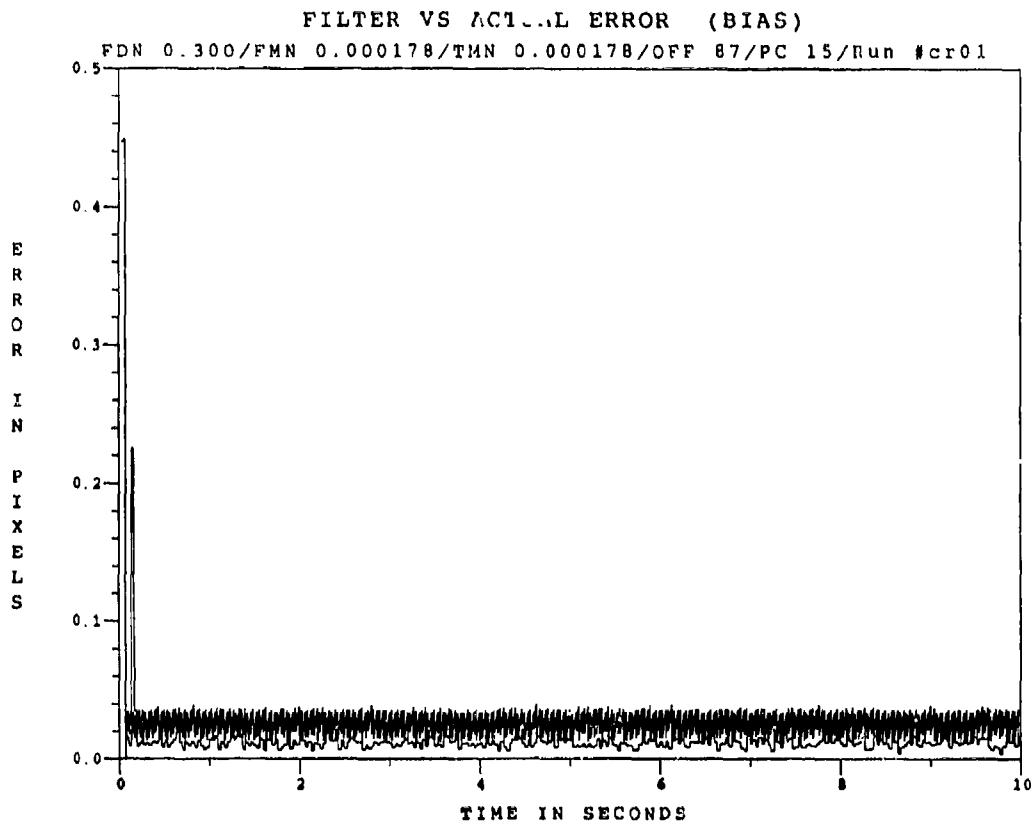


Figure F.1.4 0.53 μm Two-State Modified MAP MMAF Bias Error, SNR=10, $P_m = -0.0$

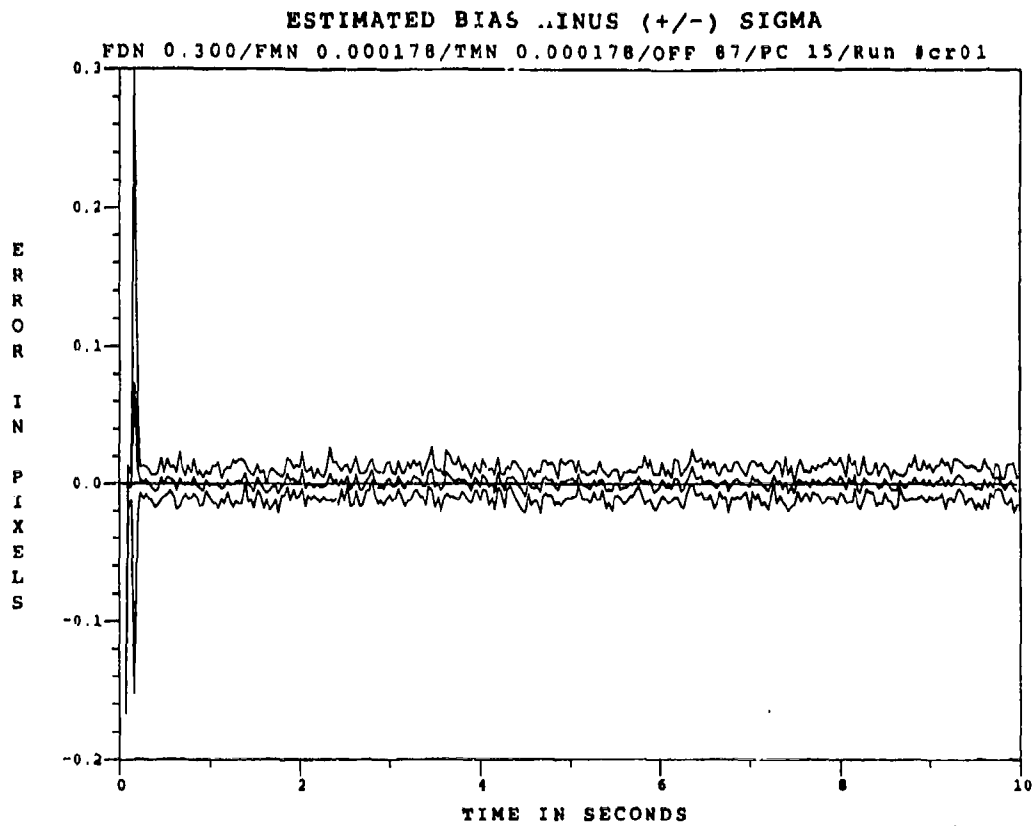


Figure F.1.5 0.53 μm Two-State Modified MAP MMAF Bias Error, SNR=10, $P_m = -0.0$, at t_i^-

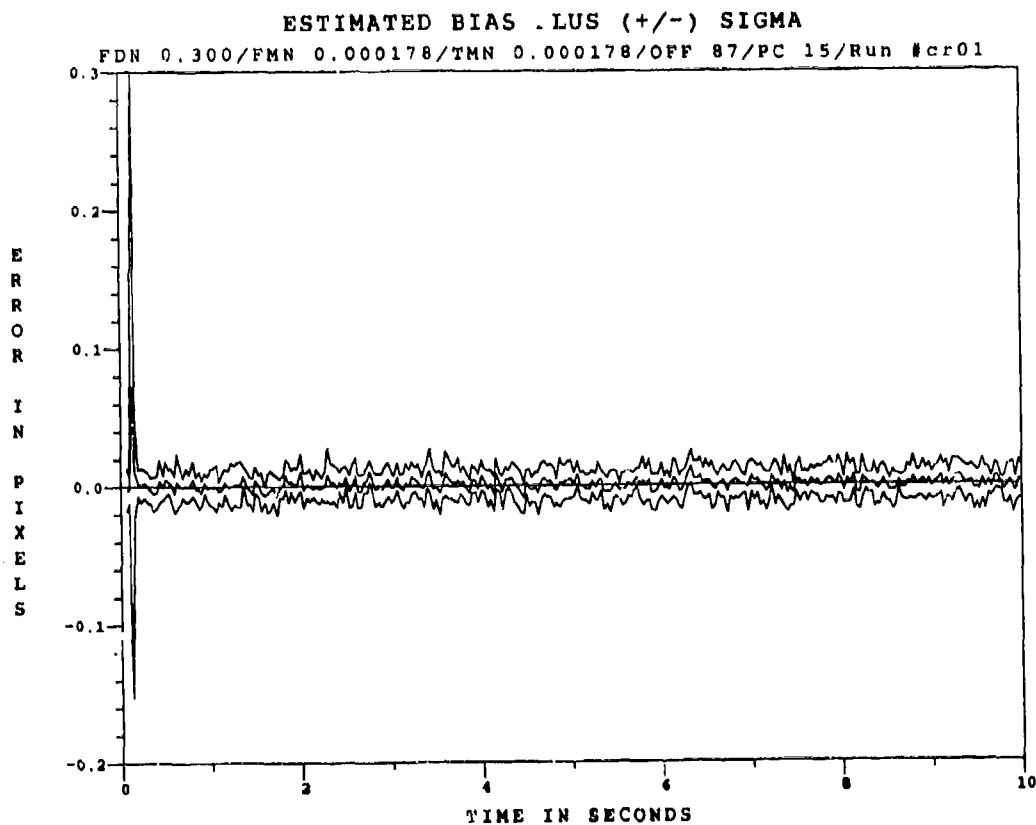


Figure F.1.6 0.53 μm Two-State Modified MAP MMAF Bias Error, SNR=10, $P_m = 0.0$, at t_i^+

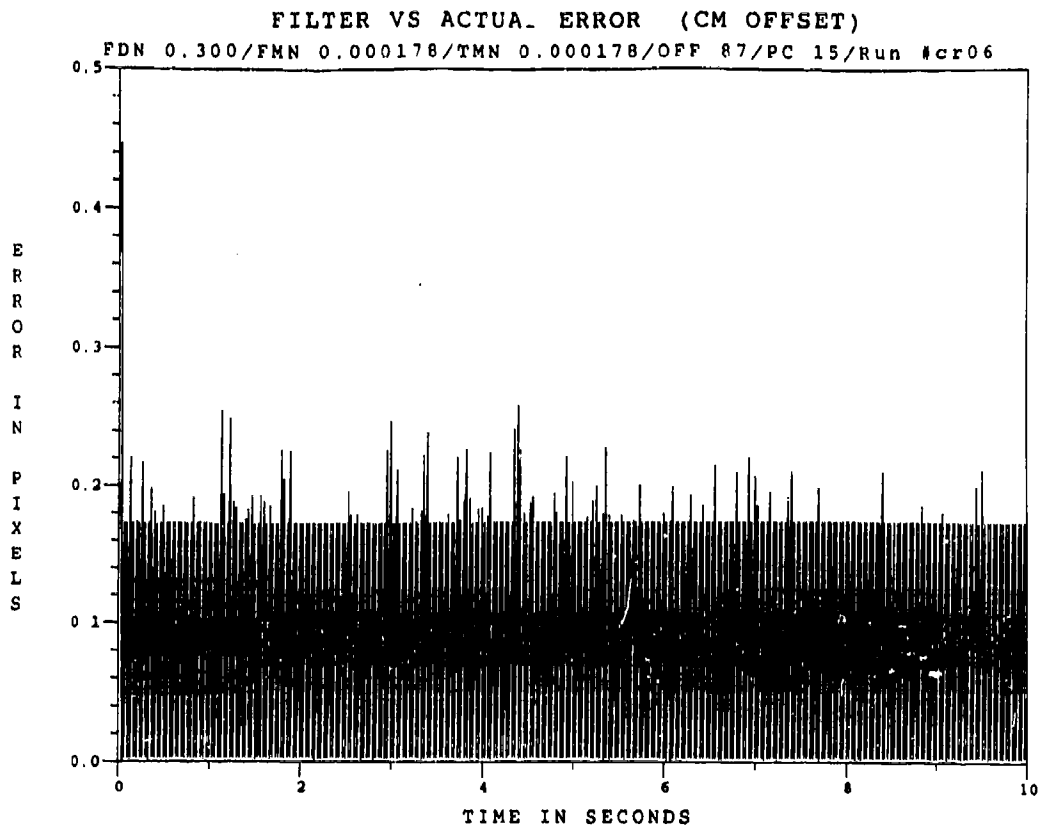


Figure F.1.7 0.53 μm Two-State Modified MAP MMAF Offset Error, SNR = 10, $P_m = 0.05$

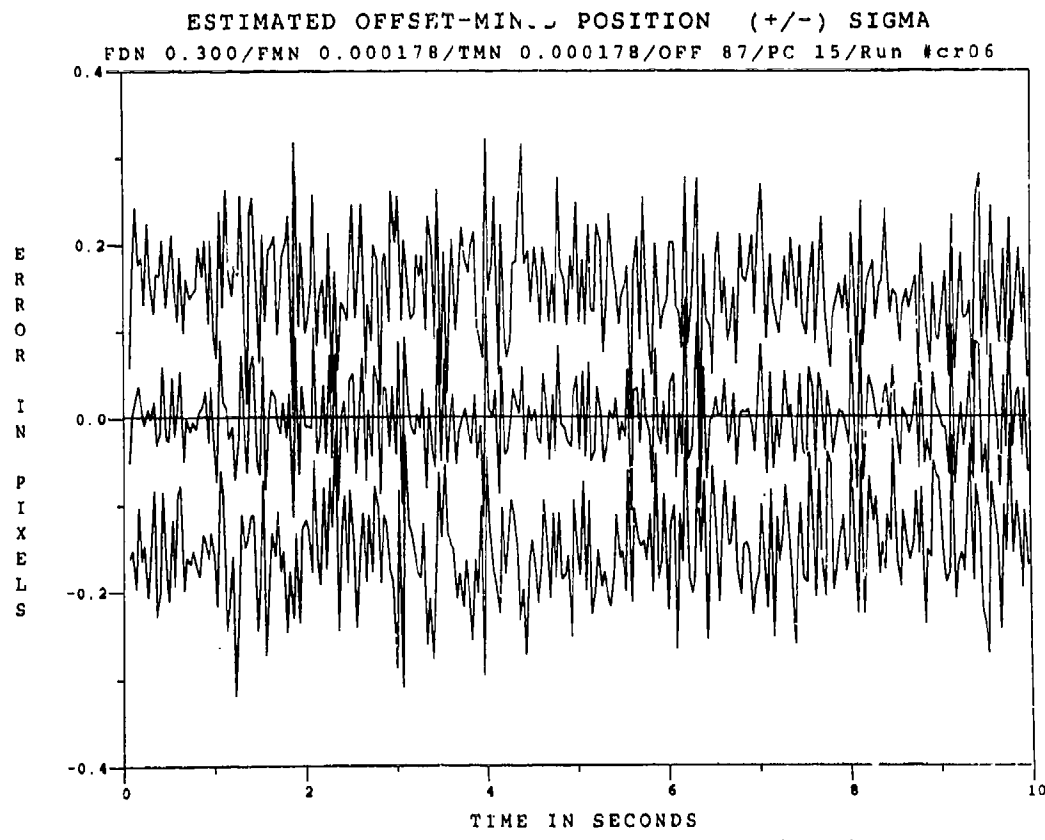


Figure F.1.8 0.53 μm Two-State Modified MAP MMAF Offset Error, SNR=10, $P_m = 0.05$, at t_1^*

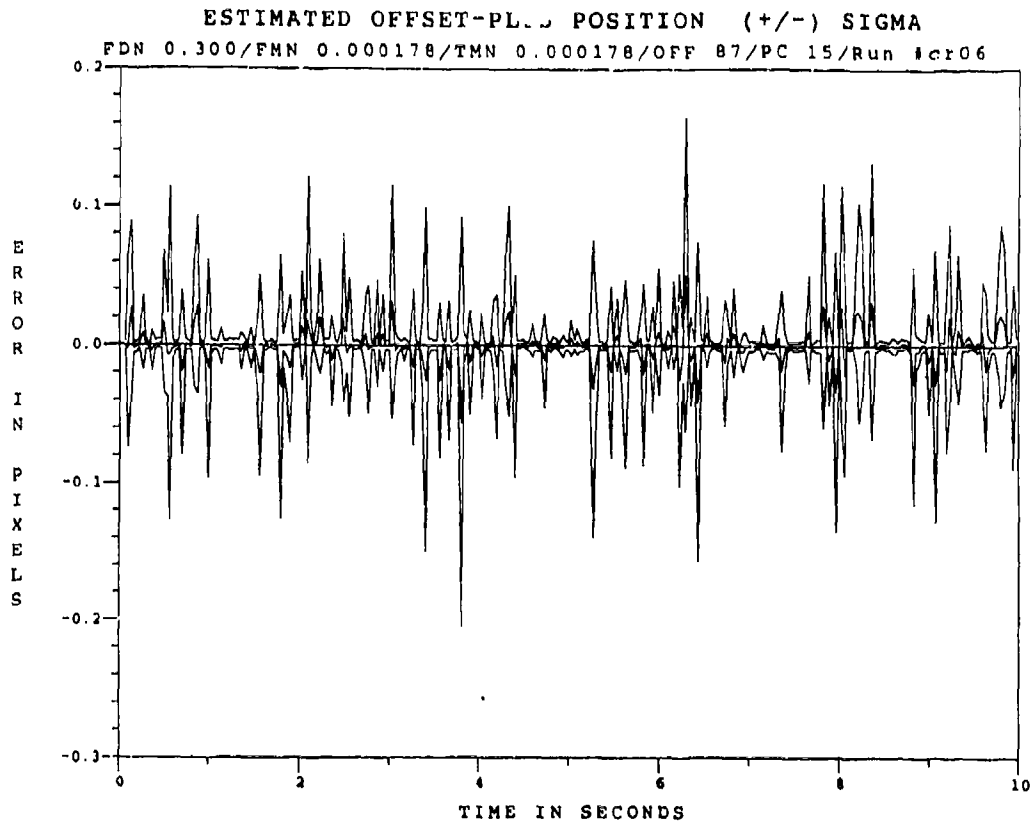


Figure F.1.9 0.53 μ m Two-State Modified MAP MMAE Offset Error, SNR=10, $P_m = -0.05$, at t_i^+

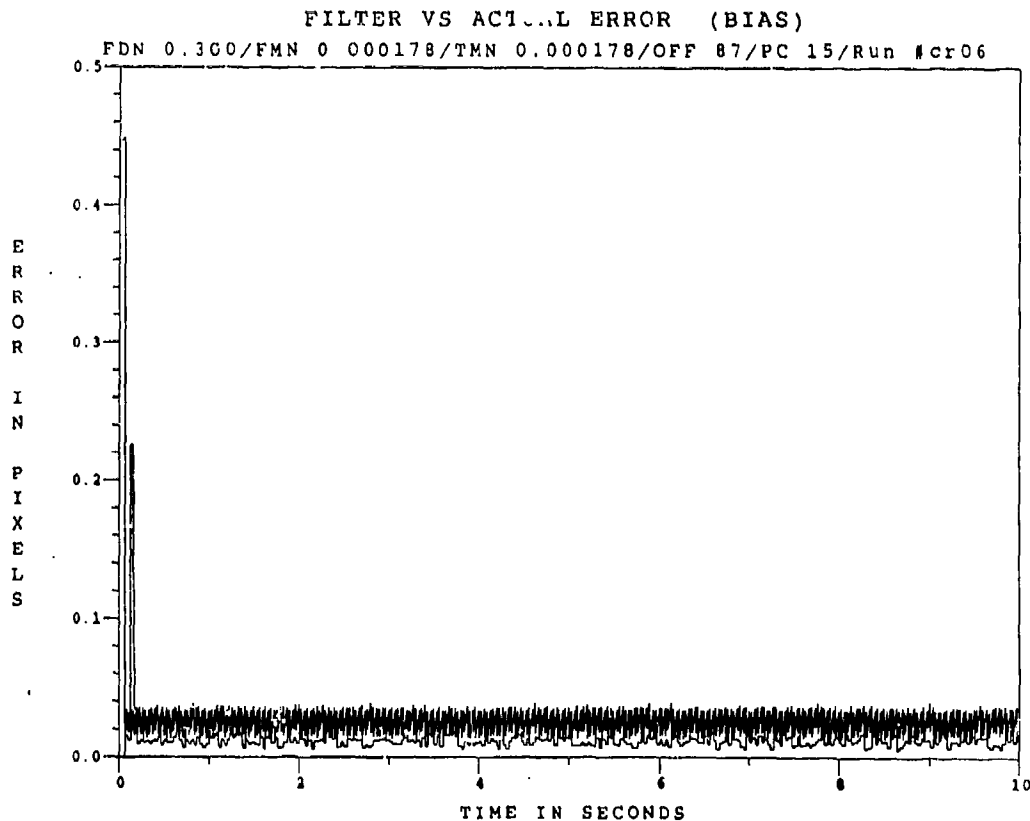


Figure F.1.10 0.53 μ m Two-State Modified MAP MMAF Bias Error, SNR = 10, $P_m = 0.05$

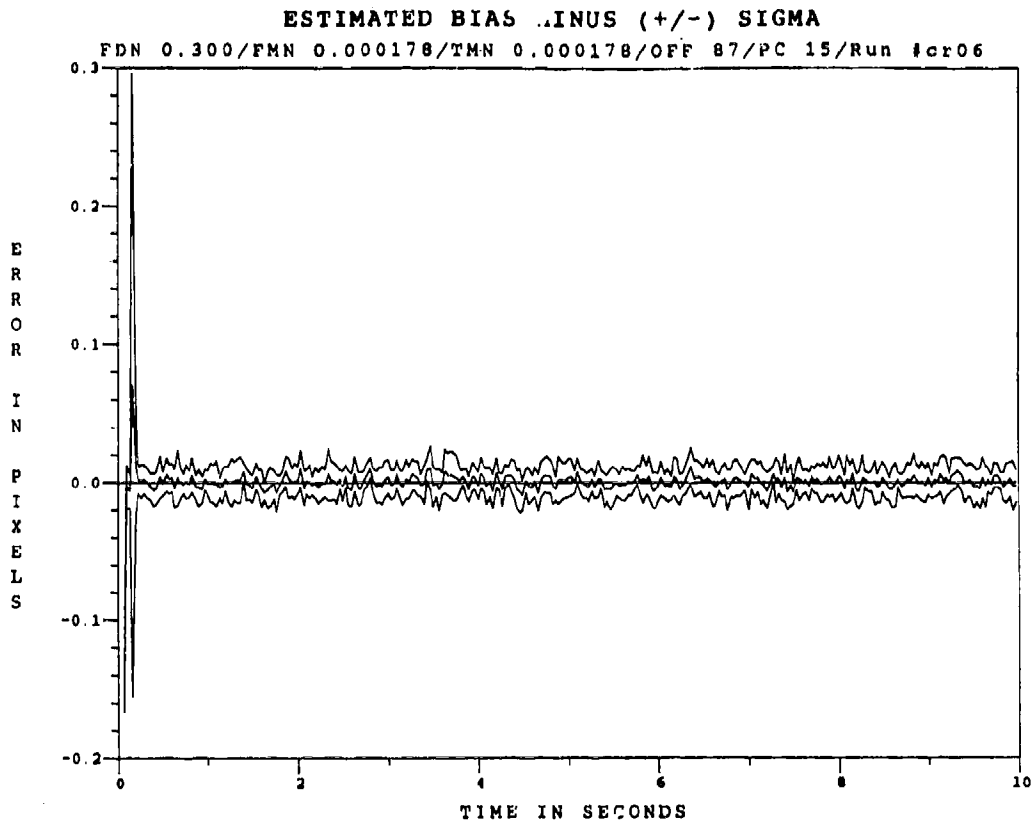


Figure F.1.11 0.53 μm Two-State Modified MAP MMAF Bias Error, SNR=10, $P_m = -0.05$, at t_i^-

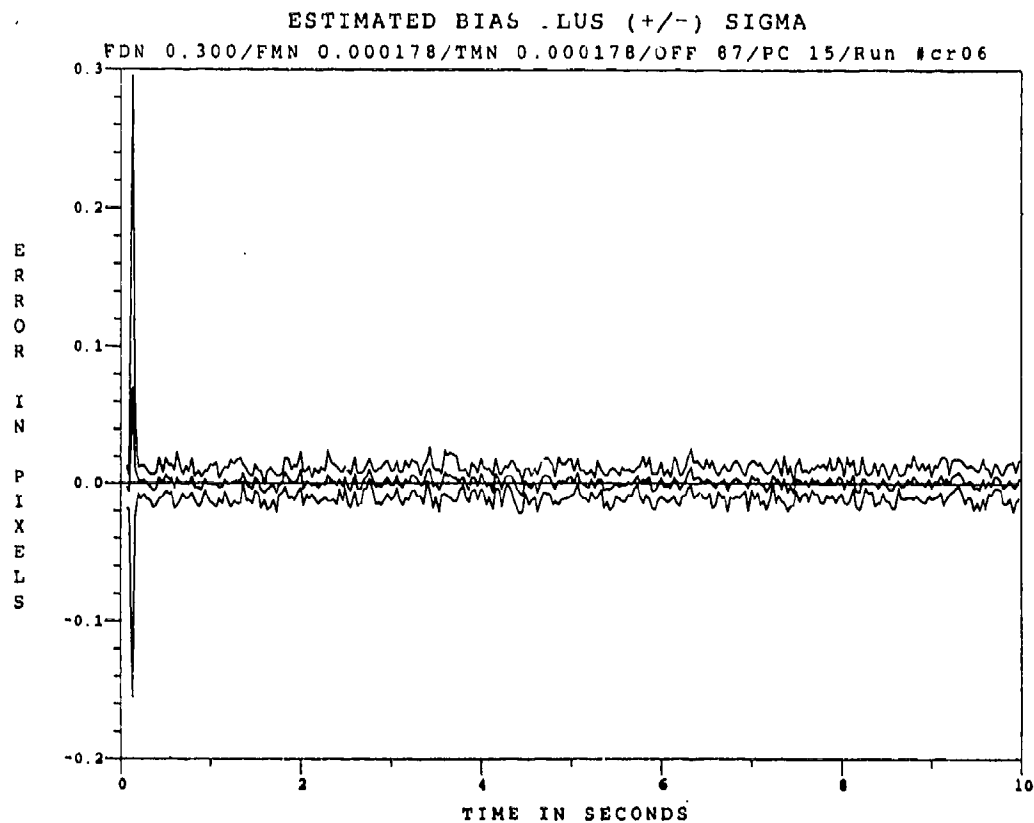


Figure F.1.12 0.53 μm Two-State Modified MAP MMAE Bias Error, SNR=10, $P_m = -0.05$, at t_i^+

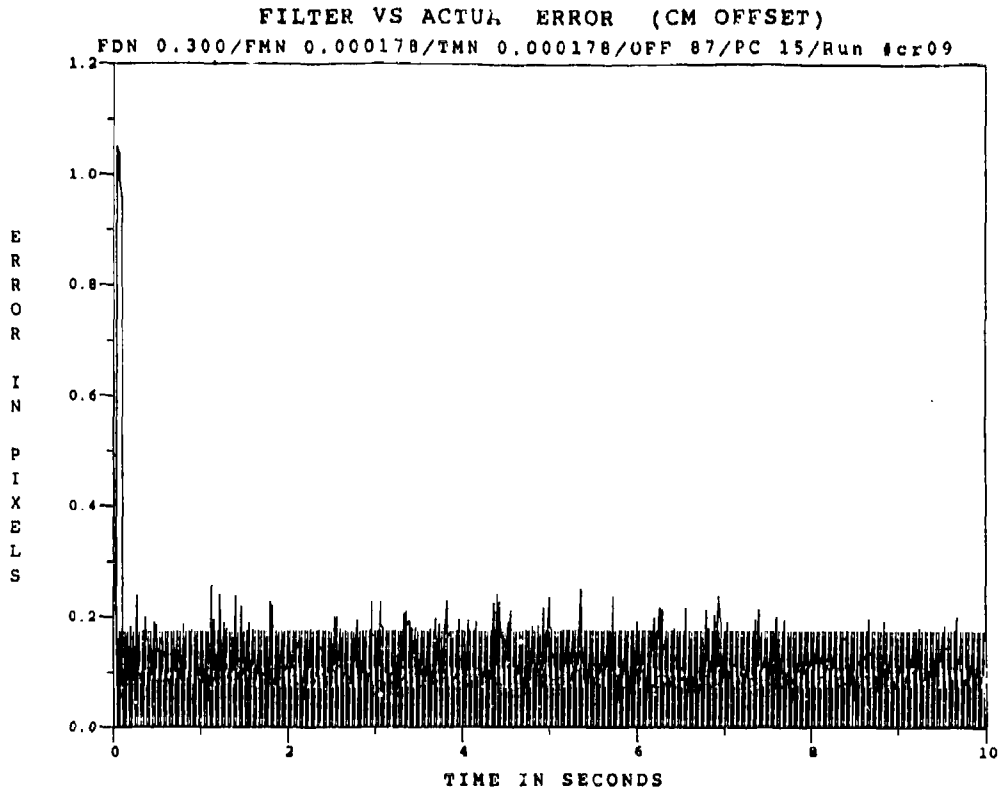


Figure F.1.13 0.53 μ m Two-State Modified MAP MMAF Offset Error, SNR = 10, $P_m = 0.30$

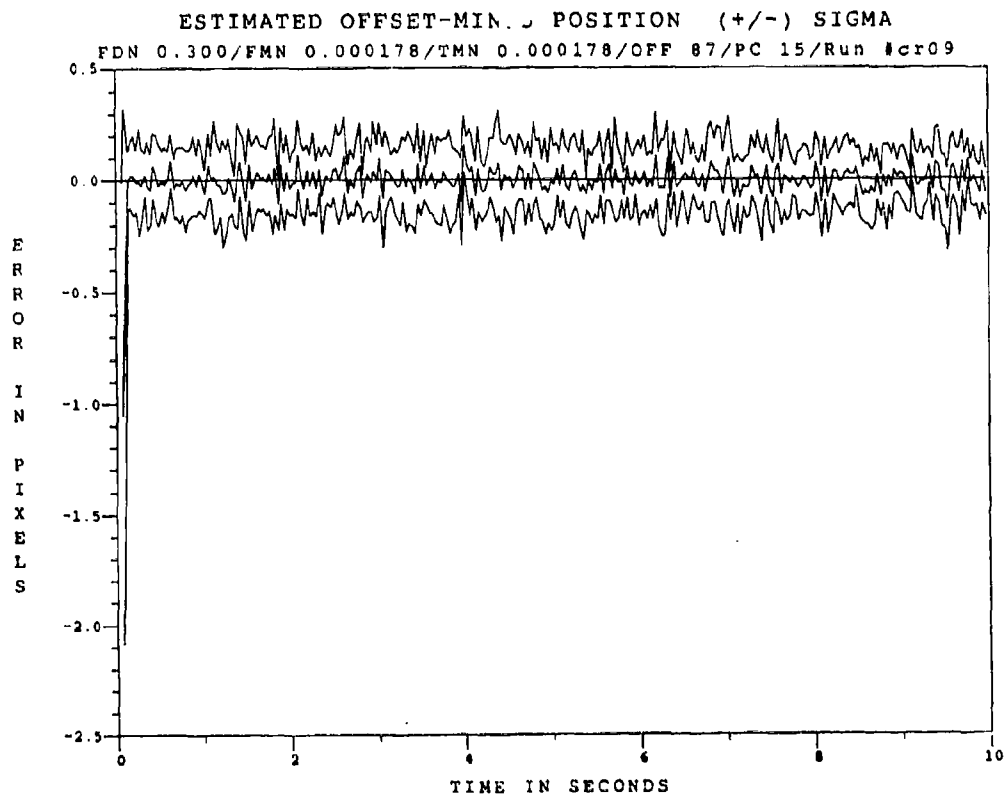


Figure F.1.14 0.53 μ m Two-State Modified MAP MMAF Offset Error, SNR=10, $P_m=0.30$, at t_i

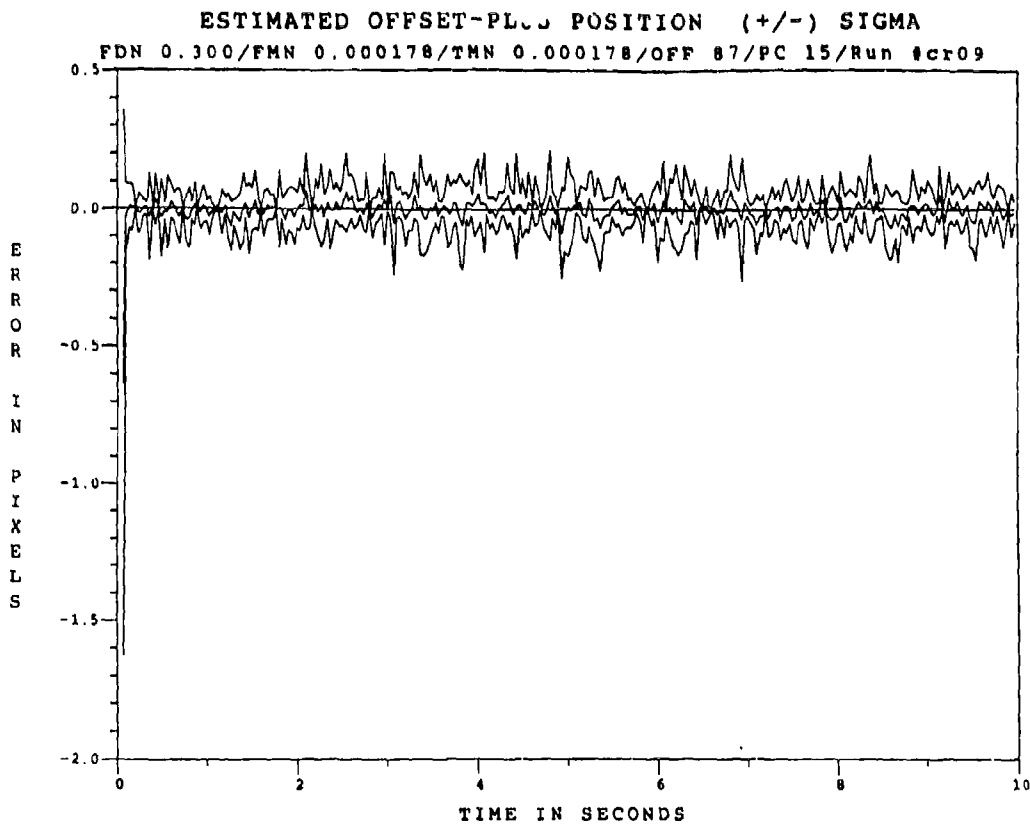


Figure F.1.15 0.53 μ m Two-State Modified MAP MMAE Offset Error, SNR=10, $P_m = -0.30$, at t_i^+

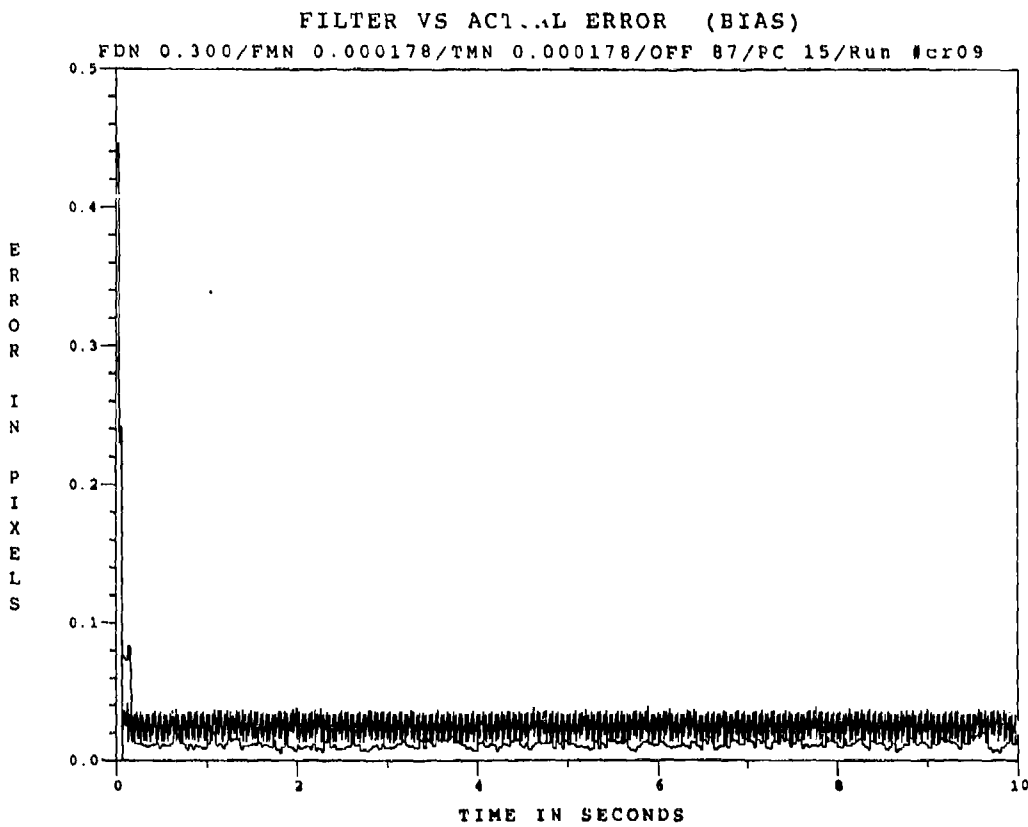


Figure F.1.16 0.53 μ m Two-State Modified MAP MMAF Bias Error, SNR = 10, $P_m = -0.30$

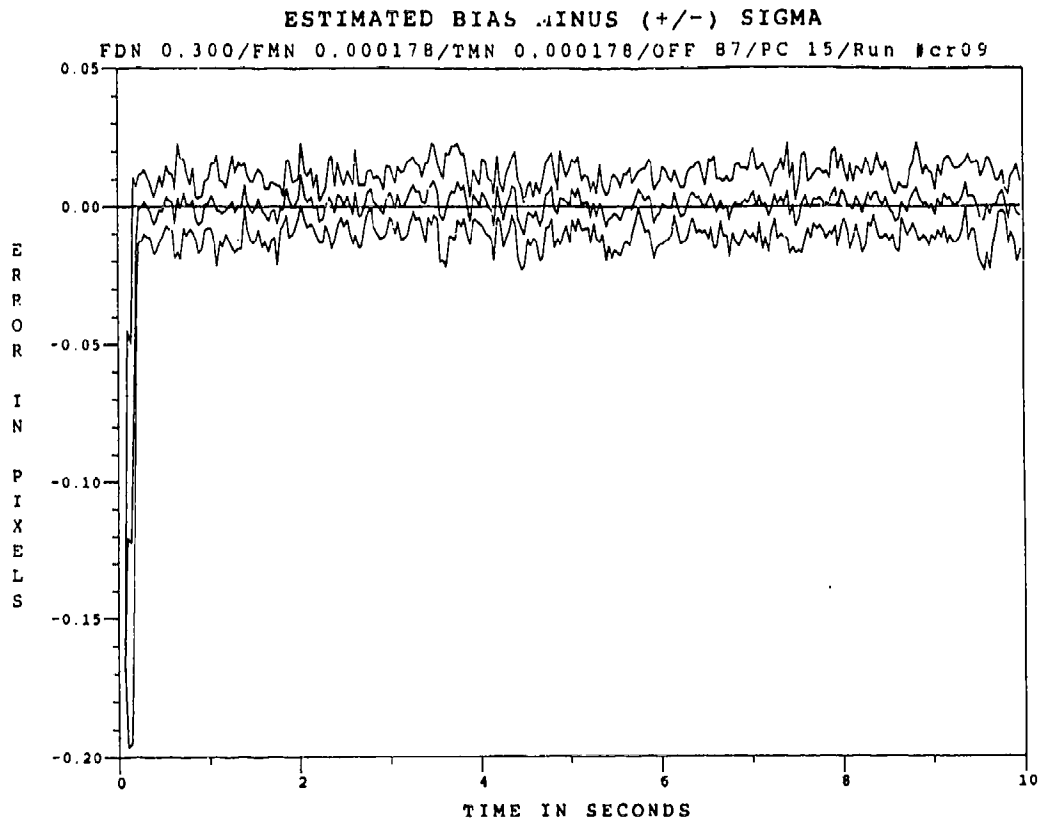


Figure F.1.17 0.53 μ m Two-State Modified MAP MMAF Bias Error, SNR=10, $P_m = -0.30$, at t_i^T

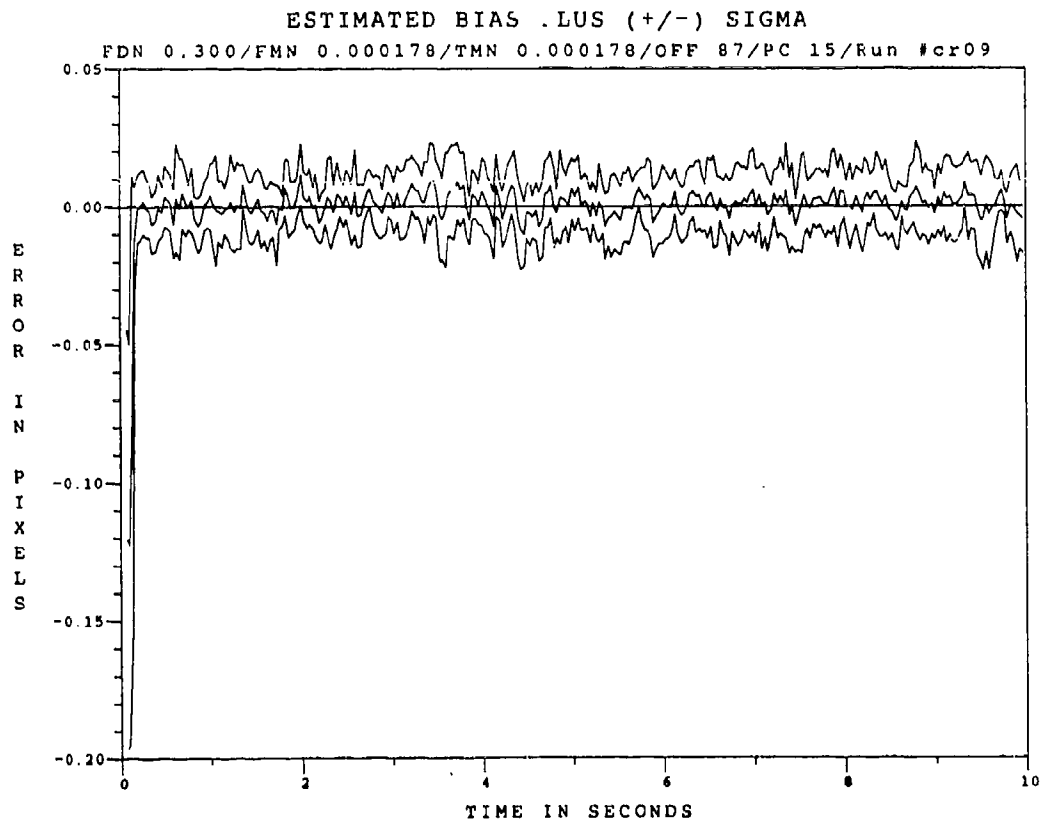


Figure F.1.18 0.53 μ m Two-State Modified MAP MMAE Bias Error, SNR=10, $P_m = -0.30$, at t_i^T

Appendix F.2

Two-State Center-of-Mass

Modified MAP MMAF

with

0.53 μm Doppler Return Measurements

at SNR = 4

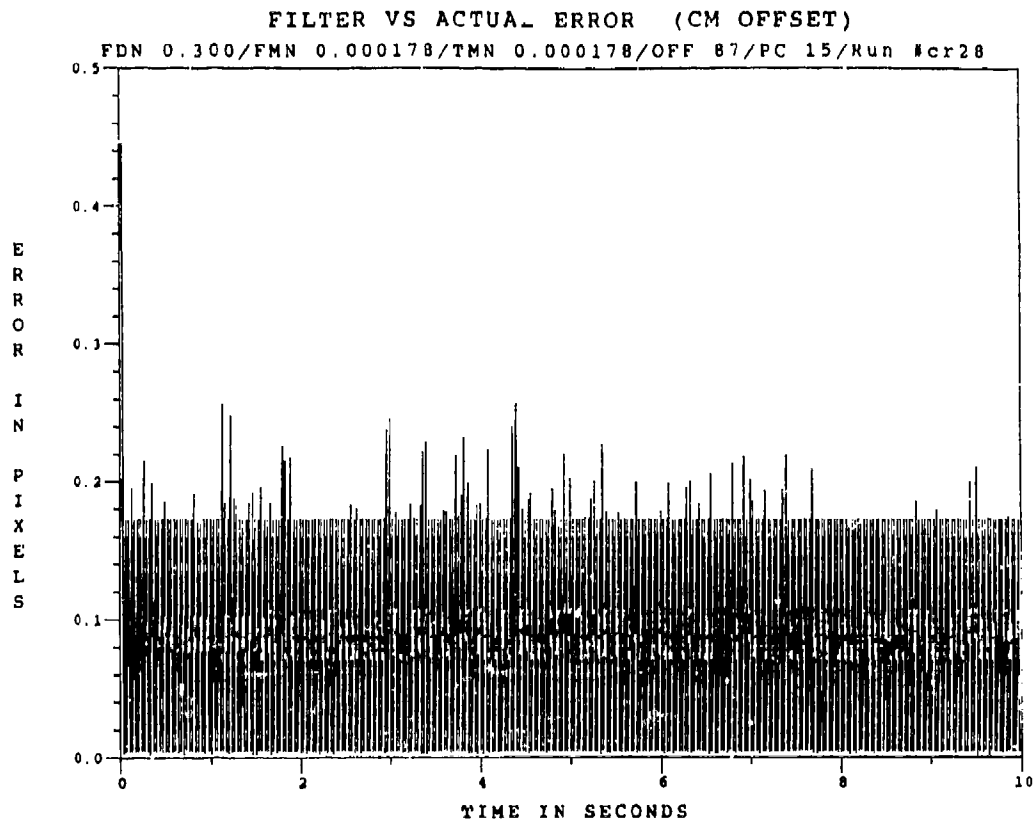


Figure F.2.1 0.53 μm Two-State Modified MAP MMAF Offset Error, SNR=4, $P_n = -0.0$

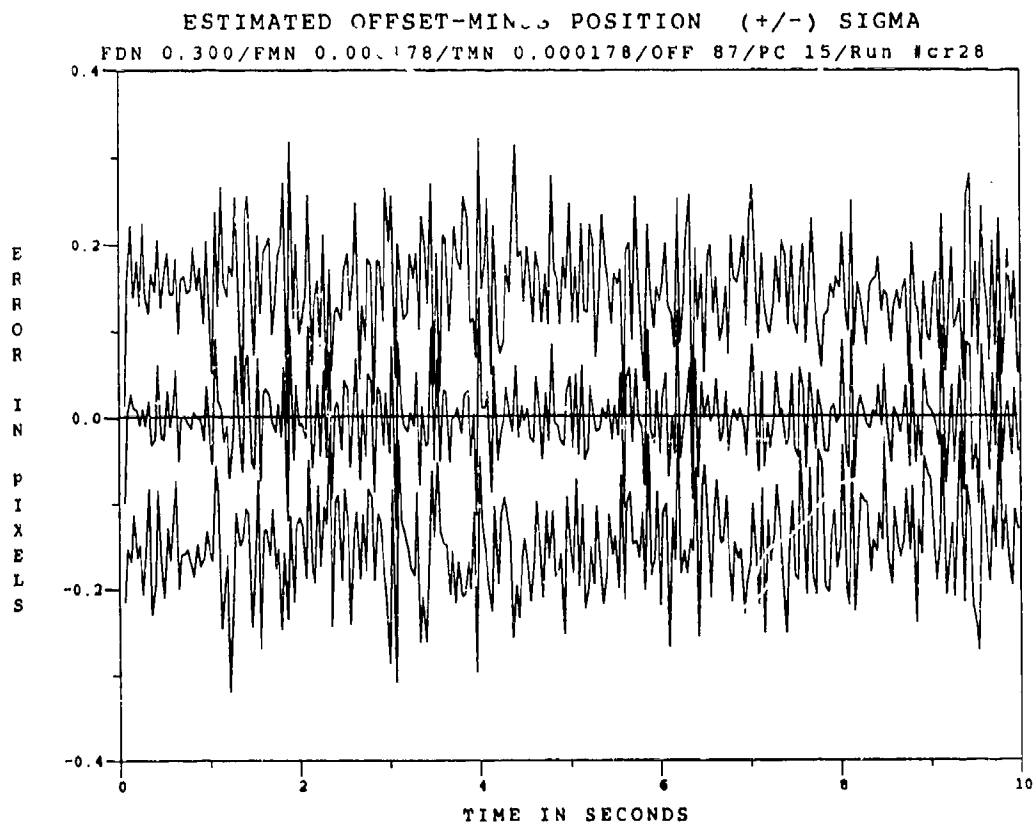


Figure F.2.2 0.53 μm Two-State Modified MAP MMAF Offset Error, SNR=4, $P_n = -0.0$, at t_i

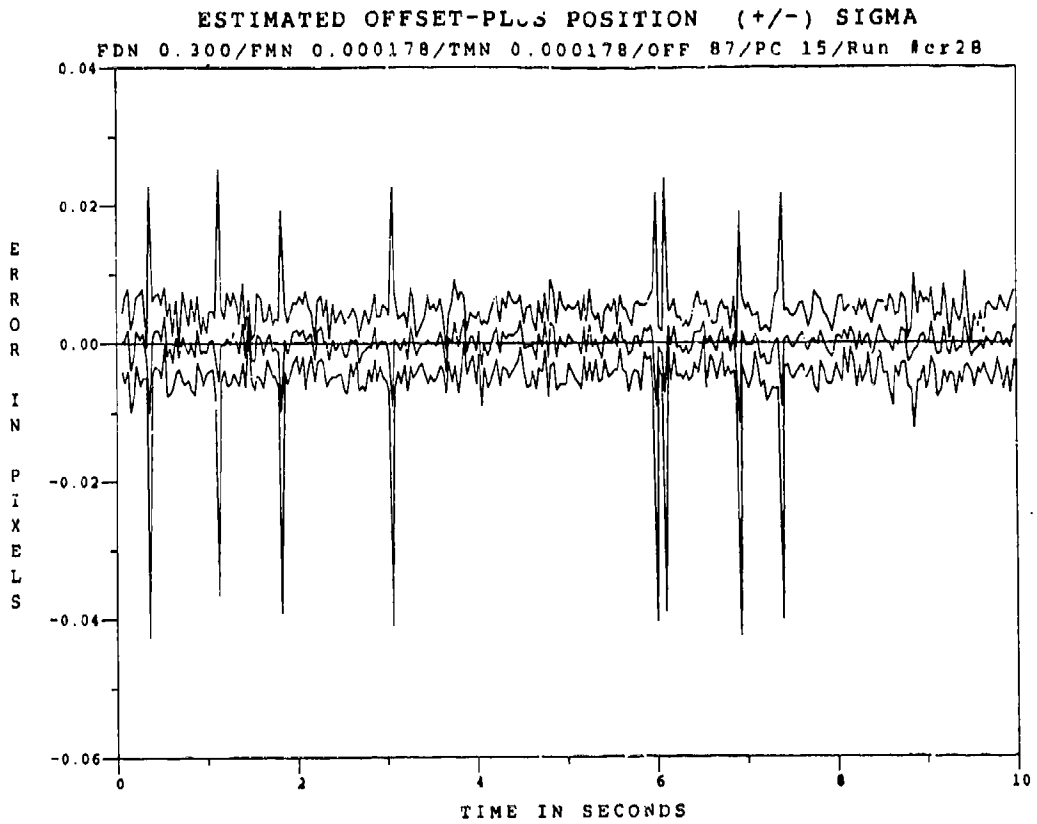


Figure F.2.3 0.53 μm Two-State Modified MAP MMAF Offset Error, SNR=4, $P_n = -0.0$, at t_i^+

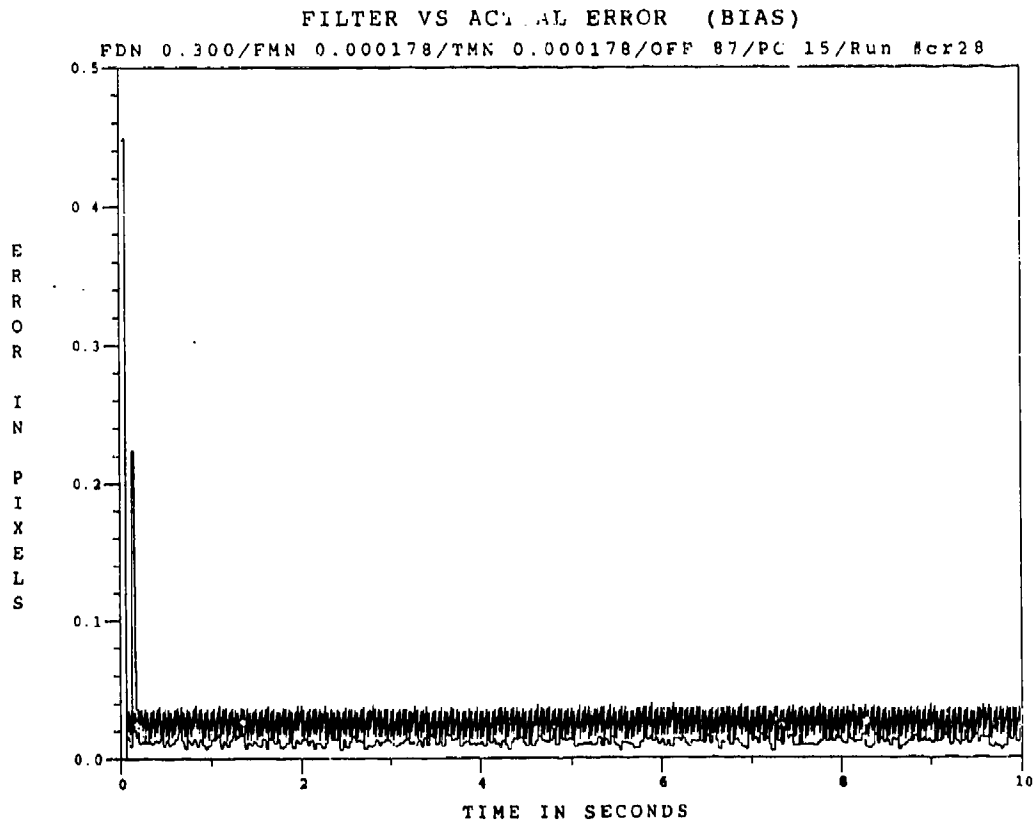


Figure F.2.4 0.53 μm Two-State Modified MAP MMAF Bias Error, SNR=4, $P_n = -0.0$

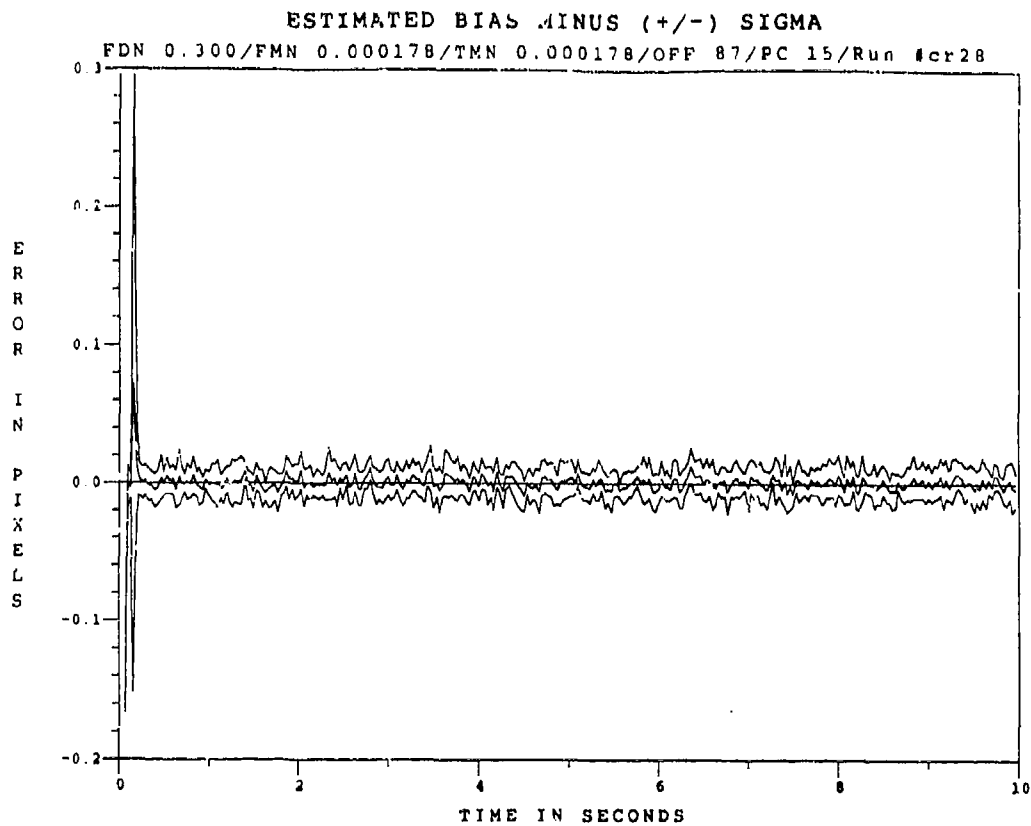


Figure F.2.5 0.53 μm Two-State Modified MAP MMAF Bias Error, SNR=4, $P_m = -0.0$, at t_i^-

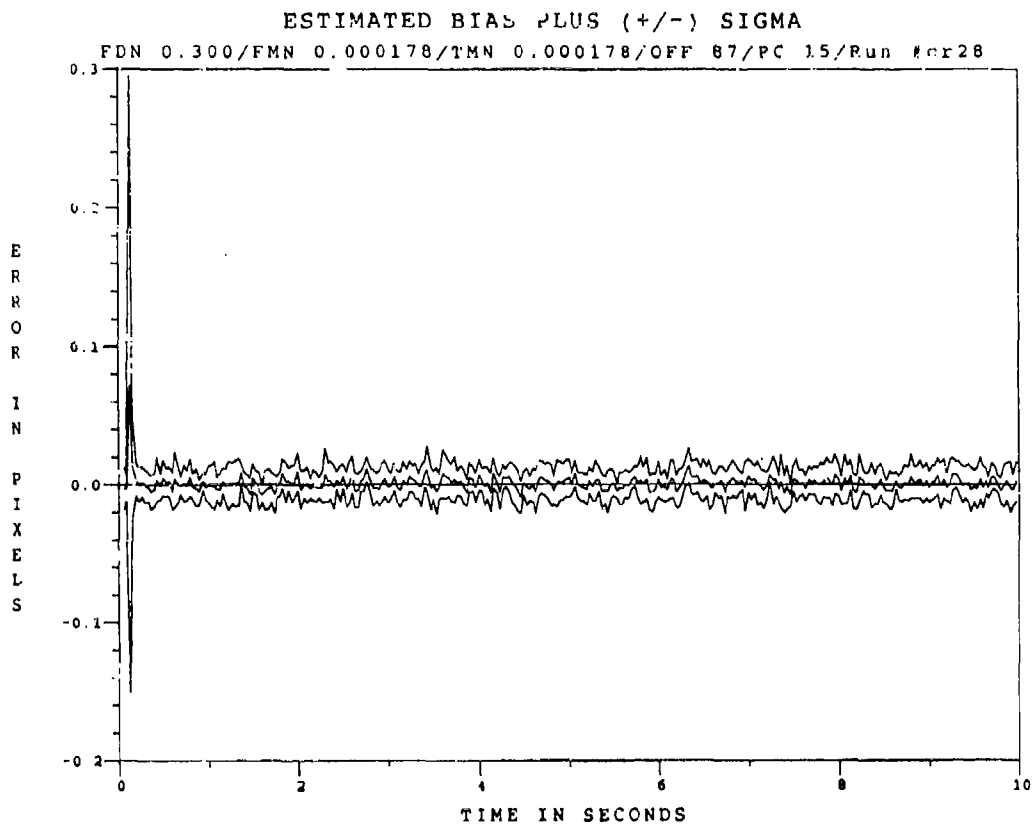


Figure F.2.6 0.53 μm Two-State Modified MAP MMAF Bias Error, SNR=4, $P_m = -0.0$, at t_i^+

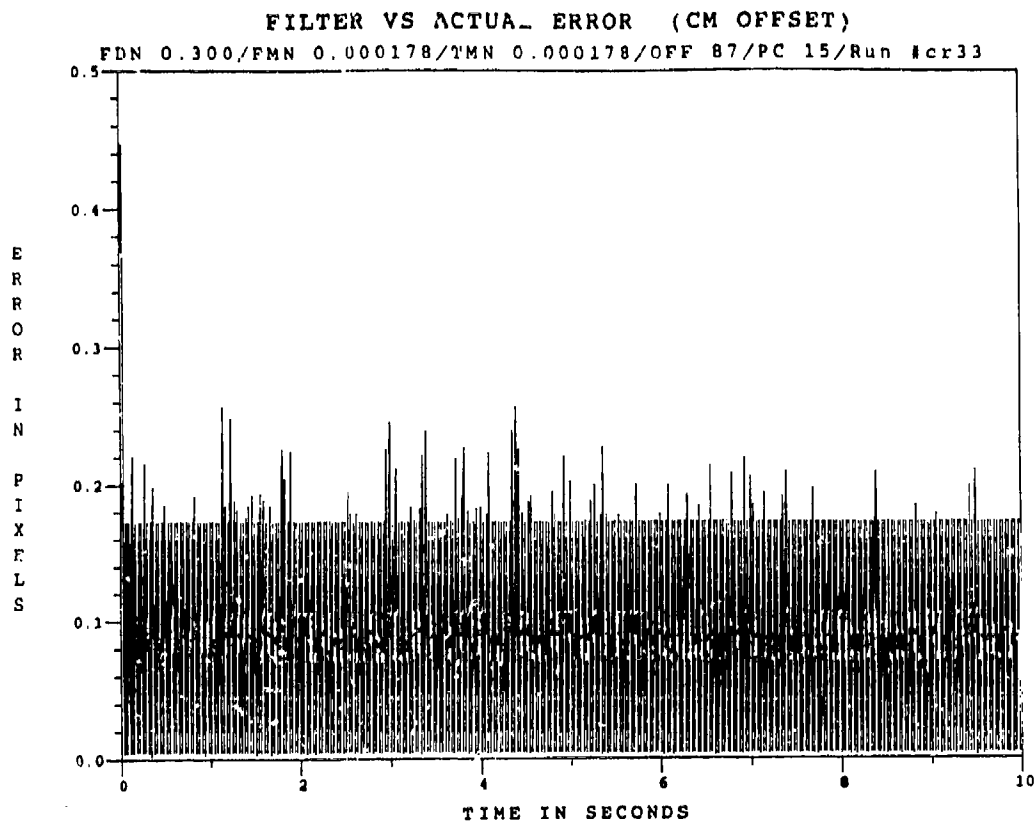


Figure F.2.7 0.53 μm Two-State Modified MAP MMAF Offset Error, SNR = 4, $P_m = 0.05$

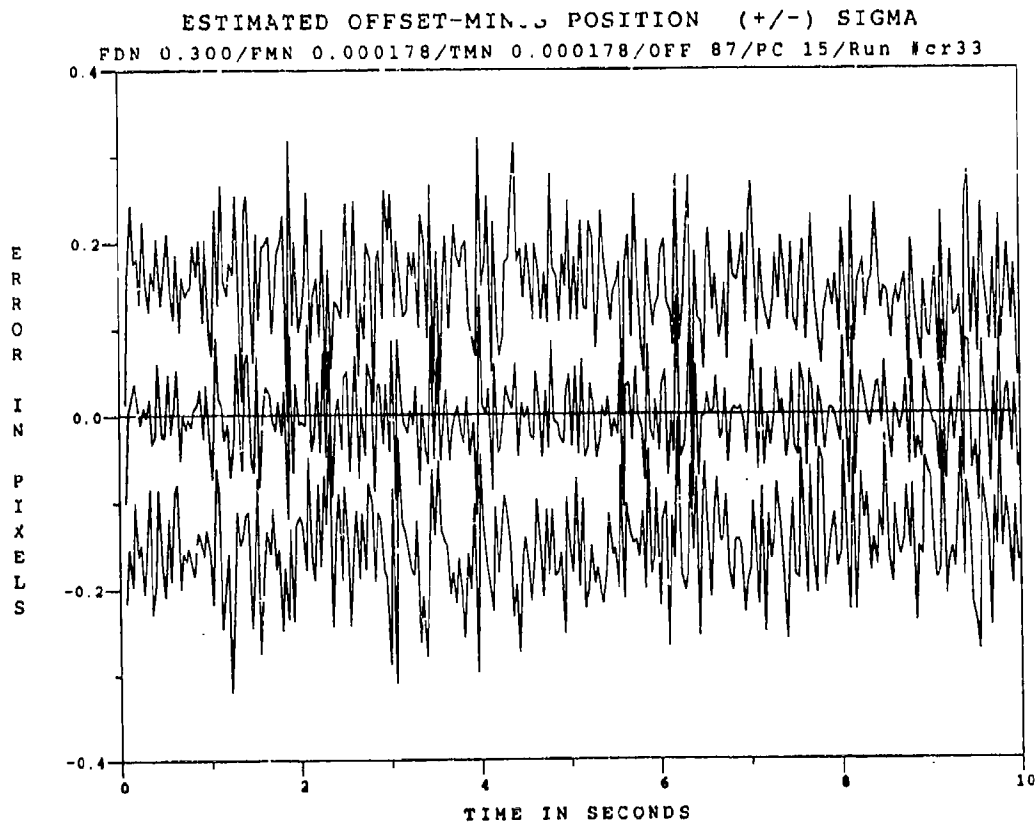


Figure F.2.8 0.53 μm Two-State Modified MAP MMAF Offset Error, SNR=4, $P_m = 0.05$, at t_i

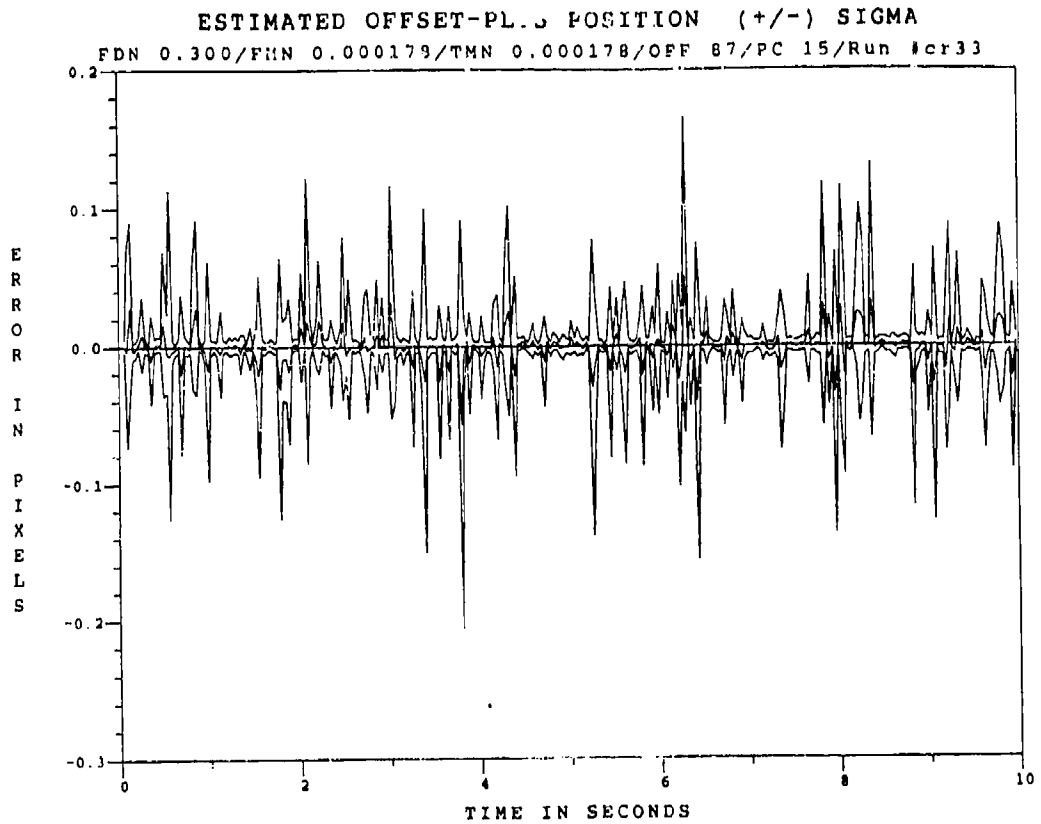


Figure F.2.9 0.53 μ m Two-State Modified MAP MMAF Offset Error, SNR=4, $P_m = 0.05$, at t_1^+

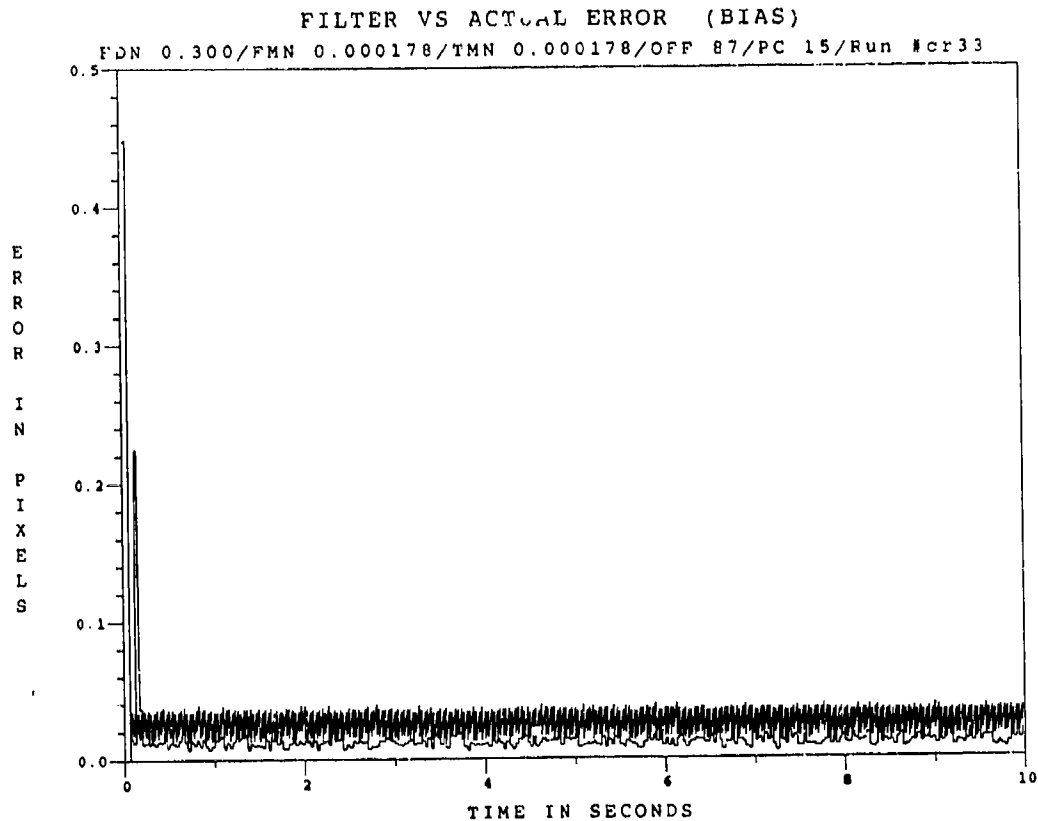


Figure F.2.10 0.53 μ m Two-State Modified MAP MMAF Bias Error, SNR = 4, $P_m = 0.05$

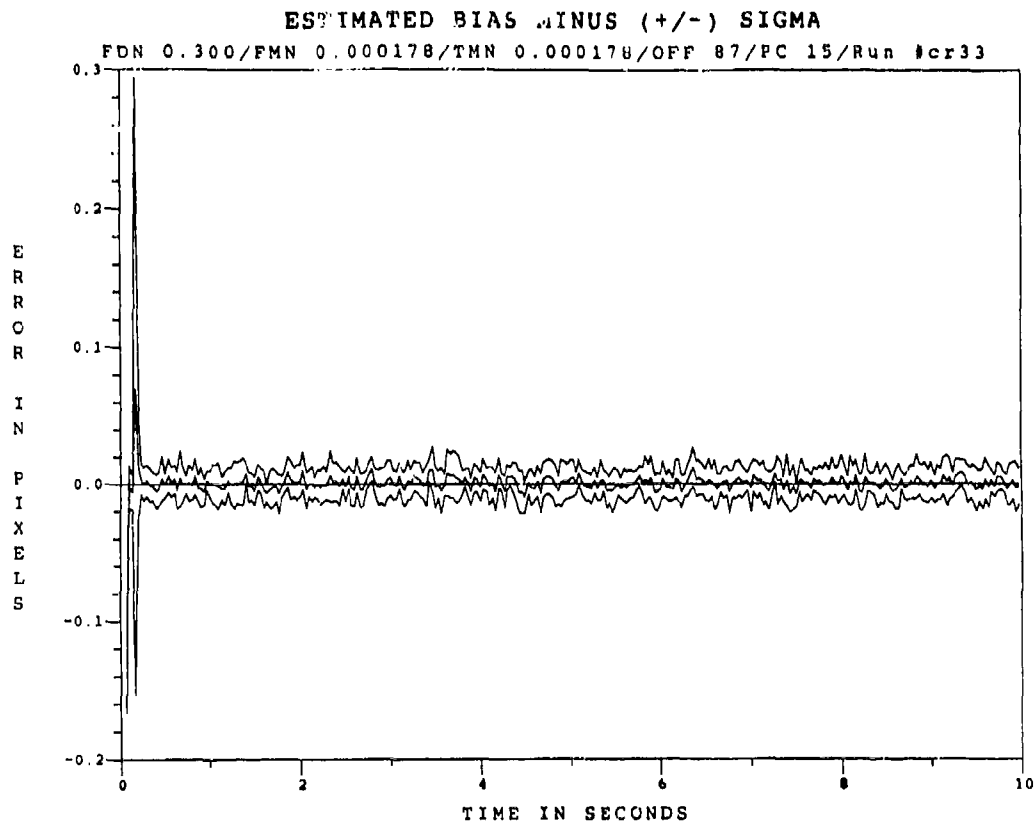


Figure F.2.11 0.53 μm Two-State Modified MAP MMAF Bias Error, SNR=4, $P_m = -0.05$, at t_i^-

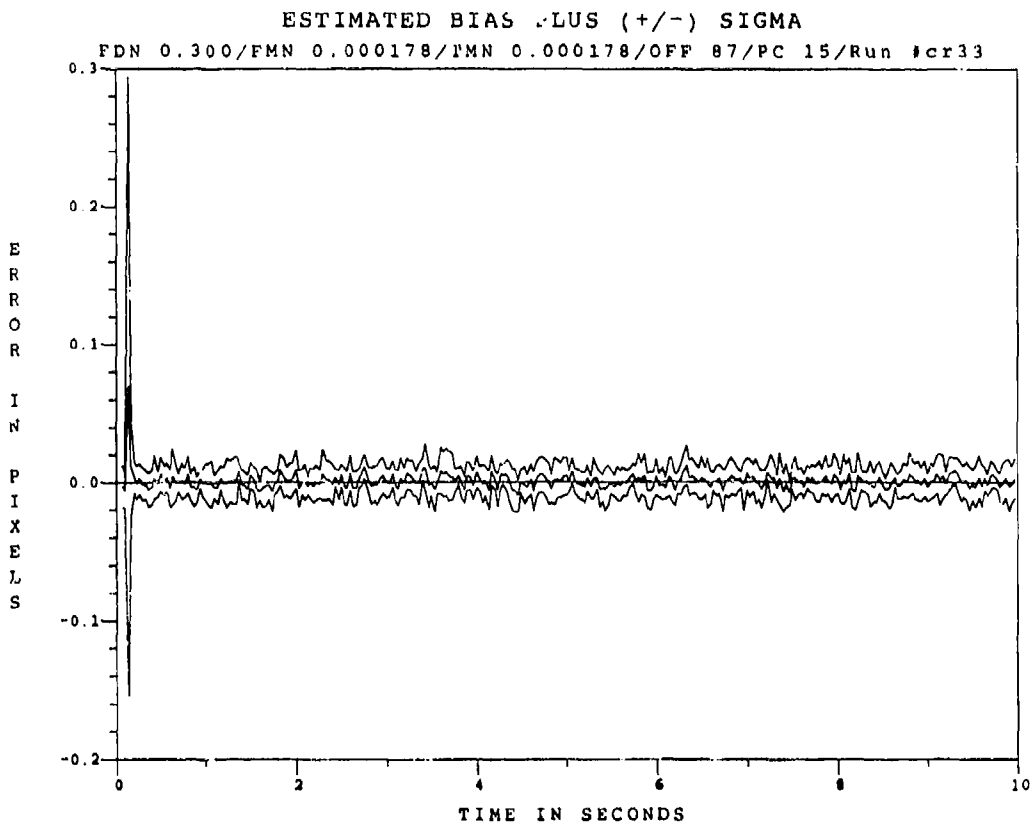


Figure F.2.12 0.53 μm Two-State Modified MAP MAE Bias Error, SNR=4, $P_m = -0.05$, at t_i^+

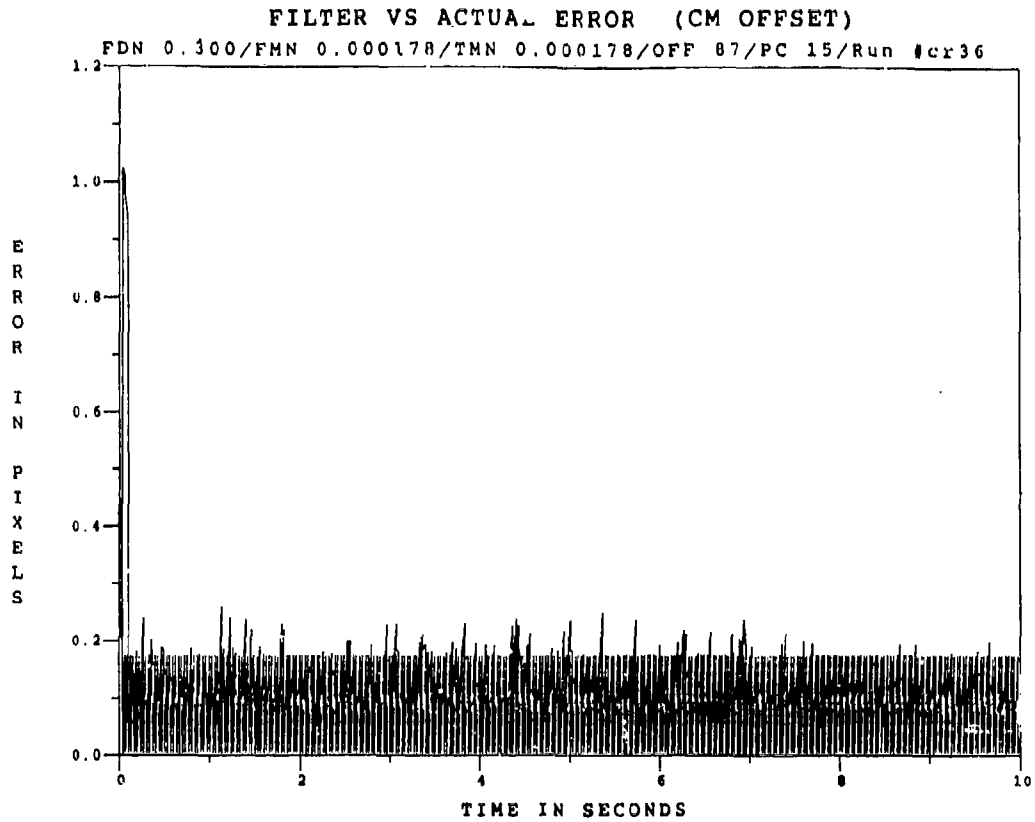


Figure F.2.13 0.53 μ m Two-State Modified MAP MMAF Offset Error, SNR = 4, $P_m = 0.30$

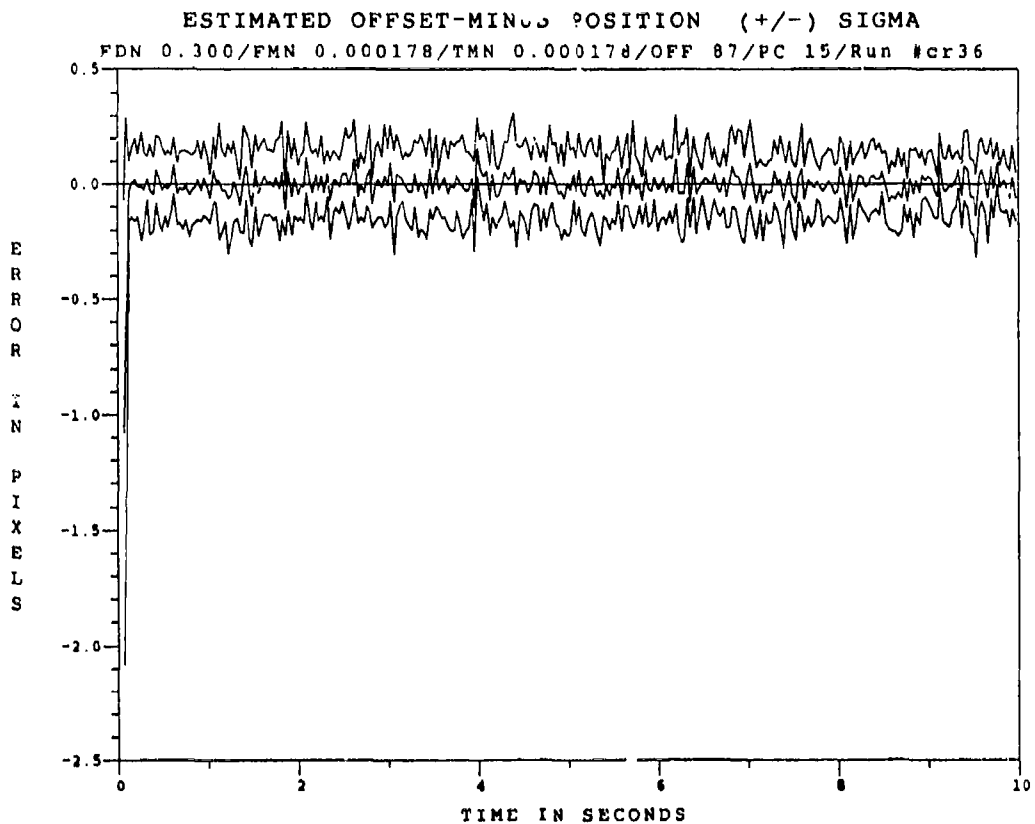


Figure F.2.14 0.53 μ m Two-State Modified MAP MMAF Offset Error, SNR=4, $P_m=0.30$, at t_i

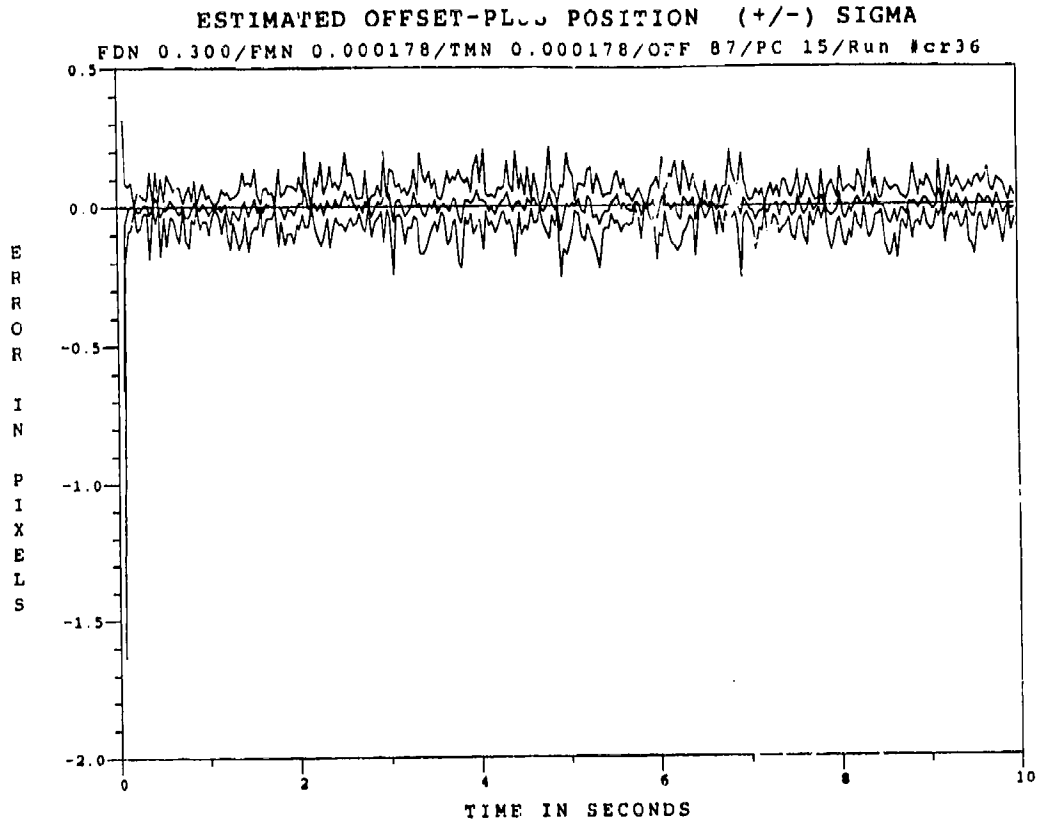


Figure F.2.15 0.53 μ m Two-State Modified MAP MMAE Offset Error; SNR=4, $P_m = -0.30$, at t_i^+

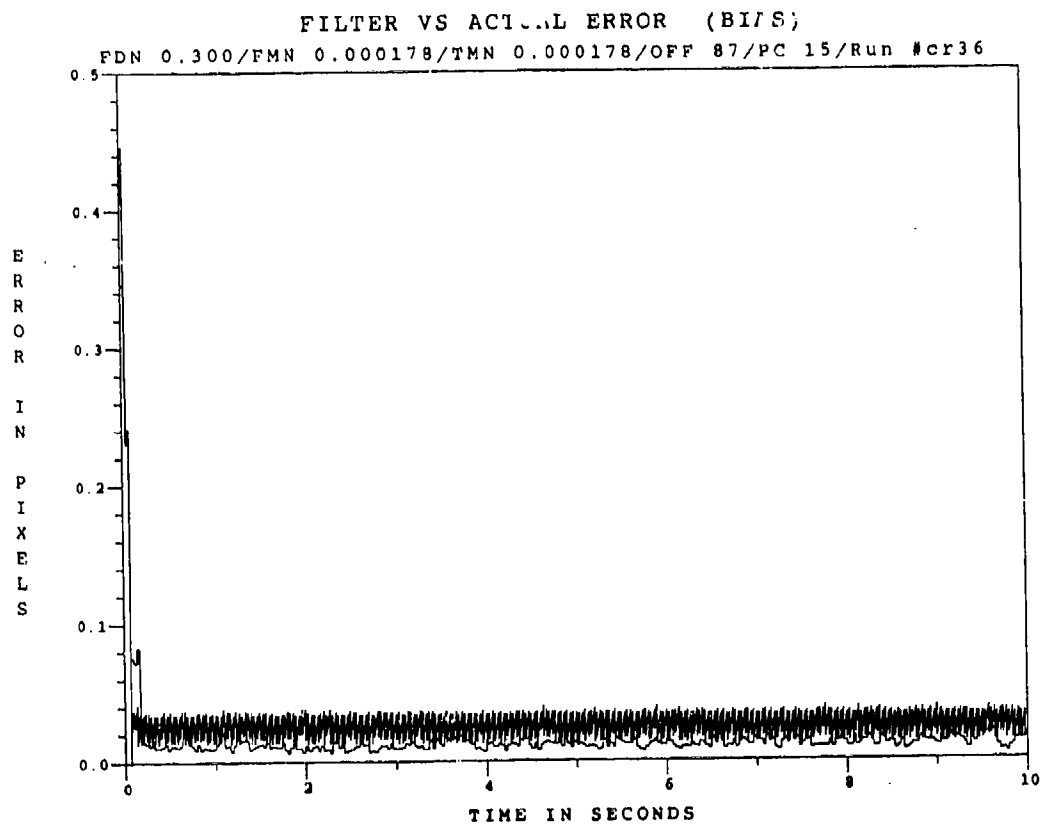


Figure F.2.16 0.53 μ m Two-State Modified MAP MMAF Bias Error, SNR = 4, $P_m = -0.30$

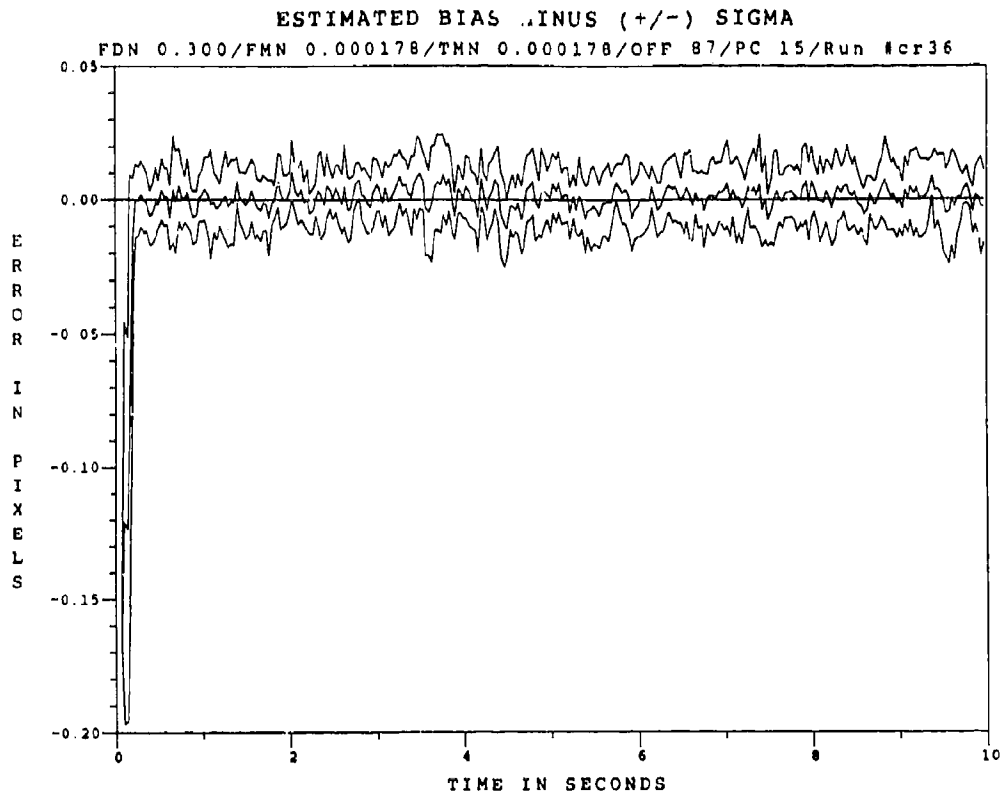


Figure F.2.17 0.53 μ m Two-State Modified MAP MMAF Bias Error, SNR=4, $P_m = -0.30$, at t_i^-

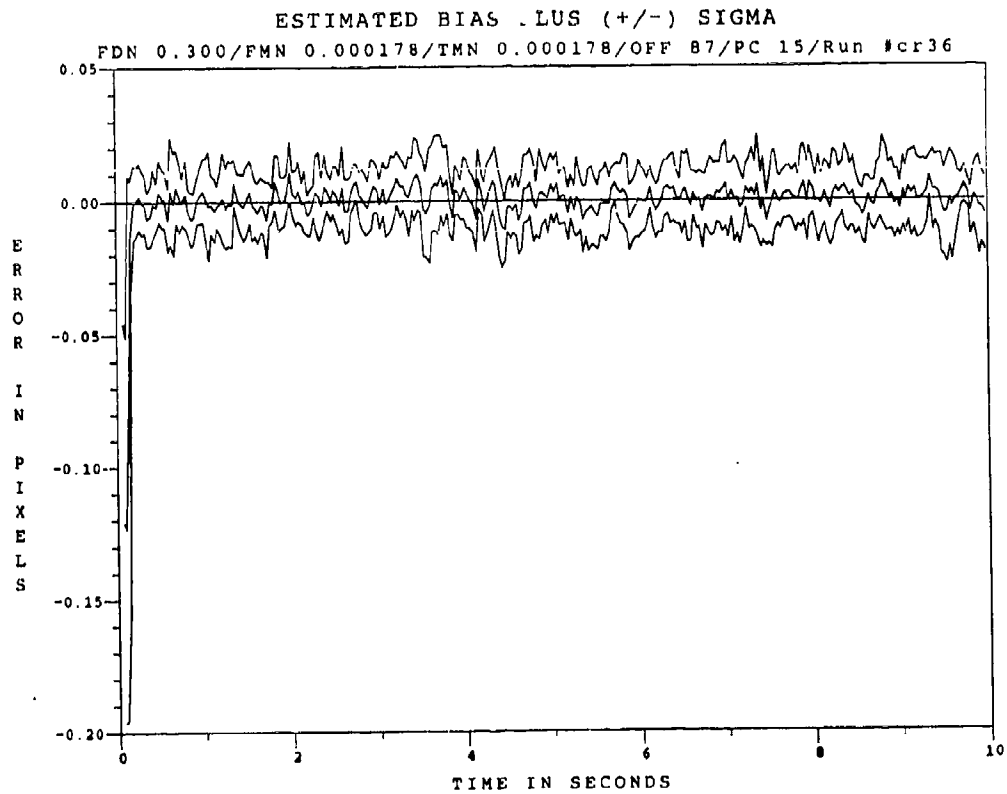


Figure F.2.18 0.53 μ m Two-State Modified MAP MMAE Bias Error, SNR=4, $P_m = -0.30$, at t_i^+

Appendix F.3

Two-State Center-of-Mass

Modified MAP MMAF

with

2.01 μm Doppler Return Measurements

at SNR = 10

FILTER VS ACTUAL ERROR (CM OFFSET)

RUNCRO73

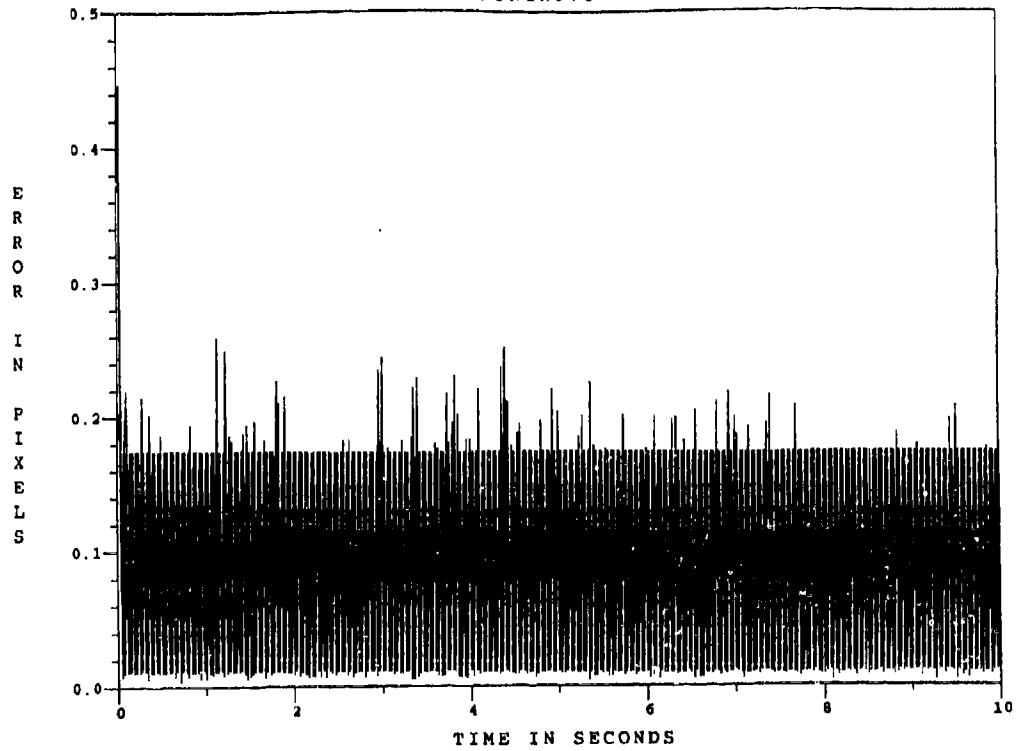


Figure F.3.1 2.01 μm Two-State Modified MAP MMAF Offset Error, SNR=10, $P_m=0.0$

ESTIMATED OFFSET-MINUS POSITION (+/-) SIGMA

RUNCRO73

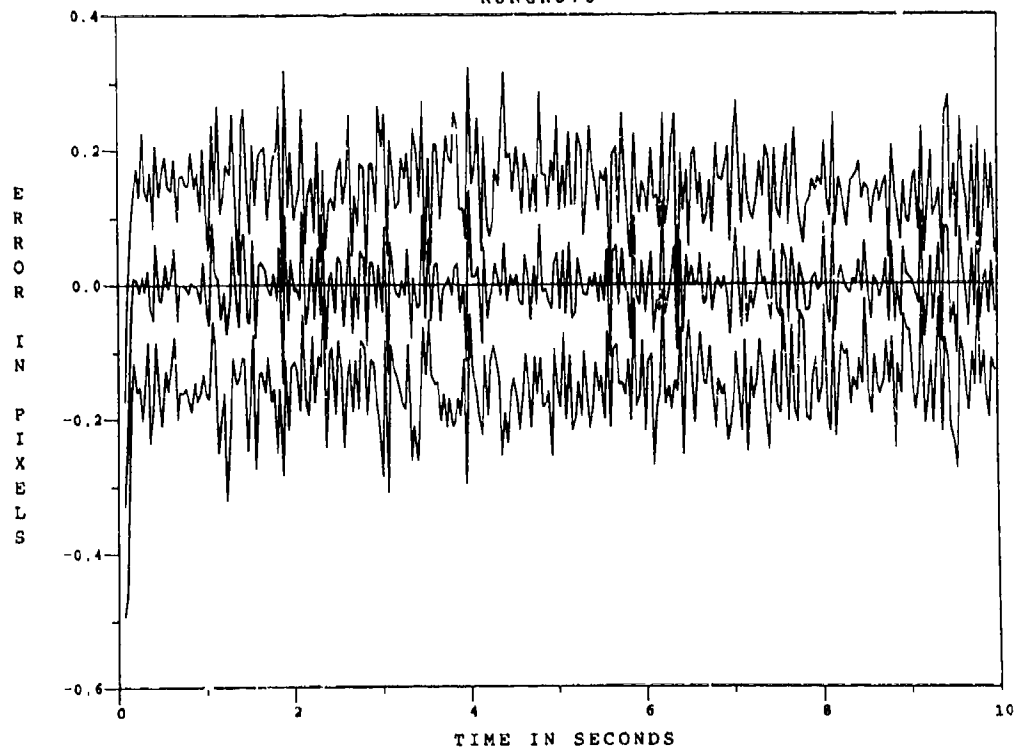


Figure F.3.2 2.01 μm Two-State Modified MAP MMAF Offset Error, SNR=10, $P_m=0.0$, at t_i

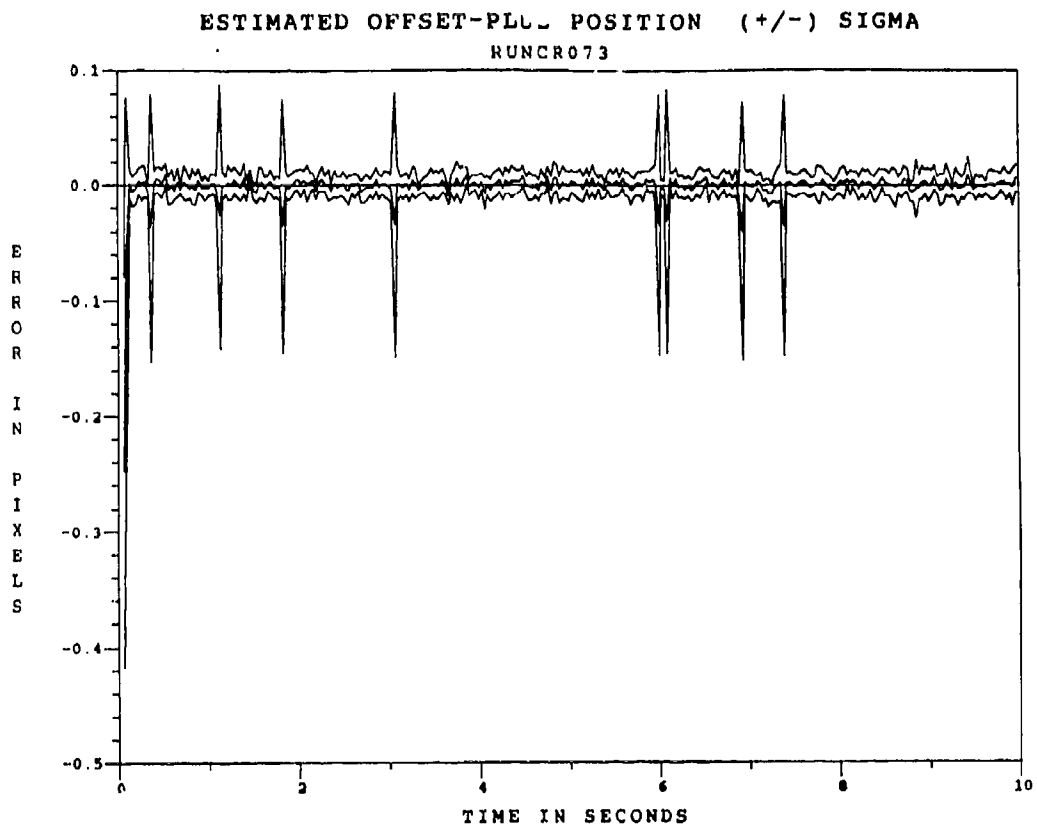


Figure F.3.3 2.01 μm Two-State Modified MAP MMAF Offset Error, SNR=10, $P_m = -0.0$, at t_i^+

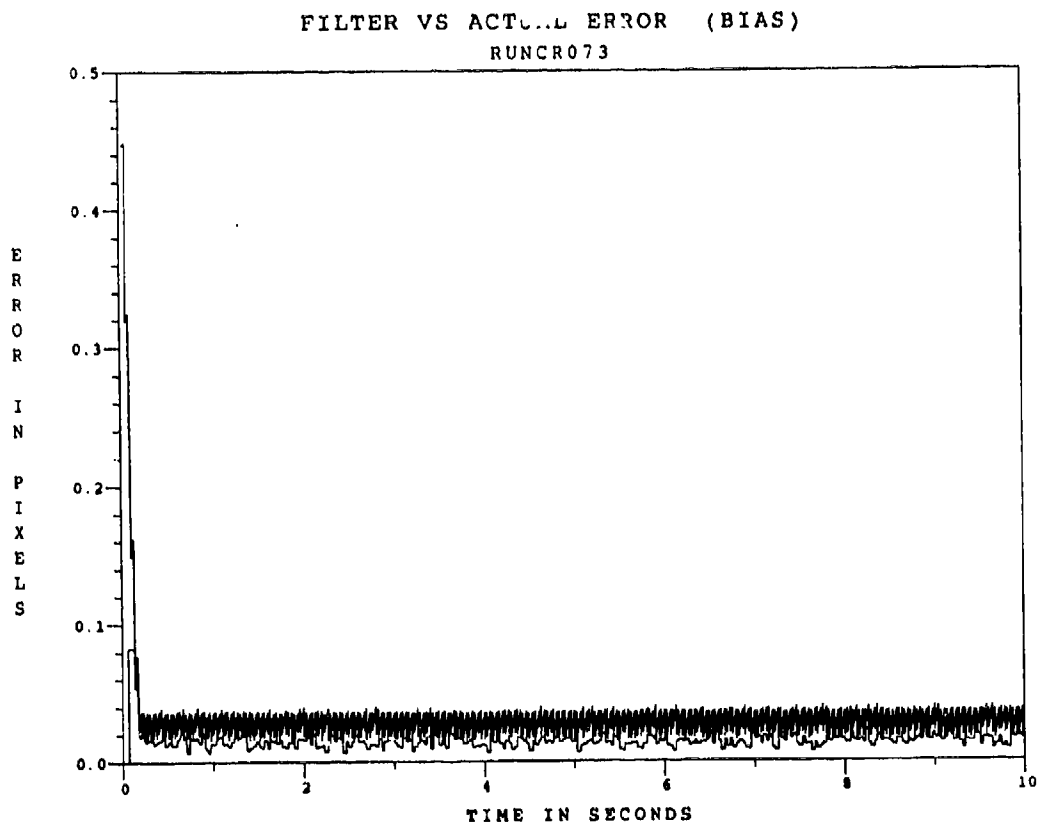


Figure F.3.4 2.01 μm Two-State Modified MAP MMAF Bias Error, SNR=10, $P_m = -0.0$

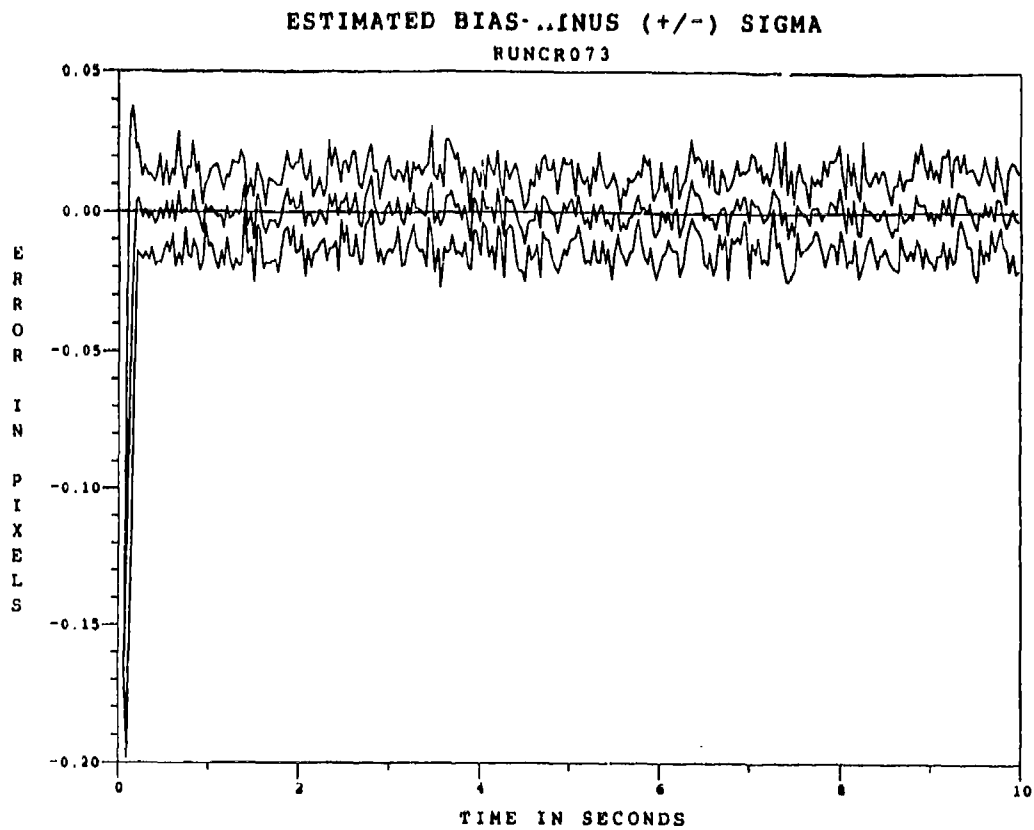


Figure F.3.5 2.01 μm Two-State Modified MAP MMAF Bias Error, SNR=10, $P_m=0.0$, at t_i^-

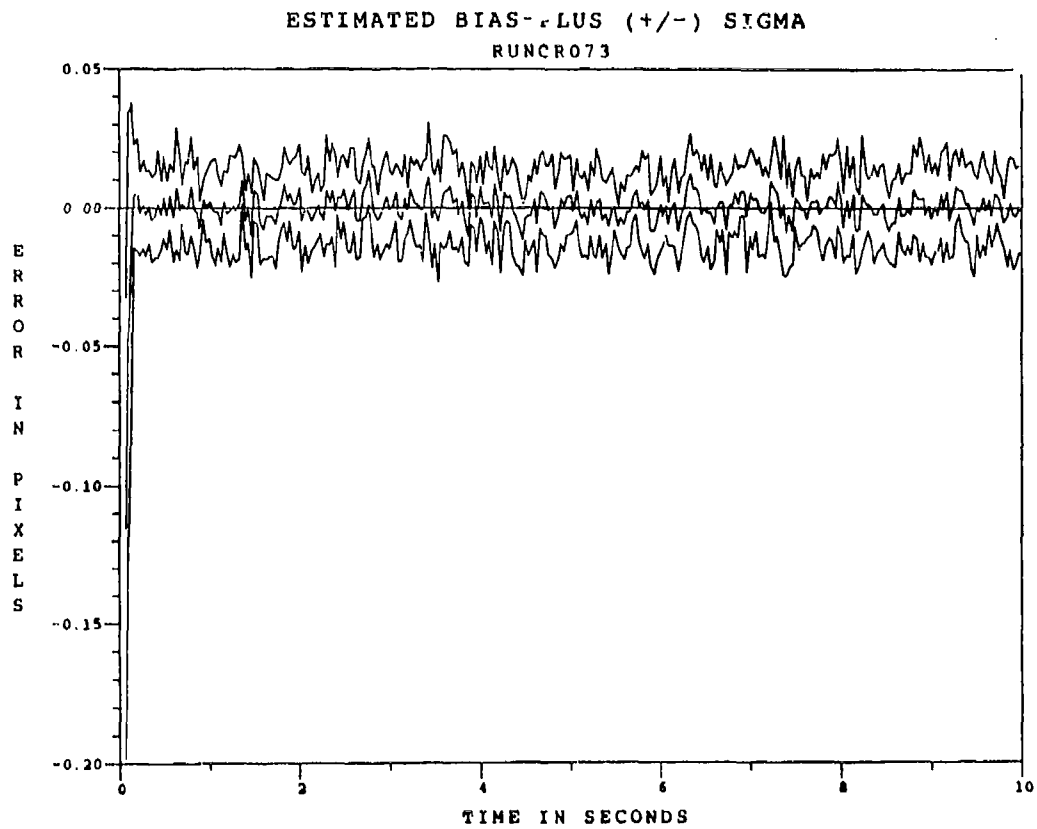


Figure F.3.6 2.01 μm Two-State Modified MAP MMAF Bias Error, SNR=10, $P_m=0.0$, at t_i^+

FILTER VS ACTUAL ERROR (CM OFFSET)

RUNCR078

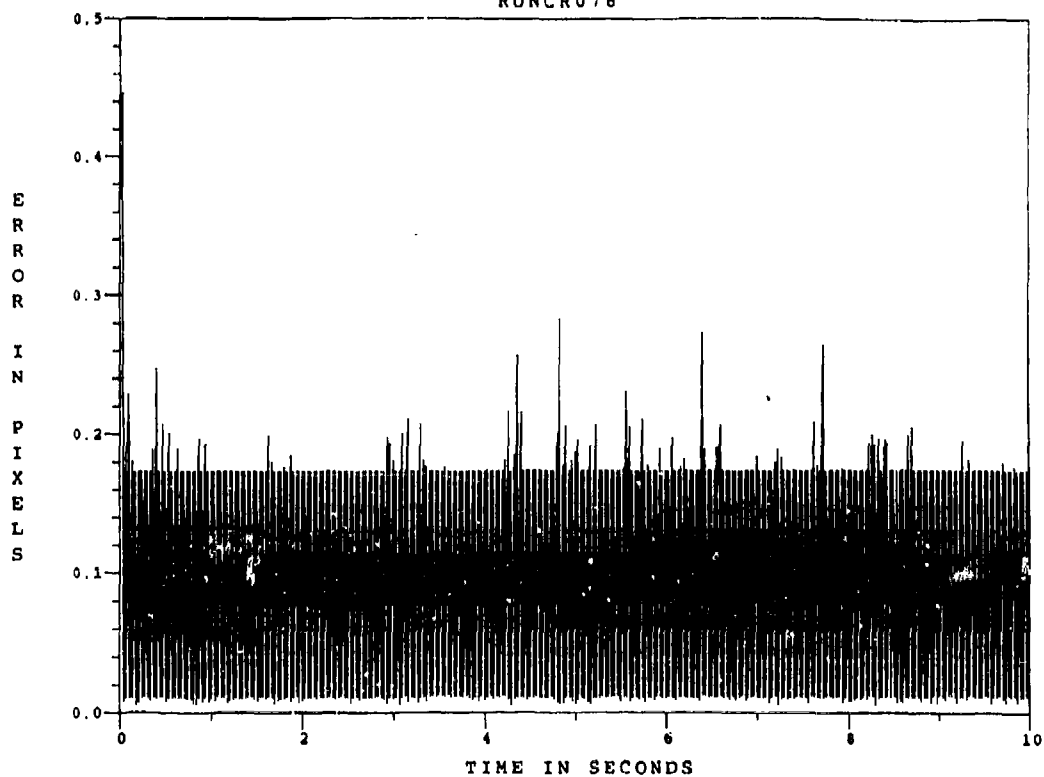


Figure F.3.7 2.01 μm Two-State Modified MAP MMAF Offset Error, SNR = 10, $P_m = 0.05$

ESTIMATED OFFSET-MINUS POSITION (+/-) SIGMA

RUNCR078

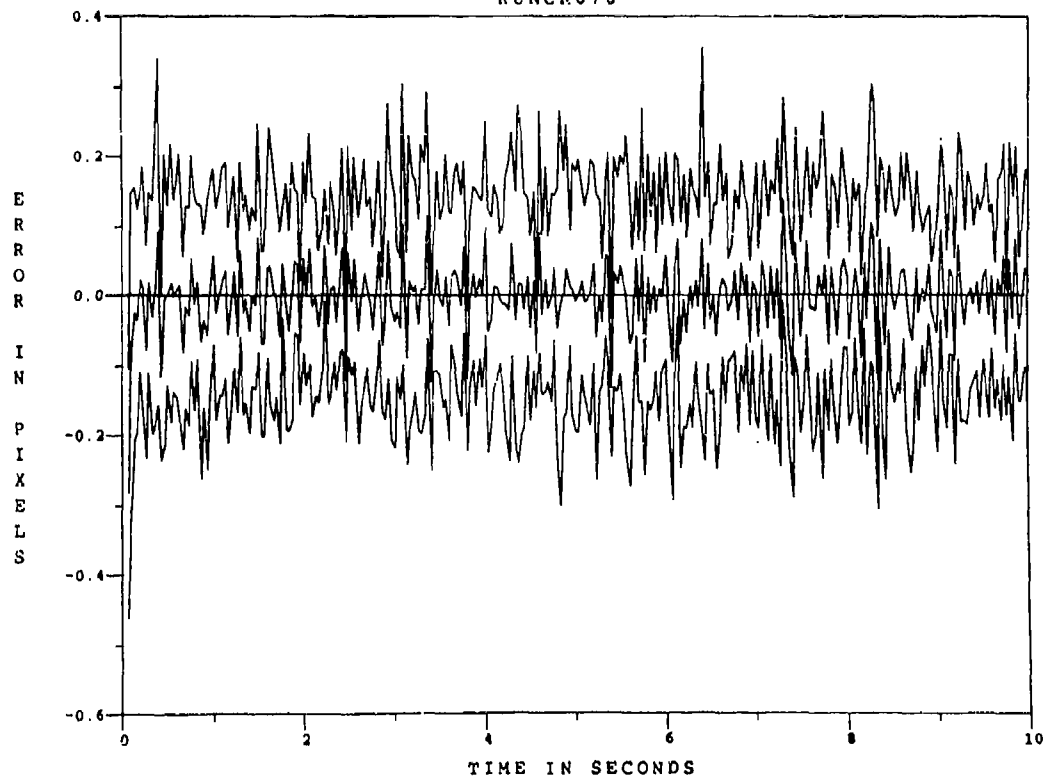


Figure F.3.8 2.01 μm Two-State Modified MAP MMAF Offset Error, SNR=10, $P_m=0.05$, at t_i

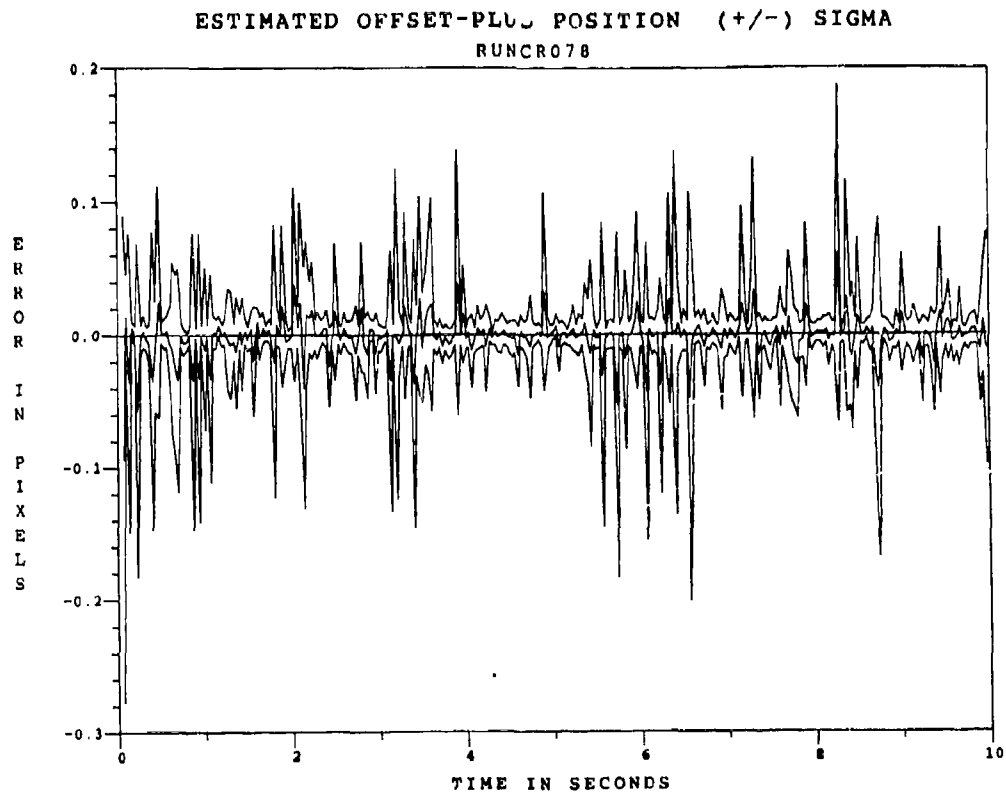


Figure F.3.9 2.01 μ m Two-State Modified MAP MMAE Offset Error, SNR=10, $P_m = -0.05$, at t_i^+

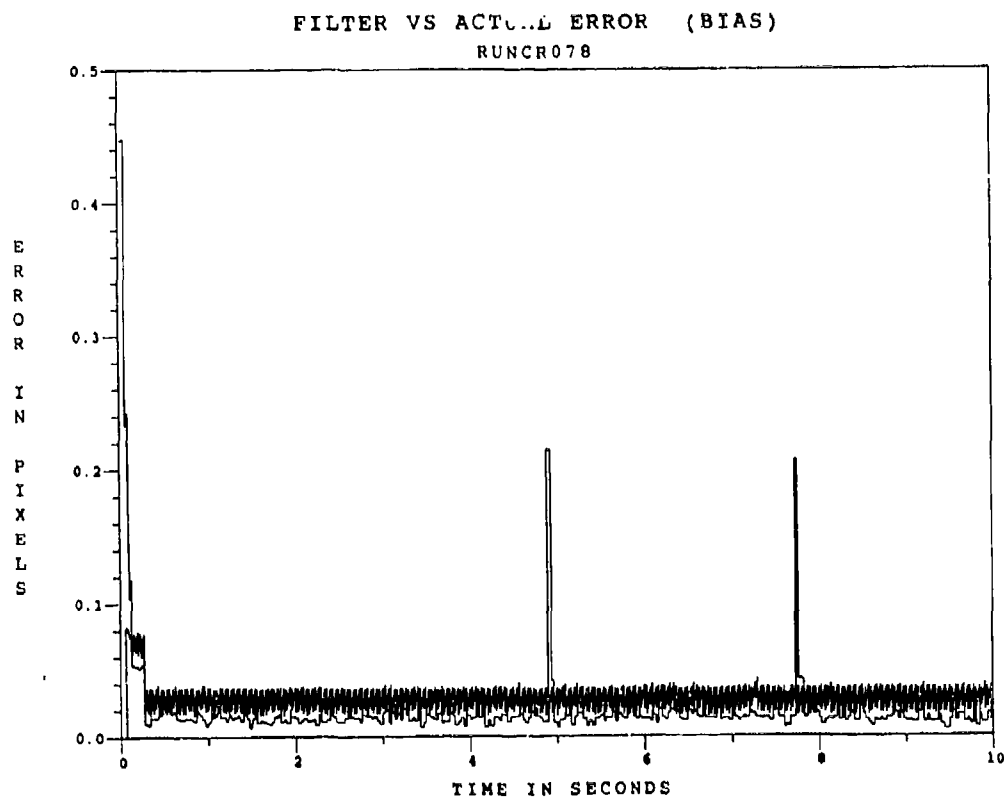


Figure F.3.10 2.01 μ m Two-State Modified MAP MMAF Bias Error, SNR = 10, $P_m = -0.05$

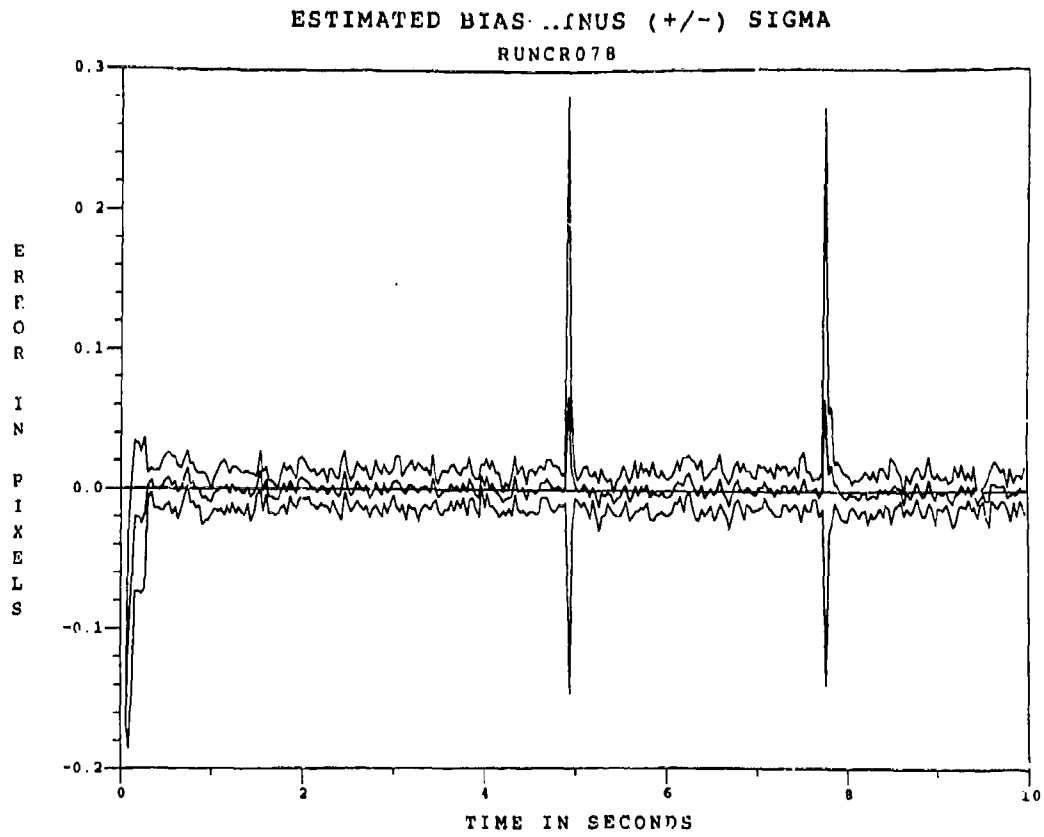


Figure F.3.11 2.01 μm Two-State Modified MAP MMAF Bias Error, SNR=10, $P_m = 0.05$, at t_i^-

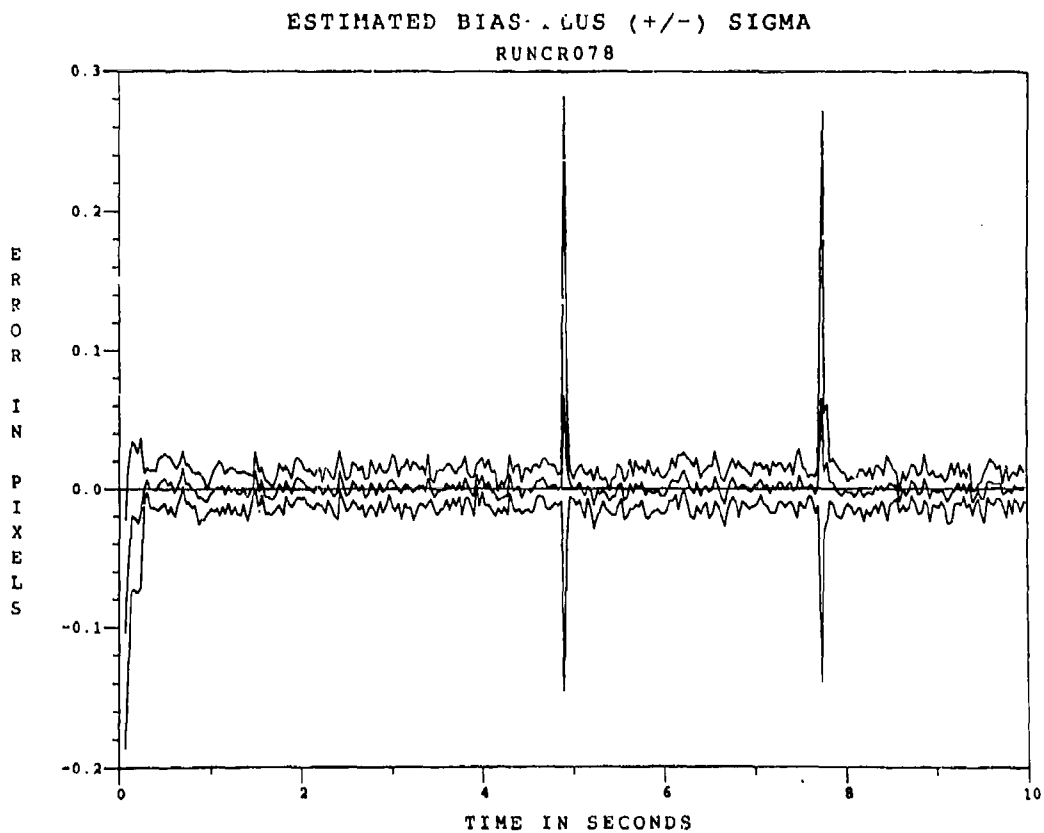


Figure F.3.12 2.01 μm Two-State Modified MAP MMAE Bias Error, SNR=10, $P_m = 0.05$, at t_i^+

FILTER VS ACTUAL ERROR (CM OFFSET)

RUNCRO81

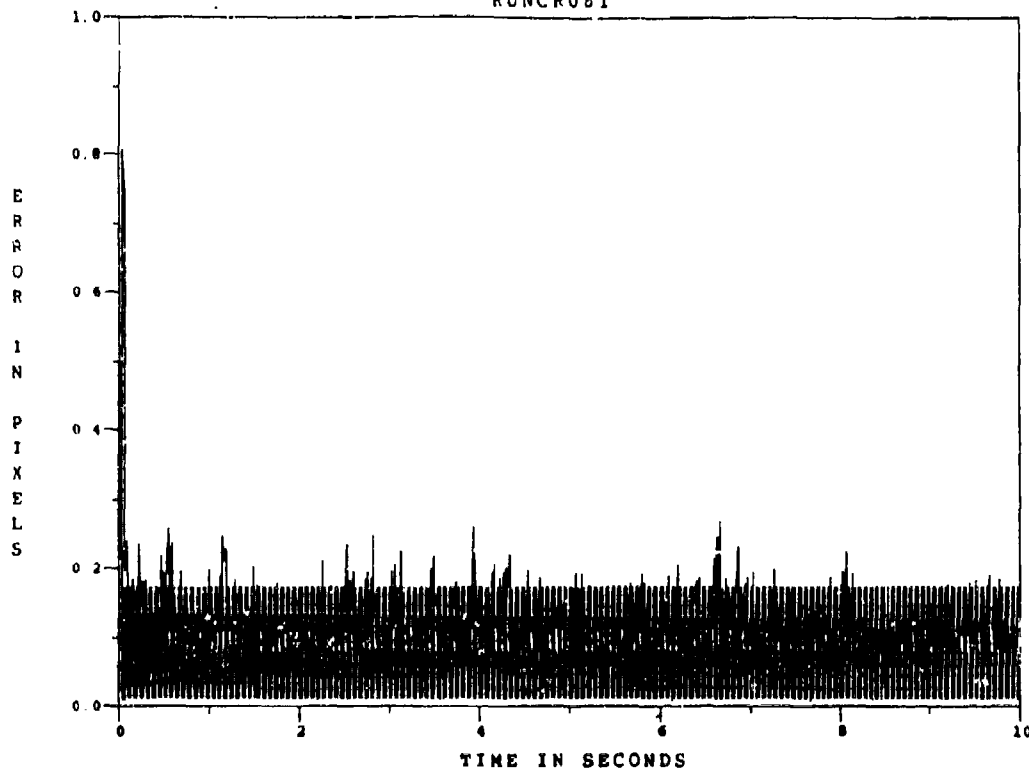


Figure F.3.13 2.01 μm Two-State Modified MAP MMAF Offset Error, SNR = 10, $P_m = 0.30$

ESTIMATED OFFSET-MINUS POSITION (+/-) SIGMA

RUNCRO81

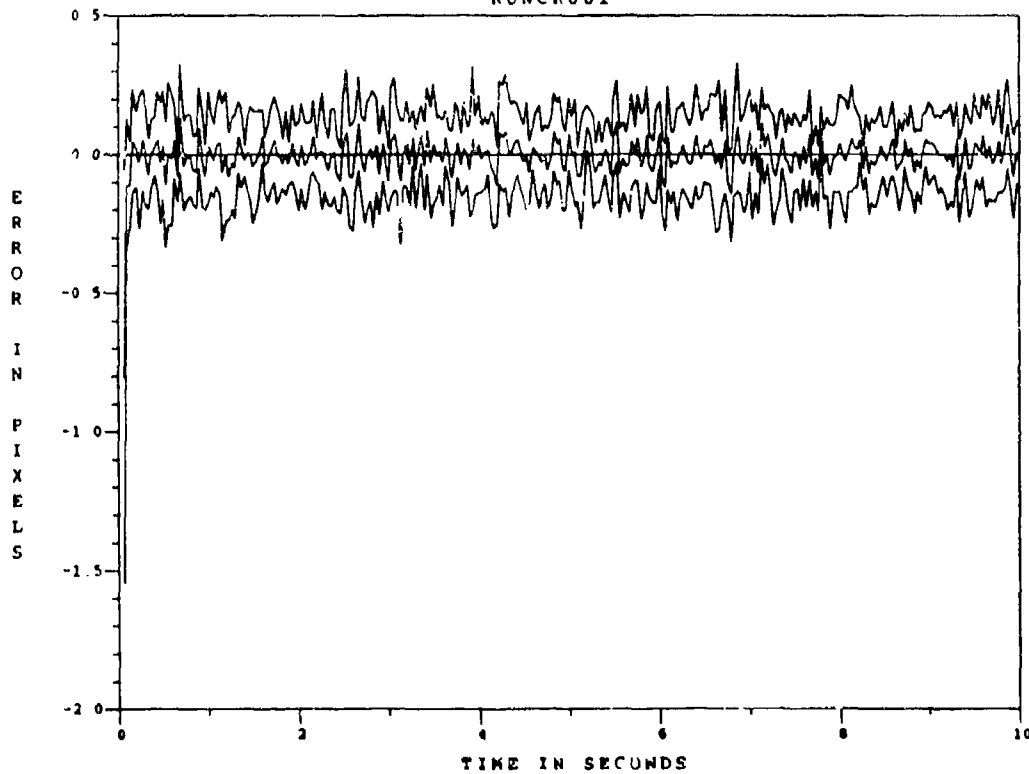


Figure F.3.14 2.01 μm Two-State Modified MAP MMAF Offset Error, SNR=10, $P_m = 0.30$, at t_1

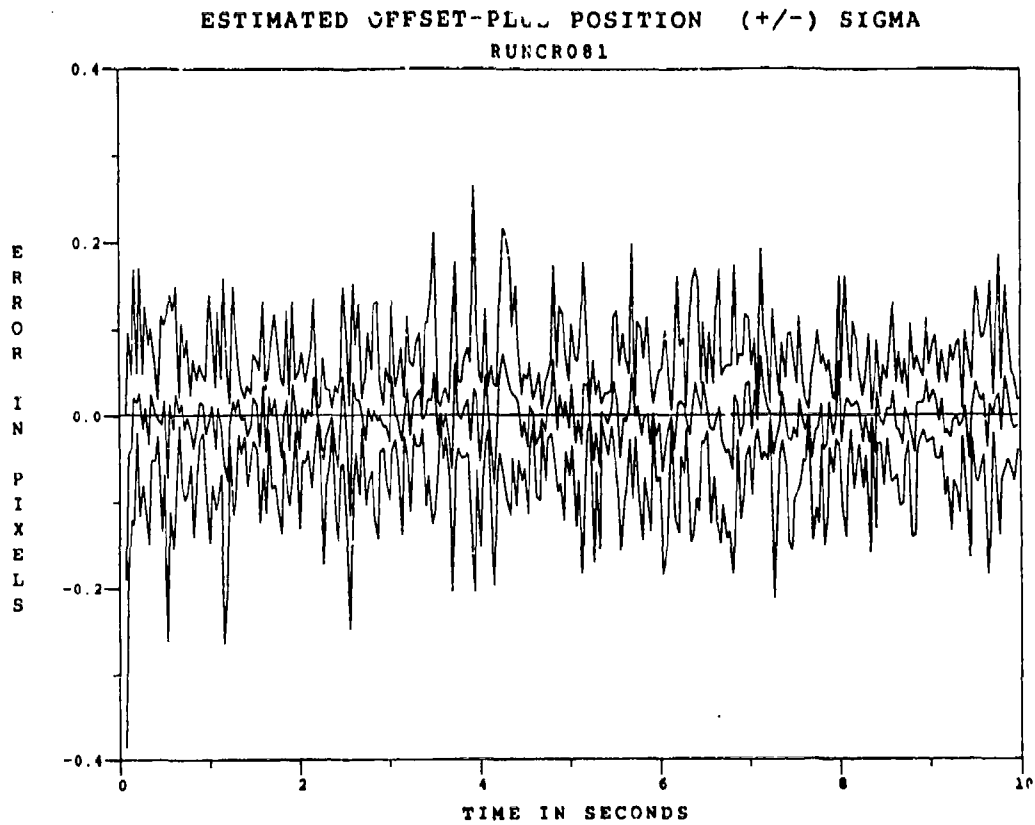


Figure F.3.15 2.01 μ m Two-State Modified MAP MMAE Offset Error, SNR=10, $P_m = -0.30$, at t_i^+

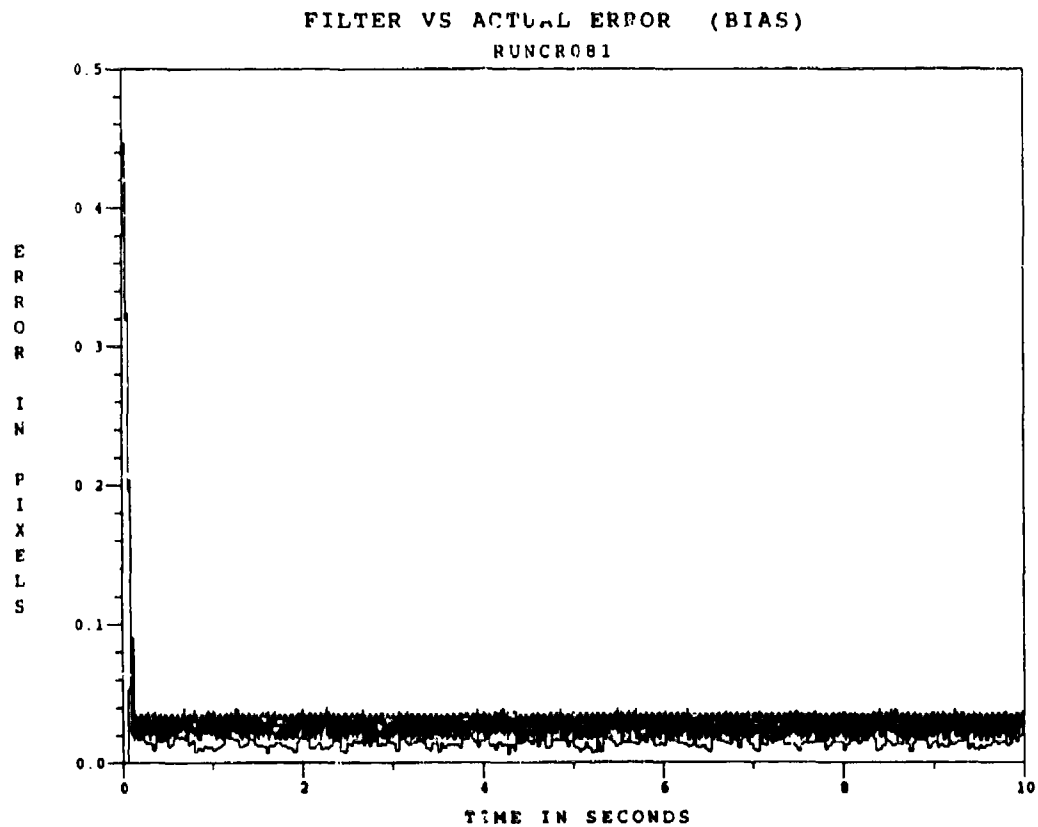


Figure F.3.16 2.01 μ m Two-State Modified MAP MMAF Bias Error, SNR = 10, $P_m = 0.30$

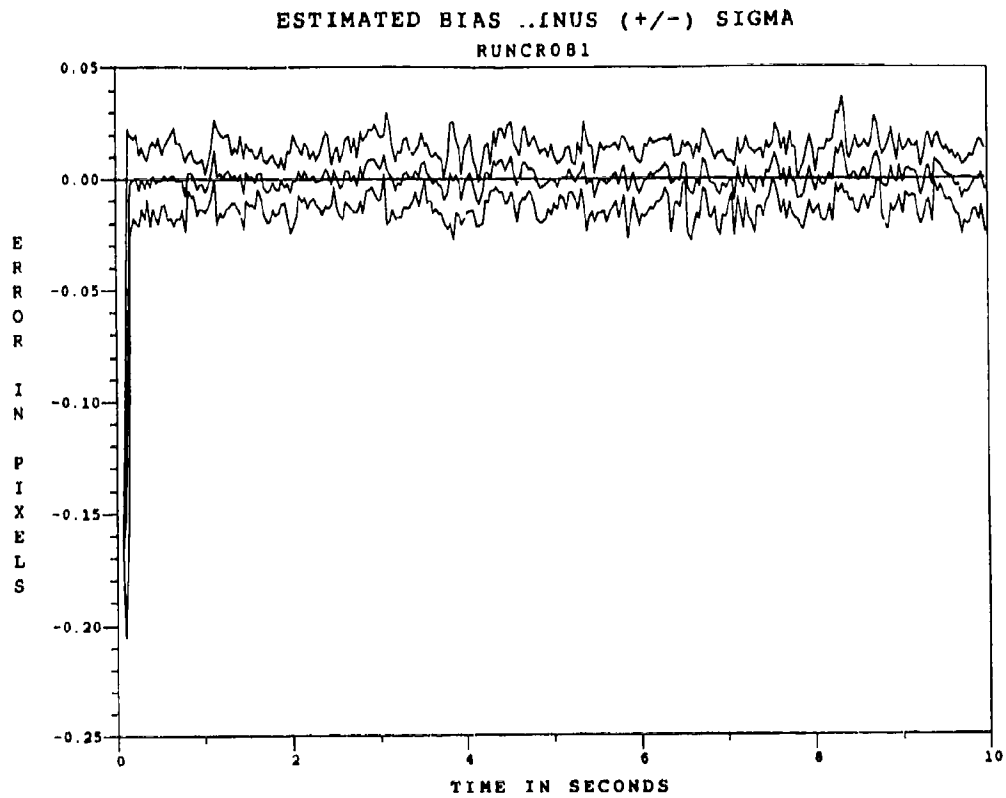


Figure F.3.17 2.01 μ m Two-State Modified MAP MMAF Bias Error, SNR=10, $P_n = -0.30$, at t_i^-

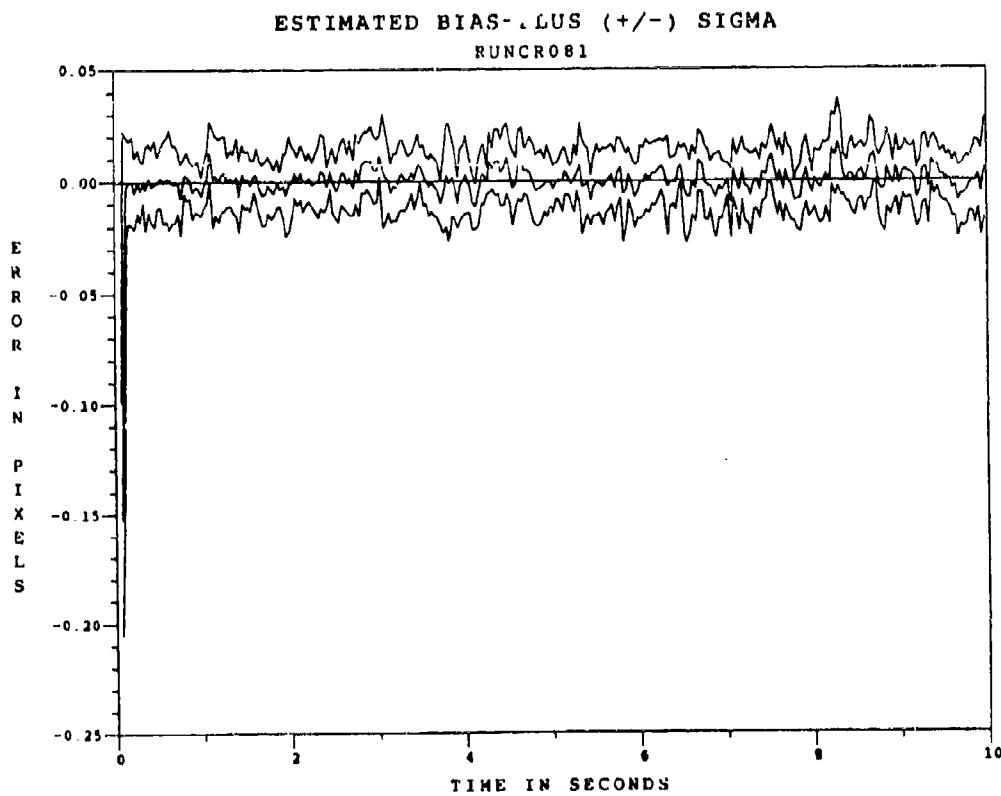


Figure F.3.18 2.01 μ m Two-State Modified MAP MMAE Bias Error, SNR=10, $P_n = -0.30$, at t_i^+

Appendix F.4

Two-State Center-of-Mass

Modified MAP MMAF

with

2.01 μm Doppler Return Measurements

at SNR = 4

FILTER VS ACTUAL ERROR (CM OFFSET)

RUNCR100

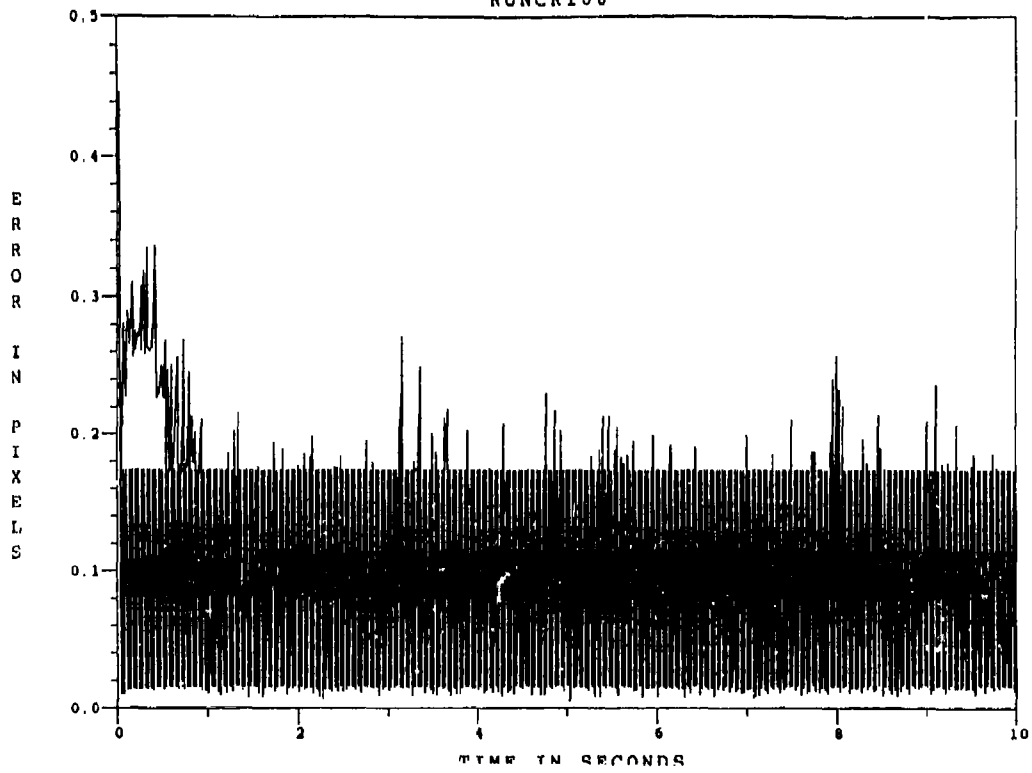


Figure F.4.1 2.01 μm Two-State Modified MAP MMAF Offset Error, SNR=4, $P_m = 0.0$

ESTIMATED OFFSET-MINUS POSITION (+/-) SIGMA

RUNCR100

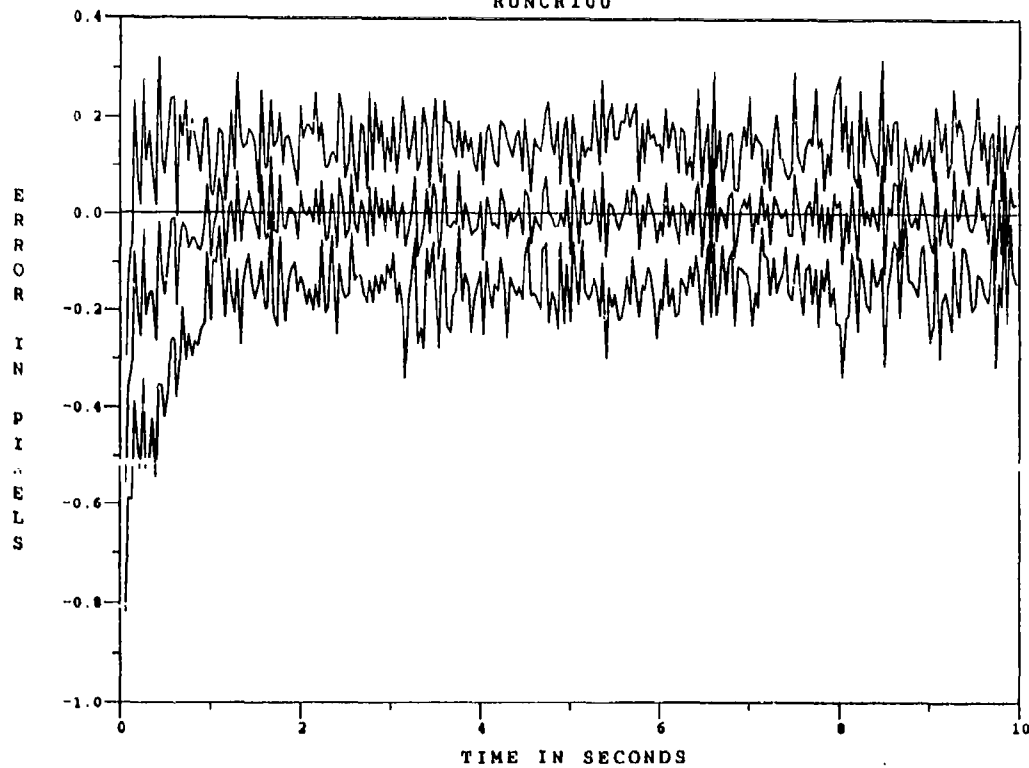


Figure F.4.2 2.01 μm Two-State Modified MAP MMAF Offset Error, SNR=4, $P_m = 0.0$, at t_i

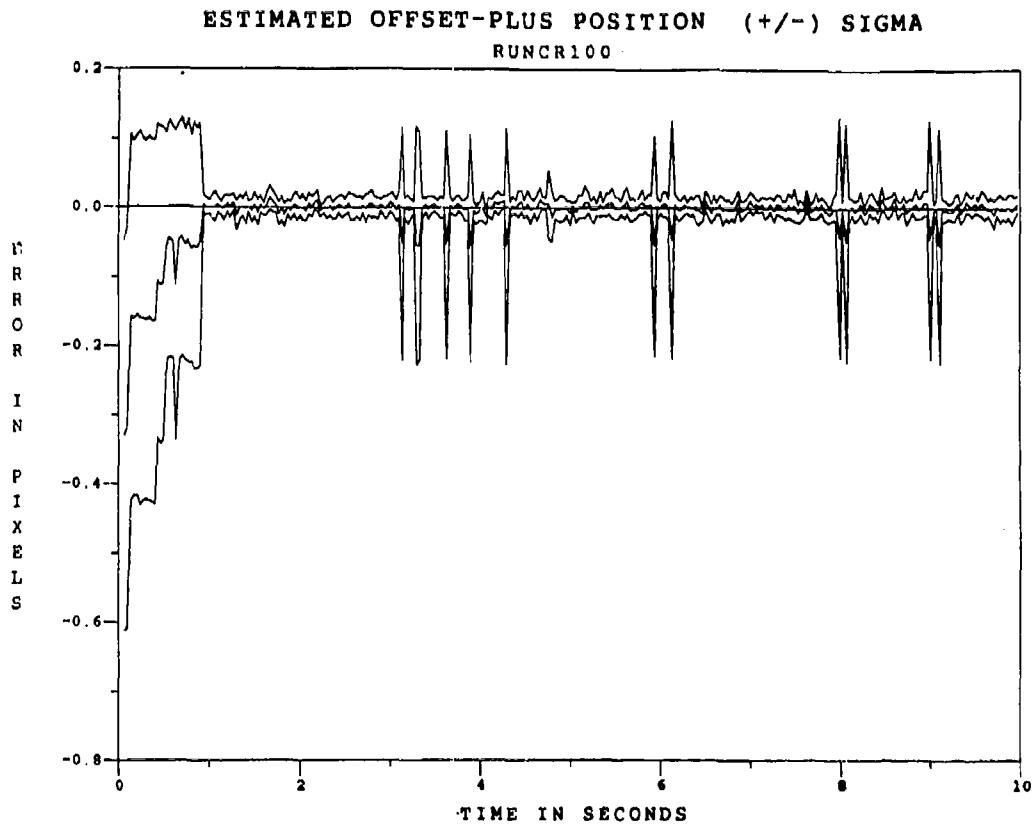


Figure F.4.3 2.01 μm Two-State Modified MAP MMAF Offset Error, SNR=4, $P_m = -0.0$, at t_1^+

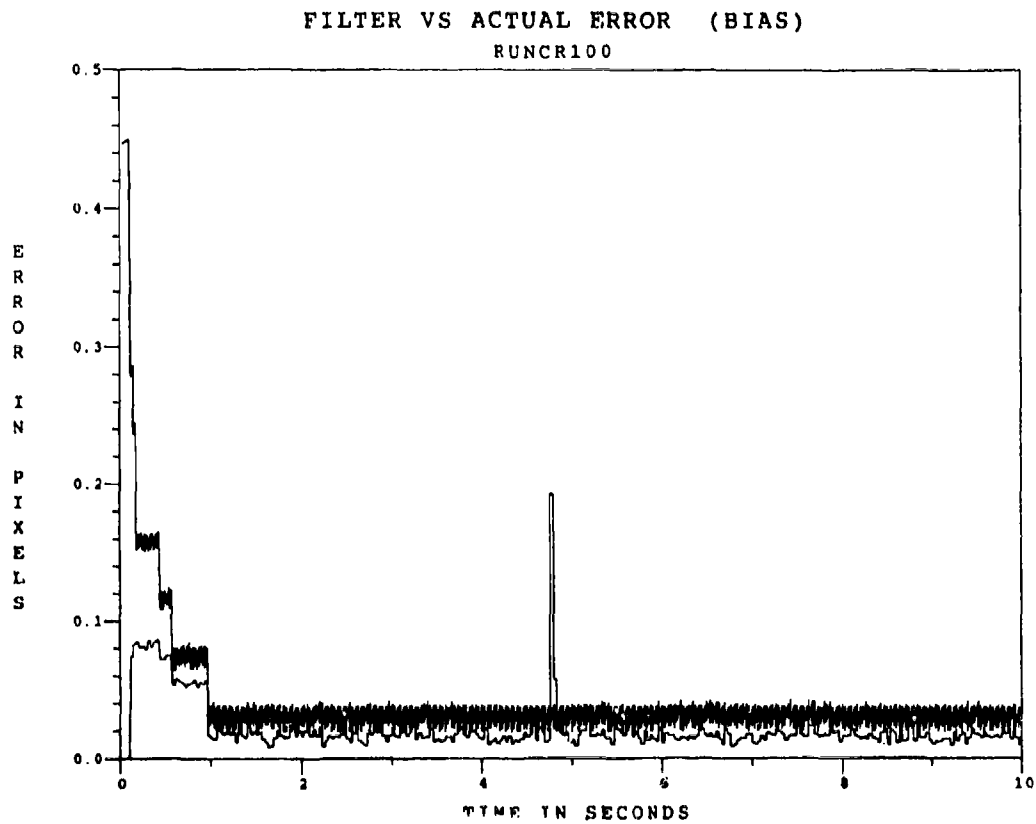


Figure F.4.4 2.01 μm Two-State Modified MAP MMAF Bias Error, SNR=4, $P_m = -0.0$

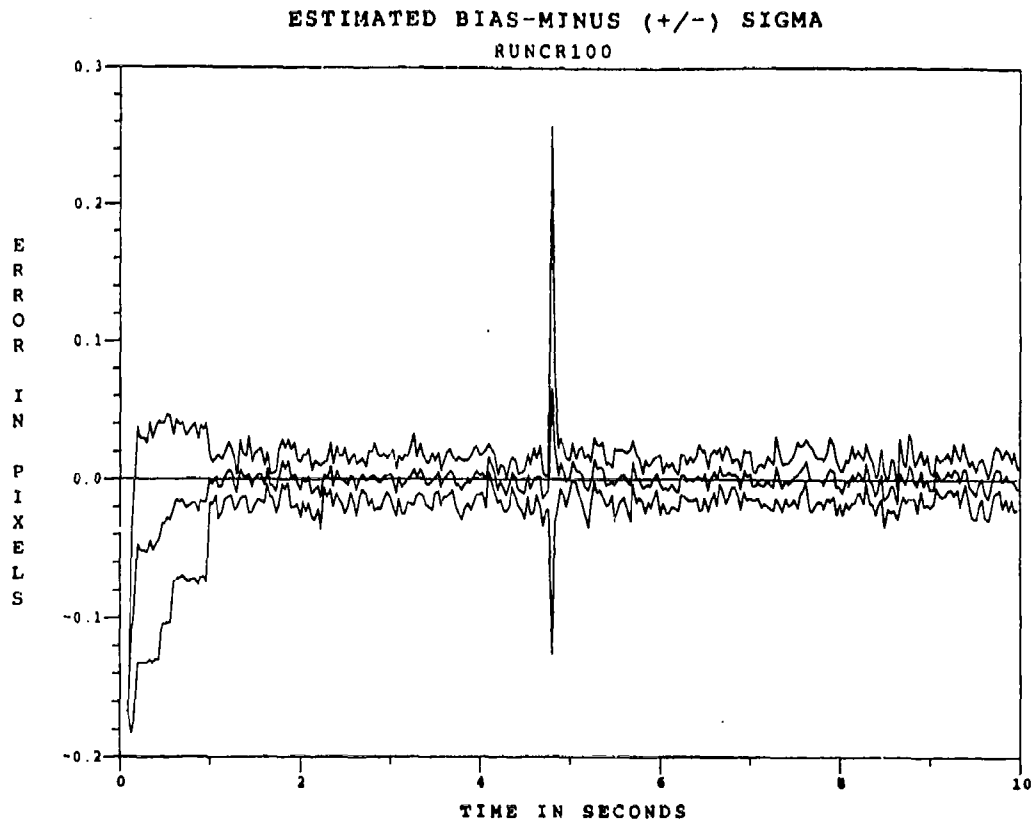


Figure F.4.5 2.01 μm Two-State Modified MAP MMAF Bias Error, SNR=4, $P_m = -0.0$, at t_i^-

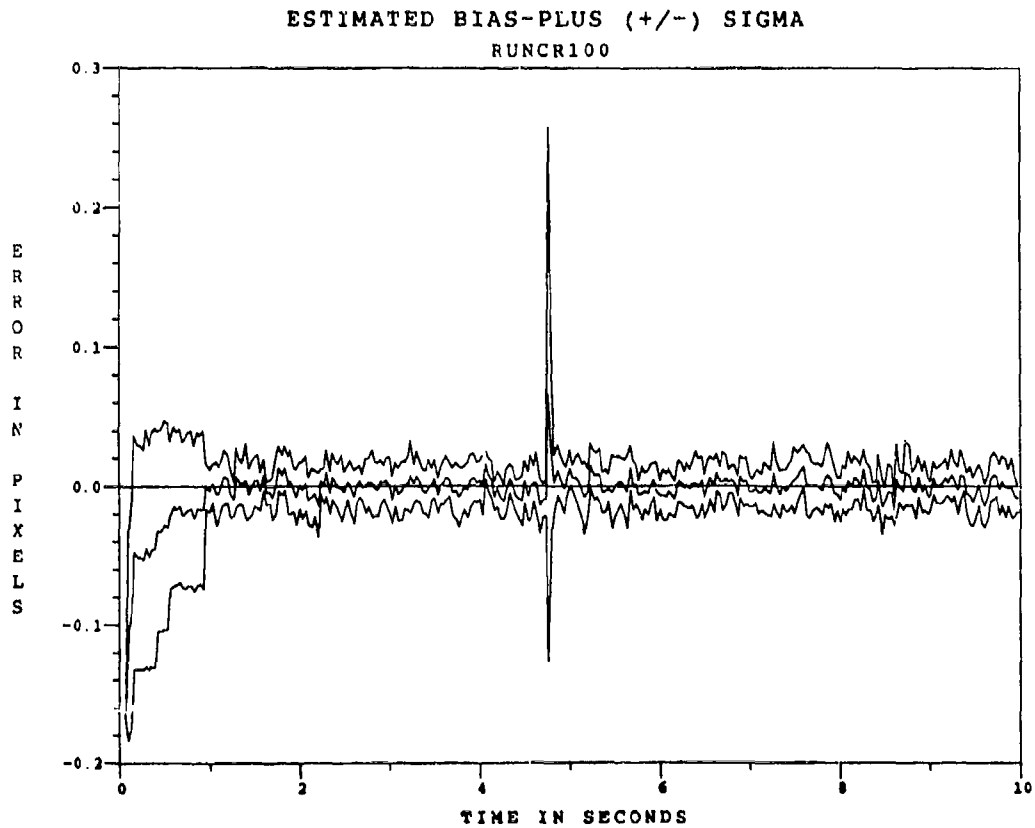


Figure F.4.6 2.01 μm Two-State Modified MAP MMAF Bias Error, SNR=4, $P_m = -0.0$, at t_i^+

FILTER VS ACTUAL ERROR (CM OFFSET)

RUNCR105

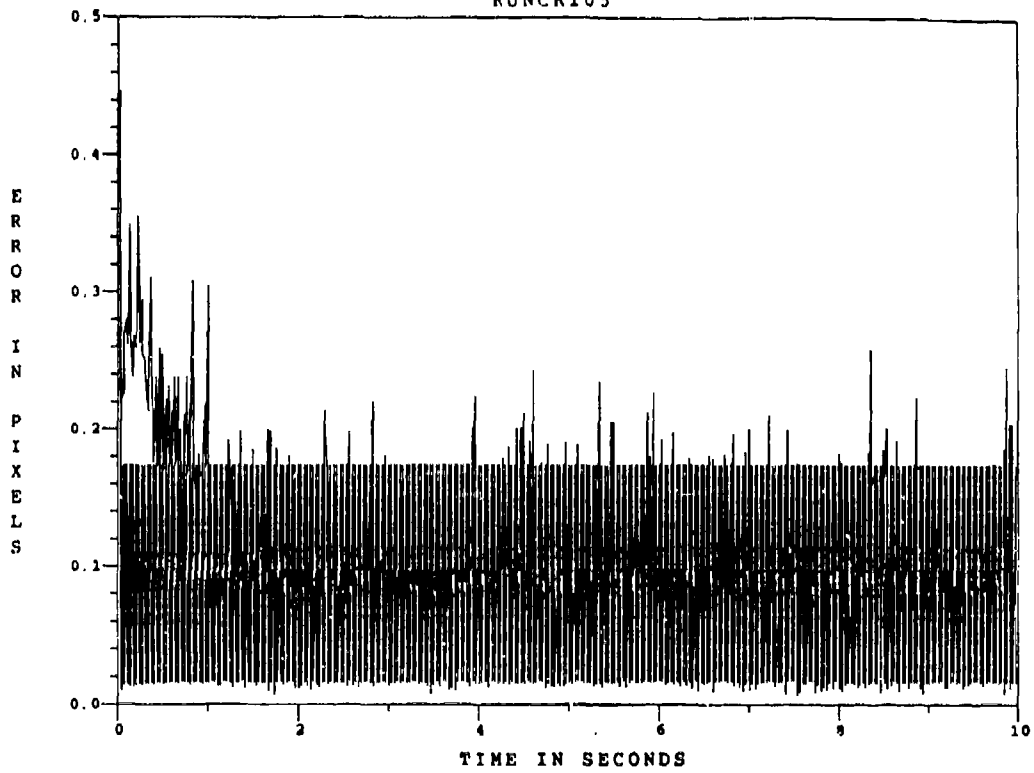


Figure F.4.7 2.01 μm Two-State Modified MAP MMAF Offset Error, SNR = 4, $P_m = 0.05$

ESTIMATED OFFSET-MINUS POSITION (+/-) SIGMA

RUNCR105

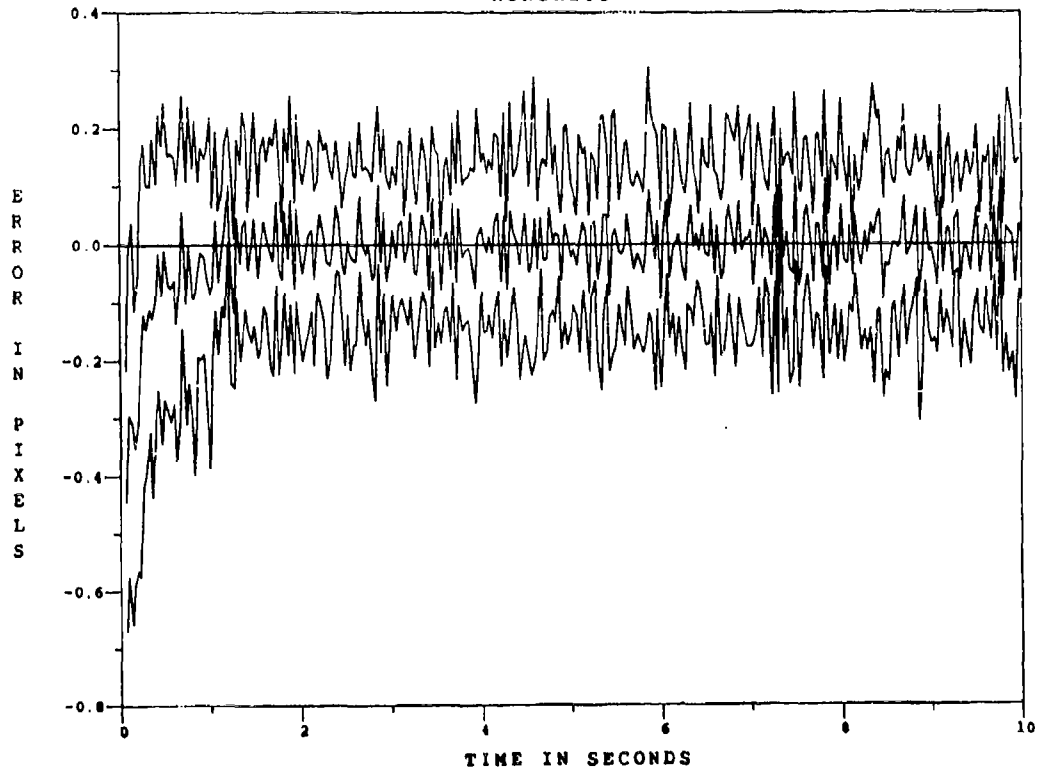


Figure F.4.8 2.01 μm Two-State Modified MAP MMAF Offset Error, SNR=4, $P_m = 0.05$, at t_1

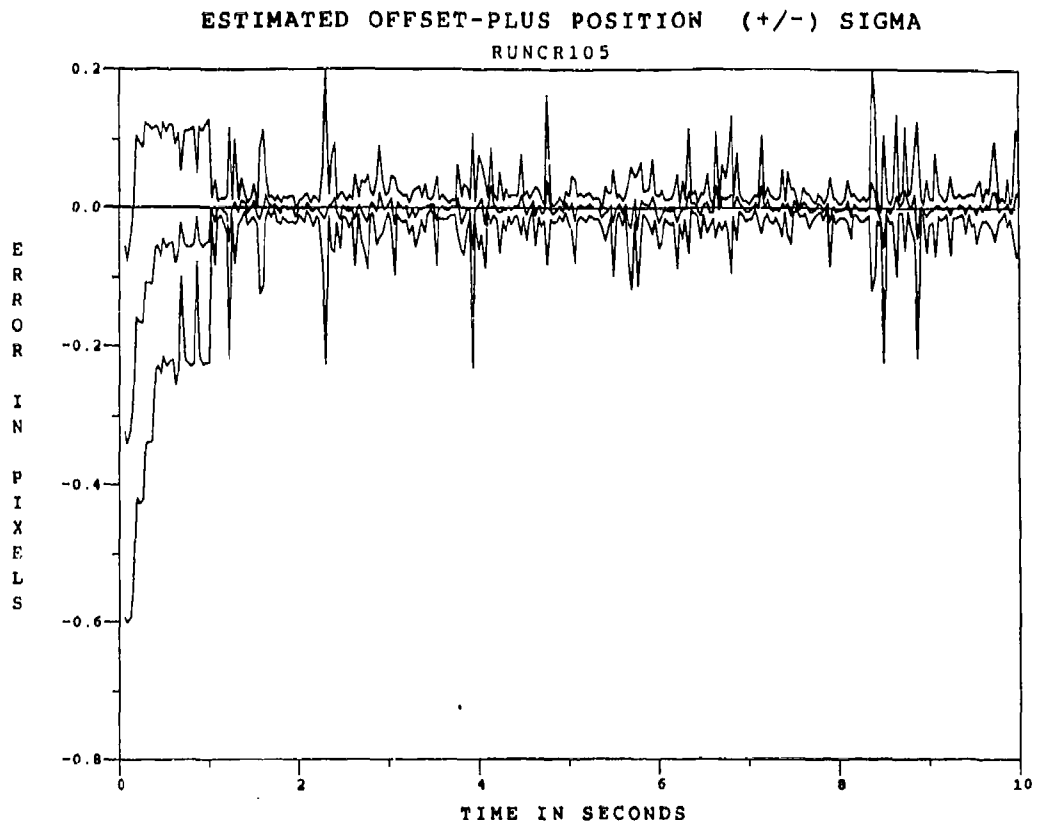


Figure F.4.9 2.01 μm Two-State Modified MAP MMAE Offset Error, SNR=4, $P_m = -0.05$, at t_i^+

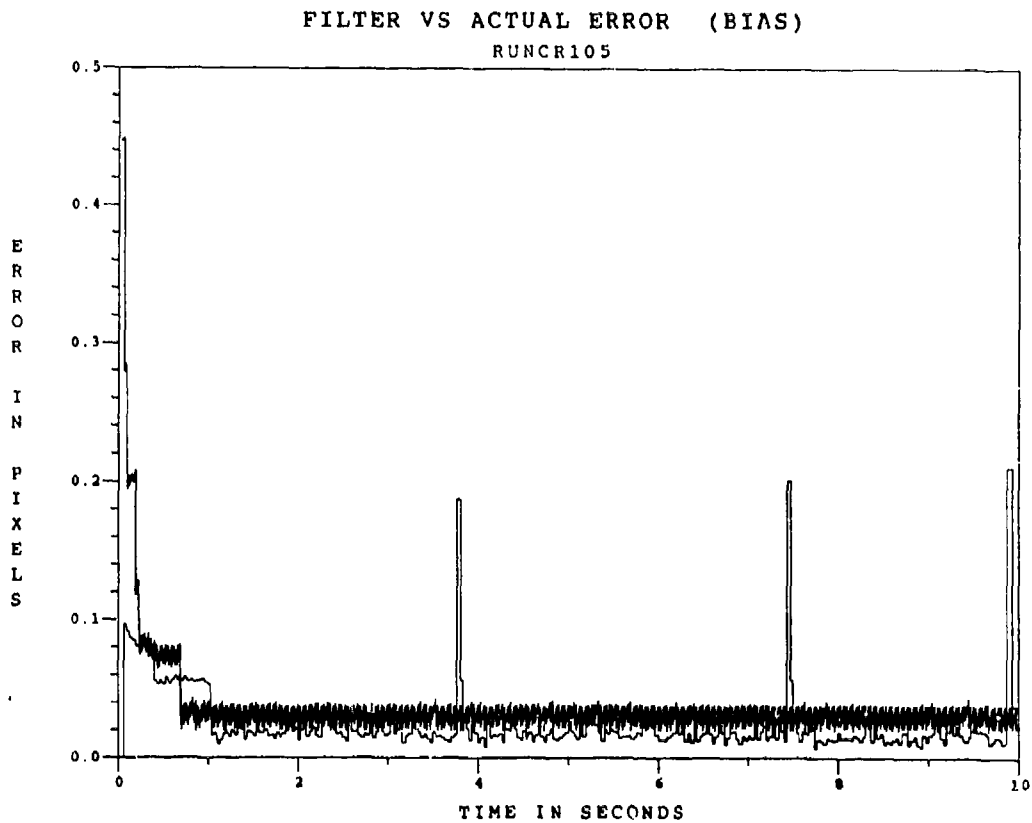


Figure F.4.10 2.01 μm Two-State Modified MAP MMAF Bias Error, SNR = 4, $P_m = 0.05$

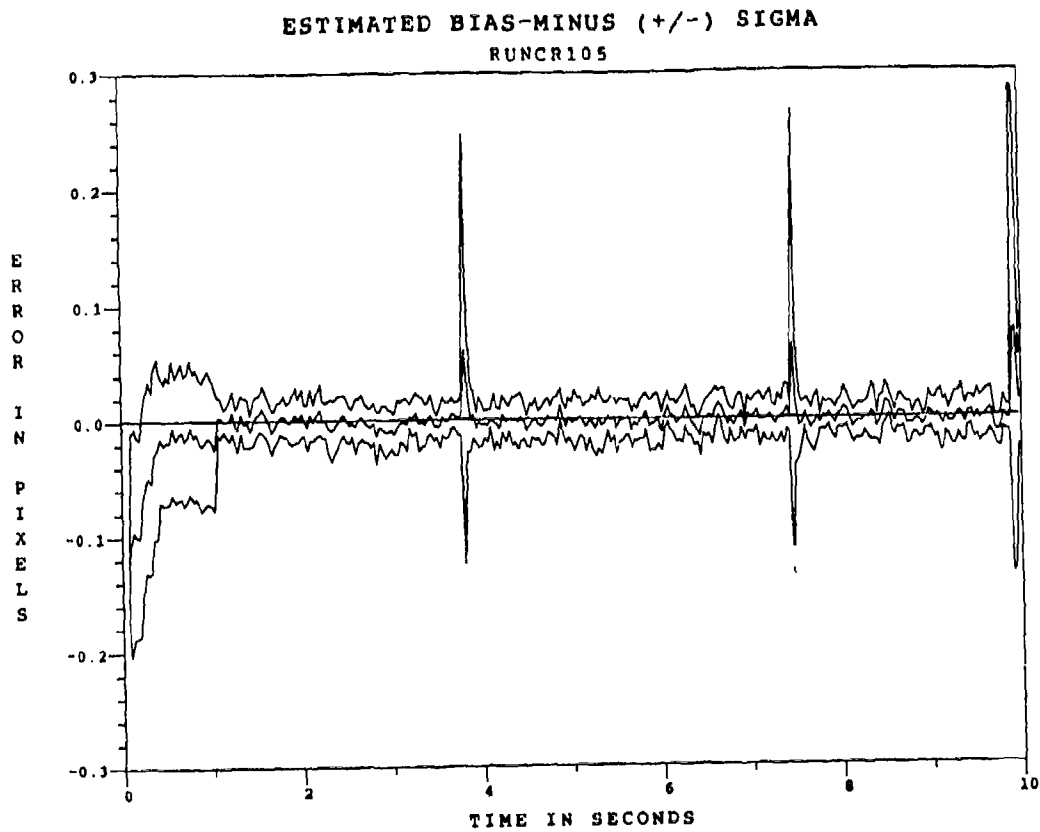


Figure F.4.11 2.01 μm Two-State Modified MAP MMAF Bias Error, SNR=4, $P_w = -0.05$, at t_i^-

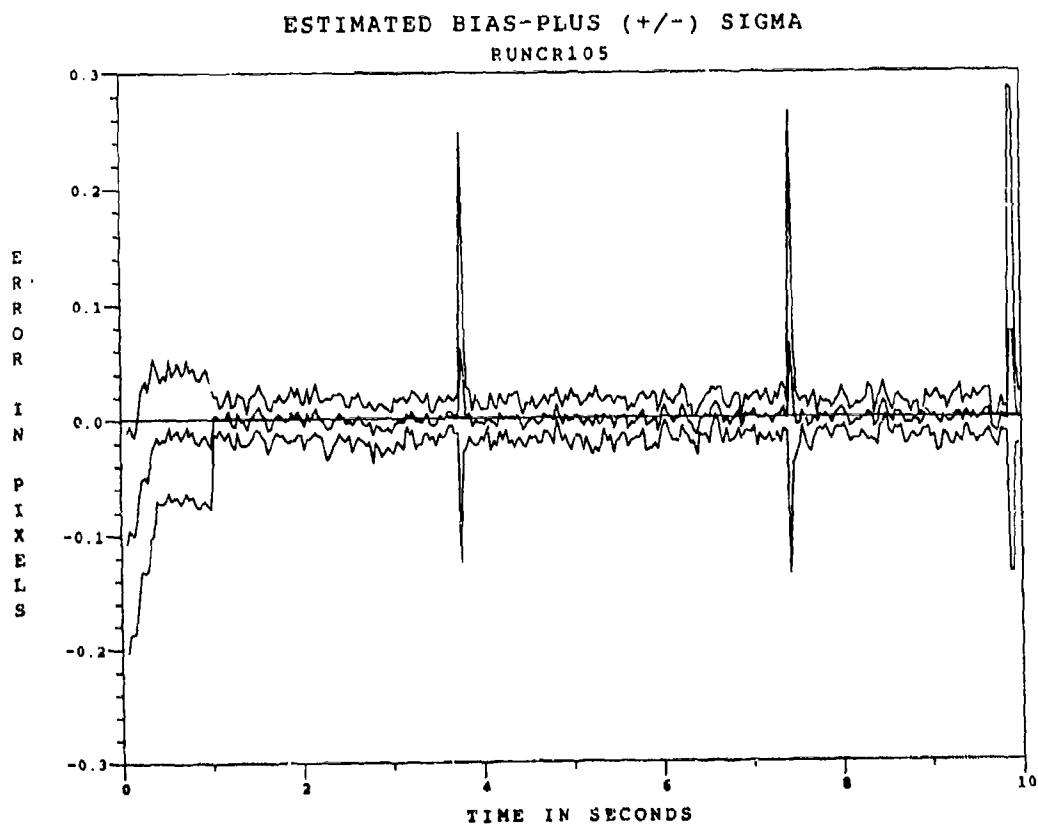


Figure F.4.12 2.01 μm Two-State Modified MAP MMAE Bias Error, SNR=4, $P_w = -0.05$, at t_i^+

FILTER VS ACTUAL ERROR (CM OFFSET)

RUNCR108

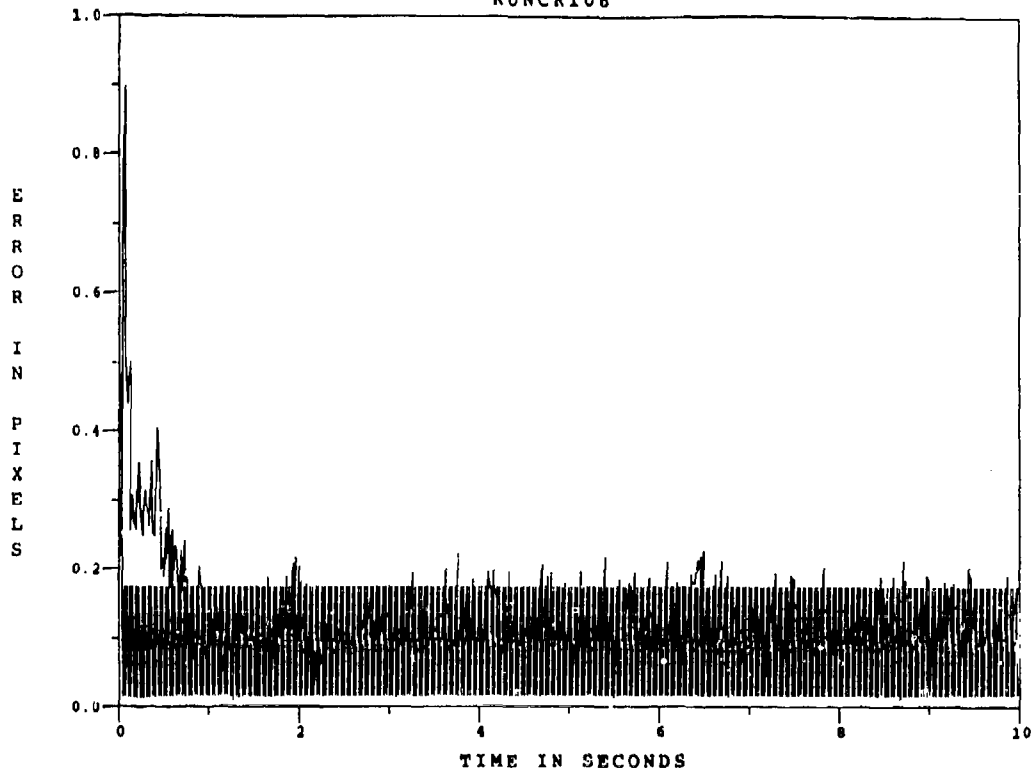


Figure F.4.13 2.01 μ m Two-State Modified MAP MMAF Offset Error, SNR = 4, $P_m = 0.30$

ESTIMATED OFFSET-MINUS POSITION (+/-) SIGMA

RUNCR108

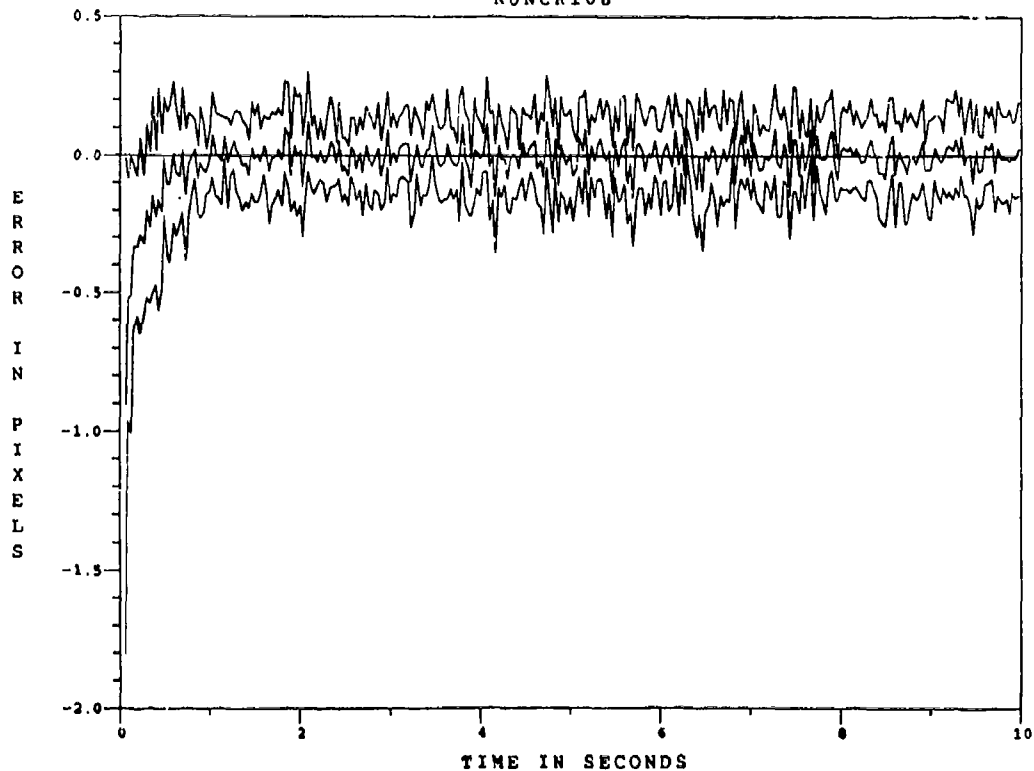


Figure F.4.14 2.01 μ m Two-State Modified MAP MMAF Offset Error, SNR=4, $P_m=0.30$, at t_i

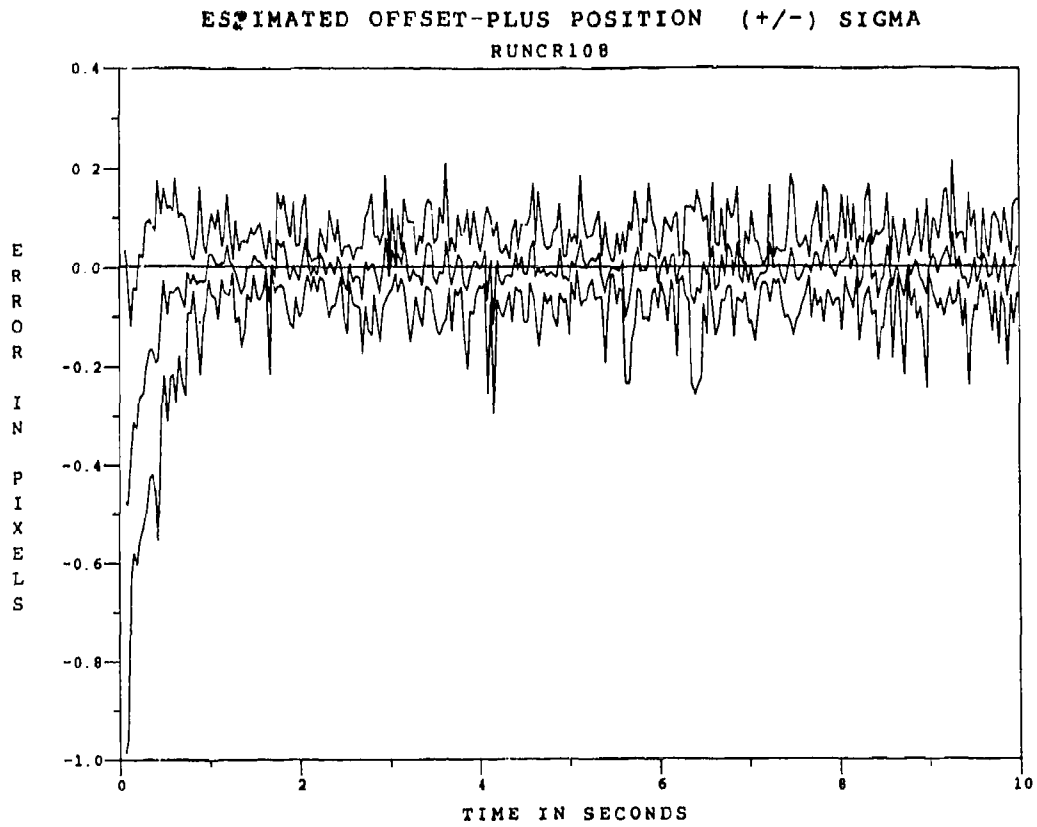


Figure F.4.15 2.01 μ m Two-State Modified MAP MMAE Offset Error, SNR=4, $P_m = -0.30$, at t_i^+

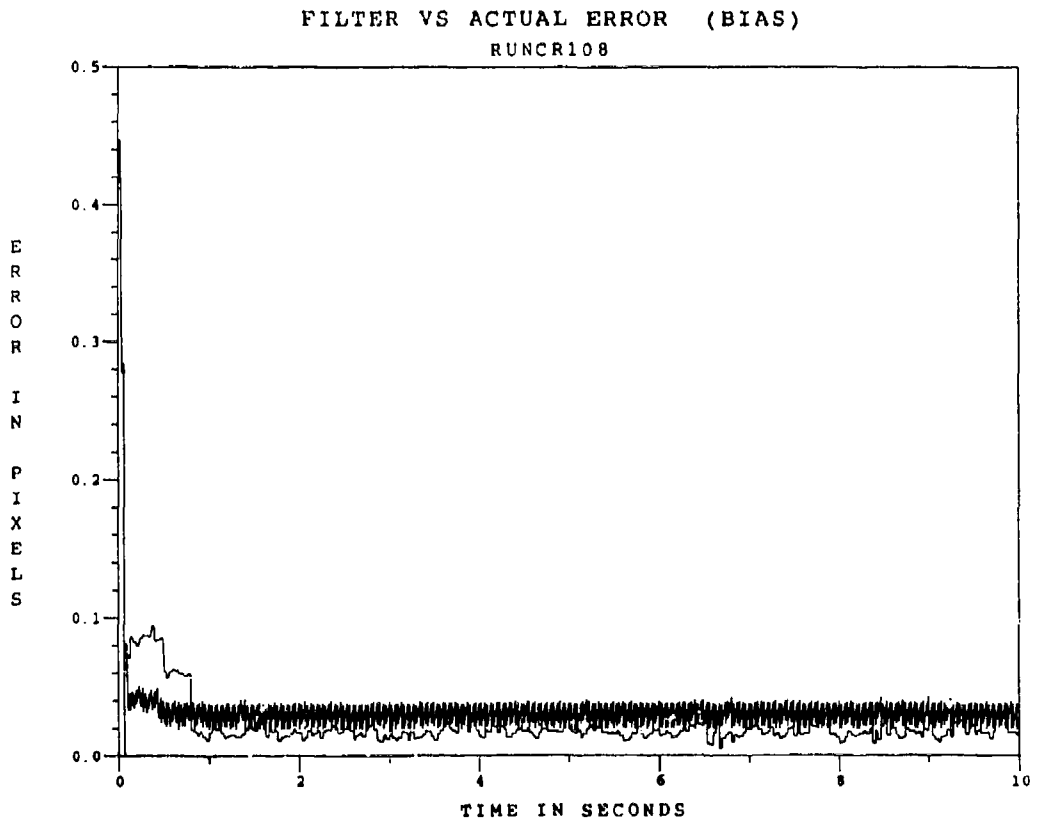


Figure F.4.16 2.01 μ m Two-State Modified MAP MMAF Bias Error, SNR = 4, $P_m = 0.30$

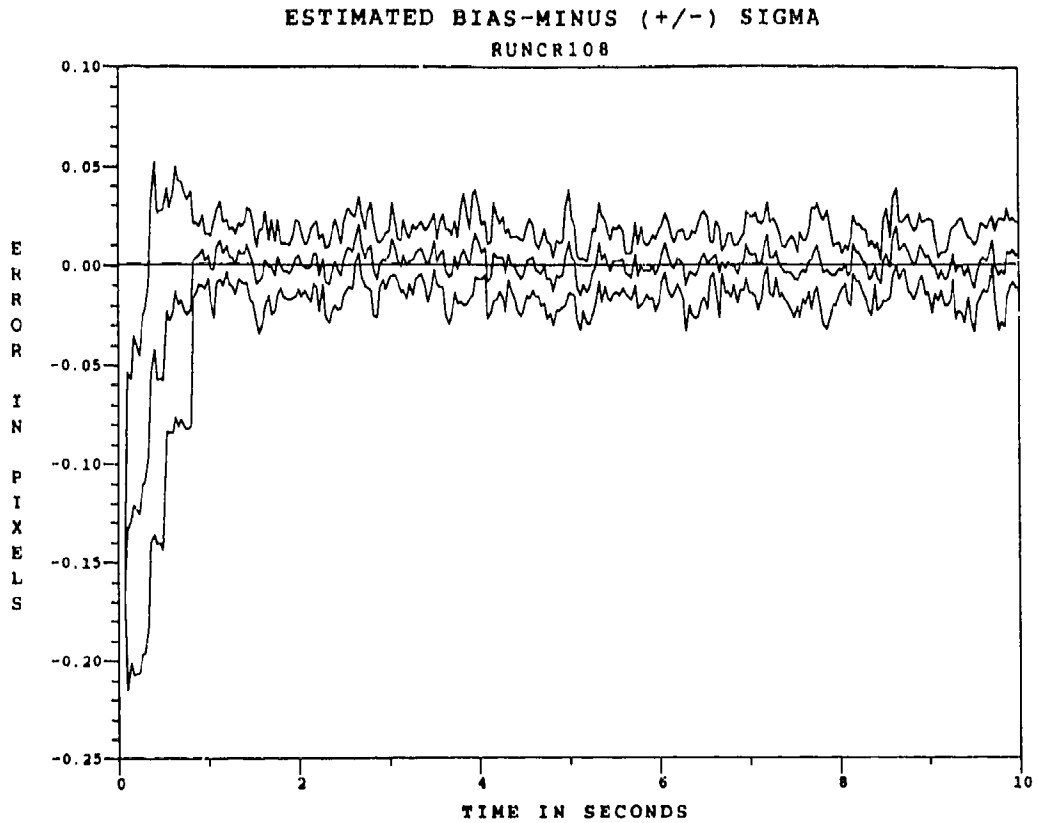


Figure F.4.17 2.01 μ m Two-State Modified MAP MMAF Bias Error, SNR=4, $P_m = -0.30$, at t_i^-

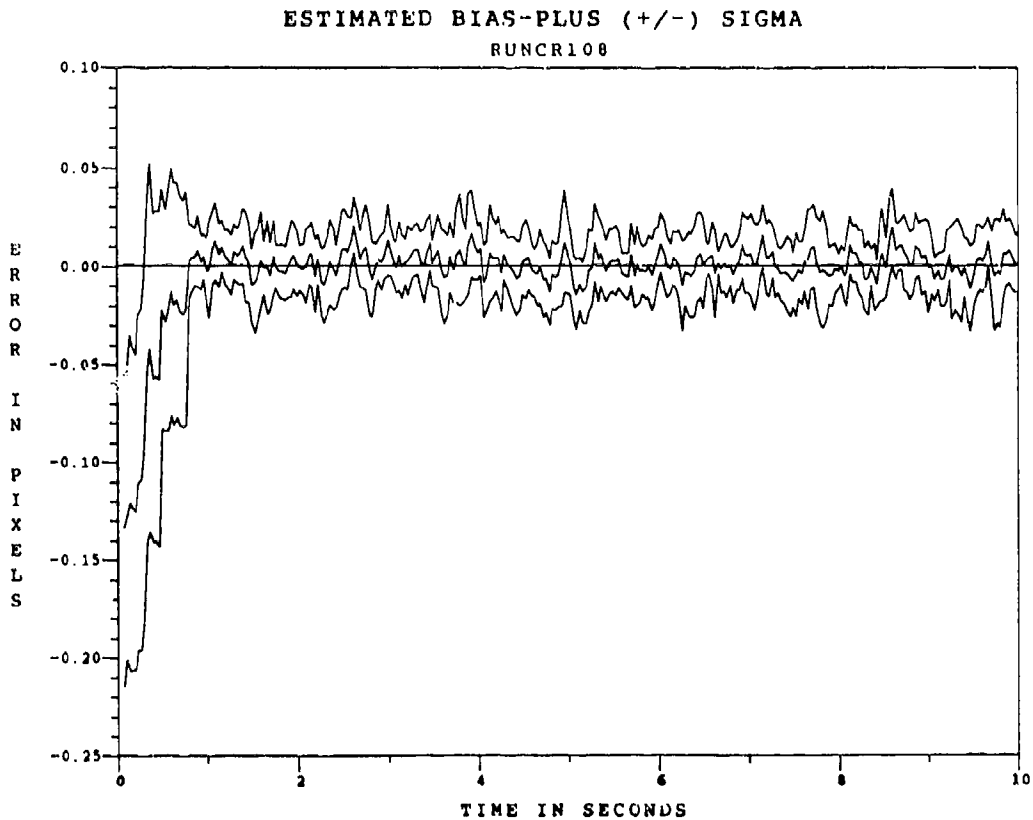


Figure F.4.18 2.01 μ m Two-State Modified MAP MMAE Bias Error, SNR=4, $P_m = -0.30$, at t_i^+

Appendix F.5

Two-State Center-of-Mass

Modified MAP MMAF

with

10.5 μm Doppler Return Measurements

at SNR = 10

FILTER VS ACTUAL ERROR (CM OFFSET)

RUNCR217

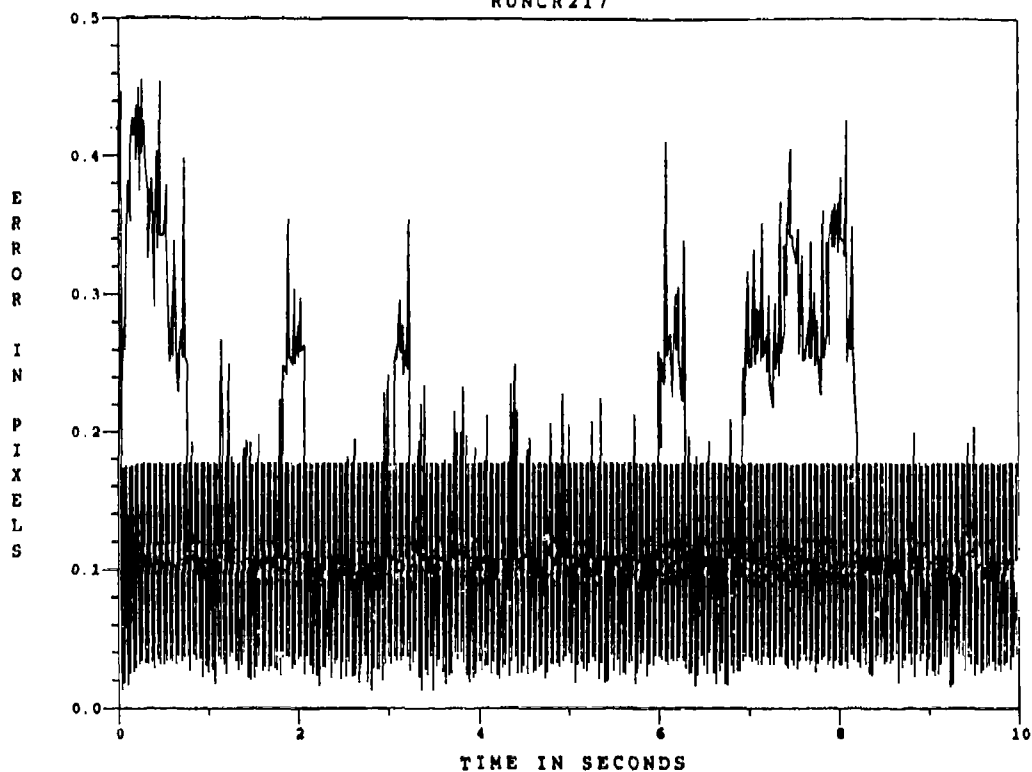


Figure F.5.1 10.5 μm Two-State Modified MAP MMAF Offset Error, SNR=10, $P_m = 0.0$

ESTIMATED OFFSET-MINUS POSITION (+/-) SIGMA

RUNCR217

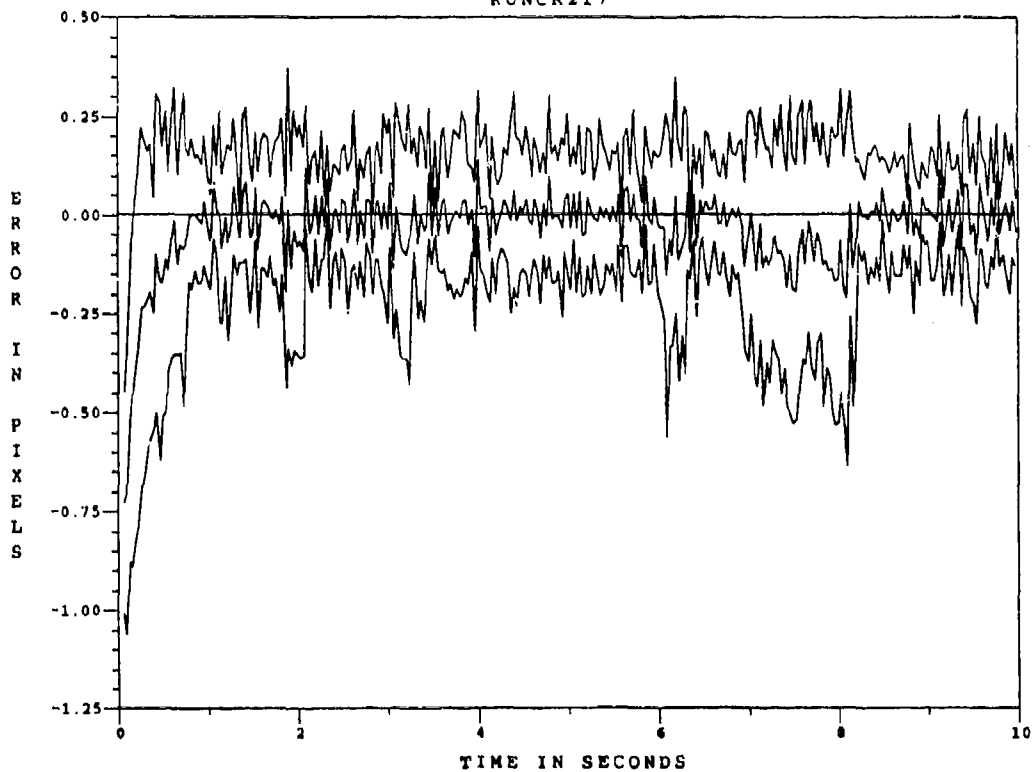


Figure F.5.2 10.5 μm Two-State Modified MAP MMAF Bias Error, SNR=10, $P_m = 0.0$, at t_i

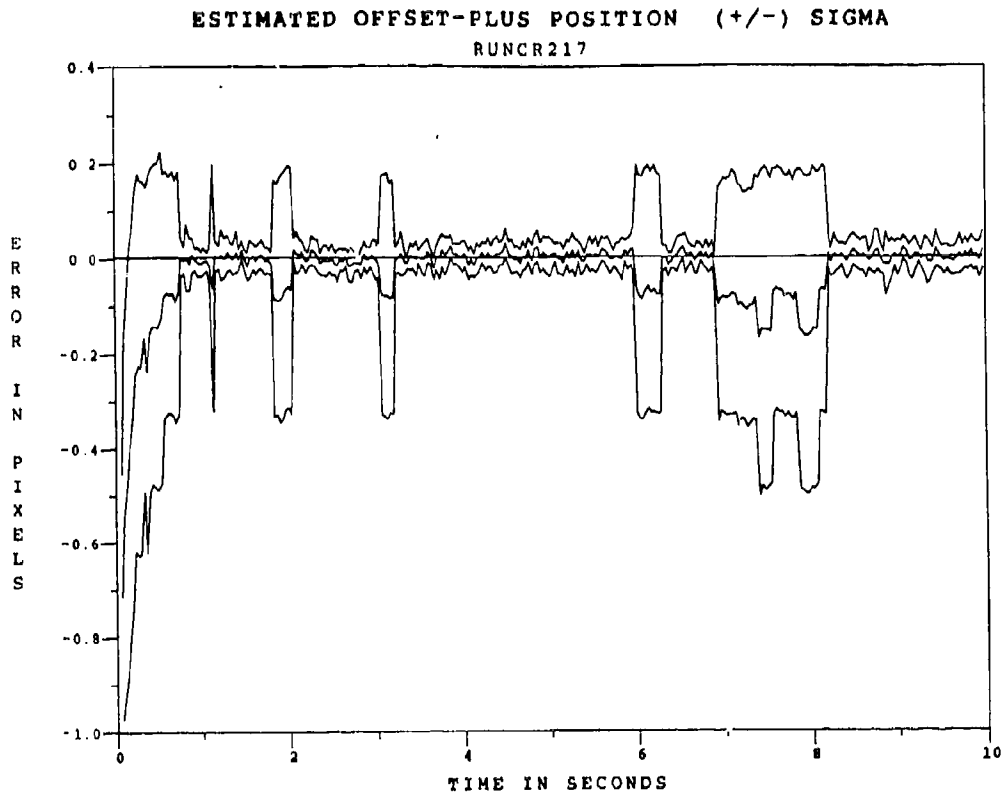


Figure F.5.3 10.5 μm Two-State Modified MAP MMAF Offset Error, SNR=10, $P_m = -0.0$, at t_1^+

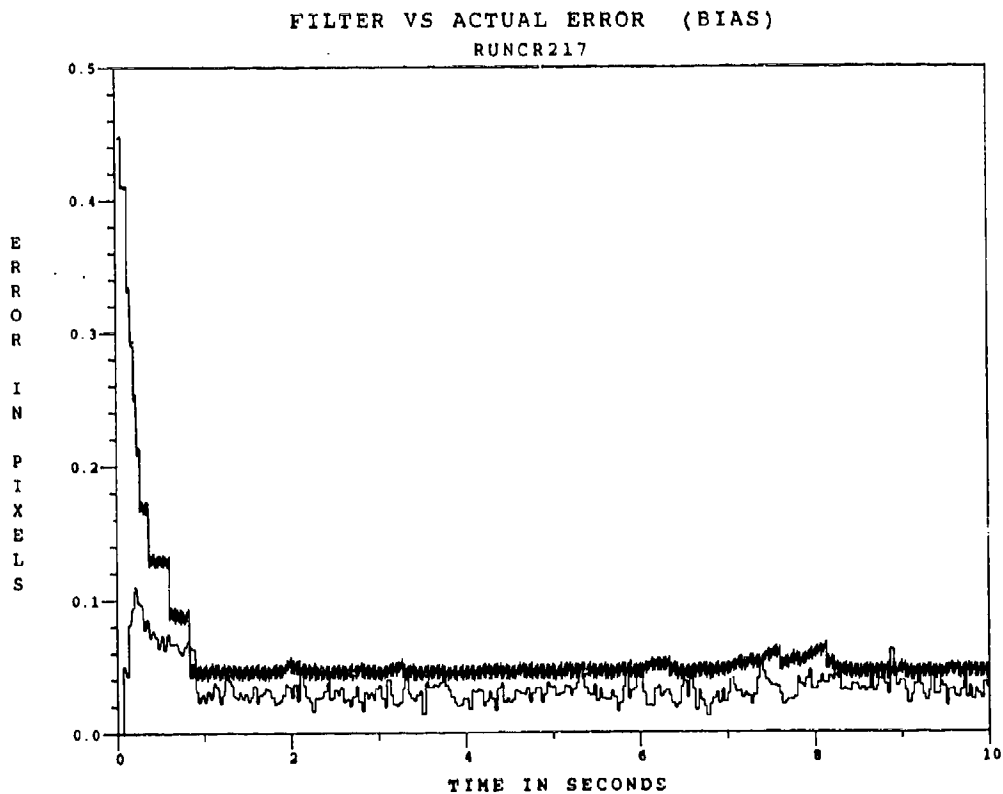


Figure F.5.4 10.5 μm Two-State Modified MAP MMAF Bias Error, SNR=10, $P_m = -0.0$

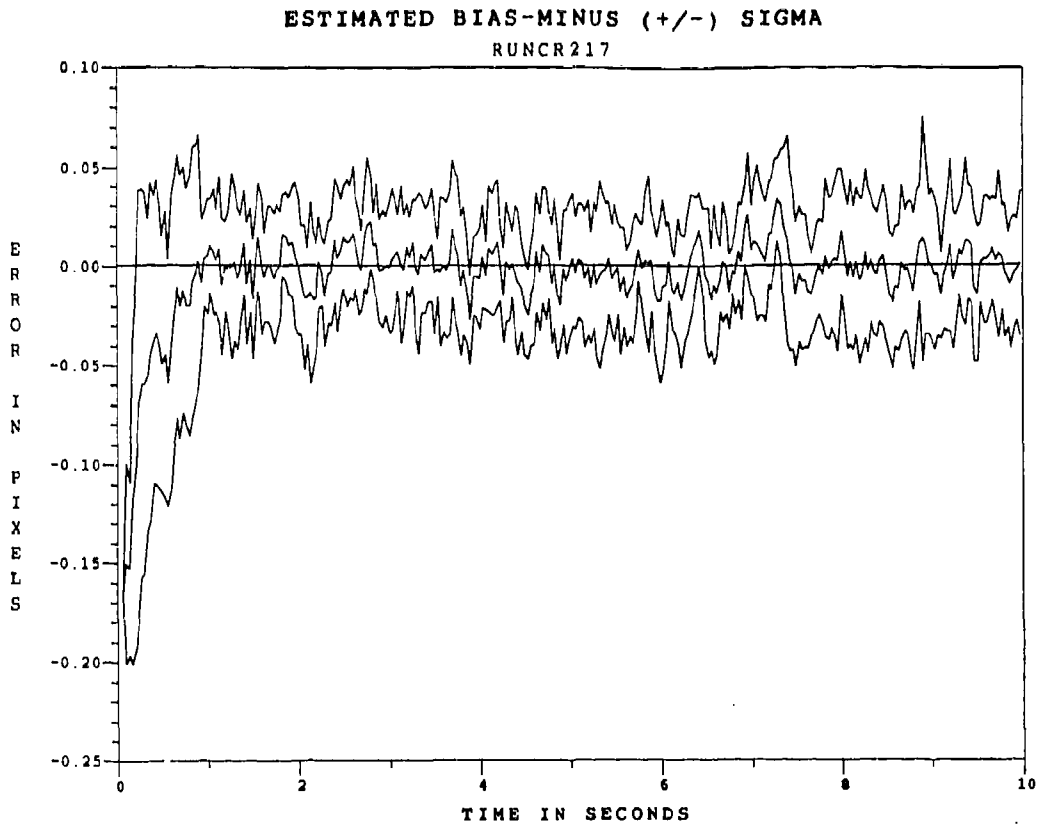


Figure F.5.5 10.5 μm Two-State Modified MAP MMAF Bias Error, SNR=10, $P_m = 0.0$, at t_i^-

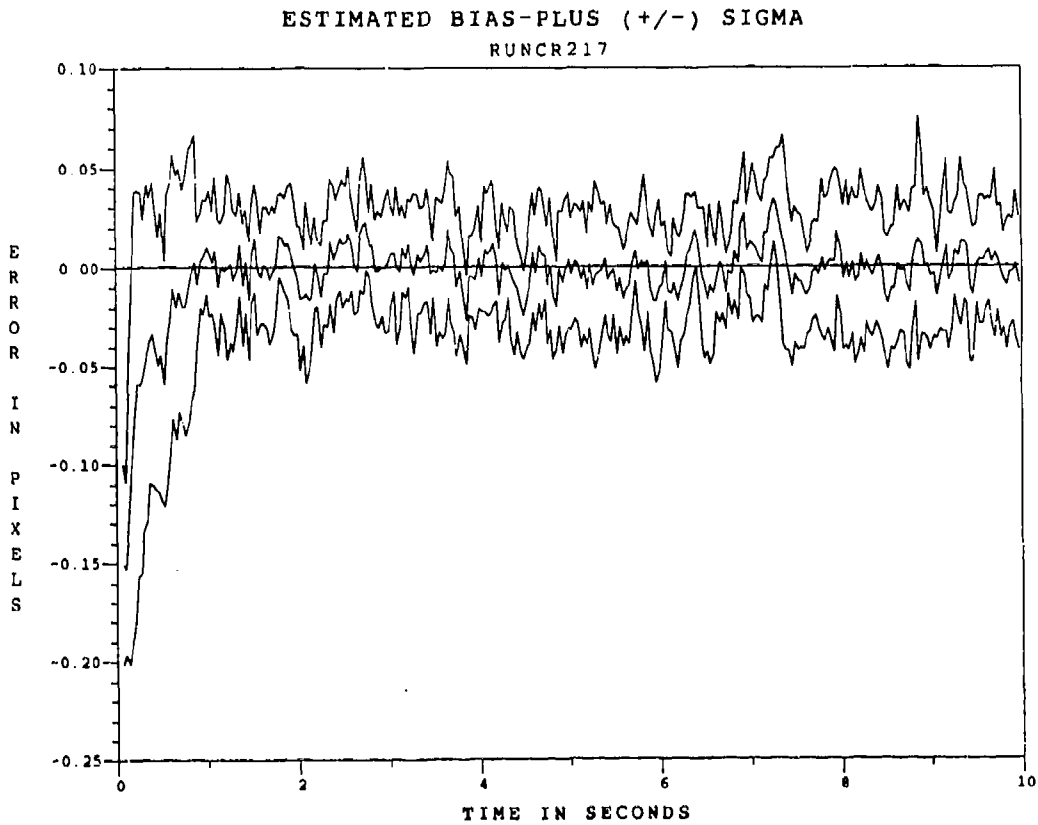


Figure F.5.6 10.5 μm Two-State Modified MAP MMAF Bias Error, SNR=10, $P_m = 0.0$, at t_i^+

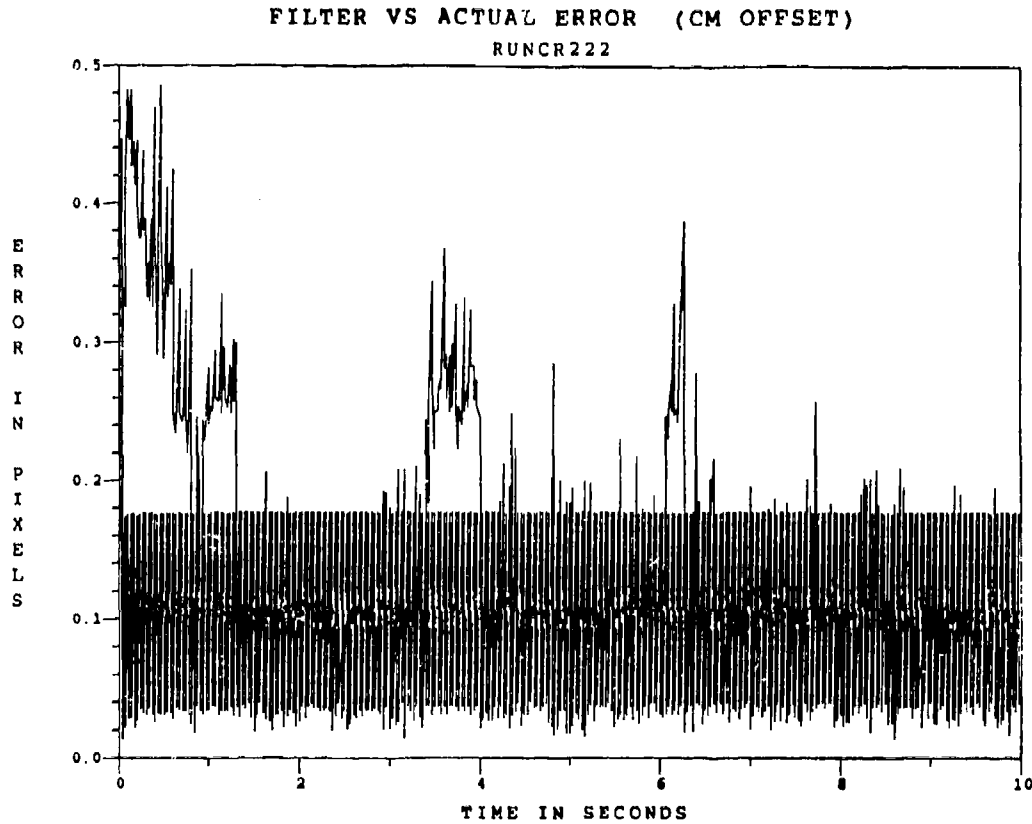


Figure F.5.7 10.5 μm Two-State Modified MAP MMAF Offset Error, SNR = 10, $P_{\text{m}} = 0.05$

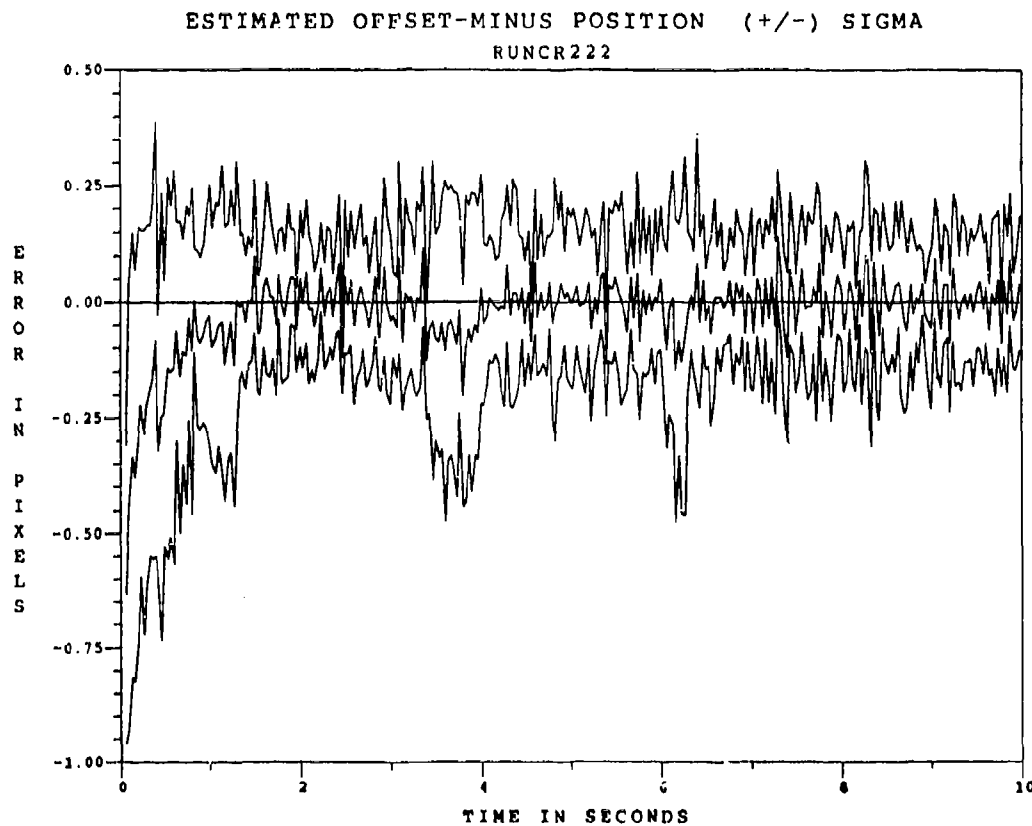


Figure F.5.8 10.5 μm Two-State Modified MAP MMAF Offset Error, SNR=10, $P_{\text{m}}=0.05$, at t_1

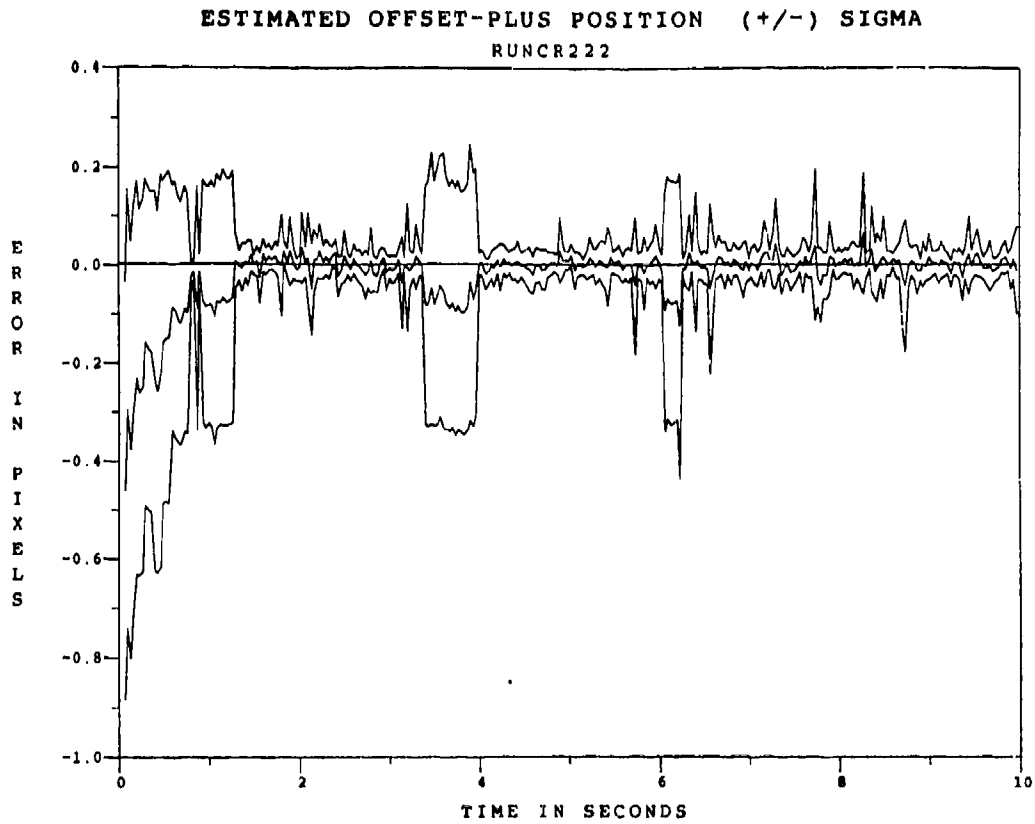


Figure F.5.9 10.5 μ m Two-State Modified MAP MMAE Offset Error, SNR=10, $P_m = -0.05$, at t_i^+

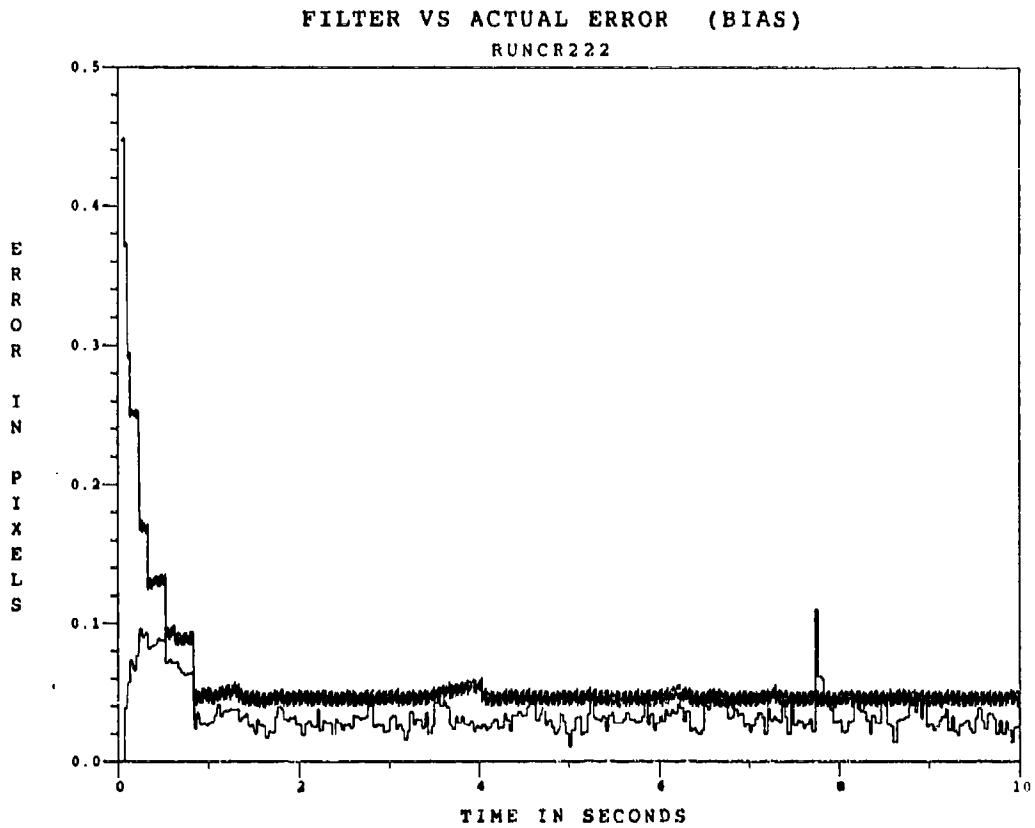


Figure F.5.10 10.5 μ m Two-State Modified MAP MMAF Bias Error, SNR = 10, $P_m = 0.05$

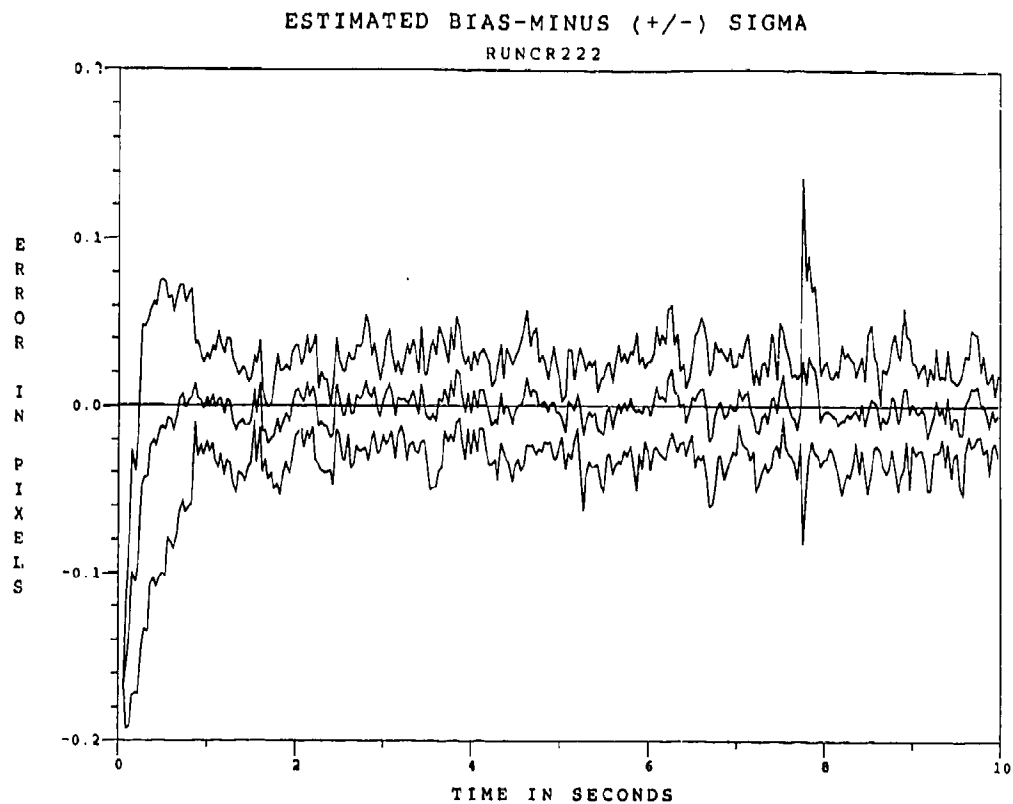


Figure F.5.11 10.5 μm Two-State Modified MAP MMAF Bias Error, SNR=10, $P_m = 0.05$, at t_i^-

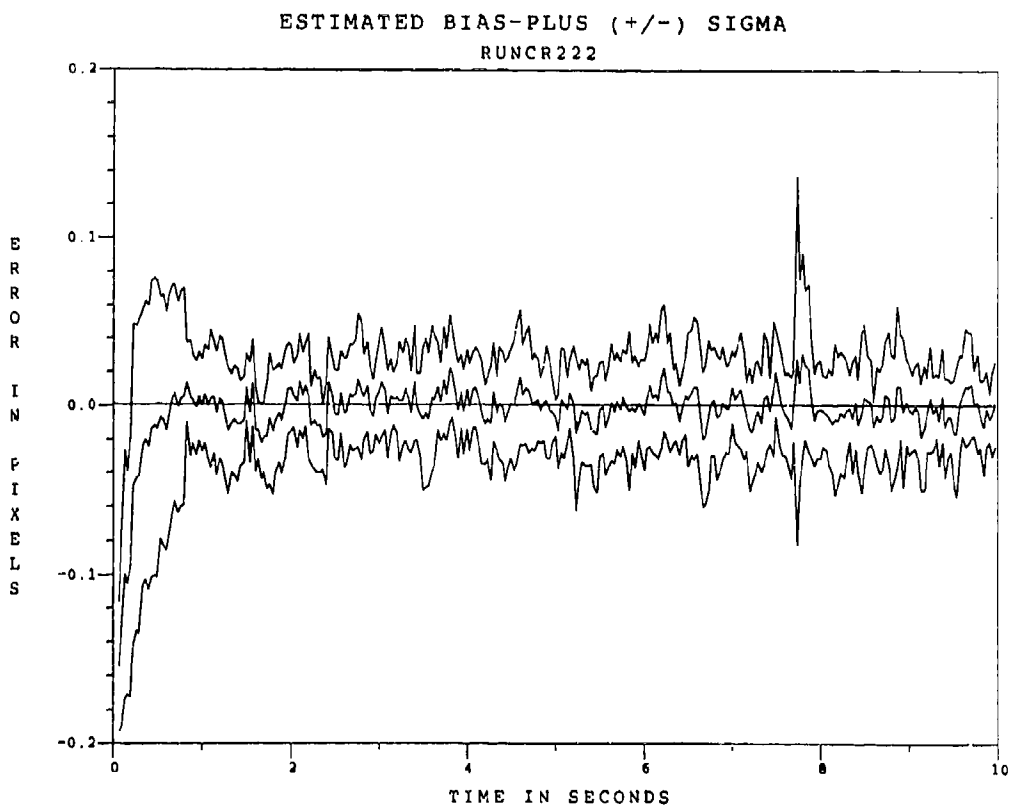


Figure F.5.12 10.5 μm Two-State Modified MAP MMAE Bias Error, SNR=10, $P_m = 0.05$, at t_i^+

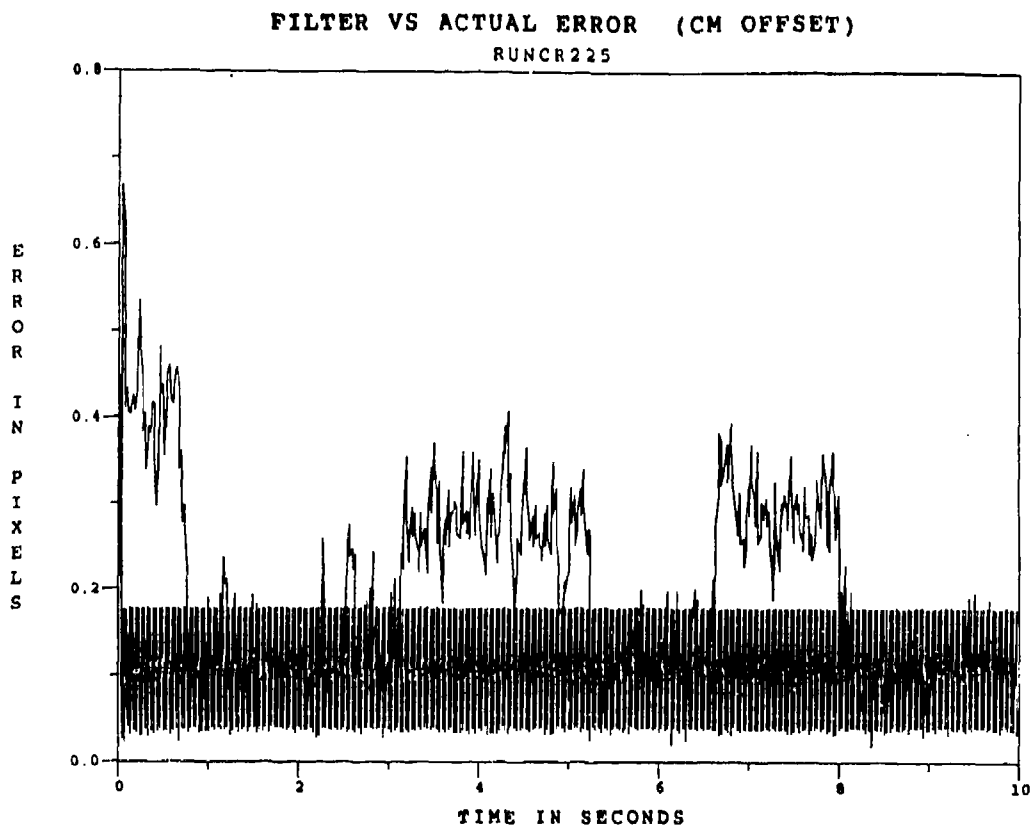


Figure F.5.13 10.5 μ m Two-State Modified MAP MMAF Offset Error, SNR = 10, $P_m = 0.30$

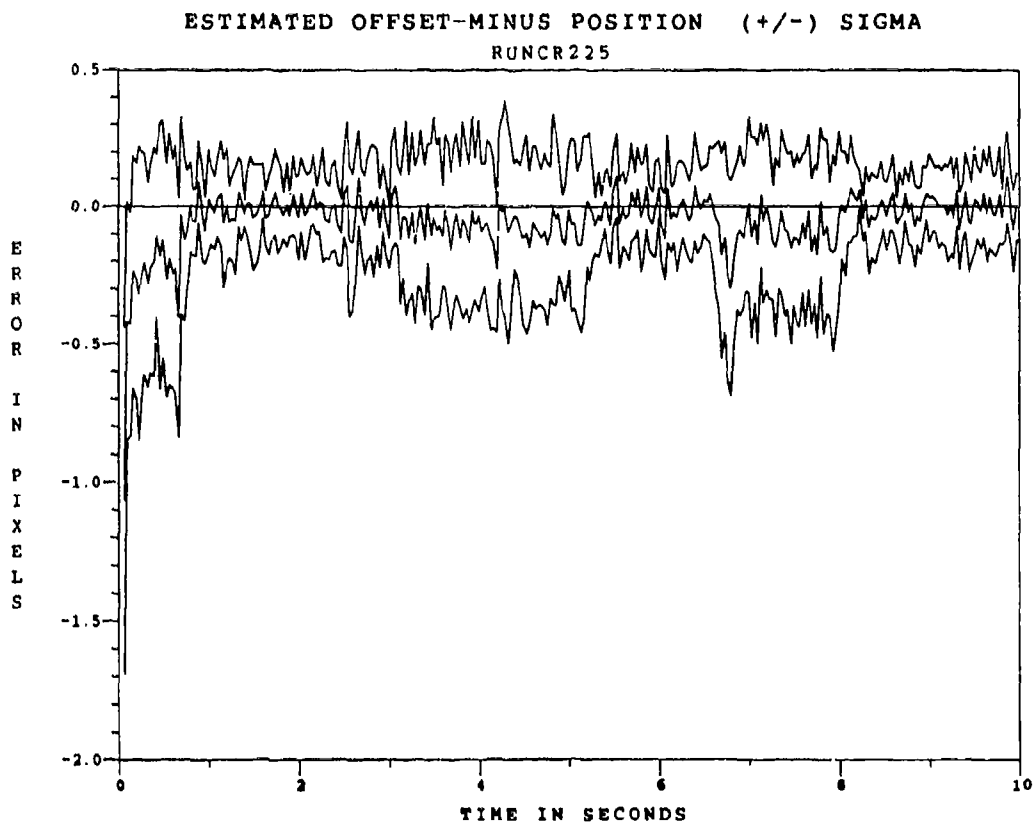


Figure F.5.14 10.5 μ m Two-State Modified MAP MMAF Offset Error, SNR=10, $P_m=0.30$, at t_i

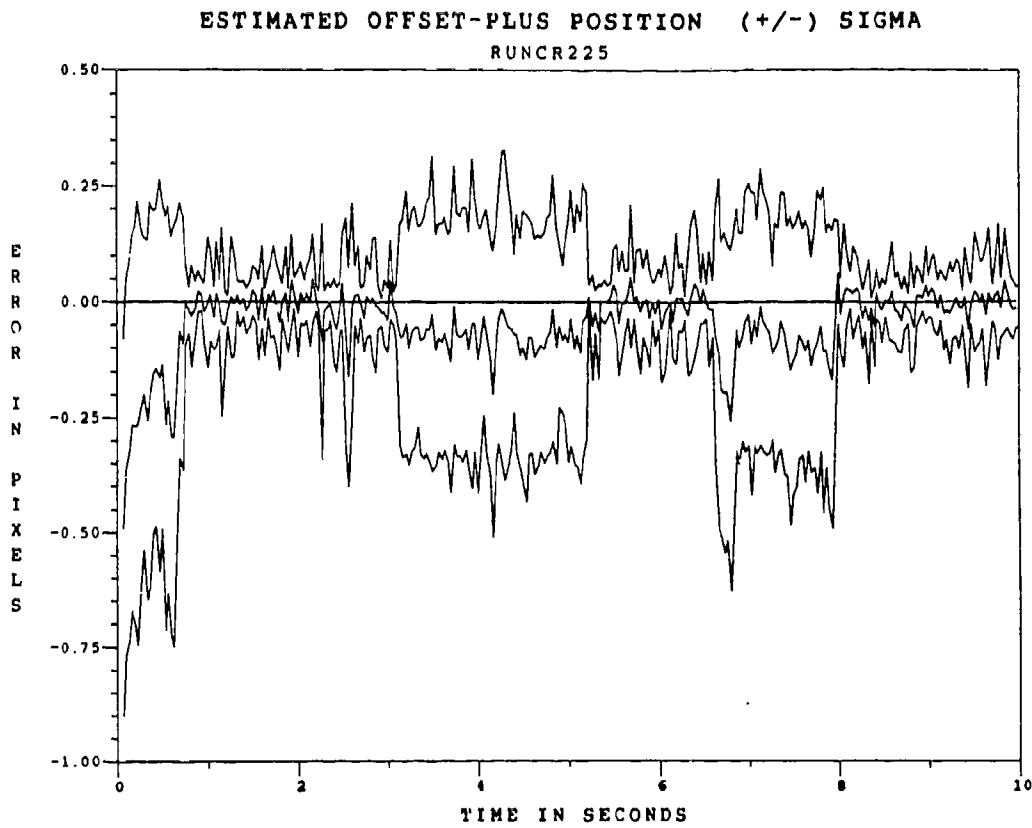


Figure F.5.15 10.5 μ m Two-State Modified MAP MMAE Offset Error, SNR=10, $P_m = 0.30$, at t_i^+

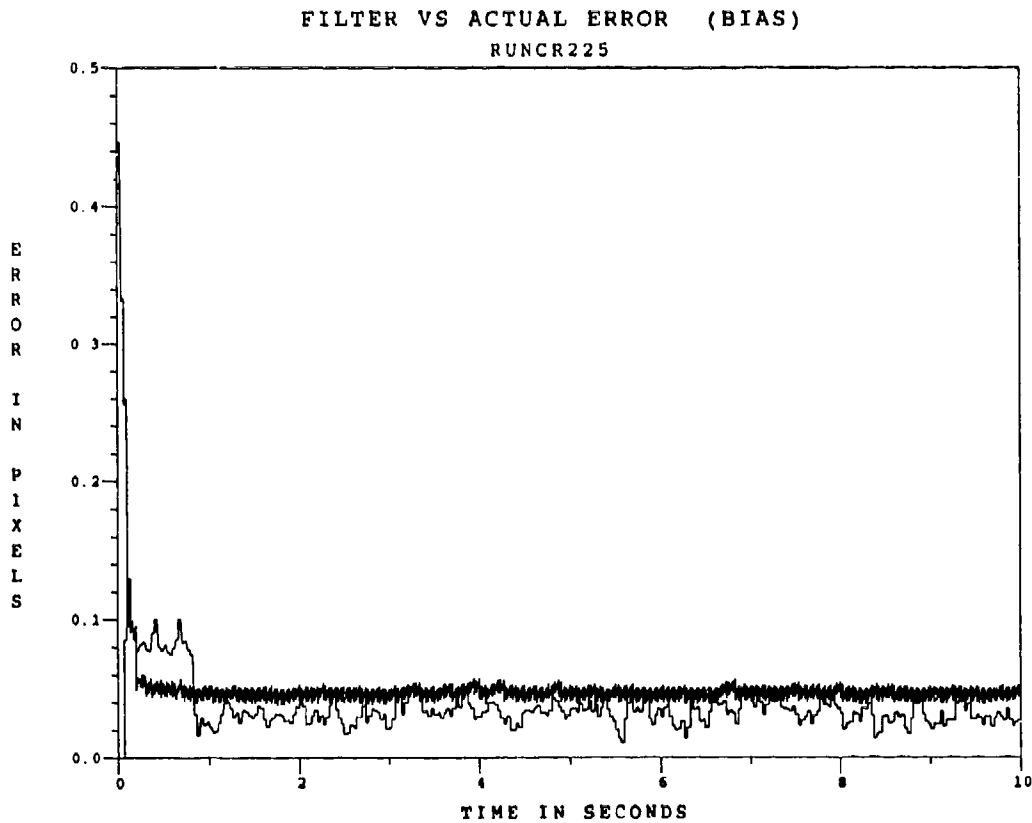


Figure F.5.16 10.5 μ m Two-State Modified MAP MMAF Bias Error, SNR = 10, $P_m = 0.30$

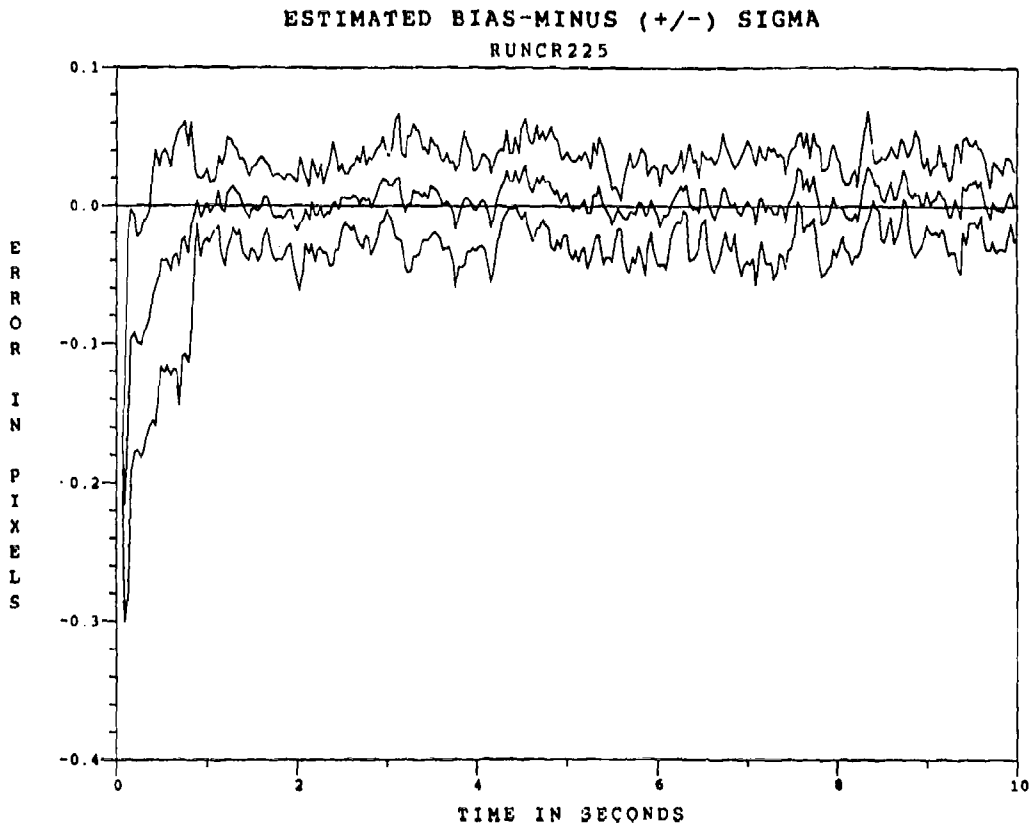


Figure F.5.17 10.5 μ m Two-State Modified MAP MMAF Bias Error, SNR=10, $P_m = -0.30$, at t_i^-

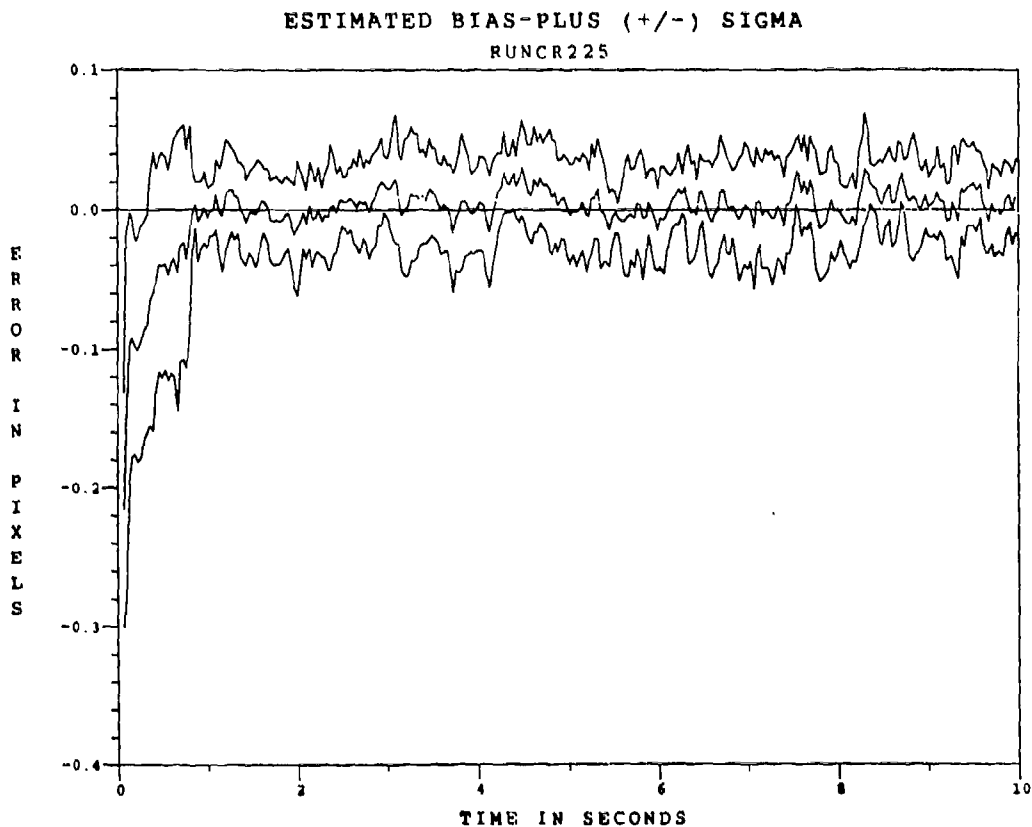


Figure F.5.18 10.5 μ m Two-State Modified MAP MMAE Bias Error, SNR=10, $P_m = -0.30$, at t_i^+

Appendix F.6

Two-State Center-of-Mass

Modified MAP MMAF

with

10.5 μm Doppler Return Measurements

at SNR = 4

FILTER VS ACTUAL ERROR (CM OFFSET)

RUNCR244

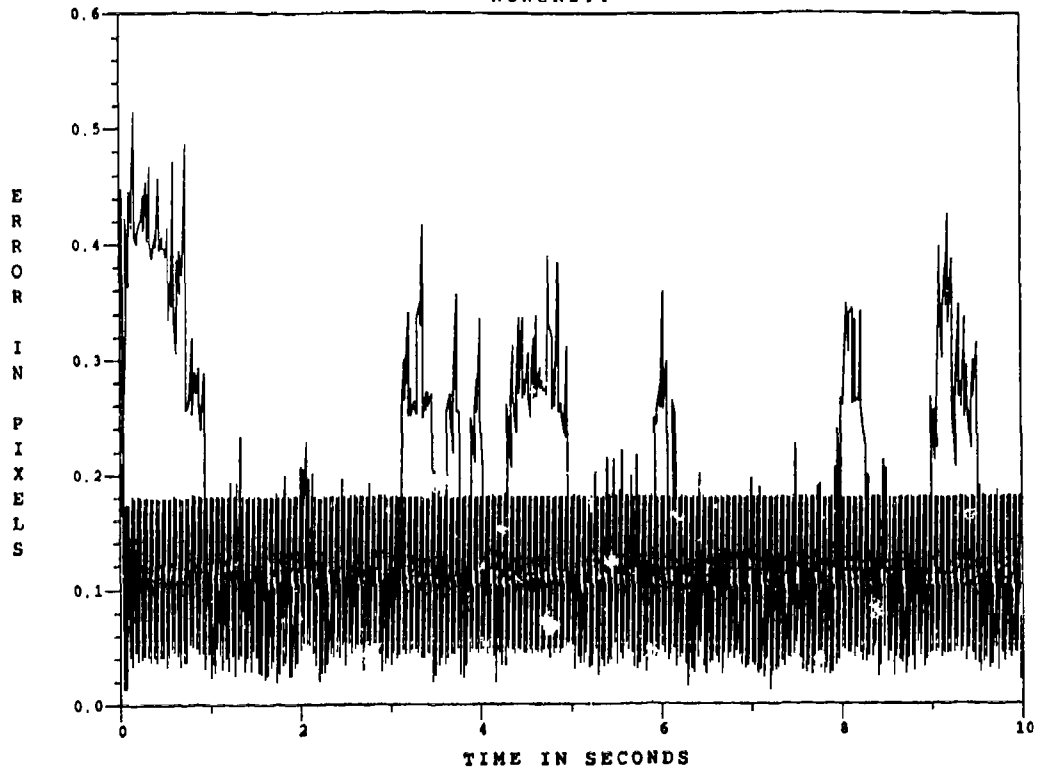


Figure F.6.1 10.5 μm Two-State Modified MAP MMAF Offset Error, SNR=4, $P_m = -0.0$

ESTIMATED OFFSET-MINUS POSITION (+/-) SIGMA

RUNCR244

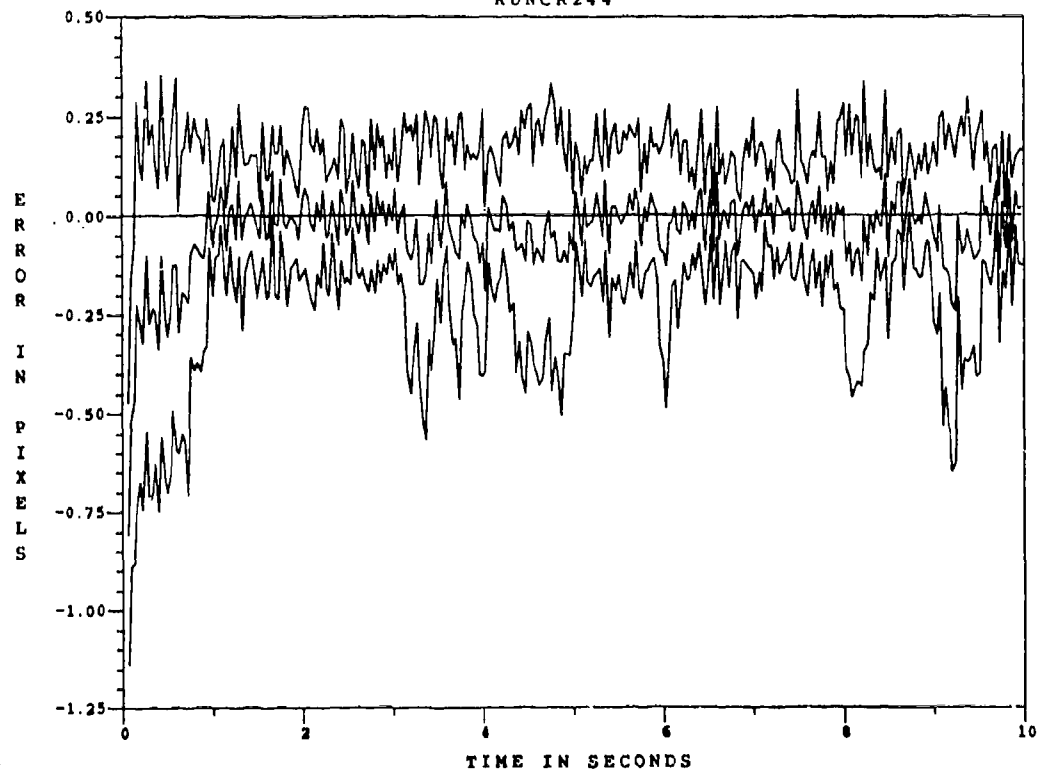


Figure F.6.2 10.5 μm Two-State Modified MAP MMAF Bias Error, SNR=4, $P_m = -0.0$, at t_i

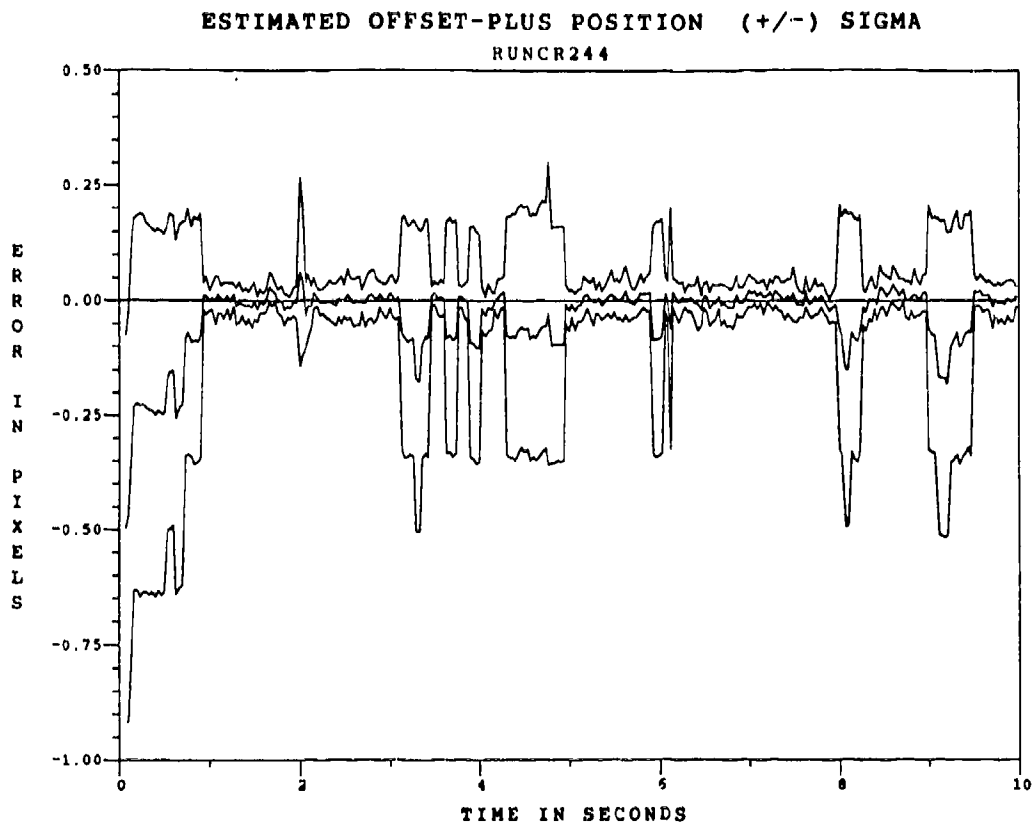


Figure F.6.3 10.5 μm Two-State Modified MAP MMAF Offset Error, SNR=4, $P_m = -0.0$, at t_i^+

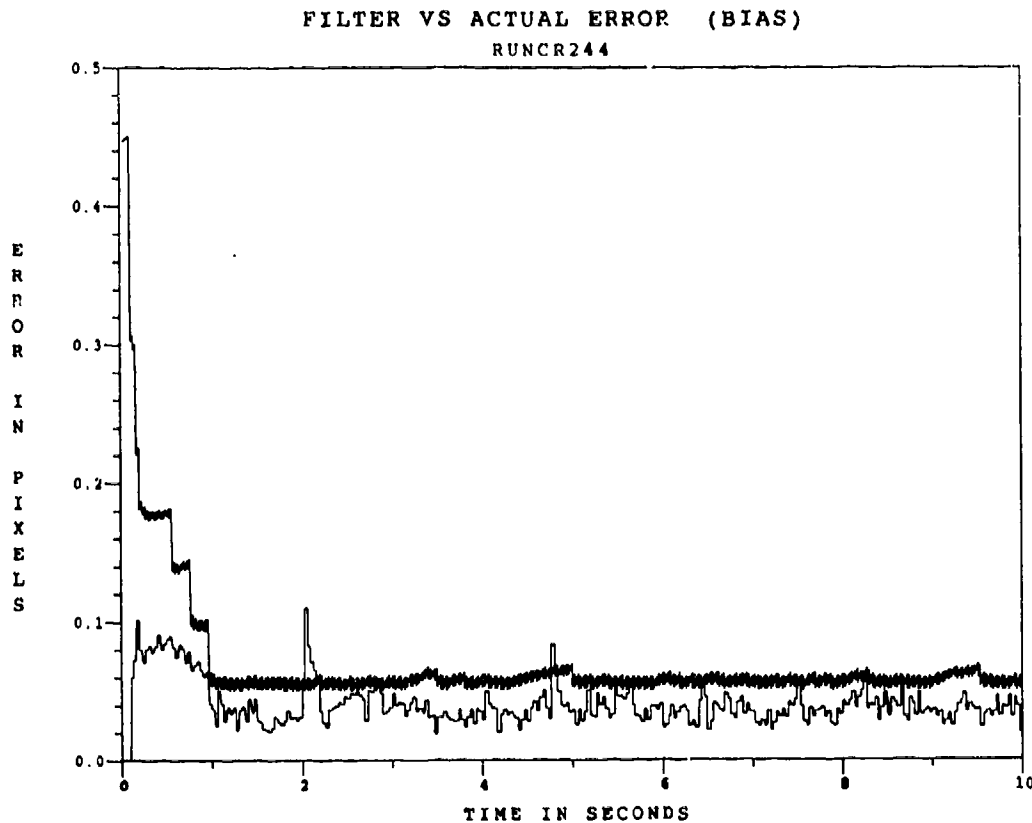


Figure F.6.4 10.5 μm Two-State Modified MAP MMAF Bias Error, SNR=4, $P_m = -0.0$

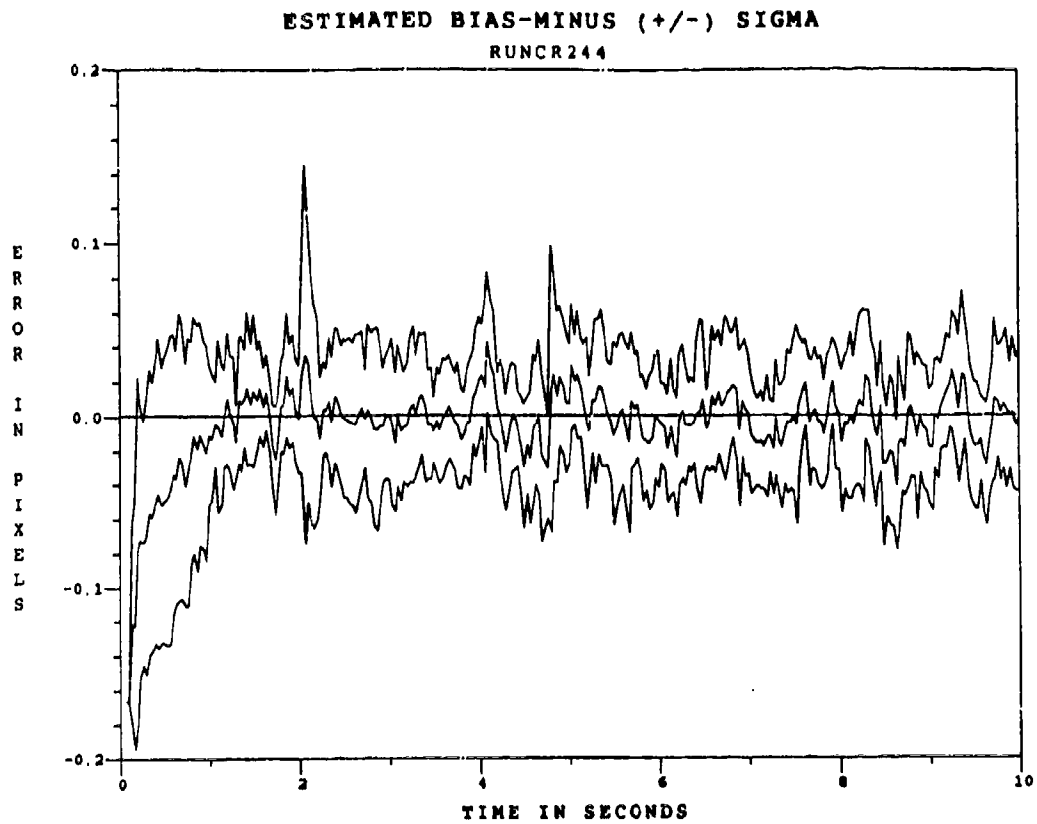


Figure F.6.5 10.5 μm Two-State Modified MAP MMAF Bias Error, SNR=4, $P_{\text{m}} = -0.0$, at t_i^-

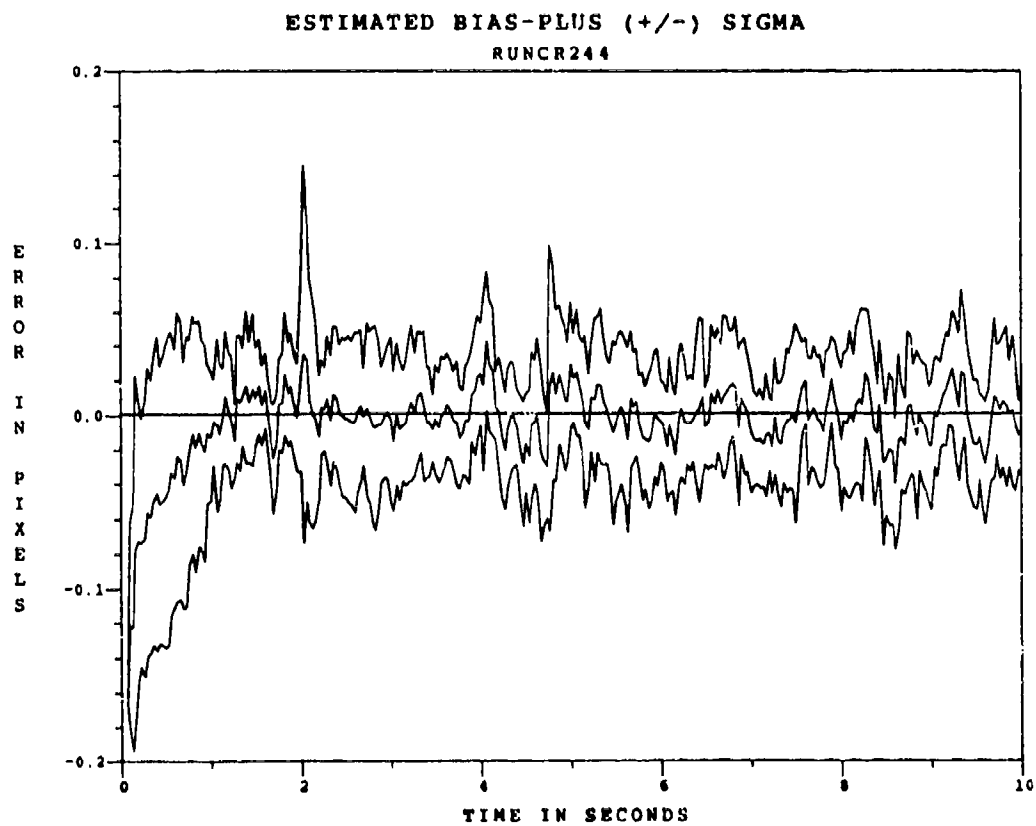


Figure F.6.6 10.5 μm Two-State Modified MAP MMAF Bias Error, SNR=4, $P_{\text{m}} = -0.0$, at t_i^+

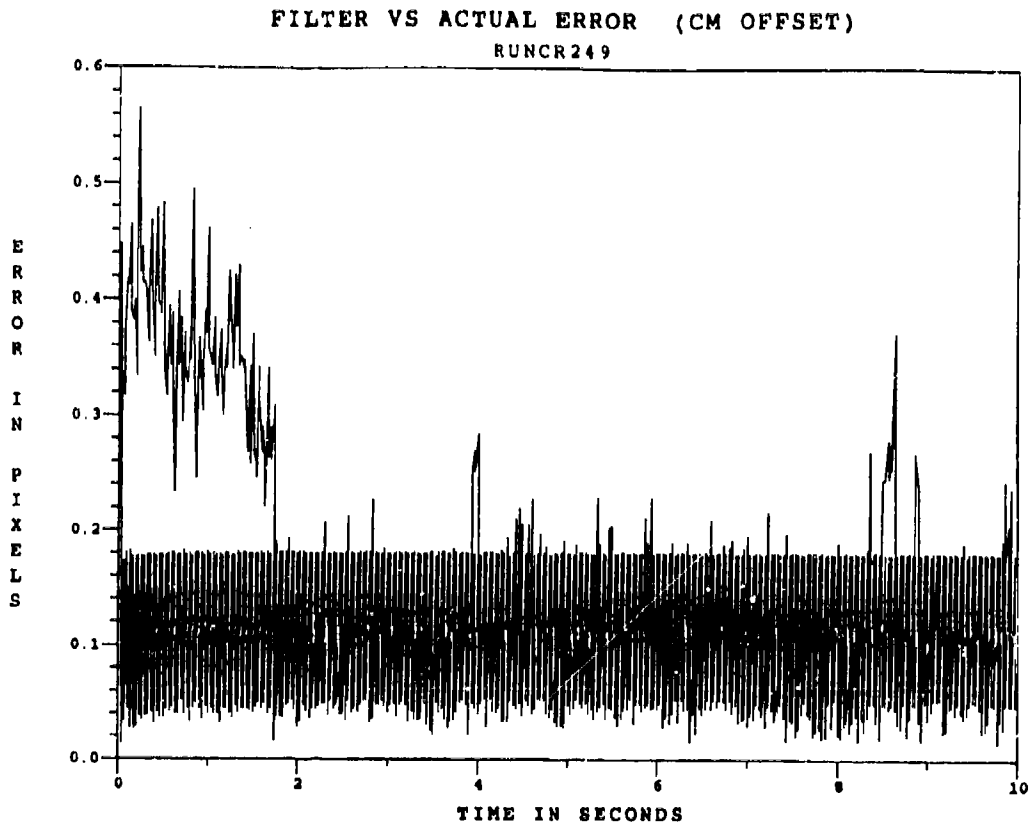


Figure F.6.7 10.5 μm Two-State Modified MAP MMAF Offset Error, SNR = 4, $P_m = 0.05$

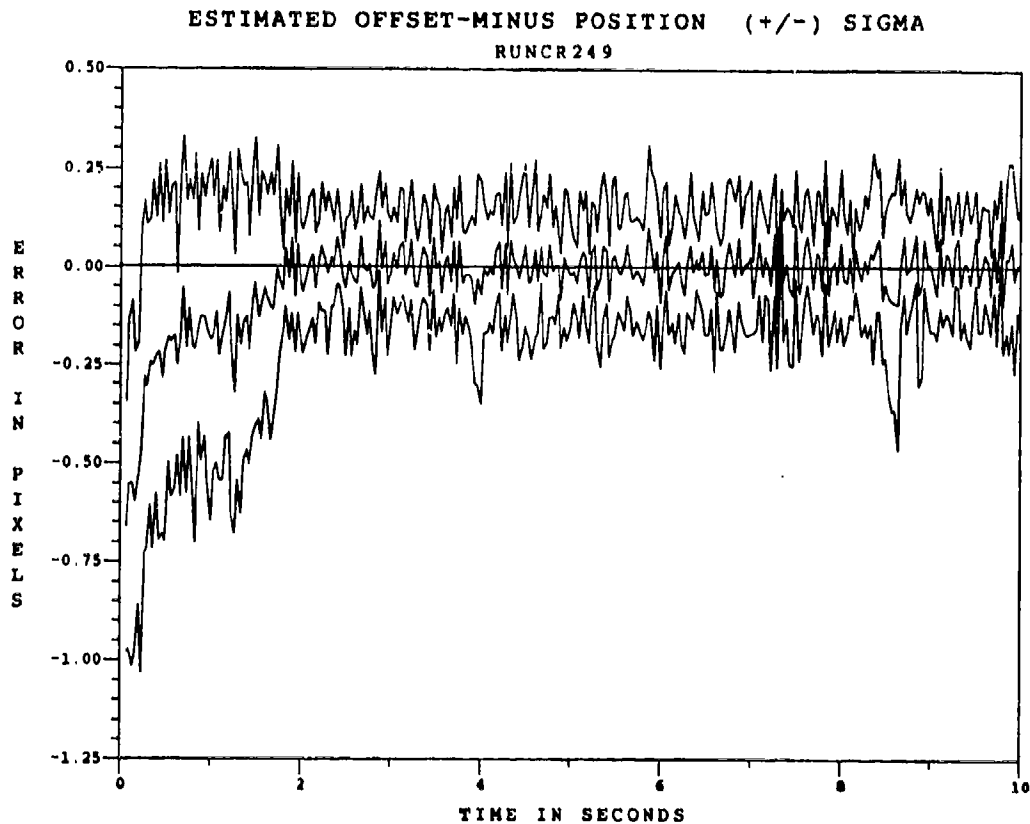


Figure F.6.8 10.5 μm Two-State Modified MAP MMAF Offset Error, SNR=4, $P_m = 0.05$, at t_1^*

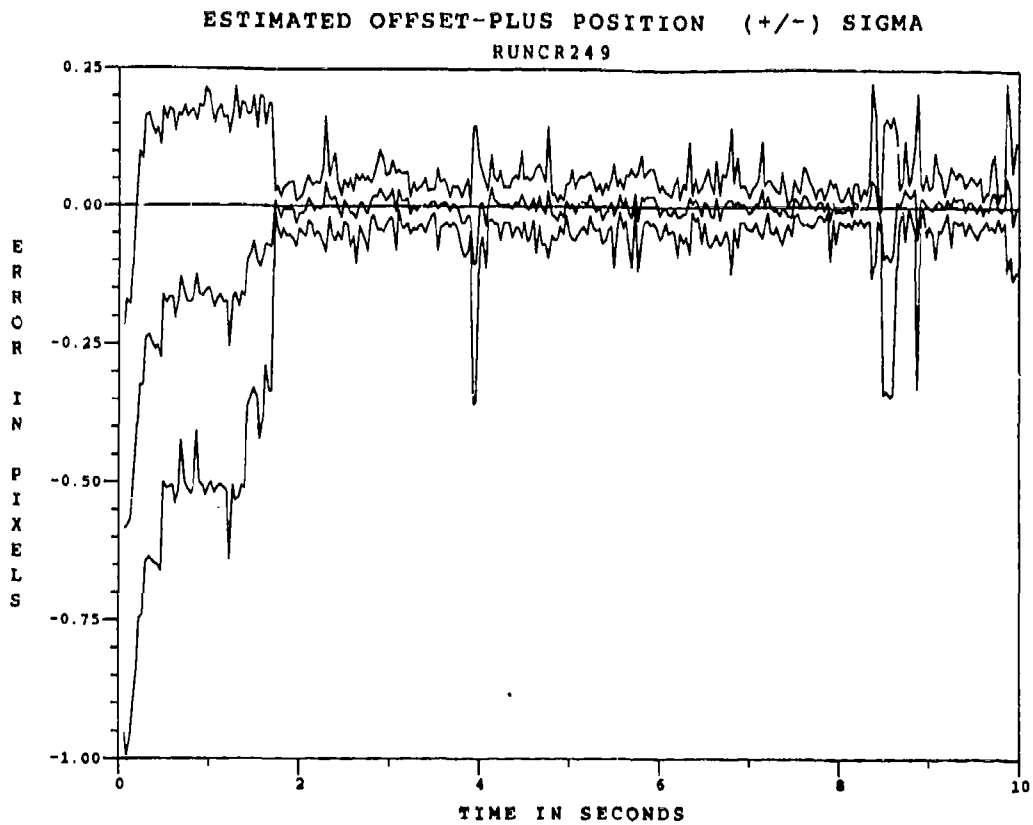


Figure F.6.9 10.5 μ m Two-State Modified MAP MMAE Offset Error, SNR=4, $P_m = -0.05$, at t_i^+

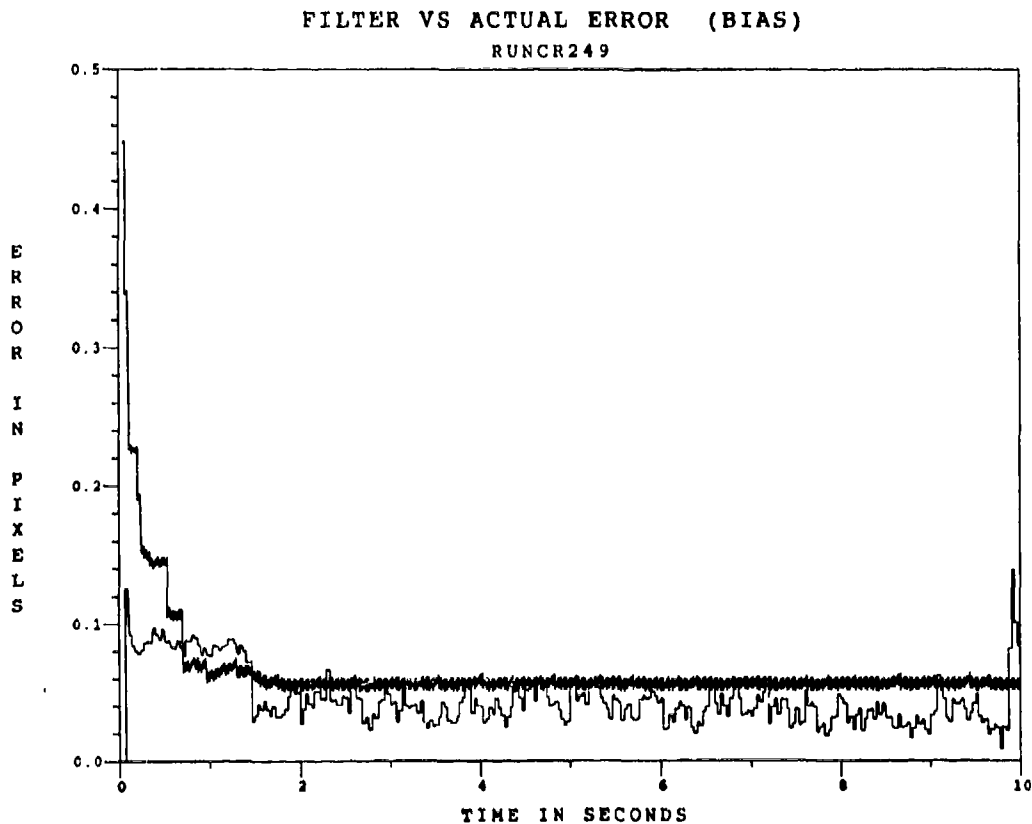


Figure F.6.10 10.5 μ m Two-State Modified MAP MMAF Bias Error, SNR = 4, $P_m = 0.05$

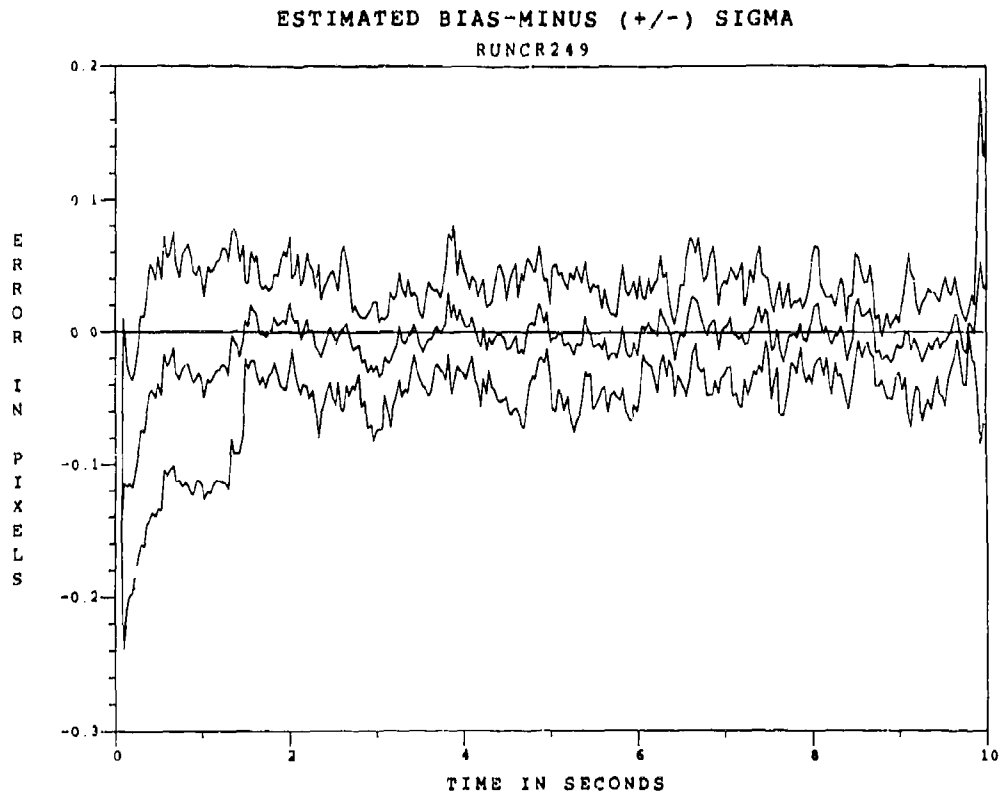


Figure F.6.11 10.5 μm Two-State Modified MAP MMAF Bias Error, $\text{SNR}=4, P_m = 0.05, \text{at } t_i^-$

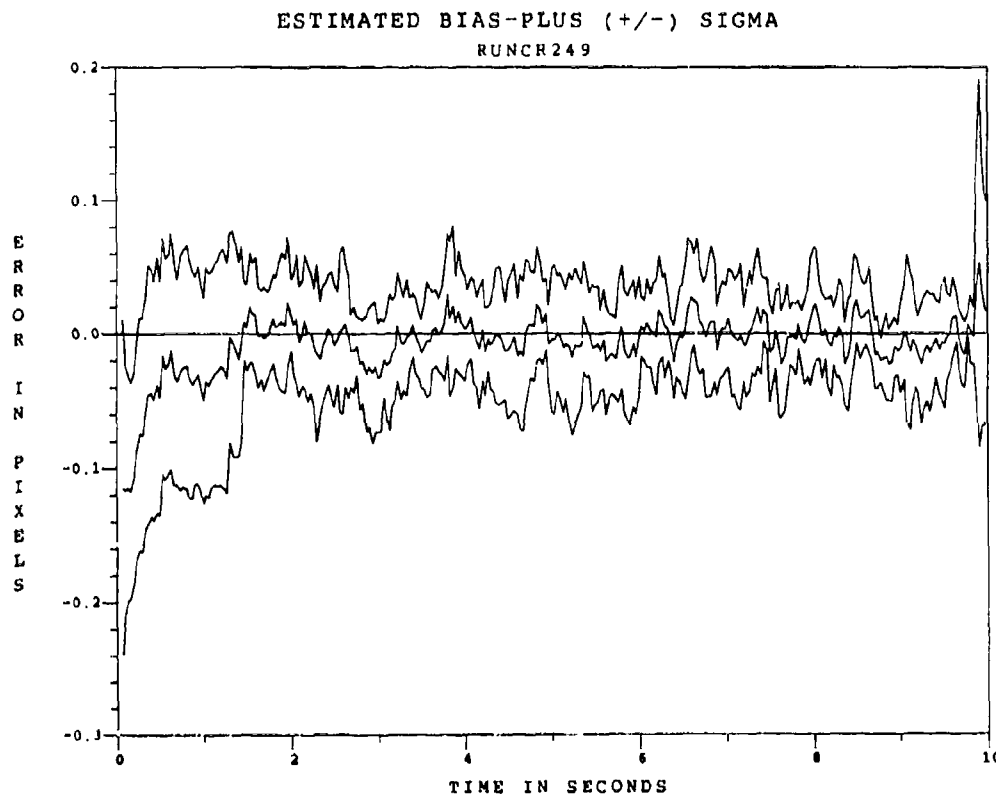


Figure F.6.12 10.5 μm Two-State Modified MAP MMAE Bias Error, $\text{SNR}=4, P_m = 0.05, \text{at } t_i^+$

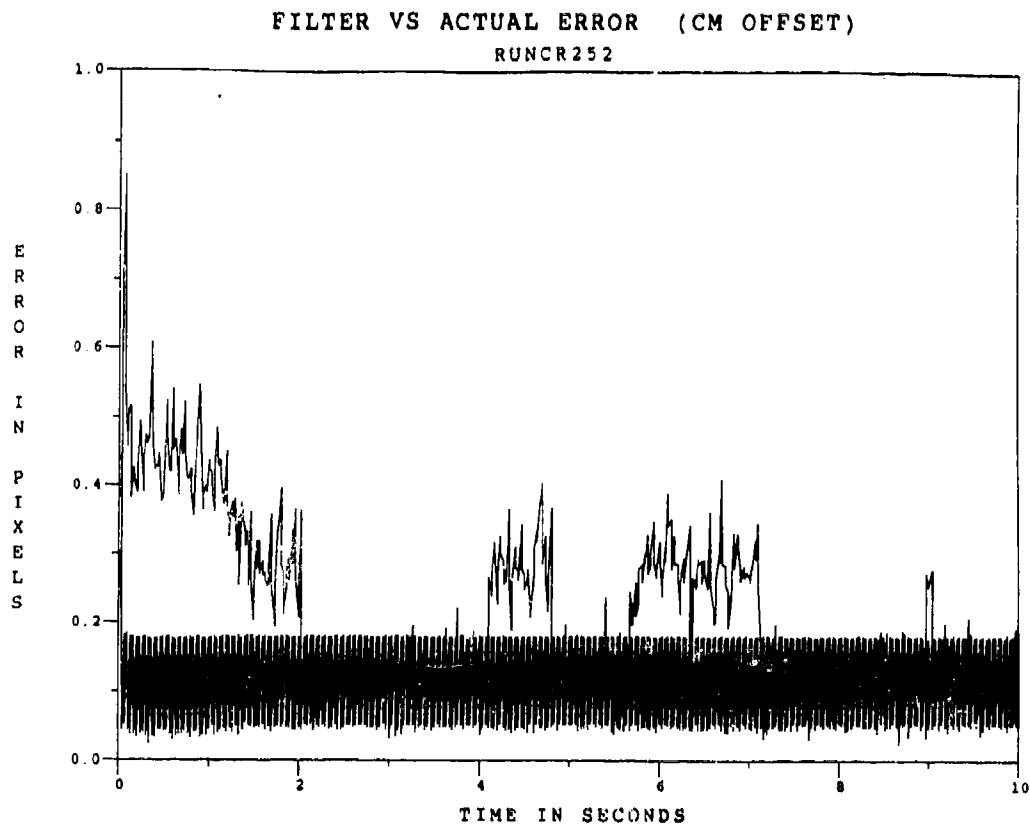


Figure F.6.13 10.5 μ m Two-State Modified MAP MMAF Offset Error, SNR = 4, $P_m = 0.30$

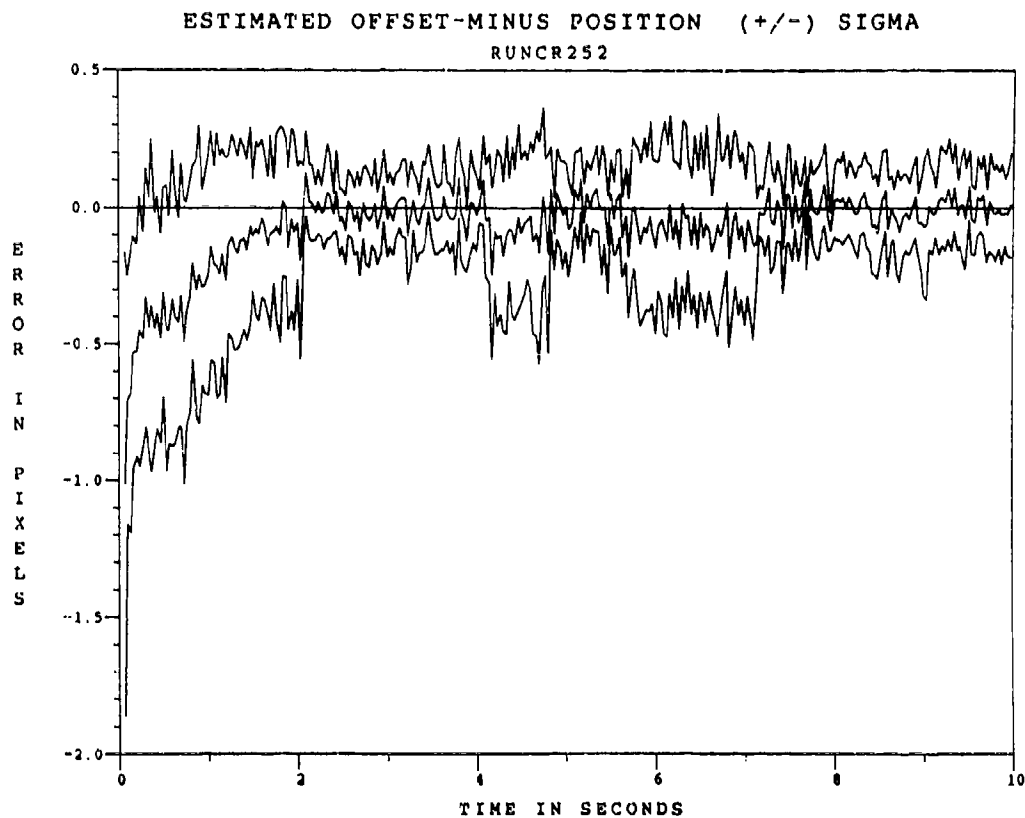


Figure F.6.14 10.5 μ m Two-State Modified MAP MMAF Offset Error, SNR=4, $P_m = 0.30$, at t_i

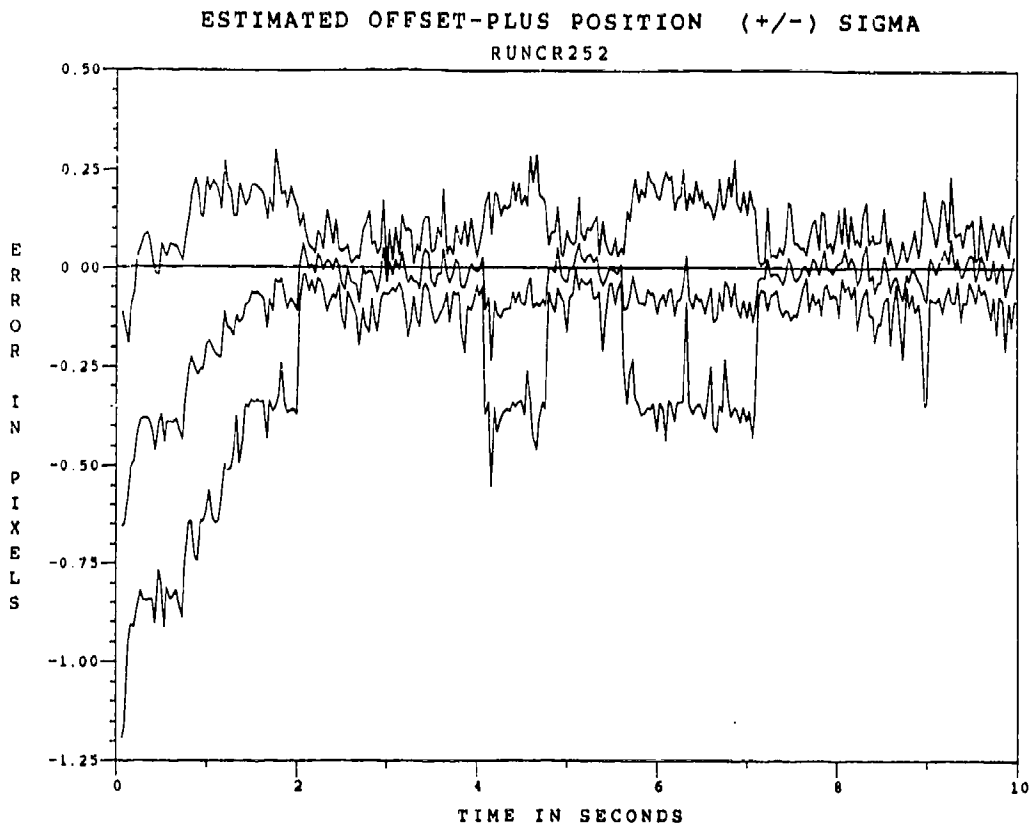


Figure F.6.15 10.5 μ m Two-State Modified MAP MMAE Offset Error, SNR=4, $P_m = 0.30$, at t_i^+

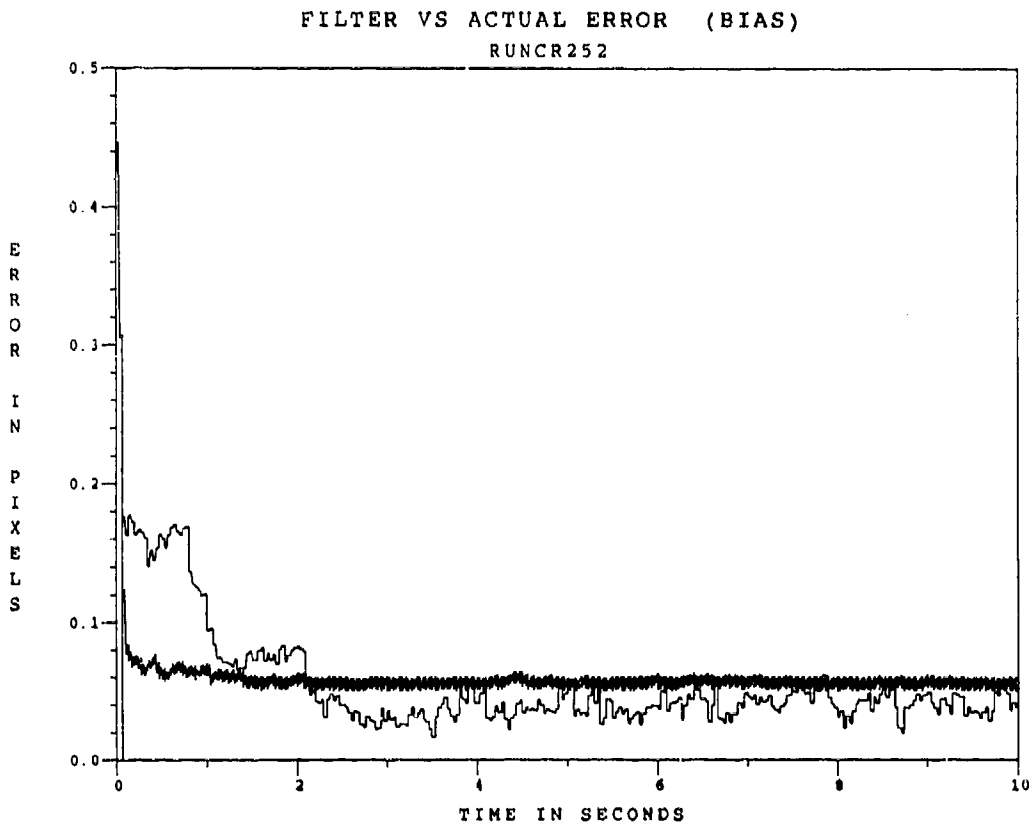


Figure F.6.16 10.5 μ m Two-State Modified MAP MMAF Bias Error, SNR = 4, $P_m = 0.30$

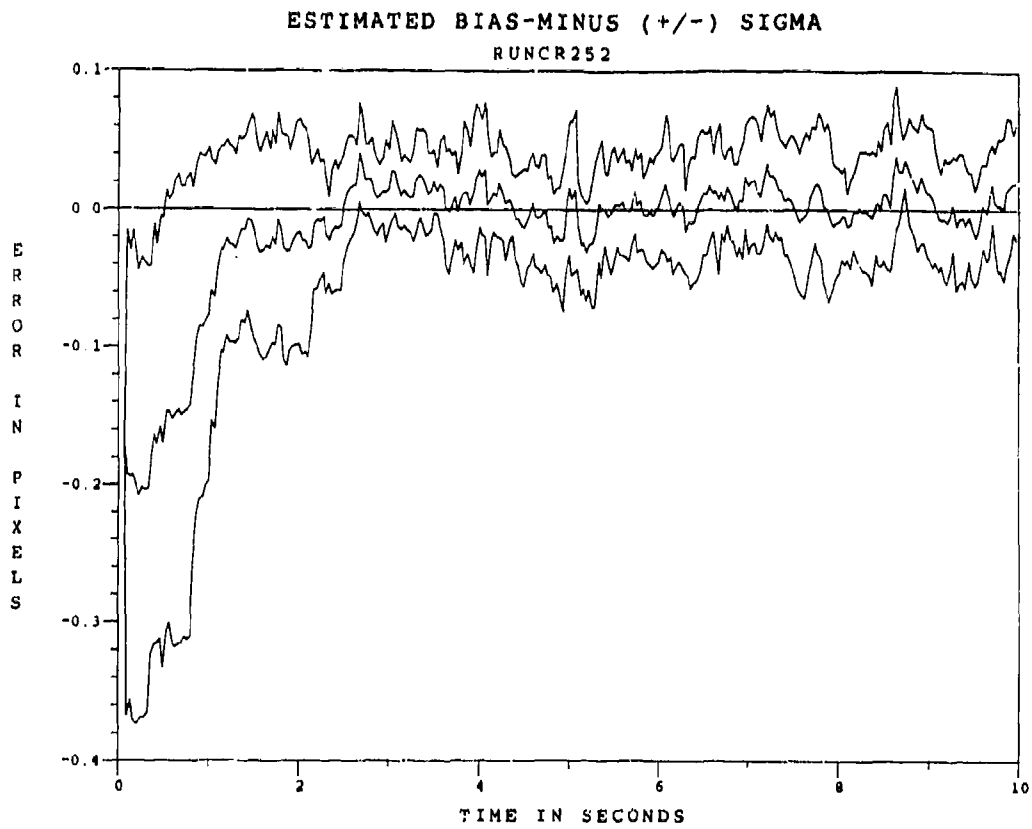


Figure F.6.17 10.5 μ m Two-State Modified MAP MMAF Bias Error, SNR=4, $P_m = -0.30$, at t_i^-

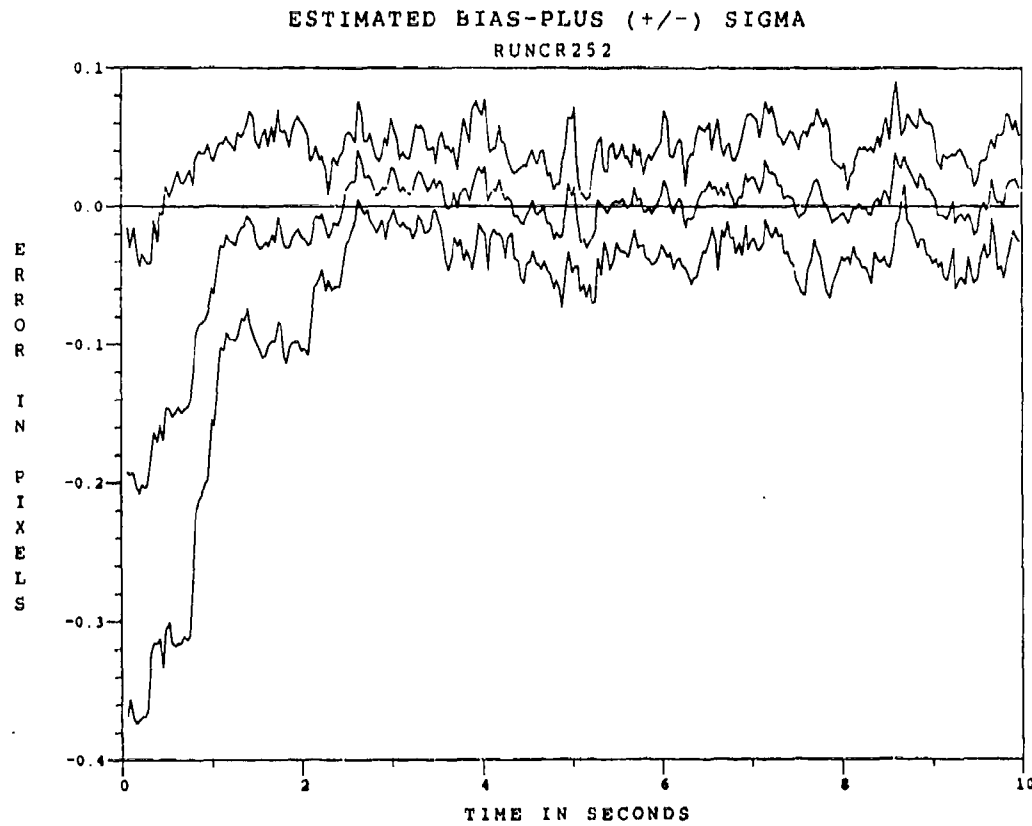


Figure F.6.18 10.5 μ m Two-State Modified MAP MMAE Bias Error, SNR=4, $P_m = -0.30$, at t_i^+

Appendix G
RMS Error Plots
for the
One-State Doppler Filter
and
Two-State Modified MAP MMAF

The graphs contained in this appendix plot the compiled performance results of the sensitivity analysis conducted upon the one-state Doppler filter and Case 1 and 2 of the two-state Modified MAP MMAF. The graphs are shown in two sets: one set presents parametric curves that give RMS errors, in units of pixels, as a function of probability-of-miss (P_m), while the parametric curves in the second set are functions of signal-to-noise ratio (SNR). This appendix is partitioned into two subappendices in the following manner:

<u>Subappendix</u>	<u>Category</u>
G.1	RMS Errors as a function of P_m
G.2	RMS Errors as a function of SNR

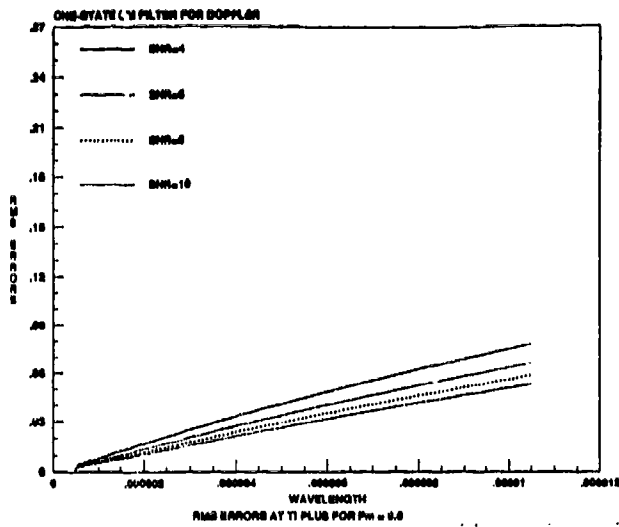
Each subappendix begins with the RMS errors at t_i^+ to present the performance after measurement, and subsequently illustrates the outcome and quality, at t_i^- , of state estimate propagation. The reader should note the difference in the RMS axis (ordinate) scale when transitioning from t_i^+ to t_i^- .

Appendix G.1

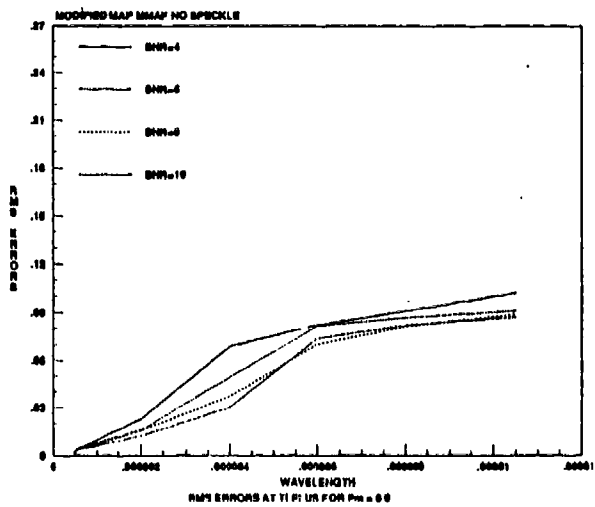
RMS Errors versus Wavelength

for a

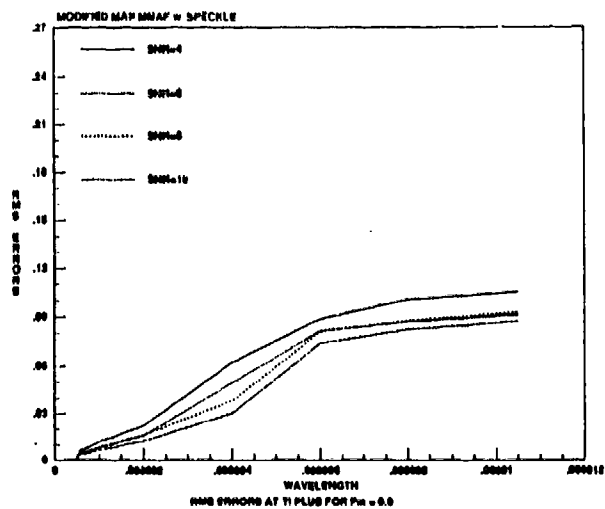
Given Probability-of-Miss



(a) One-State Doppler Filter

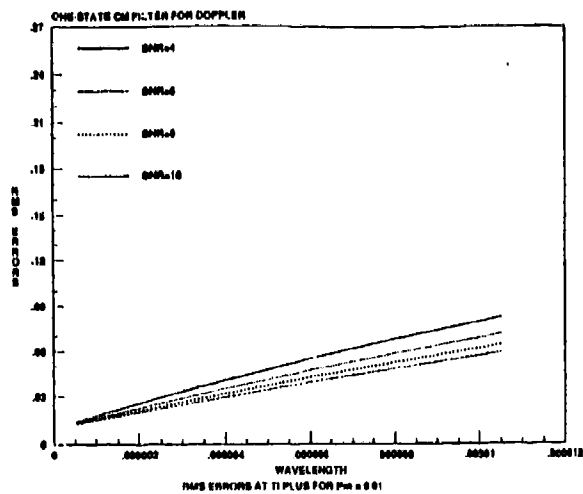


(b) Two-State Modified MAP MMAF: Case 1

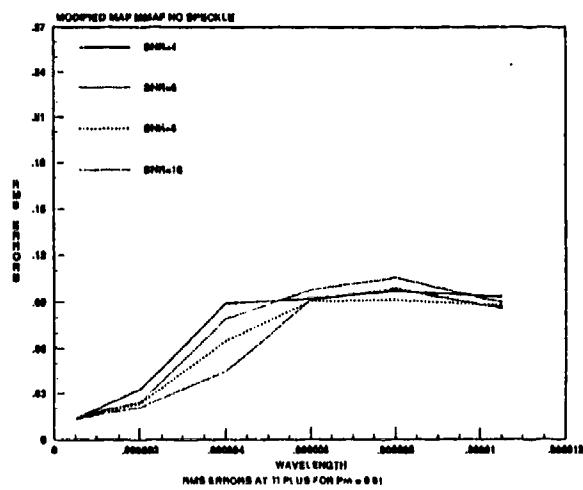


(c) Two-State Modified MAP MMAF: Case 2

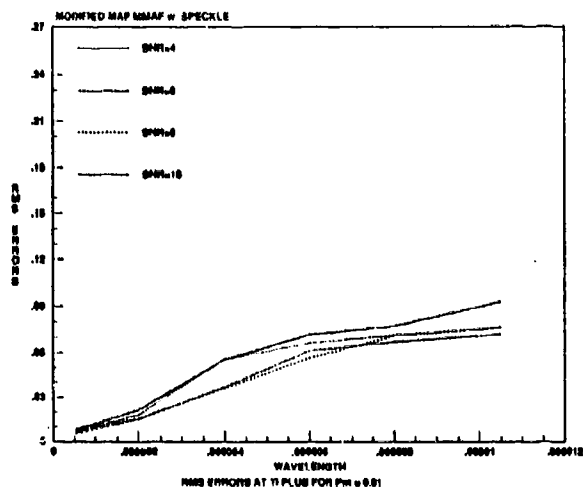
Figure G.1.1 RMS Errors for $P_m = 0.0$ at t_1^+



(a) One-State Doppler Filter

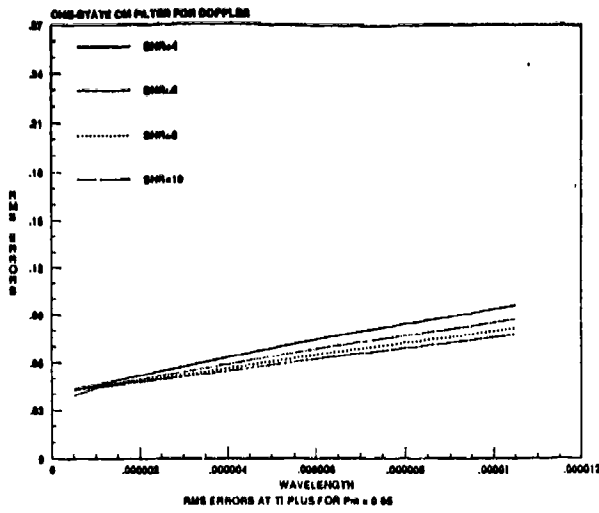


(b) Two-State Modified MAP MMAF: Case 1

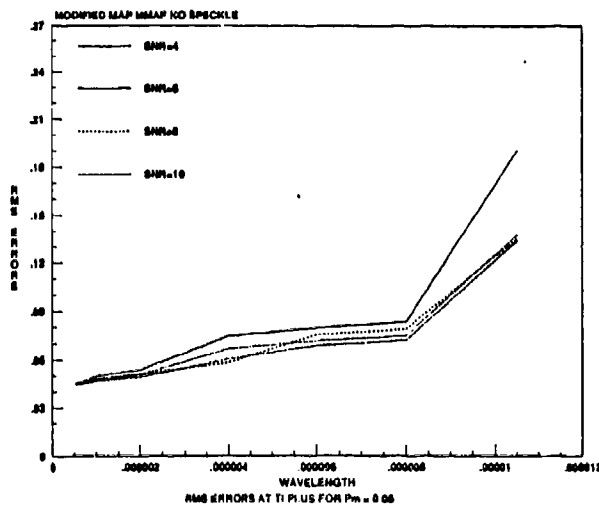


(c) Two-State Modified MAP MMAF: Case 2

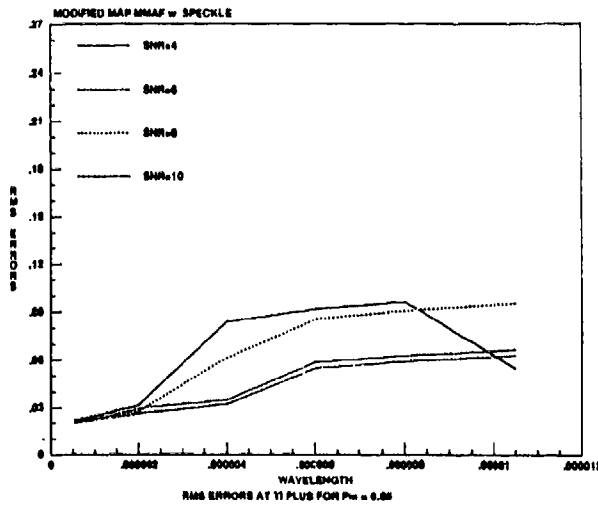
Figure G.1.2 RMS Errors for $P_m = 0.01$ at t_1^+



(a) One-State Doppler Filter

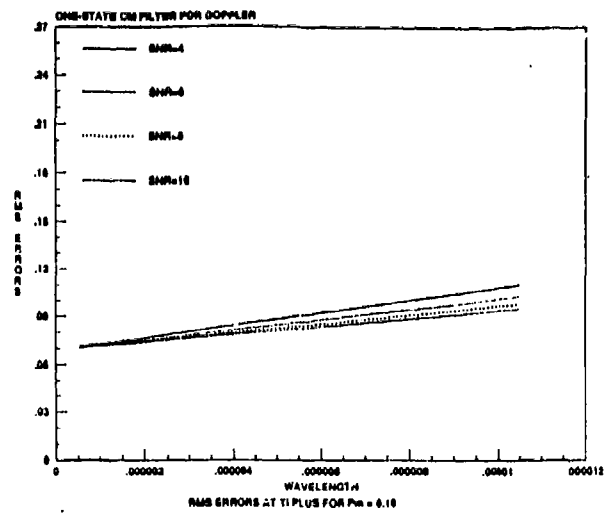


(b) Two-State Modified MAP MMAF: Case 1

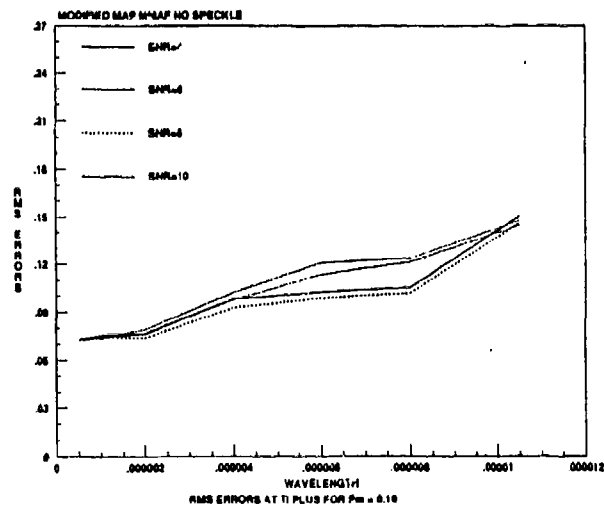


(c) Two-State Modified MAP MMAF: Case 2

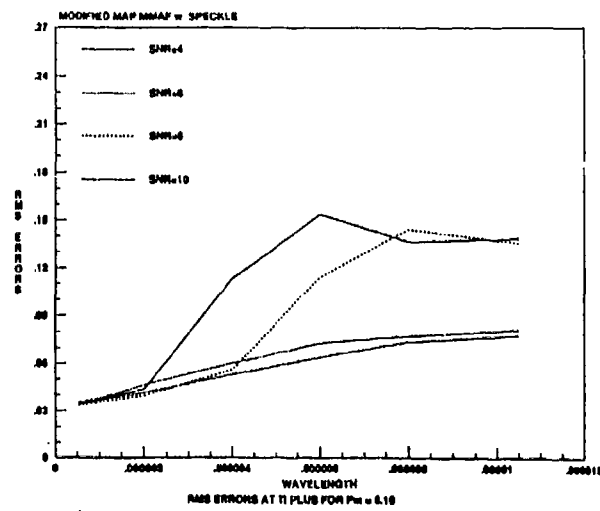
Figure G.1.3 RMS Errors for $P_m = 0.05$ at t_1^*



(a) One-State Doppler Filter

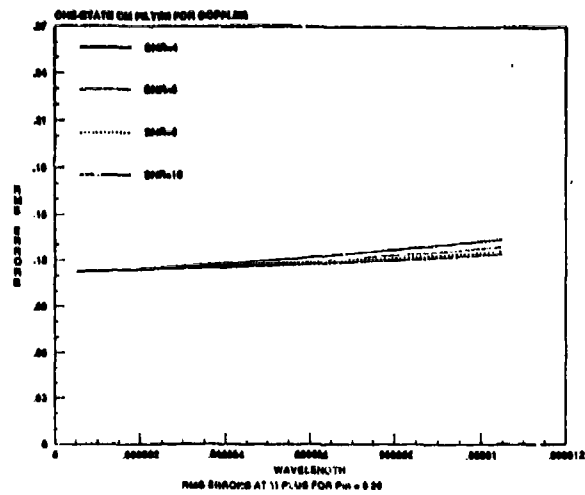


(b) Two-State Modified MAP MMAF: Case 1

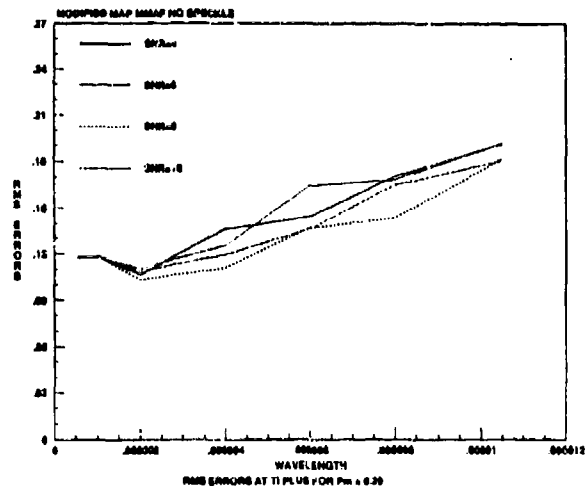


(c) Two-State Modified MAP MMAF: Case 2

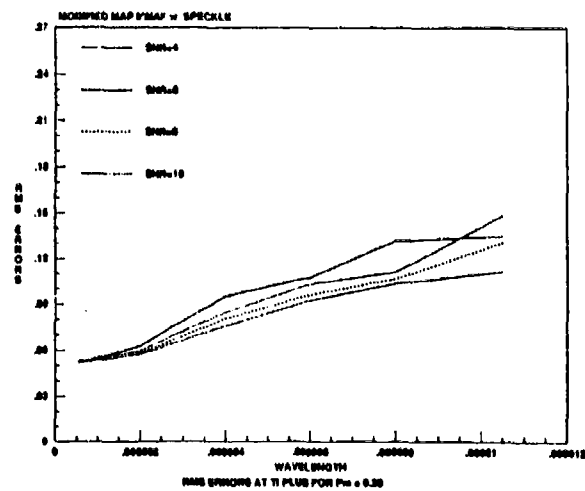
Figure G.1.4 RMS Errors for $P_m = 0.10$ at t_1^*



(a) One-State Doppler Filter

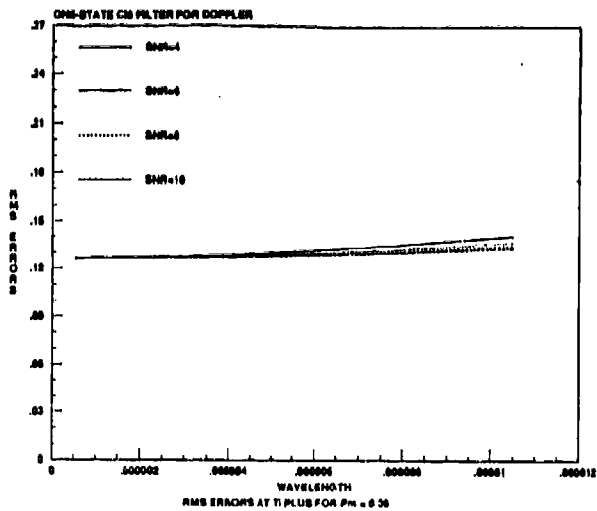


(b) Two-State Modified MAP MMAF: Case 1

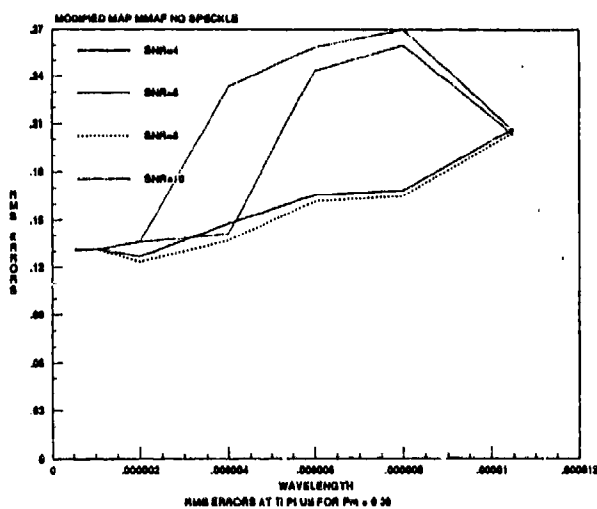


(c) Two-State Modified MAP MMAF: Case 2

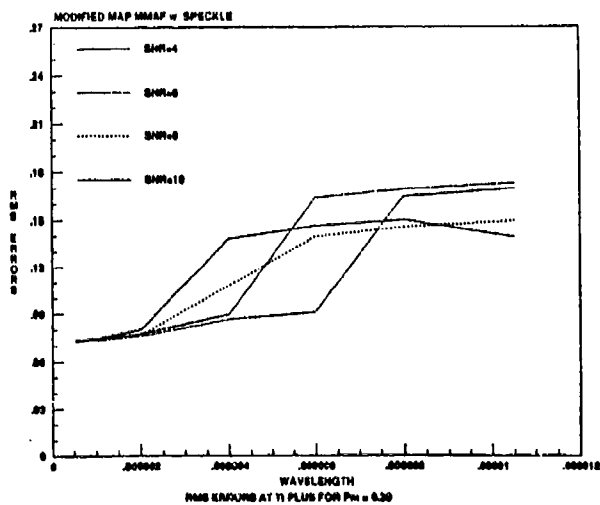
Figure G.1.5 RMS Errors for $P_m = 0.20$ at t_1^+



(a) One-State Doppler Filter

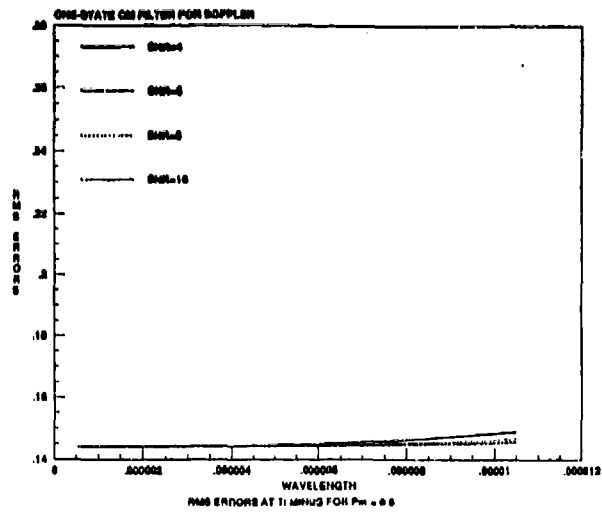


(b) Two-State Modified MAP MMAF: Case 1

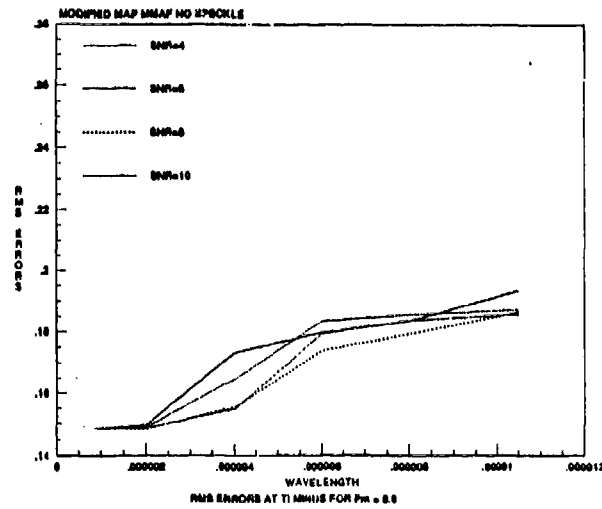


(c) Two-State Modified MAP MMAF: Case 2

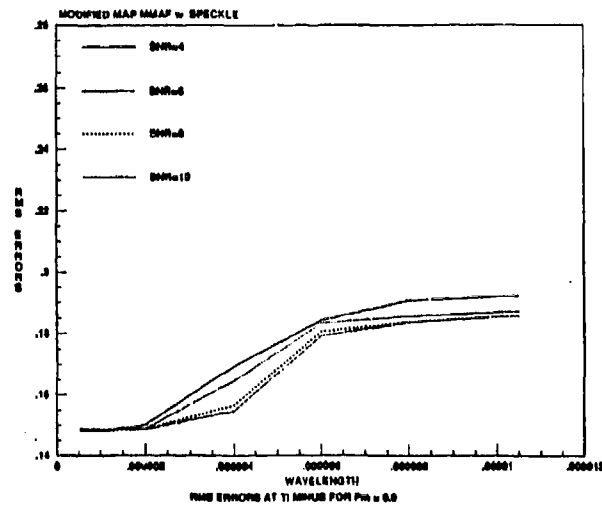
Figure G.1.6 RMS Errors for $P_n = 0.30$ at t_1^*



(a) One-State Doppler Filter

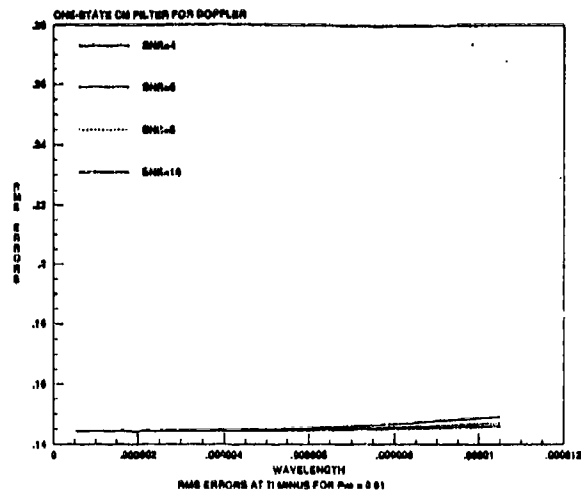


(b) Two-State Modified MAP MMAF: Case 1

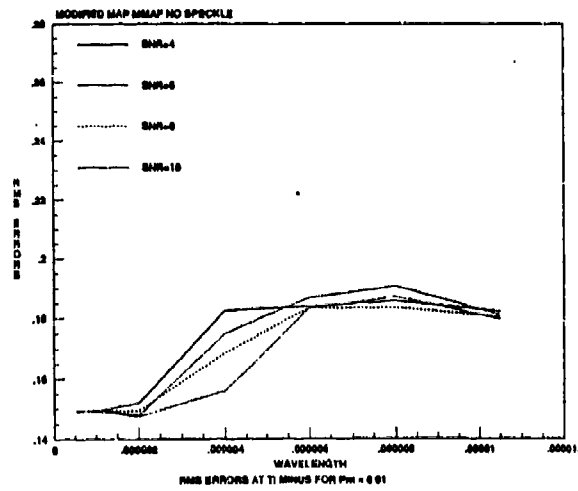


(c) Two-State Modified MAP MMAF: Case 2

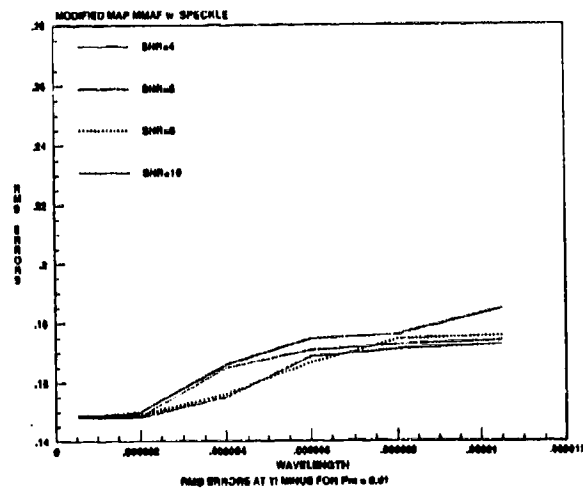
Figure G.1.7 RMS Errors for $P_{ni} = 0.0$ at t_i



(a) One-State Doppler Filter

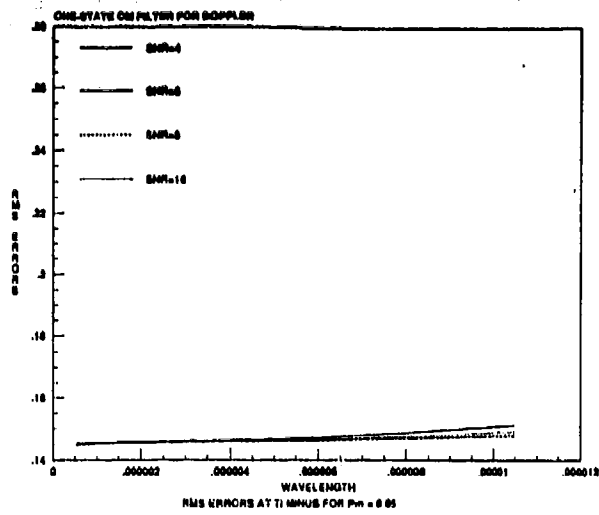


(b) Two-State Modified MAP MMAP: Case 1

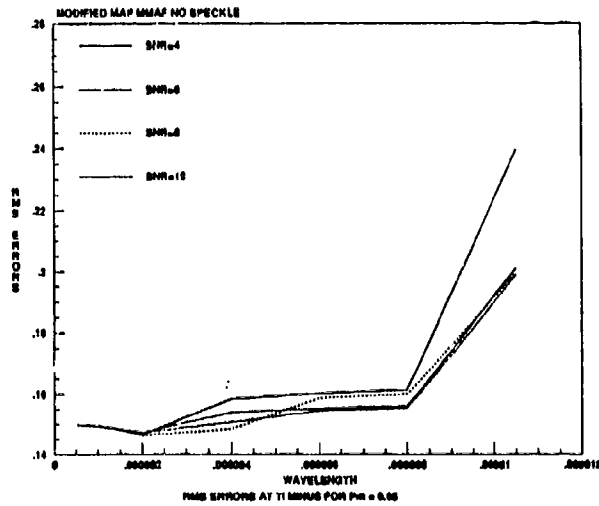


(c) Two-State Modified MAP MMAP: Case 2

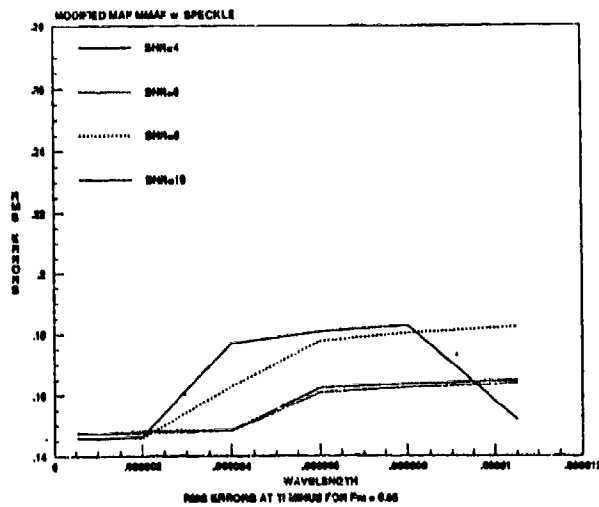
Figure G.1.8 RMS Errors for $P_m = 0.01$ at t_i



(a) One-State Doppler Filter

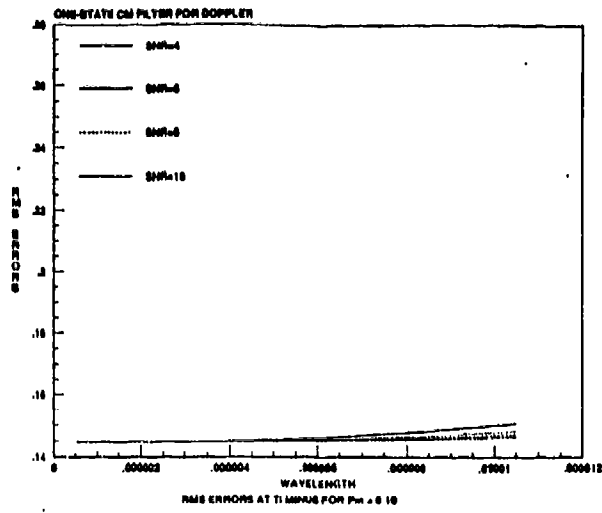


(b) Two-State Modified MAP MMAF: Case 1

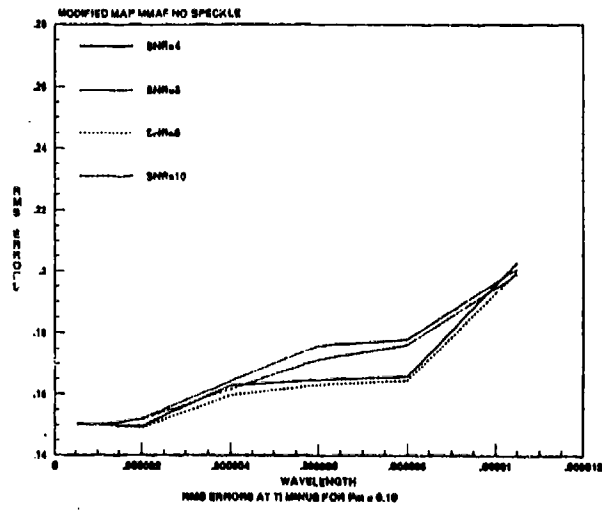


(c) Two-State Modified MAP MMAF: Case 2

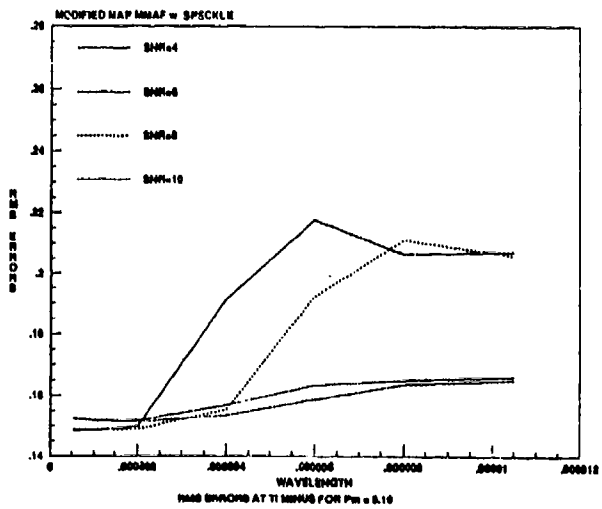
Figure G.1.9 RMS Errors for $P_{ni} = 0.05$ at t_i



(a) One-State Doppler Filter

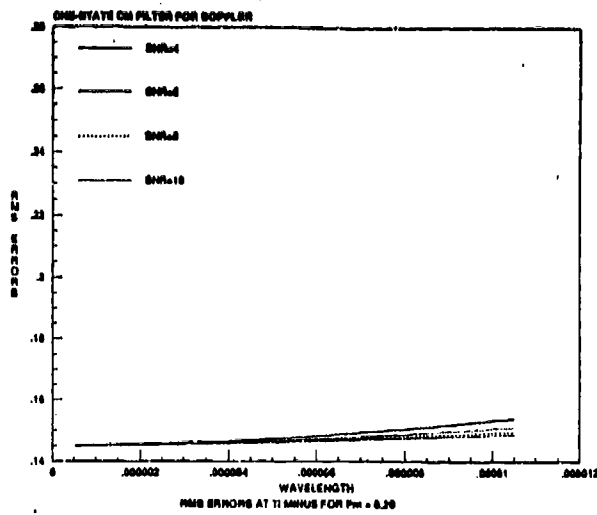


(b) Two-State Modified MAP MMAF: Case 1

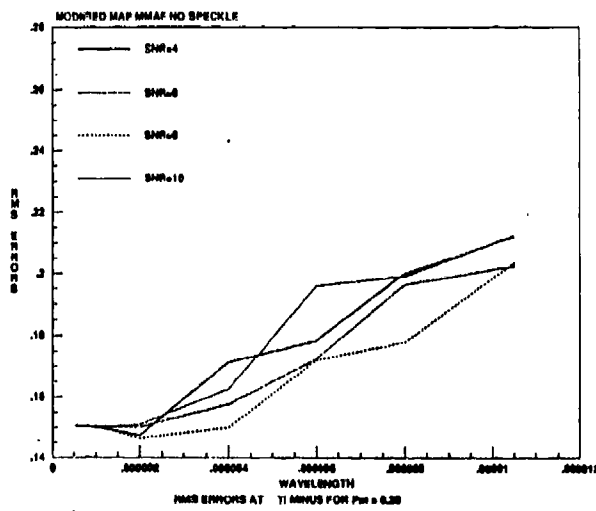


(c) Two-State Modified MAP MMAF: Case 2

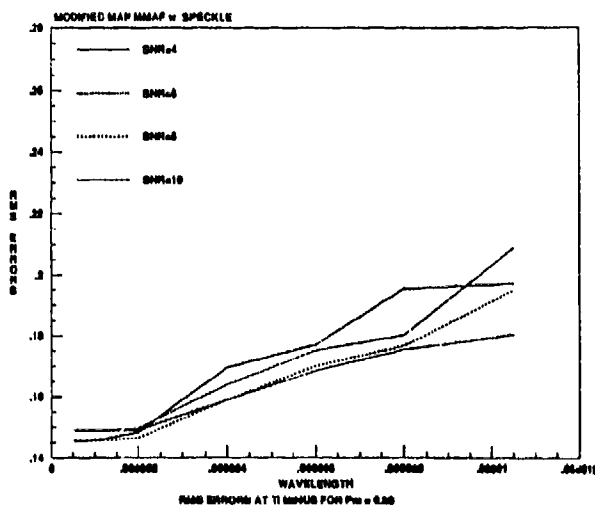
Figure G.1.10 RMS Errors for $P_m = 0.10$ at t_i



(a) One-State Doppler Filter

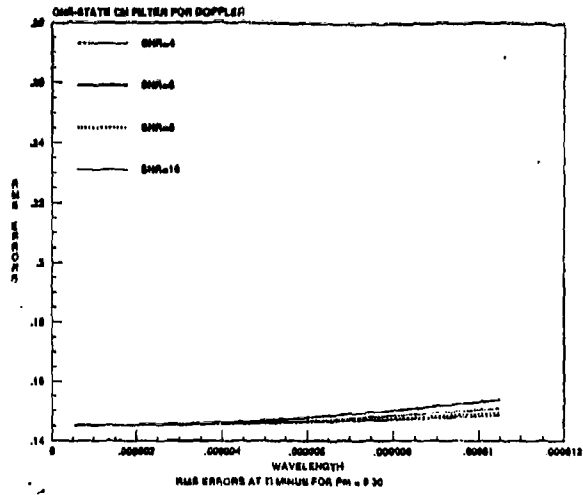


(b) Two-State Modified MAP MMAF: Case 1

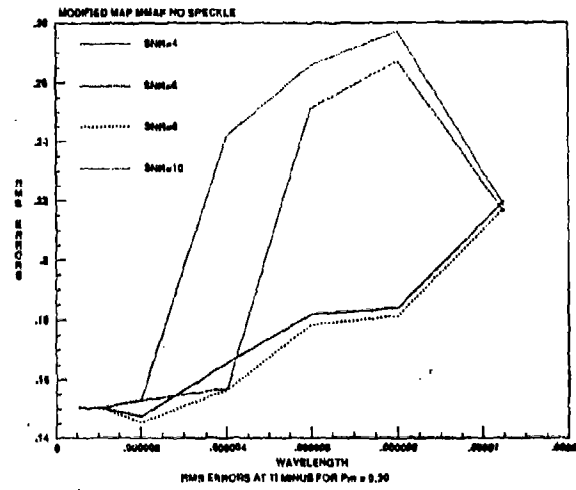


(c) Two-State Modified MAP MMAF: Case 2

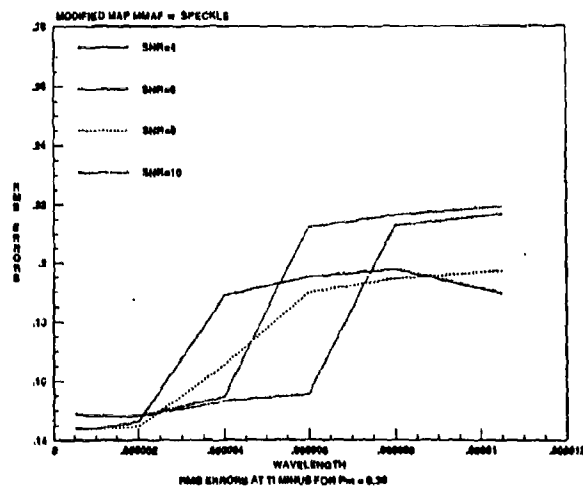
Figure G.1.11 RMS Errors for $P_m = 0.20$ at t_i



(a) One-State Doppler Filter



(b) Two-State Modified MAP MMAF: Case 1



(c) Two-State Modified MAP MMAF: Case 2

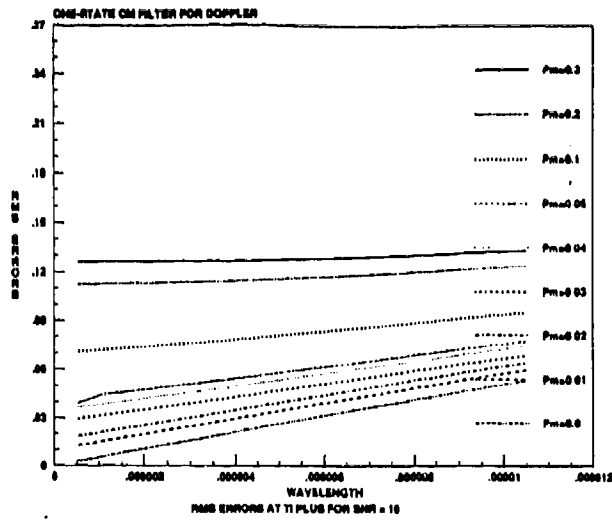
Figure G.1.12 RMS Errors for $P_m = 0.30$ at t_i

Appendix G.2

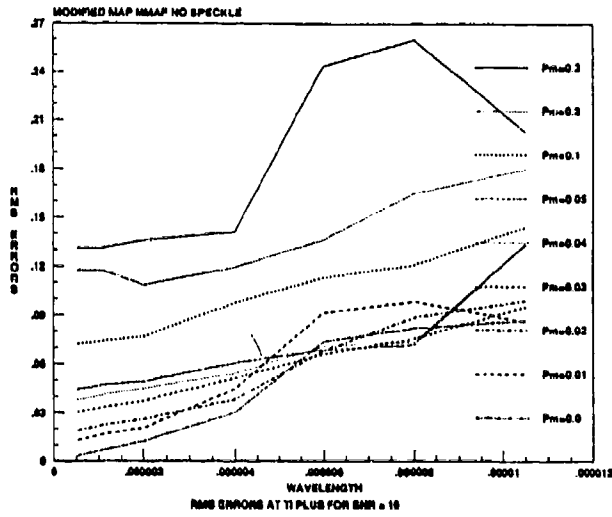
RMS Errors versus Wavelength

for a

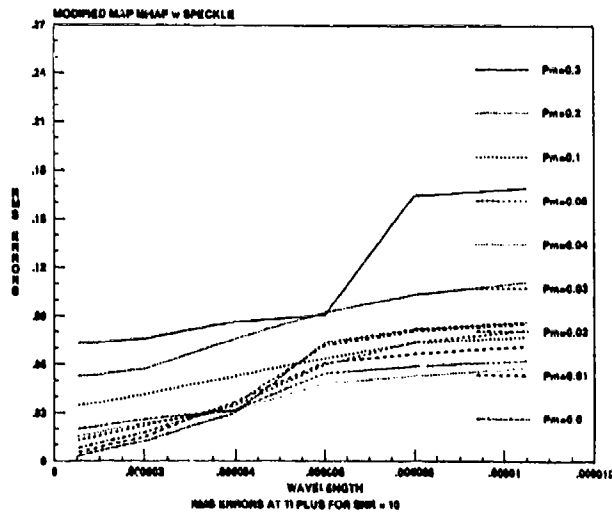
Given Signal-to-Noise Ratio



(a) One-State Doppler Filter

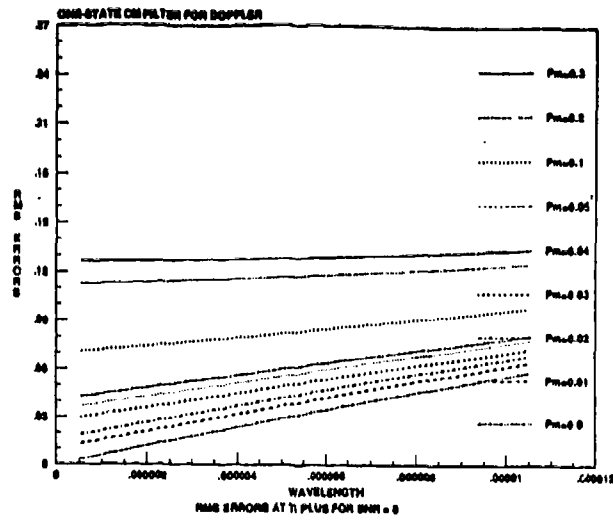


(b) Two-State Modified MAP MMAF: Case 1

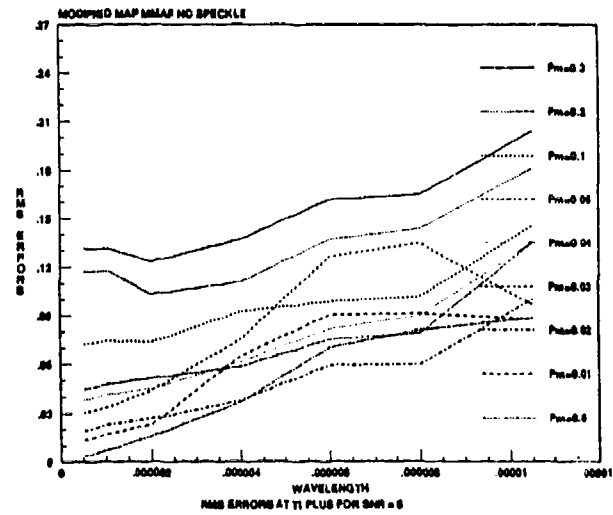


(c) Two-State Modified MAP MMAF: Case 2

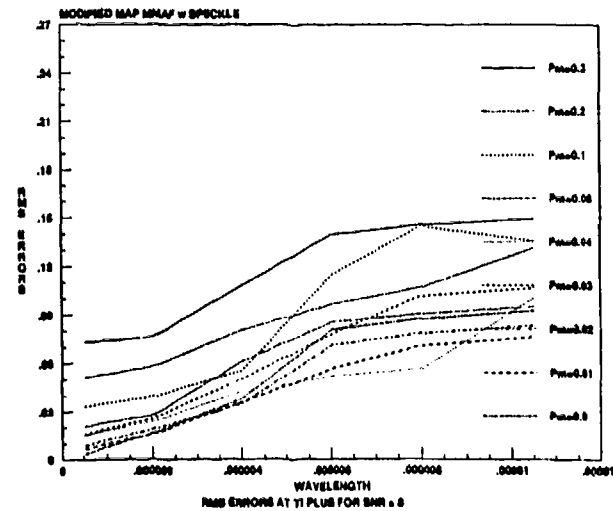
Figure G.2.1 RMS Errors for SNR = 10 at t_i^+



(a) One-State Doppler Filter

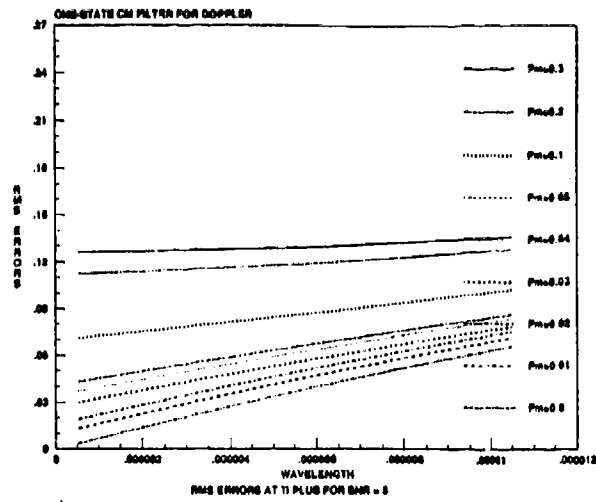


(b) Two-State Modified MAP MMAF: Case 1

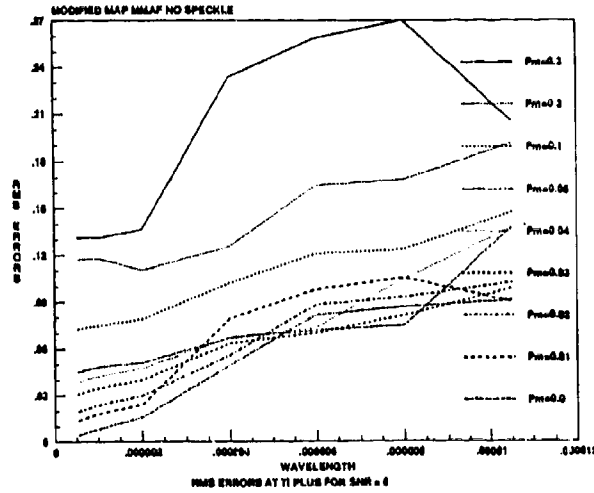


(c) Two-State Modified MAP MMAF: Case 2

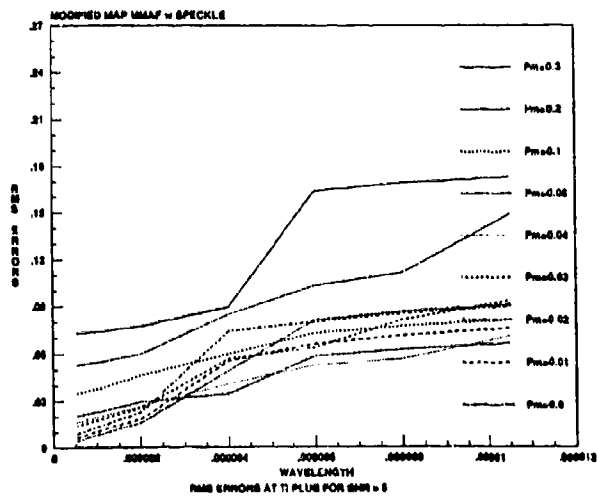
Figure G.2.2 RMS Errors for SNR = 8 at t_1^*



(a) One-State Doppler Filter

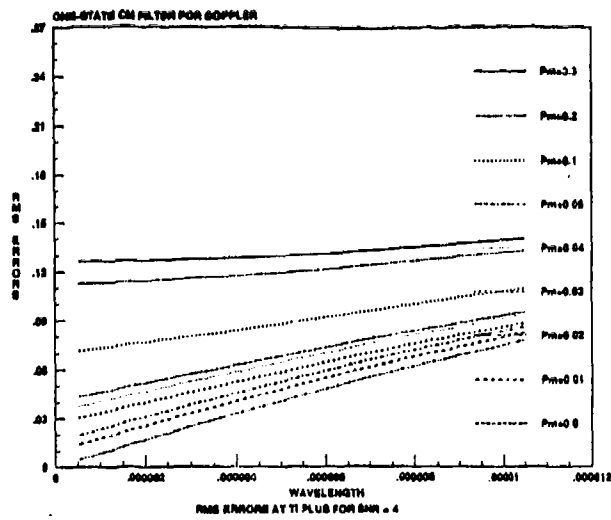


(b) Two-State Modified MAP MMAF: Case 1

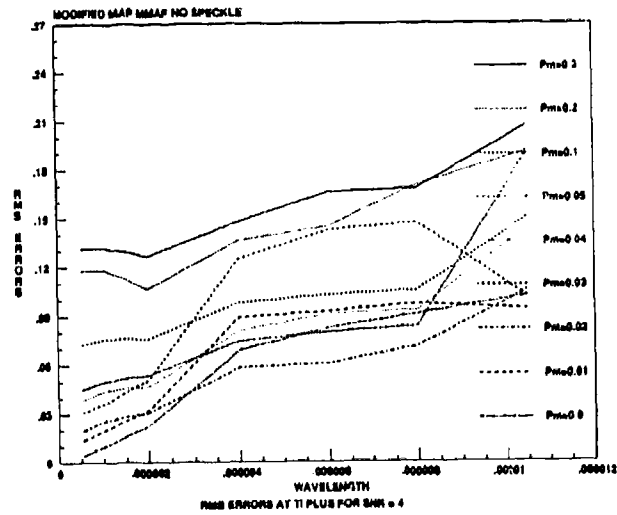


(c) Two-State Modified MAP MMAF: Case 2

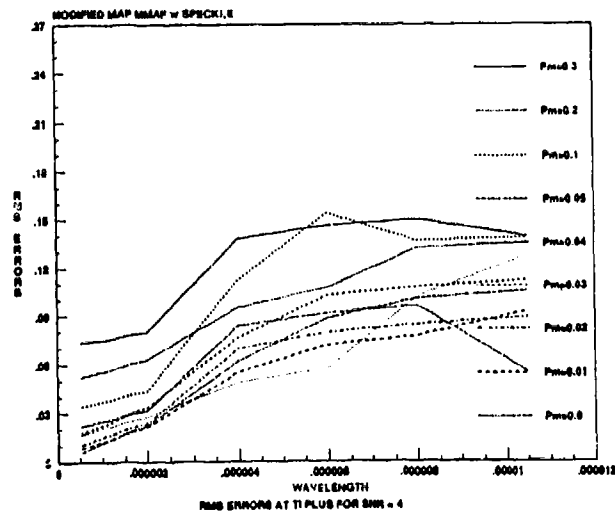
Figure G.2.3 RMS Errors for SNR = 6 at t_1^*



(a) One-State Doppler Filter

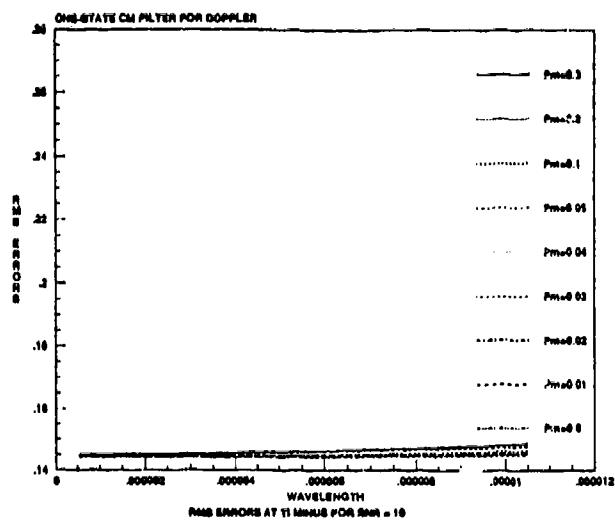


(b) Two-State Modified MAP MMAF: Case 1

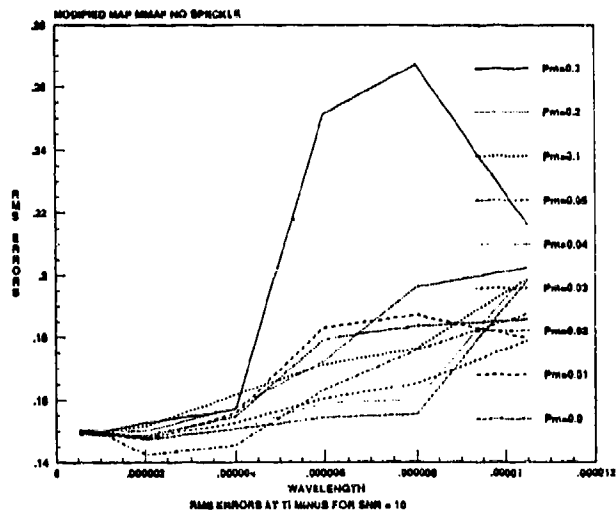


(c) Two-State Modified MAP MMAF: Case 2

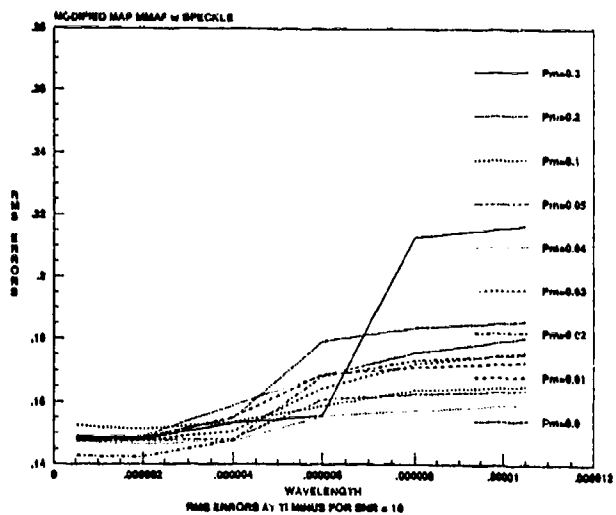
Figure G.2.4 RMS Errors for SNR = 4 at t_i^*



(a) One-State Doppler Filter

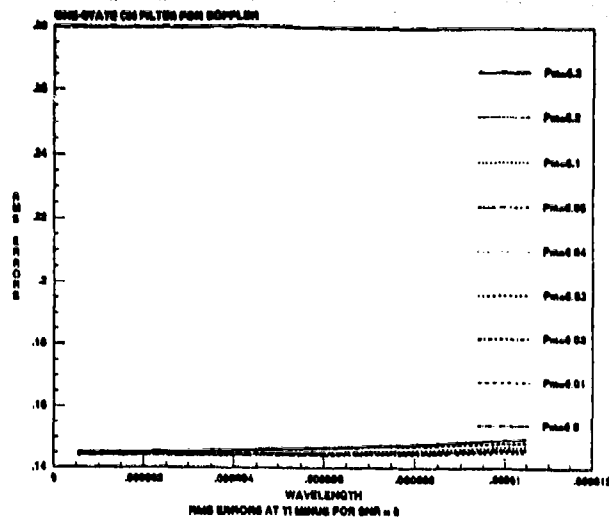


(b) Two-State Modified MAP MMAF: Case 1

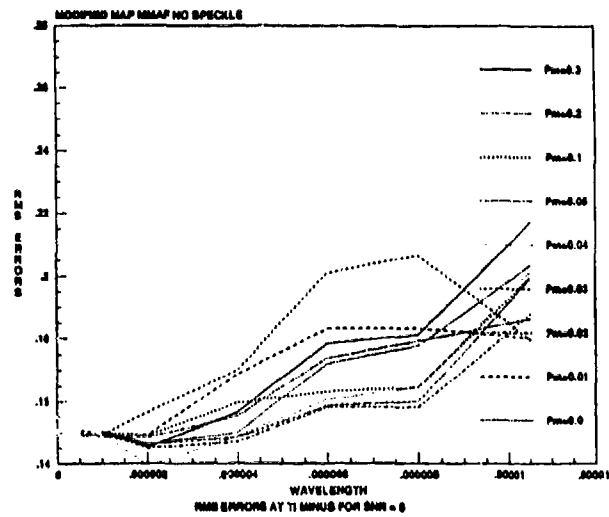


(c) Two-State Modified MAP MMAF: Case 2

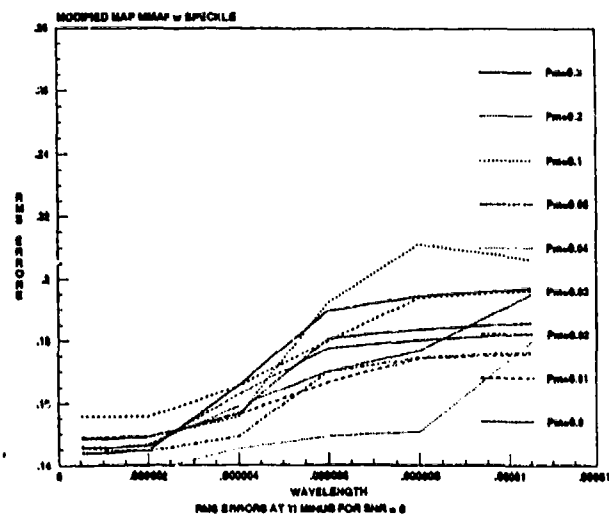
Figure G.2.5 RMS Errors for SNR = 10 at t_i



(a) One-State Doppler Filter

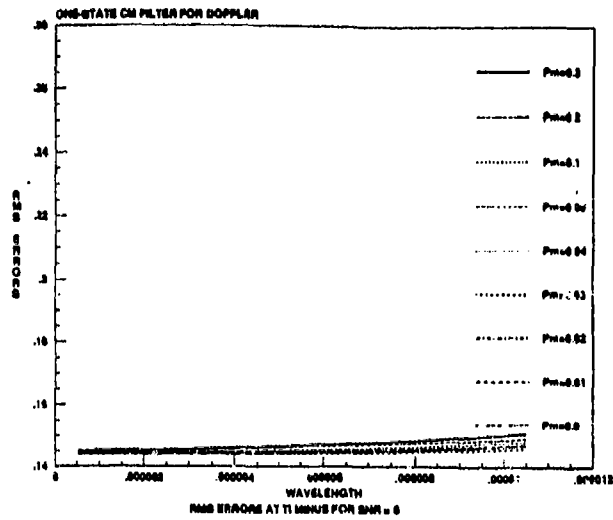


(b) Two-State Modified MAP MMAF: Case 1

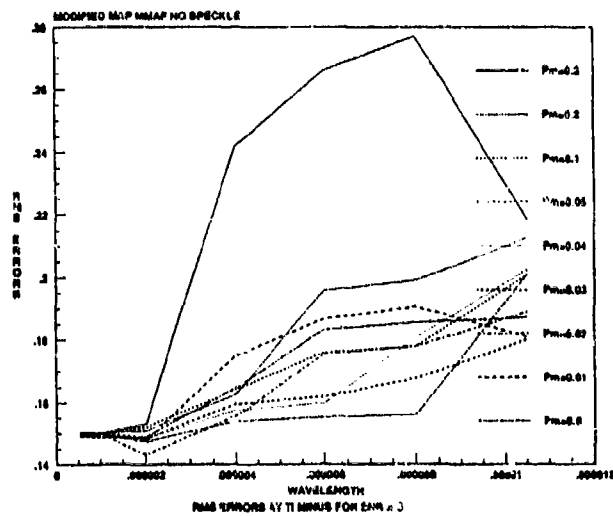


(c) Two-State Modified MAP MMAF: Case 2

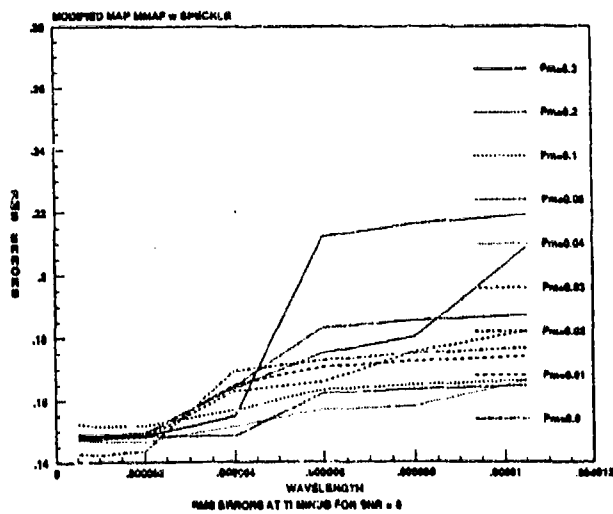
Figure G.2.6 RMS Errors for SNR = 8 at t_i



(a) One-State Doppler Filter

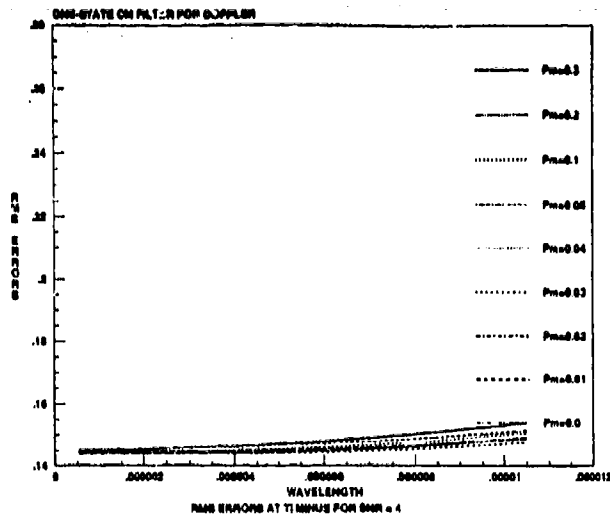


(b) Two-State Modified MAP MMAF: Case 1

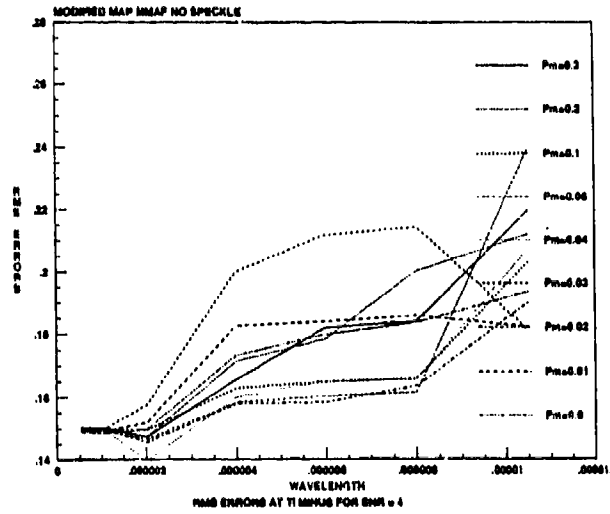


(c) Two-State Modified MAP MMAF: Case 2

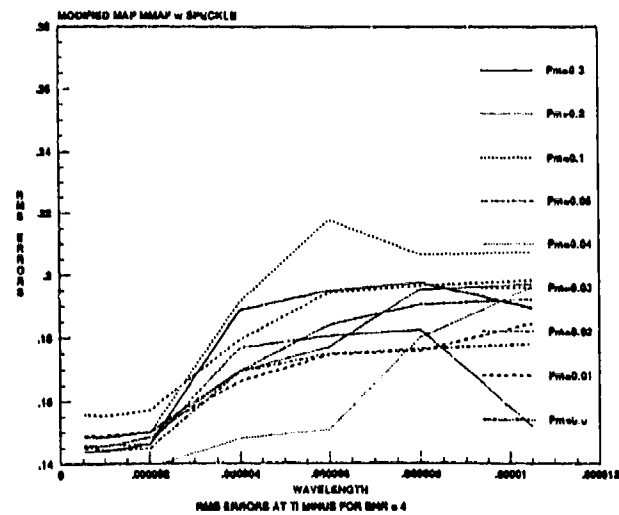
Figure G.2.7 RMS Errors for SNR = 6 at t_i



(a) One-State Doppler Filter



(b) Two-State Modified MAP MMAF: Case 1



(c) Two-State Modified MAP MMAF: Case 2

Figure G.2.8 RMS Errors for SNR = 4 at t_i

Appendix H

Tables

This appendix contains three tables that list the results of the respective sensitivity analysis performed on the one-state Doppler filter and on Cases 1 and 2 of the two-state Modified MAP MMAF. The tables list the average mean errors and average standard deviations, in units of pixels, before measurement update at t_i^- and after measurement update at t_i^+ . Note that, as a result of the output format of the Fortran-coded simulation, the data is shown with five significant figures. In actuality, three significant figures will suffice for analyzing the data.

Table H.1 One-State Doppler Filter Offset Error Statistics (in Pixels)

$\lambda, \mu\text{m}$	SNR	P_m	$\text{mean}(t_i^-)$	$\text{mean}(t_i^+)$	$1\sigma(t_i^-)$	$1\sigma(t_i^+)$
0.53	10	0.0	-0.30391E-04	0.15079E-03	0.14402E+00	0.28674E-02
		.01	-0.13520E-03	0.14715E-02	0.14436E+00	0.12484E-01
		.02	-0.55185E-03	0.16988E-02	0.14479E+00	0.18428E-01
		.03	-0.85223E-03	0.94931E-03	0.14461E+00	0.29420E-01
		.04	-0.44544E-03	0.85601E-04	0.14509E+00	0.36668E-01
		.05	0.27581E-03	0.64996E-03	0.14478E+00	0.39320E-01
		.10	0.44882E-03	0.50387E-03	0.14477E+00	0.70834E-01
		.20	0.31482E-02	0.39645E-02	0.14495E+00	0.11249E+00
		.30	0.30750E-02	0.32894E-02	0.14520E+00	0.12629E+00
			8	0.0	-0.13815E-04	0.16873E-03
.01	-0.12149E-03			0.14870E-02	0.14436E+00	0.12800E-01
.02	-0.53712E-03			0.17176E-02	0.14480E+00	0.18733E-01
.03	-0.83849E-03			0.96113E-03	0.14461E+00	0.29670E-01
.04	-0.43344E-03			0.97137E-04	0.14509E+00	0.36905E-01
.05	-0.59301E-04			0.32913E-03	0.14524E+00	0.42879E-01
.10	0.45783E-03			0.50925E-03	0.14477E+00	0.70968E-01
.20	0.31588E-02			0.39750E-02	0.14496E+00	0.11253E+00
.30	0.30816E-02			0.32949E-02	0.14520E+00	0.12630E+00
	6			0.0	0.90539E-05	0.19443E-03
		.01	-0.10140E-03	0.15119E-02	0.14436E+00	0.13258E-01
		.02	-0.51895E-03	0.17452E-02	0.14482E+00	0.19176E-01
		.03	-0.81892E-03	0.97926E-03	0.14459E+00	0.30039E-01
		.04	-0.41581E-03	0.11512E-03	0.14508E+00	0.37255E-01
		.05	-0.33936E-04	0.34924E-03	0.14526E+00	0.43200E-01
		.10	0.46960E-03	0.51677E-03	0.14477E+00	0.71165E-01
		.20	0.31751E-02	0.39916E-02	0.14498E+00	0.11259E+00
		.30	0.30933E-02	0.33013E-02	0.14520E+00	0.12631E+00
			4	0.0	0.51095E-04	0.23792E-03
.01	-0.68101E-04			0.15506E-02	0.14437E+00	0.14030E-01
.02	-0.48477E-03			0.17917E-02	0.14485E+00	0.19918E-01
.03	-0.78556E-03			0.10110E-02	0.14457E+00	0.30657E-01
.04	-0.38538E-03			0.14446E-03	0.14507E+00	0.37841E-01
.05	0.46723E-05			0.38337E-03	0.14528E+00	0.43738E-01
.10	0.49465E-03			0.53090E-03	0.14477E+00	0.71501E-01
.20	0.31985E-02			0.40154E-02	0.14501E+00	0.11270E+00
.30	0.31100E-02			0.33113E-02	0.14521E+00	0.12634E+00

$\lambda, \mu\text{m}$	SNR	P_m	$\text{mean}(t_i^-)$	$\text{mean}(t_i^+)$	$1\sigma(t_i^-)$	$1\sigma(t_i^+)$		
1.06	10	0.0	0.10966E-03	0.30011E-03	0.14399E+00	0.57299E-02		
		.01	-0.18792E-04	0.16088E-02	0.14437E+00	0.15143E-01		
		.02	-0.43944E-03	0.18588E-02	0.14490E+00	0.20993E-01		
		.03	-0.73669E-03	0.10555E-02	0.14453E+00	0.31550E-01		
		.04	-0.34100E-03	0.18836E-03	0.14506E+00	0.38690E-01		
		.05	0.61238E-04	0.43743E-03	0.14532E+00	0.44521E-01		
		.10	0.52479E-03	0.54857E-03	0.14476E+00	0.71983E-01		
		.20	0.32340E-02	0.40506E-02	0.14506E+00	0.11285E+00		
		.30	0.31360E-02	0.33297E-02	0.14521E+00	0.12639E+00		
			8	0.0	0.14194E-03	0.33509E-03	0.14399E+00	0.64031E-02
				.01	0.86867E-05	0.16399E-02	0.14437E+00	0.15769E-01
.02	-0.40992E-03			0.18991E-02	0.14493E+00	0.21599E-01		
.03	-0.70981E-03			0.10797E-02	0.14452E+00	0.32057E-01		
.04	-0.31472E-03			0.21480E-03	0.14505E+00	0.39171E-01		
.05	0.95668E-04			0.46626E-03	0.14534E+00	0.44960E-01		
.10	0.54414E-03			0.56194E-03	0.14476E+00	0.72260E-01		
.20	0.32550E-02			0.40729E-02	0.14509E+00	0.11294E+00		
.30	0.31499E-02			0.33371E-02	0.14522E+00	0.12642E+00		
	6			0.0	0.18916E-03	0.38860E-03	0.14399E+00	0.73915E-02
				.01	0.46878E-04	0.16886E-02	0.14438E+00	0.16686E-01
		.02	-0.37135E-03	0.19551E-02	0.14496E+00	0.22486E-01		
		.03	-0.67082E-03	0.11159E-02	0.14449E+00	0.32798E-01		
		.04	-0.27818E-03	0.25151E-03	0.14504E+00	0.39875E-01		
		.05	0.13868E-03	0.50515E-03	0.14553E+00	0.45659E-01		
		.10	0.57420E-03	0.58121E-03	0.14476E+00	0.72665E-01		
		.20	0.32855E-02	0.41035E-02	0.14513E+00	0.11308E+00		
		.30	0.31693E-02	0.33490E-02	0.14523E+00	0.12646E+00		
			4	0.0	0.27054E-03	0.47438E-03	0.14399E+00	0.90476E-02
				.01	0.11542E-03	0.17660E-02	0.14439E+00	0.18225E-01
.02	-0.30594E-03			0.20457E-02	0.14503E+00	0.23970E-01		
.03	-0.60589E-03			0.11753E-02	0.14445E+00	0.34044E-01		
.04	-0.21550E-03			0.30985E-03	0.14502E+00	0.41059E-01		
.05	0.21941E-03			0.58013E-03	0.14543E+00	0.46695E-01		
.10	0.61749E-03			0.60915E-03	0.14476E+00	0.73352E-01		
.20	0.33364E-02			0.41543E-02	0.14521E+00	0.11332E+00		
.30	0.32044E-02			0.33708E-02	0.14525E+00	0.12655E+00		

$\lambda, \mu\text{m}$	SNR	P_m	$\text{mean}(t_i^-)$	$\text{mean}(t_i^+)$	$1\sigma(t_i^-)$	$1\sigma(t_i^+)$
2.01	10	0.0	0.36007E-03	0.56858E-03	0.14399E+00	0.10843E-01
		.01	0.18846E-03	0.18493E-02	0.14439E+00	0.19898E-01
		.02	-0.23438E-03	0.21442E-02	0.14510E+00	0.25584E-01
		.03	-0.53112E-03	0.12396E-02	0.14440E+00	0.35400E-01
		.04	-0.14913E-03	0.37758E-03	0.14500E+00	0.42347E-01
		.05	0.30485E-03	0.65790E-03	0.14549E+00	0.47879E-01
		.10	0.66959E-03	0.64378E-03	0.14476E+00	0.74103E-01
		.20	0.33901E-02	0.42120E-02	0.14529E+00	0.11359E+00
		.30	0.32428E-02	0.33960E-02	0.14523E+00	0.12665E+00
			8	0.0	0.42186E-03	0.63403E-03
.01	0.23947E-03			0.19071E-02	0.14440E+00	0.21080E-01
.02	-0.18464E-03			0.22135E-02	0.14515E+00	0.26728E-01
.03	-0.47973E-03			0.12874E-02	0.14437E+00	0.36365E-01
.04	-0.10038E-03			0.42364E-03	0.14499E+00	0.43262E-01
.05	0.36534E-03			0.71350E-03	0.14553E+00	0.48721E-01
.10	0.70537E-03			0.66689E-03	0.14476E+00	0.74643E-01
.20	0.34280E-02			0.42508E-02	0.14535E+00	0.11379E+00
.30	0.32698E-02			0.34130E-02	0.14530E+00	0.12673E+00
	6			0.0	0.51366E-03	0.73359E-03
		.01	0.31640E-03	0.19946E-02	0.14442E+00	0.22816E-01
		.02	-0.10962E-03	0.23134E-02	0.14522E+00	0.28401E-01
		.03	-0.40409E-03	0.13527E-02	0.14433E+00	0.37779E-01
		.04	-0.26314E-04	0.49365E-03	0.14497E+00	0.44610E-01
		.05	0.45673E-03	0.79641E-03	0.14559E+00	0.49958E-01
		.10	0.75925E-03	0.70574E-03	0.14477E+00	0.75444E-01
		.20	0.34868E-02	0.43103E-02	0.14544E+00	0.11409E+00
		.30	0.33089E-02	0.34390E-02	0.14535E+00	0.12686E+00
			4	0.0	0.66680E-03	0.89720E-03
.01	0.44352E-03			0.21331E-02	0.14444E+00	0.25713E-01
.02	0.17095E-04			0.24826E-02	0.14535E+00	0.31197E-01
.03	-0.27951E-03			0.14609E-02	0.14426E+00	0.40153E-01
.04	0.92439E-04			0.60917E-03	0.14495E+00	0.46868E-01
.05	0.60920E-03			0.93585E-03	0.14569E+00	0.52037E-01
.10	0.84940E-03			0.77198E-03	0.14478E+00	0.76803E-01
.20	0.35800E-02			0.44078E-02	0.14560E+00	0.11463E+00
.30	0.33720E-02			0.34791E-02	0.14543E+00	0.12712E+00

$\lambda, \mu\text{m}$	SNR	P_m	$\text{mean}(t_i)$	$\text{mean}(t_i^+)$	$1\sigma(t_i)$	$1\sigma(t_i^+)$
4.00	10	0.0	0.88503E-03	0.11266E-02	0.14405E+00	0.21422E-01
		.01	0.61875E-03	0.23269E-02	0.14449E+00	0.29768E-01
		.02	0.19279E-03	0.27151E-02	0.14554E+00	0.35110E-01
		.03	-0.99467E-04	0.16167E-02	0.14419E+00	0.43492E-01
		.04	0.26297E-03	0.77425E-03	0.14494E+00	0.50050E-01
		.05	0.82315E-03	0.11343E-02	0.14585E+00	0.54963E-01
		.10	0.98073E-03	0.87060E-03	0.14483E+00	0.78756E-01
		.20	0.37164E-02	0.45488E-02	0.14584E+00	0.11545E+00
		.30	0.34632E-02	0.35422E-02	0.14560E+00	0.12753E+00
			8	0.0	0.10083E-02	0.12613E-02
.01	0.72330E-03			0.24355E-02	0.14453E+00	0.32077E-01
.02	0.29406E-03			0.28441E-02	0.14565E+00	0.37338E-01
.03	0.29633E-05			0.17043E-02	0.14416E+00	0.45401E-01
.04	0.36379E-03			0.86913E-03	0.14495E+00	0.51877E-01
.05	0.94634E-03			0.12471E-02	0.14594E+00	0.56644E-01
.10	0.10556E-02			0.93094E-03	0.14487E+00	0.79897E-01
.20	0.37955E-02			0.46310E-02	0.14600E+00	0.11595E+00
.30	0.35150E-02			0.35785E-02	0.14571E+00	0.12781E+00
	6			0.0	0.11916E-02	0.14537E-02
		.01	0.87399E-03	0.25925E-02	0.14459E+00	0.35431E-01
		.02	0.44414E-03	0.30297E-02	0.14582E+00	0.40574E-01
		.03	0.15307E-03	0.18306E-02	0.14413E+00	0.48184E-01
		.04	0.50964E-03	0.10079E-02	0.14496E+00	0.54545E-01
		.05	0.11307E-02	0.14170E-02	0.14609E+00	0.59098E-01
		.10	0.11680E-02	0.10248E-02	0.14494E+00	0.81588E-01
		.20	0.39087E-02	0.47516E-02	0.14624E+00	0.11671E+00
		.30	0.35906E-02	0.36329E-02	0.14590E+00	0.12825E+00
			4	0.0	0.14979E-02	0.17753E-02
.01	0.11244E-02			0.28443E-02	0.14474E+00	0.40959E-01
.02	0.69651E-03			0.33354E-02	0.14614E+00	0.45913E-01
.03	0.40438E-03			0.20375E-02	0.14413E+00	0.52800E-01
.04	0.75705E-03			0.12430E-02	0.14504E+00	0.58981E-01
.05	0.14392E-02			0.17069E-02	0.14636E+00	0.63183E-01
.10	0.13569E-02			0.11878E-02	0.14513E+00	0.84474E-01
.20	0.41007E-02			0.49574E-02	0.14669E+00	0.11809E+00
.30	0.37231E-02			0.37318E-02	0.14630E+00	0.12910E+00

$\lambda, \mu\text{m}$	SNR	P_m	$\text{mean}(t_i^-)$	$\text{mean}(t_i^+)$	$1\sigma(t_i^-)$	$1\sigma(t_i^+)$
6.00	10	0.0	0.14140E-02	0.16854E-02	0.14422E+00	0.31744E-01
		.01	0.10539E-02	0.27736E-02	0.14470E+00	0.39426E-01
		.02	0.62434E-03	0.32516E-02	0.14604E+00	0.44433E-01
		.03	0.33358E-03	0.19815E-02	0.14413E+00	0.51516E-01
		.04	0.68899E-03	0.11772E-02	0.14502E+00	0.57747E-01
		.05	0.13532E-02	0.16268E-02	0.14628E+00	0.62046E-01
		.10	0.13041E-02	0.11411E-02	0.14507E+00	0.83661E-01
		.20	0.40462E-02	0.48994E-02	0.14655E+00	0.11769E+00
		.30	0.36844E-02	0.37010E-02	0.14618E+00	0.12885E+00
			8	0.0	0.16012E-02	0.18818E-02
.01	0.12085E-02			0.29272E-02	0.14481E+00	0.42756E-01
.02	0.77850E-03			0.34334E-02	0.14625E+00	0.47651E-01
.03	0.48676E-03			0.21050E-02	0.14415E+00	0.54310E-01
.04	0.84140E-03			0.13206E-02	0.14508E+00	0.60432E-01
.05	0.15435E-02			0.18029E-02	0.14646E+00	0.64523E-01
.10	0.14205E-02			0.12423E-02	0.14521E+00	0.85439E-01
.20	0.41661E-02			0.50278E-02	0.14685E+00	0.11857E+00
.30	0.37653E-02			0.37634E-02	0.14645E+00	0.12940E+00
	6			0.0	0.18759E-02	0.21697E-02
		.01	0.14338E-02	0.31433E-02	0.14501E+00	0.47536E-01
		.02	0.10032E-02	0.36957E-02	0.14658E+00	0.52271E-01
		.03	0.71164E-03	0.22901E-02	0.14424E+00	0.58336E-01
		.04	0.10666E-02	0.15307E-02	0.14524E+00	0.64322E-01
		.05	0.18225E-02	0.20654E-02	0.14676E+00	0.68108E-01
		.10	0.15928E-02	0.13997E-02	0.14547E+00	0.88070E-01
		.20	0.43385E-02	0.52164E-02	0.14733E+00	0.11991E+00
		.30	0.38856E-02	0.38595E-02	0.14692E+00	0.13030E+00
			4	0.0	0.23391E-02	0.26514E-02
.01	0.18136E-02			0.34963E-02	0.14548E+00	0.55251E-01
.02	0.13823E-02			0.41139E-02	0.14724E+00	0.59747E-01
.03	0.10865E-02			0.25931E-02	0.14454E+00	0.64899E-01
.04	0.14460E-02			0.18803E-02	0.14563E+00	0.70634E-01
.05	0.22959E-02			0.25115E-02	0.14735E+00	0.73976E-01
.10	0.18811E-02			0.16687E-02	0.14608E+00	0.92525E-01
.20	0.46301E-02			0.55404E-02	0.14827E+00	0.12232E+00
.30	0.40884E-02			0.40281E-02	0.14788E+00	0.13200E+00

$\lambda, \mu\text{m}$	SNR	P_m	$\text{mean}(t_i^-)$	$\text{mean}(t_i^+)$	$1\sigma(t_i^-)$	$1\sigma(t_i^+)$
8.00	10	0.0	0.19439E-02	0.22399E-02	0.14458E+00	0.41636E-01
		.01	0.14906E-02	0.31961E-02	0.14507E+00	0.48686E-01
		.02	0.10584E-02	0.37586E-02	0.14667E+00	0.53385E-01
		.03	0.76491E-03	0.23346E-02	0.14427E+00	0.59310E-01
		.04	0.11208E-02	0.15823E-02	0.14528E+00	0.65264E-01
		.05	0.18910E-02	0.21305E-02	0.14684E+00	0.68975E-01
		.10	0.16342E-02	0.14379E-02	0.14555E+00	0.88717E-01
		.20	0.43800E-02	0.52606E-02	0.14745E+00	0.12025E+00
		.30	0.39126E-02	0.38808E-02	0.14705E+00	0.13053E+00
			8	0.0	0.21958E-02	0.25006E-02
.01	0.16938E-02			0.33873E-02	0.14531E+00	0.52889E-01
.02	0.12617E-02			0.39878E-02	0.14702E+00	0.57456E-01
.03	0.96914E-03			0.24981E-02	0.14443E+00	0.62883E-01
.04	0.13278E-02			0.17709E-02	0.14549E+00	0.68726E-01
.05	0.21477E-02			0.23705E-02	0.14715E+00	0.72168E-01
.10	0.17912E-02			0.15842E-02	0.14587E+00	0.91132E-01
.20	0.45390E-02			0.54383E-02	0.14796E+00	0.12155E+00
.30	0.40240E-02			0.39739E-02	0.14756E+00	0.13145E+00
	6			0.0	0.25648E-02	0.28823E-02
		.01	0.19985E-02	0.36637E-02	0.14576E+00	0.58836E-01
		.02	0.15666E-02	0.43169E-02	0.14762E+00	0.63227E-01
		.03	0.12653E-02	0.27363E-02	0.14475E+00	0.67975E-01
		.04	0.16331E-02	0.20469E-02	0.14589E+00	0.73673E-01
		.05	0.25264E-02	0.27281E-02	0.14769E+00	0.76737E-01
		.10	0.20209E-02	0.18025E-02	0.14645E+00	0.94681E-01
		.20	0.47711E-02	0.56986E-02	0.14879E+00	0.12354E+00
		.30	0.41878E-02	0.41133E-02	0.14842E+00	0.13289E+00
			4	0.0	0.31902E-02	0.35196E-02
.01	0.25070E-02			0.41203E-02	0.14676E+00	0.68220E-01
.02	0.20732E-02			0.48462E-02	0.14882E+00	0.72366E-01
.03	0.17611E-02			0.31388E-02	0.14557E+00	0.76115E-01
.04	0.21448E-02			0.25011E-02	0.14682E+00	0.81610E-01
.05	0.31614E-02			0.33303E-02	0.14878E+00	0.84081E-01
.10	0.24046E-02			0.21738E-02	0.14772E+00	0.10060E+00
.20	0.51610E-02			0.61399E-02	0.15043E+00	0.12707E+00
.30	0.44774E-02			0.43719E-02	0.15014E+00	0.13559E+00

$\lambda, \mu\text{m}$	SNR	P_m	$\text{mean}(t_i^-)$	$\text{mean}(t_i^+)$	$1\sigma(t_i^-)$	$1\sigma(t_i^+)$
10.5	10	0.0	0.26115E-02	0.29295E-02	0.14534E+00	0.53274E-01
		.01	0.20358E-02	0.36996E-02	0.14583E+00	0.59557E-01
		.02	0.16022E-02	0.43570E-02	0.14770E+00	0.63928E-01
		.03	0.13037E-02	0.27672E-02	0.14480E+00	0.68595E-01
		.04	0.16703E-02	0.20807E-02	0.14594E+00	0.74279E-01
		.05	0.25731E-02	0.27723E-02	0.14776E+00	0.77298E-01
		.10	0.20497E-02	0.18295E-02	0.14653E+00	0.95123E-01
		.20	0.47999E-02	0.57305E-02	0.14890E+00	0.12380E+00
		.30	0.42102E-02	0.41334E-02	0.14854E+00	0.13309E+00
			8	0.0	0.29443E-02	0.32696E-02
.01	0.23072E-02			0.39434E-02	0.14633E+00	0.64631E-01
.02	0.18750E-02			0.46408E-02	0.14832E+00	0.68865E-01
.03	0.15675E-02			0.29808E-02	0.14521E+00	0.72986E-01
.04	0.19443E-02			0.23233E-02	0.14642E+00	0.78556E-01
.05	0.29113E-02			0.30912E-02	0.14833E+00	0.81255E-01
.10	0.22554E-02			0.20283E-02	0.14718E+00	0.98289E-01
.20	0.50071E-02			0.59651E-02	0.14975E+00	0.12567E+00
.30	0.43640E-02			0.42693E-02	0.14943E+00	0.13450E+00
	6			0.0	0.34352E-02	0.37659E-02
		.01	0.27089E-02	0.42957E-02	0.14723E+00	0.71686E-01
		.02	0.22730E-02	0.50484E-02	0.14936E+00	0.75751E-01
		.03	0.19556E-02	0.32947E-02	0.14598E+00	0.79150E-01
		.04	0.23476E-02	0.26767E-02	0.14727E+00	0.84579E-01
		.05	0.34120E-02	0.35648E-02	0.14928E+00	0.86833E-01
		.10	0.25535E-02	0.23192E-02	0.14831E+00	0.10288E+00
		.20	0.53125E-02	0.63133E-02	0.15115E+00	0.12851E+00
		.30	0.45938E-02	0.44776E-02	0.15090E+00	0.13672E+00
			4	0.0	0.42651E-02	0.45982E-02
.01	0.33884E-02			0.48892E-02	0.14910E+00	0.82539E-01
.02	0.29406E-02			0.57096E-02	0.15147E+00	0.86402E-01
.03	0.26006E-02			0.38282E-02	0.14766E+00	0.88773E-01
.04	0.30215E-02			0.32559E-02	0.14908E+00	0.94020E-01
.05	0.42458E-02			0.43537E-02	0.15119E+00	0.95596E-01
.10	0.30541E-02			0.28026E-02	0.15063E+00	0.11036E+00
.20	0.58285E-02			0.69039E-02	0.15386E+00	0.13345E+00
.30	0.49931E-02			0.48497E-02	0.15375E+00	0.14073E+00

Table H.2 Two-State Modified MMAF Offset Error Statistics (in Pixels) for Case 1

$\lambda, \mu\text{m}$	SNR	P_m	mean(t_i)	mean(t_i^*)	$1\sigma(t_i)$	$1\sigma(t_i^*)$
0.53	10	0.0	0.33822E-04	-0.18678E-04	0.14904E+00	0.31945E-02
		.01	-0.39903E-03	0.32547E-03	0.14932E+00	0.12852E-01
		.02	-0.89191E-03	0.43935E-03	0.14954E+00	0.18845E-01
		.03	-0.12107E-02	-0.24677E-03	0.14989E+00	0.30205E-01
		.04	-0.69277E-03	-0.97808E-03	0.14988E+00	0.37895E-01
		.05	-0.13571E-03	-0.38331E-03	0.15000E+00	0.44448E-01
		.10	0.27966E-03	-0.35659E-03	0.15038E+00	0.72172E-01
		.20	0.15996E-02	0.20021E-02	0.15063E+00	0.11733E+00
		.30	0.13357E-02	0.16175E-02	0.15053E+00	0.13116E+00
			8	0.0	0.20463E-04	-0.32822E-04
.01	-0.42603E-03			0.29957E-03	0.14930E+00	0.13258E-01
.02	-0.91313E-03			0.41181E-03	0.14952E+00	0.19215E-01
.03	-0.12392E-02			-0.28571E-03	0.14988E+00	0.30532E-01
.04	-0.73057E-03			-0.10223E-02	0.14984E+00	0.38217E-01
.05	-0.17422E-03			-0.42909E-03	0.14993E+00	0.44729E-01
.10	0.25508E-03			-0.38802E-03	0.15035E+00	0.72341E-01
.20	0.15679E-02			0.19653E-02	0.15057E+00	0.11734E+00
.30	0.13047E-02			0.15885E-02	0.15050E+00	0.13115E+00
	6			0.0	-0.13042E-05	-0.52716E-04
		.01	-0.47029E-03	0.25518E-03	0.14927E+00	0.13865E-01
		.02	-0.94834E-03	0.37101E-03	0.14949E+00	0.19772E-01
		.03	-0.12849E-02	-0.34905E-03	0.14986E+00	0.31022E-01
		.04	-0.81988E-03	-0.11022E-02	0.14972E+00	0.38708E-01
		.05	-0.23537E-03	-0.49898E-03	0.14983E+00	0.45154E-01
		.10	0.21631E-03	-0.43852E-03	0.15030E+00	0.72594E-01
		.20	0.15713E-02	0.19594E-02	0.15054E+00	0.11738E+00
		.30	0.12517E-02	0.15399E-02	0.15044E+00	0.13112E+00
			4	0.0	-0.13042E-05	-0.52716E-04
.01	-0.47029E-03			0.25518E-03	0.14927E+00	0.13865E-01
.02	-0.94834E-03			0.37101E-03	0.14949E+00	0.19772E-01
.03	-0.12849E-02			-0.34905E-03	0.14986E+00	0.31022E-01
.04	-0.81988E-03			-0.11022E-02	0.14972E+00	0.38708E-01
.05	-0.23537E-03			-0.49898E-03	0.14983E+00	0.45154E-01
.10	0.21631E-03			-0.43852E-03	0.15030E+00	0.72594E-01
.20	0.15713E-02			0.19594E-02	0.15054E+00	0.11738E+00
.30	0.12517E-02			0.15399E-02	0.15044E+00	0.13112E+00

$\lambda, \mu\text{m}$	SNR	P_m	$\text{mean}(t_i^-)$	$\text{mean}(t_i^+)$	$1\sigma(t_i^-)$	$1\sigma(t_i^+)$
1.06	10	0.0	-0.12165E-03	-0.16674E-03	0.14875E+00	0.66395E-02
		.01	-0.69267E-03	0.31986E-04	0.14919E+00	0.16450E-01
		.02	-0.11325E-02	0.15841E-03	0.14941E+00	0.22165E-01
		.03	-0.15199E-02	-0.66019E-03	0.14981E+00	0.33155E-01
		.04	-0.11580E-02	-0.14696E-02	0.14945E+00	0.40857E-01
		.05	-0.54761E-03	-0.84976E-03	0.14948E+00	0.47025E-01
		.10	0.87363E-06	-0.71307E-03	0.15011E+00	0.73745E-01
		.20	0.13787E-02	0.17158E-02	0.15025E+00	0.11748E+00
		.30	0.98720E-03	0.12974E-02	0.15023E+00	0.13102E+00
			8	0.0	-0.16676E-03	-0.21155E-03
.01	-0.77630E-03			-0.53336E-04	0.14920E+00	0.17320E-01
.02	-0.12020E-02			0.76889E-04	0.14941E+00	0.22982E-01
.03	-0.16080E-02			-0.77689E-03	0.14981E+00	0.33891E-01
.04	-0.12853E-02			-0.16061E-02	0.14940E+00	0.41606E-01
.05	-0.66489E-03			-0.97689E-03	0.14940E+00	0.47680E-01
.10	-0.81334E-04			-0.81625E-03	0.15007E+00	0.74161E-01
.20	0.13067E-02			0.16249E-02	0.15017E+00	0.11754E+00
.30	0.81920E-03			0.11374E-02	0.15026E+00	0.13108E+00
	6			0.0	-0.23381E-03	-0.27715E-03
		.01	-0.90322E-03	-0.17720E-03	0.14924E+00	0.18588E-01
		.02	-0.13053E-02	-0.41636E-04	0.14945E+00	0.24183E-01
		.03	-0.17400E-02	-0.94986E-03	0.14985E+00	0.34985E-01
		.04	-0.14730E-02	-0.18117E-02	0.14937E+00	0.42718E-01
		.05	-0.84016E-03	-0.11702E-02	0.14932E+00	0.48658E-01
		.10	-0.20527E-03	-0.97569E-03	0.15005E+00	0.74795E-01
		.20	0.11993E-02	0.14881E-02	0.15008E+00	0.11765E+00
		.30	0.74260E-03	0.10743E-02	0.15039E+00	0.13128E+00
			4	0.0	-0.34877E-03	-0.38813E-03
.01	-0.11124E-02			-0.38811E-03	0.14940E+00	0.20652E-01
.02	-0.14801E-02			-0.24482E-03	0.14959E+00	0.26163E-01
.03	-0.19570E-02			-0.12408E-02	0.14999E+00	0.36808E-01
.04	-0.19036E-02			-0.21504E-02	0.14944E+00	0.44572E-01
.05	-0.11325E-02			-0.14852E-02	0.14932E+00	0.50310E-01
.10	-0.41163E-03			-0.12404E-02	0.15012E+00	0.75902E-01
.20	0.10232E-02			0.12622E-02	0.15000E+00	0.11792E+00
.30	0.49984E-03			0.85359E-03	0.15047E+00	0.13146E+00

$\lambda, \mu\text{m}$	SNR	P_m	$\text{mean}(t_i^-)$	$\text{mean}(t_i^+)$	$1\sigma(t_i^-)$	$1\sigma(t_i^+)$
2.01	10	0.0	-0.45957E-03	-0.49394E-03	0.14870E+00	0.12443E-01
		.01	-0.12408E-02	-0.23504E-02	0.14747E+00	0.20557E-01
		.02	-0.69788E-03	-0.20630E-02	0.14232E+00	0.26077E-01
		.03	-0.10382E-02	-0.89523E-03	0.14823E+00	0.37409E-01
		.04	-0.49185E-03	-0.13671E-02	0.14797E+00	0.45259E-01
		.05	0.19771E-03	0.37456E-03	0.14733E+00	0.49297E-01
		.10	-0.17522E-02	-0.12557E-02	0.15180E+00	0.76836E-01
		.20	0.87361E-03	0.87518E-03	0.15014E+00	0.10868E+00
		.30	0.18422E-01	0.18320E-01	0.15178E+00	0.13459E+00
			8	0.0	-0.19404E-02	-0.18046E-02
.01	-0.13023E-02			-0.12213E-02	0.14933E+00	0.23181E-01
.02	-0.48919E-03			-0.87413E-03	0.14510E+00	0.26764E-01
.03	-0.21437E-02			-0.24676E-02	0.15656E+00	0.43858E-01
.04	-0.31918E-03			0.96144E-03	0.13921E+00	0.45021E-01
.05	0.66977E-03			-0.93208E-03	0.14631E+00	0.51428E-01
.10	-0.19856E-02			-0.26873E-02	0.14913E+00	0.73590E-01
.20	-0.89986E-03			-0.12004E-02	0.14635E+00	0.10328E+00
.30	0.36289E-02			0.46550E-02	0.14528E+00	0.12320E+00
	6			0.0	-0.80556E-03	-0.83279E-03
		.01	-0.16134E-02	-0.27107E-02	0.14786E+00	0.23985E-01
		.02	-0.13049E-02	-0.26119E-02	0.14296E+00	0.29760E-01
		.03	-0.13981E-02	-0.13508E-02	0.14854E+00	0.39936E-01
		.04	-0.71835E-03	-0.15378E-02	0.14836E+00	0.47784E-01
		.05	0.13491E-03	0.27798E-03	0.14738E+00	0.51066E-01
		.10	-0.23579E-02	-0.19627E-02	0.15209E+00	0.78830E-01
		.20	0.28728E-03	0.31967E-03	0.15101E+00	0.11036E+00
		.30	0.18175E-01	0.18112E-01	0.15210E+00	0.13519E+00
			4	0.0	-0.32932E-02	-0.31397E-02
.01	-0.33141E-02			-0.32291E-02	0.15189E+00	0.32314E-01
.02	-0.98558E-03			-0.13796E-02	0.14561E+00	0.31069E-01
.03	-0.40762E-02			-0.42124E-02	0.15748E+00	0.51092E-01
.04	-0.32898E-03			0.11863E-02	0.13978E+00	0.46989E-01
.05	0.50116E-03			-0.10566E-02	0.14657E+00	0.53971E-01
.10	-0.25768E-02			-0.31636E-02	0.14960E+00	0.75933E-01
.20	-0.15304E-02			-0.22255E-02	0.14749E+00	0.10642E+00
.30	0.19264E-02			0.31013E-02	0.14733E+00	0.12655E+00

$\lambda, \mu\text{m}$	SNR	P_m	$\text{mean}(t_i^-)$	$\text{mean}(t_i^+)$	$1\sigma(t_i^-)$	$1\sigma(t_i^+)$
4.00	10	0.0	-0.41279E-02	-0.38862E-02	0.15473E+00	0.29990E-01
		.01	-0.75068E-02	-0.88362E-02	0.15566E+00	0.43897E-01
		.02	-0.28136E-02	-0.43038E-02	0.14554E+00	0.38045E-01
		.03	-0.45103E-02	-0.48597E-02	0.15271E+00	0.51099E-01
		.04	-0.19585E-02	-0.26528E-02	0.15067E+00	0.54189E-01
		.05	-0.24800E-02	-0.23962E-02	0.15075E+00	0.60649E-01
		.10	-0.96501E-02	-0.94083E-02	0.16138E+00	0.97202E-01
		.20	-0.42394E-02	-0.36662E-02	0.15759E+00	0.11937E+00
		.30	0.15810E-01	0.15814E-01	0.15622E+00	0.14008E+00
			8	0.0	-0.70734E-02	-0.68968E-02
.01	-0.13339E-01			-0.13245E-01	0.16809E+00	0.63618E-01
.02	-0.22060E-02			-0.26045E-02	0.14699E+00	0.37809E-01
.03	-0.11865E-01			-0.11970E-01	0.16956E+00	0.74304E-01
.04	-0.56950E-02			-0.36051E-02	0.14885E+00	0.61371E-01
.05	-0.46611E-03			-0.19872E-02	0.14847E+00	0.58503E-01
.10	-0.84825E-02			-0.92542E-02	0.15935E+00	0.92049E-01
.20	-0.26565E-02			-0.35143E-02	0.15002E+00	0.11089E+00
.30	-0.34531E-02			-0.21258E-02	0.15654E+00	0.13690E+00
	6			0.0	-0.96441E-02	-0.93674E-02
		.01	-0.17947E-01	-0.19290E-01	0.17404E+00	0.76768E-01
		.02	-0.83157E-02	-0.94930E-02	0.15551E+00	0.54951E-01
		.03	-0.85248E-02	-0.86749E-02	0.15928E+00	0.62879E-01
		.04	-0.54886E-02	-0.61132E-02	0.15745E+00	0.66854E-01
		.05	-0.39164E-02	-0.38618E-02	0.15390E+00	0.66793E-01
		.10	-0.11062E-01	-0.10897E-01	0.16385E+00	0.10155E+00
		.20	-0.62229E-02	-0.58621E-02	0.16249E+00	0.12528E+00
		.30	-0.62672E-01	-0.62648E-01	0.23357E+00	0.22484E+00
			4	0.0	-0.17437E-01	-0.17239E-01
.01	-0.20234E-01			-0.20155E-01	0.18135E+00	0.86726E-01
.02	-0.79146E-02			-0.83046E-02	0.15773E+00	0.57777E-01
.03	-0.28570E-01			-0.28945E-01	0.19790E+00	0.12153E+00
.04	-0.11960E-01			-0.10371E-01	0.15959E+00	0.80043E-01
.05	-0.64088E-02			-0.78721E-02	0.15824E+00	0.74093E-01
.10	-0.10304E-01			-0.11038E-01	0.16254E+00	0.97456E-01
.20	-0.15379E-01			-0.15761E-01	0.17066E+00	0.13527E+00
.30	-0.93830E-02			-0.81853E-02	0.16537E+00	0.14741E+00

$\lambda, \mu\text{m}$	SNR	P_m	mean(t_i^-)	mean(t_i^+)	$1\sigma(t_i^-)$	$1\sigma(t_i^+)$
6.00	10	0.0	-0.18991E-01	-0.18695E-01	0.17825E+00	0.71339E-01
		.01	-0.22457E-01	-0.24065E-01	0.18172E+00	0.88191E-01
		.02	-0.11969E-01	-0.13122E-01	0.16289E+00	0.66766E-01
		.03	-0.89645E-02	-0.91385E-02	0.16028E+00	0.65344E-01
		.04	-0.59487E-02	-0.68517E-02	0.15905E+00	0.70503E-01
		.05	-0.40804E-02	-0.40412E-02	0.15446E+00	0.68580E-01
		.10	-0.14850E-01	-0.15030E-01	0.17074E+00	0.11227E+00
		.20	-0.11364E-01	-0.16721E-01	0.17206E+00	0.13583E+00
		.30	-0.66505E-01	-0.66464E-01	0.24236E+00	0.23407E+00
			8	0.0	-0.17715E-01	-0.17517E-01
.01	-0.20486E-01			-0.20401E-01	0.18211E+00	0.88101E-01
.02	-0.80249E-02			-0.84123E-02	0.15807E+00	0.58721E-01
.03	-0.28970E-01			-0.29344E-01	0.19888E+00	0.12307E+00
.04	-0.12136E-01			-0.10547E-01	0.16011E+00	0.81034E-01
.05	-0.65162E-02			-0.79775E-02	0.15855E+00	0.74858E-01
.10	-0.10504E-01			-0.11232E-01	0.16286E+00	0.98118E-01
.20	-0.15561E-01			-0.15953E-01	0.17130E+00	0.13609E+00
.30	-0.16863E-01			-0.15943E-01	0.17764E+00	0.16082E+00
	6			0.0	-0.20526E-01	-0.20209E-01
		.01	-0.23522E-01	-0.25139E-01	0.18520E+00	0.94512E-01
		.02	-0.18272E-01	-0.19392E-01	0.17462E+00	0.85790E-01
		.03	-0.95590E-02	-0.97586E-02	0.16169E+00	0.69176E-01
		.04	-0.56784E-02	-0.65475E-02	0.15976E+00	0.73083E-01
		.05	-0.42377E-02	-0.42181E-02	0.15527E+00	0.71452E-01
		.10	-0.17393E-01	-0.17656E-01	0.17514E+00	0.11929E+00
		.20	-0.24955E-01	-0.24581E-01	0.19430E+00	0.16261E+00
		.30	-0.72899E-01	-0.72845E-01	0.25577E+00	0.24806E+00
			4	0.0	-0.21006E-01	-0.20787E-01
.01	-0.19591E-01			-0.19473E-01	0.18277E+00	0.90248E-01
.02	-0.70838E-02			-0.74465E-02	0.15818E+00	0.60103E-01
.03	-0.34144E-01			-0.34523E-01	0.20889E+00	0.13787E+00
.04	-0.14108E-01			-0.12531E-01	0.16443E+00	0.89863E-01
.05	-0.70131E-02			-0.84579E-02	0.16014E+00	0.79176E-01
.10	-0.11617E-01			-0.12315E-01	0.16438E+00	0.10165E+00
.20	-0.18172E-01			-0.18606E-01	0.17739E+00	0.14312E+00
.30	-0.18061E-01			-0.16836E-01	0.18098E+00	0.16470E+00

$\lambda, \mu\text{m}$	SNR	P_m	$\text{mean}(t_i^-)$	$\text{mean}(t_i^+)$	$1\sigma(t_i^-)$	$1\sigma(t_i^+)$
8.00	10	0.0	-0.20609E-01	-0.20290E-01	0.18242E+00	0.79447E-01
		.01	-0.23616E-01	-0.25236E-01	0.18557E+00	0.95226E-01
		.02	-0.18380E-01	-0.19498E-01	0.17492E+00	0.86390E-01
		.03	-0.11481E-01	-0.11707E-01	0.16482E+00	0.74676E-01
		.04	-0.56622E-02	-0.65277E-02	0.15990E+00	0.73502E-01
		.05	-0.42490E-02	-0.42284E-02	0.15536E+00	0.71805E-01
		.10	-0.17566E-01	-0.17838E-01	0.17539E+00	0.11974E+00
		.20	-0.25101E-01	-0.24726E-01	0.19471E+00	0.16310E+00
		.30	-0.73388E-01	-0.73331E-01	0.25695E+00	0.24929E+00
			8	0.0	-0.20793E-01	-0.20573E-01
.01	-0.19472E-01			-0.19363E-01	0.18232E+00	0.89207E-01
.02	-0.70499E-02			-0.74200E-02	0.15797E+00	0.59304E-01
.03	-0.31816E-01			-0.32191E-01	0.20423E+00	0.13073E+00
.04	-0.14005E-01			-0.12424E-01	0.16404E+00	0.89011E-01
.05	-0.69417E-02			-0.83873E-02	0.15989E+00	0.78455E-01
.10	-0.11430E-01			-0.12135E-01	0.16416E+00	0.10108E+00
.20	-0.18087E-01			-0.18515E-01	0.17691E+00	0.14248E+00
.30	-0.17797E-01			-0.16584E-01	0.18056E+00	0.16412E+00
	6			0.0	-0.21056E-01	-0.20723E-01
		.01	-0.24755E-01	-0.26361E-01	0.18900E+00	0.10204E+00
		.02	-0.19094E-01	-0.20181E-01	0.17692E+00	0.90708E-01
		.03	-0.12669E-01	-0.12909E-01	0.16720E+00	0.79998E-01
		.04	-0.16848E-01	-0.17659E-01	0.17993E+00	0.10314E+00
		.05	-0.42565E-02	-0.42459E-02	0.15606E+00	0.74557E-01
		.10	-0.19193E-01	-0.19208E-01	0.17692E+00	0.12197E+00
		.20	-0.26007E-01	-0.25629E-01	0.19739E+00	0.16646E+00
		.30	-0.77297E-01	-0.77223E-01	0.26601E+00	0.25866E+00
			4	0.0	-0.22166E-01	-0.21940E-01
.01	-0.19984E-01			-0.19832E-01	0.18460E+00	0.94965E-01
.02	-0.10521E-01			-0.10530E-01	0.16313E+00	0.70090E-01
.03	-0.35183E-01			-0.35542E-01	0.21136E+00	0.14253E+00
.04	-0.13817E-01			-0.12274E-01	0.16499E+00	0.92248E-01
.05	-0.73049E-02			-0.87551E-02	0.16132E+00	0.82720E-01
.10	-0.12545E-01			-0.13215E-01	0.16538E+00	0.10432E+00
.20	-0.30064E-01			-0.30522E-01	0.19777E+00	0.16761E+00
.30	-0.19262E-01			-0.17987E-01	0.18292E+00	0.16711E+00

$\lambda, \mu\text{m}$	SNR	P_m	$\text{mean}(t_i^-)$	$\text{mean}(t_i^+)$	$1\sigma(t_i^-)$	$1\sigma(t_i^+)$
10.5	10	0.0	-0.21071E-01	-0.20738E-01	0.18448E+00	0.84377E-01
		.01	-0.16689E-01	-0.15960E-01	0.17880E+00	0.84557E-01
		.02	-0.20723E-01	-0.18649E-01	0.18634E+00	0.97423E-01
		.03	-0.17178E-01	-0.16382E-01	0.17808E+00	0.93890E-01
		.04	-0.29128E-01	-0.29388E-01	0.19848E+00	0.13033E+00
		.05	-0.26703E-01	-0.27624E-01	0.19660E+00	0.13089E+00
		.10	-0.26909E-01	-0.27012E-01	0.19716E+00	0.14193E+00
		.20	-0.26618E-01	-0.26112E-01	0.20074E+00	0.17841E+00
		.30	-0.35108E-01	-0.34632E-01	0.21324E+00	0.20015E+00
			8	0.0	-0.21158E-01	-0.20820E-01
.01	-0.16794E-01			-0.16067E-01	0.17943E+00	0.86262E-01
.02	-0.20868E-01			-0.18780E-01	0.18683E+00	0.98344E-01
.03	-0.17274E-01			-0.16466E-01	0.17864E+00	0.95353E-01
.04	-0.29407E-01			-0.29676E-01	0.19937E+00	0.13197E+00
.05	-0.26829E-01			-0.27724E-01	0.19748E+00	0.13254E+00
.10	-0.27096E-01			-0.27208E-01	0.19800E+00	0.14329E+00
.20	-0.26715E-01			-0.26209E-01	0.20174E+00	0.17959E+00
.30	-0.35362E-01			-0.34886E-01	0.21427E+00	0.20127E+00
	6			0.0	-0.21197E-01	-0.20854E-01
		.01	-0.16881E-01	-0.16156E-01	0.18017E+00	0.88395E-01
		.02	-0.20967E-01	-0.18881E-01	0.18771E+00	0.10054E+00
		.03	-0.17312E-01	-0.16498E-01	0.17928E+00	0.97158E-01
		.04	-0.29710E-01	-0.29985E-01	0.20036E+00	0.13391E+00
		.05	-0.27667E-01	-0.28184E-01	0.19900E+00	0.13482E+00
		.10	-0.27264E-01	-0.27388E-01	0.19896E+00	0.14494E+00
		.20	-0.31213E-01	-0.30710E-01	0.21020E+00	0.18897E+00
		.30	-0.35511E-01	-0.35046E-01	0.21542E+00	0.20250E+00
			4	0.0	-0.23786E-01	-0.23439E-01
.01	-0.16894E-01			-0.16176E-01	0.18136E+00	0.92106E-01
.02	-0.21026E-01			-0.18947E-01	0.18884E+00	0.10353E+00
.03	-0.17262E-01			-0.16431E-01	0.18008E+00	0.99596E-01
.04	-0.32105E-01			-0.32382E-01	0.20460E+00	0.14033E+00
.05	-0.47341E-01			-0.47771E-01	0.23468E+00	0.18452E+00
.10	-0.28458E-01			-0.28269E-01	0.20094E+00	0.14764E+00
.20	-0.30184E-01			-0.29689E-01	0.20984E+00	0.18882E+00
.30	-0.35536E-01			-0.35092E-01	0.21675E+00	0.20395E+00

Table H.3 Two-State Modified MAP MMAF Offset Error Statistics (in Pixels) for Case 2

$\lambda, \mu\text{m}$	SNR	P_m	mean(t_i^-)	mean(t_i^+)	$1\sigma(t_i^-)$	$1\sigma(t_i^+)$
0.53	10	0.0	0.33822E-04	-0.18678E-04	0.14904E+00	0.31945E-02
		.01	-0.10650E-03	-0.25523E-03	0.14831E+00	0.53584E-02
		.02	0.27202E-03	0.11516E-03	0.14269E+00	0.79514E-02
		.03	-0.43156E-03	-0.16704E-03	0.14806E+00	0.13082E-01
		.04	-0.37338E-03	-0.14840E-03	0.14744E+00	0.15582E-01
		.05	-0.11909E-03	0.20641E-04	0.14750E+00	0.19875E-01
		.10	-0.11103E-02	-0.11407E-02	0.15249E+00	0.34393E-01
		.20	0.56603E-04	0.27481E-03	0.14906E+00	0.52569E-01
		.30	-0.44194E-03	-0.32322E-03	0.14890E+00	0.72982E-01
			8	0.0	-0.25316E-03	-0.16467E-03
.01	-0.84196E-03			-0.49823E-03	0.14893E+00	0.68223E-02
.02	0.55623E-03			0.50270E-03	0.14534E+00	0.89088E-02
.03	-0.11046E-02			-0.10615E-02	0.15570E+00	0.15989E-01
.04	0.50046E-03			0.10022E-02	0.13875E+00	0.15377E-01
.05	0.10049E-03			0.23059E-03	0.14600E+00	0.20810E-01
.10	-0.20527E-02			-0.17224E-02	0.14874E+00	0.33363E-01
.20	-0.23921E-02			-0.24090E-02	0.14549E+00	0.51411E-01
.30	-0.11327E-02			-0.98018E-03	0.14389E+00	0.73278E-01
	6			0.0	-0.13042E-05	-0.52716E-04
		.01	-0.16196E-03	-0.31161E-03	0.14824E+00	0.63403E-02
		.02	0.16909E-03	0.98771E-05	0.14257E+00	0.89130E-02
		.03	-0.52300E-03	-0.26268E-03	0.14797E+00	0.13945E-01
		.04	-0.43809E-03	-0.21380E-03	0.14728E+00	0.16331E-01
		.05	-0.13451E-03	0.63315E-05	0.14748E+00	0.20473E-01
		.10	-0.12692E-02	-0.13008E-02	0.15231E+00	0.34963E-01
		.20	-0.12043E-04	0.20691E-03	0.14901E+00	0.52882E-01
		.30	-0.58934E-03	-0.47167E-03	0.14873E+00	0.73080E-01
			4	0.0	-0.42414E-03	-0.33754E-03
.01	-0.91824E-03			-0.57512E-03	0.14887E+00	0.82736E-02
.02	0.43942E-03			0.38938E-03	0.14511E+00	0.10417E-01
.03	-0.12666E-02			-0.12221E-02	0.15557E+00	0.17398E-01
.04	0.41729E-03			0.92052E-03	0.13861E+00	0.16539E-01
.05	0.58756E-04			0.18977E-03	0.14590E+00	0.21870E-01
.10	-0.21232E-02			-0.17971E-02	0.14866E+00	0.34161E-01
.20	-0.26346E-02			-0.26733E-02	0.14541E+00	0.52123E-01
.30	-0.13965E-02			-0.12422E-02	0.14380E+00	0.73377E-01

$\lambda, \mu\text{m}$	SNR	P_m	$\text{mean}(t_i^-)$	$\text{mean}(t_i^+)$	$1\sigma(t_i^-)$	$1\sigma(t_i^+)$
1.06	10	0.0	-0.12165E-03	-0.16674E-03	0.14875E+00	0.66395E-02
		.01	-0.34912E-03	-0.49723E-03	0.14806E+00	0.88671E-02
		.02	-0.14757E-03	-0.30480E-03	0.14229E+00	0.11451E-01
		.03	-0.80021E-03	-0.54304E-03	0.14777E+00	0.16229E-01
		.04	-0.65515E-03	-0.43315E-03	0.14686E+00	0.18365E-01
		.05	-0.18483E-03	-0.45245E-04	0.14741E+00	0.21990E-01
		.10	-0.17426E-02	-0.17711E-02	0.15185E+00	0.36598E-01
		.20	-0.31244E-03	-0.93781E-04	0.14882E+00	0.53927E-01
		.30	-0.10101E-02	-0.89500E-03	0.14832E+00	0.73559E-01
			8	0.0	-0.71891E-03	-0.63264E-03
.01	-0.97292E-03			-0.63199E-03	0.14890E+00	0.10167E-01
.02	0.23657E-03			0.18742E-03	0.14480E+00	0.12623E-01
.03	-0.15349E-02			-0.14946E-02	0.15545E+00	0.19506E-01
.04	0.27908E-03			0.77921E-03	0.13844E+00	0.18273E-01
.05	-0.24617E-04			0.10774E-03	0.14578E+00	0.23441E-01
.10	-0.22549E-02			-0.19340E-02	0.14860E+00	0.35410E-01
.20	-0.30417E-02			-0.31100E-02	0.14541E+00	0.53421E-01
.30	-0.18117E-02			-0.16546E-02	0.14379E+00	0.73699E-01
	6			0.0	-0.23381E-03	-0.27715E-03
		.01	-0.52603E-03	-0.67178E-03	0.14800E+00	0.10983E-01
		.02	-0.44348E-03	-0.60041E-03	0.14216E+00	0.13609E-01
		.03	-0.10518E-02	-0.79903E-03	0.14768E+00	0.18178E-01
		.04	-0.86355E-03	-0.64367E-03	0.14660E+00	0.20142E-01
		.05	-0.23345E-03	-0.95542E-04	0.14738E+00	0.23255E-01
		.10	-0.21702E-02	-0.21957E-02	0.15154E+00	0.38118E-01
		.20	-0.58375E-03	-0.36472E-03	0.14876E+00	0.54979E-01
		.30	-0.13877E-02	-0.12754E-02	0.14809E+00	0.74195E-01
			4	0.0	-0.11564E-02	-0.10716E-02
.01	-0.11066E-02			-0.76732E-03	0.14890E+00	0.12884E-01
.02	-0.72216E-04			-0.12204E-03	0.14454E+00	0.15686E-01
.03	-0.20518E-02			-0.20114E-02	0.15520E+00	0.22778E-01
.04	-0.45738E-04			0.45359E-03	0.13818E+00	0.21080E-01
.05	-0.36317E-04			0.92692E-04	0.14585E+00	0.25364E-01
.10	-0.24608E-02			-0.21501E-02	0.14866E+00	0.37276E-01
.20	-0.36507E-02			-0.37706E-02	0.14572E+00	0.55560E-01
.30	-0.24200E-02			-0.22567E-02	0.14406E+00	0.74904E-01

$\lambda, \mu\text{m}$	SNR	P_m	$\text{mean}(t_i^-)$	$\text{mean}(t_i^+)$	$1\sigma(t_i^-)$	$1\sigma(t_i^+)$
2.01	10	0.0	-0.45957E-03	-0.49394E-03	0.14870E+00	0.12443E-01
		.01	-0.86927E-03	-0.10156E-02	0.14819E+00	0.15144E-01
		.02	-0.10440E-02	-0.12024E-02	0.14232E+00	0.17888E-01
		.03	-0.18569E-02	-0.16089E-02	0.14759E+00	0.22171E-01
		.04	-0.12858E-02	-0.10667E-02	0.14644E+00	0.23761E-01
		.05	-0.47967E-03	-0.34617E-03	0.14755E+00	0.26227E-01
		.10	-0.30232E-02	-0.30411E-02	0.15131E+00	0.41426E-01
		.20	-0.11163E-02	-0.89814E-03	0.14899E+00	0.57322E-01
		.30	-0.21351E-02	-0.20301E-02	0.14803E+00	0.75903E-01
			8	0.0	-0.16023E-02	-0.15162E-02
.01	-0.12362E-02			-0.90166E-03	0.14902E+00	0.15770E-01
.02	-0.39803E-03			-0.44523E-03	0.14456E+00	0.18931E-01
.03	-0.23595E-02			-0.23216E-02	0.15544E+00	0.25607E-01
.04	-0.30890E-03			0.18956E-03	0.13828E+00	0.23902E-01
.05	-0.11822E-03			0.95353E-05	0.14594E+00	0.27696E-01
.10	-0.26857E-02			-0.23840E-02	0.14892E+00	0.39394E-01
.20	-0.43041E-02			-0.44778E-02	0.14644E+00	0.58025E-01
.30	-0.30664E-02			-0.29006E-02	0.14468E+00	0.76561E-01
	6			0.0	-0.80556E-03	-0.83279E-03
		.01	-0.11027E-02	-0.12479E-02	0.14858E+00	0.18453E-01
		.02	-0.20709E-02	-0.22280E-02	0.14346E+00	0.22886E-01
		.03	-0.23380E-02	-0.20966E-02	0.14801E+00	0.25482E-01
		.04	-0.15887E-02	-0.13756E-02	0.14664E+00	0.26683E-01
		.05	-0.97454E-03	-0.84237E-03	0.14828E+00	0.29611E-01
		.10	-0.44613E-02	-0.44739E-02	0.15175E+00	0.46205E-01
		.20	-0.18820E-02	-0.16645E-02	0.14965E+00	0.59942E-01
		.30	-0.27042E-02	-0.26037E-02	0.14835E+00	0.77492E-01
			4	0.0	-0.23257E-02	-0.22422E-02
.01	-0.20302E-02			-0.16982E-02	0.15005E+00	0.21492E-01
.02	-0.10081E-02			-0.10582E-02	0.14491E+00	0.23964E-01
.03	-0.42251E-02			-0.41811E-02	0.15707E+00	0.33630E-01
.04	-0.61153E-03			-0.11602E-03	0.13876E+00	0.27786E-01
.05	-0.40743E-03			-0.28042E-03	0.14638E+00	0.31682E-01
.10	-0.33908E-02			-0.31044E-02	0.14984E+00	0.43704E-01
.20	-0.56010E-02			-0.58369E-02	0.14825E+00	0.62616E-01
.30	-0.43593E-02			-0.41875E-02	0.14626E+00	0.79954E-01

$\lambda, \mu\text{m}$	SNR	P_m	$\text{mean}(t_i^-)$	$\text{mean}(t_i^+)$	$1\sigma(t_i^-)$	$1\sigma(t_i^+)$
4.00	10	0.0	-0.41279E-02	-0.38862E-02	0.15473E+00	0.29990E-01
		.01	-0.59830E-02	-0.61286E-02	0.15502E+00	0.36508E-01
		.02	-0.52957E-02	-0.54529E-02	0.14770E+00	0.35216E-01
		.03	-0.41895E-02	-0.39613E-02	0.15052E+00	0.34296E-01
		.04	-0.17352E-02	-0.15254E-02	0.14735E+00	0.31308E-01
		.05	-0.50094E-03	-0.37906E-03	0.14810E+00	0.32010E-01
		.10	-0.58107E-02	-0.58123E-02	0.15343E+00	0.52470E-01
		.20	-0.72123E-02	-0.70033E-02	0.15876E+00	0.75646E-01
		.30	-0.61799E-02	-0.60901E-02	0.15314E+00	0.86421E-01
			8	0.0	-0.62068E-02	-0.61190E-02
.01	-0.54995E-02			-0.51770E-02	0.15612E+00	0.35670E-01
.02	-0.35297E-02			-0.35883E-02	0.14899E+00	0.34865E-01
.03	-0.93655E-02			-0.90617E-02	0.16508E+00	0.49895E-01
.04	-0.45838E-02			-0.40901E-02	0.14520E+00	0.42412E-01
.05	-0.99506E-02			-0.98315E-02	0.16234E+00	0.60585E-01
.10	-0.71797E-02			-0.69079E-02	0.15527E+00	0.55335E-01
.20	-0.12356E-01			-0.12641E-01	0.15842E+00	0.79751E-01
.30	-0.15983E-01			-0.15821E-01	0.16467E+00	0.10702E+00
	6			0.0	-0.96441E-02	-0.93674E-02
		.01	-0.11034E-01	-0.11182E-01	0.16472E+00	0.54421E-01
		.02	-0.17724E-01	-0.17881E-01	0.16864E+00	0.72172E-01
		.03	-0.12094E-01	-0.12150E-01	0.16260E+00	0.55640E-01
		.04	-0.40456E-02	-0.38360E-02	0.15157E+00	0.40895E-01
		.05	-0.52880E-03	-0.40847E-03	0.14846E+00	0.34730E-01
		.10	-0.79540E-02	-0.79509E-02	0.15667E+00	0.59464E-01
		.20	-0.10057E-01	-0.98537E-02	0.16361E+00	0.84425E-01
		.30	-0.71976E-02	-0.71139E-02	0.15464E+00	0.89429E-01
			4	0.0	-0.13730E-01	-0.13637E-01
.01	-0.10485E-01			-0.10169E-01	0.16586E+00	0.54429E-01
.02	-0.13904E-01			-0.13976E-01	0.16875E+00	0.68328E-01
.03	-0.16962E-01			-0.16941E-01	0.17859E+00	0.74756E-01
.04	-0.54432E-02			-0.49586E-02	0.14783E+00	0.48900E-01
.05	-0.16567E-01			-0.16455E-01	0.17610E+00	0.82419E-01
.10	-0.27752E-01			-0.27497E-01	0.18944E+00	0.10966E+00
.20	-0.17676E-01			-0.17996E-01	0.16860E+00	0.93736E-01
.30	-0.28038E-01			-0.27885E-01	0.18670E+00	0.13553E+00

$\lambda, \mu\text{m}$	SNR	P_m	$\text{mean}(t_i^-)$	$\text{mean}(t_i^+)$	$1\sigma(t_i^-)$	$1\sigma(t_i^+)$
6.00	10	0.0	-0.18991E-01	-0.18695E-01	0.17825E+00	0.71339E-01
		.01	-0.12860E-01	-0.13010E-01	0.16817E+00	0.59808E-01
		.02	-0.16482E-01	-0.16636E-01	0.16730E+00	0.70041E-01
		.03	-0.12709E-01	-0.12780E-01	0.16387E+00	0.58649E-01
		.04	-0.59192E-02	-0.57118E-02	0.15528E+00	0.48078E-01
		.05	-0.70042E-02	-0.68899E-02	0.16061E+00	0.54230E-01
		.10	-0.89353E-02	-0.89293E-02	0.15850E+00	0.63415E-01
		.20	-0.12209E-01	-0.12306E-01	0.16806E+00	0.91860E-01
		.30	-0.75701E-02	-0.74936E-02	0.15537E+00	0.90751E-01
			8	0.0	-0.19705E-01	-0.19609E-01
.01	-0.10596E-01			-0.10279E-01	0.16626E+00	0.55509E-01
.02	-0.14095E-01			-0.14167E-01	0.16932E+00	0.69575E-01
.03	-0.17219E-01			-0.17201E-01	0.17920E+00	0.75983E-01
.04	-0.61135E-02			-0.56361E-02	0.14899E+00	0.51629E-01
.05	-0.16745E-01			-0.16635E-01	0.17679E+00	0.83682E-01
.10	-0.28100E-01			-0.27846E-01	0.19036E+00	0.11109E+00
.20	-0.17927E-01			-0.18253E-01	0.16917E+00	0.94658E-01
.30	-0.28482E-01			-0.28327E-01	0.18766E+00	0.13673E+00
	6			0.0	-0.20526E-01	-0.20209E-01
		.01	-0.13266E-01	-0.13414E-01	0.17028E+00	0.64940E-01
		.02	-0.18459E-01	-0.18604E-01	0.17187E+00	0.77995E-01
		.03	-0.13614E-01	-0.13702E-01	0.16538E+00	0.62600E-01
		.04	-0.59435E-02	-0.57368E-02	0.15700E+00	0.52439E-01
		.05	-0.73153E-02	-0.72023E-02	0.16206E+00	0.58081E-01
		.10	-0.11475E-01	-0.11474E-01	0.16306E+00	0.72251E-01
		.20	-0.16801E-01	-0.16918E-01	0.17444E+00	0.10191E+00
		.30	-0.39179E-01	-0.39113E-01	0.20868E+00	0.15935E+00
			4	0.0	-0.20638E-01	-0.20535E-01
.01	-0.14199E-01			-0.13893E-01	0.17406E+00	0.70409E-01
.02	-0.15840E-01			-0.15586E-01	0.17425E+00	0.78007E-01
.03	-0.25230E-01			-0.25227E-01	0.19283E+00	0.99619E-01
.04	-0.63934E-02			-0.59210E-02	0.15069E+00	0.57014E-01
.05	-0.17370E-01			-0.17268E-01	0.17980E+00	0.89947E-01
.10	-0.41346E-01			-0.41429E-01	0.21389E+00	0.14834E+00
.20	-0.21440E-01			-0.21785E-01	0.17589E+00	0.10550E+00
.30	-0.30944E-01			-0.30804E-01	0.19265E+00	0.14317E+00

$\lambda, \mu\text{m}$	SNR	P_m	$\text{mean}(t_i^-)$	$\text{mean}(t_i^+)$	$1\sigma(t_i^-)$	$1\sigma(t_i^+)$
8.00	10	0.0	-0.20609E-01	-0.20290E-01	0.18242E+00	0.79447E-01
		.01	-0.13289E-01	-0.13437E-01	0.17051E+00	0.65542E-01
		.02	-0.18575E-01	-0.18717E-01	0.17215E+00	0.78608E-01
		.03	-0.16971E-01	-0.17063E-01	0.17126E+00	0.72113E-01
		.04	-0.59357E-02	-0.57304E-02	0.15713E+00	0.52894E-01
		.05	-0.73417E-02	-0.72280E-02	0.16223E+00	0.58550E-01
		.10	-0.11565E-01	-0.11563E-01	0.16323E+00	0.72722E-01
		.20	-0.16894E-01	-0.17014E-01	0.17470E+00	0.10239E+00
		.30	-0.39394E-01	-0.39327E-01	0.20921E+00	0.16000E+00
			8	0.0	-0.20529E-01	-0.20428E-01
.01	-0.14137E-01			-0.13829E-01	0.17373E+00	0.69453E-01
.02	-0.15734E-01			-0.15481E-01	0.17385E+00	0.76966E-01
.03	-0.24996E-01			-0.24991E-01	0.19231E+00	0.98542E-01
.04	-0.63647E-02			-0.58918E-02	0.15042E+00	0.56111E-01
.05	-0.17319E-01			-0.17216E-01	0.17934E+00	0.88950E-01
.10	-0.37139E-01			-0.37220E-01	0.20794E+00	0.13980E+00
.20	-0.21254E-01			-0.21594E-01	0.17546E+00	0.10474E+00
.30	-0.30618E-01			-0.30474E-01	0.19206E+00	0.14235E+00
	6			0.0	-0.21056E-01	-0.20723E-01
		.01	-0.13280E-01	-0.13421E-01	0.17209E+00	0.70102E-01
		.02	-0.19363E-01	-0.19503E-01	0.17405E+00	0.83053E-01
		.03	-0.18773E-01	-0.18877E-01	0.17461E+00	0.79101E-01
		.04	-0.57616E-02	-0.55662E-02	0.15805E+00	0.56410E-01
		.05	-0.74731E-02	-0.73652E-02	0.16342E+00	0.62167E-01
		.10	-0.12261E-01	-0.12258E-01	0.16453E+00	0.76323E-01
		.20	-0.20045E-01	-0.20180E-01	0.17917E+00	0.10968E+00
		.30	-0.40754E-01	-0.40694E-01	0.21266E+00	0.16435E+00
			4	0.0	-0.23238E-01	-0.23126E-01
.01	-0.14704E-01			-0.14401E-01	0.17533E+00	0.75697E-01
.02	-0.16224E-01			-0.15960E-01	0.17589E+00	0.82792E-01
.03	-0.26240E-01			-0.26259E-01	0.19491E+00	0.10442E+00
.04	-0.21180E-01			-0.20373E-01	0.17886E+00	0.99493E-01
.05	-0.17373E-01			-0.17275E-01	0.18172E+00	0.94465E-01
.10	-0.33927E-01			-0.33695E-01	0.20385E+00	0.13256E+00
.20	-0.31354E-01			-0.31708E-01	0.19289E+00	0.12838E+00
.30	-0.32397E-01			-0.32268E-01	0.19502E+00	0.14663E+00

$\lambda, \mu\text{m}$	SNR	F_m	mean(t_i^-)	mean(t_i^+)	$1\sigma(t_i^-)$	$1\sigma(t_i^+)$
10.5	10	0.0	-0.21071E-01	-0.20738E-01	0.18448E+00	0.84377E-01
		.01	-0.13267E-01	-0.13409E-01	0.17218E+00	0.70387E-01
		.02	-0.19407E-01	-0.19548E-01	0.17415E+00	0.83323E-01
		.03	-0.18826E-01	-0.18930E-01	0.17470E+00	0.79366E-01
		.04	-0.63974E-02	-0.62002E-02	0.15939E+00	0.57878E-01
		.05	-0.74758E-02	-0.73681E-02	0.16349E+00	0.62397E-01
		.10	-0.12305E-01	-0.12303E-01	0.16461E+00	0.76550E-01
		.20	-0.20081E-01	-0.20217E-01	0.17927E+00	0.10990E+00
		.30	-0.40824E-01	-0.40763E-01	0.21284E+00	0.16459E+00
			8	0.0	-0.20912E-01	-0.20800E-01
.01	-0.14680E-01			-0.14378E-01	0.17501E+00	0.74605E-01
.02	-0.16143E-01			-0.15881E-01	0.17550E+00	0.81590E-01
.03	-0.25993E-01			-0.26005E-01	0.19443E+00	0.10323E+00
.04	-0.21088E-01			-0.20283E-01	0.17832E+00	0.98229E-01
.05	-0.17408E-01			-0.17312E-01	0.18126E+00	0.93336E-01
.10	-0.33771E-01			-0.33536E-01	0.20328E+00	0.13146E+00
.20	-0.31115E-01			-0.31468E-01	0.19238E+00	0.12747E+00
.30	-0.32037E-01			-0.31904E-01	0.19448E+00	0.14580E+00
	6			0.0	-0.21197E-01	-0.20854E-01
		.01	-0.12930E-01	-0.13061E-01	0.17352E+00	0.74756E-01
		.02	-0.20057E-01	-0.20198E-01	0.17559E+00	0.87317E-01
		.03	-0.22550E-01	-0.22299E-01	0.18066E+00	0.90690E-01
		.04	-0.94444E-02	-0.92588E-02	0.16618E+00	0.70383E-01
		.05	-0.74815E-02	-0.73805E-02	0.16460E+00	0.66016E-01
		.10	-0.13015E-01	-0.13010E-01	0.16580E+00	0.79998E-01
		.20	-0.38965E-01	-0.39117E-01	0.20522E+00	0.14376E+00
		.30	-0.41698E-01	-0.41641E-01	0.21524E+00	0.16781E+00
			4	0.0	-0.23344E-01	-0.23223E-01
.01	-0.18769E-01			-0.18477E-01	0.18358E+00	0.90538E-01
.02	-0.16465E-01			-0.16187E-01	0.17719E+00	0.87058E-01
.03	-0.27113E-01			-0.27153E-01	0.19645E+00	0.10856E+00
.04	-0.28952E-01			-0.28138E-01	0.19392E+00	0.12448E+00
.05	-0.67151E-04			0.35709E-05	0.15185E+00	0.54615E-01
.10	-0.33658E-01			-0.33433E-01	0.20460E+00	0.13460E+00
.20	-0.32079E-01			-0.32443E-01	0.19449E+00	0.13145E+00
.30	-0.28231E-01			-0.27757E-01	0.18730E+00	0.13638E+00

Vita

Capt Theodore D. Herrera was born on 11 July 1952, in Sharon, Pennsylvania. He graduated from Brent School, Inc., Baguio City, Philippines, in 1970. He enlisted in the U.S. Air Force in July 1973 and worked as a jet engine mechanic from 1974 - 76. In 1977, he cross-trained into the flight simulator technician career field. Capt Herrera was accepted into the Airman Education Commissioning Program in 1983 and in December 1985, graduated summa cum laude with a Bachelor of Science in Engineering from Northern Arizona University, in Flagstaff, Arizona. Upon graduation from Officer Training School in 1986, Capt Herrera was assigned to the Kinetic Energy Weapons SPO, Space Division, in Los Angeles Air Force Station. In 1987, he received a cross-broadening assignment into the Civil Engineering field, where he served as an Electrical Engineer and eventually became the project manager for the design of military construction projects. He attended the University of the Philippines and received a Master's of Business Management in May 1990. Capt Herrera was selected to attend the Air Force Institute of Technology in May 1990 to pursue a Master's of Science degree in Electrical Engineering (Guidance and Control).

Bibliography

1. "Accords on SDI, Cruise Missiles, Mobile ICBMs Aid START Process," *Aviation Week and Space Technology*, Vol 131, 25, October 2, 1989.
2. Bergin, J., Capt, Phillips Laboratory, Kirtland AFB, NM. Letter. 18 March 1991.
3. Bergin, J., Capt. Personal Interview. Phillips Laboratory, Kirtland AFB, NM, 13 - 16 June 1991.
4. Durst, F., A. Melling, and J. H. Whitelaw. *Principles and Practice of Laser-Doppler Anemometry*. New York: Academic Press, 1981.
5. Eden, Claude W. *Enhanced Tracking of Ballistic Targets Using Forward Looking Infrared Measurements With Active Target Illumination*. MS Thesis, AFIT/GE/ENG/89D-11. School of Engineering, Air Force Institute of Technology (AU), Wright-Patterson AFB, OH December 1989.
6. Evans, Roger J. *Kalman Filter Tracking of a Reflective Target Using Forward Looking Infrared Measurements and Laser Illumination*. MS Thesis, AFIT/GE/ENG/90D-20. School of Engineering, Air Force Institute of Technology (AU), Wright-Patterson AFB, OH, December 1990.
7. Fairbanks, Ronald R., Capt, Headquarters 6585th Test Group. Holloman AFB, NM. Letter and Unclassified Empirical Radar Information. 19 June 1990.
8. Flynn, P. M. *Alternative Dynamics Models and Multiple Model Filtering for a Short Range Tracker*. MS Thesis, AFIT/GE/ENG/81D. School of Engineering, Air Force Institute of Technology (AU), Wright-Patterson AFB, OH, December 1981.
9. Gill, T. P. *The Doppler Effect*. New York: Academic Press, 1965.
10. Harnly, Douglas A., and Robert L. Jensen. *An Adaptive Distributed-Measurement Extended Kalman Filter for a Short Range Tracker*. MS Thesis, AFIT/GA/EE/79-1. School of Engineering, Air Force Institute of Technology (AU), Wright-Patterson AFB, OH, December 1979.
11. Kozemchak, Mark R. *Enhanced Image Tracking: Analysis of Two Acceleration Models in Tracking Multiple Hot-Spot Images*. MS Thesis, AFIT/GE/ENG/82D. School of Engineering, Air Force Institute of Technology (AU), Wright-Patterson AFB, OH, December 1982.
12. Leeney, T. A. *A Multiple Model Adaptive Tracking Algorithm Against Airborne Targets*. MS Thesis, AFIT/GE/ENG/87D-37. School of Engineering, Air Force Institute of Technology (AU), Wright-Patterson AFB, OH, December 1987.
13. Levanon, Nadav. *Radar Principles*. New York: John Wiley and Sons, 1988.

14. Loving, Phyllis A. *Bayesian vs. MAP Multiple Model Adaptive Estimation for Field of View Expansion in Tracking Airborne Targets*. MS Thesis, AFIT/GE/ENG/85M. School of Engineering, Air Force Institute of Technology (AU), Wright-Patterson AFB, OH, March 1985.
15. McManamon, Paul F. *Active/Passive Sensor for Strategic Defense*. Electro-Optics Branch, Mission Avionics Division, Wright Laboratories, Wright-Patterson AFB, OH, 16 April 1991.
16. McManamon, Paul F. Senior Engineer. Personal Interviews. Electro-Optical Techniques Group, Electro-Optics Branch, Mission Avionics Division, Wright Laboratories, Wright-Patterson AFB, OH, April through December 1991.
17. Maybeck, Peter S. *Stochastic Models, Estimation and Control, Volume I*. New York: Academic Press, 1979.
18. - - - - -. *Stochastic Models, Estimation and Control, Volume II*. New York: Academic Press, 1982.
19. - - - - -. "Adaptive Tracking of Maneuvering Targets Based on IR Image Data." *Kalman Filter Integration of Modern Guidance and Navigation Systems*, Proceedings of the North Atlantic Treaty Organization (NATO), AGARD Lecture Series No. 166, 7-1 - 7-18, London, England, 1989.
20. - - - - -. Professor of Electrical Engineering. Personal Interviews. Air Force Institute of Technology (AU), School of Engineering, Wright-Patterson AFB, OH, January through December 1991.
21. - - - - -, D. A. Harnly and R. L. Jensen. "An Adaptive Extended Kalman Filter for Target Image Tracking," *IEEE Transactions on Aerospace and Electronic Systems*, Vol. AES-17, No. 2, 173-180, March 1981.
22. - - - - - and D. E. Mercier. "A Target Tracker Using Spatially Distributed Infrared Measurements," *IEEE Transactions on Automatic Control*, Vol. AC-25, No. 2, 222-225, April 1980.
23. - - - - - and S. K. Rogers. "Adaptive Tracking of Multiple Hot-Spot Target IR Images," *IEEE Transactions on Automatic Control*, Vol. AC-28, No. 10, 937-943, October 1983.
24. - - - - - and R. I. Suizu. "Adaptive Tracker Field of View Variation Via Multiple Model Filtering," *IEEE Transactions of Aerospace and Electronic Systems*, Vol. AES-21, No. 4, 529-539, July 1985.
25. - - - - -, W. H. Worsley, and P. M. Flynn. "Investigation of Constant Turn-Rate Dynamics Models in Filters for Airborne Vehicle Tracking," *Proceedings of the IEEE National Aerospace and Electronics Conference*, Dayton, OH, 896-903, May 1982.
26. Meer, David E., LCol. Professor of Electrical Engineering. Personal Interviews. Air Force Institute of Technology (AU), School of Engineering, Wright-Patterson AFB, OH, April through December 1991.

27. Mercier, D. E. *An Extended Kalman Filter for Use in a Shared Aperture Medium Range Tracker*. MS Thesis, AFIT/GA/EE/78D-3. School of Engineering, Air Force Institute of Technology (AU), Wright-Patterson AFB, OH, December 1978.
28. Miller, Judith. *Doppler Tracking Program*. Briefing Slides. Phillips Lab, Kirtland AFB, New Mexico, 27 February 1991.
29. Millner, P. P. *Enhanced Tracking of Airborne Targets Using a Correlator/Kalman Filter*. MS Thesis, AFIT/GE/ENG/82M. School of Engineering, Air Force Institute of Technology (AU), Wright-Patterson AFB, OH, December 1982.
30. Murphy, P. J. *Laser Scattering and Extinction Techniques for Rocket Plume Diagnostics*. Technical Report AEDC-TR-89-16. Arnold Engineering Development Center, Air Force Systems Command, Arnold Air Force Base, Tennessee, April 1990.
31. Nawrocki, Paul J. and Robert Papa. *Atmospheric Processes*. New Jersey: Prentice-Hall Inc., 1963.
32. Netzer, Allan S. *Characteristics of Bayesian Multiple Model Adaptive Estimation for Tracking Airborne Targets*. MS Thesis, AFIT/GAE/ENG/85D-2. School of Engineering, Air Force Institute of Technology (AU), Wright-Patterson AFB, OH, December 1985.
33. Norton, John E. *Multiple Adaptive Tracking of Airborne Targets*. MS Thesis, AFIT/GA/ENG/88D-2. School of Engineering, Air Force Institute of Technology (AU), Wright-Patterson AFB, OH, December 1988.
34. Nowakowski, J. and A. Kalisz. *Measurement of Doppler Signatures*. Technical Report FR-1/B78-705. Air Force Weapons Laboratory (AFSC), Kirtland AFB, New Mexico, 15 August 1990.
35. Rizzo, David R. *Enhanced Tracking of Ballistic Targets Using Forward Looking Infrared Measurements*. MS Thesis, AFIT/GE/ENG/89M-7. School of Engineering, Air Force Institute of Technology (AU), Wright-Patterson AFB, OH, March 1989.
36. Rogers, Steven K. *Advanced Tracking of Airborne Targets Using Forward Looking Infrared Measurements*. MS Thesis, AFIT/GE/ENG/81D. School of Engineering, Air Force Institute of Technology (AU), Wright-Patterson AFB, OH, December 1981.
37. Singletery, J. *Adaptive Laser Pointing and Tracking Problem*. MS Thesis, AFIT/GEO/EE/ENG/80D-12. School of Engineering, Air Force Institute of Technology (AU), Wright-Patterson AFB, OH, December 1980.
38. Skolnik, Merril I. *Introduction to Radar Systems*. New York: McGraw-Hill, Inc., 1962.
39. Stimson, George W. *Introduction to Airborne Radar*. Hughes Aircraft Company, El Segundo, CA., 1983.

40. Suizu, Robert I. *Advanced Tracking of Airborne Targets Using Multiple Model Adaptive Filtering Techniques for Adaptive Field of View Expansion*. MS Thesis, AFIT/GE/ENG/83D. School of Engineering, Air Force Institute of Technology (AU), Wright-Patterson AFB, OH December 1983.
41. Tobin, David M. *A Multiple Model Adaptive Tracking Algorithm for a High Energy Laser Weapon System*. MS Thesis, AFIT/GE/ENG/86D-37. School of Engineering, Air Force Institute of Technology (AU), Wright-Patterson AFB, OH, December 1986.
42. Tobin, David M., and Peter S. Maybeck. "Substantial Enhancements to a Multiple Model Adaptive Estimator for Tracking Image Tracking," *Proceedings of the IEEE Conference on Decision and Control*, Los Angeles, CA, 2002-2011, December 1987.
43. Tobin, David M., and Peter S. Maybeck. "Enhancements to a Multiple Model Adaptive Estimator/Image Tracker," *IEEE Transactions on Aerospace and Electronic Systems*, Vol. AES-24, No. 4, pp 417-426, July 1988.
44. Toomay, J. C. *Radar Principles for the Non-Specialist*. Belmont, Ca: Wadsworth, Inc., 1982.
45. Wlodawski, M., et. al. *Measurements of Scattering by Particulates in Rocket Exhaust Plumes*. Technical Report TR-1/B78-7-05, Air Force Weapons Laboratory, Kirtland AFB, New Mexico, 23 January 1990.

Best Available Copy